Controlling Charge Transfer and Excited State Conversion Processes for Efficient OLEDs

Der Universität Bayreuth
zur Erlangung des Grades eines
Doktors der Naturwissenschaften (Dr. rer. nat.)
vorgelegte Abhandlung

von

Rishabh Saxena

aus Pilibhit, Indien

1. Gutachterin:	Prof. Dr. Anna Köhler
2. Gutachter:	Prof. Dr. Georg Herink

Tag der Einreichung:	15.08.2022
Tag des Kolloquiums:	28.10.2022

The present work was carried out in the period from December 2018 to August 2022 at the chair of Soft Matter Optoelectronics (Experimental Physics II) at University of Bayreuth under the supervision of Prof. Dr. Anna Köhler.

Acting director of the graduate school: Prof. Dr. Hans Keppler

Dissertation submitted on: 15.08.2022

Date of PhD defense: 28.10.2022

Examination committee:

First reviewer:	Prof. Dr. Anna Köhler
Second reviewer:	Prof. Dr. Georg Herink
Third examiner:	Prof. Dr. Matthias Weiss
Chairperson:	Prof. Dr. Stephan Gekle

Cogito, ergo sum.

I think, therefore I am.

René Descartes

(1596-1650)

Deutsche Kurzzusammenfassung

Da ein erheblicher Teil der modernen Anzeigegeräte auf der Technologie der organischen Leuchtdioden (OLED) basiert, gehören OLEDs neben den Fotokopierern zu den kommerziell erfolgreichsten Beispielen für organische optoelektronische Bauelemente. Nach der Erfindung der amorphen Dünnschicht-OLED durch Tang und VanSlyke bei Kodak im Jahr 1987 haben umfangreiche Forschungsarbeiten, die sich auf die Entwicklung neuer Materialien und Bauelementearchitekturen sowie auf die Physik von OLEDs konzentrierten, zur Marktreife dieser bahnbrechenden Technologie geführt. Diese Forschungsarbeiten wurden durch Studien zum Ladungs- und Anregungstransport zwischen den organischen Chromophoren sowie zur Übertragung von Anregungen innerhalb jedes einzelnen Chromophors ergänzt. Die Untersuchungen zum intermolekularen Ladungs- und Anregungstransport sind aufgrund der amorphen Natur der heutigen organischen Halbleiterfilme von entscheidender Bedeutung. Darüber hinaus ist das Verständnis der intramolekularen Umwandlungsprozesse in angeregten Zuständen aufgrund des exzitonischen Charakters der elektronischen Struktur organischer Halbleiter von entscheidender Bedeutung.

Die mikroskopisch ungeordnete Natur der amorphen organischen Halbleiterfilme (AOSFs) impliziert, dass der Ladungs- und Exzitonentransport sowohl von der statischen Unordnung als auch von der dynamischen Kopplung an die intra- und intermolekularen Schwingungen gesteuert wird. Für die Entwicklung von OLED-Materialien mit guten Transporteigenschaften und für ein besseres grundlegendes Verständnis des Ladungs- und Exzitonentransports in AOSFs ist es daher notwendig, die wichtigen Parameter zu verstehen, die den Hüpftransport von Ladungen und Exzitonen in AOSFs beeinflussen. Im Zusammenhang mit OLEDS ist es besonders wichtig, den Transport von Triplett-Exzitonen über Triplett-Diffusion zu verstehen, da eine bimolekulare Wechselwirkung zwischen zwei Tripletts, nämlich ein Triplett-Triplett-Annihilationsprozess (TTA), genutzt werden kann, um die interne Quanteneffizienz eines Emitters zu erhöhen, wenn er zur verzögerten Fluoreszenz beiträgt, indem er den Singulett-Anregungszustand des Emitters auffüllt. Andererseits können thermisch aktivierte RISC-Prozess (Reverse Intersystem Crossing, RISC) auch zum Übergang von einem Triplett- zu einem Singulett-Zustand führen, was wiederum in einer zeitlich verzögerten Fluoreszenz resultiert, die daher als thermisch aktivierte verzögerte Fluoreszenz (TADF) bezeichnet wird. Dieser Mechanismus ist die Grundlage für die neueste Generation von OLED-Bauelementen und daher sind TADF-Emitter von großem Interesse für die aktuelle OLED-Forschung. In

diesem Zusammenhang ist es von entscheidender Bedeutung, die Parameter zu verstehen, die den RISC-Prozess beeinflussen, und zu wissen, wie sie moduliert werden können, um eine hohe RISC-Rate zu erreichen, was wiederum zu einer höheren Quanteneffizienz des Emitters führen kann. In der Emissionsschicht einer solchen OLED werden TADF-Emitter häufig in Wirtsmaterialien dotiert, um durch Konzentrationslöschung bedingte Verluste bei der Strahlungseffizienz des Emitters zu vermeiden. Eine wesentliche Bedingung hierfür ist, dass die Triplett-Energie des Wirtsmaterials höher sein muss als die des Emitters. Diese Bedingung für blau emittierende OLEDs schwer zu erfüllen. Daher ist es eine wesentliche Aufgabe, die Struktur-Eigenschafts-Beziehungen zu untersuchen, um Strategien für die Entwicklung eines stabilen Wirtsmaterials mit hoher Triplett-Energie zu entwickeln.

Um einen Beitrag zu den oben genannten Aufgaben zu leisten, wird in dieser Arbeit zunächst ein besseres Verständnis der Materialparameter entwickelt, die den intermolekularen Ladungs- (Kapitel 8 und Kapitel 9) und Triplett-Transport (Kapitel 10) mit Hilfe von kinetischen Monte-Carlo-Simulationen (KMC) steuern. Anschließend werden spektroskopische Messungen eingesetzt, um die intramolekularen Ladungs- und Triplett-Transferprozesse experimentell zu untersuchen, mit dem Ziel, das Design von TADF-Emittern (Kapitel 11 und Kapitel 12) und Wirtsmaterialien (Kapitel 13) für eine verbesserte OLED-Leistung zu optimieren.

In Kapitel 8 ging es in erster Linie darum, die Auswirkungen der dynamischen Unordnung, die durch die Reorganisationsenergie quantifiziert wird, auf den Ladungstransport in AOSFs zu untersuchen. Durch die Verwendung von KMC-Simulationsergebnissen für die Analyse von experimentellen temperaturabhängigen Ladungstransportdaten konnte ich zeigen, dass dynamische Unordnung nicht viel zum Ladungstransport beiträgt. Nachdem ich verstanden hatte, dass statische energetische Unordnung eine dominante Rolle bei der Beeinflussung des Ladungstransports spielt, konnte ich in Kapitel 9 weiter veranschaulichen, wie die räumlichen Korrelationen zwischen den Energien der organischen Moleküle eine entscheidende Rolle bei der energetischen Entspannung der Ladungen innerhalb der Zustandsdichte (DOS) bei niedrigen Temperaturen spielen können.

Nachdem ich in Kapitel 10 wichtige Faktoren für den Ladungstransport in AOSFs identifiziert hatte, war ich daran interessiert, die entscheidenden Materialparameter und morphologischen Eigenschaften zu ermitteln, die erforderlich sind, um die Triplettdiffusion so zu steuern, dass die bimolekulare TTA anstelle der monomolekularen Löschung der Tripletts an den nicht strahlenden Fallenstellen in einem amorphen Film aus konjugierten Polymeren gefördert wird. Ich habe herausgefunden, dass es möglich ist, die TTA auf der Grundlage der verzögerten Fluoreszenz anstelle der Löschung zu optimieren, und dass diese Optimierung einen dispersiven Transport (hohe Unordnung), eine hohe Probenreinheit und eine Morphologie und Konjugationslänge erfordert, die isotropes Hüpfen ermöglicht.

Wie bereits erwähnt, ist TADF eine zweite Möglichkeit, den Singulett-Zustand eines Emittermoleküls besetzen und die Quanteneffizienz eines OLED potenziell zu erhöhen. Daher

konzentrierten sich die Studien in Kapitel 11 und Kapitel 12 auf die systematische Untersuchung der Struktur-Eigenschafts-Beziehungen in einer Reihe von TADF-Dendrimeren, um Designstrategien zur Optimierung der Struktur von TADF-Emittern aufzudecken. Die Dendrimere wiesen mehrere dendritische, auf Carbazol basierende Donor-Erweiterungen (als Dendrone bezeichnet) auf, die mit dem auf Triazin basierenden Akzeptorkern über eine *para*- oder *meta*-Phenylenbrücke verbunden waren. In Kapitel 11 entdeckte ich, dass das stärker konjugierte *para*-Dendrimer zwar eine größere Oszillatorstärke und eine höhere Strahlungszerfallsrate besitzt, die *meta*-Dendrimere jedoch strukturelle Vorteile in Bezug auf eine höhere RISC-Rate aufweisen. Detaillierte photophysikalische Analysen in Kombination mit quantenchemischen Berechnungen ergaben, dass eine kleine Singulett-Triplett-Lücke (ΔE_{ST}), eine höhere Spin-Bahn-Kopplung (SOC) und eine geringere intramolekulare Reorganisationsenergie zu einer höheren RISC-Rate, einer verbesserten TADF und somit zu einer verbesserten Elektrolumineszenzleistung der *meta*-Dendrimer-OLEDs führen. Während sich in der Vergangenheit das molekulare Design von TADF-Emittern oft auf die Minimierung ΔE_{ST} oder die Verbesserung des SOC konzentrierte, wurde die Rolle der molekularen Reorganisation häufig übersehen. In Kapitel 11 habe ich hervorgehoben, dass die Änderung der Geometrie zwischen dem Triplett- und dem Singulett-Zustand mit der niedrigsten Energie ein wichtiger Parameter ist, insbesondere im Fall von sperrigen Dendrimeren, und als allgemeines Designprinzip verwendet werden kann. Des Weiteren habe ich in Kapitel 12 gezeigt, dass ein Dendrimer mit synergistischen *meta*- und *para*-basierten Verbindungen nicht nur eine hohe RISC-Rate (von *meta*-verbundenen Dendronen), eine große Oszillatorstärke und eine hohe Strahlungsabklingrate (von *para*-verbundenen Dendronen) aufweist, sondern auch ein gewünschtes unterdrücktes Konzentrationsquenching zeigt, was die Herstellung von in Lösung verarbeiteten OLEDs mit nicht dotierten emittierenden Schichten ermöglicht.

In Kapitel 13 schließlich untersuchte ich eine Reihe von bipolaren Wirtsmaterialien des Donor-Akzeptor-Typs auf der Grundlage von einem Acridin-Derivat (Donor) mit drei verschiedenen Pyrimidin-Einheiten (Akzeptoren) mit unterschiedlicher Konjugationslänge. Ich habe dies getan, um den wichtigen Aspekt der Struktur-Eigenschafts-Beziehung bei OLED-Wirtsmaterialien ebense systematisch wie zuvor bei den Emittern zu behandeln, mit besonderem Augenmerk auf ihre Verwendung als Wirte für TADF-Emitter, wie sie in den vorherigen Kapiteln untersucht wurden. Anhand von Steady-State-Absorptions- und Emissionsstudien konnte ich zeigen, dass es innerhalb der untersuchten Serien möglich ist, die Triplett-Energie des Wirtsmaterials zu erhöhen, indem einfach die π-Konjugation innerhalb der Akzeptoreinheit erniedrigt wird. Das vielversprechendste Wirtsmaterial 1MPA (1MP: Methylpyrimidin, A: Acridin), bei dem die Konjugation des Akzeptors auf nur einen Pyrimidinring beschränkt ist, wies die höchste Triplett-Energie auf (= 3,07 eV). Darüber hinaus erwies sich 1MPA als geeigneter Wirt für die Herstellung effizienter OLEDs auf Basis blauer TADF-Emitter mit hohem Wirkungsgrad und geringem Effizienz-Roll-off-Effekt.

English abstract

With a significant proportion of modern display units being based on organic light emitting diode (OLED) technology, OLEDs are among the commercially most successful example of organic optoelectronic devices along with the photocopier machines. Following the invention of amorphous thin film OLED by Tang and VanSlyke at Kodak in 1987, extensive research focusing on the design of new materials and device architectures, and on the device physics of OLEDs have resulted in the commercial viability of this breakthrough technology. This research was further supplemented by the studies on charge and excitation transport between the organic chromophores as well as the transfer of excitations within each individual chromophore. The studies pertaining to the intermolecular transfer of charges and excitations are crucial because of the amorphous nature of today's organic semiconductor films. Moreover, understanding the intramolecular excited state conversion processes is imperative because of the excitonic character of the electronic structure of organic semiconductors.

The microscopically disordered nature of the amorphous organic semiconductor films (AOSFs) implies that the charge and exciton transport is controlled by the static disorder as well as the dynamic coupling to the intra and intermolecular vibrations. Thus, for establishing the design rules of OLED materials with good transport properties as well as for a better fundamental understanding of charge and exciton transport in AOSFs, it is necessary to comprehend the important parameters affecting the hopping transport of both charges and excitons in AOSFs. In the context of OLEDS, it is especially important to understand the transport of triplet excitons via triplet diffusion because a bimolecular interaction of two triplets, namely a triplet-triplet annihilation (TTA) process, can be utilized to increase the internal quantum efficiency of an emitter when it contributes to delayed fluorescence by populating the emitter's singlet excited state. On the other hand, thermally activated reverse intersystem crossing (RISC) process can also result in the transition from a triplet to a singlet state, leading to fluorescence at a delayed time, which is hence referred to as thermally activated delayed fluorescence (TADF). This mechanism is the basis for the latest generation of OLEDs and consequently, TADF emitters are of high interest in the topical OLED research. In this context, it is crucial to understand the parameters affecting the RISC process and how they can be modulated to achieve a high RISC rate, which in turn may result in a higher quantum efficiency of the emitter. In the emissive layer of such an OLED, TADF emitters are often doped in host materials to avoid concentration quenching

related losses on the radiative efficiency of the emitter. An essential condition to achieve this is that the triplet energy of the host material must be higher than that of the emitter. This condition is hard to fulfill for blue-emitting OLEDs. Therefore, it is an essential task to investigate structure-property relationships with an objective to establish design strategies for obtaining a stable host material with high triplet energy.

To contribute to the tasks mentioned above, this thesis will first develop a better understanding of material parameters controlling the intermolecular charge (Chapter 8 and Chapter 9) and triplet (Chapter 10) transport using kinetic Monte Carlo (KMC) simulations. Next, spectroscopic measurements will be utilized to experimentally investigate the intramolecular charge and triplet transfer processes, with an objective to optimize the design of TADF emitters (Chapter 11 and Chapter 12) and host materials (Chapter 13) for enhanced OLED performance.

In Chapter 8, the primary goal was to investigate the impact of dynamic disorder, as quantified by reorganization energy, on the charge transport in AOSFs. By utilizing KMC simulation results for the analysis of experimental temperature-dependent charge transport data, I could show that dynamic disorder does not contribute much to charge transport. Having understood that static energetic disorder has a dominant role in affecting the charge transport, in Chapter 9 I could further illustrate how the spatial correlations among the energies of the organic molecules can play a crucial role in the energetic relaxation of the charges within the density of states (DOS) at low temperatures.

Having identified important factors for charge transport in AOSFs, in Chapter 10, I was then interested in identifying the crucial material parameters and morphological properties required to control triplet diffusion in a way that bimolecular TTA is promoted instead of monomolecular quenching of triplets at the non-radiative trap sites, in an amorphous film of conjugated polymers. I found that it is possible to optimize TTA based delayed fluorescence instead of quenching and that this optimization requires dispersive transport (high disorder), high sample purity and a morphology and conjugation length that allows for isotropic hopping.

As pointed out above, TADF is a second possibility to populate the singlet state of an emitter molecule and potentially increase the overall quantum efficiency of an OLED. Therefore, the studies in Chapter 11 and Chapter 12 were focused on systematically investigating the structure-property relationships in a set of TADF dendrimers in order to unveil design strategies for optimizing the structure of TADF emitters. The dendrimers featured multiple dendritic carbazole-based donor extensions (referred as dendrons) connected to the triazine based acceptor core via a *para*- or *meta*-phenylene bridge. In Chapter 11 I discovered that while the more conjugated *para*-dendrimer owns a larger oscillator strength and higher radiative decay rate, the *meta*-dendrimers have design advantages in terms of achieving higher RISC rate. Detailed photophysical analysis in combination with quantum chemical

calculations revealed that small singlet-triplet gap (ΔE_{ST}), higher spin-orbit coupling (SOC) and lower intramolecular reorganization energy result in higher RISC rate, improved TADF and thus improved electroluminescence performance of the *meta*-dendrimer OLEDs. While in the past the molecular design of TADF emitters was often focused on either minimizing ΔE_{ST} or enhancing SOC, the role of molecular reorganization was frequently overlooked. In Chapter 11, I emphasized that the change in geometry between lowest energy triplet and singlet state is an important parameter, especially in case of bulky dendrimers and can be used as a general design principle. Further, in Chapter 12 I revealed that a dendrimer with synergistic *meta*- and *para*-based connections not only inherits a high RISC rate (from *meta*-connected dendrons), large oscillator strength and high radiative decay rate (from *para*-connected dendrons), but also exhibits a desired suppressed concentration quenching thus allowing the fabrication of solution-processed OLEDs with non-doped emissive layers. Finally, in Chapter 13 I investigated a series of donor-acceptor type bipolar host materials based on an acridine derivative (donor) and three different pyrimidine moieties (acceptors) of different conjugation. I did this in order to equally systematically address the important aspect of the structure-property relationship in OLED-host materials with special focus on their use as hosts for TADF emitters, like the ones studied in the previous chapters. With steady-state absorption and emission studies I could show that within the investigated series, it is possible to increase the triplet energy of the host material simply by reducing the π-conjugation within the acceptor moiety. The most promising host material 1MPA (1MP: methylpyrimidine, A: acridine) where the conjugation of the acceptor is limited to just one pyrimidine ring exhibited the highest triplet energy ($= 3.07$ eV). Furthermore, 1MPA was shown to be a suitable host for the fabrication of efficient and low efficiency roll-off OLEDs, employing blue TADF emitters.

Contents

Part I

Introduction

1 Motivation

Modern society is heavily reliant on the use of smart electronic devices. Our laptops, tablets, televisions and of course mobile phones are ubiquitous and all of them have displays. Displays made up of OLEDs are the disruptive technology that is replacing the existing liquid crystal displays (LCDs). OLED has introduced innovations such as ultrahigh 4K resolution, a much larger color gamut and a faster response time, which LCDs cannot match. This is so compelling that Apple launched iPhone X as their first OLED phone.[1] Furthermore, OLEDs can be fabricated on a much larger range of substrates, opening new fields of applications such as foldable phones (for e.x., the new Samsung Galaxy Z Fold 3).[2] More and more display makers are adopting flexible OLEDs as they offer design freedom in addition to being lighter and more durable as compared to rigid glass-based displays.

Smartphones with OLED display constituted 35.6% of the market in 2020 and this number is projected to reach 50% by 2023. Samsung Display started producing active matrix OLED (AMOLED) displays in 2017 and currently they dominate the smartphone OLED display market while LG Display is the major OLED television producer.[4] OLED TV sales in 2019 reached 3 million units constituting a 1.3% share of the TV market and the revenue is expected to exceed $7 billion by 2024.[5] OLED display market grew rapidly in the last few years

Figure 1.1: Comparison of display panel revenue between liquid crystal display (LCD) and OLED technology from 2016-2024. (source: DSCC, 2020)[3]

reaching $30 billion in revenues in 2020. Display Supply Chain Consultants (DSCC) predicts that by 2024, the production of OLED panels will cross the mark of 1 billion which will drive OLED sales to reach approximately $50 billion, with OLEDs constituting a share of 39.5% of all the display technologies, as shown in Figure 1.1.[3]

Even though OLEDs have become a commercially viable technology, economic, scientific and technological challenges remain. Firstly, understanding and improving the OLED *efficiency* is still an ongoing process. Improving the *device lifetime* is a strict requirement for the longevity

of the commercial products, especially for their use in large-area displays and high luminance lighting. The *color point* of the monochromatic OLED pixels needs to remain stable during the OLED operation and throughout the device lifetime. And last but not the least, *cost* of OLED panels is still an obstruction to their application in inexpensive light sources in mass-market applications.

To improve the efficiency of an OLED, it is necessary to first understand the basic working principle of a multilayer OLED stack. Though the very first OLEDs consisted of simpler monolayers or bilayers of one material sandwiched between two electrodes,[6] specialization of materials and the need for higher efficiencies have resulted in much complex device stacks consisting of many layers, possibly consisting of many materials, each fulfilling its own function (Figure 1.2). Going from outside inwards, we first encounter the electrodes. The anode typically consists of indium tin oxide (ITO), a transparent conducting oxide and the cathode can consist of any metal depending on the desired work function. Then hole and electron transport layers (HTL, ETL) are introduced to bridge the gap between the energy levels of the electrodes to the emissive layer (EML). This reduces the barrier for charge injection into the EML, thus reducing the turn-on voltage needed for light emission and the associated power consumption of an OLED. Finally, in the middle of the device, we find the EML. Most EMLs usually consist of two materials, i.e., an emitter which generates light and a host material which facilitates the charge transport. Additionally, state-of-the art OLEDs can also consist of hole/electron injection layers (usually dopant materials[7]) to facilitate injection into the transport layers and hole/electron blocking layers to confine the carriers to the EML, ensuring that they recombine. OLEDs require well controlled functionality of each layer material for their efficient operation.

At low current densities, the *internal quantum efficiency* (η_{IQE}) of an OLED, i.e., the ratio between the number of generated photons and injected charge carriers,[8] is determined by a number of factors: i) the recombination efficiency η_{rec}, i.e., the percentage of injected charges that recombine to form an exciton, ii) η_{ST}, the fraction of emitting excitons (which depends on the exciton spin) and, iii) η_r, the intrinsic radiative efficiency of the emitter. Furthermore, η_{IQE} needs to be multiplied with the outcoupling efficiency (η_{out}) of the device to yield the external quantum efficiency (η_{EQE}) of an OLED:

$$\eta_{EQE} = \eta_{out} \times \eta_{IQE} = \eta_{out} \times \eta_{rec} \times \eta_{ST} \times \eta_r \tag{1.1}$$

This simple outline and Equation 1.1 already shows that a number of processes contribute individually to the overall efficiency and need to be optimized separately. For example, a generated photon can be trapped inside the OLED cavity and is thus lost for light generation. The outcoupling efficiency (η_{out}) quantifies the probability of a photon generated inside an OLED to be extracted from the cavity. For normal planar devices, η_{out} is about 20%,[8,9]
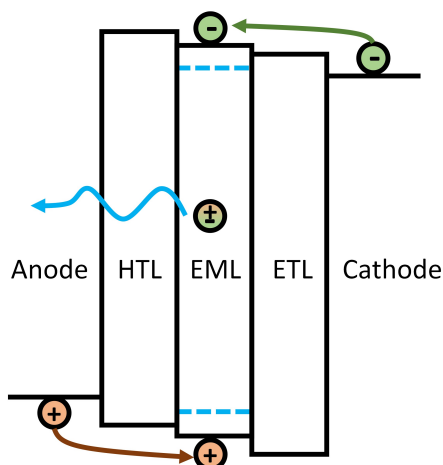
Figure 1.2: A schematic energy level diagram of a multilayer OLED stack. From left to right: anode, hole transport layer (HTL), emissive layer (EML), electron transport layer (ETL), and cathode. EML consists of a host material and an emitter (energy levels shown by dashed blue lines). The path of hole and electron transport is indicated by arrows. Injected holes and electrons recombine on the emitter sites to form an exciton which decays radiatively to emit a photon.

nevertheless, it can be improved by optimizing the optical microcavity, using high refractive index substrates, scattering layers, patterned outcoupling foils as well as by making use of the preferential orientation of the molecule.[10–12]

η_{rec} defines the probability that the injected charge carriers recombine inside the device instead of getting discharged at the opposite electrodes. A further consideration needs to adhere to the position of the recombination zone, i.e., the position inside the device where the electrons and holes recombine to generate excitons. This should ideally be in the center of the EML; which requires a balanced charge transport, or in other words, similar mobilities of electrons and holes. If, for example, the hole mobility is much larger than the electron mobility, the recombination zone will shift close to the cathode compromising both, the color point as well as the device lifetime of the OLED (piling up of charges at the layer interfaces leads to enhanced quenching and degradation processes).[13] In contrast to inorganic semiconductors where band transport occurs because of the delocalized nature of the charge wavefunction, in organic semiconductors charge transport is due to hopping, i.e., thermally assisted non-coherent jumps between localized sites.[14] In this case, transport is controlled by a number of material parameters as well as morphological properties. From these considerations, it becomes obvious that, it is important to better understand the impact of the material parameters on the charge transport to be able to control charge transport in an OLED.

The recombination of injected electrons and holes can result in the formation of singlet and triplet exciton with a spin-statistics based probability of 0.25 and 0.75, respectively. Unfortunately for purely organic molecules, radiative transition of triplet excitons is spin-
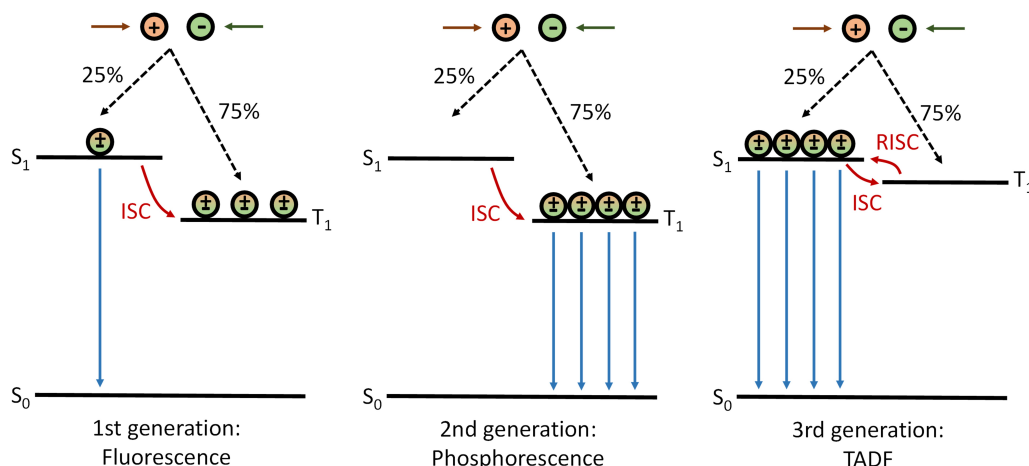
Figure 1.3: The three generation of OLEDs are depicted. In the first generation OLEDs fluorescent emitters were used. Second generation OLEDs utilized phopshorescent emitters for triplet harvesting, i.e., using the triplets generated in the device to emit light. In the third generation OLEDs, thermally activated delayed fluorescence (TADF) is used, i.e., triplets are up-converted to singlets via thermal activation and can decay radiatively at delayed times.

forbidden and hence the triplet excitons are lost via non-radiative transitions. In the first generation of fluorescent OLEDs (Figure 1.3) the maximum η_{ST} was thus limited to 25%.[6] The concept of *triplet harvesting* was first utilized in the second generation of OLEDs: the phosphorescent OLEDs, pioneered by the Forrest group.[15] Phosphorescent emitters are organometallic complexes having a heavy metal atom (such as iridium or platinum) incorporated in their chemical structure. This heavy metal atom can induce an admixture of singlet state to the triplet state, via spin-orbit coupling mechanism. This admixture is sufficient enough to make the transition from a triplet excited state to a singlet ground state a spin-allowed transition and therefore phosphorescent OLEDs achieved a η_{ST} of $> 95\%$ in an OLED, i.e., nearly 100% triplet harvesting and around 20-25% η_{EQE}.[16,17] Current commercial OLED products use red and green phosphorescent OLEDs,[18] however, in the blue (emission wavelength below 460 nm), they generally suffer from suboptimal IQEs.[19] Additionally, the weak chemical bond between ligands and iridium renders the blue phosphorescent OLEDs to be fundamentally unstable having short lifetimes.[19,20] Therefore, the commercial OLED products use blue triplet-triplet annihilation (TTA) based delayed fluorescent emitters (current $\eta_{EQE,max} = 12.5\%$, Idemitsu Kosan[21]) and thus the efficiency of blue pixels is much lower than that of green and red pixels.

Delayed fluorescent emitters employ the conversion of triplet excitons into emissive singlet excitons by either a thermally assisted reverse intersystem crossing (RISC) process or a TTA process.[22,23] In conventional fluorescent emitters, triplet excitons are lost via non-radiative transitions, however they can be converted into singlet excitons by small singlet-triplet energy

difference driven RISC process to yield thermally activated delayed fluorescence (TADF) or by a process involving the triplet-triplet collision process.[22,23] TTA can lead to the formation of tiplet pair state. In such a state, a quantum mechanically allowed spin conversion can occur such that when the triplet pair state decays, one triplet can decay to the ground state while simultaneously promoting the other molecule to a higher energy singlet state from which the radiative transition is allowed.[23] However, since there are competing decay pathways for the triplet pair state it leads to maximum theoretical η_{ST} of 62.5%.[24] Nevertheless, no matter how efficient the triplet-to-singlet upconversion process is, a first requisite is that the two triplets meet efficiently and do not end up at the non-radiative quenching centers. This aspect of optimizing triplet diffusion through the matrix to find each other and form a triplet pair state is very rarely discussed.

On the other hand, complete triplet to singlet up-conversion via TADF can result in 100% η_{ST} in third generation TADF based OLEDs (Figure 1.3). The most relevant design of TADF emitters involves a donor-acceptor (D-A) strategy. These molecular geometries lead to strongly localized hole and electron densities which results in the minimization of electronic exchange energy and thus reduced ΔE_{ST} values; which is a necessary yet not sufficient requirement for the exothermic RISC to occur.[25] Since their first report in 2009,[26] the design of small molecule TADF emitters have evolved significantly and vacuum-deposited OLEDs have achieved impressive $\eta_{EQE} > 20\%$ for all primary colors. So, these can be envisioned to replace phosphorescent emitters in commercial display panels. However, the cost of fabrication, inefficient use of materials and limitations on pixel size are some of the detracting features of the vacuum deposition technology. An alternative materials- and cost-efficient technology is solution-processing.[27] Nonetheless, what is required are devices that exhibit comparable performance metrics as vacuum-deposited devices, and this is underpinned by high-performance solution-processable emitter materials. Unlike small molecules, dendrimers and polymers allow for easy solution-processed manufacturing. However, the molecular weight distribution of polymers leads to batch-to-batch deviation of their properties, dendrimers on the other hand have a definite molecular weight. Nevertheless, the potential of TADF dendrimers in solution-processed OLEDs has to date not yet been realized because of the poor understanding of structure-property relationship in dendrimers.[28–31]

Furthermore, the emission of a photon is influenced by two factors (Equation 1.1), the intrinsic radiative efficiency of the emitter (η_r) and the fraction of emitting excitons (η_{ST}). To reduce the interactions among the emitter molecules that could lead to concentration quenching and resulting decrease in η_r of the emitters, they are often dispersed in a host matrix within the EML (Figure 1.2).[32,33] The amount of concentration quenching depends on the extent of trapping of diffusive excitons by either the aggregates of molecules or traps of varied nature (such as microcrystal interfaces and impurities). Moreover, doping of emitters in a host matrix is also essential to prevent diffusion-assisted detrimental processes caused by long-lived triplet

excitons.[34,35] The host materials must exhibit good thermal, morphological and chemical stability, suitable electronic energy levels for OLED applications and a high triplet energy; high enough to confine the excitons on the emitter. Implementing the last requirement is particularly challenging for blue-emitting OLEDs.[33] The majority of hosts are either carbazole or phosphine oxide based materials.[32,33] While phosphine oxide hosts are chemically unstable, carbazole based hosts show dominant hole transport.[36,37] The unbalanced charge transport leads to poor η_{rec} or leads to the formation of recombination zone near the interface of EML and ETL which is not good for the color purity, device efficiency as well as device lifetime. Hence, there is an urgent need of bipolar host materials. D-A type host materials show good electrical performance as they provide good charge carrier balance owing to their bipolar nature as compared to only donor or only acceptor type (monopolar) hosts.[38,39] However, the presence of donor and acceptor moeities leads to the formation of intramolecular charge transfer states, which results in a reduced triplet energy.[33] Overall, host materials remain less developed as compared to emitters, therefore some strategies and design guidenlines could be beneficial for the progress of this field.

From these considerations, it becomes obvious that it is highly desirable to develop a better understanding of charge and excitation transport between the organic chromophores as well as the transfer of excitations within each individual chromophore. Both aspects are therefore the focus of this thesis. On one hand, this thesis will contribute to the understanding of material parameters and morphological properties that control intermolecular charge transfer (Chapter 8 and Chapter 9) and triplet transfer (Chapter 10) by employing kinetic Monte Carlo (KMC) simulations. On the other hand, spectroscopic methods such as absorption and emission spectroscopy will be applied to experimentally investigate the intramolecular charge and triplet transfer processes, with the goal of optimizing the design of TADF dendrimers (Chapter 11 and Chapter 12) and bipolar host materials (Chapter 13) for enhanced OLED performance.

In particular, in Chapter 8 of this thesis, I assessed the relative impact of static and dynamic disorder on intermolecular charge transport. Building on this work, in Chapter 9 I investigated whether or not the spatial correlations among the energies of the lattice sites have an impact on energetic relaxation of charges within the DOS. Having identified important factors for charge transport in AOSFs, I then focused on understanding the parameters affecting triplet diffusion and how these parameters can be modulated to obtain efficient TTA in polymeric emitters (Chapter 10). It is specifically important to develop methodologies of increasing TTA in the framework of OLEDs as TTA can be utilized to increase the internal quantum efficiency of an OLED when it contributes to delayed fluorescence by populating the emitter's singlet excited state. As pointed out above, TADF is another alternative to populate the singlet state of an emitter molecule and possibly increase the internal quantum efficiency of an OLED. Therefore, the studies in Chapter 11 and Chapter 12 of this thesis were

focused on methodically examining structure-property relationships in a set of dendrimers to reveal design strategies for optimizing their TADF properties. Finally, the investigations in Chapter 13 were focused on methodically examining the role of chemical motifs with restricted π-conjugation in yielding high triplet energy bipolar host materials.

The thesis is structured in three parts. Part I gives an overview of the relevant concepts and the current state of research pertinent to the work done in this thesis. Chapter 2 explains the fundamental concepts regarding the transitions between different excited states which can be used to understand the photophysical studies done in this thesis. Chapter 3 reviews the mechanisms of hopping transport in organic semiconductors and discusses the impending issues related to the appropriateness of different hopping mechanisms that have been a recurring theme in the literature. Chapter 4 summarizes the current state of research on the TADF emitters and bipolar host materials. Part II gives an overview of the thesis. Chapter 5 presents a summary and the interconnection of my individual publications. The content of each publication is summarized in Chapter 6, with a separate section outlining the author contributions of each publication. Overall conclusions of this thesis are presented in Chapter 7. The publications, in their original form, are reprinted in Part III (Chapters 8-13). Full list of my publications is presented in Chapter 14.

2

Excited states and optical processes in organic semiconductors

This chapter recapitulates the basic concepts of molecular photophysics such as the nature of electronic states in organic semiconductors and how they are formed (Chapter 2.1), radiative and non-radiative transitions between these states (Chapter 2.2) as well as the bimolecular processes relevant for OLEDs (Chapter 2.3).

2.1 From atomic orbitals to molecular orbitals to states

A molecular orbital (MO) can be approximated by a linear combination of atomic orbitals (LCAO) involved in the bonding. For example the molecular σ-orbital formed by the combination of two 1s orbitals, ϕ_a and ϕ_b, of two hydrogen atoms can be expressed as $\phi_\pm = c_1\phi_a \pm c_2\phi_b$, where c_1 and c_2 are positive normalization constants and $\phi_\pm$ represents bonding (anti-bonding) orbitals formed as a result of constructive (destructive) interference of the atomic orbitals. Energy of the two MOs thus formed can be calculated by using the Schrödinger equation ($\hat{H}\psi = E\psi$) with the Hamiltonian operator ($\hat{H}$) as the sum of kinetic and potential energies to yield

$$E_\pm = E_{at} + J \pm K_{ab} \tag{2.1}$$

where E_{at} is the energy of the hydrogen $1s$ orbital, Coulomb integral $J = \int \phi_a H \phi_a$ gives a measure of the Coulomb interaction of electron on one nucleus with the other nucleus and exchange (resonance) integral $K_{ab} = \int \phi_a H \phi_b$ expresses an interaction between the nucleus and the overlap of two atomic orbitals. The resonance integral controls the splitting between the two molecular orbitals thus formed ($\Delta E = E_- - E_+ = 2K_{ab}$). The enhanced charge density in bonding orbital, owing to constructive interference, leads to its lower energy as compared to the anti-bonding orbital.[40]

Organic semiconductors mainly consist of carbon-carbon and carbon-hydrogen bonds. Atomic carbon has six electrons in its ground state with a configuration $1s^2 2s^2 2p_x{}^1 2p_y{}^1 2p_z{}^0$. When a carbon atom is approached by a hydrogen or another carbon atom as bonding partners, it can form energetically favorable hybrid orbitals from a linear combination of $2s$ and $2p$ orbitals.
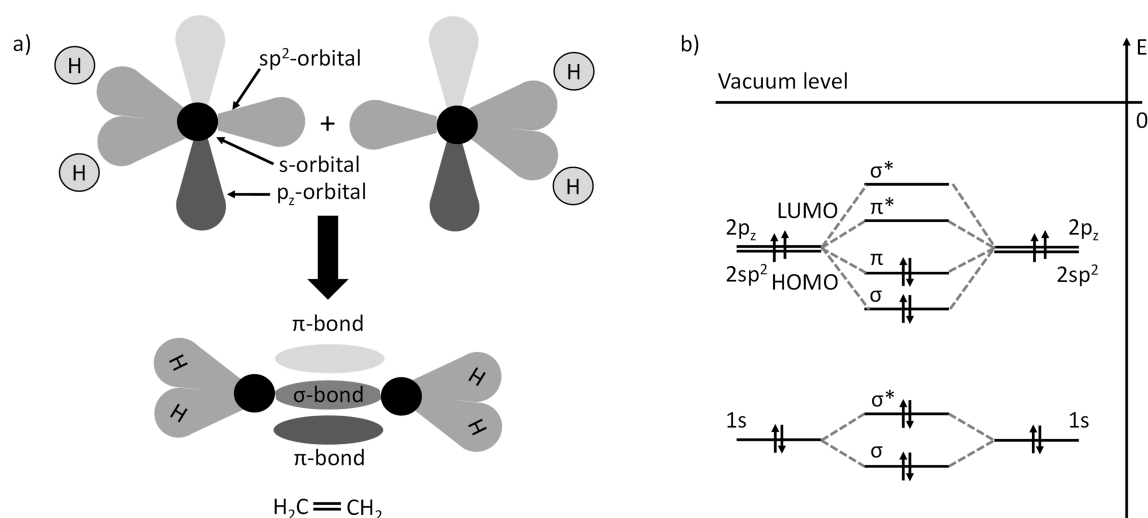
Figure 2.1: a) The combination of four hydrogen atoms and two sp^2 hybridized carbon atoms to form ethene with the formation of a σ-bond and a π-bond along the internuclear axis. After Köhler and Bässler.[41] b) Energy level diagram depicting the formation of σ and π-bonds of ethene from atomic orbitals of carbon. The two $2sp^2$ hybrid orbitals forming bonds with hydrogen are omitted for simplicity. After Atkins.[40]

The number of hybrid and remaining p-orbitals determine the number and nature of the bonds (molecular orbitals). The electrons of hybrid orbitals overlap to form a covalent σ bond (σ-orbital) while the electrons of the orbitals not involved in the hybridization form a π-bond (π-orbital). To construct the molecular orbitals as LCAOs, for example in ethene, two carbon atoms each with one 1s orbital, one threefold degenerate $2sp^2$ orbitals and one unoccupied $2p_z$ need to be considered (Figure 2.1a). The $1s$ orbitals which are near the core with negligible exchange interaction between them form a σ and σ^* orbital with little splitting between them (Figure 2.1b). The $2sp^2$ orbitals along the internuclear axis form σ and σ^* orbital with large splitting because of high amount of charge overlap. Two other degenerate $2sp^2$ orbitals form carbon-hydrogen bonds, with similar MO character. Interaction of $2p_z$ orbitals located at some distance leads to negligible resonance integral and thus weaker splitting between the bonding π and anti-bonding π^* orbitals. Filling of electrons in these MOs determines that the *highest occupied molecular orbital* (HOMO) in ethene is a π-orbital and the *lowest unoccupied molecular orbital* (LUMO) is π^* orbital. The weaker splitting of π and π^* orbitals as compared to σ and σ^* orbitals render their energy levels favorable for charge injection from metal electrodes as well as for absorption and emission of visible light, thus making the organic semiconductors suitable for optoelectronic applications. Furthermore, conjugated polymers are often distinguished by alternate single and double bonds and thus the electrons in the π orbitals delocalize over several repeating units. The corresponding span of electronic wave function delocalization is known as *conjugation length*.

When considering molecules, an important distinction can be illustrated between orbitals
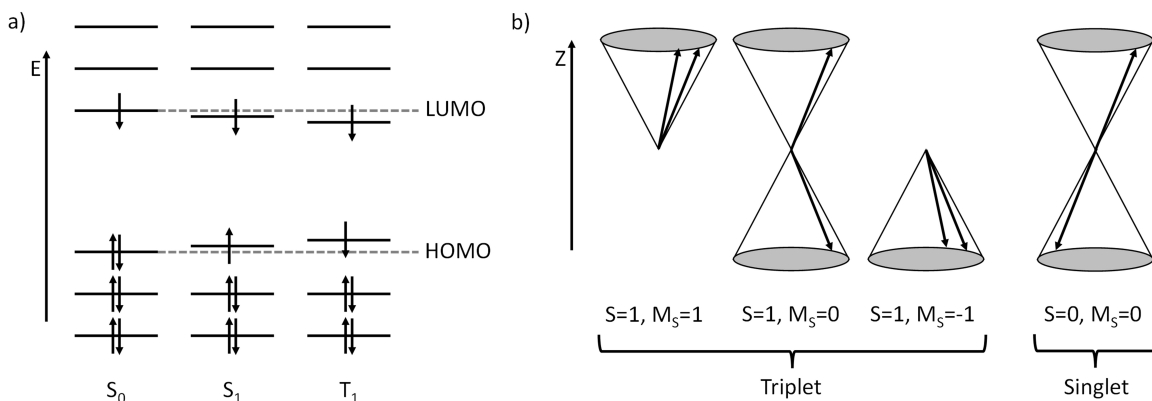
Figure 2.2: Singlet and triplet states depicted in a) an orbital configuration scheme with arrows indicating the spin of the electron. Coulom and exchange energies are explicitly included for the illustration of HOMO and LUMO levels of the excited singlet and triplet states in comparison to the ground state and, b) as a vector diagram. The two electron spins process around a magnetic field directed along z-direction. The corresponding eigenvalues of S and M_S are also shown. After Köhler and Bässler.[41]

and states by considering the configuration with one electron in HOMO and one in LUMO, as shown in Figure 2.2a). Though they have the same configuration, the spin-parallel and spin-antiparallel case correspond to different energies, wavefunctions and excited states of the molecule. This can be considered by describing the total wavefunction as the product of electronic wavefunction ψ_{el} (a function of electron's spatial coordinates) and a spin wavefunction ψ_{spin} (a function of electron's spin). If α and β denote the one-electron state spin wavefunctions with magnetic spin quantum number $m_s = 1/2$ and $m_s = -1/2$, the two particle spin wavefunction eigenstates can be written as:

$$\psi_{spin,T_{+1}} = \alpha_1 \alpha_2 \tag{2.2a}$$

$$\psi_{spin,T_0} = \frac{1}{\sqrt{2}} \left(\alpha_1 \beta_2 + \beta_1 \alpha_2 \right) \tag{2.2b}$$

$$\psi_{spin,T_{-1}} = \beta_1 \beta_2 \tag{2.2c}$$

$$\psi_{spin,S_0} = \frac{1}{\sqrt{2}} \left(\alpha_1 \beta_2 - \beta_1 \alpha_2 \right) \tag{2.2d}$$

The arrangement of first three symmetric wavefunctions with total spin $S = 1$ and different z-component of the spin ($M_S = 1, 0, -1$) is called a *triplet* state and the fourth, antisymmetric wavefunction with $S = 0$ and only single possible value of $M_S = 0$ is referred as *singlet*. In terms of vector representation, the spins are always in phase for triplet wavefunctions whereas they are 180° out of phase for singlet wavefunction, as shown in Figure 2.2b. According to Equation 2.1, the energy difference between the singlet and triplet states is equal to two times the resonance integral, $E(S_i) - E(T_i) = 2K_i$.

2.2 Transitions between states

2.2.1 Radiative transitions: absorption and emission

The transitions between different molecular states are accessible by means of optical spectroscopy and are therefore related to the photophysics of a molecule. A framework to understand the fundamentals of absorption and emission spectra of organic molecules is *Franck-Condon principle*. It results from the application of *Born-Oppenheimer approximation* to the *Fermi's golden rule*.[42] The Born-Oppenheimer approximation utilizes the fact that electronic transitions occur on a much faster time scale (typically in the order of 10^{-15} s) than the motion of atomic nucleus (in the order of 10^{-13} s) to separate their dynamics.[42,43] The total wavefunction (ψ_{tot}) of an electronic state can then be described as a product of electronic wavefunction (ψ_{el}), spin wavefunction (ψ_{spin}) and vibrational wavefunction (ψ_{vib}). For the case of emission or absorption, the dipole operator provides the coupling between the electronic states and the electromagnetic radiation field,[42] and thus can be used as a perturbing Hamiltonian in the expression for Fermi's golden rule describing the rate of transition k_{if} from an initial state $|\psi_i\rangle$ to $|\psi_f\rangle$

$$k_{if} = \frac{2\pi}{\hbar} |\langle \Psi_{\text{el,f}}|e\hat{\boldsymbol{r}}|\Psi_{\text{el,i}}\rangle|^2 \cdot |\langle \Psi_{\text{vib,f}}|\Psi_{\text{vib,i}}\rangle|^2 \cdot |\langle \Psi_{\text{spin,f}}|\Psi_{\text{spin,i}}\rangle|^2 \rho \qquad (2.3)$$

ρ is the density of final states. The electronic factor $|\langle \Psi_{\text{el,f}}|e\hat{\boldsymbol{r}}|\Psi_{\text{el,i}}\rangle|$ determines the selection rules and states whether a particular transition is dipole-allowed or not. Furthermore, the value of the integral is roughly proportional to the overlap between the initial and final electronic wavefunctions. This implies that the rates between the orbitals centered on the same parts of the molecules (e.g., $\pi - \pi^*$ transitions, i.e., locally excited transitions) will be larger than rates between orbitals occupying different spaces (e.g., charge transfer transitions or $n - \pi^*$ transition).[44] Experimentally, the strength of a transition is described by it's *oscillator strength* (f) which can be estimated as:[44]

$$f = 4.39 \times 10^{-19} \int \epsilon dv \qquad (2.4)$$

where ϵ denotes the molar decadic extinction coefficient. The absorption signal strength can therefore be utilized to identify the nature of the transitions.[41]

The vibrational factor or the Franck-Condon factor $|\langle \Psi_{\text{vib,f}}|\Psi_{\text{vib,i}}\rangle|^2$ determines the relative intensities of the vibronic structure arising from the vibrations of the nuclei. Near the equilibrium generalized coordinate (Q) of the nuclei, the potential energy curve can be approximated as a harmonic oscillator potential.[45] Figure 2.3 shows two oscillator potentials representing ground state (S_0) and excited state (S_1) in the presence of a single vibrational mode of energy $\hbar\omega_{vib}$ for both the states. The states are displaced by their equilibrium coordinate difference ΔQ. According to Franck-Condon principle, the generalized coordinate
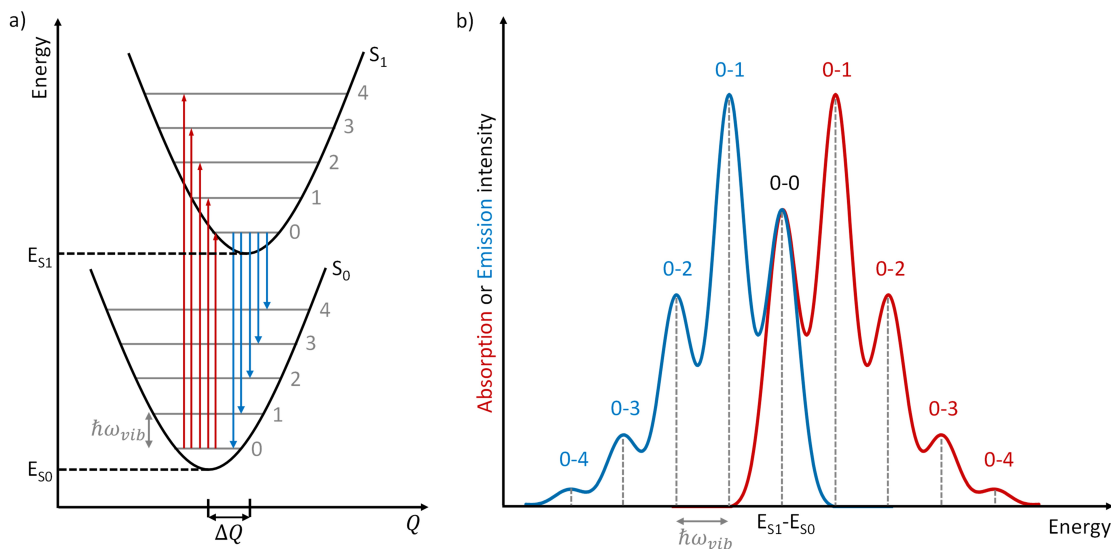
Figure 2.3: Franck-Condon principle. a) Electronic energies of the ground (S_0) and excited (S_1) singlet states as a function of generalized coordinate Q within the harmonic approximation. S_0 and S_1 are displaced by ΔQ. The first five vibrational levels with a vibrational quanta $\hbar\omega_{vib}$ are also indicated. b) Absorption and emission spectra resulting from the vertical transitions illustrated in a).

is assumed to stay constant during a transition so that it appears as a vertical tranistion in the energy diagram, starting from the lowest vibrational level.[46] Hence the transition probability I_{0-m} between the 0th vibrational level of S_0 and the mth level of S_1 can be described by a Poisson distribution,[45] provided that the thermal energy $k_B T >> \hbar\omega_{vib}$:

$$I_{0-m} = \frac{S^m e^{-S}}{m!} \tag{2.5}$$

S is called the Huang-Rhys parameter and evidently (from Equation 2.5) it can be described as the ratio of 0-0 and 0-1 vibrational peak intensities. After the vertical transition, the molecule relaxes into the new equilibrium coordinate and the associated reorganization energy can be estimated as $\lambda = S\hbar\omega_{vib}$. Furthermore, in solutions as well as amorphous films the transitions are inhomogenously broadened (and are not sharp lines). Thus, the vibrational intensities are often multiplied by a Gaussian lineshape function (see Chapter 3.1) to model absorption/emission spectra.

2.2.2 Spin factor and spin-orbit coupling

The final term in Equation 2.3 is the spin factor $|\langle \Psi_{\mathrm{spin,f}} | \Psi_{\mathrm{spin,i}} \rangle|$ which is equal to 0 or 1, depending on whether the spin of the initial and final states involved in the transition are

different or same. Thus, only the transitions within the same spin manifold (ex. $S_1 \leftarrow S_0$ or $T_n \leftarrow T_1$) are *spin-allowed* and the transitions such as $T_1 \rightarrow S_0$ are *spin-forbidden*. Nevertheless, if the orbital angular momentum (l) and spin angular momentum (s) couple for an electron, then in order to conserve the total angular momentum ($j = l + s$) during the transition, change in l can compensate for the change in s. Thus, *spin-orbit coupling* (SOC) can provide a perturbation such that triplet state acquires some singlet admixture (i.e., contribution of a singlet state wavefunction to the triplet state wavefunction) and as a result the spin-forbidden $T_1 \rightarrow S_0$ can also obtain a finite decay rate. This is the reason behind the observation of *phosphorescence* ($T_1 \rightarrow S_0$) emission, which is distinct from *fluorescence* ($S_1 \rightarrow S_0$) emission. The magnitude of SOC is proportional to the fourth power of atomic charge ($\hat{H}_{SOC} \propto Z^4$), therefore, a strong phosphorescence is observed for organometallic complexes like Ir-complexes (or Pt-complexes) making them suitable for phosphorescent OLEDs (Figure 1.3).[16] Even for purely organic TADF emitters (no heavy atom effect), SOC plays a crucial role in determining the reverse intersystem crossing (RISC) rate for the triplet to singlet upconversion (see subsection 4.1.1).[47,48]

2.2.3 Non-radiative transitions: internal conversion and intersystem crossing

An isoenergetic transition from the 0th vibrational level of the initial state to the mth vibrational level of the final state is termed as non-radiative transition and is usually followed by rapid thermal relaxation. In contrast to the radiative transitions which are represented by a vertical arrow, non-radiative transition is indicated by a horizontal arrow in the configuration coordinate diagram. When the non-radiative transitions take place between two states of the same spin manifold it is referred as *internal conversion* (e.g., $S_n \rightarrow S_1$ or $T_n \rightarrow T_1$) and when it takes place between the states with different spin it is referred as *intersystem crossing* (e.g., $S_1 \rightarrow T_1$ or viceversa $T_1 \rightarrow S_1$). For the description of experimental results, the theory of non-radiative transitions was developed in the 1960s[45,49–54] and it describes that the radiationless transition rate exhibits an exponential dependence on the energy gap (ΔE) between the initial and final state, the so called *energy gap law*:[54]

$$k_{IC} = exp\left(-\gamma \frac{\Delta E}{\hbar \omega_m}\right) \tag{2.6}$$

where γ is a constant and $\hbar \omega_m$ is the vibrational energy of the final state.

2.3 Bimolecular processes

In addition to the intrinsic radiative and non-radiative processes discussed in Chapter 2.2, the excitons can also interact bimolecularly with other excitons or polarons (charges). In an *exciton-exciton annihilation* process, which occurs as a result of the interaction of two excitons,
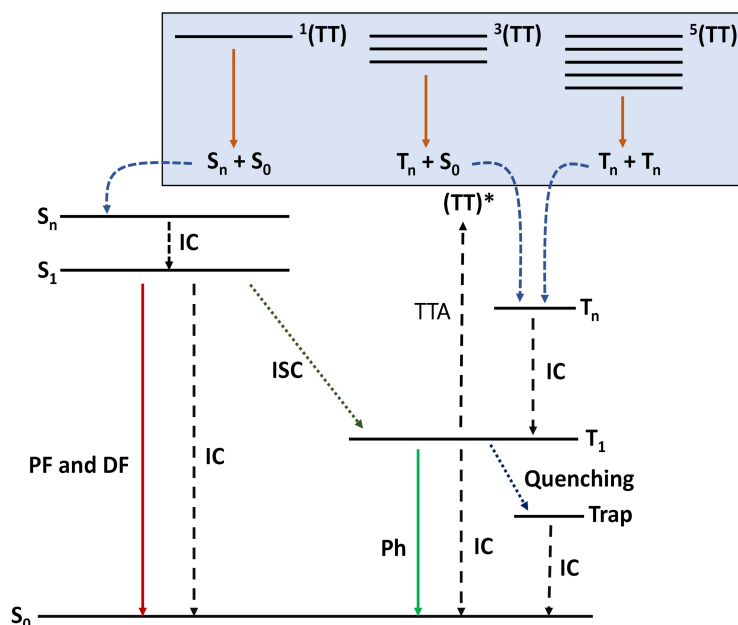
Figure 2.4: Schematic illustrating the bimolecular triplet-triplet annihilation (TTA) process along with other monomolecular decay processes (PF, prompt fluorescence; DF, delayed fluorescence; IC, internal conversion; ISC, intersystem crossing; Ph, phosphorescence). The reaction of TTA can be given as $T_1 + T_1 \rightarrow (TT)^*$. Reproduced from Chapter 10.

one or both of these excitons are lost. While, in principle, both singlets and triplets can interact, literature on *singlet-singlet annihilation* (SSA) and *singlet-triplet annihilation* (STA) is rather limited and is mainly relevant to organic laser applications.[55,56] This is because the lifetime of singlet excitons is short and additionally, the singlet density in OLEDs under typical operating (quasi-steady state) conditions is low. *Triplet-triplet annihilation* (TTA), on the other hand, is a well documented process. Based on spin-statistics, the intermediate triplet pair state (TT^*) created as result of the interaction of two triplets can give rise to singlets, triplets and quintets with a probability of $1/9$ (if $S_{TT} = 0$), $3/9$ (if $S_{TT} = 1$) and $5/9$ (if $S_{TT} = 2$), respectively (Figure 2.4).[41] However, the high energy of quintets prevents these species from forming. Rather, the encounter results in the scattering of the triplets.[57]

As mentioned in Chapter 1, the singlet excitons formed as a result of TTA process can produce additional emission at delayed timescales (and hence the name, *delayed fluorescence*) which is distinct from the spontaneous emission of singlet excitons (*prompt fluorescence*).[23] This is shown schematically in Figure 2.4. Thus, TTA can enhance the IQE of fluorescent OLEDs when it contributes to DF via an up-conversion mechanism, however, it can be detrimental to the performance of phosphoescent or TADF-based OLEDs since it leads to the loss of a triplet exciton.[58,59] In addition, triplets can also be quenched due to an interaction with polarons (charges) and the process is known as *triplet-polaron quenching* (TPQ).[60,61]

Both TTA and TPQ are considered to be the principle contributors towards the decrease of OLED efficiency at high luminance, the so called *roll-off effect* in phosphorescent and TADF-based OLEDs. *Singlet-polaron quenching* (SPQ) is not relevant in OLEDs due to short singlet lifetime, however, it can play a significant role in organic lasers with high singlet as well as high polaron densities.[62,63]

3   **Mechanisms of hopping transport**

This chapter reviews the current understanding of hopping transport in organic semiconductors, introduces the relevant theoretical formulations and describes how they can be utilized to build a mechanistic model of charge and exciton transport in amorphous organic semiconductor films. Concomitantly, this chapter also highlights the issues pertaining to the appropriateness of different hopping mechanisms that have been a center of debate in the literature.

3.1 Polaronic and disorder-controlled transport

Organic conducting materials can be roughly categorized into three broad groups: molecular crystals, polymers and amorphous molecular materials. Present day OLED fabrication utilizes the thermal deposition of amorphous molecular materials. Polymer LEDs offer another cost- and material-efficient alternative as they can be manufactured by utilizing potentially cheaper solution processing methods such as spin-coating, ink-jet printing or roll-to-roll printing.[27] In either case, the deposited films show little or no structural order. In this case, charge (and exciton) transport is controlled by i) electronic coupling between the hopping sites, ii) the static disorder (present due to variations in the intermolecular distances and orientations due to the morphology of a film), and iii) the dynamic disorder due to the coupling of electronic excitations to the intra- as well as intermolecular vibrations.

If the static or dynamic disorder effects become comparable to the nearest neighbor electronic coupling, the wavefunction of a charge carrier gets localized to the molecular sites and the transport can no longer be described by band transport. Hopping transport was first introduced by Conwell and Mott in 1956,[64,65] for impurity conduction in inorganic semiconductors, when they found out that the conductivity increases with temperature in these systems - an opposite effect to what is generally observed in inorganic semiconductors. This led to the description of charge transport as a series of thermally activated non-coherent transfer events, which is referred as hopping transport. The same behavior was observed in molecular semiconductors. In 1959, Holstein developed a hopping transport model to describe the charge transport in molecular crystals.[66]

The delocalized transport band can be destroyed either because of too much variation in site energies (hereby referred as disorder-controlled transport) or too much change in the geometry

of a molecule between its neutral and charged/excited state (hereby referred as polaronic transport). The pioneering theories of polaronic transport in the context of molecular crystals were formulated by Austin and Mott,[67] Emin[68] and Holstein[66] and the resulting transport mechanism is similar to the Marcus theory of electron transfer in solution.[69,70] Polaronic transport happens if in a perfectly ordered crystal, the dynamic disorder leads to very small coupling among the hopping sites as compared to electron-phonon coupling. As the charged molecule couples to the surrounding molecules, it forms a small-polaron and the transport of charge leads to structural reorganization of the organic molecule or a subunit of a π-conjugated polymer. This results in a thermally activated nature of the transfer process. In a semiclassical approach, starting with the Fermi's golden rule, the rate of electron transfer between isonergetic molecules can then be expressed as:[67,69]

$$k_{ij,Marcus} = \frac{2\pi}{\hbar} \ J^2 \ \sqrt{\frac{1}{4\pi\lambda k_B T}} \ exp\left(-\frac{\lambda}{4k_B T}\right) \tag{3.1}$$

where λ is the reorganization energy; J is called the transfer integral and represents the electronic coupling between the initial and final molecular site. Classical Marcus theory is equivalent to the high-temperature limit of Holstein's theory of small polarons.[66,69] This implies an Arrhenius-type temperature dependence of mobility:

$$\mu(T) = \mu_0 \ exp\left(-\frac{E_a}{k_B T}\right), \quad E_a = \lambda/4 \tag{3.2}$$

However, most organic semiconductors used in OLEDs are non-crystalline with variations in the sites energies (static disorder or energetic disorder) and intermolecular distances (positional disorder). The electron (hole) is located in the LUMO (HOMO) of a molecule and hops to the LUMO (HOMO) of a neighboring molecule, but the LUMO and HOMO energies vary from one molecule to the next. This is because, in an amorphous film, the intermolecular distances vary randomly and lead to a varied amount of polarization shifts (i.e., the electrostatic interaction energy of the charge on a molecule with the induced dipole moment on the neighboring molecules) for each molecule depending on it's local environment.[71–74] Conjugated polymers can
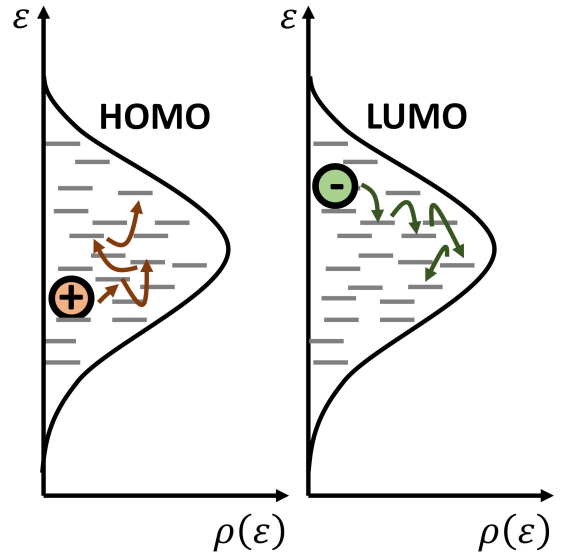
Figure 3.1: Illustration of Gaussian density of states (Equation 3.3). Holes hop within the HOMO distribution while the electrons within the LUMO distribution.

have an additional contribution as a consequence of the structural disorder of the polymer chains. Using the central limit theorem, a Gaussian DOS (Figure 3.1) can then be used to describe the distribution of energies[14,75]

$$\rho(\epsilon) = \frac{1}{\sqrt{2\pi}\sigma} \, exp\left(-\frac{(\varepsilon - \varepsilon_0)^2}{2\sigma^2}\right) \tag{3.3}$$

where ε is the energy of a molecule and σ is the energetic width (disorder) of the Gaussian DOS. Like charges, the excitonic states are also energetically disordered in organic semiconductors (as mentioned previously in Chapter 2.1) and hence the excitons also show thermal activation of transport.[76–79] Nevertheless, exciton is a neutral excitation and as a consequence it is less susceptible to polarization shifts induced by the local dielectric environment, therefore, the energetic width of the excitonic DOS is often smaller as compared to the HOMO or LUMO width.

For polaronic transport between isoenergetic molecules there is no difference between a forward jump (from site i to j) and a backward jump (from site j to i), implying $k_{ij} = k_{ji}$. After the introduction of static energetic disorder this symmetry is no longer preserved. The uphill transitions require an activation energy while the excess energy is dissipated during a downhill transition. In 1960, Miller and Abrahams formulated an expression for impurity hopping in an n-type semiconductor.[80] They assumed a constant density of final states which leads to a constant rate when the energy difference between the sites $\Delta\varepsilon = \varepsilon_j - \varepsilon_i < 0$ and the rate of transition is weighed by a Boltzmann activation factor for $\Delta\epsilon > 0$:

$$k_{ij,MA} = J^2 \, \upsilon_0 \, exp\left(-\frac{|\Delta\varepsilon| + \Delta\varepsilon}{2k_BT}\right) \tag{3.4}$$

The prefactor υ_0 is known as attempt-to-hop frequency and is often fit to reproduce experimental results. The theory is physically correct for molecular systems if the transfer at $\Delta\epsilon \neq 0$ is activated by the absorption or emission of a single molecular vibration.[81] Within such a regime, the temperature dependence of low concentration, quasi-equilibrium mobility deviates from an Arrhenius law and exhibits a

$$\mu(T) = \mu_0 \, exp\left[-C_{MA}\left(\frac{\sigma}{k_BT}\right)^2\right] \tag{3.5}$$

law (where $C_{MA} \approx 0.44$ for a three dimensional system),[14] assuming that the effects due to geometrical relaxation are unimportant.

3.1.1 Superposition of polaronic and disorder effects

Though the pertinent static disorder as described by Bässler's GDM (Equation 3.3) can account for a wide range of experimental observations in amorphous organic semiconductor
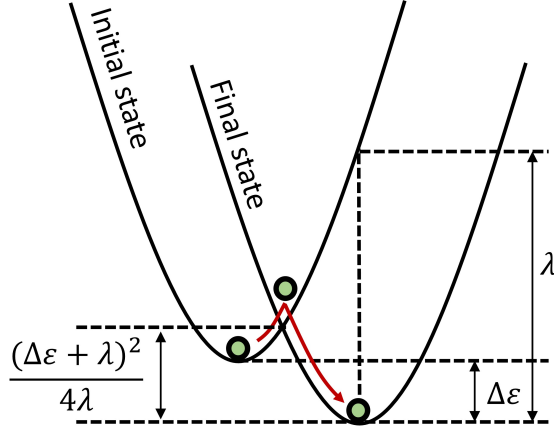
Figure 3.2: Schematic illustration of Marcus theory of charge transfer when $\Delta\epsilon$ is the energy difference and λ is the reorganization energy between the initial and final states. The activation process required for charge transfer is indicated by red arrows. Transfer from initial state to the final state occurs at the point of intersection of the two potentials.

films (AOSFs), such as the transition from non-dispersive to dispersive transport or the temperature and field-dependence of mobility, in some systems dynamic disorder needs to be considered.[14,82–84] Depending on the magnitude of reorganization energy it could result in a significant polaronic nature of charge transport.[85,86] This superposition must also be reflected in the transition rate of charge carriers among the molecular sites. In Marcus theory[69,70] one can account for the energy difference between the initial and final state present due to the static disorder by including the term $\Delta\varepsilon$ in the activation energy, thus resulting in the form

$$k_{ij,Marcus} = \frac{2\pi}{\hbar}\, J^2\, \sqrt{\frac{1}{4\pi\lambda k_B T}}\, exp\left(-\frac{(\lambda + \Delta\varepsilon)^2}{4\lambda k_B T}\right) \tag{3.6}$$

Strictly speaking, Equation 3.1 and Equation 3.6, based on classical Marcus theory are valid only at high temperatures when thermal energy is much greater than the energies of all relevant phonon modes ($k_B T >> \hbar\omega$). If this is no longer the case, the reorganization energy needs to be separated into a contribution from high energy vibrations treated in a quantum mechanical manner (λ_{qm}) and a contribution from low energy vibrations treated classically (λ_{cl}). The corresponding expression for transfer rate is often referred to as Marcus-Levich-Jortner formalism and it extends the validity of Marcus theory to intermediate temperatures.[87–89]

To account for the superposition of polaronic and disorder-controlled transport, the temperature dependence of mobility needs to be modulated as well. An important step in this direction was made by Parris,[90] who formulated a corresponding analytic theory for one dimensional polaronic hopping in a disordered landscape. Currently, there is a consensus that the activation energy for the temperature dependence of mobility can be decoupled into

a disorder and a polaron contribution and their relative weight can be quantified by the so called C factor in the expression for the effective polaron mobility:[85,86,90–96]

$$\mu(T) = \mu_0 \; exp\left[-\frac{E_a}{k_B T} - C\left(\frac{\sigma}{k_B T}\right)^2\right] \tag{3.7}$$

While the study by Fischuk *et al.*[86] showed that the C factor depends on the ratio of σ and E_a, a point of debate is whether the universal scaling relation (implying a constant C factor) regarding the polaron formation energy is really obeyed, as recently claimed in the literature.[85,96] Also, though it is commonly accepted that both static and dynamic disorder can contribute to charge transport, an issue is related to the question whether or not the simpler material-independent MA type hopping rate is sufficient for the interpretation of charge transport measurements instead of Marcus rate.[97] These impending issues have been investigated in Chapter 8 of this thesis.

3.2 Transfer integrals: Förster and Dexter transfer

While, in the previous sections, we discussed different regimes of transport and the associated transition rate theories which can account for hopping between molecular sites, we did not discuss the perturbation term J in Equation 3.1, Equation 3.4 and Equation 3.6 which allows the carrier transfer to occur. Carrier transfer can take place via two mechanisms: Förster resonant energy transfer (FRET) and Dexter energy transfer (DET).

The excitation transfer phenomenon between fluorescent molecules was described by Theodor Förster in 1948.[98] Utilizing the first order perturbation theory, Förster described the transfer integral (J) for excitation transfer by the transition dipole coupling of the donor and acceptor molecules[99]

$$J^2_{F\ddot{o}rster} \propto \frac{\mu_D^2 \mu_A^2}{R^6} \tag{3.8}$$

In Förster theory, the squared transition dipole moment of the donor (μ_D^2) is obtained from the donor lifetime (τ) and the acceptor squared transition dipole moment (μ_A^2) is obtained from the spectral overlap of the donor emission spectrum and acceptor absorption spectrum, which is included in the parameter called Förster radius (R_F), to yield:

$$J^2_{F\ddot{o}rster} = \frac{1}{\tau}\left(\frac{R_F}{R}\right)^6 \tag{3.9}$$

It is important to note that for the Förster transfer to occur, the transition from the excited state to the ground state has to be an allowed transition. This implies that in fluorescent molecules only the Förster transfer of singlets is allowed, while it is forbidden for triplets. In

phosphorescent molecules, owing to strong spin-orbit coupling, Förster transfer is allowed for triplets as well.

In 1953, Dexter developed a more general theory for excitation transfer in inorganic solids based on exchange mechanism.[100] Based on Dexter mechanism, the interaction exhibits an exponential dependence on the wavefunction overlap:

$$J_{Dexter}^2 = exp(-2\gamma R) \tag{3.10}$$

where γ is called the inverse localization length. Charge transport as well as triplet transport in fluorescent molecules occurs via Dexter exchange mechanism.

3.3 Spatially correlated energy landscape

The experimental electron or hole mobility (μ) is often found to obey the empirical Poole-Frenkel $ln(\mu) \propto \sqrt{F}$ dependence on electric field (F).[101] Within GDM (Equation 3.3)[14] as well as it's subsequent extension, the so-called extended GDM (EGDM)[102–104] developed to include the carrier density dependence of mobility, such a field dependence is indeed found; albeit only in a narrow field range. Gartstein and Conwell argued that a wider field range applicability of Poole-Frenkel type dependence requires that the energy levels must be spatially correlated.[105] In Bässler's GDM (and EGDM) such spatial correlations between the energies of the hopping sites were diregarded, however, they can be can expected in real world organic solids. The physical origin of such correlations could be ascribed to the permanent dipole moments present in some molecules,[105–108] the quadrupole moment present in all π-conjugated polymers, short-range order due to the packing of the film or long-range thermal fluctuations in molecular geometries.[109] After the incorporation of correlation effects, an extended range of Poole-Frenkel field-dependence was indeed found by Novikov and coworkers.[107,108] The dominant contribution to such correlations comes from the charge carrier interaction with the field of randomly oriented permanent dipoles. The resulting energy E_i of the site i is then taken to be the electrostatic energy resulting from the charge carrier interaction with the permanent dipole moments ($\boldsymbol{d_j}$) of equal magnitude d but randomly oriented on all other organic molecules $j \neq i$[110]

$$E_i = -\sum_{j \neq i} \frac{e\boldsymbol{d_j} \cdot \boldsymbol{R_{ij}}}{\epsilon_0 \epsilon_r |\boldsymbol{R_{ij}}|^3} \tag{3.11}$$

where e is the unit charge, ϵ_0 is the vacuum permittivity and ϵ_r is the dielectric constant of the material. The resulting DOS is Gaussian,[107,111] with an energetic width, $\sigma \propto d$ and the correlation function (C_{ij}), which quantifies the degree of correlation between sites separated by a distance R_{ij}, exhibits a $1/R_{ij}$ dependence.[108] The energy landscape thus obtained can
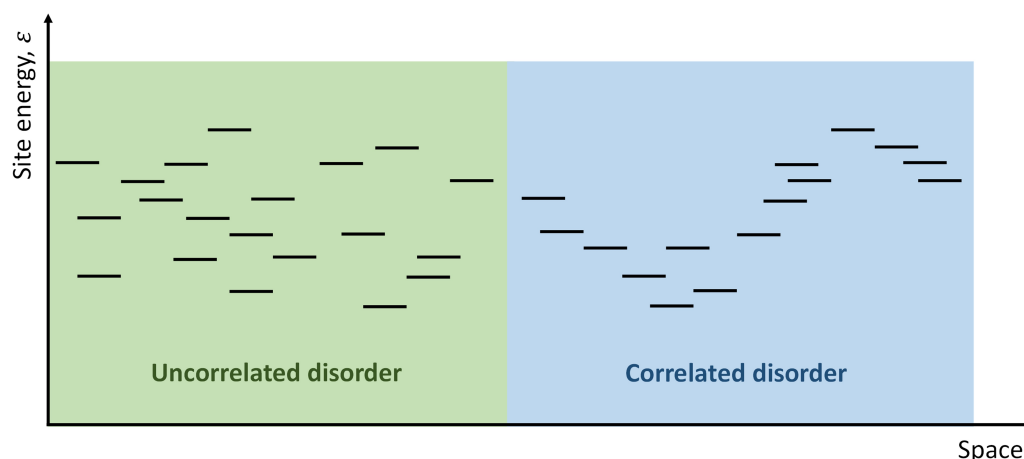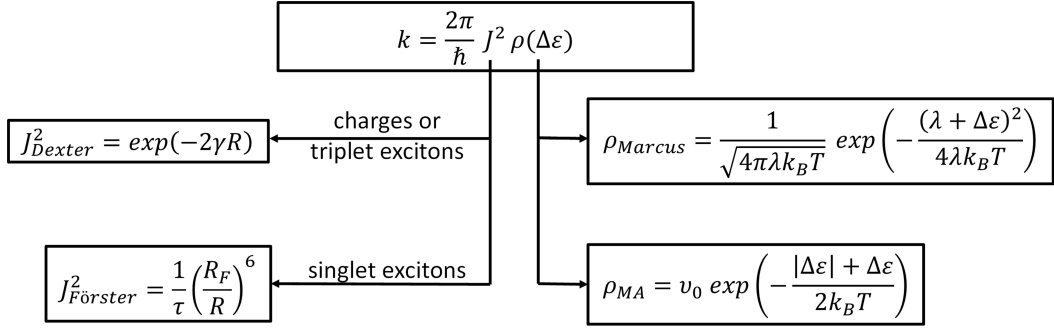
Figure 3.3: Illustration of spatially correlated disorder. The variation of site energy with space is shown for a system with a) uncorrelated (random) disorder b) correlated disorder. After Novikov *et al.*[107]

be thought as one in which large-scale potential energy variation superimposes on small scale fluctuations in energy, as depicted in Figure 3.3. This amended version of GDM is called correlated disorder model (CDM).

Correlation effects play a lesser role at high electric fields and for the case of non-polar materials, however differences between GDM and CDM arise when describing the motion of charges at low electric fields ($< 10^5 \, V/cm$) and in particular with molecules carrying some permanent dipole moment. The effects are also less important when considering the motion of excitons (neutral excitations). Though CDM has been crucial in predicting the field dependence of mobility in organic semiconductors, nevertheless, it has not been considered important for reproducing the temperature dependence of mobility or for describing the energetic relaxation of charges within the DOS. This is precisely the subject of study in Chapter 9 of this thesis.

3.4 Mechanistic modeling of charge and exciton transport

The theories described for charge and exciton transport (Chapter 3.1) can all be linked with the expressions of transfer integral (Chapter 3.2). This general scheme is schematically depicted in Figure 3.4. Now that we know different charge and exciton transfer theories and different parameters which can affect such transport we will discuss how to simulate the transport on the scale of a film (or device). Transport to a particular site j is controlled by its (time-dependent) occupational probability p_j and the rate of transport from site i to site j, k_{ij}. The hopping transport can then be described by a general master equation:[112]

$$k = \frac{2\pi}{\hbar} J^2 \rho(\Delta\varepsilon)$$

$$J^2_{Dexter} = exp(-2\gamma R)$$

charges or
triplet excitons

$$\rho_{Marcus} = \frac{1}{\sqrt{4\pi\lambda k_B T}} \, exp\left(-\frac{(\lambda + \Delta\varepsilon)^2}{4\lambda k_B T}\right)$$

$$J^2_{F\ddot{o}rster} = \frac{1}{\tau}\left(\frac{R_F}{R}\right)^6$$

singlet excitons

$$\rho_{MA} = \nu_0 \, exp\left(-\frac{|\Delta\varepsilon| + \Delta\varepsilon}{2k_B T}\right)$$

Figure 3.4: Schematic linking the different exciton and charge transfer theories to the transfer integral (J) and density of states (ρ) in Fermi's golden rule.

$$\frac{dp_i(t)}{dt} = \sum_{j\neq i}[-k_{ij}p_i(t)[1 - p_j(t)] + k_{ji}p_j(t)[1 - p_i(t)]] \tag{3.12}$$

In the limit of low carrier concentration, $p_i p_j \approx 0$. Additionally, the lifetime of a charge and especially of an exciton is not infinite i.e., they can decay with a rate λ_i. After incorporating these into the master equation:[82]

$$\frac{dp_i(t)}{dt} = \sum_{j}[-k_{ij}p_i(t) + k_{ji}p_j(t)] - \lambda_i p_i(t) \tag{3.13}$$

Equation 3.13 can be solved numerically using 3D master equation simulations or analytically by using theories such as effective medium approach[75,82,86,113] and multiple trapping and release formalism[112,114–119] (see Chapter 8 for more details). Alternatively, mechanistic kinetic Monte Carlo (KMC) simulations can be utilized with an arbitrarily adjustable degree of disorder.[14,120–122]

In recent years, off-lattice simulations considering actual morphologies of the molecular materials, generated by molecular dynamics simulations, have been extensively developed to include increasing amount of molecular details.[123–127] This is done as a part of an endeavor to predict the macroscopic properties of organic semiconductors (such as mobility) starting from their molecular structure. However, in this thesis I have utilized lattice based KMC simulations, except for the case of triplet transport in conjugated polymers (Chapter 10). In the latter case, the approach suggested by Athanasopoulus *et al.*[78,79] is used to generate simple (parallel or grid-like) chromophore morphologies. Though more complex morphologies can be generated using the more sophisticated approaches (as discussed above), the simple approaches used in this thesis have often been found to sufficiently capture the essential physical aspects at a reasonable computational cost. After the morphology generation, the lattice sites are assigned energies based on GDM (Equation 3.3) or CDM (Equation 3.11) and either single excitation (Chapter 8, Chapter 9) or multiple excitations (Chapter 10) are

generated within the DOS. The excitations can hop based on their respective transition rates (Figure 3.4) or decay according to their respective decay rates in a stochastic manner; which in this thesis has been implemented by using mechanistic KMC simulations. The protocol adopted for the kinetic implementation of KMC simulations is as follows. For each event i (of each excitation) the rate k_i is calculated. For the selection of an event, firstly for each event i the partial sum $S_i = \sum_{\beta=1}^{i} k_\beta$ is evaluated. A random number $\phi \in (0, 1]$ is drawn randomly and from all possible events, the event i for which $S_{i-1} < \phi \, k_T \leqslant S_i$ holds is selected, with $k_T = \sum_{\beta=1}^{N} k_\beta$, N being the total number of events. The selected event is executed and the simulation time (t) is updated by the waiting time, $\tau_w = -ln(X)/k_T$, where X is a random number between 0 and 1. Results are obtained by averaging over several number of trials. Specific details regarding the simulation technique relevant to individual chapters (Chapter 8-10) are detailed therein.

4 Donor-acceptor strategy for the design of TADF emitters and bipolar hosts

The chemical design of thermally activated delayed fluorescence (TADF) emitters as well as bipolar host materials relies heavily on the donor-acceptor strategy in which donor (D) and acceptor (A) moieties are linked either directly or via an aromatic bridge.[22,32,33,128–130] This chapter summarizes the state-of-the-art chemical design strategies of TADF emitters and bipolar host materials as well as the current state of research on the photophysical and reverse intersystem crossing (RISC) mechanism studies of TADF emitters.

4.1 Emission from intramolecular charge transfer states

TADF was first reported in 1929 by Perrin *et al.*[131] and subsequently characterized in detail by Lewis *et al.*[132] in solid state and Parker *et al.*[133,134] using Eosin dye. This study on Eosin is the reason that TADF was also known as E-type delayed fluorescence in the past. In 2012, Adachi and coworkers,[22] exploited the TADF mechanism for triplet harvesting in OLEDs and demonstrated highly efficient electroluminescence with purely organic molecules. This pioneering work has been a driving force for a significant research interest in understanding the photophysics of TADF process. As discussed in Chapter 2, the performance of TADF emitters depends on the energy difference (ΔE_{ST}) between the lowest energy singlet and triplet excited states which in turn depends on the exchange energy (K) between the two unpaired electrons (one in HOMO and the other in LUMO) in the excited state (Chapter 2.1).[25] Thus, ΔE_{ST} can be minimized by minimizing K, i.e., by decreasing the overlap between the HOMO and LUMO.[25,135,136] D-A type molecules, which favor D to A electron transfer in the excited state, thus prove to be quite useful in obtaining small ΔE_{ST} values and hence in achieving an efficient up-conversion of triplets via RISC mechanism.[137]

In view of this background, the development of small molecule (or in other words, low molecular weight amorphous molecular materials) TADF emitters relied robustly upon the minimization of ΔE_{ST}.[128,138] In general, adopting a D-A type architecture leads to reduced ΔE_{ST}, as discussed above. However, further reductions in ΔE_{ST} were reported using various other strategies. For example:

- as reported by Dias *et al.*,[139,140] twisted geometries with near-orthogonal D-A relative orientation lead to even smaller ΔE_{ST} values.

- increasing the D-A distance (by introducing an aromatic linker between them) also leads to similar effects.[141–143]

- even with identical D-A dihedral environments, owing to positional differences in the acceptor strengths associated with inductive and resonance effects in the aromatic π-systems, smaller ΔE_{ST} values are achieved in *meta*-isomers as compared to *para*-isomers.[144,145] For further discussion regarding the effect of relative position of donor and acceptor moieties on the TADF properties, the reader is referred to the review article by Xie *et al.*[146]

The strong D-A nature of TADF emitters and the associated D to A electron transfer in the excited state, results in the formation of excited states with intramolecular charge transfer (CT) character.[147–149] Experimental evidence of the CT character of excited states comes from the solvatochromism observed in their emission. The bathochromic spectral shift with increasing solvent polarity is a result of the electrostatic interaction between the dipole of the solvent molecules and the excited state dipole of the TADF molecules, the latter arising as a consequence of the redistribution of electronic density in a CT state.[149] Unfortunately, as outlined in the article by Olivier *et al.*[150] as well as in the review article by Dias *et al.*,[139] a subtle trade-off exists between the RISC efficiency and the oscillator strength (cf. subsection 2.2.1) of the excited singlet state. While negligible orbital overlap leads to small ΔE_{ST}, it also leads to weak electronic coupling between the ground and excited state which results in low oscillator strengths, low radiative rates and, as a consequence reduced radiative efficiency values.[139,150]

A simplified three-level energy diagram depicting the rates of radiative and non-radiative transitions from and between the first excited singlet and triplet states for a TADF emitter is shown in Figure 4.1a. TADF can be identified experimentally from a transient PL decay profile, as illustrated in Figure 4.1b. The PL decay for a TADF emitter comprises of a prompt fluorescence (PF) decay in the timescale of a few ns to $\approx$100 ns and a delayed fluorescence (DF) decay in the μs time scale.[135,138,139,151–154] The RISC process within the regime of first order perturbation theory has been proposed to increase exponentially with increasing temperature (T) i.e., $k_{RISC} \propto exp\left(-\Delta E_{ST}/k_B T\right)$, therefore, the intensity of DF increases with increasing temperature (Figure 4.1b). This is considered as an indication of TADF.[137]

4.1.1 Reverse intersystem crossing mechanism

Using the classical Marcus expression (Equation 3.6) for the Franck-Condon weighted density of final states, k_{RISC} can be expressed within the limit of first order perturbation theory by
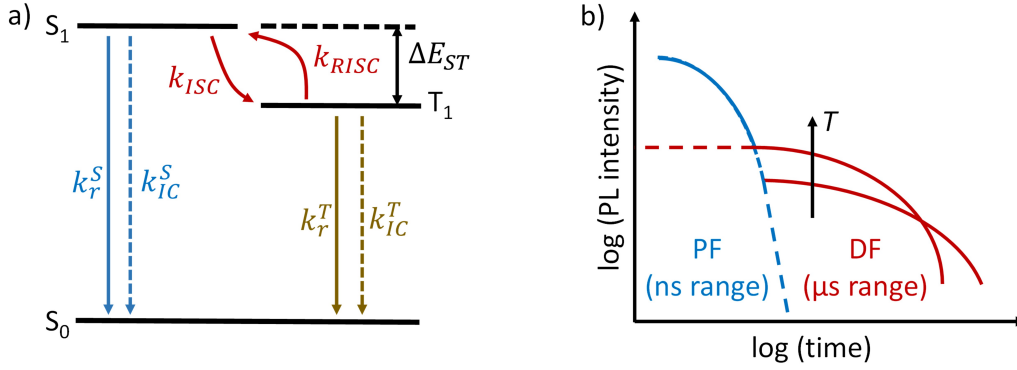
Figure 4.1: a) A three-level Jabolinski diagram showing transitions from and between lowest energy singlet (S_1) and triplet (T_1) excited states. k_r and k_{IC} indicate radiative decay and internal conversion rates, respectively. The rate of conversion of singlet state to the triplet state and the reverse process are denoted as intersystem crossing rate k_{ISC} and reverse intersystem crossing rate k_{RISC}, respectively. b) Schematic illustration of transient PL decay on a log-log scale consisting of prompt fluorescence (PF) decay in the ns time scale and delayed fluorescence (DF) decay in the μs time scale. Also shown is the evolution of DF intensity with increasing temperature (T).

Fermi's golden rule:[48,155–161]

$$k_{RISC} = \frac{2\pi}{\hbar} \, |\langle S_1|\hat{H}_{SOC}|T_1\rangle|^2 \, \sqrt{\frac{1}{4\pi\lambda k_B T}} \, exp\left[-\frac{(\lambda + \Delta E_{ST})^2}{4\lambda k_B T}\right] \quad (4.1)$$

where λ represents the Marcus reorganization energy and $\langle S_1|\hat{H}_{SOC}|T_1\rangle$ represents the spin-orbit coupling (SOC) matrix element for the transition from T_1 to the S_1 state. However, in D-A type TADF emitters, both, the lowest singlet and triplet states are of CT character, thus, the direct RISC between these states should be very inefficient because of the vanishing SOC between the states of similar character.[160,162,163] This is because, for the singlet and triplet states with the same spatial orbital occupation, any change in spin cannot be compensated by a corresponding change in orbital angular momentum and as a consequence the total angular momentum can no longer be conserved (El-Sayed rule).[164,165] To justify the RISC mechanism in these molecules, Monkman, Penfold and coworkers[166–170] proposed that the non-adiabatic vibronic coupling ($\hat{H}_{vib}$) between a triplet CT (^{3}CT) state and a higher energy triplet locally excited (^{3}LE) state can promote the RISC by opening the possibility of second order coupling effects to allow the spin-orbit coupling to the singlet CT (^{1}CT) state, yielding

$$k_{RISC} = \frac{2\pi}{\hbar} \left| \frac{\langle ^1\Psi_{CT}|\hat{H}_{SOC}|^3\Psi_{LE}\rangle \, \langle ^3\Psi_{LE}|\hat{H}_{vib}|^3\Psi_{CT}\rangle}{\delta\left(^3E_{LE} - \, ^3E_{CT}\right)} \right|^2 \delta\left(^3E_{LE} - \, ^1E_{CT}\right) \quad (4.2)$$

where ψ and E represent the wavefunction and energy value of the respective CT and LE states; δ represents a delta function.[166,170] Nevertheless, there is a plethora of CT-type molecules to

which this mechanism does not apply, for example, the molecules where the locally excited states are much higher in energy than both S_1 (^{1}CT) and T_1 (^{3}CT) states.[22,29,47,150,171] Thus, any higher lying locally excited T_n state is also too destabilized to be implicated in any significant fashion to the RISC process via second order spin-vibronic coupling mechanism. As detailed in Chapter 11, this is also the case for TADF dendrimers investigated in this thesis (Chapter 11 and Chapter 12). Therefore, in this case, the RISC rate warrants consideration of other factors (ΔE_{ST}, SOC, λ) within the limit of first order perturbation theory.

4.2 Bipolar host materials

As mentioned in Chapter 1, neat emitter layers show self quenching which results in the decrease of radiative efficiency of the emitter with increasing emitter concentration and thus it is necessary to disperse the emitters in suitable host matrices. These hosts have several requirements such as, having a high singlet and triplet energy, suitable HOMO and LUMO levels for the device applications, chemical and thermal stability and balanced hole and electron mobilities (i.e., bipolar transport).[33,172] One of the recent challenges is the development of efficient and stable blue host-emitter systems which can replace the less efficient 1st generation fluorescent ones, currently used in commercial OLED displays.[173] So far, the reported hosts with a triplet energy suitable for blue OLEDs ($E_T > 3$ eV) are mostly unipolar. A majority of them use less stable groups such as phosphine oxide,[33,174–178] DPEPO (bis(2-(diphenylphosphino)phenyl)ether oxide; $E_T = 3$ eV) being one of the most commonly used host material for blue TADF emitters.[36] With the advantage of being stable, carbazole based hosts have also been developed.[128] Most of these carbazole-based hosts are suitable for greenish-blue emitters but not for blue OLEDs as their triplet energy is less than 3 eV. Additionally, the dominating hole transporting nature of these host materials leads to the recombination of injected charges to be near the interface of emissive layer and electron transport layer.[36,37] This is detrimental to the efficiency, color point as well as lifetime of the OLEDs.

Host materials based on the D-A type architecture show good electrical performance in terms of balanced charge carrier transport as compared to only D- or A-type (unipolar) host materials.[38,39,179] There are several reports of enhanced efficiency and reduced efficiency roll-off at high luminance when using bipolar D-A type hosts.[33,180] However, as mentioned above for the case of TADF emitters, the D-A chemical design leads to strong intramolecular CT character of the lowest triplet state and consequently a lower E_T. The formation of a CT state can be impeded either through *meta*-substitution which lacks the resonance, or by using a sterically twisted geometry, or by using linkers to interrupt the π-conjugation or by using chemical motifs with disrupted π-conjugation.[181–183] In general, bipolar host materials remain less developed in comparison to the emitters, therefore some structure-property

relationship investigations need to be performed to establish chemical design strategies for the advancement of this field. To contribute to the development of these strategies, the role of acceptor motifs with restricted π-conjugation in achieving high triplet energies is investigated in Chapter 13 of this thesis.
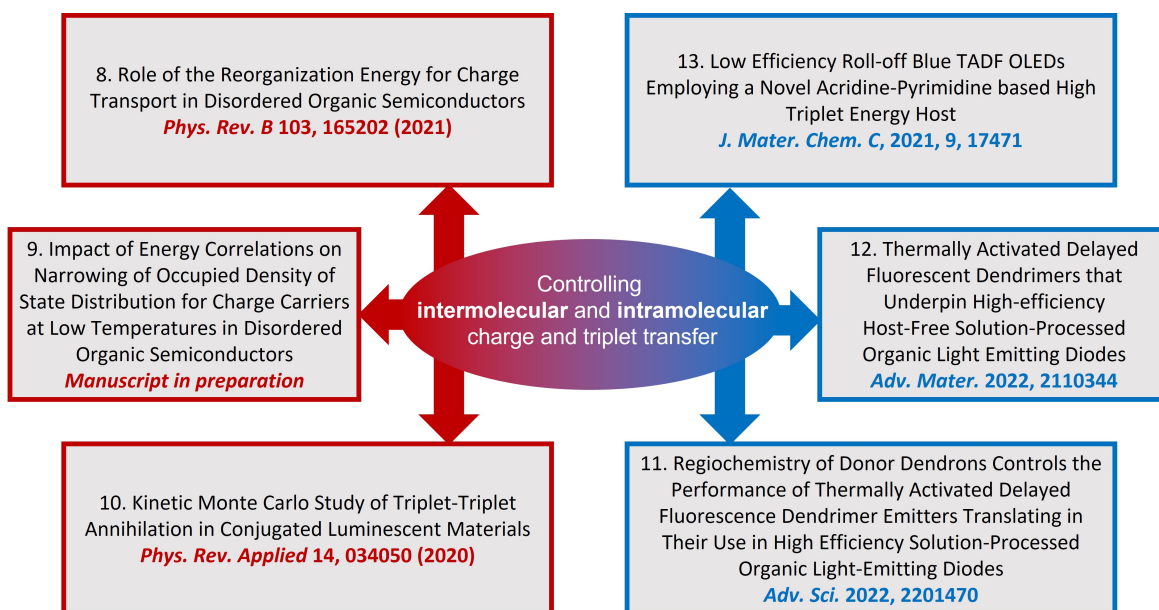
Part II

Overview of the thesis

5 Overall context and summary

The aim of this thesis is to develop a deeper understanding of charge and triplet transport in organic semiconductors. In particular, the objective is to comprehend which molecular parameters control the transfer of charges and excitons within and between the chromophores. I also aim to use the insight gained to optimize the intramolecular energy transfer with a view to optimize the OLED materials for enhanced OLED performance. This dissertation addresses this issue in six chapters. They can be grouped into two parts. An overview over the relation between different chapters is depicted in Figure 5.1.

In the first part of this thesis (Chapters 8-10), I focus on understanding the intermolecular charge and triplet transport using kinetic Monte Carlo (KMC) simulations. With KMC simulations, I was able to disentangle the effect of each individual material parameter (such as the degree of electronic coupling between the hopping sites, the static energetic disorder and the reorganization energy) and morphological property on charge transport and various photophysical processes associated with the triplet excitons. This allowed me to determine the crucial parameters affecting the transport of charges and triplet excitons in microscopically disordered materials such as amorphous organic semiconductor films (AOSFs). In Chapter 8, I investigated the relative impact of static and dynamic disorder on charge transport in organic semiconductors. Further, I advanced the single-excitation KMC algorithm developed during the previous work to investigate the impact of spatial correlations among the energies of the organic molecules on the energetic relaxation of charges within the DOS in Chapter 9. Having understood the important factors for charge transport in AOSFs, I then turned my attention to triplet transport in Chapter 10 and investigated triplet-triplet annihilation (TTA) in a system of conjugated polymers using multi-excitation KMC simulations. TTA involves the collision of two triplets and thus depends on the diffusivity of triplet excitons. Therefore, studying TTA in a model system allowed me to understand the fundamentals behind the intermolecular triplet transport in AOSFs. Additionally, this also allowed me to systematically comprehend which material parameters need to be optimized for obtaining efficient room temperature TTA in polymeric semiconductors. This information is useful for the design of efficient TTA-based delayed fluorescent emitters. Likewise, for establishing the design rules of an efficient TADF emitter, it is imperative to determine the molecular parameters affecting the RISC process. Thus, the investigations in the second part (Chapters 11-13) of this thesis are concerned with the intramolecular charge transfer (CT) processes

8. Role of the Reorganization Energy for Charge Transport in Disordered Organic Semiconductors
Phys. Rev. B **103, 165202 (2021)**

13. Low Efficiency Roll-off Blue TADF OLEDs Employing a Novel Acridine-Pyrimidine based High Triplet Energy Host
J. Mater. Chem. C, **2021, 9, 17471**

9. Impact of Energy Correlations on Narrowing of Occupied Density of State Distribution for Charge Carriers at Low Temperatures in Disordered Organic Semiconductors
Manuscript in preparation

Controlling **intermolecular** and **intramolecular** charge and triplet transfer

12. Thermally Activated Delayed Fluorescent Dendrimers that Underpin High-efficiency Host-Free Solution-Processed Organic Light Emitting Diodes
Adv. Mater. **2022, 2110344**

10. Kinetic Monte Carlo Study of Triplet-Triplet Annihilation in Conjugated Luminescent Materials
Phys. Rev. Applied **14, 034050 (2020)**

11. Regiochemistry of Donor Dendrons Controls the Performance of Thermally Activated Delayed Fluorescence Dendrimer Emitters Translating in Their Use in High Efficiency Solution-Processed Organic Light-Emitting Diodes
Adv. Sci. **2022, 2201470**

Figure 5.1: Schematic overview of the structure of the thesis.

and transitions between the excited states. For this purpose, detailed insight in molecular photophysics is required and I aimed to obtain this by using spectroscopic methods such as absorption and emission spectroscopy. In Chapter 11, I systematically investigated the effect of regiochemistry of the dendrimers, notably the connection of donor and acceptor moeities via *meta-* or *para-* position on a phenyl ring, on the intramolecular reorganization energy and how this affects the RISC rate. The insights obtained in Chapter 11 were utilized in Chapter 12 to illustrate how the design of TADF dendrimers can be improved further by combining the synergistic effects of *para-* and *meta-*connected dendrons. Moreover, TADF emitters are often doped in a host matrix to prevent diffusion assisted detrimental bimolecular effects caused by long-lived triplet states. Aside from other electrical, thermal, and chemical properties, host materials must have high triplet energy; high enough to confine the excitons on the emitter, which is particularly challenging for blue-emitting OLEDs. Therefore, in Chapter 13, I equally systematically investigated the role of chemical motifs with restricted π-conjugation in yielding high triplet energies.

The following text summarizes the content of individual chapters forming this dissertation. A more detailed description is given in Chapter 6. In the study presented in Chapter 8, I address the role of dynamic disorder, as expressed in terms of reorganization energy, on charge transport in AOSFs. As outlined in Chapter 3.1, while it is generally accepted that the activation energy of thermally activated transport can be decoupled into a disorder and a polaron contribution, their relative weight is still debatable. This feature is quantified in terms of the so-called C factor in the expression for the effective polaron mobility:

$\mu_e = exp[-E_a/k_BT - C(\sigma/k_BT)^2)]$, where E_a and σ are the polaron activation energy and the energy width of a Gaussian DOS, respectively. A key issue is whether the universal scaling relation (implying a constant C factor) regarding the polaron formation energy is really obeyed, as recently claimed in the literature.[96] To investigate this issue, I developed a single particle grid-based kinetic Monte Carlo (KMC) code to monitor the motion of excitations as hopping events in a three-dimensional simulation box based on Marcus theory for polaron hopping rates. In conventional "DOS simulations", the excitation generated at an arbitrary site within the DOS exhibits an initial non-equilibrium transport, until a quasi-equilibrium between the downward hops and thermally activated upward hops is attained.[82] This non-equilibrium nature of the simulated diffusivity affects the resulting transport properties. Therefore, to differentiate equilibrium transport from non-equilibrium transport, I introduced "ODOS simulations" (ODOS: occupational DOS) where the initial ($t = 0$) energy of the charge is chosen from a DOS centered at the equilibrium energy ($\epsilon_{eq} = -\sigma^2/k_BT$) below the DOS center with the same energetic width σ. I demonstrated that the C factor turns out to depend on whether the transport has reached equilibrium or not, and on the degree of carrier localization, i.e., the electronic coupling between the hopping sites. Moreover, it changes with the σ/E_a ratio. This clarified the non-existence of universal scaling law. Furthermore, I utilized the KMC results to analyze the experimental charge transport data available in literature,[184] and demonstrated that virtually the same disorder parameters (σ) are determined irrespective of whether the data are interpreted in terms of Marcus or Miller-Abrahams (MA) rate. This implies that molecular reorganization, i.e., dynamic disorder, contributes only weakly to charge transport. Thus, this work "legitimizes" the use of simple MA rate model for the description of charge transport in AOSFs. This is a key message of this study, especially relevant for experimentalists, who routinely use GDM for the analysis of charge transport measurements and naturally want to know to what extent this zero-order material-independent approach is accurate in determination of the width of the DOS.

In addition to charge transport measurements, the low temperature thermally stimulated luminescence (TSL) technique can also be applied to probe the energetic disorder of localized states in organic semiconductors. The TSL curve maps the distribution of these localized charge carriers within the ODOS. TSL experiments conducted by Andrei Stankevych (Institute of Physics, Kiev), on the thin films of 18 commonly used small molecule OLED materials (used as hosts, emitters, hole/electron transport materials in OLEDs) demonstrated a quite general phenomenon, i.e., σ scales linearly with σ_{ODOS} and that it leads to an universal ratio of $\sigma_{ODOS}/\sigma \approx 2/3$. This implies a significant narrowing of ODOS distribution formed at low temperatures as compared to the DOS width. In order to gain deeper insight into this effect I performed variable time step KMC (vt-KMC) simulations of charge-carrier energy relaxation process as vt-KMC simulations, owing to a non-linear increase in the time step as charge

carriers relax in energy, allow us to probe the long-time limit of the relaxation of the charges (at reasonable computational cost). This renders the simulation results to be suitable for comparison with the TSL experimental results. In the work presented in Chapter 9, using vt-KMC simulations, I found that such "spectral narrowing" effect is a genuine property of the hopping carrier relaxation at low temperature within a Gaussian distribution of localized states. However, a quantitative agreement with the TSL experimental data for the ODOS width could only be obtained after the inclusion of energy correlations, that are indeed present in polar OLED materials (Chapter 3.3). This is a key finding of this work, as in the previous studies correlations have never been considered important for reproducing the temperature dependence of the mobility or to describe the energetic relaxation of the charges.

Like charges in AOSFs, triplets also diffuse via short range exchange mechanism and hence triplet diffusion, and consequently the bimolecular TTA process, is thermally activated. Moreover, revived interest in TTA is stimulated by the present endeavor towards the development of efficient delayed fluorescence (DF) based OLEDs since TTA can enhance the internal quantum efficiency of OLEDs when it contributes to DF via an up-conversion mechanism. No matter how efficient the triplet-to-singlet up-conversion process is, a first requisite is that the two triplets meet efficiently and do not end up at the non-radiative quenching centers. Thus, in the study presented in Chapter 10, I focused on understanding the material parameters and the morphological properties affecting triplet diffusion and established ground rules for obtaining efficient TTA in polymeric semiconductors at RT (where devices typically operate). I advanced the KMC simulations from single-excitation simulations to multi-excitation simulations, to account for the annihilation effects. These simulations were also advanced to contemplate different morphologies for the consideration of conjugation effects in the polymeric systems, as suggested by Athanasopoulos *et al.*[79] In the study presented in Chapter 10, I utilized these KMC simulations to study the complex interplay between bimolecular TTA and monomolecular quenching processes (at non-radiative trap sites). An essential message of this study is that the DF features a maximum at a temperature that scales as $\sigma/k_B T$. I found that optimizing the TTA process, and concomitantly the yield of DF, to peak at RT is possible. This requires (i) a high disorder and therefore dispersive transport (in the range of $\sigma/k_B T \approx 3$), (ii) a high sample purity ($< 10^{17}$ quenching sites per cm^3), and (iii) a transport morphology and conjugation length with many contact points that enables isotropic hopping. In addition, a key message of this study is that energetic disorder has an additional role in promoting bimolecular TTA process. It causes filamentary transport which enhances the triplet density in the energetic valleys, thus increasing the probability of two triplets to encounter each other rather than an impurity. Moreover, the choice of hopping rate (Marcus or MA rate) is not critical when considering the yield of TTA events. This implies that geometric reorganization has little to no impact on charge (Chapter 8) as well as triplet (Chapter 10) transport between the chromophores.

Forming a transition to the next part of this thesis, it is necessary to emphasize that while on one hand, the TTA-based delayed fluorescent emitters employ diffusion assisted TTA process for the conversion of non-emissive triplet states to the emissive singlet states, on the other hand, TADF-based emitters employ the small singlet-triplet energy difference driven RISC process to mediate the transition from triplet excited state to the singlet excited state. Therefore, it is important to investigate the material parameters controlling the intramolecular charge transfer and transitions between the excited states. For this purpose, I adopted an experimental approach involving steady-state and time-resolved photophysical measurements (in solutions and in films) along with the interpretation of quantum chemical calculation results.

In the study presented in Chapter 11, I investigated TADF dendrimers with multiple dendritic electron-donating moieties (carbazole based donor dendrons) connected to a central electron-withdrawing triazine core via a *para*- or a *meta*-phenylene bridge. Dendrimers allow for easy solution-processed manufacture of large-area devices. However, the potential of dendrimers exhibiting TADF as emitters in solution-processed OLEDs has to date not yet been realized. This in part is due to a poor understanding of the structure-property relationship in dendrimers where reports of detailed photophysical characterization and RISC mechanism are lacking. To address this void, I utilized absorption and solvatochromic photoluminescence studies in solution to probe the origin and nature of the lowest excited states in these systems. Moreover, I did comparative time-resolved and temperature-dependent solid-state photoluminescence measurements to show that the *meta*-dendrimers possess smaller adiabatic singlet-triplet gap (ΔE_{ST}), several times higher reverse intersystem crossing rate (k_{RISC}) and thus the corresponding OLEDs exhibit improved electroluminescence (EL) performance. ΔE_{ST} was found to be lower in *meta*-dendrimer (tBuCz3mTRZ) as compared to *para*-dendrimer (tBuCz3pTRZ) (80 *vs.* 100 meV). However, according to Boltzmann distribution this ΔE_{ST} difference can only lead to 40% (1.4 times) enhancement of RISC and thus was not sufficient to explain the seven-fold increase in k_{RISC}, in going from *para*- to *meta*-connected dendrimer alone. Thus, I elicited other factors within the first order perturbation theory that can be considered in the chemical design other than ΔE_{ST} (see subsection 4.1.1 for more details). Combining photophysical results with quantum chemical calculation results, I demonstrated that smaller ΔE_{ST}, greater spin orbit coupling (SOC), and smaller reorganization energy (λ) blend to lead to a faster k_{RISC} in *meta*-dendrimer as compared to the *para*-analogue. Though the molecular design of donor-acceptor TADF emitters has most often focused on either the minimization of ΔE_{ST} or the enhancement of SOC, the role of λ has been frequently overlooked. What Chapter 11 describes is, that λ can play an important role in enhancing k_{RISC}, and that this can be modulated as a function of the regiochemistry of the donor dendrons about the central acceptor.

As detailed in Chapter 4.1, the donor-acceptor strategy adopted for the design of TADF

emitters results in the minimization of electronic exchange energy and thus reduced ΔE_{ST} values. However, this also leads to low oscillator strength and radiative singlet decay rate. The conclusions derived from the study presented in Chapter 11 clearly revealed that *meta-*connection dendrimers possess several design advantages over *para-*connection dendrimer with respect to enhancing RISC. It also demonstrated that the more conjugated *para-*connected dendrimer exhibited higher radiative decay rate, owing to the greater hole-electron density overlap of the lowest energy singlet charge transfer (^{1}CT) state. These results were used to further improve the design of TADF dendrimers in the work presented in Chapter 12; by combining the synergistic effects of *meta-* and *para-*connected dendrimers. Through the introduction of both *para-* and *meta-*connected donor dendrons about the triazine acceptor, the dendrimer tBuCz2m2pTRZ was then found to not only inherit a high RISC rate, large oscillator strength, but also exhibited a desired suppressed concentration quenching as evident by the improved OLED performance.

Aside from emitters, host materials need to be optimized as well for the fabrication of efficient and stable OLEDs. In particular, the detrimental effects of longer-lived triplet excitons (Chapter 2.3) need to be suppressed by their confinement on the emitter molecules for which host materials with high triplet energy is an essential requirement. This is particularly challenging for blue OLEDs as it requires a host triplet energy to be greater than 3 eV. So finally in the work presented in Chapter 13, I investigated a series of donor-acceptor type bipolar host materials based on acridine (donor) and three different pyrimidine moieties (acceptors) with a different size of the conjugated system of pyrimidine, namely 2-phenylpyrimidine (2PhPy), 1-phenylpyrimidine (1PhPy) and methylpyrimidine (MePy). I performed steady state photophysical measurements in solution (toluene and mTFH) to illustrate how, via careful molecular modifications, it is possible to limit the conjugation of pyrimidine leading to high triplet energies (of >3 eV). While for 2PPA and 1PPA (2PP, 1PP and A represent 2PhPy, 1PhPy and acridine, respectively), the ^{3}LE state localized on the acceptor moieties 2PhPy and 1PhPy is the lowest triplet energy with an onset at around 2.9 eV, this is no longer the case when the conjugation is reduced to MePy in 1MPA (1MP and A represent MePy and acridine, respectively). The triplet state for the MePy unit is found to be well above the onset of phosphorescence of acridine unit. As a result, in 1MPA, the lowest triplet state is found to have an onset at 3.07 eV. Through detailed spectroscopic investigation and quantum chemical calculations, the nature of this triplet state is attributed to a mixed CT-LE character, where the LE contribution is from the acridine unit. To demonstrate the potential of 1MPA as a host material, sky blue TADF OLEDs with electroluminescence peak at 491 nm and a maximum external quantum efficiency of 13.6%, combined with low roll-off were achieved. The host 1MPA was also shown suitable for deep blue TADF OLEDs.

# 6 Contents of the individual publications

The following sections provide detailed summaries of the publications included in this thesis. The author's contributions for all the publications are detailed in Chapter 6.7.

6.1 Role of the Reorganization Energy for Charge Transport in Disordered Organic Semiconductors

The work presented in Chapter 8 deals with the relative impact of static and dynamic disorder on charge transport in amorphous organic semiconductor films (AOSFs). As outlined in subsection 3.1.1, charge transport in AOSFs can be described by a superposition of polaronic and disorder-controlled transport. There is a consensus within the community that the transition rate for charge transport among the molecular sites can be described by classical Marcus theory (Equation 3.6) and that the activation energy of the thermally activated transport can be split into a disorder-controlled term and a polaronic term (reproducing Equation 3.7):

$$\mu(T) = \mu_0 \, exp\left[-\frac{E_a}{k_B T} - C\left(\frac{\sigma}{k_B T}\right)^2\right] \tag{6.1}$$

where μ_0 is the infinite temperature mobility, E_a (= a quarter of the reorganization energy, λ) is the polaron activation energy, and σ is the energetic width of a Gaussian DOS. However, what has been in debate over the years is, the numerical value of C factor, which weighs the relative contribution of disorder and polaron effects in Equation 6.1. Recently, this issue was investigated by Fishchuk *et al.* by combining effective medium approximation (EMA) calculations and KMC simulations.[86] They showed a dependence of C factor on the σ/E_a ratio which has also been confirmed by various other approaches.[93–95] Nonetheless, there have also been contrasting reports questioning the variability of C factor in Equation 6.1.[96] In view of this, I specifically intended to answer two conceptual questions in this work: i) Whether an universal scaling relation, implying a constant C factor, regarding the polaron formation energy is really obeyed or not? ii) If the C factor varies with material parameters, or in other words, if it varies with experimental conditions, what is the impact of this variation on the analysis of temperature-dependent experimental transport data?
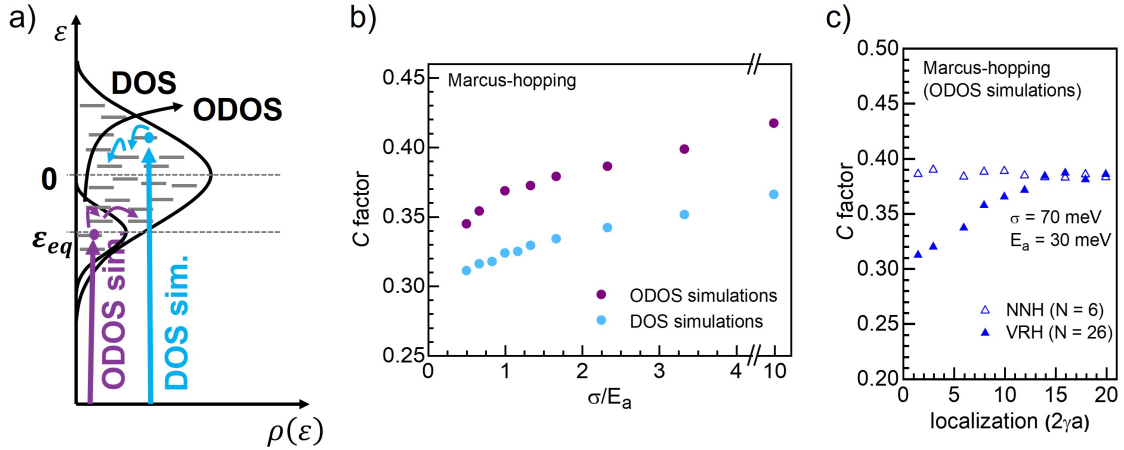
Figure 6.1: a) Schematic illustration of the two simulation approaches used in Chapter 8, namely DOS simulation approach and ODOS simulation approach (see text for details). b) Variation of C factor with the σ/E_a ratio for both, DOS and ODOS simulations. c) Variation of C factor with the localization parameter $2\gamma a$ for nearest neighbor hopping (NNH) and variable range hopping (VRH) regime.

I addressed the first question on the basis of the Marcus transition model (Equation 3.6) for charge transport by using KMC simulations. The site energies were drawn randomly from a Gaussian distribution (Equation 3.3). As explained briefly in Chapter 5, the simulations were done using the conventional '*DOS approach*' ($\varepsilon_0 = 0$ in Equation 3.3) as well as '*ODOS approach*' ($\varepsilon_0 = \varepsilon_{eq} = -\sigma^2/k_B T$ in Equation 3.3). The latter simulations were performed to exclude the effect of initial non-equilibrium, time-dependent nature of the energetic relaxation process on the simulated diffusivity. After the excitation was generated (either within DOS or ODOS, see Figure 6.1a), the diffusion of the excitation was executed and diffusivity was calculated as, $D = \Delta x^2/t$ (where Δx is the net displacement of the excitation and t is the simulation time).

We systematically examined the dependence of C factor on the polaronic contribution magnitude and we obtained that the factor C in Equation 6.1 increases with increasing σ/E_a ratio, i.e., with increasing relative strength of disorder (Figure 6.1b). This observation was in agreement with Fishchuk *et al.*[86] Simulations performed using the conventional DOS approach resulted in a lower value of the C factor as compared to the ODOS simulations, i.e., a smaller contribution of disorder to the transport, depending on how far the transport occurs from equilibrium. Moreover, the C factor obtained after including the polaronic effects was always smaller than the one obtained using Miller-Abrahams (MA) rate ($C_{MA} \approx 0.44$). However, in the limiting case of vanishing E_a, as represented by the data point with $\sigma/E_a = 10$ in Figure 6.1b, the MA result was obtained asymptotically. This further illustrated that any contribution from the geometric reorganization of the molecule leads to a reduced relative weight of the contribution of disorder to the transport.

The simulations discussed above (Figure 6.1b) were performed within the premise of nearest-neighbor hopping (NNH). It is known, however, that jumps to the non-nearest neighboring sites can also contribute to excitation transport, as described within the premise of variable range hopping (VRH). The probabilities for such jumps are determined by the localization parameter of the excitation ($2\gamma a$). VRH was implemented in KMC simulations by allowing hops to sites more distant than the nearest ones. The results for an exemplary case where long-distance jumps to up to 26 neighbors were considered, i.e., up to the third nearest neighbor, are shown in Figure 6.1c. Since, irrespective of the inverse localization length (γ) value the NNH is preserved at N = 6, no dependence is observed in the variation of C factor for this case. However, for VRH, the C factor increases with increasing $2\gamma a$ value and the values converge to the value of NNH at large localizations, since at large localization (or poor electronic coupling) NNH becomes dominating.

Overall, the simulation results showed that the value of C factor decreases whenever the contribution of disorder to the transport decreases. This happens when i) the transport is not in equilibrium, ii) when reorganization contributes to the transport and iii) when the wavefunction of the excitation is delocalized. In conclusion, the simulation study demonstrated that an "universal scaling relation" is not followed, at least not in the strict mathematical sense. For practical purpose, it is safe to assume that under thermal equilibrium, C ranges around 0.40 ± 0.05 and therefore as a next step, I evaluated the impact of this variation on the analysis of experimental transport data.

A frequently adopted procedure in the community to obtain the energetic disorder (σ) is to analyze the T-dependence of zero-field mobility assuming $C_{MA} = 0.44$ within a purely disorder-controlled MA formalism (i.e., $E_a = 0$ in Equation 6.1), as established by previous KMC and theoretical approaches:

$$\mu(T) = \mu_0 \, exp\left[-0.44\left(\frac{\sigma}{k_B T}\right)^2\right] \tag{6.2}$$

However, this procedure has a shortcoming, because disorder and reorganization energy are entangled, as reflected in Equation 6.1. So, we illustrated how much difference can be expected in the σ values when different formalisms are used to fit the data. For this assessment, I analyzed the T-dependence of zero-field time of flight (TOF) mobility for holes in four phenanthrene indenofluorine copolymers reported by Hoffmann *et al.*[184] labeled as copolymer 1, 3, 7 and 9 (see Chapter 8 for chemical structure and experimental data). To assess the dependence of the σ values on the C factor, the E_a values calculated using density functional theory were used in Equation 6.1 for several values of C factor. A comparison of the fits to the experimental data using Equation 6.1 ($C = 0.35, 0.4$ and 0.44) and Equation 6.2 is shown exemplary for copolymer-1 in Figure 6.2. It illustrates that the fits with different approaches are indistinguishable. We observed that the σ values obtained using different approaches differ
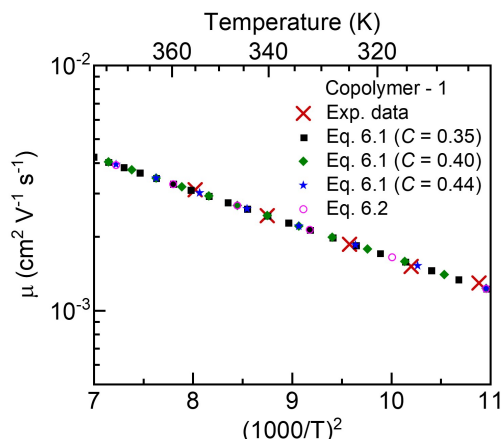
Figure 6.2: Comparison of the fits done by using Equation 6.1 with $C = 0.35, 0.4$ and 0.44 and by using Equation 6.2 (MA rate) for an exemplary case of copolymer 1 from Hoffmann *et al.*[184]

by less than 10% from each other for all the copolymers (Table II, Chapter 8). These results implied that the consideration of polaronic contribution to the transport description is not critical for the determination of disorder value, as long as C ranges around $C = 0.40 \pm 0.05$. This work also provided a "legitimization" of the use of simple and material-independent MA rate model for the description of charge transport in realistic disordered films; a message which is especially relevant for the experimentalists who routinely use GDM for their data analysis and naturally want to know to what extent this zero-order approach is accurate for the determination of DOS width.

6.2 Impact of Energy Correlations on Narrowing of Occupied Density of State Distribution for Charge Carriers at Low Temperatures in Disordered Organic Semiconductors

The study presented in Chapter 9 is about the impact of energy correlations on the relaxation of charges within the regime of dispersive charge transport. Since in the previous study (Chapter 8), I learned that reorganization energy does not contribute significantly to charge transport in AOSFs, the analysis in Chapter 9 was performed by describing the hopping rates in terms of purely disorder-controlled MA rate equation (Equation 3.4). In this work, low temperature thermally stimulated luminescence (TSL) experimental data was used as a benchmark for the KMC investigations.

As explained in Chapter 5 and Chapter 6.1 (Figure 6.1a), in the regime of non-dispersive quasi-equilibrium transport, ODOS is formed by the charges distributed around the thermal equilibrium energy ($\varepsilon_{eq} = -\sigma_{DOS}^2/k_B T$). However, at low temperatures ($\sigma_{DOS}/k_B T << 1$) thermal equilibrium is unattainable. Therefore, at such temperatures, the photogenerated
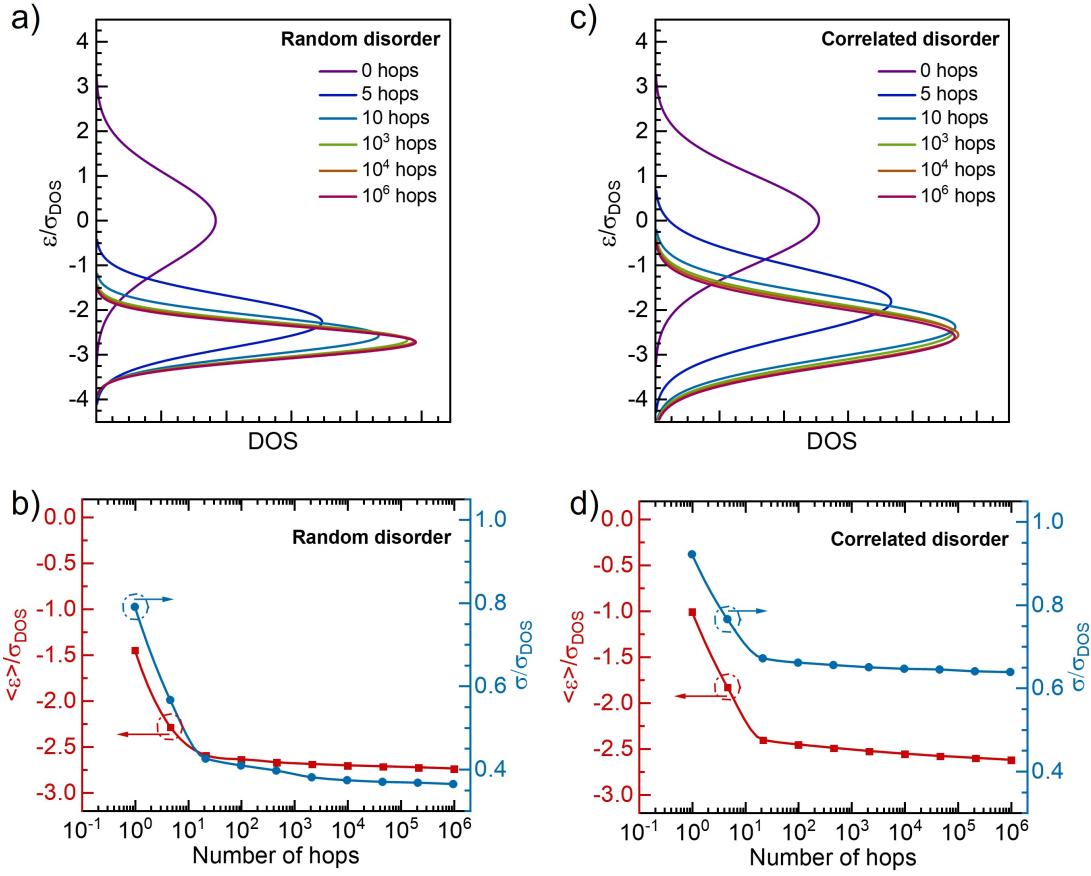
Figure 6.3: Evolution of charge distribution with the number of hops for a system with a) random and c) correlated disorder. The data illustrated are the Gaussian fit results of the energy distribution of charges obtained after the specified number of hops. Variation of mean energy ($< \varepsilon >$) and width (σ) of the energy distribution (both normalized by the DOS width, σ_{ODOS}) with the number of hops, for b) random and d) correlated disorder.

charge carriers hop preferentially towards the lower energy sites until they reach the band tail where the probability of further downward hops is so low that the charge carriers get trapped in these tail states to form the ODOS. TSL curve maps the distribution of these localized charge carriers within the ODOS. The high-temperature wing of the TSL curve is an exact replica of the deeper portion of the DOS distribution and thus, it's Gaussian analysis yielded the effective DOS width, σ_{DOS}. Moreover, a Gaussian fit of the whole TSL curve allowed us to determine the ODOS width (σ_{ODOS}). TSL experiments conducted on films of eighteen commonly used OLED materials (performed by Andrei Stankevych at IOP, Kiev; see Chapter 6.7 for author contributions) led to a rather general observation, that the ODOS distribution formed at low temperatures is narrower as compared to the DOS, and that it leads to an universal ratio of $\sigma_{ODOS}/\sigma_{DOS} \approx 2/3$.

In order to gain deeper insight into this effect, I utilized the variable time step KMC (vt-KMC)

simulations developed in Chapter 8. In vt-KMC, the time step is evaluated as the inverse of the hopping rate thus, as the charges relax within the DOS, the hopping rates can decrease abruptly which leads to a non-linear increase in the time step during the relaxation process. For comparison with the TSL experiments, it was necessary to probe the long-time limit of the energetic relaxation of the charges and therefore I decided to consider vt-KMC simulations for such an analysis. Figure 6.3a shows the vt-KMC results for the evolution of the distribution of charge carriers (with $\sigma_{DOS} = 50$ meV) in a system with random disorder at $T = 5$ K. The data illustrated are the Gaussian fits of the energy distribution of the charges after a certain number of hops and suggests that the charge carrier ensemble moves to deeper states and gets narrower with the increasing number of hops. Figure 6.3b plots the variation of mean energy ($< \varepsilon >$) and the width (σ) of the charge carrier ensemble, both normalized by σ_{DOS}, as a function of number of hops. Since only newly visited sites contribute to the energetic relaxation process, $< \varepsilon >$ and σ decrease significantly within the first 20 hops followed by a decrease in the relaxation rate. The charge carrier ensemble after 10^6 hops was considered as the ODOS distribution and the width of this ODOS distribution (σ_{ODOS}) was compared with the width of the TSL signal. It was observed that the calculated $\sigma_{ODOS} = 0.36\,\sigma_{DOS}$ did not match the experimental results. The system with random disorder was therefore considered unsuitable for the correct explanation of the TSL results. This observation also served as a motivation behind the exploration of an alternative approach.

While it is known that, energy correlations have a significant role in describing the field dependence of mobility; before this work, they were never considered important for the description of energetic relaxation of charges within the DOS. Nevertheless, since TSL experiments are performed at zero-fields and most of the studied organic materials used in this study are polar in nature (cf. Chapter 3.3), I advanced the vt-KMC simulations to include the effect of energy correlations. Figure 6.3c shows the evolution of charge carrier distribution in a system with correlated disorder. Like the system with random disorder, the charge carrier ensemble shifts to deeper states with the increasing number of hops. However, unlike the system with random disorder, the narrowing effects are less significant. As shown in Figure 6.3b and d, the shift in mean energy ($< \varepsilon >$) after 10^6 hops is almost equal for both systems, however, the narrowing of the charge carrier distribution within the first 20 hops is drastically suppressed in the case of system with correlated disorder. This led to a higher ODOS width of $\sigma_{ODOS} = 0.64\,\sigma_{DOS}$ for the medium with spatially correlated disorder (Figure 6.3d), in quantitative agreement with the TSL experimental data. Evidently, in the case of random disorder all hops to the new sites contribute to the narrowing, whereas hops among the correlated sites with almost the same energies do not.

In brief, the vt-KMC simulation based study illustrated that the "spectral narrowing" effect as observed in TSL experiments, is a genuine property of the carrier relaxation within the Gaussian DOS at low temperature and that spatial correlations among the energy of the

hopping sites have a significant effect on this narrowing effect. Moreover, though it was never considered important in the past, a key finding of this work is that the introduction of energy correlations, which are indeed present in organic media, allows reproducing experimentally obtained values for the ODOS width, i.e., σ_{ODOS} in a correlated system $\approx$ TSL σ_{ODOS}.

6.3 Kinetic Monte Carlo Study of Triplet-Triplet Annihilation in Conjugated Luminescent Materials

After understanding the impact of material parameters on charge transport in AOSFs, I investigated the transport of (neutral) triplet excitations through the inhomogenously disordered medium such as AOSF. This was achieved by studying triplet-triplet annihilation (TTA) in a model system of conjugated polymers because TTA, being a bimolecular process, involves the interaction of two triplet excitons and thus depends on triplet diffusivity. Concomitantly, the fundamental understanding developed in the process of understanding triplet diffusion was utilized to determine the crucial parameters which need to be tuned to obtain a high yield of TTA based delayed fluorescence (DF) in conjugated polymers, at room temperature (where devices typically operate).

The motivation for the latter objective comes from the fact that triplet transport (like charge transport) in AOSFs is thermally activated, therefore, an increase in temperature enables bimolecular TTA leading to increased DF by the up-conversion process. However, it also enables monomolecular quenching of the triplet excitons at the impurity centers. This leads to a peak in the temperature dependence of DF intensity, with the maximum DF obtained at temperature below RT. This was explicitly shown in the experimental findings by Hoffmann *et al.* in a series of poly(p-phenylene) derivatives,[185] and more recently by Raišys *et al.* for anthracene derivatives.[186] Thus, the KMC code developed to study the effect of material parameters on charge transport in previous studies (Chapter 8 and Chapter 9) was further advanced from single-excitation simulations to multi-excitation simulations; to account for the bimolecular exciton-exciton annihilation processes. In the work presented in Chapter 10, I employed these KMC simulations to study the complex interplay between bimolecular TTA and monomolecular quenching of triplets at the non-radiative trap sites. For this purpose the effects of morphology and different system parameters such as the length of a conjugated chromophore (n), inverse localization length along ($\gamma_{\parallel}$) and perpendicular ($\gamma_{\perp}$) to the conjugated chromophore, trap concentration (c_t) and energetic disorder (σ) on the temperature dependence of quenching, DF, and phosphorescence (Ph) efficiency were simulated.

Following the approach of Athanasopoulos *et al.*,[79] we described a conjugated chromophore as a segment of 'n' isoenergetic lattice sites, as depicted in Figure 6.4a. Different values for

inverse localization length (γ) between the sites parallel to the chain ($\gamma_\parallel$) and perpendicular to the chain ($\gamma_\perp$) were used to obtain different electronic coupling for triplet transport parallel and perpendicular to the conjugated chromophores. Thus, the ratio $\gamma_\parallel : \gamma_\perp$ was used to control the directionality of triplet transport. Moreover, since each conjugated chromophore consisted of lattice sites with identical energy, while the energy differed between the conjugated segments, the hops within a conjugated segment were expected to be inherently faster than the hops between the conjugated segments. This procedure allowed us to treat the conjugation effects in a stochastic manner. Furthermore, triplet transport also depends on the number of accessible sites and for conjugated polymers different morphologies result in a different number of accessible neighbors. In a realistic film, the morphology is much complex and more sophisticated approaches exist to represent them, however, two limiting real morpholigies is one where all chains are aligned and one where all chains cross each other heavily. We realized these two limiting cases in our model through two design morpholigies, referred to as parallel (Figure 6.4b) and grid (Figure 6.4c) lattice. For the parallel lattice, the chain orientation is the same in each layer, whereas, for grid lattice, the chain is rotated by 90° between alternative layers. This gridlike arrangement increases the number of contact points to next neighbors in the layer above and below from previously only two contacts in total to several contacts (Figure S3, Chapter 10). As a consequence, more hops to sites of different energy are possible, and this impacts triplet diffusion significantly.

When comparing the effect of two lattices, we observed less quenching and more DF for the grid lattice (green circles in Figure 6.4d) as compared to parallel lattice (blue open circles) at a fixed conjugation length ($n = 10$). This applies not only to the peak value but, also to the value at 300 K. Evidently, the film morphology plays a key role in determining the relative extent of bimolecular and monomolecular recombination. A morphology of mostly parallel chains, conducive for directional transport, favors quenching at the trap sites whereas a gridlike morphology of many crossing chains that allows for more isotropic hopping enhances the fraction of TTA events. Furthermore, our study of delocalization effects suggested that increasing the length of conjugated segments, e.g. from $n = 10$ to $n = 40$ (green open *vs.* solid circles in Figure 6.4d) improves DF by raising the number of readily accessible crossing points to other chains, thus increasing the isotropy of transport. However, no significant effect was observed when varying the $\gamma_\parallel : \gamma_\perp$ ratio.

For a closer inspection on the impact of static energetic disorder, the variation of quenching and DF was simulated for different energetic disorder values, as shown in Figure 6.5a. We found that with the increase in energetic disorder, both TTA and quenching rates slow down and as a result the DF peak value remains the same but shifts to higher temperatures (Figure 6.5a). In fact, the same curves are just stretched towards higher temperatures because of the inherent scalibility between disorder and temperature within the MA hopping regime (Equation 3.5). This is illustrated in Figure 6.5b, where the same data is displayed on a
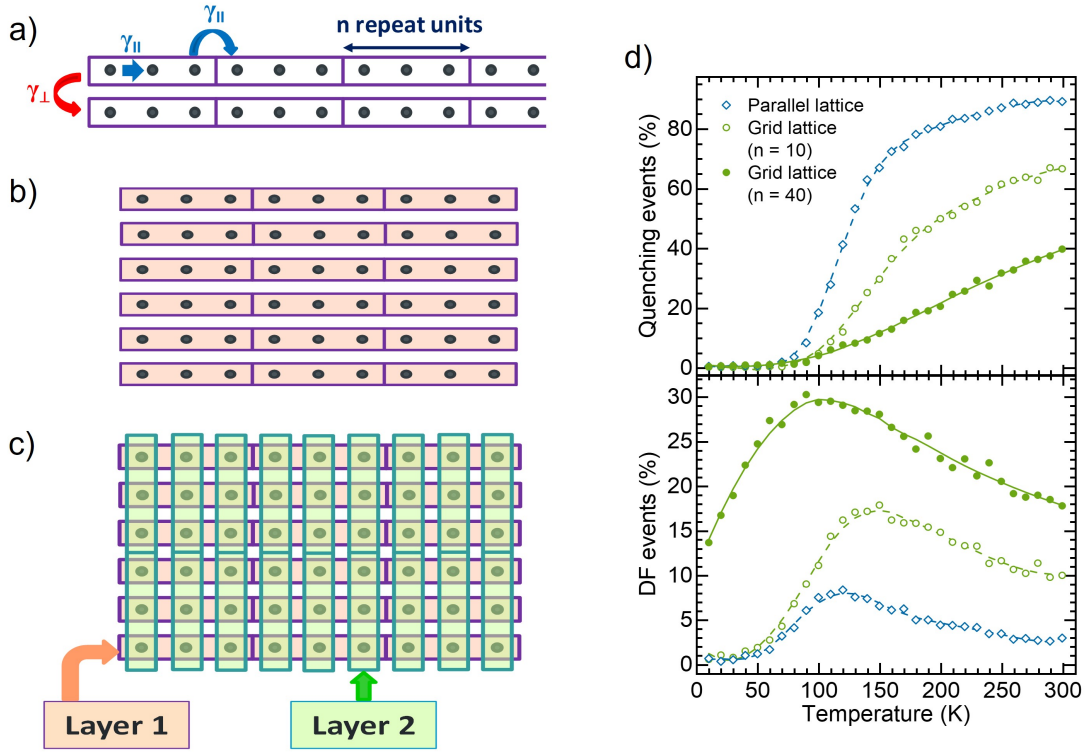
Figure 6.4: a) Pictorial representation of the design of a conjugated segment with "n" isoenergetic repeat units and separate inverse localization lengths for triplet transport parallel and perpendicular to the chain. (b) Top view of the parallel lattice with all the chains along y direction in all the layers. (c) Top view of the grid lattice with all the chains in layer 1 and layer 2 aligned along y and x direction, respectively. d) Comparison of simulated quenching and DF events for grid (green circles) and and parallel lattice (blue diamonds). Effect of delocalization in the case of grid lattice is shown by varying the length of conjugated segment (n) from 10 (green open circles) to 40 (green solid circles). Lines serve as a guide to the eye.

logarithmic scale as a function of σ/k_BT. The quenching and DF events superimpose on each other for similar σ/k_BT values and the DF peaks at $\sigma/k_BT \approx 3$ for all values of energetic disorder. In addition, we also explored the effects of polaronic contributions to hopping rates by using Marcus transition rates (Equation 3.6) and we found that, the choice of hopping rates is not critical for determining the TTA yield and that changes in reorganization energy do not affect the intensity of room temperature DF (Chapter 10).

Moreover, the role of disorder was found to be twofold. Firstly, it changes the hopping rate such that high disorder (dispersive transport) favors bimolecular TTA over monomolecular quenching at the trap sites. The second and perhaps less appreciated, though relevant, role is that it causes filamentary transport. In other words, by changing the energy landscape it modifies the spatial distribution of the triplet states. For $\sigma/k_BT > 1$, the triplets relax energetically and hop predominantly through the valleys resulting in a nonuniform spatial distribution of triplets. As TTA is a bimolecular process, the TTA events also take place
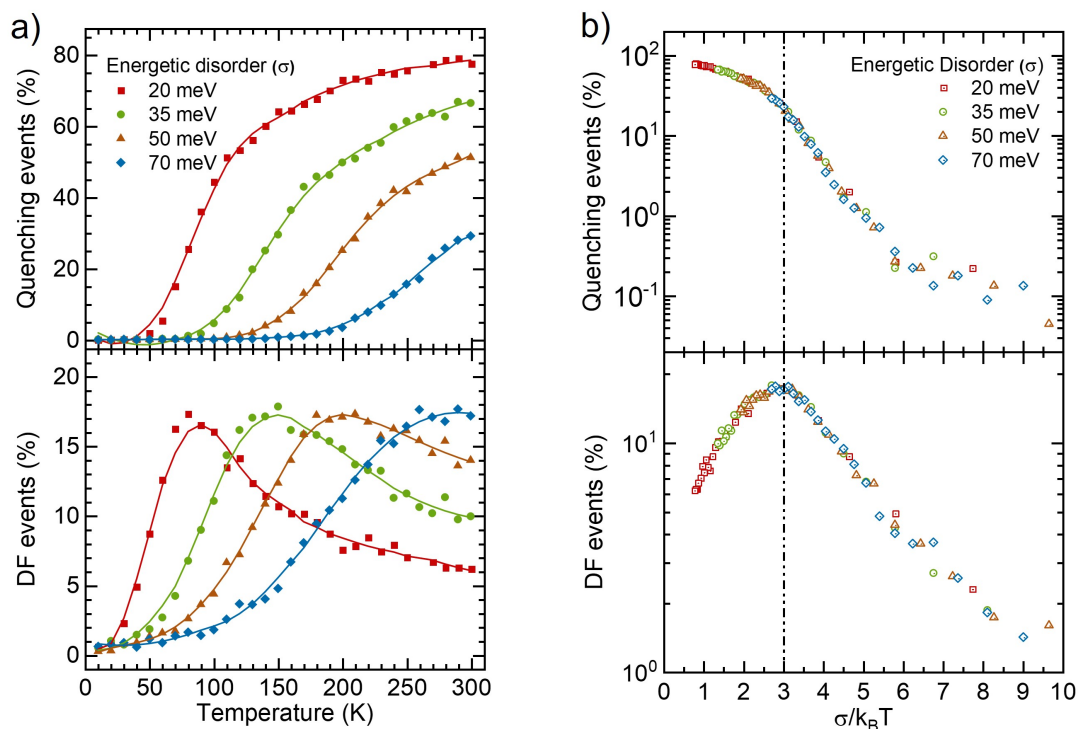
Figure 6.5: Effect of static disorder (σ) is investigated on the temperature dependence of quenching and DF events for Miller-Abrahams rate. b) shows data in a) represented with respect to thermal energy normalized disorder ($\sigma/k_B T$) values instead of temperature on a semilog scale. A grid morphology with the length of the conjugated segment $n = 3$ and a constant coupling along and perpendicular to the chain ($\gamma_{\parallel} = 1.5\,nm^{-1}$ and $\gamma_{\perp} = 2\,nm^{-1}$) was used. Solid lines serve as a guide to the eye.

predominantly in the valleys. This implies a higher effective TTA rate than expected from spatially averaged triplet density. Evidently, a high $\sigma/k_B T$ value ensures a high TTA yield.

6.4 Regiochemistry of Donor Dendrons Controls the Performance of Thermally Activated Delayed Fluorescence Dendrimer Emitters Translating in Their Use in High Efficiency Solution-Processed Organic Light-Emitting Diodes

In the publication presented in Chapter 10, I focused on understanding the crucial material parameters affecting (intermolecular) triplet transport between the chromophores with an objective of establishing design rules for the optimization of TTA based DF emitters. Next, I turned my attention towards contributing to the understanding of intramolecular excitation transfer from the lowest energy triplet state to the lowest energy singlet state, the so called reverse intersystem crossing (RISC) process, and how it can be optimized for the design

of efficient TADF dendrimers. To date, there have been only a few reports using TADF dendrimers and most of them show far less efficiencies than small molecule (low molecular weight) TADF emitters. This in part is due to a poor understanding of their photophysics and the RISC mechanism. Therefore, firstly in Chapter 11, I focused on investigating the effect of regiochemistry, notably the connection of donor dendrons and acceptor moieties via *meta-* or *para-* position on a bridging phenyl ring, on the photophysical properties and RISC mechanism. The insights obtained in Chapter 11 were exploited in Chapter 12 to further improve the TADF dendrimer design.

As a first step, I investigated the nature of lowest energy singlet excited states in solution. Figure 6.6a shows the chemical structure of the dendrimers investigated in Chapter 11. The RT absorption and emission spectra of the dendrimers as well as the dendron unit (dendritic carbazoles shown with blue color in Figure 6.6a) in toluene solution at low concentration are shown in Figure 6.6b and c (semilogarithmic plots). The absorption of all the dendrimers is characterized by two distinct bands. The strongly absorbing band below 3.5 eV arises from the locally excited (LE) transitions on the dendron unit. By comparison with the absorption spectra of the reference chemical units, it was shown that this structured dendron absorption comprised of two vertical excitation processes: i) a lower energy absorption from an excitation localized on the central electron-rich carbazole (denoted as LE_1) and ii) a higher energy absorption localized on the peripheral carbazoles (denoted as LE_2). In addition, tBuCz3pTRZ was characterized by the presence of a broad, strong absorption band in the range of $2.8 - 3.4$ eV. This feature remained at the same energy, but the extinction coefficient reduced by over an order of magnitude when the more conjugated *para*-connection was replaced by the less conjugated *meta*-connection in tBuCz2mTRZ, tBuCz3mTRZ and tBuCz4mTRZ. We ascribed the nature of this lowest excited state as a charge transfer (CT) transition from the dendron donors to the triazine (TRZ) acceptor. The comparable extinction coefficients of CT_1 and LE_1 bands in tBuCz3pTRZ indicated a significant electron-hole wavefunction overlap and consequently some admixture of both $\pi - \pi^*$ and CT character. Moreover, the *meta*-dendrimers were also characterized by a distinct CT_2 band, with larger extinction coefficient than the CT_1 band. Emission exhibited simpler spectral features (Figure 6.6c). All dendrimers exhibited a CT_1 emission, and, in addition, *meta*-dendrimers also showed a high-energy LE_1 emission band of the dendron unit. This non-Kasha emission, or in other words, simultaneous emission from different energy states can only be observed when the rate of internal conversion from the LE_1 to CT_1 state is slow enough to compete with the rate of radiative decay from LE_1 state. Internal conversion from LE to CT state requires electron transfer to the TRZ acceptor moiety which is expected to be slow in the poorly conjugated *meta*-dendrimers as compared to tBuCz3pTRZ and thus explains the origin of non-Kasha emission in *meta*-dendrimers.

Next, I investigated the photophysics of triplet excited states and TADF properties in
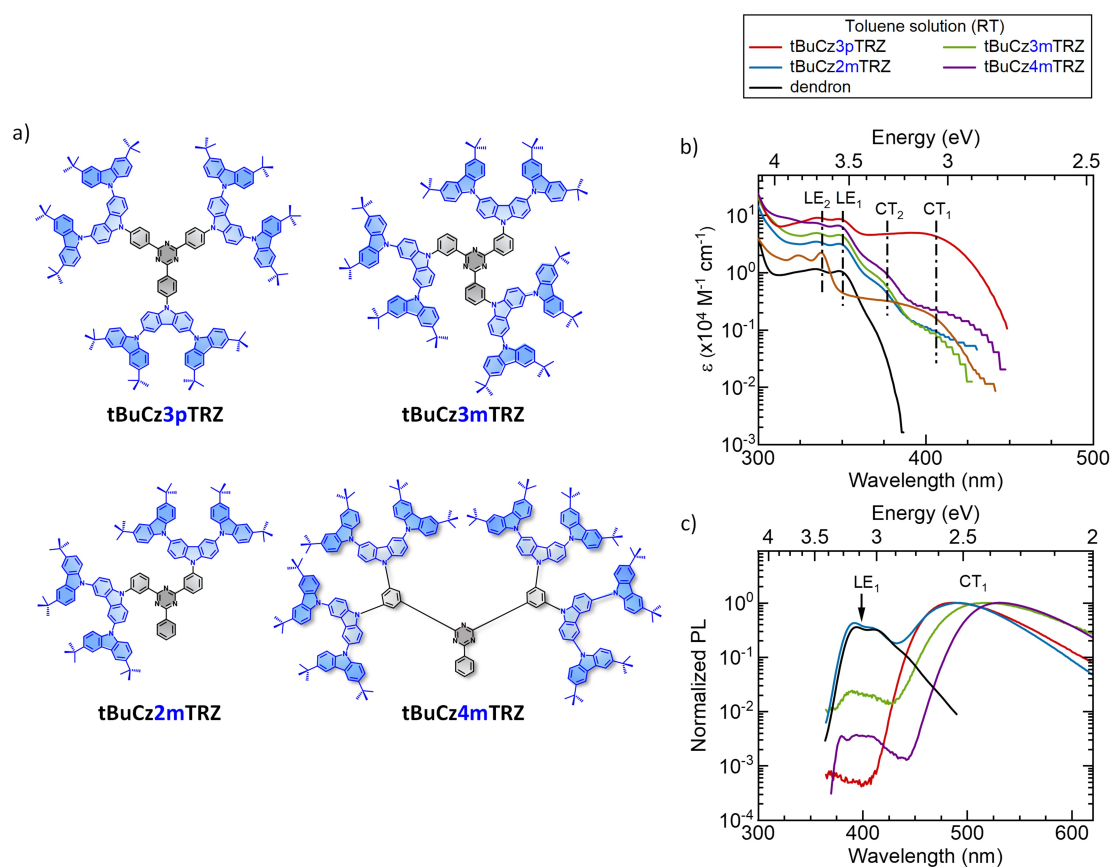
Figure 6.6: a) Molecular structures of tBuCz3pTRZ, tBuCz3mTRZ, tBuCz2mTRZ and tBuCz4mTRZ. RT solution photophysics of the dendrimer and model compounds: b) Molar absorptivity and c) normalized emission spectra (excitation wavelength, $\lambda_{exc} = 300$ nm) in toluene on a log scale. LE_1, LE_2, CT_1, CT_2 refer to the lower and higher energy singlet LE and CT states as described in the text.

doped films (10 wt% dendrimer in mCP; mCP: 1,3-Di(9H-carbazol-9-yl)benzene). For TADF materials, the energy difference between the lowest singlet and triplet excited states (ΔE_{ST}) is a crucial parameter. The 5 K prompt fluorescence, PF (delay time: 10 ns; gating time: 7 ns) and phosphorescence, Ph (delay time: 10 ms; gating time: 1 ms) were measured in doped films to estimate ΔE_{ST}. These spectra are shown in Figure 6.7a. The ΔE_{ST} value decreases from 100 meV to 80 meV, when moving from *para*-dendrimer tBuCz3pTRZ to *meta*-dendrimer tBuCz3mTRZ. Temperature dependent photoluminescence (PL) decay curves showing temperature activation of delayed fluorescence for tBuCz3pTRZ and tBuCz3mTRZ are shown in Figure 6.6b. PL decay curves at 300 K along with the respective PL quantum yield (PLQY) values were used to calculate the quantum efficiencies and rate constants associated with different kinetic processes. Though the PLQY value for tBuCz3pTRZ (89%) was higher than tBuCz3mTRZ (81%), the contribution of DF to the PL was higher in
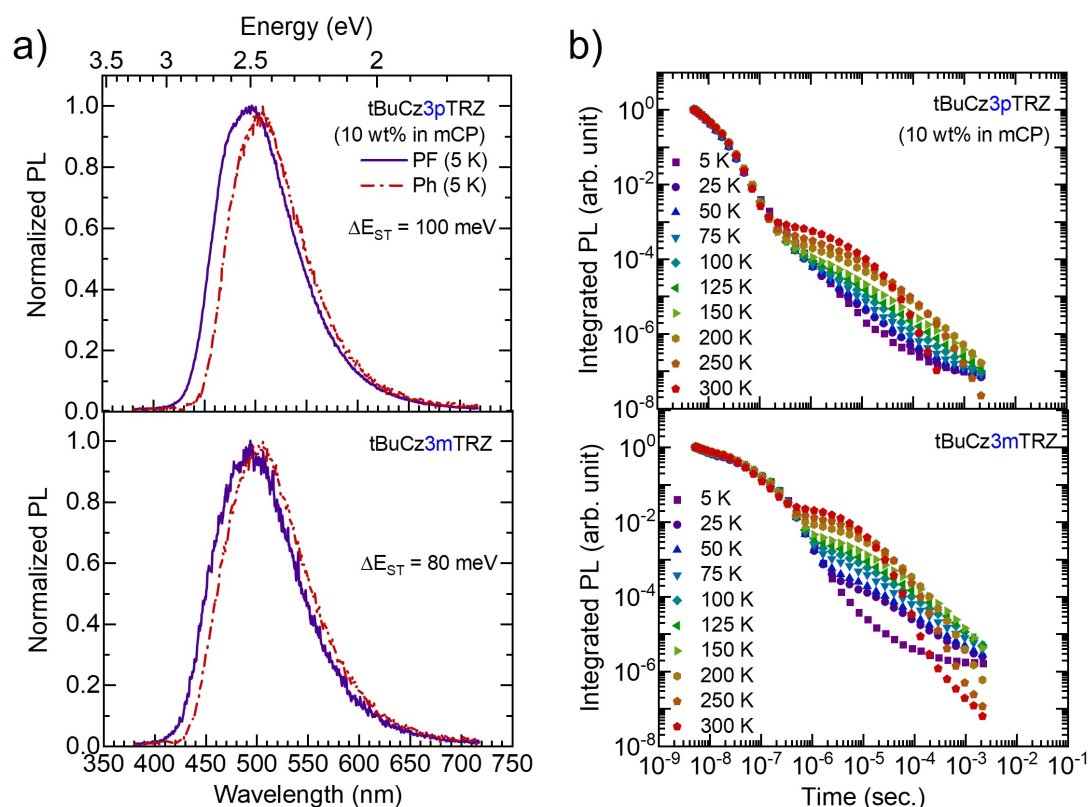
Figure 6.7: a) 5 K prompt fluorescence (delay time: 10 ns, blue solid line) and 5 K phosphorescence (delay time: 10 ms, red dash-dotted line) and b) temperature dependent PL decay curves for 10 wt% dendrimer films doped in mCP (excitation wavelength, λ_{exc} = 355 nm).

tBuCz3mTRZ (ϕ_{DF} = 0.63) as compared to tBuCz3pTRZ (ϕ_{DF} = 0.19), suggesting higher RISC efficiency in *meta*-connected dendrimer. Moreover, while the ISC rate constant (k_{ISC}) remained approximately constant, the RISC rate (k_{RISC}) increased by about 7 times in going from tBuCz3pTRZ to tBuCz3mTRZ.

Though, this was the first report where *meta*-connected dendrimers were reported, for small molecule TADF emitters, *meta*-isomers were often found to perform better than *para*-isomers because of the reduced ΔE_{ST} in *meta*-isomers as a result of the reduced conjugation between the donor and acceptor units (see Chapter 4.1 for more details). In this work as well, the extinction coefficient for more conjugated *para*-dendrimer was found to be much higher as compared to that of less conjugated *meta*-dendrimer (Figure 6.6b) and consequently *meta*-dendrimers were found to exhibit reduced ΔE_{ST} values as compared to the *para*-dendrimer. However, the decrease in conjugation and the associated decrease in ΔE_{ST} alone could not explain the increase in k_{RISC} in going from *para*- to *meta*-connected dendrimers. Therefore, I recalled other factors within the first order perturbation theory (see subsection 4.1.1 for details) which need to be considered in the chemical design of dendrimers other than ΔE_{ST},
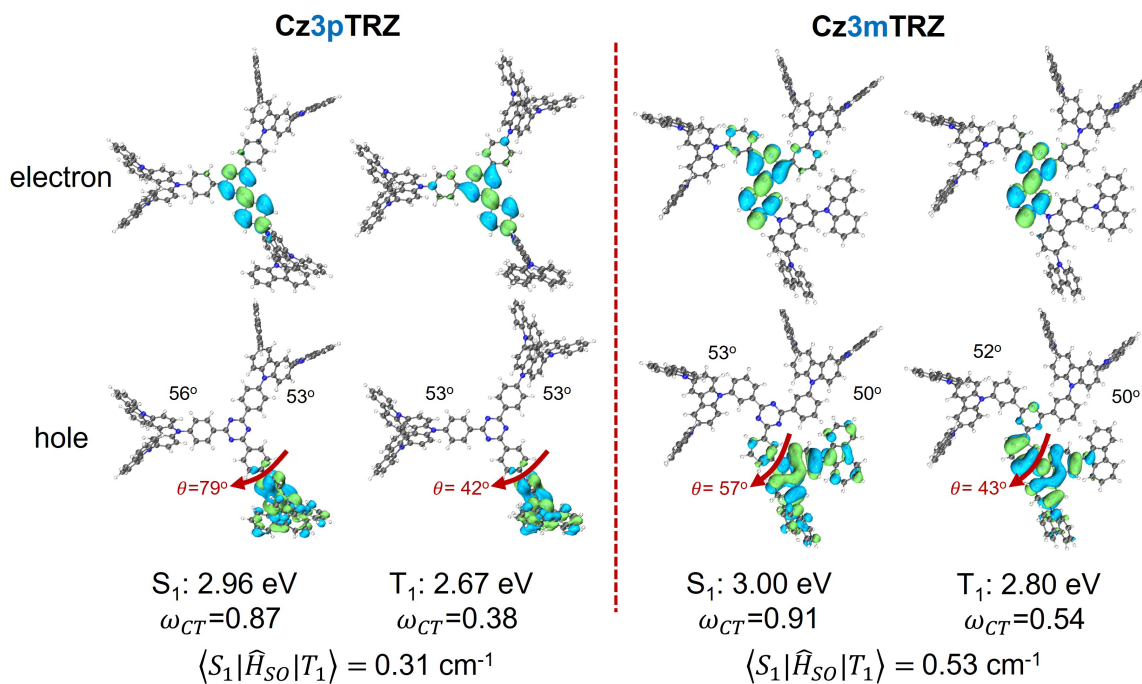
Figure 6.8: Natural transition orbital (NTO) pairs for the S_1 and T_1 states of Cz3pTRZ and Cz3mTRZ. The spin-orbit coupling (SOC) matrix elements are also provided.

namely the SOC matrix element for the RISC process and the reorganization energy.

Subsequently, quantum chemical calculations were performed by Dianming Sun (University of St. Andrews) and Stavros Athanasopoulos (Universidad Carlos III de Madrid), coordinated by me. The reader is referred to Chapter 6.7 for details regarding the author contributions of this publication. The calculation results, summarized in Figure 6.8, depict the hole and electron natural transition orbitals (NTOs) for the S_1 and T_1 states for Cz3pTRZ and Cz3mTRZ. It is important to note that tBu groups were replaced with hydrogen atoms for computational reasons. The S_1 states for both the dendrimers were found to be CT states, while the T_1 states were found to be hybrid CT-LE states. The SOC matrix element ($\langle S_1|\hat{H}_{SOC}|T_1\rangle$) was found to be higher for *meta*-dendrimer (0.53 cm^{-1}) as compared to *para*-dendrimer (0.31 cm^{-1}). The higher SOC in *meta*-dendrimer was ascribed to a change in the orbital character for the hole NTO between S_1 and T_1 states (while there was no change for Cz3pTRZ), which in accordance with El-Sayed rule should lead to higher SOC in Cz3mTRZ. The calculated intramolecular reorganization energy (λ_{intra}) for Cz3pTRZ (275 meV) was found to be higher as compared to Cz3mTRZ (155 meV). This is because, while the geometric relaxation in Cz3mTRZ is sterically restricted, it is possible for Cz3pTRZ to exhibit larger changes in dihedral angles. This implied a higher reorganization energy for the $T_1 \rightarrow S_1$ transition for Cz3pTRZ as compared to Cz3mTRZ.

In summary, we illustrated that lower ΔE_{ST}, higher SOC and lower λ combine to yield higher k_{RISC} in *meta*-dendrimers as compared to *para*-dendrimer. Though in the previous reports, the molecular design strategy of TADF emitters was focused on the minimization of ΔE_{ST} or increasing the SOC, the role of reorganization energy (λ) was often neglected. The study in Chapter 11 shows that λ can play an important role in controlling the RISC process, especially for the case of bulky dendrimers and that this can be changed as a function of the regiochemistry of the dendrimers.

6.5 Thermally Activated Delayed Fluorescent Dendrimers that Underpin High-efficiency Host-Free Solution-Processed Organic Light Emitting Diodes

Increasing RISC is a central issue for the design of TADF emitters and Chapter 11 highlights the design advantages of *meta*-dendrimers over *para*-densrimers with respect to achieving higher RISC rate. The findings of Chapter 11 also illustrate that the more conjugated *para*-dendrimer possessed higher radiative decay rates and higher oscillator strength of the lowest energy intramolecular CT transition. In fact, as summarized in Chapter 4.1, a key issue with the design of TADF emitters is to obtain high RISC rate and high radiative decay rates, simultaneously.

With the knowledge gained in Chapter 11, we surmised that a targeted emitter tBuCz2m2pTRZ (see Figure 6.9a for chemical structure) would inherit the key properties from both *para-* and *meta*-connected model dendrimers, i.e., a high radiative decay rate of tBuCz2pTRZ and a high k_{RISC} of tBuCz2mTRZ. To test this hypothesis, the relevant dendrimers were synthesized (by Dianming Sun, University of St. Andrews). Together with my colleague Eimantas Duda (see Chapter 6.7 for author contributions), I investigated their absorption and emission properties in solution and in solid-state. This study is presented in Chapter 12. Figure 6.9b shows the absorption spectra for the three dendrimers in toluene solution. For the reasons discussed in the previous section (Chapter 6.4), the molar extinction coefficient of lowest excited CT_1 state reduces from $\epsilon = 3500\,M^{-1}cm^{-1}$ for tBuCz2pTRZ to $\epsilon = 300\,M^{-1}cm^{-1}$ for tBuCz2mTRZ. Interestingly, the CT_1 absorption strength for tBuCz2m2pTRZ ($\epsilon = 1500\,M^{-1}cm^{-1}$) is found to be comparable to that of tBuCz2pTRZ. Since the strength of the extinction coefficient can be related to the oscillator strength of the dendrimers (cf. Equation 2.4), it is evident that the high oscillator strength of *para*-connected dendrons is conserved in tBuCz2m2pTRZ. Figure 6.9c shows the PL decay curves for neat dendrimer films at 300 K. The kinetic analysis of PL decay curves showed that for tBuCz2m2pTRZ, the radiative decay rate was about half as compared to tBuCz2pTRZ, yet four times greater than tBuCz2mTRZ. k_{RISC} in tBuCz2mTRZ and tBuCz2m2pTRZ was calculated to be 3-5 times higher as compared
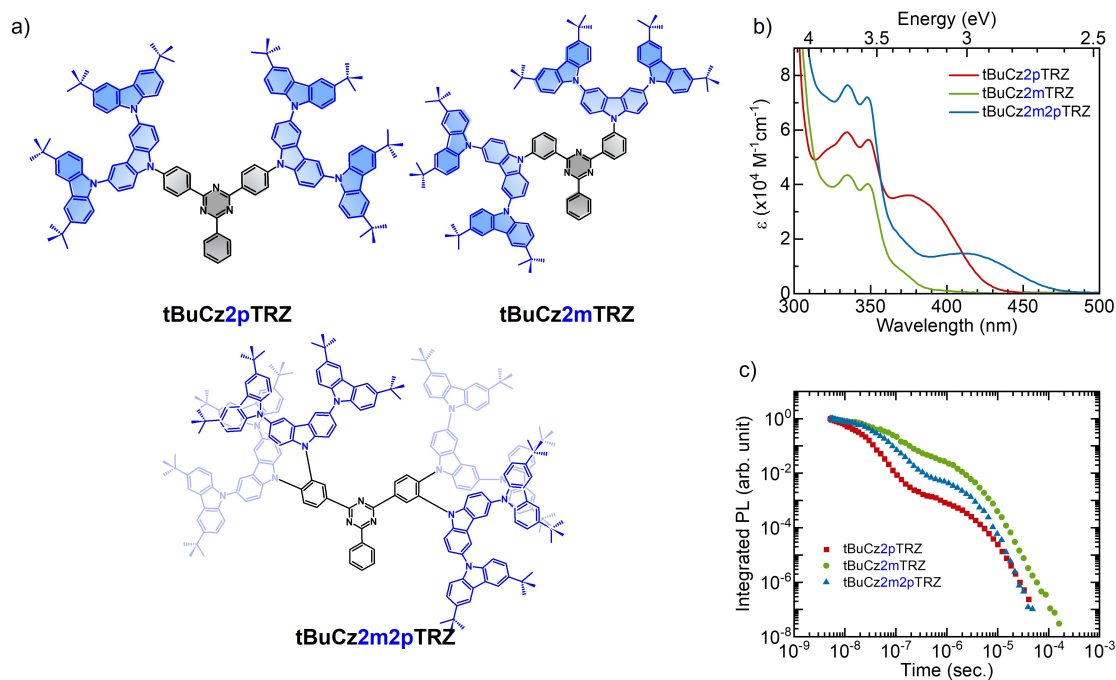
Figure 6.9: a) Molecular structures b) molar absorptivity measured in toluene solution and c) room temperature PL decay of neat films (excitation wavelength, $\lambda_{exc} = 355$ nm) of the dendrimers tBuCz2pTRZ, tBuCz2mTRZ and tBuCz2m2pTRZ studied in Chapter 12.

to tBuCz2pTRZ. Evidently, tBuCz2m2pTRZ embodies the best of both: higher radiative decay rate and RISC rate from *para-* and *meta*-connected dendrons. Furthermore, under N_2, tBuCz2pTRZ and tBuCz2mTRZ exhibited similar PLQY values of 61% and 59%, while tBuCz2m2pTRZ exhibited the highest PLQY of 86% in neat films. High PLQY in neat films illustrated another intrinsic advantage of tBuCz2m2pTRZ, i.e., a larger number of dendrons in tBuCz2m2pTRZ, as compared to the model dendrimers tBuCz2mTRZ and tBuCz2pTRZ, suppresses emitter to emitter interactions leading to reduced concentration quenching (see Chapter 4.2). Host-free solution processed OLEDs with tBuCz2m2pTRZ as emitters exhibited an excellent maximum external quantum efficiency (EQE_{max}) of 28.7%. Importantly, the severe efficiency roll-off of the OLEDs at practical luminescence efficiencies was found to be significantly improved when the non-doped (host-free) emissive layer was replaced with a doped emissive layer.

6.6 Low Efficiency Roll-off Blue TADF OLEDs Employing a Novel Acridine-Pyrimidine based High Triplet Energy Host

The investigations presented in Chapter 11 and Chapter 12 deal with the parameters affecting the RISC process so that the EQE_{max} of the TADF emitter based OLEDs can be enhanced.

Though, this is a necessary condition for the design of efficient OLEDs, it is not a sufficient one. Additional constraint is, obtaining high EQE at practical brightness levels (for ex. at 1000 cd m^{-1}), which can be ensured by optimizing the efficiency roll-off of the device. As illustrated in Chapter 12, it can be achieved by using doped emissive layers. This could either be done to balance the electron and hole transport in the emissive layer (cf. Chapter 12) or to confine the triplet excitons to emitters so that the detrimental bimolecular effects (described in Chapter 2.3) associated with the long-lived triplet excitons can be suppressed. In any case, a strict requirement is that the triplet energy (E_T) of the host material must be higher than that of the TADF emitter. This is particularly challenging for blue-emitting OLEDs as they require a $E_T > 3$ eV. As detailed in Chapter 4.2, additional complexities arise in bipolar D-A hosts due to the formation of intramolecular CT states, which leads to a narrower band gap and thus reduced E_T.

In the work presented in Chapter 13, acridine (donor) and pyrimidine (acceptor) were chosen as building blocks for the design of host materials because of their high triplet energies. In particular, the objective was to strategically use pyrimidine acceptor motifs with disrupted π-conjugation with an aim to increase the E_T of donor-acceptor type bipolar host materials. I investigated the host molecules 2PPA, 1PPA and 1MPA (Figure 6.10), based on acridine and three different pyrimidine groups, namely 2-phenylpyrimidine (2PhPy), 1-phenylpyrimidine (1PhPy) and methylpyrimidine (MePy). In order to estimate the triplet energies of the host materials, phosphorescence measurements were performed in toluene solution (concentration of $6-9 \times 10^{-5}$ M) at liquid nitrogen temperature (77 K). For 2PPA and 1PPA, the phosphorescence was found to be structured with 0-0 vibrational peaks at 2.81 eV (442 nm) and 2.76 eV (449 nm), respectively (Figure 6.10a and b). The lower energy for T_1 state in 1PPA as compared to 2PPA was accounted on the basis of the nature of this state, as the phosphorescence spectra of 2PPA and 1PPA were similar to the phosphorescence spectra of their respective pyrimidine acceptor motifs (2PhPy and 1PhPy). This indicated that the triplet in 2PPA and 1PPA has a localized exciton character (^{3}LE). Based on quantum chemical calculations (by Stavros Athanasopoulos, Universidad Carlos III de Madrid; see Chapter 6.7 for author contributions), the lower T_1 energy in 1PPA was attributed to the observation that the phenyl ring is planar with pyrimidine in 1PPA whereas there is a torsion in 2PPA. I measured the spectra at different excitation wavelengths between 300 and 350 nm, and found no change in the spectra. However, as shown in Figure 6.10c, the phosphorescence of 1MPA was found to depend on the excitation wavelength. When exciting with 300 nm (4.13 eV) and 320 nm (3.88 eV), I obtained a structured phosphorescence band with 0-0 vibrational peak at 3.18 eV. However, for excitation at 335 nm (3.70 eV) and 350 nm (3.54 eV), the phosphorescence band had a similar shape but was shifted to lower energy (with onset at 3.07 eV). To understand the nature and origin of these two bands, I measured the phosphorescence of acridine (donor) and MePy (acceptor), as well as the phosphorescence
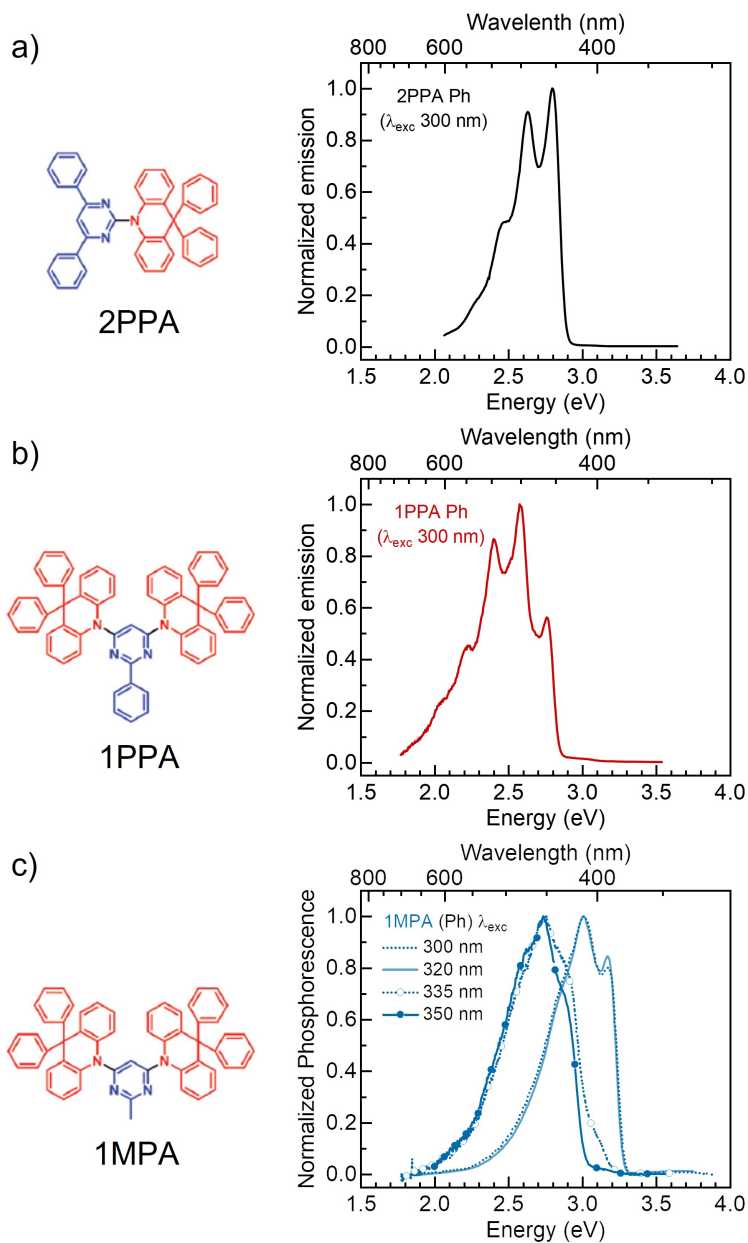
Figure 6.10: The phosphorescence (Ph) spectra (delay time: 150 ms, gate width: 50 ms) of a) 2PPA, b) 1PPA and c) 1MPA measured at 77 K in toluene glass. The excitation wavelengths (λ_{exc}) used for the measurements are specified in the respective plots. Molecular structures of 2PPA, 1PPA and 1MPA are also shown.

excitation spectra. Based on this data, we ultimately attributed the higher energy (T_2) state to be a ^{3}LE state localized on acridine and the lower energy T_1 state to be a state with mixed CT-LE character, where the LE contribution would be from the acridine.

In summary, the insights obtained in Chapter 13 exemplify the impact of reducing the conjugation length of the acceptor unit on E_T in D-A type bipolar host materials. While for 2PPA and 1PPA, the ^{3}LE state localized on the respective acceptor motifs (2PhPy and 1PhPy) were found to be the lowest energy triplet states, with an onset at about 2.9 eV. This was no longer the case when the conjugation was reduced to MePy with a phosphorescence 0-0 peak at 3.42 eV; well above the onset of phosphorescence of acridine motif. As a result of this reordering of the lowest energy triplet excited states, the T_1 state in 1MPA (E_T = 3.07 eV) became one with a mixed CT-LE character with the LE contribution from acridine. Furthermore, the host material 1MPA, with $E_T > 3$ eV, was combined with blue emitter to fabricate TADF OLED with low efficiency roll-off, even beyond the practical brightness of 1000 cd m^{-1}.

6.7 Author's contributions

Role of the Reorganization Energy for Charge Transport in Disordered Organic Semiconductors

This work is published in Physical Review B (*Phys. Rev. B*, **2021**, 103, 165202) and reprinted in Chapter 8. The authors are:

Rishabh Saxena, *V. R. Nikitenko*, *I. I. Fishchuk*, *Ya. V. Burdakov*, *Yu. V. Metel*, *Jan Genoe*, *Heinz Bässler*, *Anna Köhler*, and *Andrey Kadashchuk.*

I, V. R. Nikitenko, and Andrey Kadashchuk designed the study and wrote the manuscript. I wrote the Python program for KMC study, managed all the simulations, and interpreted the KMC data. V. R. Nikitenko, Ya. V. Burdakov, and Yu. V. Metel were responsible for multiple trapping and release (MTR) calculations. I. I. Fishchuk performed effective medium approximation (EMA) calculations. I analyzed the experimental data based on theoretical and simulation results after the discussions with Heinz Bässler and Anna Köhler. Jan Genoe, Heinz Bässler and Anna Köhler discussed the results and critically revised the manuscript.

Impact of Energy Correlations on Narrowing of Occupied Density of State Distribution for Charge Carriers at Low Temperatures in Disordered Organic Semiconductors

This work is in preparation and the draft is reprinted in Chapter 9. The authors are:

Andrei Stankevych,‡ **Rishabh Saxena**,‡ *Alexander Vakhnin*, *Christof Pflumm*, *Jan Genoe*, *Heinz Bässler*, *Anna Köhler*, and *Andrey Kadashchuk.*

‡ Andrei Stankevych and I contributed equally to this work.
Andrey Kadashchuk initiated this study, analyzed experimental results, and wrote a part of the manuscript. I wrote the Python program for variable time step (vt-KMC) approach, managed vt-kMC simulations, adapted kMC simulations to account for energy correlation effects, interpreted the simulation results and wrote a part of manuscript. Andrei Stankevych wrote the Python program for constant time step kinetic Monte Carlo (ct-kMC) approach, managed ct-kMC simulations, interpreted his simulation data, was responsible for experimental thermally simulated luminescence (TSL) studies, contributed to upgrading the TSL experimental set-up and to writing the manuscript. Alexander Vakhnin contributed to TSL measurements. Christof Pflumm provided especially synthetized high-quality OLED

materials for this study. Andrei Stankevych, I and Andrey Kadashchuk formulated major conclusions of this paper after discussions with Heinz Bässler and Anna Köhler. Jan Genoe, Heinz Bässler and Anna Köhler discussed the results and critically revised the manuscript

Kinetic Monte Carlo Study of Triplet-Triplet Annihilation in Conjugated Luminescent Materials

This work is published in Physical Review Applied (*Phys. Rev. Applied*, **2020**, 14, 034050) and reprinted in Chapter 10. The authors are:

Rishabh Saxena, *Tobias Meier*, *Stavros Athanasopoulos*, *Heinz Bässler*, and *Anna Köhler*.

I designed and organized the work, wrote the Python program used for the kinetic Monte Carlo (KMC) study, managed all the simulations, interpreted the data, and wrote the manuscript. Tobias Meier wrote the Python code for the generation of a parallel morphology; I used this code to generate the code for the grid morphology and integrated both morphologies in the main KMC code. Stavros Athanasopoulos provided crucial suggestions regarding the development of the morphology code as well as the KMC code. Heinz Bässler and Anna Köhler supervised the work, helped with the interpretation of simulation data, and critically edited the manuscript. All authors reviewed the manuscript.

Regiochemistry of Donor Dendrons Controls the Performance of Thermally Activated Delayed Fluorescence Dendrimer Emitters Translating in Their Use in High Efficiency Solution-Processed Organic Light-Emitting Diodes

This work is published in Advanced Science (*Adv. Sci.*, **2022**, 2201470) and reprinted in Chapter 11. The authors are:

Dianming Sun,[‡] **Rishabh Saxena**,[‡] *Xiaochun Fan*, *Stavros Athanasopoulos*, *Eimantas Duda*, *Ming Zhang*, *Sergey Bagnich*, *Xiaohong Zhang*, *Eli Zysman-Colman*, and *Anna Köhler*.

[‡] Dianming Sun and I contributed equally to this work.
Dianming Sun designed and synthesized the molecules, performed electrochemical measurements, carried out device fabrication and measurements. I performed the photophysical measurements. Eimantas Duda assisted me in these measurements. Sergey Bagnich helped in the interpretation of the photophysical data. Xiaochun Fan scaled up the synthesis. Ming Zhang participated in making devices. The quantum chemical calculations were performed by

Dianming Sun and Stavros Athanasopoulos, coordinated by me. I discussed the calculation results with Dianming Sun, Stavros Athanasopoulos and Anna Köhler, and proposed the RISC mechanism and its dependence on the regiochemistry of the molecules. Dianming Sun, I, Anna Köhler and Eli Zysman-Colman discussed all the data and wrote the manuscript. In particular, I wrote some parts of introduction section, and major parts of results and discussion section of the manuscript. Xiaohong Zhang, Anna Köhler and Eli Zysman-Colman supervised the work in their respective groups. All authors discussed the progress of research and reviewed the manuscript.

Thermally Activated Delayed Fluorescent Dendrimers that Underpin High-efficiency Host-Free Solution-Processed Organic Light Emitting Diodes

This work is published in Advanced Materials (*Adv. Mater.*, **2022**, 2110344) and reprinted in Chapter 12. The authors are:

Dianming Sun,[‡] *Eimantas Duda,*[‡] *Xiaochun Fan*, **Rishabh Saxena**, *Ming Zhang, Sergey Bagnich, Xiaohong Zhang, Anna Köhler*, and *Eli Zysman-Colman.*

[‡] Dianming Sun and Eimantas Duda contributed equally to this work.
Dianming Sun designed and synthesized the molecules, performed electrochemical measurements, carried out device fabrication and measurements, and performed quantum chemical calculations. Eimantas Duda performed the photophysical measurements. I and Sergey Bagnich helped Eimantas Duda with the photophysical measurements, with the interpretation of the data obtained and with the writing of photophysics section of the manuscript. In particular, I carried out PLQY measurements. Xiaochun Fan scaled up the synthesis. Ming Zhang participated in making devices. Dianming Sun, Eimantas Duda, Anna Köhler and Eli Zysman-Colman discussed all the data and wrote the manuscript. Xiaohong Zhang, Anna Köhler and Eli Zysman-Colman supervised the work in their respective groups. All authors discussed the progress of research and reviewed the manuscript.

Low Efficiency Roll-off Blue TADF OLEDs Employing a Novel Acridine-Pyrimidine based High Triplet Energy Host

This work is published in Journal of Materials Chemistry C (*J. Mater. Chem. C*, **2021**, 9, 17471) and reprinted in Chapter 13. The authors are:

Francesco Rodella, **Rishabh Saxena**, *Sergey Bagnich, Dovydas Banevičius, Gediminas*

Kreiza, Stavros Athanasopoulos, Saulius Juršėnas, Karolis Kazlauskas, Anna Köhler, and *Peter Strohriegl.*

Francesco Rodella performed the synthesis and characterization of the host materials, as well as the thermal and electrochemical analysis. I performed the photophysical studies. Sergey Bagnich helped with the interpretation of the photophysical data. Dovydas Banevičius and Gediminas Kreiza fabricated OLEDs. Stavros Athanasopoulos was responsible for quantum chemical calculations. I, Stavros Athanasopoulos, and Anna Köhler interpreted the calculation results with reference to the photophysical measurements. Francesco Rodella, I, Stavros Athanasopoulos and Karolis Kazlauskas wrote the manuscript. In particular, I wrote the photophysics section of the manuscript. Saulius Juršėnas, Karolis Kazlauskas, Anna Köhler, and Peter Strohriegl supervised the experiments and corrected the manuscript.

7 Conclusions and outlook

Overall, the investigations presented in this thesis contribute to the understanding of parameters affecting the intermolecular charge and triplet transport as well as the transitions between the lowest energy triplet and singlet excited states. From the work in Chapter 8-10, I can conclude that dynamic disorder, as expressed in terms of the reorganization energy, contributes only weakly to charge and triplet transport within the inhomogenously broadened DOS. The investigations presented in Chapter 8 justify the use of the material-independent Miller-Abrahams rate for the extraction of DOS width from the analysis of temperature-dependent charge transport measurements. In Chapter 9, I found that the distribution of charge carriers narrows as the charge carriers relax to deeper states within the DOS at low temperatures and that this "spectral narrowing" is a genuine property of energetic relaxation within the regime of dispersive transport. Moreover, consideration of spatial correlations among the lattice sites has a significant impact on this narrowing effect. Additionally, as highlighted in Chapter 10, dispersive transport is crucial for promoting bimolecular TTA instead of monomolecular quenching of triplets at the non-radiative trap sites. Static disorder has an additional role in promoting TTA, as it modifies the energetic landscape to increase the spatial density of triplets in the energetic valleys, thus increasing the bimolecular TTA rate and the associated delayed fluorescence yield in conjugated polymers.

The work in Chapter 11 and Chapter 12 indicates that regiochemistry, notably the connection of donor dendrons and acceptor moieties via *meta-* or *para-* position on a bridging phenyl ring, can be used to modulate the intramolecular reorganization energy and hence the RISC rate in the dendrimers. Further, I illustrated that it is possible to resolve the conflicting requirements of simultaneously achieving high RISC rate and a large oscillator strength by incorporating both, *meta-* as well as *para-*connected donor dendrons, about the acceptor core in the dendrimer molecular structure. Finally in Chapter 13, I demonstrated that varying the extent of π-conjugation within the acceptor unit results in a reordering of the energy of the lowest energy locally excited and intramolecular charge transfer states and that by careful molecular modification, it is possible to design a donor-acceptor type bipolar host material with a triplet energy higher than 3 eV.

In terms of optimizing the KMC simulation protocol, I suggest that the future studies regarding the modelling of charge and exciton transport should focus on reducing the amount of "useless events": events that occur frequently but do not contribute to the convergence of

simulations, such as back-and-forth hopping of a carrier between two sites of almost equal energy. This can be resolved by identifying such sites and replacing them with an "aggregate site": a site with properties of both sites. Such an approximation should have no influence on the macroscopic properties of the system; however, it can lead to a significant reduction of the computational cost. Additionally, it is important to remember that if conventional DOS simulations are being used for comparison with the analytical results derived under the premise of equilibrium transport, one needs to be sure that the simulations have converged to the equilibrium value, i.e., the results do not exhibit any time dependence. This might be computationally demanding and thus ODOS simulations, as introduced in Chapter 8, can be utilized as an alternative for such a purpose.

Previous experimental and KMC studies on spectral diffusion of excitons focused extensively on their energetic relaxation within the DOS while the spectral narrowing effect was often overlooked. In view of the study presented in Chapter 9, it would be interesting to investigate the effect of energy correlations on spectral narrowing associated with triplet diffusion and it's evolution when moving from the dispersive to non-dispersive transport regime. The KMC simulations in Chapter 10 were performed using simplified morphologies. However, more realistic morphologies can be generated with *ab initio* methods and it is worth investigating the role of such microscopic details on the diffusion-assisted bimolecular processes.

As seen in Chapter 11 and Chapter 12, understanding the RISC mechanism is still an ongoing process and the dependence of RISC rate on reorganization energy is relatively less recognized. Though the intramolecular reorganization energy can be evaluated from quantum chemical calculations, it is often difficult to account for the solvent (or matrix) effects in such calculations. As an experimental alternative, Franck-Condon analysis of absorption and emission spectra can be quite useful in this case. Firstly, we need to identify the crucial vibrational modes (using Raman spectra, for example) and then utilize this information to extract reorganization energy for a set of dendrimers with different molecular structures. Such a study combined with steady-state and time-resolved photophysical studies should enable us to quantify the exact role of reorganization energy on the RISC process.

Finally, I would like to emphasize that dendrimers are an excellent class of emitters because they can be utilized for the fabrication of efficient non-doped solution-processed OLEDs with simplified device architectures; thus providing a cost-effective alternative to vacuum-deposited OLEDs. However, they suffer from severe efficiency roll-off at high luminescence. Different mechanisms can contribute to this roll-off effect, such as imbalanced charge transport, field-induced exciton dissociation as well as bimolecular processes such as exciton-exciton annihilation and exciton-polaron quenching. Contribution of these processes to the net roll-off of these non-doped OLEDs needs to be quantified because overcoming this problem would bring us closer to the commercialization of dendrimer based solution-processed OLEDs for their application in economical mass-market applications.

References

[1] OLED-info. *Apple: OLED company spotlight, updated on April 4, 2021. Last accessed: 16.03.2022.*

[2] Wikipedia. *Samsung Galaxy Z Fold 3. Last accessed: 16.03.2022.*

[3] DSCC. *DSCC Revised 2020 Display Market Revenues, posted on June 7, 2020. Last accessed: 16.03.2022.*

[4] Kyulux. *The OLED Market. Last accessed: 16.03.2022.*

[5] OLED-info. *IHS: global OLED TV sales reached 1.1 million in Q4 2019, posted on March 3, 2020. Last accessed: 16.03.2022.*

[6] C. W. Tang and S. A. VanSlyke (1987). Organic electroluminescent diodes. *Applied physics letters* **51** (12), 913–915.

[7] M. Pfeiffer, A. Beyer, T. Fritz, and K. Leo (1998). Controlled doping of phthalocyanine layers by cosublimation with acceptor molecules: A systematic Seebeck and conductivity study. *Applied Physics Letters* **73** (22), 3202–3204.

[8] T. Tsutsui, E. Aminaka, C. Lin, and D.-U. Kim (1997). Extended molecular design concept of molecular materials for electroluminescence: sublimed–dye films, molecularly doped polymers and polymers with chromophores. *Philosophical Transactions of the Royal Society of London. Series A: Mathematical, Physical and Engineering Sciences* **355** (1725), 801–814.

[9] A. Salehi, Y. Chen, X. Fu, C. Peng, and F. So (2018). Manipulating refractive index in organic light-emitting diodes. *ACS applied materials & interfaces* **10** (11), 9595–9601.

[10] W. Brütting (2005). Introduction to the physics of organic semiconductors. *Physics of organic semiconductors*, 1–14.

[11] T. D. Schmidt, T. Lampe, P. I. Djurovich, M. E. Thompson, W. Brütting, et al. (2017). Emitter orientation as a key parameter in organic light-emitting diodes. *Physical Review Applied* **8** (3), 037001.

[12] A. Hofmann, M. Schmid, and W. Brütting (2021). The many facets of molecular orientation in organic optoelectronics. *Advanced Optical Materials* **9** (21), 2101004.

[13] S. Nowy, W. Ren, A. Elschner, W. Lövenich, and W. Brütting (2010). Impedance spectroscopy as a probe for the degradation of organic light-emitting diodes. *Journal of Applied Physics* **107** (5), 054501.

[14] H. Bässler (1993). Charge transport in disordered organic photoconductors. A Monte Carlo simulation study. *Physica Status Solidi B (Basic Research);(Germany)* **175** (1).

[15] M. A. Baldo, D. F. O'Brien, Y. You, A. Shoustikov, S. Sibley, M. E. Thompson, and S. R. Forrest (1998). Highly efficient phosphorescent emission from organic electroluminescent devices. *Nature* **395** (6698), 151–154.

[16] C. Adachi, M. A. Baldo, M. E. Thompson, and S. R. Forrest (2001). Nearly 100% internal phosphorescence efficiency in an organic light-emitting device. *Journal of Applied Physics* **90** (10), 5048–5051.

[17] Y. Kawamura, K. Goushi, J. Brooks, J. J. Brown, H. Sasabe, and C. Adachi (2005). 100% phosphorescence quantum efficiency of Ir (III) complexes in organic semiconductor films. *Applied Physics Letters* **86** (7), 071104.

[18] Y. Im, S. Y. Byun, J. H. Kim, D. R. Lee, C. S. Oh, K. S. Yook, and J. Y. Lee (2017). Recent progress in high-efficiency blue-light-emitting materials for organic light-emitting diodes. *Advanced Functional Materials* **27** (13), 1603007.

[19] A. Monkman (2021). Why Do We Still Need a Stable Long Lifetime Deep Blue OLED Emitter? *ACS Applied Materials & Interfaces*.

[20] J. C. Deaton and F. N. Castellano (2017). Archetypal Iridium (III) Compounds for Optoelectronic and Photonic Applications: Photophysical Properties and Synthetic Methods. *Iridium (III) in optoelectronic and photonics applications*, 1–69.

[21] J. Wang, F. Zhang, J. Zhang, W. Tang, A. Tang, H. Peng, Z. Xu, F. Teng, and Y. Wang (2013). Key issues and recent progress of high efficient organic light-emitting diodes. *Journal of Photochemistry and Photobiology C: Photochemistry Reviews* **17**, 69–104.

[22] H. Uoyama, K. Goushi, K. Shizu, H. Nomura, and C. Adachi (2012). Highly efficient organic light-emitting diodes from delayed fluorescence. *Nature* **492** (7428), 234–238.

[23] D. Kondakov, T. Pawlik, T. Hatwar, and J. Spindler (2009). Triplet annihilation exceeding spin statistical limit in highly efficient fluorescent organic light-emitting diodes. *Journal of Applied Physics* **106** (12), 124510.

[24] D. Di, L. Yang, J. M. Richter, L. Meraldi, R. M. Altamimi, A. Y. Alyamani, D. Credgington, K. P. Musselman, J. L. MacManus-Driscoll, and R. H. Friend (2017). Efficient triplet exciton fusion in molecularly doped polymer light-emitting diodes. *Advanced Materials* **29** (13), 1605987.

[25] F. B. Dias, T. J. Penfold, and A. P. Monkman (2017). Photophysics of thermally activated delayed fluorescence molecules. *Methods and applications in fluorescence* **5** (1), 012001.

[26] A. Endo, M. Ogasawara, A. Takahashi, D. Yokoyama, Y. Kato, and C. Adachi (2009). Thermally activated delayed fluorescence from Sn4+–porphyrin complexes and their application to organic light emitting diodes—A novel mechanism for electroluminescence. *Advanced Materials* **21** (47), 4802–4806.

[27] D. B. Mitzi, L. L. Kosbar, C. E. Murray, M. Copel, and A. Afzali (2004). High-mobility ultrathin semiconducting films prepared by spin coating. *Nature* **428** (6980), 299–303.

[28] K. Matsuoka, K. Albrecht, K. Yamamoto, and K. Fujita (2017). Mulifunctional dendritic emitter: aggregation-induced emission enhanced, thermally activated delayed fluorescent material for solution-processed multilayered organic light-emitting diodes. *Scientific reports* **7** (1), 1–9.

[29] K. Albrecht, K. Matsuoka, D. Yokoyama, Y. Sakai, A. Nakayama, K. Fujita, and K. Yamamoto (2017). Thermally activated delayed fluorescence OLEDs with fully solution processed organic layers exhibiting nearly 10% external quantum efficiency. *Chemical Communications* **53** (16), 2439–2442.

[30] Y. Li, G. Xie, S. Gong, K. Wu, and C. Yang (2016). Dendronized delayed fluorescence emitters for non-doped, solution-processed organic light-emitting diodes with high efficiency and low efficiency roll-off simultaneously: two parallel emissive channels. *Chemical science* **7** (8), 5441–5447.

[31] M. Huang, Y. Li, K. Wu, J. Luo, G. Xie, L. Li, and C. Yang (2018). Carbazole-dendronized thermally activated delayed fluorescent molecules with small singlet-triplet gaps for solution-processed organic light-emitting diodes. *Dyes and Pigments* **153**, 92–98.

[32] T. Chatterjee and K.-T. Wong (2019). Perspective on host materials for thermally activated delayed fluorescence organic light emitting diodes. *Advanced Optical Materials* **7** (1), 1800565.

[33] M. Godumala, S. Choi, M. J. Cho, and D. H. Choi (2019). Recent breakthroughs in thermally activated delayed fluorescence organic light emitting diodes containing non-doped emitting layers. *Journal of Materials Chemistry C* **7** (8), 2172–2198.

[34] Z. Yang, Z. Mao, Z. Xie, Y. Zhang, S. Liu, J. Zhao, J. Xu, Z. Chi, and M. P. Aldred (2017). Recent advances in organic thermally activated delayed fluorescence materials. *Chemical Society Reviews* **46** (3), 915–1016.

[35] Y. Wang, J. H. Yun, L. Wang, and J. Y. Lee (2021). High triplet energy hosts for blue organic light-emitting diodes. *Advanced Functional Materials* **31** (12), 2008332.

[36] C. Han, Y. Zhao, H. Xu, J. Chen, Z. Deng, D. Ma, Q. Li, and P. Yan (2011). A Simple Phosphine–Oxide Host with a Multi-insulating Structure: High Triplet Energy Level for Efficient Blue Electrophosphorescence. *Chemistry–A European Journal* **17** (21), 5800–5803.

[37] P. Schrögel, N. Langer, C. Schildknecht, G. Wagenblast, C. Lennartz, and P. Strohriegl (2011). Meta-linked CBP-derivatives as host materials for a blue iridium carbene complex. *Organic Electronics* **12** (12), 2047–2055.

[38] A. Chaskar, H.-F. Chen, and K.-T. Wong (2011). Bipolar host materials: a chemical approach for highly efficient electrophosphorescent devices. *Advanced Materials* **23** (34), 3876–3895.

[39] Y. Tao, Q. Wang, C. Yang, Q. Wang, Z. Zhang, T. Zou, J. Qin, and D. Ma (2008). A simple carbazole/oxadiazole hybrid molecule: an excellent bipolar host for green and red phosphorescent OLEDs. *Angewandte Chemie International Edition* **47** (42), 8104–8107.

[40] P. W. Atkins and R. S. Friedman (2011). *Molecular quantum mechanics.* Oxford university press.

[41] A. Köhler and H. Bässler (2015). *Electronic processes in organic semiconductors: An introduction.* John Wiley & Sons.

[42] M. Pope and C. E. Swenberg (1982). *Electronic processes in organic crystals*. Clarendon Press.

[43] H. Haken and H. C. Wolf (2013). *Molecular Physics and Quantum Chemistry: Introduction to the Experimental and Theoretical Foundations*. Springer-Verlag.

[44] S. P. McGlynn, T. Azumi, M. Kinoshita, et al. (1969). Molecular spectroscopy of the triplet state.

[45] W. Siebrand (1967). Radiationless transitions in polyatomic molecules. I. Calculation of Franck—Condon factors. *The Journal of Chemical Physics* **46** (2), 440–447.

[46] M. Kasha (1950). Characterization of electronic transitions in complex molecules. *Discussions of the Faraday society* **9**, 14–19.

[47] T. Hosokai, H. Matsuzaki, H. Nakanotani, K. Tokumaru, T. Tsutsui, A. Furube, K. Nasu, H. Nomura, M. Yahiro, and C. Adachi (2017). Evidence and mechanism of efficient thermally activated delayed fluorescence promoted by delocalized excited states. *Science advances* **3** (5), e1603282.

[48] P. K. Samanta, D. Kim, V. Coropceanu, and J.-L. Brédas (2017). Up-conversion intersystem crossing rates in organic emitters for thermally activated delayed fluorescence: impact of the nature of singlet vs triplet excited states. *Journal of the American Chemical Society* **139** (11), 4042–4051.

[49] G. W. Robinson and R. Frosch (1962). Theory of electronic energy relaxation in the solid phase. *The Journal of Chemical Physics* **37** (9), 1962–1973.

[50] G. W. Robinson and R. Frosch (1963). Electronic excitation transfer and relaxation. *The Journal of Chemical Physics* **38** (5), 1187–1203.

[51] W. Siebrand (1966). Mechanism of radiationless triplet decay in aromatic hydrocarbons and the magnitude of the Franck—Condon factors. *The Journal of Chemical Physics* **44** (10), 4055–4057.

[52] J. Jortner (1969). Radiation-less transitions in photochemistry. *Adv. Photochem.* **7**, 149–309.

[53] K. F. Freed and J. Jortner (1970). Multiphonon processes in the nonradiative decay of large molecules. *The Journal of Chemical Physics* **52** (12), 6272–6291.

[54] R. Englman and J. Jortner (1970). The energy gap law for radiationless transitions in large molecules. *Molecular Physics* **18** (2), 145–164.

[55] M. Lehnhardt, T. Riedl, T. Weimann, and W. Kowalsky (2010). Impact of triplet absorption and triplet-singlet annihilation on the dynamics of optically pumped organic solid-state lasers. *Physical Review B* **81** (16), 165206.

[56] S. Forget and S. Chénais (2013). *Organic solid-state lasers*. Vol. 175. Springer.

[57] M. Pope, C. E. Swenberg, et al. (1999). *Electronic processes in organic crystals and polymers*. Vol. 56. Oxford University Press on Demand.

[58] M. A. Baldo, C. Adachi, and S. R. Forrest (2000). Transient analysis of organic electrophosphorescence. II. Transient analysis of triplet-triplet annihilation. *Physical Review B* **62** (16), 10967.

[59] C. Murawski, K. Leo, and M. C. Gather (2013). Efficiency roll-off in organic light-emitting diodes. *Advanced Materials* **25** (47), 6801–6827.

[60] S. Wehrmeister, L. Jäger, T. Wehlus, A. F. Rausch, T. C. Reusch, T. D. Schmidt, and W. Brütting (2015). Combined electrical and optical analysis of the efficiency roll-off in phosphorescent organic light-emitting diodes. *Physical Review Applied* **3** (2), 024008.

[61] S. Reineke and M. A. Baldo (2012). *Recent progress in the understanding of exciton dynamics within phosphorescent OLEDs.*

[62] M. Inoue, K. Goushi, K. Endo, H. Nomura, and C. Adachi (2013). Reduced amplified spontaneous emission threshold in organic semiconductor laser structure with relaxed roll-off characteristics under high current densities. *Journal of luminescence* **143**, 754–758.

[63] C. Gärtner, C. Karnutsch, U. Lemmer, and C. Pflumm (2007). The influence of annihilation processes on the threshold current density of organic laser diodes. *Journal of Applied Physics* **101** (2), 023107.

[64] E. M. Conwell (1956). Impurity band conduction in germanium and silicon. *Physical Review* **103** (1), 51.

[65] N. Mott (1956). On the transition to metallic conduction in semiconductors. *Canadian journal of physics* **34** (12A), 1356–1368.

[66] T. Holstein (1959). Studies of polaron motion: Part I. The molecular-crystal model. *Annals of physics* **8** (3), 325–342.

[67] I. Austin and N. F. Mott (1969). Polarons in crystalline and non-crystalline materials. *Advances in physics* **18** (71), 41–102.

[68] D. Emin (1975). Phonon-assisted transition rates I. Optical-phonon-assisted hopping in solids. *Advances in Physics* **24** (3), 305–348.

[69] R. A. Marcus (1956). On the theory of oxidation-reduction reactions involving electron transfer. I. *The Journal of chemical physics* **24** (5), 966–978.

[70] R. A. Marcus (1993). Electron transfer reactions in chemistry. Theory and experiment. *Reviews of Modern Physics* **65** (3), 599.

[71] A. Amirav, U. Even, and J. Jortner (1980). Spectroscopy of large molecules in inert gas clusters. *Chemical Physics Letters* **72** (1), 16–20.

[72] A. Amirav, U. Even, and J. Jortner (1981). Microscopic solvation effects on excited-state energetics and dynamics of aromatic molecules in large van der Waals complexes. *The Journal of Chemical Physics* **75** (6), 2489–2512.

[73] P. Borsenberger and H. Bässler (1991). Concerning the role of dipolar disorder on charge transport in molecularly doped polymers. *The Journal of chemical physics* **95** (7), 5327–5331.

[74] R. H. Young, T.-M. Kung, J. A. Sinicropi, N. G. Rule, J. J. Fitzgerald, J. E. Eilers, C. H. Chen, and N. W. Boaz (1996). Effect of group and net dipole moments on electron transport in molecularly doped polymers. *The Journal of Physical Chemistry* **100** (45), 17923–17930.

[75] V. I. Arkhipov, I. I. Fishchuk, A. Kadashchuk, and H. Bässler (2007). Charge transport in neat and doped random organic semiconductors. In: *Semiconducting Polymers: Chemistry, Physics and Engineering*. Vol. 1. Wiley-VCH, 275–384.

[76] J.-L. Brédas, D. Beljonne, V. Coropceanu, and J. Cornil (2004). Charge-transfer and energy-transfer processes in π-conjugated oligomers and polymers: a molecular picture. *Chemical reviews* **104** (11), 4971–5004.

[77] S. Athanasopoulos, E. V. Emelianova, A. B. Walker, and D. Beljonne (2009). Exciton diffusion in energetically disordered organic materials. *Physical Review B* **80** (19), 195209.

[78] S. T. Hoffmann, S. Athanasopoulos, D. Beljonne, H. Bässler, and A. Köhler (2012). How do triplets and charges move in disordered organic semiconductors? A Monte Carlo study comprising the equilibrium and nonequilibrium regime. *The Journal of Physical Chemistry C* **116** (31), 16371–16383.

[79] S. Athanasopoulos, S. T. Hoffmann, H. Bässler, A. Köhler, and D. Beljonne (2013). To hop or not to hop? Understanding the temperature dependence of spectral diffusion in organic semiconductors. *The Journal of Physical Chemistry Letters* **4** (10), 1694–1700.

[80] A. Miller and E. Abrahams (1960). Impurity conduction at low concentrations. *Physical Review* **120** (3), 745.

[81] V. Coropceanu, J. Cornil, D. A. da Silva Filho, Y. Olivier, R. Silbey, and J.-L. Brédas (2007). Charge transport in organic semiconductors. *Chemical reviews* **107** (4), 926–952.

[82] B. Movaghar, M. Grünewald, B. Ries, H. Bassler, and D. Würtz (1986). Diffusion and relaxation of energy in disordered organic and inorganic materials. *Physical Review B* **33** (8), 5545.

[83] H. Bässler and A. Köhler (2011). Charge transport in organic semiconductors. *Unimolecular and supramolecular electronics I*, 1–65.

[84] P. Borsenberger and D. Weiss (1998). Organic Photoreceptors for Xerography. Marcel Dekker Inc.

[85] J. Cottaar, L. Koster, R. Coehoorn, and P. Bobbert (2011). Scaling theory for percolative charge transport in disordered molecular semiconductors. *Physical review letters* **107** (13), 136601.

[86] I. I. Fishchuk, A. Kadashchuk, S. T. Hoffmann, S. Athanasopoulos, J. Genoe, H. Bässler, and A. Köhler (2013). Unified description for hopping transport in organic semiconductors including both energetic disorder and polaronic contributions. *Physical Review B* **88** (12), 125202.

[87] J. Jortner (1976). Temperature dependent activation energy for electron transfer between biological molecules. *The Journal of Chemical Physics* **64** (12), 4860–4867.

[88] N. R. Kestner, J. Logan, and J. Jortner (1974). Thermal electron transfer reactions in polar solvents. *The Journal of Physical Chemistry* **78** (21), 2148–2166.

[89] M. Bixon and J. Jortner (1982). Quantum effects on electron-transfer processes. *Faraday Discussions of the Chemical Society* **74**, 17–29.

[90] P. E. Parris, V. M. Kenkre, and D. H. Dunlap (2001). Nature of charge carriers in disordered molecular solids: Are polarons compatible with observations? *Physical Review Letters* **87** (12), 126601.

[91] H. Bässler, P. Borsenberger, and R. Perry (1994). Charge transport in poly (methylphenyl-silane): The case for superimposed disorder and polaron effects. *Journal of Polymer Science Part B: Polymer Physics* **32** (9), 1677–1685.

[92] I. Fishchuk, A. Kadashchuk, H. Bässler, and S. Nesprek (2003). Nondispersive polaron transport in disordered organic solids. *Physical Review B* **67** (22), 224303.

[93] N. Lu, L. Li, W. Banerjee, P. Sun, N. Gao, and M. Liu (2015). Charge carrier hopping transport based on Marcus theory and variable-range hopping theory in organic semiconductors. *Journal of Applied Physics* **118** (4), 045701.

[94] N. Lu, L. Li, D. Geng, and M. Liu (2018). A review for polaron dependent charge transport in organic semiconductor. *Organic Electronics* **61**, 223–234.

[95] V. Rodin, F. Symalla, V. Meded, P. Friederich, D. Danilov, A. Poschlad, G. Nelles, F. von Wrochem, and W. Wenzel (2015). Generalized effective-medium model for the carrier mobility in amorphous organic semiconductors. *Physical Review B* **91** (15), 155203.

[96] K. Seki and M. Wojcik (2016). Temperature scaling of effective polaron mobility in energetically disordered media. *The Journal of Chemical Physics* **145** (3), 034106.

[97] X. de Vries, P. Friederich, W. Wenzel, R. Coehoorn, and P. A. Bobbert (2018). Full quantum treatment of charge dynamics in amorphous molecular semiconductors. *Physical Review B* **97** (7), 075203.

[98] T. Förster (1948). Intermolecular Energy Migration and Fluorescence. *Annals of Physics* **437** (1-2), 55–75.

[99] G. D. Scholes (2003). Long-range resonance energy transfer in molecular systems. *Annual review of physical chemistry* **54** (1), 57–87.

[100] D. L. Dexter (1953). A theory of sensitized luminescence in solids. *The journal of chemical physics* **21** (5), 836–850.

[101] W. Gill (1972). Drift mobilities in amorphous charge-transfer complexes of trinitrofluorenone and poly-n-vinylcarbazole. *Journal of Applied Physics* **43** (12), 5033–5040.

[102] R. Coehoorn, W. Pasveer, P. Bobbert, and M. Michels (2005). Charge-carrier concentration dependence of the hopping mobility in organic materials with Gaussian disorder. *Physical Review B* **72** (15), 155206.

[103] S. Baranovskii, T. Faber, F. Hensel, and P. Thomas (1997). The applicability of the transport-energy concept to various disordered materials. *Journal of Physics: Condensed Matter* **9** (13), 2699.

[104] S. Baranovskii, H. Cordes, F. Hensel, and G. Leising (2000). Charge-carrier transport in disordered organic solids. *Physical Review B* **62** (12), 7934.

[105] Y. N. Gartstein and E. Conwell (1995). High-field hopping mobility in molecular systems with spatially correlated energetic disorder. *Chemical Physics Letters* **245** (4-5), 351–358.

[106] D. H. Dunlap, P. E. Parris, and V. M. Kenkre (1996). Charge-dipole model for the universal field dependence of mobilities in molecularly doped polymers. *Physical review letters* **77** (3), 542.

[107] S. V. Novikov, D. H. Dunlap, V. M. Kenkre, P. E. Parris, and A. V. Vannikov (1998). Essential role of correlations in governing charge transport in disordered organic materials. *Physical Review Letters* **81** (20), 4472.

[108] S. V. Novikov and A. V. Vannikov (1995). Cluster structure in the distribution of the electrostatic potential in a lattice of randomly oriented dipoles. *The Journal of Physical Chemistry* **99** (40), 14573–14576.

[109] Z. Yu, D. Smith, A. Saxena, R. Martin, and A. Bishop (2000). Molecular geometry fluctuation model for the mobility of conjugated polymers. *Physical review letters* **84** (4), 721.

[110] J. Van der Holst, F. Van Oost, R. Coehoorn, and P. Bobbert (2011). Monte Carlo study of charge transport in organic sandwich-type single-carrier devices: Effects of Coulomb interactions. *Physical Review B* **83** (8), 085206.

[111] R. H. Young (1995). Dipolar lattice model of disorder in random media analytical evaluation of the gaussian disorder model. *Philosophical Magazine B* **72** (4), 435–457.

[112] W. Pasveer, J. Cottaar, C. Tanase, R. Coehoorn, P. Bobbert, P. Blom, D. De Leeuw, and M. Michels (2005). Unified description of charge-carrier mobilities in disordered semiconducting polymers. *Physical review letters* **94** (20), 206601.

[113] I. Fishchuk (2001). On the theory of hopping transport in organic solids with super-imposed disorder and polaron effects. *Philosophical Magazine B* **81** (6), 561–568.

[114] S. Baranovskii, I. Zvyagin, H. Cordes, S. Yamasaki, and P. Thomas (2002). Percolation approach to hopping transport in organic disordered solids. *physica status solidi (b)* **230** (1), 281–288.

[115] F. W. Schmidlin (1977). Theory of trap-controlled transient photoconduction. *Physical Review B* **16** (6), 2362.

[116] M. D. Khan, V. R. Nikitenko, A. P. Tyutnev, and R. S. Ikhsanov (2018). Joint application of transport level and effective temperature concepts for an analytic description of the quasi-and nonequilibrium charge transport in disordered organics. *The Journal of Physical Chemistry C* **123** (3), 1653–1659.

[117] V. Arkhipov and A. Rudenko (1982). Drift and diffusion in materials with traps: II. Non-equilibrium transport regime. *Philosophical Magazine B* **45** (2), 189–207.

[118] V. Arkhipov, E. Emelianova, and H. Bässler (2001). Equilibrium carrier mobility in disordered hopping systems. *Philosophical Magazine B* **81** (9), 985–996.

[119] N. Apsley and H. Hughes (1975). Temperature-and field-dependence of hopping conduction in disordered systems, II. *Philosophical Magazine* **31** (6), 1327–1339.

[120] H. Van Eersel, P. Bobbert, and R. Coehoorn (2015). Kinetic Monte Carlo study of triplet-triplet annihilation in organic phosphorescent emitters. *Journal of Applied Physics* **117** (11), 115502.

[121] R. Coehoorn, H. Van Eersel, P. Bobbert, and R. Janssen (2015). Kinetic Monte Carlo study of the sensitivity of OLED efficiency and lifetime to materials parameters. *Advanced Functional Materials* **25** (13), 2024–2037.

[122] H. Van Eersel, P. Bobbert, R. Janssen, and R. Coehoorn (2014). Monte Carlo study of efficiency roll-off of phosphorescent organic light-emitting diodes: Evidence for dominant role of triplet-polaron quenching. *Applied Physics Letters* **105** (14), 156_1.

[123] P. Friederich, V. Meded, A. Poschlad, T. Neumann, V. Rodin, V. Stehr, F. Symalla, D. Danilov, G. Lüdemann, R. F. Fink, et al. (2016). Molecular origin of the charge carrier mobility in small molecule organic semiconductors. *Advanced Functional Materials* **26** (31), 5757–5763.

[124] P. Kordt, J. J. van der Holst, M. Al Helwi, W. Kowalsky, F. May, A. Badinski, C. Lennartz, and D. Andrienko (2015). Modeling of organic light emitting diodes: From molecular to device properties. *Advanced Functional Materials* **25** (13), 1955–1971.

[125] N. B. Kotadiya, A. Mondal, S. Xiong, P. W. Blom, D. Andrienko, and G.-J. A. Wetzelaer (2018). Rigorous characterization and predictive modeling of hole transport in amorphous organic semiconductors. *Advanced Electronic Materials* **4** (12), 1800366.

[126] F. Liu, A. Massé, P. Friederich, F. Symalla, R. Nitsche, W. Wenzel, R. Coehoorn, and P. A. Bobbert (2016). Ab initio modeling of steady-state and time-dependent charge transport in hole-only α-NPD devices. *Applied Physics Letters* **109** (24), 243301.

[127] A. Massé, P. Friederich, F. Symalla, F. Liu, R. Nitsche, R. Coehoorn, W. Wenzel, and P. A. Bobbert (2016). Ab initio charge-carrier mobility model for amorphous molecular semiconductors. *Physical Review B* **93** (19), 195209.

[128] M. Y. Wong and E. Zysman-Colman (2017). Purely organic thermally activated delayed fluorescence materials for organic light-emitting diodes. *Advanced Materials* **29** (22), 1605444.

[129] T.-A. Lin, T. Chatterjee, W.-L. Tsai, W.-K. Lee, M.-J. Wu, M. Jiao, K.-C. Pan, C.-L. Yi, C.-L. Chung, K.-T. Wong, et al. (2016). Sky-blue organic light emitting diode with 37% external quantum efficiency using thermally activated delayed fluorescence from spiroacridine-triazine hybrid. *Advanced Materials* **28** (32), 6976–6983.

[130] F. Rodella, S. Bagnich, E. Duda, T. Meier, J. Kahle, S. Athanasopoulos, A. Köhler, and P. Strohriegl (2020). High Triplet Energy Host Materials for Blue TADF OLEDs—A Tool Box Approach. *Frontiers in chemistry*, 657.

[131] F. Perrin (1929). La fluorescence des solutions-Induction moléculaire.–Polarisation et durée d'émission.–Photochimie. In: *Annales de physique*. Vol. 10. 12. EDP Sciences, 169–275.

[132] G. N. Lewis, D. Lipkin, and T. T. Magel (1941). Reversible photochemical processes in rigid media. A study of the phosphorescent state. *Journal of the American Chemical Society* **63** (11), 3005–3018.

[133] C. Parker and C. Hatchard (1963). Delayed fluorescence of pyrene in ethanol. *Transactions of the Faraday Society* **59**, 284–295.

[134] C. Parker and T. A. Joyce (1968). Activation-controlled delayed fluorescence of benzil. *Chemical Communications (London)* (22), 1421–1422.

[135] Y. Tao, K. Yuan, T. Chen, P. Xu, H. Li, R. Chen, C. Zheng, L. Zhang, and W. Huang (2014). Thermally activated delayed fluorescence materials towards the breakthrough of organoelectronics. *Advanced materials* **26** (47), 7931–7958.

[136] N. J. Turro, V. Ramamurthy, V. Ramamurthy, and J. C. Scaiano (2009). *Principles of molecular photochemistry: an introduction.* University science books.

[137] B. Milián-Medina and J. Gierschner (2012). Computational design of low singlet–triplet gap all-organic molecules for OLED application. *Organic Electronics* **13** (6), 985–991.

[138] F. B. Dias, K. N. Bourdakos, V. Jankus, K. C. Moss, K. T. Kamtekar, V. Bhalla, J. Santos, M. R. Bryce, and A. P. Monkman (2013). Triplet harvesting with 100% efficiency by way of thermally activated delayed fluorescence in charge transfer OLED emitters. *Advanced Materials* **25** (27), 3707–3714.

[139] F. B. Dias, J. Santos, D. R. Graves, P. Data, R. S. Nobuyasu, M. A. Fox, A. S. Batsanov, T. Palmeira, M. N. Berberan-Santos, M. R. Bryce, et al. (2016). The role of local triplet excited states and D-A relative orientation in thermally activated delayed fluorescence: photophysics and devices. *Advanced Science* **3** (12), 1600080.

[140] R. S. Nobuyasu, Z. Ren, G. C. Griffiths, A. S. Batsanov, P. Data, S. Yan, A. P. Monkman, M. R. Bryce, and F. B. Dias (2016). Rational design of TADF polymers using a donor–acceptor monomer with enhanced TADF efficiency induced by the energy alignment of charge transfer and local triplet excited states. *Advanced Optical Materials* **4** (4), 597–607.

[141] S. K. Mellerup and S. Wang (2018). Isomerization and rearrangement of boriranes: from chemical rarities to functional materials. *Science China Materials* **61** (10), 1249–1256.

[142] G. Valchanov, A. Ivanova, A. Tadjer, D. Chercka, and M. Baumgarten (2016). Understanding the fluorescence of TADF light-emitting dyes. *The Journal of Physical Chemistry A* **120** (35), 6944–6955.

[143] H. F. Higginbotham, C.-L. Yi, A. P. Monkman, and K.-T. Wong (2018). Effects of ortho-phenyl substitution on the rISC rate of D–A type TADF molecules. *The Journal of Physical Chemistry C* **122** (14), 7627–7634.

[144] C. S. Oh, H. L. Lee, S. H. Han, and J. Y. Lee (2019). Rational Molecular Design Overcoming the Long Delayed Fluorescence Lifetime and Serious Efficiency Roll-Off in Blue Thermally Activated Delayed Fluorescent Devices. *Chemistry–A European Journal* **25** (2), 642–648.

[145] D. R. Lee, J. M. Choi, C. W. Lee, and J. Y. Lee (2016). Ideal molecular design of blue thermally activated delayed fluorescent emitter for high efficiency, small singlet–triplet energy splitting, low efficiency roll-off, and long lifetime. *ACS applied materials & interfaces* **8** (35), 23190–23196.

[146] F.-M. Xie, J.-X. Zhou, Y.-Q. Li, and J.-X. Tang (2020). Effects of the relative position and number of donors and acceptors on the properties of TADF materials. *Journal of Materials Chemistry C* **8** (28), 9476–9494.

[147] A. Marini, A. Munoz-Losa, A. Biancardi, and B. Mennucci (2010). What is solvatochromism? *The Journal of Physical Chemistry B* **114** (51), 17128–17135.

[148] Z. R. Grabowski, K. Rotkiewicz, and W. Rettig (2003). Structural changes accompanying intramolecular electron transfer: focus on twisted intramolecular charge-transfer states and structures. *Chemical reviews* **103** (10), 3899–4032.

[149] F. B. Dias, S. Pollock, G. Hedley, L.-O. Pålsson, A. Monkman, I. I. Perepichka, I. F. Perepichka, M. Tavasli, and M. R. Bryce (2006). Intramolecular charge transfer assisted by conformational changes in the excited state of fluorene-dibenzothiophene-S, S-dioxide co-oligomers. *The Journal of Physical Chemistry B* **110** (39), 19329–19339.

[150] Y. Olivier, B. Yurash, L. Muccioli, G. D'Avino, O. Mikhnenko, J.-C. Sancho-Garcia, C. Adachi, T.-Q. Nguyen, and D. Beljonne (2017). Nature of the singlet and triplet excitations mediating thermally activated delayed fluorescence. *Physical Review Materials* **1** (7), 075602.

[151] C. Baleizão and M. N. Berberan-Santos (2007). Thermally activated delayed fluorescence as a cycling process between excited singlet and triplet states: Application to the fullerenes. *The Journal of chemical physics* **126** (20), 204510.

[152] F. B. Dias (2015). Kinetics of thermal-assisted delayed fluorescence in blue organic emitters with large singlet–triplet energy gap. *Philosophical Transactions of the Royal Society A: Mathematical, Physical and Engineering Sciences* **373** (2044), 20140447.

[153] C. Baleizão and M. N. Berberan-Santos (2011). The brightest fullerene: a new isotope effect in molecular fluorescence and phosphorescence. *ChemPhysChem* **12** (7), 1247–1250.

[154] M. N. Berberan-Santos and J. M. Garcia (1996). Unusually strong delayed fluorescence of C70. *Journal of the American Chemical Society* **118** (39), 9391–9394.

[155] L. Wang, Q. Ou, Q. Peng, and Z. Shuai (2021). Theoretical Characterizations of TADF Materials: Roles of Δ G and the Singlet–Triplet Excited States Interconversion. *The Journal of Physical Chemistry A* **125** (7), 1468–1475.

[156] I. E. Serdiuk, M. Mońka, K. Kozakiewicz, B. Liberek, P. Bojarski, and S. Y. Park (2021). Vibrationally assisted direct intersystem crossing between the same charge-transfer states for thermally activated delayed fluorescence: analysis by Marcus–Hush theory including reorganization energy. *The Journal of Physical Chemistry B* **125** (10), 2696–2706.

[157] E. Cho, M. Hong, V. Coropceanu, and J.-L. Brédas (2021). The Role of Intermolecular Interactions on the Performance of Organic Thermally Activated Delayed Fluorescence (TADF) Materials. *Advanced Optical Materials* **9** (14), 2002135.

[158] X.-K. Chen, B. W. Bakr, M. Auffray, Y. Tsuchiya, C. D. Sherrill, C. Adachi, and J.-L. Bredas (2019). Intramolecular noncovalent interactions facilitate thermally activated delayed fluorescence (TADF). *The Journal of Physical Chemistry Letters* **10** (12), 3260–3268.

[159] L.-S. Cui, A. J. Gillett, S.-F. Zhang, H. Ye, Y. Liu, X.-K. Chen, Z.-S. Lin, E. W. Evans, W. K. Myers, T. K. Ronson, et al. (2020). Fast spin-flip enables efficient and stable organic electroluminescence from charge-transfer states. *Nature Photonics* **14** (10), 636–642.

[160] H. Noda, X.-K. Chen, H. Nakanotani, T. Hosokai, M. Miyajima, N. Notsuka, Y. Kashima, J.-L. Brédas, and C. Adachi (2019). Critical role of intermediate electronic states for spin-flip processes in charge-transfer-type organic molecules with multiple donors and acceptors. *Nature Materials* **18** (10), 1084–1090.

[161] X.-K. Chen, S.-F. Zhang, J.-X. Fan, and A.-M. Ren (2015). Nature of highly efficient thermally activated delayed fluorescence in organic light-emitting diode emitters: nonadiabatic effect between excited states. *The Journal of Physical Chemistry C* **119** (18), 9728–9733.

[162] C. M. Marian (2016). Mechanism of the triplet-to-singlet upconversion in the assistant dopant ACRXTN. *The Journal of Physical Chemistry C* **120** (7), 3715–3721.

[163] B. T. Lim, S. Okajima, A. Chandra, and E. Lim (1981). Radiationless transitions in electron donor-acceptor complexes: selection rules for S1→ T intersystem crossing and efficiency of S1→ S0 internal conversion. *Chemical Physics Letters* **79** (1), 22–27.

[164] M. El-Sayed (1963). Spin—orbit coupling and the radiationless processes in nitrogen heterocyclics. *The Journal of Chemical Physics* **38** (12), 2834–2838.

[165] C. M. Marian (2012). Spin–orbit coupling and intersystem crossing in molecules. *Wiley Interdisciplinary Reviews: Computational Molecular Science* **2** (2), 187–203.

[166] M. K. Etherington, J. Gibson, H. F. Higginbotham, T. J. Penfold, and A. P. Monkman (2016). Revealing the spin–vibronic coupling mechanism of thermally activated delayed fluorescence. *Nature communications* **7** (1), 1–7.

[167] J. Gibson, A. P. Monkman, and T. J. Penfold (2016). The importance of vibronic coupling for efficient reverse intersystem crossing in thermally activated delayed fluorescence molecules. *ChemPhysChem* **17** (19), 2956–2961.

[168] P. Data, P. Pander, M. Okazaki, Y. Takeda, S. Minakata, and A. P. Monkman (2016). Dibenzo [a, j] phenazine-Cored Donor–Acceptor–Donor Compounds as Green-to-Red/NIR Thermally Activated Delayed Fluorescence Organic Light Emitters. *Angewandte Chemie* **128** (19), 5833–5838.

[169] P. L. Santos, J. S. Ward, P. Data, A. S. Batsanov, M. R. Bryce, F. B. Dias, and A. P. Monkman (2016). Engineering the singlet–triplet energy splitting in a TADF molecule. *Journal of Materials Chemistry C* **4** (17), 3815–3824.

[170] T. J. Penfold, E. Gindensperger, C. Daniel, and C. M. Marian (2018). Spin-vibronic mechanism for intersystem crossing. *Chemical reviews* **118** (15), 6975–7025.

[171] E. Duda, D. Hall, S. Bagnich, C. L. Carpenter-Warren, R. Saxena, M. Y. Wong, D. B. Cordes, A. M. Slawin, D. Beljonne, Y. Olivier, et al. (2022). Enhancing thermally activated delayed fluorescence by fine-tuning the dendron donor strength. *The Journal of Physical Chemistry B*.

[172] Y. Tao, C. Yang, and J. Qin (2011). Organic host materials for phosphorescent organic light-emitting diodes. *Chemical Society Reviews* **40** (5), 2943–2970.

[173] X. Cai and S.-J. Su (2018). Marching toward highly efficient, pure-blue, and stable thermally activated delayed fluorescent organic light-emitting diodes. *Advanced Functional Materials* **28** (43), 1802558.

[174] S. Hirata, Y. Sakai, K. Masui, H. Tanaka, S. Y. Lee, H. Nomura, N. Nakamura, M. Yasumatsu, H. Nakanotani, Q. Zhang, et al. (2015). Highly efficient blue electroluminescence based on thermally activated delayed fluorescence. *Nature materials* **14** (3), 330–336.

[175] W.-C. Chen, C.-S. Lee, and Q.-X. Tong (2015). Blue-emitting organic electrofluorescence materials: progress and prospective. *Journal of Materials Chemistry C* **3** (42), 10957–10963.

[176] S.-H. Hwang et al. (2015). Stable blue thermally activated delayed fluorescent organic light-emitting diodes with three times longer lifetime than phosphorescent organic light-emitting diodes. *Advanced materials* **27** (15), 2515–2520.

[177] K. S. Yook and J. Y. Lee (2016). Bipolar host materials for organic light-emitting diodes. *The Chemical Record* **16** (1), 159–172.

[178] J. Zhang, D. Ding, Y. Wei, F. Han, H. Xu, and W. Huang (2016). Multiphosphine-Oxide Hosts for Ultralow-Voltage-Driven True-Blue Thermally Activated Delayed Fluorescence Diodes with External Quantum Efficiency beyond 20%. *Advanced Materials* **28** (3), 479–485.

[179] L. Xiao and Z. Chen (2011). B. Qu, J. Luo, S. Kong, Q. Gong and J. Kido. *Adv. Mater* **23** (8), 926.

[180] W. Li, J. Li, D. Liu, and Q. Jin (2016). Simple bipolar host materials for high-efficiency blue, green, and white phosphorescence OLEDs. *ACS Applied Materials & Interfaces* **8** (34), 22382–22391.

[181] S. O. Jeon and J. Y. Lee (2012). Comparison of symmetric and asymmetric bipolar type high triplet energy host materials for deep blue phosphorescent organic light-emitting diodes. *Journal of Materials Chemistry* **22** (15), 7239–7244.

[182] S. O. Jeon, S. E. Jang, H. S. Son, and J. Y. Lee (2011). External quantum efficiency above 20% in deep blue phosphorescent organic light-emitting diodes. *Advanced Materials* **23** (12), 1436–1441.

[183] Y. J. Cho, S. K. Jeon, and J. Y. Lee (2016). Molecular Engineering of High Efficiency and Long Lifetime Blue Thermally Activated Delayed Fluorescent Emitters for Vacuum and Solution Processed Organic Light-Emitting Diodes. *Advanced Optical Materials* **4** (5), 688–693.

[184] S. T. Hoffmann, F. Jaiser, A. Hayer, H. Bässler, T. Unger, S. Athanasopoulos, D. Neher, and A. Köhler (2013). How do disorder, reorganization, and localization influence the hole mobility in conjugated copolymers? *Journal of the American Chemical Society* **135** (5), 1772–1782.

[185] S. T. Hoffmann, J.-M. Koenen, U. Scherf, I. Bauer, P. Strohriegl, H. Bässler, and A. Köhler (2011). Triplet–triplet annihilation in a series of poly (p-phenylene) derivatives. *The Journal of Physical Chemistry B* **115** (26), 8417–8423.

[186] S. Raišys, O. Adomėnienė, P. Adomėnas, A. Rudnick, A. Köhler, and K. Kazlauskas (2021). Triplet exciton diffusion and quenching in matrix-free solid photon upconversion films. *The Journal of Physical Chemistry C* **125** (7), 3764–3775.

Part III

Publications

8

Role of the Reorganization Energy for Charge Transport in Disordered Organic Semiconductors

Rishabh Saxena, *V. R. Nikitenko, I. I. Fishchuk, Ya. V. Burdakov, Yu. V. Metel, Jan Genoe, Heinz Bässler, Anna Köhler*, and *Andrey Kadashchuk*

Role of the reorganization energy for charge transport in disordered organic semiconductors

R. Saxena ⬤,[1] V. R. Nikitenko ⬤,[2] I. I. Fishchuk ⬤,[3,4] Ya. V. Burdakov ⬤,[2] Yu. V. Metel,[2] J. Genoe ⬤,[5] H. Bässler,[6] A. Köhler ⬤,[1,6] and A. Kadashchuk ⬤[4,5,*]

[1]*Soft Matter Optoelectronics and Bavarian Polymer Institute (BPS), Universitätsstrasse 30, 95448 Bayreuth, Germany*
[2]*National Research Nuclear University "MEPhI" (Moscow Engineering Physics Institute), Kashirskoe Shosse 31, 115409 Moscow, Russia*
[3]*Institute for Nuclear Research, National Academy of Science of Ukraine, Prospect Nauky 47, 03028 Kyiv, Ukraine*
[4]*Institute of Physics, National Academy of Sciences of Ukraine, Prospect Nauky 46, 03028 Kyiv, Ukraine*
[5]*IMEC, Kapeldreef 75, B-3001 Leuven, Belgium*
[6]*Bayreuth Institute of Macromolecular Research (BIMF), Universitätsstrasse 30, 95448 Bayreuth, Germany*

While it is commonly accepted that the activation energy of the thermally activated polaron hopping transport in disordered organic semiconductors can be decoupled into a disorder and a polaron contribution, their relative weight is still controversial. This feature is quantified in terms of the so-called C factor in the expression for the effective polaron mobility: $\mu_e \propto \exp[-E_a/k_B T - C(\sigma/k_B T)^2]$, where E_a and σ are the polaron activation energy and the energy width of a Gaussian density of states (DOS), respectively. A key issue is whether the universal scaling relation (implying a constant C factor) regarding the polaron formation energy is really obeyed, as recently claimed in the literature [Seki and Wojcik, J. Chem. Phys. **145**, 034106 (2016)]. In the present work, we reinvestigate this issue on the basis of the Marcus transition rate model using extensive kinetic Monte Carlo simulations as a benchmark tool. We compare the polaron-transport simulation data with results of analytical calculations by the effective medium approximation and multiple trapping and release approaches. The key result of this study is that the C factor for Marcus polaron hopping depends on first the degree of carrier localization, i.e., the coupling between the sites, further whether quasiequilibrium has indeed been reached, and finally the σ/E_a ratio. This implies that there is no universal scaling with respect to the relative contribution of polaron and disorder effect. Finally, we demonstrate that virtually the same values of the disorder parameter σ are determined from available experimental data using the C factors obtained here irrespective of whether the data are interpreted in terms of Marcus or Miller-Abrahams rates. This implies that molecular reorganization contributes only weakly to charge transport, and it justifies the use of the zero-order Miller-Abrahams rate model for evaluating the DOS width from temperature-dependent charge transport measurements regardless of whether or not polaron effects are accounted for.

I. INTRODUCTION

Charge-carrier transport in amorphous organic semiconductors (AOSs) occurs by noncoherent hopping through the manifold of localized states distributed in space and energy, which is commonly described by a Gaussian density of states (DOS) distribution of energetic width σ. The latter is a measure of the energetic disorder that is generally accepted to be a dominant factor governing the charge transport in AOS films. Although the pertinent energetic disorder can account for a broad variety of experimental observations in AOSs, such as the mobility temperature and electric-field dependences, or the transition from nondispersive to dispersive transport regimes upon lowering temperature [1], in some organic systems polaron formation is sometimes taken into account. This is because an organic molecule or a subunit of a conjugated polymer can undergo structural reorganization upon charging. Depending on the value of the reorganization energy, this could result in a significant polaronic nature of charge transport, and consequently, the observed temperature dependence of the carrier mobility may be governed by the superposition of disorder and polaron effects.

Although a large amount of work was done on the description of charge-carrier transport in AOSs for the last decades, an adequate theoretical description of the polaronic transport in disordered media remains challenging. In particular, there has been a long-standing discussion concerning the expression for the effective polaron mobility μ_e obtained for energetically disordered organic semiconductors when using a Marcus-type intersite hopping rate model. The commonly accepted relation, which was heuristically suggested, splits the activation energy of the zero electric field mobility into a disorder and a polaron term. It reads as follows [2]:

$$\mu_e = \mu_0 \exp\left[-\frac{E_a}{k_B T} - C\left(\frac{\sigma}{k_B T}\right)^2\right]. \quad (1)$$

The argument presumes that transport occurs by hopping in a Gaussian-shaped distribution of energy sites, but each jump

*kadash@iop.kiev.ua

is associated with an additional constant activation energy, that is, the polaron activation energy E_a, which is equal to a quarter of the total reorganization energy associated with the charge transfer ($E_a = \lambda/4$). The prefactor μ_0 is the infinite temperature mobility. What has been in dispute for decades is the numerical value of the C factor (coefficient) which weights the relative contribution of disorder and polaron effects. In their original paper [2], Bässler *et al.* suggested a long time ago to consider the C factor in Eq. (1) as a constant that is determined entirely by the energetic disorder effects and, consequently, to adopt the same value as that derived before for the charge transport in a polaron free system (i.e., $C = 4/9 \approx 0.44$) within the Miller-Abrahams rate model [1]. Recently, this issue was thoroughly investigated [3–5] by combining Monte Carlo simulation studies and analytical calculations using an effective medium approximation (EMA), and a dependence of the C factor on the σ/E_a ratio was shown. The latter effect has also been confirmed by several different theoretical approaches [6–8].

Nevertheless, recently Seki and Wojcik [9] have questioned the variability of the C factor in Eq. (1) and the existence of a nonlinear dependence of the relative weights of polaron and disorder contributions to the hopping transport on the σ/E_a ratio. They performed both kinetic Monte Carlo (KMC) numerical simulations and EMA calculations considering the nearest-neighbor hopping regime. They used Marcus rates and found that the C factor is virtually independent of E_a. A value of $C \cong 1/2$ was obtained by EMA, while the KMC data revealed slightly different values of $C = 0.42$ and 0.5 for three-dimensional (3D) and two-dimensional (2D) transport systems, respectively. This would imply a universal scaling relation for the polaronic mobility with the polaron formation energy. A similar conclusion was also drawn in Ref. [10] where a very weak σ/E_a dependence of the C factor was reported. It is important to mention that the authors of Ref. [9] actually used a simplified Marcus relation, where the prefactor was assumed to be constant.

In the present paper, we reinvestigate the C factor issue on the basis of Marcus theory for polaron hopping rates by combining kinetic Monte Carlo simulations and two alternative theoretical approaches EMA and a multiple trapping and release (MTR) formalism. We have advanced these methods for considering the hopping transport problem for different rates, and obtained the C factor in the context of Eq. (1). Our work brings additional insights to light on aspects related to *polaronic* hopping transport that have not been considered so far. We demonstrate that the C factor turns out to depend on whether transport has reached equilibration or not, and on the degree of carrier localization. Moreover, it changes with the σ/E_a ratio. Thus, our study is in sharp contrast to the notion of a "universal scaling law" recently published by Seki and Wojcik in Ref. [9], and we clarify that and why there is no universal scaling regarding the polaron formation energy. The present results help to build an understanding on the interplay of disorder and polaronic effects, and their quantitative dependence on different transport parameters.

This paper is organized as follows. First, we describe our kinetic Monte Carlo simulation method (Sec. II) and the theoretical formulation of our EMA and MTR analytic approaches (Sec. III). In Sec. IV we present the results

of the KMC simulations and the theoretical calculations of the temperature-dependent diffusivity obtained for Miller-Abrahams (MA) and Marcus hopping rates for the nearest-neighbor hopping regime, and the corresponding C factors are evaluated as a function of the σ/E_a ratio. Subsequently we consider the impact of variable-range hopping. In Sec. V we apply our results to reanalyze available experimental data, and a concluding discussion is given in Sec. VI.

II. MONTE CARLO SIMULATIONS

The thermally activated hopping of excitations in a disordered organic solid is studied using a grid-based kinetic Monte Carlo (KMC) method to monitor the motion of excitations as hopping events. We place a particular emphasis on the dependence of the C factor on the σ/E_a ratio and the degree of excitation localization. The excitation can, in principle, be equally well a charge carrier or a triplet exciton since (i) both move by an exchange mechanism, and (ii) the transfer of a triplet can, to first order, be described as a correlated exchange of two charges. The physical meaning of the excitation depends on the value chosen for the energetic disorder and the reorganization energy. The KMC simulations were done by employing an isotropic three-dimensional (3D) simulation box ($50 \times 50 \times 50$ lattice sites) with a lattice constant of 1.5 nm. Since energetic disorder is inherent to conventional thin-film organic semiconductors, the lattice sites are assigned a random energy drawn from a Gaussian distribution $g(\varepsilon)$ with a standard deviation σ centered at zero energy, i.e., $\varepsilon_0 = 0$.

$$g(\varepsilon) = \frac{N}{\sigma\sqrt{2\pi}} \exp\left[-\frac{1}{2}\left(\frac{\varepsilon - \varepsilon_0}{\sigma}\right)^2\right], \qquad (2)$$

where N is the density of localized states. To describe the diffusion of excitations through the disordered medium, both Miller-Abrahams (MA) and Marcus hopping rates have been used. This is done to find out whether the hopping process and thus the value of the C factor is altered by the hopping rate chosen for determining the diffusivity of the excitations. The MA hopping rate between an initial site of energy ε_i and final site of energy ε_j is given by [11]

$$W_{ij} = W_0 \exp\left[-\frac{|\varepsilon_j - \varepsilon_i| + (\varepsilon_j - \varepsilon_i)}{2k_BT}\right],$$
$$W_0 = \nu_0 \exp(-2\gamma R_{ij}), \qquad (3)$$

where W_0, the MA rate prefactor, is determined by the hopping distance R_{ij}. The inverse localization radius γ is related to the electronic coupling matrix element between adjacent sites. ν_0 is the attempt to escape frequency usually being close to an intermolecular phonon frequency, k_B is the Boltzmann constant, and T is temperature. The parameter γ is assumed to be isotropic in all directions. The MA formalism does not consider any polaronic effects related to the reorganization energy. These effects can be taken into account by considering a semiclassical Marcus-type hopping rate [12,13]:

$$W_{ij} = W_1 \exp\left[-\frac{E_a}{k_BT} - \frac{\varepsilon_j - \varepsilon_i}{2k_BT} - \frac{(\varepsilon_j - \varepsilon_i)^2}{16E_ak_BT}\right],$$
$$W_1 = (J_{ij}/\hbar)\sqrt{\pi/4E_ak_BT}, \qquad (4)$$

where W_1 denotes the Marcus prefactor that, in contrast to the MA rate, depends on temperature. $J_{ij} = J_0^2 \exp(-2\gamma R_{ij})$ represents the electronic coupling, J_0 is the nearest-neighbor coupling constant, E_a is the small-polaron activation energy related to the reorganization energy λ by $E_a = \lambda/4$.

In conventional Monte Carlo simulations, the initial site energy is typically sampled from the DOS distribution centered at $\varepsilon_0 = 0$. Therefore, an excitation generated at a site with arbitrary energy in the DOS first energetically relaxes toward the tail states. While the energetically downward hops are dominant initially, a quasiequilibrium between the thermally activated upward hops and the downward hops is eventually obtained at later times. Therefore, the diffusivity within a disordered semiconductor is time dependent until the excitation has relaxed to a mean equilibrium energy below the center of the DOS ($\varepsilon_{\mathrm{eq}} = -\sigma^2/k_B T$). This time dependence, i.e., the nonequilibrium nature of the simulated diffusivity, affects the resulting transport properties [14,15]. Thus, the diffusion coefficient can critically depend on whether the initial energy is chosen from the DOS (centered at 0 eV) or the occupied DOS (ODOS) distribution centered at the equilibrium energy $\varepsilon_{\mathrm{eq}}$ below the DOS center, with the same σ. The analytical theories in the present paper (and, in general) are formulated under the premise of equilibrium transport; in order to provide an adequate comparison with the analytical results, our KMC simulations are thus performed under the conditions that the initial energy of an excitation is sampled from a Gaussian ODOS distribution of width σ centered at $\varepsilon_0 = \varepsilon_{\mathrm{eq}} = -\sigma^2/K_B T$. Hereafter we refer to this as the "ODOS approach" to distinguish it from the conventional "DOS approach."

At the beginning of the simulation, $t = 0$, an excitation is generated randomly at one of the lattice sites. In the case that the simulation is intended to start with an excitation in the ODOS, the energy of that lattice site is manually adjusted to be part of the ODOS. At each kinetic step, the excitation can hop to any of the nearest-neighbor sites. For the case of variable-range hopping (VRH) simulations, excitations are also allowed to access non-nearest hopping sites. Every permissible hop is treated as an event and for each event i, the rate W_i is calculated. For the selection of an event, firstly, for each event i the partial sum $S_i = \sum_{\beta=1}^{i} W_\beta$ is calculated. A random number φ is drawn from the interval $(0, W_T]$, with $W_T = \sum_{\beta=1}^{N_E} W_\beta$, N_E being the total number of events (permissible hops). From all possible events, the event i for which $S_{i-1} < \varphi \leqslant S_i$ holds is selected. The selected event is executed for the corresponding excitation and the simulation time (t) is updated by the waiting time, $\tau_w = -\ln(X)/W_T$ where X is a random number between 0 and 1. The simulation stops after 10^5 hops. The initial ($t = 0$) and final (after 10^5 hops) position of the excitation in the lattice are used to determine the values for mean diffusivity, $D = \Delta x^2/t$. Results are obtained by averaging over 5000 simulation trials accounting for different disorder configurations. The simulations do not take the effect of conjugation or correlated disorder into consideration.

III. THEORETICAL FORMULATION

A. Effective medium approximation approach

The effective medium approximation (EMA) is an analytic method that has been often used to describe different aspects of the charge transport properties in disordered semiconducting materials. This approach is conventionally used for the nearest-neighbor hopping transport in a periodic cubic lattice of different spatial dimensionalities from one dimensional (1D) to 3D. Within the EMA approach, the disordered organic medium with localized states for charge carriers is replaced by an effective ordered cubic 3D lattice with spacing $a = N^{-1/3}$ equal to the average distance between the localized states, where N is the density of the localized states. We consider that the energy ε of the localized states is randomly distributed and their DOS can be described by a Gaussian function with width σ, represented by Eq. (2). Such kind of DOS distribution is applicable for both charged and neutral excitations (excitons) in organic disordered solids. Polaron effects arising at sufficiently large electron-phonon coupling and/or high enough temperatures can be accounted for by employing the Marcus rate for nonadiabatic hopping transfer given by Eq. (4). Recently, we suggested a generalized EMA approach [5] which is applicable for an arbitrary polaron activation energy E_a compared to the energetic disorder parameter σ. This approach is based on the following self-consistency equation suggested earlier by Kirkpatrick [16] for the effective conductivity $\sigma_e = G_e/a$ characterizing the whole disordered system,

$$\left\langle \frac{\sigma_{12} - \sigma_e}{\sigma_{12} + (d-1)\sigma_e} \right\rangle = 0, \tag{5}$$

where $\sigma_{12} = G_{12}/a$ is conductivity in two-site cluster approximation, d is the dimensionality of the hopping transport system, G_{12} is two-site conductance, and angular brackets $\langle \cdots \rangle$ denote the configuration averaging. The above-mentioned EMA study, similar to that in the paper by Seki and Wojcik [9], was done using a constant Marcus rate prefactor $W_1 = 1$ in Eq. (4). This approach will be hereafter referred to as a "simplified Marcus" rate approach.

In the present work, we performed EMA calculations of the effective diffusion coefficient by using the full Marcus rate equation, i.e., explicitly taking into account the temperature-dependent prefactor. We focus our consideration here on the low carrier concentration transport regime and the limit of weak electric fields, when $eF \Delta R_{ij} \ll \sigma$. ΔR_{ij} is the hopping distance which, implicitly, depends on the energetic disorder. As demonstrated in Ref. [5], the effective diffusivity is $D_e = a^2 W_e$, where W_e is the effective jump rate between neighboring localized sites. It can be derived within the EMA approach by the following integral equation obtained as a result of configuration averaging in Eq. (5):

$$\int_{-\infty}^{\infty} dt_1 \int_{-\infty}^{\infty} dt_2 \exp\left[-\frac{1}{2}\left(t_1^2 + t_2^2\right)^2\right] \frac{x^{1/2} \exp\left[-\frac{x}{16x_a}(t_1 - t_2)^2 - \frac{x}{2}(t_1 + t_2) - \frac{1}{2}x^2\right] - X_e}{x^{1/2} \exp\left[-\frac{x}{16x_a}(t_1 - t_2)^2 - \frac{x}{2}(t_1 + t_2) - \frac{1}{2}x^2\right] + (d-1)X_e} = 0, \tag{6}$$

where $X_e = D_e/D_0$, $D_0 = a^2(J/\hbar)\sqrt{\pi/4E_a\sigma}\exp(-x\,x_a)$, $x = \sigma/k_BT$, and $x_a = E_a/\sigma$. It is worth noting that in the EMA approach we use direct configurational averaging over a DOS distribution, which avoids shortcomings involved in the effective transport energy $\varepsilon_{\text{trans}}$ or percolation concepts. The EMA is in particular a suitable method for studying hopping transport in disordered materials with not very large energetic disorder and it naturally allows accounting for the dimensionality of the system.

B. Multiple trapping and release approach

The multiple trapping and release (MTR) theory was initially developed for the description of trap-controlled transport in inorganic semiconductors with band conduction. Thus, according to the MTR, charge carriers can only be transported via conductive delocalized states lying above the so-called mobility edge ε_c. The carriers interact with localized states (traps) through trapping and thermal release. Despite the fact that all electronic states in conventional organic semiconductors are localized, a relatively simple MTR formalism can still be used to describe the hopping transport. The MTR description is commonly based on the concept of the transport energy $\varepsilon_{\text{trans}}$ playing the role of the mobility edge in the classical MTR model. There are two general approaches to defining the transport energy. The first one considers the transport level $\varepsilon_{\text{trans}}$ as a characteristic energy of the states predominantly contributing to the electric conductivity [17–20]. Due to the energetic disorder, such "conductive states" are actually distributed over a certain energy interval. Another approach (the effective transport energy concept) [18,19,21–26] considers the transport level as a parameter in the mean release rate of carriers from rather deep, mostly populated states. This release rate can be approximated in a form similar to the MTR model:

$$\omega(\varepsilon) = \omega_0 \, \exp\left(-\frac{\varepsilon_{\text{trans}} - \varepsilon}{k_BT}\right), \quad (7)$$

where ε is the energy of the initial state, and ω_0 is the frequency factor which is different from W_0 in Eq. (3).

It should be noted that there are many reports (see, for instance, [17–21,24,25]) on derivations of the transport energy for nonpolaronic hopping transport in Gaussian DOS, which were formulated for the Miller-Abrahams rate. There have been few applications of the effective transport energy concept to the Marcus rate model, except to its truncated form [22,23]. On the other hand, the transport energy approach does not need to be invoked explicitly to apply the MTR method to the hopping transport. Instead, the problem of defining the transport energy can be circumvented in the event that one can split all the available states into "transporting" states, which provide the principal contribution to the transport and "trapping" states, which delay carriers. The former states can be referred to as conductive states in a similar manner to the classical MTR model, and the latter ones can be considered as traps. This idea was proposed long ago by Schmidlin [27]; however, more work needs to be done on developing a general calculation method to obtain transport parameters with this approach. Below, we present our MTR approach, which makes use of this idea by Schmidlin. Our approach is quite

general and is suitable for the description of hopping transport irrespective of a jump rate model. We apply it to the analysis of temperature-dependent carrier diffusivity for both MA and Marcus rates in the limit of small carrier concentration and low electric fields. The gist of our approach lies essentially in reducing the well-known master equation of hopping transport [24,27,28] to the balance equation of the MTR model at arbitrary jump rates (see the Appendix for more details).

In practice, we identify a "conductive" state by the condition that the escape time from this state does not exceed a certain time t_0. Since the carrier release is a stochastic process, the probability that a given state is conductive, is determined by the Poisson distribution as

$$\varphi(\varepsilon) = 1 - \exp[-\omega(\varepsilon)t_0] \approx \omega(\varepsilon)t_0, \ \omega(\varepsilon)t_0 \ll 1, \quad (8)$$

provided that the critical time t_0 is rather small relative to a typical hopping time. Note that the approximation (7) is not relevant anymore to Eq. (8) and to the subsequent equations. The trap-controlled diffusivity in the MTR approach can then be expressed as [25,29]

$$D = D_c\frac{p_c}{p} \approx (a^2/t_0)\frac{\int_{-\infty}^{\infty} d\varepsilon\, g_{\text{ODOS}}(\varepsilon)\varphi(\varepsilon)}{\int_{-\infty}^{\infty} d\varepsilon\, g_{\text{ODOS}}(\varepsilon)}, \quad (9)$$

where p_c and p are the carrier concentration in "conductive" states and the total concentration, respectively. $D_c \approx a^2/t_0$ is the carrier diffusivity in conductive states, $a \approx N^{-1/3}$ is the mean hopping distance in conductive states, and $g_{\text{ODOS}}(\varepsilon)$ is the ODOS distribution proportional to the product $g(\varepsilon)\exp(-\varepsilon/k_BT)$ under quasiequilibrium conditions. The parameter t_0 cancels in Eq. (9) after combining Eqs. (8) and (9), and therefore the diffusivity is proportional to the mean release rate averaged over the ODOS distribution. The resulting relation reads as

$$D \approx a^2\langle\omega(\varepsilon)\rangle = a^2\frac{\int_{-\infty}^{\infty} d\varepsilon\, \omega(\varepsilon)g(\varepsilon)\exp\left(-\varepsilon/k_BT\right)}{\int_{-\infty}^{\infty} d\varepsilon\, g(\varepsilon)\exp\left(-\varepsilon/k_BT\right)}. \quad (10)$$

Further, to determine the mean release rate $\omega(\varepsilon)$ and to consider the variable-range hopping (VRH) regime, we use the *mean hopping parameter* method suggested by Arkhipov *et al.* [30], which is very similar to the method proposed by Apsley and Hughes [31] for a weak electric field and low carrier concentration limit. The function $\omega(\varepsilon)$ can be expressed as follows:

$$\omega(\varepsilon) = \omega_0 e^{-\langle u\rangle(\varepsilon)}, \quad \langle u\rangle(\varepsilon) = \int_0^{\infty} du\, e^{-n(\varepsilon,u)}, \quad (11)$$

where u is the hopping parameter; $n(\varepsilon, u)$ is the average number of target neighbor sites whose hopping rates are not smaller than a given value of $\omega_0\exp(-u)$. An important modification was done here with respect to the previous works [30,31] in order to preclude multiple carrier jumps within pairs of occasionally close localized states: Hopping neighbors for which return jumps to initially occupied states are more probable than jumps to other states are excluded from $n(\varepsilon, u)$. This also implies including the percolation effects [24,32,33] in a first approximation (see the Appendix for details). If the oscillations of a carrier within pairs of localized states are not excluded, then our MTR approach for the MA rate leads to a similar low-field mobility as obtained in

Ref. [30]. This similarity applies within the accuracy of the prefactor a^2, and using the Einstein relation $\mu = eD/k_BT$. It should be mentioned that results of the calculation with Eq. (11) for the MA rates showed that Eq. (7) can be considered as a good approximation for the release frequency $\omega(\varepsilon)$ when the localized states are rather deep, $\varepsilon < \varepsilon_{\text{trans}}$. Upon applying Eq. (7) and the Einstein relation, Eq. (10) reduces to the well-known result from the transport level method: $\mu \approx (e\omega_0 a^2/kT)\exp\left[-\varepsilon_{\text{trans}}/k_BT - 0.5(\sigma/k_BT)^2\right]$ [17–21,24,25]. However, using Eq. (7) as an approximation is generally inappropriate in the case of the Marcus rate model.

IV. RESULTS

A. *C* factor in the limit of purely disorder-controlled transport

To find the value of the C factor, which weighs the polaronic and disorder contributions to the temperature dependence of the mobility [Eq. (1)], we first consider simulations of charge-carrier transport using the kinetic Monte Carlo method. We differentiate between two cases, that is, transport in thermal equilibrium, and transport out of thermal equilibrium. It is well known that, in many experimental situations, e.g., in time of flight (TOF) and transient electroluminescence (TEL) measurements, one observes an initial short, sharp spikelike decay of the signal. This is because immediately after carrier injection or creation somewhere within the DOS, the carrier is usually *not* in thermal equilibrium. Rather, it relaxes energetically through a sequence of energetically downhill jumps until a quasiequilibrium transport is achieved, where thermally activated uphill jumps are in balance with downhill jumps. Experimentally, this is visible as a plateau in the intensity of the transient signal. This implies that the carrier moves between states that are energetically distributed, statistically with the same width (σ) as before, yet centered around an equilibrium energy, $\varepsilon_{\text{eq}} = -\sigma^2/k_BT$, below the center of the full DOS. The energetic distribution of these states is referred to as occupied density of states (ODOS). The relaxation behavior is well reproduced in KMC simulations when a carrier is initially placed at a random site within the full DOS. Following the carrier's trajectory implies following the relaxation process [1,14,15]. Transport in thermal equilibrium is reached and monitored eventually, yet long simulation times may be needed to arrive at this stage. A different situation prevails when the carrier moves under equilibrium conditions. This is the case, for example, in charge extraction by linearly increasing voltage (CELIV) experiments. Here, the carrier moves only within the ODOS. In KMC simulations, this can be realized by imposing the condition that the carrier starts its trajectory on a site within the equilibrium distribution, i.e., within the ODOS. The impact of nonequilibrium transport on the diffusivity is thus eliminated. For our KMC study, we consider both transport under equilibrium and out of equilibrium. The analytical EMA method and the MTR formalism in the present study apply only to the case of equilibrium transport.

Here, we first assess the impact of the two different KMC simulation approaches (DOS vs ODOS) on the temperature dependence of a quasiparticle diffusion coefficient (D) within the premise of the *Miller-Abrahams* rate model, using Eq. (3)
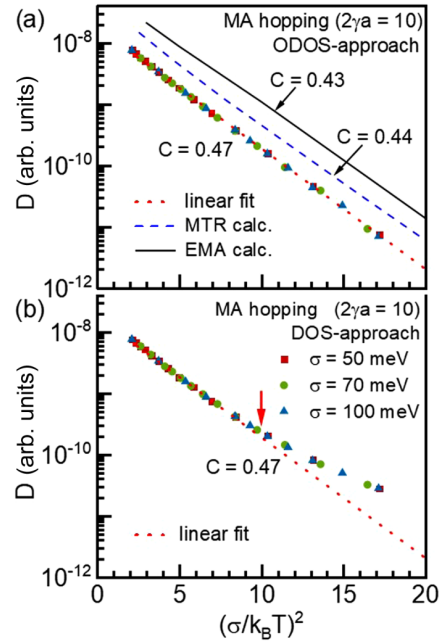
FIG. 1. Kinetic Monte Carlo simulations (symbols) of the diffusion coefficient as a function of disorder-normalized temperature for the *Miller-Abrahams rate* and the nearest-neighbor hopping regime in an isotropic 3D disordered organic system with different energetic disorder values ($\sigma = 50, 70,$ and 100 meV, indicated by red squares, green circles, and blue triangles, respectively). The KMC simulations are performed (a) for equilibrium transport, using the ODOS and (b) for nonequilibrium transport, using a conventional DOS as starting distribution. Dotted lines in both figures represent a linear fit to $\ln(D) \propto -C(\sigma/k_BT)^2$. Dashed and solid curves in (a) are the results obtained by MTR and EMA theories, respectively. These calculated curves are shifted vertically relative to each other for clarity. The arrow in (b) depicts the crossover from nondispersive to dispersive transport.

for the hopping rate. This implies that we neglect any polaronic disorder, corresponding to the situation of $E_a = 0$ in Eq. (1). We expect $\ln(D)$ to be proportional to $-C(\sigma/k_BT)^2$ from Eq. (1), so that the value of C corresponds to the slope in a $\ln(D)$ vs $(\sigma/k_BT)^2$ plot, as shown in Fig. 1. The results obtained for equilibrium transport are compared against those obtained using the EMA method and the MTR formalism in Fig. 1(a). The simulations were done employing our ODOS-simulation method for a lattice representing an isotropic 3D disordered organic system with different widths of the Gaussian ODOS ($\sigma = 50, 70,$ and 100 meV), and considering solely the nearest-neighbor hopping (coordination number $N = 6$). Since all excitations are thermally equilibrated right from the start of the simulation, a perfect linear dependence of $\ln(D)$ vs $(\sigma/k_BT)^2$, depicted by a dotted line, is observed over a broad temperature range irrespective of the energetic disorder. The slope of this dependence yields a C factor of about 0.47. The temperature dependences of the diffusion coefficient calculated by effective medium and MTR theories are presented by solid and dashed lines, respectively, and are vertically translated for clarity of display. They demonstrate almost perfect agreement with the KMC simulation data over
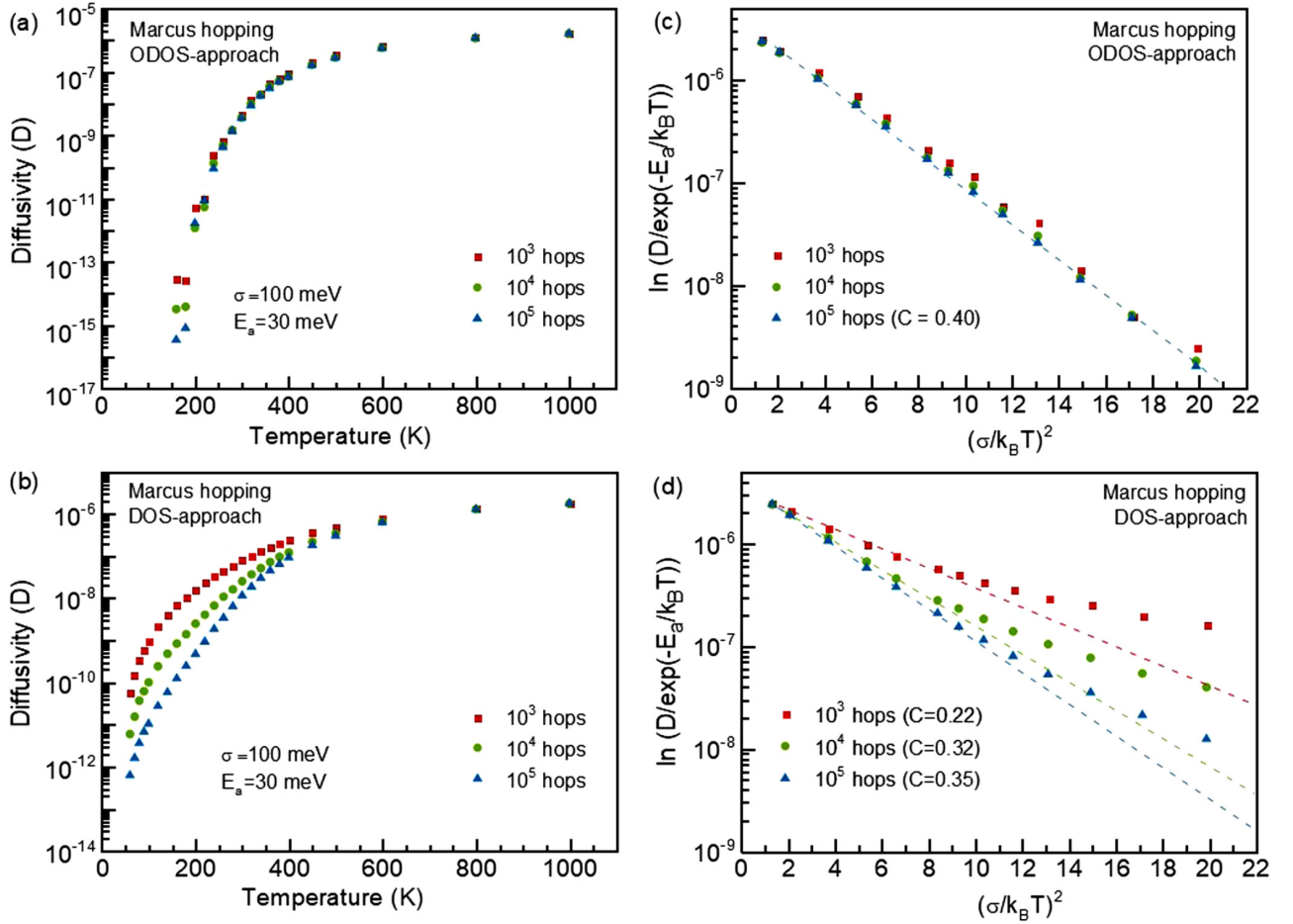
90

FIG. 2. Temperature dependencies of the diffusion coefficient obtained for the *Marcus rate* by kinetic Monte Carlo simulations (symbols) for the nearest-neighbor hopping in an isotropic 3D disordered organic system at different number of hops during simulations (ranging from 10^3 to 10^5) performed using (a), (c) conventional DOS and (b), (d) equilibrated ODOS-simulation approaches. Simulations are done at $\sigma = 100$ meV and $E_a = 30$ meV. Straight lines in (c), (d) represent the linear fit of the above simulated super-Arrhenius plot (symbols) made in the temperature range where the $\ln[D/\exp(-E_a/k_BT)] \propto (\sigma/k_BT)^2$ law is obeyed.

a broad range of σ/k_BT, yielding virtually the same C factor (0.43–0.44) for the Miller-Abrahams hopping in conjunction with the nearest-neighbor hopping regime. This testifies the reliability of our ODOS-based simulation approach, which can be adequately compared against analytic theories formulated just for the nondispersive transport in disordered organic solids.

Figure 1(b) presents the temperature-dependent diffusivity simulated in the more conventional way, i.e., when the energy of an initial site is sampled from the DOS distribution. The figure demonstrates that the diffusion coefficient obtained by the conventional DOS-simulation approach follows the predicted $\ln(D) \propto -C(\sigma/k_BT)^2$ dependence (depicted by a dotted line) only at relatively low energetic disorder or high temperatures ($\sigma/k_BT \leqslant 3.3$). The dependence progressively deviates from a straight line at larger σ/k_BT values. This is a well expected result indicative of the contribution from the nonequilibrium (dispersive) transport to the simulated diffusivity, which consequently leads to an overestimation of diffusion coefficients at larger σ/k_BT. Hence, the C factor can be derived only from the high-temperature branch of the obtained

dependence, where it is 0.47 as in the case of equilibrium transport.

B. *C* factor when a polaronic contribution is considered

Next, we test our equilibrated Monte Carlo simulation approach for the *Marcus rate* model, using Eq. (4) for the hopping rate. This is equivalent to the situation of $E_a \neq 0$, and $\sigma \neq 0$ in Eq. (1). Figures 2(a) and 2(b) show temperature-dependent diffusion coefficients, parametric in the number of hops during simulations, obtained for equilibrium transport (ODOS approach) and nonequilibrium transport (DOS approach), respectively. We used $\sigma = 100$ meV and $E_a = 30$ meV, and hopping is restricted to the nearest-neighbor lattice sites. A general observation is that the diffusivity increases as the temperature increases, and this is accompanied by a decrease in the rate of increment. This is a typical behavior for thermally activated hopping transport [1]. The results for the two simulation approaches differ insofar that for the ODOS approach, representing equilibrium transport, the temperature dependence of diffusivity remains almost identical

irrespective of the number of hops after which the diffusion coefficient is evaluated. When plotting $\ln[D/\exp(-E_a/k_BT)]$ vs $(\sigma/k_BT)^2$ such as to readily read off the value of C from the slope in Fig. 2(c), the expected linear dependence (with $C = 0.4$) is obtained irrespective of the number of hops executed by the excitation (with minor deviations at lower number of hops). In contrast, when transport is not in equilibrium, represented by the conventional DOS approach, the temperature dependence of the diffusivity depends on the number of hops executed, and $\ln[D/\exp(-E_a/k_BT)]$ deviates significantly from the linear dependence on $(\sigma/k_BT)^2$, suggesting an overestimation of diffusivity values at lower temperatures [Fig. 2(d)], analogous to the behavior of the diffusivity for the case of MA rates in Fig. 1(b). Moreover, the dependence on the number of hops complicates the determination of the exact C factor even when considering the high-temperature (low σ/k_BT) range since the lower the number of hops, the further away the transport is from equilibrium. Extrapolating the high-temperature regime by linear fits, shown as dashed lines in Fig. 2(d), yields a C factor that increases progressively from $C = 0.22$ (for 10^3 hops) to 0.32 (10^4 hops) and to 0.35 (10^5 hops).

To summarize the results obtained so far, in Sec. IV A we considered the value of C, allowing for only nearest-neighbor hops, for a *purely disorder-controlled* transport for the case of transport both in and out of equilibrium. In thermal equilibrium, the values obtained by three independent approaches, that is, KMC simulation, EMA theory, and the MTR formalism, agree on a value of $C = 0.45 \pm 0.02$. Out of thermal equilibrium, KMC predicts a lower value that depends on the deviation from the equilibrium situation. In Sec. IV B we extended our KMC study to the case of transport in a disordered energy landscape *with consideration of reorganization energy*, exemplarily using $\sigma = 100$ meV and $E_a = 30$ meV ($\frac{\sigma}{E_a} = 3.3$). A value of $C = 0.40$ is approached asymptotically as carriers reach thermal equilibrium. This value is lower than what we obtained for the case when polaronic contributions are neglected. In the next section, we focus on the dependence of the C factor on the relative size of the disorder to the reorganization energy, still restraining our simulations to nearest-neighbor hops.

C. Impact of the reorganization energy on the C factor

Having seen that the value of the C factor is modified when a polaronic contribution to the transport is taken into account, we systematically addressed the dependence of the C factor on the magnitude of the polaronic contribution. Figure 3 presents the C factor as a function of the σ/E_a ratio. As before, we used the Marcus-type hopping rate in the presence of disorder, Eq. (4), and allowed only for nearest-neighbor hops. In addition to the results obtained for equilibrium (ODOS) and nonequilibrium (DOS) transport, we show the results from the MTR formalism and the EMA calculations, which treat the equilibrium situation. For comparison, we also include the values obtained with the simplified Marcus expression used previously by Seki and Wojcik [9], where the preexponential factor [W_1 in Eq. (4)] is approximated by a constant ($W_1 = 1$).

For all approaches we obtain the same qualitative result, that is, that the factor C increases with increasing σ/E_a ratio,
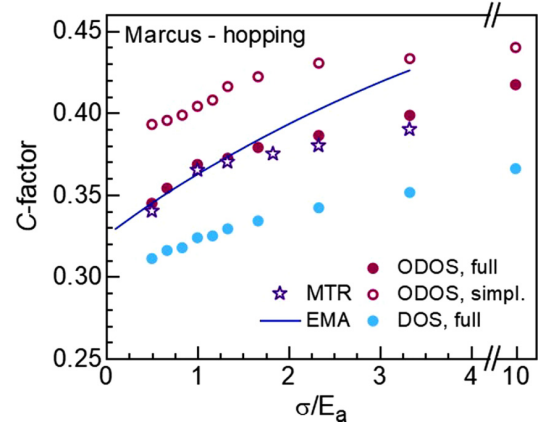
FIG. 3. C factor vs σ/E_a derived from kinetic Monte Carlo simulations of the nearest-neighbor hopping diffusivity $D(T)$ using a Marcus rate in an isotropic 3D system and $2\gamma a = 10$. Also shown are results from analytic MTR and EMA calculations. The KMC simulations marked "DOS, full" refer to the case of nonequilibrated transport; all other data are obtained for transport under equilibrium. For comparison, values obtained using a Marcus-type hopping rate with a constant preexponential factor is also shown ("ODOS, simpl.")

i.e., with increasing the relative strength of the disorder effect. This is in line with our previous finding [5]. We note that the C factor obtained under inclusion of polaronic effects is always smaller than that obtained using a pure Miller-Abrahams rate ($C \cong 0.44$). Evidently, any contribution from geometric reorganization of the molecule reduces the relative weight of the disorder contribution to transport. However, in the limit of vanishing E_a, exemplified by the data point at $\sigma/E_a = 10$ in Fig. 3, the MA result is recovered asymptotically.

Regarding the results, we again find a gratifying quantitative agreement between the three different equilibrium nearest-neighbor hopping (NNH) approaches used, that is, the KMC simulation (ODOS), the MTR formalism, and the EMA calculations, as depicted in Fig. 3 by stars and solid line, respectively. As expected, the EMA calculations agree with simulation data only at low to moderate energetic disorder ($\sigma/E_a < 2$), where EMA formalism is more justified. In the present study we used a conventional EMA approach based on a self-consistency equation (5), which is not suitable for a strongly inhomogeneous medium, or in other words, for high disorders. This explains the disagreement between the KMC ODOS simulations and EMA at large σ/E_a values [34]. The agreement between the three different and independent approaches gives confidence in the absolute values obtained for the factor C.

Analogous to the results in the previous sections, calculations carried out using a conventional KMC approach, where the carrier is placed at random in the DOS and then relaxes, yield a reduced value of the factor C as compared to the ODOS approach, i.e., a lower contribution of the disorder to transport, depending on how far from equilibrium the transport takes place. In contrast, an increased value of the factor C is obtained when the Marcus-type hopping rate is simplified by assuming a constant prefactor. We obtain principally the same results as that obtained before for $W_1 = 1$ in the paper by Seki
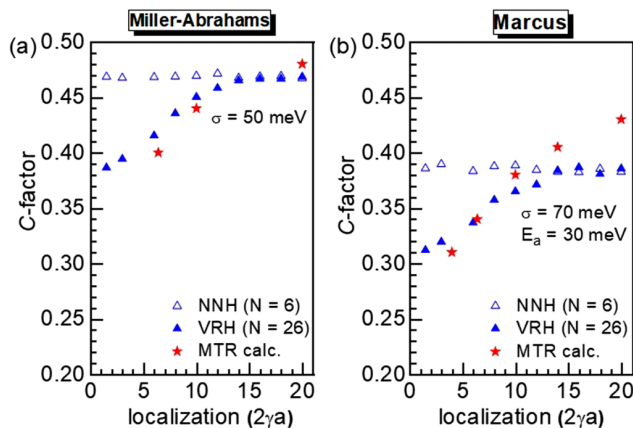
FIG. 4. The C factor as a function of localization derived from kinetic Monte Carlo simulations of hopping diffusivity $D(T)$ in both the nearest-neighbor hopping (empty symbols) and variable-range hopping (filled symbols) regimes using (a) a Miller-Abrahams or (b) a Marcus-type hopping rate. Results of analytic MTR calculations in the VRH regime for MA and Marcus rates are shown by red stars in (a), (b), respectively.

and Wojcik [9]. Evidently, this simplification is a rather coarse approximation that overestimates the C factor.

D. C factor in variable-range hopping (VRH) regime

The nearest-neighbor hopping (NNH) considered in the preceding section was modeled assuming just six nearest neighbors of a site i on a cubic 3D lattice ($N = 6$). However, it is well known that hops between the non-nearest-neighboring sites can also contribute to the hopping transport. This is described by variable-range hopping (VRH) [6] which is a more general approach and considers transitions of carriers to further neighbors than the nearest ones. Here VRH was implemented in the KMC simulations by allowing long-distance jumps to as many as $N = 26$ neighbors in total, i.e., up to the third-nearest neighbor. The probabilities of such jumps are determined by the carrier localization parameter ($2\gamma a$). Figure 4 presents the C factor obtained as a function of $2\gamma a$, with larger values implying stronger localization. Simulation results are shown for jumps to the third-nearest neighbor ($N = 26$ sites), thus enabling the VRH regime (filled triangles), and they are compared to those allowing for hopping to next-nearest neighbors ($N = 6$, empty triangles). We only considered the case of equilibrium transport, once for purely disorder-controlled transport, using a Miller-Abrahams type hopping rate [Eq. (3)] and once when including polaronic effects through a Marcus-type hopping rate [Eq. (4)]. Also shown are values obtained using the MTR formalism. For the EMA calculations that we used in the previous section, a distinction between NNH and VRH cannot be implemented explicitly.

As expected, no dependence of the C factor on the localization length was observed for the case of NNH because this regime is preserved at $N = 6$ irrespective of the inverse localization length (γ) value. On the other hand, Figs. 4(a) and 4(b) demonstrate a clear decrease in C factor with decreasing

$2\gamma a$ in the VRH regime as found by both the KMC simulations (filled triangles) and the MTR theoretical calculations (stars). At large localization, the values converge to the value of NNH for all the simulations, which is a trivial observation, since at large localization or very poor electronic coupling, the NNH regime becomes dominating. We note the difference between the KMC and the MTR obtained values for C in the limit of large localization. While this is a minor effect for pure disorder-dominated transport, it is significant when polaronic contributions are included. We speculate whether in this case, MTR is less suitable, since the distinction between "transporting" and "trapping" states, on which this formalism is based, becomes blurred [33].

Overall, the results obtained so far have demonstrated that

(i) There is very good agreement between three approaches for the C factor for equilibrium transport. Depending on conditions, values range from 0.30 to 0.47.

(ii) The value of the C factor decreases when transport is out of equilibrium.

(iii) The value of the C factor decreases when reorganization contributes to the transport.

(iv) The value of the C factor decreases when the wave function of the charge or excitation is less localized.

This behavior is not consistent with the notion of a "universal scaling law," at least not in the strict mathematical sense. For practical purposes, one may consider that, in thermal equilibrium, the values for C range around 0.40 ± 0.05. We shall therefore evaluate the impact of this variation in the next section.

V. ANALYSIS OF EXPERIMENTAL DATA

The theoretical and simulation results obtained in the previous sections are utilized here to analyze earlier experimental transport data. A frequently encountered albeit problematic procedure adopted in the community to obtain the polaronic activation energies (E_a) for transport is to analyze the $1/T$ dependence of zero-field mobility using Eq. (1) presuming zero disorder, i.e., Eq. (12a). Similarly, the energetic disorder can be obtained by analyzing the temperature dependence of the zero-field mobility ($1/T^2$ dependence) assuming $C = 0.44$ within a purely disorder-controlled MA formalism, i.e., $E_a = 0$, as established by previous KMC and EMA approaches [1]; see Eq. (12b):

$$\mu(T) = \mu_0 \exp\left[-\left(\frac{E_a}{k_B T}\right)\right], \tag{12a}$$

$$\mu(T) = \mu_0 \exp\left[-0.44\left(\frac{\sigma}{k_B T}\right)^2\right]. \tag{12b}$$

However, this procedure has serious shortcomings, because disorder and reorganization energy are entangled, as reflected in the use of the unified model, Eq. (1).

In this section, we illustrate how much difference can be expected in the σ and E_a values when using different formalisms to fit the data. For this assessment, we analyze the temperature dependence of the zero-field TOF mobility for holes in a series of conjugated alternating phenanthrene indenofluorene copolymers reported by Hoffmann *et al.* [35]. We analyze four copolymers from this paper labeled as

TABLE I. E_a and σ values obtained from fitting with Eq. (12). Also given are E_a values obtained from DFT calculations (from Ref. [35]).

Copolymer	E_a (meV) by Eq. (12a)	σ (meV) by Eq. (12b)	E_a (meV) by DFT
1	178 ± 2	109 ± 2	46
3	235 ± 2	102 ± 2	38
7	329 ± 2	89 ± 2	25
9	397 ± 2	91 ± 2	31

copolymers 1, 3, 7, and 9 (see Sec. 1 of the Supplemental Material [36] or Ref. [35] for chemical structure). For reference, we quote in Table I the values obtained in Ref. [35] from fitting the mobilities of the copolymers with Eq. (12).

As discussed in detail in Ref. [35], it turns out that the σ values obtained from Eq. (12) are consistent with those obtained by other methods, while the E_a values are unrealistically large. Thus, one needs to obtain estimation for E_a by other means, such as density-functional theory (DFT) calculations.

If we wish to assess how the values derived for σ and E_a depend on the C factor used, a straightforward test is therefore to take the DFT-calculated E_a value and subsequently employ Eq. (1) to determine σ for several values of C. Figure 5(a) presents the experimental mobility data reported by Hoffmann *et al.* [35] (symbols) plotted against $1/T^2$ on a semilogarithmic scale. The solid lines are the corresponding fits done using Eq. (1) with $C = 0.40$ and using the DFT-calculated E_a values summarized in Table I. A comparison of the fits to the experimental data with Eq. (1) for $C = 0.35$, 0.40, and 0.44 is shown exemplarily for copolymer 1 in Fig. 5(b). It illustrates that the fits with different approaches coincide perfectly and are almost indistinguishable. Given the limited temperature range from 300 to 350 K for which the mobility was determined, this is expected. The data for copolymers 3, 7, and 9 agree similarly well and are shown in Sec. 2 of the Supplemental Material [36]. The disorder parameters obtained as a result of fittings are summarized in Table II.

We observe that the σ values obtained when using a pure MA approach, Eq. (12b), or a unified approach, i.e., Eq. (1), with different values for C differ by less than 10% from each other. This is within the typical experimental error range (note that the error given refers to the fitting procedure). Our result implies that the consideration of the polaronic contribution to the transport description, and the question of how much

FIG. 5. (a) The temperature dependence of the mobility plotted as μ vs $1/T^2$ on a semilog scale, along with the zero-field TOF mobility for copolymers 1 (red squares), 3 (green circles), 7 (pink triangles), and 9 (blue diamonds) as reported in Ref. [35]. Solid lines represent the fitting results using Eq. (1) with $C = 0.40$ and E_a values presented in Table I. (b) Comparison of the fits done by using Eq. (1) with $C = 0.35$, 0.40, and 0.44, and by using Eq. (12b) (MA rate).

weight this should be given, is *not* critical for the determination of the disorder value as long as C ranges around $C = 0.40 \pm 0.05$.

However, a very different result is obtained when the disorder value from the pure MA approach is used in Eq. (1), and E_a is determined parametric in the C factor. Table III summarizes the values obtained. The fits to the experimental data are as good as in Fig. 5. They can be found in Sec. 2 of the Supplemental Material [36] for reference. However, the

TABLE II. The σ values obtained from fitting with Eq. (1), using the DFT-calculated E_a values from Table I.

Copolymer	σ (meV) by Eq. (1), $C = 0.35$	σ (meV) by Eq. (1), $C = 0.40$	σ (meV) by Eq. (1), $C = 0.44$
1	116 ± 2	108 ± 2	103 ± 2
3	108 ± 2	101 ± 2	96 ± 2
7	95 ± 2	89 ± 2	85 ± 2
9	97 ± 2	91 ± 2	86 ± 2

TABLE III. E_a values obtained from fitting with Eq. (1), using σ values from Table I.

Copolymer	E_a (meV) by Eq. (1), $C = 0.35$	E_a (meV) by Eq. (1), $C = 0.40$	E_a (meV) by Eq. (1), $C = 0.44$
1	78 ± 2	35 ± 2	0 ± 2
3	69 ± 2	33 ± 2	0 ± 2
7	50 ± 2	21 ± 2	0 ± 2
9	54 ± 2	24 ± 2	0 ± 2

94

E_a values span a much wider range, implying that the fitting approach has a huge effect. This demonstrates that the value obtained for E_a depends more strongly on the correct choice of the C factor than the values obtained for σ. It seems that the range of values obtained using Eq. (1) with $C = 0.40 \pm 0.03$ is reasonably realistic (cf. Sec. 3 of the Supplemental Material [36] for detailed discussion), while a full neglect of disorder contributions as in a pure Marcus model, Eq. (12a), results in values that are at variance with other experiments.

VI. DISCUSSION AND CONCLUSIONS

This study illuminates several points regarding the description of charge transport. It clarifies that the relative contribution of polaron and disorder effects to the charge-carrier mobility, as quantified through the value of the C factor, depends on various factors.

One aspect is whether charge transport takes place *in equilibrium or out of equilibrium*: The further away the transport is from equilibrium, the lower is the contribution of disorder, and thus the lower is the C factor. It is straightforward that disorder should play a lesser role when hops occur mostly downward in energy. One may need to bear this in mind when analyzing experimental data where transport is far out of equilibrium, e.g., on very short timescales after carrier generation. Our study, notably Figs. 1 and 2, indicates that this is of relevance to both MA as well as Marcus rates. Correspondingly, it can become important to perform the KMC calculations under equilibrium conditions, e.g., by starting from the ODOS distribution instead of the full DOS, if one wishes to obtain a reliable value that is independent of simulation time or temperature. This is an important insight, as most available KMC simulations are premised on the condition that the initial energy of an excitation is sampled from a DOS distribution.

Another aspect is that the value of the C factor depends on the *ratio between the reorganization energy and the disorder*. This had been noted before by several groups [5,6,22], though there are also disagreeing calculations [9]. The gratifying feature in our work is the quantitative agreement of $C(\sigma, E_a)$ obtained via three independent approaches, that is, KMC simulations, EMA calculations, and the MTR formalism. As discussed above, EMA calculations apply to the range of lower disorder values, while the MTR formalism is more meaningful for the range of higher disorder values where the distinction between conducting and trapping states is maintained. KMC applies over the entire range of disorder values, though for comparison with the EMA and MTR formalism, one needs to ensure that the simulation is conducted for the quasiequilibrium case. In this context, we noticed the importance of using the full Marcus-type hopping rate, i.e., including the temperature-dependent prefactor. The evolution of $C(\sigma, E_a)$ was only rendered consistently between the three approaches when using Eq. (4) with the temperature-dependent prefactor. This may account for the difference to the work by Seki and Wojcik, who assumed a constant Marcus prefactor [9].

A further aspect concerns the dependence of the C factor on the *delocalization of the carrier wave function*. We revealed the effect of the degree of carrier localization in organic semiconductors on the C factor for Marcus polaron

hopping. It was found to feature a qualitatively similar trend to that obtained for MA hopping of nonpolaronic carriers (Fig. 4). In both cases the weak carrier localization gives rise to a significantly lower C factor. This is equivalent to the earlier noticed dependence of the C factor on lattice geometry, coordination number, or dimensionality [37–39]. Our study implies a reduced contribution of disorder when more lattice sites are accessible for transport. It is easy to see that disorder should matter less when a particular energy barrier can simply be circumvented by a different pathway, so that increases in dimensionality, coordination number, or accessible neighbor sights all reduce the contribution of disorder. This aspect is easily overlooked, and perhaps not always sufficiently appreciated. For example, in our earlier work [5], we reported a stronger dependence of the C factor on σ/E_a than here. The reason is that in the earlier work, the lattice chosen was not a strictly simple cubic lattice but a slightly orthorhombic one. This was done in order to match the experimental conditions and it resulted in a stronger evolution of $C(\sigma, E_a)$. This dependence on dimensionality and available lattice sites implies that the distribution of chromophores in a film, and in particular, any existence of partial order, will have a significant impact on the appropriate value of the C factor.

Given the variation of the C factor with experimental conditions, one may question what can be learned from an analysis of temperature-dependent mobility data in the framework of Eq. (1). The investigation we performed clearly indicated that such an analysis provides a reasonable basis for the assessment of disorder using a C factor of $C = 0.40 \pm 0.03$. "Reasonable" means here that the values are within 10% of each other and the value obtained from a pure MA approach, and agree with any other information available from experiments [35]. In this way, our work eventually provides a "legitimization" for the use of the simple MA rate model to the description of the charge transport in realistic disordered organic solids. This is a key message of our paper, especially relevant for experimentalists, who routinely use the Gaussian disorder model (GDM) for their data analysis and naturally want to know to what extent this zero-order approach is accurate in determination of the width of the DOS. We emphasize that Eq. (1) with $C = 0.40 \pm 0.03$ is fully applicable only when the carrier transport is in quasiequilibrium. This is when $(\sigma/k_BT)^2 < 10$, i.e., $\sigma/k_BT < 3.3$ as evident from Figs. 1 and 2. Experimentally, these conditions are usually fulfilled for CELIV measurements or for nondispersive TOF measurements where the plateau and the subsequent kink in the current transients are clearly visible. Note that our conclusion about the appropriateness of the MA rate is consistent with the recent finding by de Vries *et al.* in Ref. [40] based on full quantum mechanical treatment; however, in our work the problem was tackled from the standpoint of established hopping-transport theories and computer simulations. As also mentioned by de Vries, the values obtained for the reorganization energy are significantly less reliable. Typical values of the reorganization energy in conventional organic semiconductor have been estimated as $\lambda = 100$–200 meV [40].

Further, we would like to note that, although the impact of carrier equilibration on the C factor was indeed shown before for the case of nonpolaronic transport (MA rates), it has rarely been considered for the polaronic hopping transport

given by the Marcus rate. Also, the effect of the degree of carrier localization in organic semiconductors on the C factor was not reported before for the Marcus hopping rate, while it has been demonstrated for the nonpolaronic transport regime. In addition, almost all theoretical efforts in the description of variable-range hopping (VRH) in organic semiconductors were based so far just on the MA rate model and the VRH remains virtually unexplored for the Marcus rate model. Our work resolves the long-standing controversy regarding the C factor and explains why different values were obtained in the literature. We identify differences in the approaches used in the previous works and their specific aspects leading to the contradictory results.

Our initial question on how strongly the reorganization energy contributes to charge transport in disordered organic semiconductors may thus be answered in a brief way as "not much." The polymers of Ref. [35] that we used as experimental example are typical conjugated polymers insofar that their backbones consist of bridged or fused, i.e., rigid, phenyl rings as well as more flexible triphenylamines. They have a disorder parameter around 100 meV and an E_a of less than 50 meV, i.e., a reorganization energy λ of less than 200 meV. These values can be considered as representative. We found that entirely ignoring the polaronic contribution by analyzing the $\mu(T)$ data in terms of the simple Gaussian disorder model overestimates the disorder by roughly 10%. This can be taken as an indication that the polaronic contribution is small.

Finally, in the present paper we made important methodological advancements in both analytical treatment and computer simulations of polaron transport. In particular, we have extended the multiple trapping and release (MTR) theoretical approach to describe the Marcus polaron hopping. An important advantage of the suggested approach is that it allows avoiding the transport energy (TE) concept, as the calculation of the TE for Marcus rates turned out to be very problematic, which is in contrast to MA rates where this concept is conventionally used. Further, we have improved the algorithm of kinetic Monte Carlo simulations (KMC) to consider adequately the equilibrated polaron transport in a Gaussian DOS, which can be ensured under the conditions that the initial energy of an excitation is sampled from a Gaussian occupational DOS (ODOS) distribution shifted by the equilibrium energy below the DOS center. We found that this aspect has a significant impact on the polaron transport, which has normally been overlooked in previous relevant KMC simulation studies.

APPENDIX: APPLICABILITY OF THE MULTIPLE TRAPPING MODEL TO THE DESCRIPTION OF HOPPING TRANSPORT

We start from the well-known master equation of hopping transport for the occupation probability, f_i, of the ith hopping state [24,28],

$$\partial f_i/\partial t = \sum_{j \neq i} [\nu_{ji} f_j (1 - f_i) - \nu_{ij} f_i (1 - f_j)], \quad \text{(A1)}$$

where ν_{ij} is the hopping rate of a carrier from the ith state to the jth state. We assume that the release of carriers from the rather deep states i, the rate of release from which determines the magnitude of diffusivity and mobility, occurs preferably to relatively shallow energy states j having very low occupation probability, $f_j \ll 1$. This contrasts with the mechanism of the Mott-type conductance near the Fermi level, which might typically be realized in the low-temperature limit and is not considered here [25]. The low occupation probability results from low mean occupation time of these states, since most of the jumps per unit time occur via these shallow j states. Particularly, capture of carriers by the deep i states occurs from these "fast" j states. Further, we assume that the population of the "fast" states (of the energies ε_j) can be described by the quasiequilibrium Boltzmann's function, $f_j = f_0 \exp[-\varepsilon_j/k_B T]$. At the same time, the deep states of the energies ε_i can be filled with much higher probability $f_i \cong 1$; their population can also be far from a quasiequilibrium distribution if the initial energy distribution of the carriers is not equilibrated as a consequence of a rather small number of the release events from i states. Using the detailed balance principle, $\nu_{ji} = \nu_{ij} \exp[(\varepsilon_j - \varepsilon_i)/k_B T]$, and introducing the symbol $\omega_i = \sum_{j \neq i} \nu_{ij}$, one can rewrite the balance equation (A1) as follows:

$$\partial f_i/\partial t = f_0(x, t) \exp[-\varepsilon_i/k_B T](1 - f_i)\omega_i - f_i\omega_i, \quad \text{(A2)}$$

where x is the set of spatial coordinates. One may assume that the prefactor f_0 in Eq. (A2) is j independent, provided that the spatial scale and timescale of variations of this prefactor is much larger than several hopping lengths and several hopping times, respectively.

The magnitude of the release frequency of a carrier from the state i, ω_i, not only depends on its energy, ε_i, but also on other characteristics (such as energies, distances, and orientations) of the surrounding states. It is known from percolation theory that the states, which contribute to the transport predominantly, form a network with some characteristic size r_{c0} (correlation radius of percolation cluster) [32–34]. One can simplify the description of transport, provided that the function f in Eq. (A1) is averaged on the spatial scale of r_{c0} (which is temperature and disorder dependent) and on the respective timescale, t_{c0} (the diffusion time for the distance r_{c0}). One can select the "conductive" states among the "fast" states by relating the prefactor $f_0(x, t)$ and the concentration of carriers (the "mobile" carriers) in these states, $p_c(x, t)$,

$$f_0(x, t) = p_c(x, t)/N_c, \quad \text{(A3)}$$

where N_c is an effective concentration of "conductive" states. This concentration does not depend on coordinates and time due to quasiequilibrium occupation of conductive states and

macroscopic uniformity of the material. The other "fast" states and i states are considered below as traps (the shallower and the deeper fraction, respectively). Then one can rewrite Eq. (A2) in the continual form, introducing the spatially uniform energetic distribution function of traps $g_t(\varepsilon)$, energy-dependent release frequency $\omega(\varepsilon)$ instead of ω_i, the averaged occupation probability $f(\varepsilon, x, t)$, and the distribution of occupied traps $\rho(\varepsilon, x, t) = g_t(\varepsilon) f(\varepsilon, x, t)$. Multiplying Eq. (A2) by $g_t(\varepsilon)$, and using Eq. (A3), one obtains the balance equation of the MTR model [29],

$$
\frac{\partial \rho(\varepsilon, x, t)}{\partial t} \frac{1}{c(\varepsilon)}
$$
$$
= [g_t(\varepsilon) - \rho(\varepsilon, x, t)] p_c(x, t) - N_C \rho(\varepsilon, x, t) \exp\left(\frac{\varepsilon}{k_B T}\right),
$$
(A4)

where $c(\varepsilon) = [\omega(\varepsilon)/N_C] \exp(-\varepsilon/k_B T)$ is the capture rate of a carrier on a trap of given energy. A model of hopping rates, ν_{ji}, defines only the shape of the function $\omega(\varepsilon)$, and hence $c(\varepsilon)$, and the value of N_C. One can find the latter value from the equation which follows from Eq. (A3) and the definition of the function, $\varphi(E)$; see Eq. (8),

$$
p_c(x, t) = \frac{p_c(x, t)}{N_C} \int_{-\infty}^{\infty} dE \, g(\varepsilon) \varphi(\varepsilon) \exp\left(-\frac{\varepsilon}{k_B T}\right), \quad \text{(A5)}
$$

eliminating $p_c(x, t)$ from both sides of this equation. Since $\varphi(\varepsilon) \approx \omega(\varepsilon) t_0$, hence $g_t(\varepsilon) \approx g(\varepsilon)$. Provided that $p(x, t) \approx \int_{-\infty}^{\infty} d\varepsilon \rho(\varepsilon, x, t)$, under quasiequilibrium Eq. (A4) yields

$$
p(x, t) = p_c(x, t) \int_{-\infty}^{\infty} dE \frac{g(\varepsilon)}{N_C} \exp\left(-\frac{\varepsilon}{k_B T}\right). \quad \text{(A6)}
$$

Equation (10) follows from Eqs. (9), (A5), and (A6).

Thus, one needs to calculate the release frequency $\omega(\varepsilon)$ for defining $c(\varepsilon)$ and N_C in Eq. (A4). In this work, we calculate it from Eq. (11), where

$$
n(\varepsilon, u) = \iint_{\Omega(\varepsilon, u)} d\varepsilon' d^3 r g(\varepsilon') P(\varepsilon, \varepsilon', u), \quad \text{(A7)}
$$

where the integration volume $\Omega(\varepsilon, u)$ in the $\varepsilon' - r$ space (r is the distance to a neighbor state and ε' is its energy) is defined by the condition that the hopping rate from the initial state to any state in this volume is not smaller than a given value, $\omega_0 \exp(-u)$, where u is the hopping parameter; $P(\varepsilon, \varepsilon', u)$ is the probability that the jump is not followed by returning to the initial state (of the energy ε):

$$
P(\varepsilon, \varepsilon', u) = \begin{cases} 0, & n_0(\varepsilon', u') \leqslant 1 \\ 1 - e^{-[n_0(\varepsilon', u') - 1]}, & n_0(\varepsilon', u') > 1 \end{cases}, \quad \text{(A8)}
$$

where $u'(\varepsilon, \varepsilon', u) = u + (\varepsilon - \varepsilon')/k_B T$ is the hopping parameter for the returning jump, and

$$
n_0(\varepsilon, u) = \iint_{\Omega(\varepsilon, u)} d\varepsilon' d^3 r g(\varepsilon'). \quad \text{(A9)}
$$

Thus, the neighbor states, for which the initial state is the nearest hopping neighbor (in u space), are not considered. The term $n_0 - 1$ appears in Eq. (A8), because one state (the initial state) definitely persists for the most relevant (i.e., upward in energy) jumps. The integration volume Ω depends on the model of hopping rates (for example, MA or Marcus).

[1] H. Bässler, Phys. Status Solidi B **175**, 15 (1993).

[2] H. Bässler, P. M. Borsenberger, and R. J. Perry, J. Polym. Sci., Part B: Polym. Phys. **32**, 1677 (1994).

[3] P. E. Parris, V. M. Kenkre, and D. H. Dunlap, Phys. Rev. Lett. **87**, 126601 (2001).

[4] I. I. Fishchuk, A. Kadashchuk, H. Bässler, and S. Nešpůrek, Phys. Rev. B **67**, 224303 (2003).

[5] I. I. Fishchuk, A. Kadashchuk, S. T. Hoffmann, S. Athanasopoulos, J. Genoe, H. Bässler, and A. Köhler, Phys. Rev. B **88**, 125202 (2013).

[6] N. Lu, L. Li, W. Banerjee, P. Sun, N. Gao, and M. Liu, J. Appl. Phys. **118**, 045701 (2015).

[7] N. Lu, L. Li, D. Geng, and M. Liu, Org. Electron. **61**, 223 (2018).

[8] V. Rodin, F. Symalla, V. Meded, P. Friederich, D. Danilov, A. Poschlad, G. Nelles, F. von Wrochem, and W. Wenzel, Phys. Rev. B **91**, 155203 (2015).

[9] K. Seki, and M. Wojcik, J. Chem. Phys. **145**, 034106 (2016).

[10] J. Cottaar, L. J. A. Koster, R. Coehoorn, and P. A. Bobbert, Phys. Rev. Lett. **107**, 136601 (2011).

[11] A. Miller and E. Abrahams, Phys. Rev. **120**, 745 (1960).

[12] R. A. Marcus, J. Chem. Phys. **81**, 4494 (1984).

[13] R. A. Marcus, Rev. Mod. Phys. **65**, 599 (1993).

[14] B. Movaghar, M. Grünewald, B. Ries, H. Bässler, and D. Wurtz, Phys. Rev. B **33**, 5545 (1986).

[15] B. Ries, H. Bässler, M. Grünewald, and B. Movaghar, Phys. Rev. B **37**, 5508 (1988).

[16] S. Kirkpatrick, Rev. Mod. Phys. **45**, 574 (1973).

[17] S. D. Baranovskii, H. Cordes, F. Hensel, and G. Leising, Phys. Rev. B **62**, 7934 (2000).

[18] V. R. Nikitenko, H. von Seggern, and H. Bässler, J. Phys.: Condens. Matter **19**, 136210 (2007).

[19] V. R. Nikitenko and H. von Seggern, J. Appl. Phys. **102**, 103708 (2007).

[20] R. Schmechel, Phys. Rev. B **66**, 235206 (2002).

[21] V. I. Arkhipov, E. V. Emelianova, and G. J. Adriaenssens, Phys. Rev. B **64**, 125125 (2001).

[22] I. I. Fishchuk, V. I. Arkhipov, A. Kadashchuk, P. Heremans, and H. Bässler, Phys. Rev. B **76**, 045210 (2007).

[23] I. I. Fishchuk, A. Kadashchuk, V. N. Poroshin, and H. Bässler, Philos. Mag. **90**, 1229 (2010).

[24] S. D. Baranovskii, I. P. Zvyagin, H. Cordes, S. Yamasaki, and P. Thomas, Phys. Status Solidi B **230**, 281 (2002).

[25] M. D. Khan, V. R. Nikitenko, A. P. Tyutnev, and R. S. Ikhsanov, J. Phys. Chem. C **123**, 1653 (2019).

97

[26] V. R. Nikitenko and M. N. Strikhanov, J. Appl. Phys. **115**, 073704 (2014).

[27] F. W. Schmidlin, Phys. Rev. B **16**, 2362 (1977).

[28] W. F. Pasveer, J. Cottaar, C. Tanase, R. Coehoorn, P. A. Bobbert, P. W. M. Blom, D. M. de Leeuw, and M. A. J. Michels, Phys. Rev. Lett. **94**, 206601 (2005).

[29] A. I. Rudenko and V. I. Arkhipov, Philos. Mag. B **45**, 177 (1982).

[30] V. I. Arkhipov, E. V. Emelianova, and H. Bässler, Philos. Mag. B **81**, 985 (2001).

[31] N. Apsley and H. P. Hughes, Philos. Mag. **31**, 1327 (1975).

[32] O. Rubel, S. D. Baranovskii, P. Thomas, and S. Yamasaki, Phys. Rev. B **69**, 014206 (2004).

[33] S. D. Baranovskii, Phys. Status Solidi A **215**, 1700676 (2018).

[34] B. I. Shklovskii and A. L. Efros, in *Electronic Properties of Doped Semiconductors*, Springer Series Solid-State Science Vol. 45 (Springer, Berlin, Heidelberg, 1984), pp. 202–227.

[35] S. T. Hoffmann, F. Jaiser, A. Hayer, H. Bässler, T. Unger, S. Athanasopoulos, D. Neher, and A. Kohler, J. Am. Chem. Soc. **135**, 1772 (2013).

[36] See Supplemental Material at http://link.aps.org/supplemental/10.1103/PhysRevB.103.165202 for chemical structure of copolymers considered in the present study (Sec.1), the fitting of experimental data of considered copolymes (Sec. 2), and estimating a "reasonable" value for the *C* factor (Sec. 3).

[37] H. Cordes, S. D. Baranovskii, K. Kohary, P. Thomas, S. Yamasaki, F. Hensel, and J. H. Wendorff, Phys. Rev. B **63**, 094201 (2001).

[38] K. Kohary, H. Cordes, S. D. Baranovskii, P. Thomas, S. Yamasaki, F. Hensel, and J. H. Wendorff, Phys. Rev. B **63**, 094202 (2001).

[39] D. H. Dunlap, P. E. Parris, and V. M. Kenkre, Phys. Rev. Lett. **77**, 542 (1996).

[40] X. de Vries, P. Friederich, W. Wenzel, R. Coehoorn, and P. A. Bobbert, Phys. Rev. B **97**, 075203 (2018).

98

Supplemental Material

The role of the reorganization energy for charge transport in disordered organic semiconductors

R. Saxena[1], V. R. Nikitenko[2], I. I. Fishchuk[3,4], Ya. V. Burdakov[2], Yu. V. Metel[2], J. Genoe[5] H. Bässler[6], A. Köhler,[1,6] and A. Kadashchuk[4,5*]

[1]*Soft Matter Optoelectronics and Bavarian Polymer Institute (BPS), Universitätsstr. 30, 95448 Bayreuth, Germany*

[2]*National Research Nuclear University "MEPhI" (Moscow Engineering Physics Institute), Kashirskoe Shosse 31, 115409 Moscow, Russia*

[3]*Institute for Nuclear Research, National Academy of Sci. of Ukraine, Prospect Nauky 47, 03028 Kyiv, Ukraine*

[4]*Institute of Physics, National Academy of Sciences of Ukraine, Prospect Nauky 46, 03028 Kyiv, Ukraine*

[5]*IMEC, Kapeldreef 75, B-3001 Leuven, Belgium*

[6]*Bayreuth Institute of Macromolecular Research (BIMF), Universitätsstr. 30, 95448 Bayreuth, Germany*

* Corresponding author: e-mail: kadash@iop.kiev.ua

1) Chemical structure of co-polymers considered in the present study
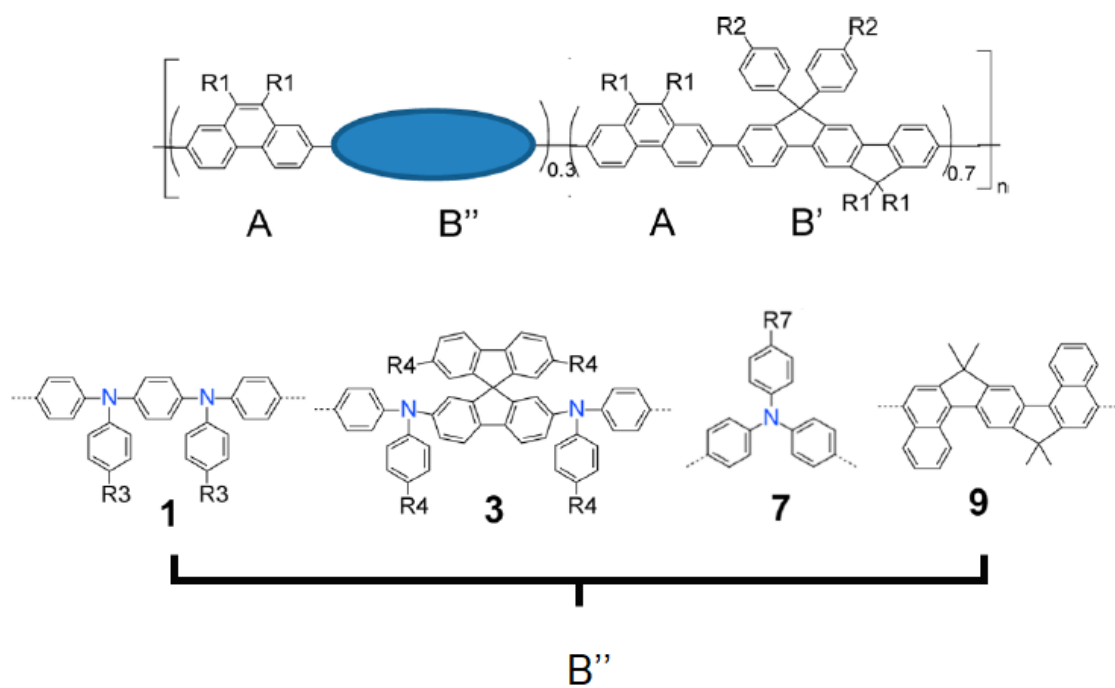
Figure S1: Chemical structure of copolymer 1, 3, 7 and 9 of Ref. 35 of main text.

2) The fitting of experimental data of considered copolymes
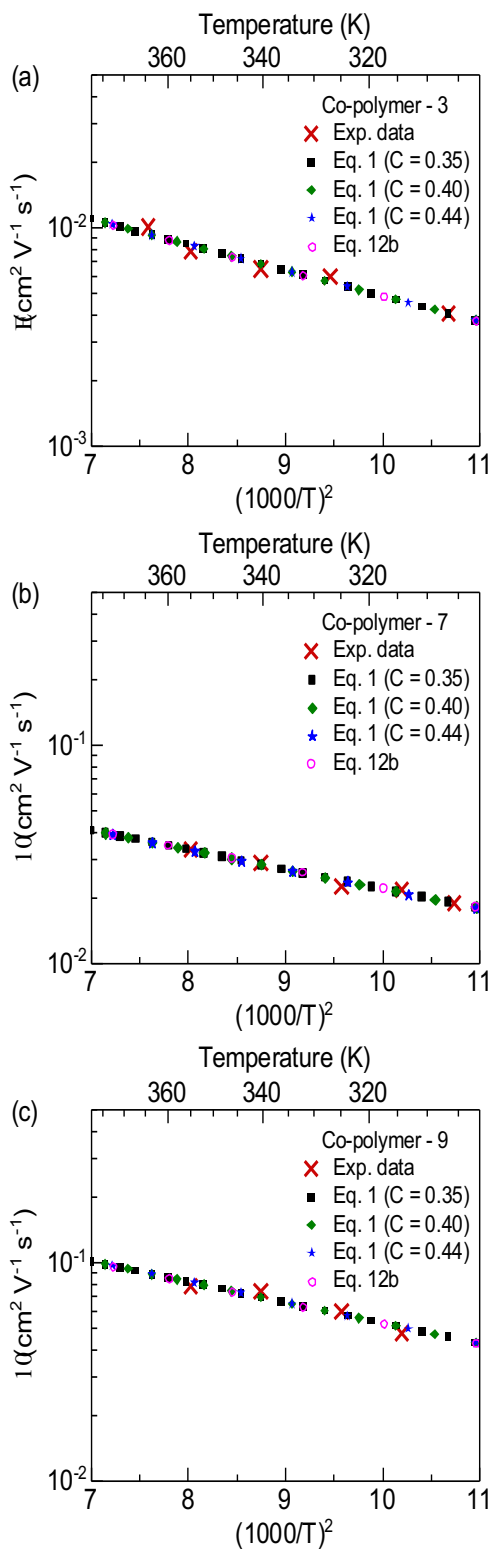
Figure S2: Comparison of fitting done by using Eq. (1) with $C=$ 0.35, 0.40 and 0.44, and by using Eq. 12b. (MA) for E_a values presented in Table 1.
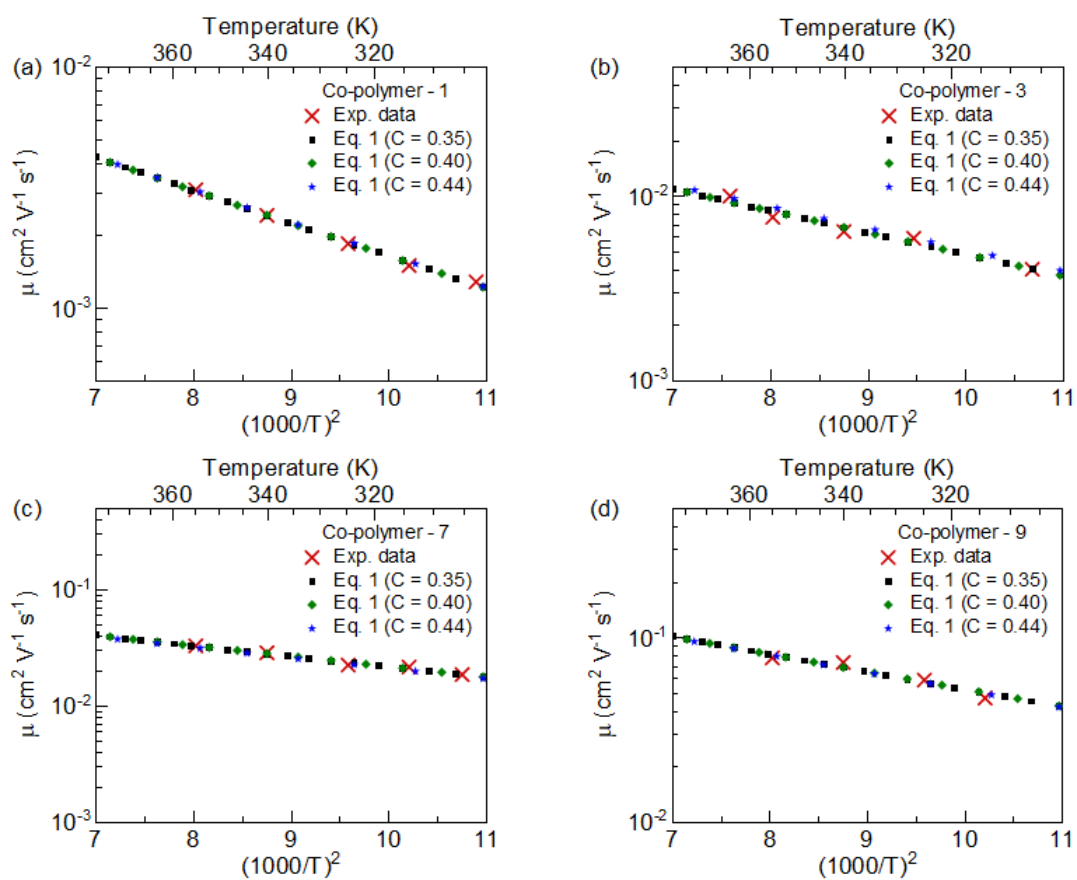
Figure S3: Comparison of fitting done by using Eq. (1) with *C*= 0.35, 0.40 and 0.44 for *σ* values presented in Table 1 of the main text.

3) Estimating a "reasonable" value for the C-factor

Values for the disorder σ can be obtained by fitting $\mu(T)$ with Eq. 1, using a given value of E_a as input. Table 2 in the manuscript shows that the values for σ vary from each by less than 10% when the value taken for the C-factor ranges from 0.35 to 0.45. We therefore consider $C = 0.40 \pm 0.05$ to be a "reasonable" value for the assessment of experimental data.

It turns out that the reorganization energy E_a is more sensitive to the value of the C-factor, as evident from Table 3. We can now do the fitting of fitting $\mu(T)$ with Eq. 1 again, using the disorder obtained from the pure MA case as input. If we take $C = 0.44$, we obtain $E_a = 0$. This is clearly an extreme lower limit. On the other hand, if we take $C = 0.35$, we obtain values for E_a that are just slightly lower than the values that have been found for the singlet exciton, using a Franck-Condon analysis of the emission spectra (see Ref. 35 in the manuscript). The reorganization energy for a charged molecule is known to be lower than that for an excited molecule. A rough estimate is that it is only about 2/3 of the reorganization energy of the excited molecule, implying that $C = 0.35$ would give a value that is slightly too high. As a first approximation, one may interpolate linearly between $C = 0.44$ and $C = 0.35$ and consider that these two values are too extreme. From this, results that $C = 0.40 \pm 0.03$ is expected to give realistic values for the reorganization energy.

9 Impact of Energy Correlations on Narrowing of Occupied Density of State Distribution for Charge Carriers at Low Temperatures in Disordered Organic Semiconductors
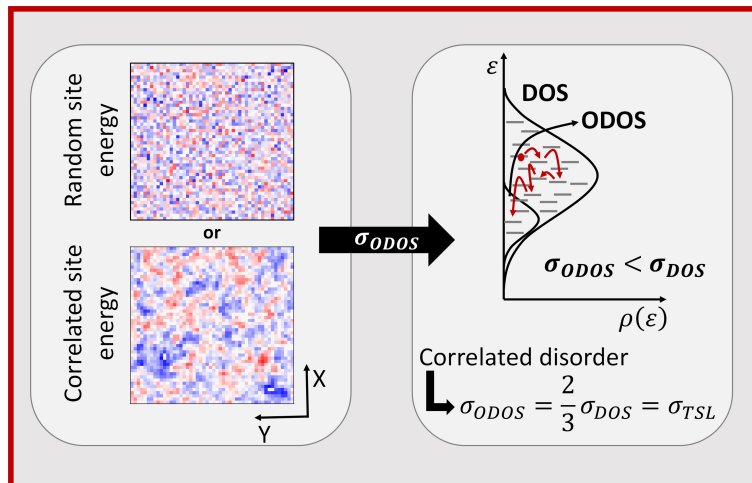
Andrei Stankevych,[‡] **Rishabh Saxena**,[‡] *Alexander Vakhnin, Christof Pflumm, Jan Genoe, Heinz Bässler, Anna Köhler*, and *Andrey Kadashchuk*

[‡] Authors contributed equally

Impact of energy correlations on narrowing of occupied density of state distribution for charge-carriers at low temperatures in disordered organic semiconductors

Andrei Stankevych,[1,2†] Rishabh Saxena,[2†] Alexander Vakhnin,[1] Christof Pflumm,[3] Jan Genoe,[4] Heinz Bässler,[5] Anna Köhler,[2,5*] and Andrey Kadashchuk[1,2,4*]

[1] Institute of Physics, National Academy of Sciences of Ukraine, Prospect Nauky 46, 03028 Kyiv, Ukraine

[2] Soft Matter Optoelectronics and Bavarian Polymer Institute (BPS), Universitätsstrasse 30, 95448 Bayreuth, Germany

[3] Merck KGaA, Display Solutions, Frankfurter Straße 250, 64293 Darmstadt, Germany.

[4] IMEC, Kapeldreef 75, B-3001 Leuven, Belgium

[5] Bayreuth Institute of Macromolecular Research (BIMF), Universitätsstrasse 30, 95448 Bayreuth, Germany

[†] Authors contributed equally to this work

*Corresponding authors: kadash@iop.kiev.ua, anna.koehler@uni-bayreuth.de

Abstract:

The dynamics of charge carriers in disordered organic semiconductors is inherently difficult to probe by spectroscopic methods. Thermally-stimulated luminescence (TSL) measurement is an approach that detects the luminescence resulting from the recombination of spatially well separated geminate charge pairs at low temperature. In this way, the density of states (DOS) for charges can be determined. Another approach to probe charge-carrier relaxation are kinetic Monte Carlo (kMC) simulations. Here we use both techniques to determine the DOS distribution of charges at low temperatures. We find that the charge dynamics is frustrated, yet this frustration can be overcome in TSL by using an infrared (IR) push pulse, and in kMC by a long simulation time that allows for long-range tunneling. Applying the IR-push TSL to pristine amorphous films of 18 commonly used low molecular weight organic light emitting diode (OLED) materials we find that the width (σ) of the ODOS universally amounts to about 2/3 of the DOS. The same result is obtained in kMC simulations that consider energetic correlation between the charge carriers. Without the explicit consideration of energetic correlation, the experimental value cannot be reproduced, which testifies to the importance of correlations for charges.

1. Introduction

Energetic relaxation of electronic excitations is a ubiquitous and well-established phenomenon in disordered organic semiconductors [1-3]. It is a direct consequence of a broad distribution of localized states in such materials, usually assumed to be a Gaussian characterized by a width σ_{DOS}. In general, the elementary excitations such as charge-carriers or neutral excitations, generated randomly within the intrinsic density of states (DOS), are not in thermodynamic equilibrium with the lattice initially and therefore tend to thermalize by occupying the lower lying states during their migration [1,2]. In the low temperature limit this is a purely dissipative process, while at finite temperatures, thermal activation competes with energetic relaxation. In the case of neutral excitations, the energetic relaxation process is manifested as "spectral diffusion" effect, which is amenable to time-resolved spectroscopy and can be easily assessed by monitoring a gradual spectral shift of the photoluminescence spectra with increasing delay time [4-6]. Spectral diffusion has been widely observed for both fluorescence and phosphorescence in various disordered organic materials, such as conjugated polymers and small molecules (low molecular weight materials). This effect has also been described both theoretically and with the help of Monte Carlo (MC) simulations, by employing the disorder formalism and the concept of random-walk of singlet and triplet excitations among localized sites within the DOS distribution.

The energetic relaxation process is determinant for charge transport in amorphous organic semiconductor films. Yet, it is commonly believed that the energy relaxation of the charge-carriers is not amenable to spectroscopic probing [1,2]. It could only be assessed *indirectly* by looking into its impact on transport properties, such as those related to the initial decay of the time-of-flight (ToF) signal and a transition from non-dispersive to dispersive transport regime occurring at a critical disorder parameter $(\sigma_{DOS}/k_B T)_{cr}$ [1,7]. To prove the concept and testify on the adequacy of the basic assumptions underlying the transport model, triplet excitations are conventionally used as probe particles as they can be monitored experimentally [1,2]. It is believed that the triplet relaxation process is analogous (at least qualitatively) to the charge-carrier relaxation process, despite the finite lifetime of triplets. This is because triplets are transported via the same short-range exchange interactions as charge-carriers - the only difference being a much larger delocalization of charge-carriers and concomitantly much shorter jump time ($\sim 10^{-13}$ s). Triplet energetic relaxation has been extensively studied in the last decades. Notably, below a characteristic temperature, the triplet

energetic relaxation was found to become progressively frustrated with further decrease in the temperature. This effect was attributed to the freezing out of thermally activated excitation jumps that otherwise promote spectral diffusion [8]. Such a regime of energetic relaxation is responsible for the dispersive charge transport that is typically observed in organic disordered media upon decreasing the temperature and/or increasing the amount of the energetic disorder [1].

So far, the energetic relaxation phenomena have been investigated under the premise of a *random energy disorder* which underlies the classical Gaussian disorder model (GDM) proposed by Bässler and coworkers [1]; implying that the energies of spatially adjacent localized sites are independent of each other. Yet, the localized sites' energies in polar organic materials can be correlated [9,10]. The spatial correlation between the energies of different localized sites is caused by electrostatic interaction of charge carrier with randomly oriented permanent dipole moments [10] and/or quadrupole moments [11] of the organic molecules. It is well established that accounting for the spatial energy correlations is important to describe a wide-field range applicability of the Poole-Frenkel-type dependence of charge mobility (μ) on the electric field (F), $\ln \mu \propto F^{1/2}$ [9,10]. Therefore, the concept of *correlated energy disorder* has been implemented in an amended version of the disorder formalism, the so-called correlated disorder model (CDM) of charge transport [9,10]. It should be noted that the presence of correlated disorder implies some flattening of the local potential energy landscape on microscopic level as compared to the random energy landscape. This circumstance *might* also have an impact on the *energetic relaxation* of charge-carriers in polar materials. On the other hand, in contrast to charge carriers, no significant spatial energy correlation effects are expected for neutral excitations because of their much weaker interactions with permanent dipoles.

In the present paper we propose that thermally-stimulated luminescence (TSL) can be used to probe energetically relaxed charge-carriers within the DOS. It turns out that the measured *TSL curve represents an occupied DOS* (ODOS) distribution formed in the course of energetic relaxation of photogenerated carriers, via their downward hopping at low temperatures. Further, our study is also aimed at revealing the role of spatial correlations on the energetic relaxation of photogenerated charge-carriers by combining both experiments and computer simulations. A trap spectroscopy technique based on TSL has been employed to determine the energy distribution of trapped carriers in amorphous films of different organic materials. We point out that the low-temperature energetic

relaxation of charge carriers is a key process determining the population of localized states occupied by trapped charge-carriers in amorphous films with a Gaussian DOS. The width of the TSL curves σ_{TSL} is found to be notably smaller than the DOS width (σ_{DOS}). However, it scales linearly with σ_{DOS}, featuring a universal ratio $\sigma_{TSL}/\sigma_{DOS} \approx 2/3$ observed for a large set of organic materials commonly used in the fabrication of thin-film organic light emitting diodes (OLEDs). This implies a significant narrowing of ODOS distribution formed at low temperatures as compared to the DOS width. Experimental result was compared against kinetic Monte Carlo (kMC) simulations of the charge-carrier energetic relaxation processes within a Gaussian DOS assuming either random or spatially correlated site energies. Our simulations have corroborated that (i) the ODOS narrowing, which is well reproduced in both cases, is a genuine property of the hopping carrier relaxation at low temperature, and (ii) demonstrated by comparison of the kMC results for both disorder models with TSL data that the energy correlations are necessary to be considered for quantitative agreement with the experimental observations in considered small molecule materials. Practical implications of this study lie in proposing a useful methodology for evaluating the σ_{DOS} parameter based on the analysis of full TSL band profile and in assessing the importance of energy correlations in amorphous organic semiconductor films.

2. Experiments

2.1. Materials

For our study we used the OLED small organic molecule materials shown in Figure 1 along with their abbreviated names. A list of full names is given in Note S1 of the supplemental material. These compounds were purchased from Sigma-Aldrich, Lumtec Taiwan, with the exception of DMAC-py-TRZ that has been provided by Eli Zysman-Colman from University of St Andrews, UK. Three materials, referred to as HTM-2, ETM-SB, and TMM were obtained from Merck, and they denote a hole-transport, electron transport, and triplet-matrix material, respectively. All materials were used as received without any further purification. Thin films of the above compounds were spin-coated from 20 mg/ml chloroform or toluene solutions onto cleaned quartz substrates (1000 rpm, 30 s) that resulted in typically 150-nm-thick layers. Subsequently, the deposited films were dried in oven at 40 °C for 10 m and then in a vacuum for 2 h to remove residual solvent.

NPB

Spiro-TAD

TPD

DMAC-TRZ

CBP

mCBP

mCP

DMAC-py-TRZ

mCBP-CN

2CzPN

NBPhen

Alq3

mCP-CN

4CzIPN

BCP
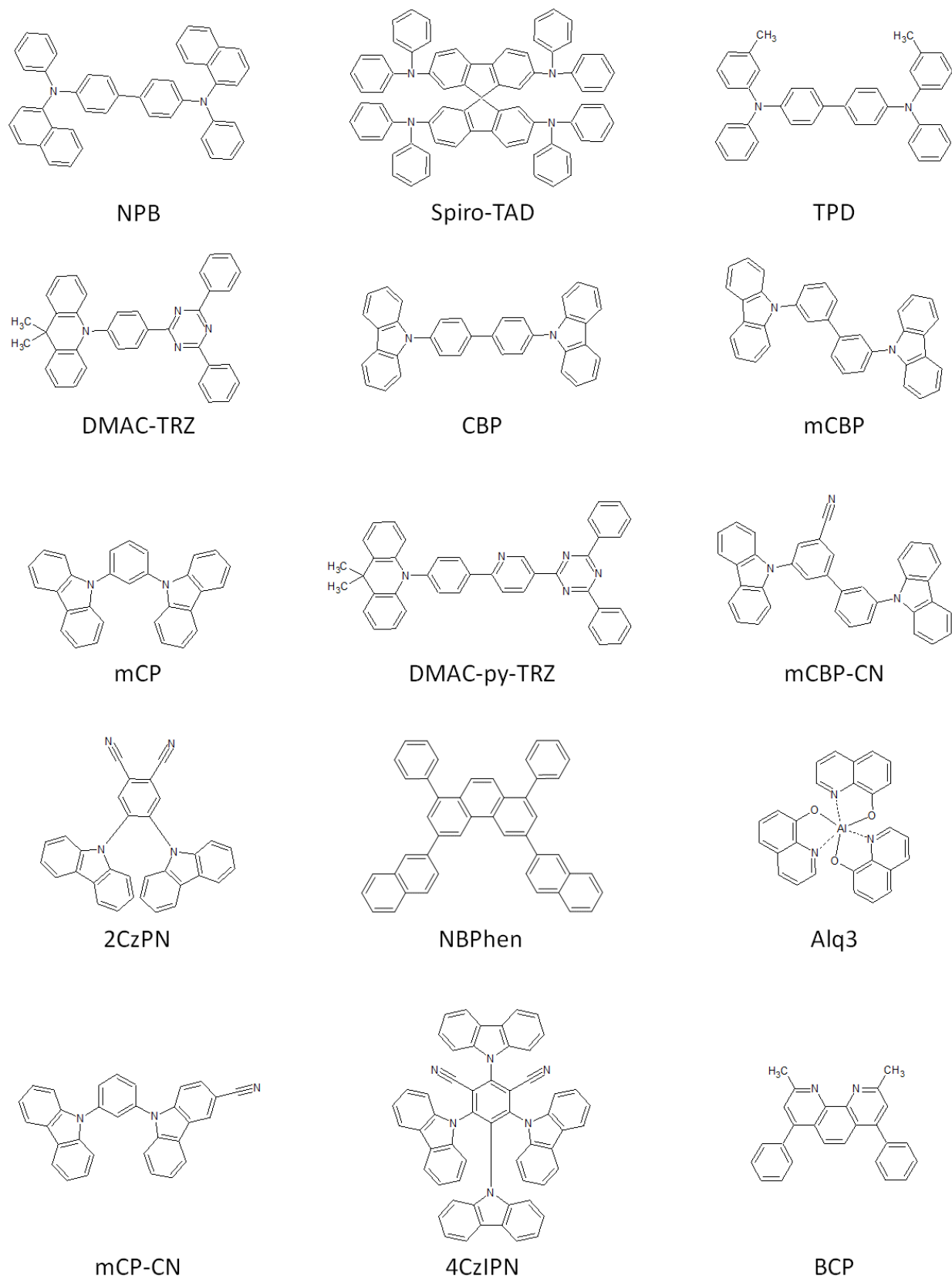
Figure 1: Molecular structures of the compounds used in this study.

2.2. TSL techniques

Thermally stimulated luminescence (TSL) is the phenomenon of light emission arising after the removal of excitation (UV light, in our case) under conditions of increasing temperature. Generally, in the TSL method, the trapping states are first populated by the photogeneration of charge carriers, usually at low temperatures. After terminating the excitation, the trapped charge carriers can be released by heating up the sample and the luminescence due to charge recombination is recorded as a function of temperature ($I_{TSL}(T)$). TSL measurements were carried out over a temperature range from 5 to 300 K using an optical temperature-regulating helium cryostat. The following text summarizes the methodology adopted for the three different regimes of TSL measurements presented in this study.

Standard TSL: In "standard TSL" experiments, samples were cooled down to 5 K and were excited at 313 nm (cw-excitation) for 3 minutes. The excitation wavelength (λ_{exc}= 313 nm) was selected from a high-pressure mercury (Hg) lamp spectrum with the help of appropriate set of cut-off filters. After that the samples were kept in the dark at a constant temperature (5 K) during a certain dwell time before the TSL heating run began to allow the long isothermal afterglow (arising due to isothermal recombination of short-range geminate pairs) to decay to a negligible value. Then TSL measurements were started upon heating the sample from 5 to 300 K with a linear heating ramp (at constant heating rate, β=0.15 K/s). TSL emission (due to the thermally activated recombination of long-range geminate pairs) was detected with a cooled photomultiplier tube operated in photon-counting mode, mounted adjacent to the cryostat window.

Infrared cleaning (IR-cleaning): After exciting the samples with λ_{exc}= 313 nm (like "standard TSL" method), samples were additionally irradiated with IR photons for 30 minutes; at 5 K. IR irradiation was selected by using an IR filter with a transparency band of 900–4500 nm from the emission spectrum of the same Hg lamp. After that, the TSL glow curve was recorded upon linear heating, just as in the case of standard TSL. We found that as a result of such additional IR irradiation, the TSL curve acquires a more symmetrical profile. Hereafter such a procedure is referred as "*IR-cleaning*" and an origin of the effect will be discussed in the succeeding section.

112

Fractional TSL: Fractional heating of TSL is widely used for quantifying trapping state energies in solids. Since TSL spectra, $I_{TSL}(T)$, of disordered organic solids display broad and unstructured bands due to a complicated convolution of contributions from different traps at different energies, additional TSL measurements in *'fractional heating'* regime must be performed to extract the information about trap energetics and distribution. In the fractional (or partial) heating technique, we apply a temperature-cycling program in which many small heating/cooling cycles are superimposed on a constant heating ramp, that allows determining the activation energies ($\langle E_a \rangle$) of the traps with high accuracy. This is especially useful when different groups of traps are not well separated in energy or are continuously distributed. The mean activation energy $\langle E_a \rangle$ during each heating cycle (of constant heating rate, β) with temperature change ΔT is determined as,

$$\langle E_a \rangle(T) = -\frac{d[ln\, I_{TSL}(T)]}{d(1/k_B T)}; \; at \; \beta = constant, \; \Delta T \ll T, \; n \ll n_{tot} \tag{1}$$

where, $I_{TSL}(T)$ is the TSL intensity, T is the temperature and k_B is the Boltzmann constant. Here n is the number of charge-carriers released during each heating cycle and n_{tot} is the total number of charge-carriers trapped by the same sort of traps. These conditions determine the "initial rise method", which is the basis for Eq. (1). Since the temperature change, ΔT, is usually much smaller than the mean value of T, $\langle E_a \rangle$ can be assumed equal to $\langle E_a \rangle(T)$ [12]. Therefore, *the $\langle E_a \rangle(T)$ dependence is the main outcome of the fractional TSL measurements*. Other essential details of this technique are summarized in Note S2 of the supplemental material. More details of the fractional TSL measurements have been described elsewhere [13-15] . We found that, for the organic materials studied in the present work, $\langle E_a \rangle$ increases linearly with temperature (Figure 2) and can be described reasonably well by the following empirical relation:

$$\langle E_a \rangle(T) = 3.2\frac{meV}{K} \times T - 91\, meV \tag{2}$$

In this work, this empirical calibration, Eq. (2), is used to convert the temperature scale to trap energy scale for the analysis of TSL data. It is worth emphasizing that such kind of linear relation for $\langle E_a \rangle(T)$ has also been justified for disordered organic semiconductors by analytical variable range hopping (VRH) calculations [16] and has also been observed in our previous experimental studies [12,17].
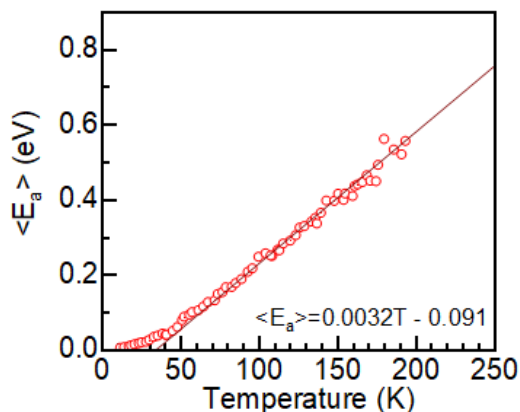
Figure 2: Example of temperature dependence of the mean activation energy $< E_a >$ as obtained for organic semiconductor materials studied in this paper by fractional heating (symbols) and extrapolation by an empirical expression, Eq. (2) (solid line).

2.2. Determination of DOS width (σ_{DOS}) by TSL

The low dielectric constant (and consequently large Coulomb capture radius) of the organic materials precludes the generation of free charge-carriers upon photoexcitation under zero electric field condition relevant to TSL experiments [2,18]. Therefore, after photogeneration at low temperatures, charge-carriers are produced in the form of geminate pairs of opposite charges [18]. The separation distance between the charges in photogenerated geminate pairs is a subject to distribution. Short-range geminate pairs are rather unstable and can recombine by tunneling, at a constant temperature, giving rise to a delayed luminescence emission [19,20] and long isothermal afterglow [21]. On the other hand, the long-range geminate pairs can avoid recombination at low temperatures (such as 5 K: relevant to TSL experiments). They can only be released, and subsequently recombine, at elevated temperatures and are therefore responsible for TSL in organic materials. It is important to note that in amorphous organic semiconductors, the mechanism of TSL differs from that commonly accepted for crystalline materials with band-type transport where a discrete trapping level model is applicable. A specific feature of amorphous solids is that the intrinsic hopping states, localized within the lower energy part of the DOS distribution of width σ_{DOS}, can act as shallow traps at very low temperatures, and therefore TSL can be observed even in chemically pure materials where the "trap-free charge transport" has been postulated [16,21]. Since TSL measurements are normally performed after a long dwell time between the photoexcitation and the onset of the heating run, the energy distribution of

the localized carriers, the so-called "occupied DOS" (ODOS) distribution is formed under the regime of low-temperature energetic relaxation of photogenerated carriers within the Gaussian shaped manifold of intrinsic localized states [16]. This is a key process determining the population of trapped carriers in disordered solids and therefore *the measured TSL curve qualitatively represents an ODOS distribution formed at low temperatures*.

Figure 3a shows the normalized TSL glow curves of several organic semiconductor films, namely, NPB, TPD, mCBP and NBPhen obtained under the same conditions by the "standard TSL" method (see section 2.2 for details). The TSL glow curve of each material represents a single broad band containing an additional shoulder-like feature on its low-temperature side, typically below 40 K. The relative intensity of this low temperature component is material specific (in some materials it is observed as an additional TSL peak). We provisionally ascribe it to either intermediate-range geminate pairs (as discussed above) or to photogenerated charge-carriers which are captured by shallow localized states.

As reported by Arkhipov *et al.* [15] using VRH calculations, an important feature of the low-temperature energy relaxation of charge-carriers is that the shape of low-energy part of the *ODOS distribution* follows the DOS distribution [16,21]. This forms the basis for the methodology of determining the DOS width, σ_{DOS}, by analyzing the shape of high-temperature wing of the TSL curve. Hereafter, this method of TSL analysis will be referred as **"Method-1"** for simplicity. Implementation of the above methodology is presented in Figure 3b. Firstly, the empirical calibration Eq. (2) is used to convert the temperature scale in Figure 3a to a trap energy scale ($\langle E_a \rangle$). Subsequently, the logarithm of TSL intensity (I_{TSL}) is plotted against $\langle E_a \rangle^2$ in Figure 3b. The high-$\langle E_a \rangle$ part of the plot in Figure 3b (and correspondingly, the high-temperature part of standard TSL in Figure 3a) reveals a Gaussian dependence ($\ln(I_{TSL}) = -\langle E_a \rangle^2 / 2\sigma_{DOS}^2$) for all samples and the slope of the straight line yields the width of the DOS (σ_{DOS}). The energetic disorder ranges from 88 to 176 meV for the least disordered NPB and the most disordered NBPhen, respectively. This method of TSL analysis (Method-1) has been extensively applied by our group to a great variety of small molecules and conjugated polymers [12-15] and the determined σ_{DOS} values were found to be in good agreement with that obtained from charge transport measurements and from molecular dynamics simulations [17]. It is worth mentioning that some films also revealed a more slowly decaying deep exponential tail at the lowest portion of the DOS, following on from the Gaussian distribution (Figure 3b). This slower decaying feature can be of a multiple origin, as described in our previous work [12], and is beyond

the scope of the present study. A determination of σ_{DOS} by this Method-1 was done for all materials considered in this study and the results are summarized in Table 1.

Furthermore, Movaghar *et al.* [22] and Bässler *et al.* [1], demonstrated that the mean ODOS energy relative to the center of the DOS distribution in zero-temperature limit is proportional to $\sigma_{DOS}[d \ ln \ ln(t/t_0)]^{1/2}$, where d is the lattice dimensionality and t_0 is a typical jump time of a carrier in a lattice without disorder. This is indeed in line with experimental observations - the TSL peak shift towards higher temperature with the increase in energetic disorder (σ_{DOS}). Interestingly, it is also accompanied by a significant *broadening of TSL band* (Figure 3a). This implies that the experimentally assessable width of the TSL band, σ_{TSL}, might somehow relate to the σ_{DOS} parameter.

2.3. Determination of ODOS width (σ_{ODOS}) by TSL

The observed trend, i.e., the TSL peak shift towards higher temperature accompanied by the broadening of the TSL band with increasing σ_{DOS}, is also observed after "IR-cleaning", as shown in Figure 3c. The IR radiation leads to a photo-induced release of the trapped carriers, an effect well documented for organic materials. The released charge-carriers can either recombine with their countercharges (i.e., the opposite charges of the geminate electron-hole pairs) giving rise to the phenomenon known as photo-stimulated luminescence [23] or be recaptured by deeper localized states. We speculate that the former process is dominated by the geminate electron-hole pairs with smaller spatial separation (and thus larger Coulomb attraction energy) which, as mentioned in Section 2.2, can contribute to the low-temperature feature of the TSL glow curve obtained using standard TSL method (Figure 3a). This speculation is supported by the experimental observations that IR-cleaning leads to an efficient removal of the low-temperature feature of TSL glow curves (Figure 3c) as well as an overall reduction in TSL intensity. Consequently, after IR-cleaning, we obtain a rather symmetrical bell-shaped TSL band. Moreover, the TSL peak shifts to a slightly higher temperature. We believe that the TSL curve after IR cleaning represents the ODOS distribution of the relaxed charge carriers. Thus, the dependence of low-temperature ODOS width on the energetic disorder (σ_{DOS}) was assessed by estimating the standard deviation of the TSL band (σ_{TSL}); by fitting the IR-cleaned TSL curve with a Gaussian function (after converting temperature scale to the energy scale by calibration Eq. (2)). Hereafter this procedure of TSL analysis is referred as **"*Method-2*"**.

At this point, it is important to distinguish between σ_{DOS} and σ_{TSL}. σ_{DOS} is determined from the high-temperature wing of the TSL curve, i.e., by analyzing the *tail of the TSL curve* obtained from standard TSL experiments by using **Method-1**. σ_{TSL} is determined by analyzing the *whole TSL curve* obtained after IR-cleaning by using **Method-2**. It should be noted that the statistical weight of the high-temperature wing of the TSL (the tail of the TSL curve analyzed in Method-1) doesn't contribute much to the fitting procedure adopted in Method-2 (< 10% for all the studied materials). *Thus, σ_{DOS} is a property of the material itself whereas σ_{TSL} is a property of the ODOS distribution of the charge-carriers ($\sigma_{TSL} = \sigma_{ODOS}$).*

2.4. General results

Figure 4 shows the IR-cleaned TSL glow curves for all 18 organic materials used in this study and, compares the σ_{TSL} derived by using "Method-2" and the σ_{DOS} parameters as estimated by the *"Method-1"* of TSL analysis. From such a comparison, we find that the σ_{TSL} scales linearly with σ_{DOS} and that the ratio $\sigma_{TSL}/\sigma_{DOS} \approx 2/3$. Surprisingly, this turns out to be a general effect for all amorphous organic semiconductor films we measured so far with a mean value of $\sigma_{TSL}/\sigma_{DOS} = 0.64 \pm 0.04$. The measurement results are summarized in Table 1. For comparison, the computed σ_{DOS} values, as obtained from QM/MM molecular dynamics simulations [12,17,24-26] are also listed in Table 1. The DOS width (σ_{DOS}) obtained from TSL measurements are in reasonable quantitative agreement with the computed σ_{DOS}.

There are two important consequences of the finding $\sigma_{TSL}/\sigma_{DOS} \approx 2/3$: (i) from a practical perspective, this "2/3-ratio" suggests a useful methodology for the DOS width determination. This is because experimentally it is relatively easy to estimate σ_{TSL} parameter by Gaussian fitting of the whole TSL curve (Method-2) measured after IR-cleaning and subsequently one can use a simple relation $\sigma_{DOS}=3/2\,\sigma_{TSL}$. (ii) From fundamental point of view, the observed ratio $\sigma_{TSL}/\sigma_{DOS} \approx 2/3$ implies a kind of "spectral-narrowing" effect occurring for the ODOS at low temperatures. This experimental finding obviously requires a theoretical justification. Therefore, we further carry out KMC simulation-based study to gain a deeper insight into charge-carrier energetic relaxation phenomena at low temperatures.
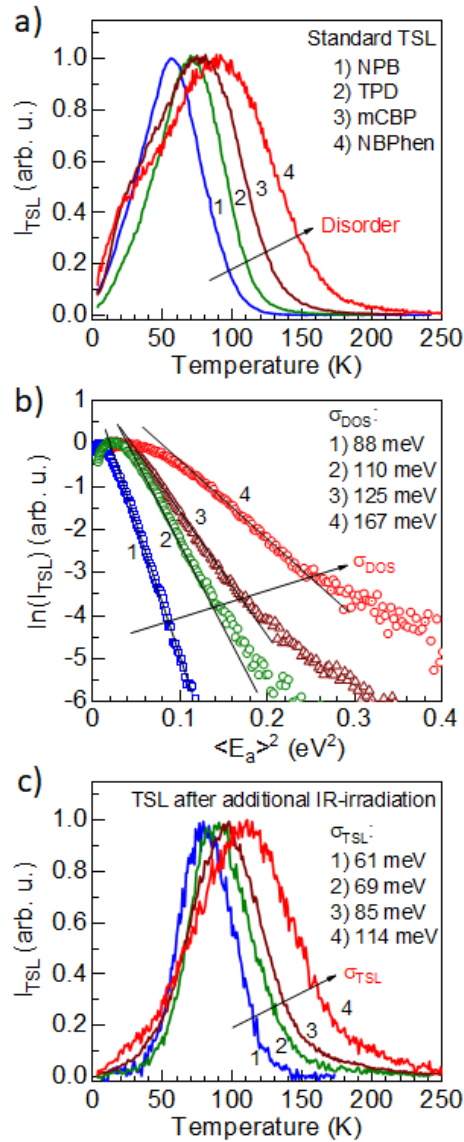
Figure 3: a) Normalized TSL intensity (I_{TSL}) curves measured at the constant heating rate 0.15 K/s after excitation with 313 nm-light for 3 min at 5 K in NPB, TPD, mCBP and NBPhen films (curve 1, 2, 3, and 4, respectively); b) Analysis by *Method-1* of the high temperature wings of the TSL curves shown in (a) (see text for details). The slope of the straight lines is a measure of the DOS width (σ_{DOS}), and the extracted σ_{DOS} -parameters are indicated in the Inset; c) Effect of IR-cleaning on the TSL curve profile NPB, CBP, mCBP and NBPhen (curve 1, 2, 3, 4 respectively). Standard deviation parameters, σ_{TSL}, inferred from such TSL peaks are also listed. Note that these values are notably smaller than corresponding σ_{DOS} for these materials (see text for more details).

Table 1: Comparison between energetic disorder parameter (σ_{DOS}), the energy width of TSL peak (σ_{TSL}), and the $\sigma_{TSL}/\sigma_{DOS}$ ratio for a set of amorphous organic semiconductors. The last column shows theoretical σ_{DOS} parameter derived from QM/MM calculations.

	Material	σ_{DOS} (meV)	σ_{TSL} (meV)	$\dfrac{\sigma_{TSL}}{\sigma_{DOS}}$	Theoretical σ_{DOS} (meV)
1	NPB	88	61	**0.69**	87 [17]
2	Spiro-TAD	110	69	**0.63**	90 [17]
3	TPD	110	69	**0.63**	-
4	DMAC-TRZ	110	66	**0.60**	129 [26]
5	CBP	125	77	**0.62**	100 [17]
6	mCBP	131	85	**0.65**	122 [17]
7	mCP	140	99	**0.70**	160 [12], 157 [24]
8	DMAC-py-TRZ	151	99	**0.66**	-
9	mCBP-CN	151	102	**0.68**	200 [17]
10	2CzPN	161	100	**0.62**	-
11	NBPhen	167	114	**0.68**	194 [17]
12	Alq3	177	99	**0.56**	150 [25]
13	mCP-CN	177	115	**0.65**	240 [17]
14	4CzIPN	213	125	**0.59**	220 [26]
15	BCP	226	147	**0.65**	190 [17]
16	HTM-2	73	49	**0.67**	-
17	ETM-1	103	65	**0.63**	-
18	TMM-1	132	90	**0.68**	-
			Mean	**0.64±0.04**	
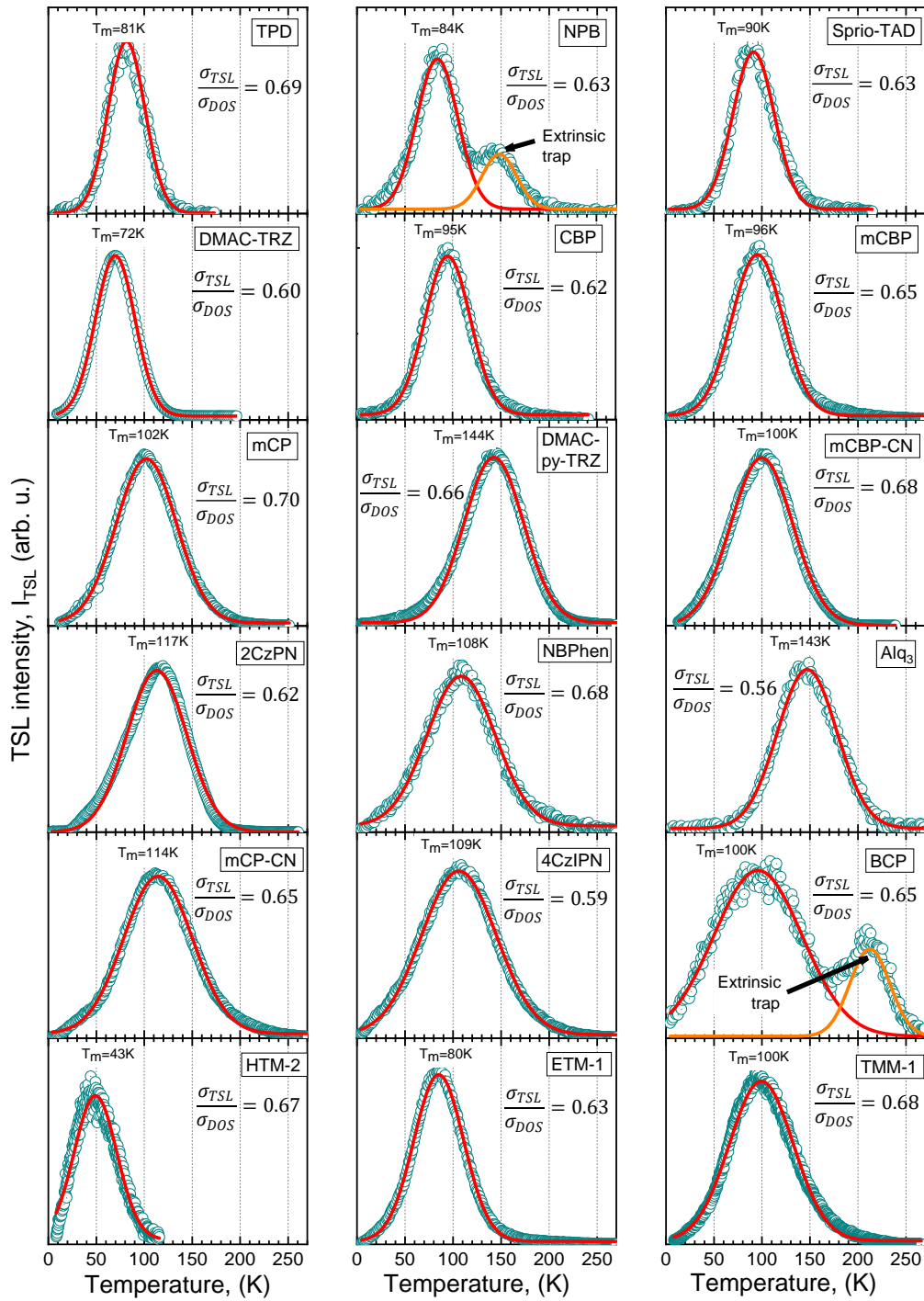
Figure 4: The TSL curves of different organic semiconductor films obtained after IR-cleaning. Experimental data are shown by symbols and the solid lines are the fitted Gaussians. The $\sigma_{TSL}/\sigma_{DOS}$ ratios are also indicated for each material.

3. Kinetic Monte Carlo simulations

3.1. Simulation techniques

The energetic relaxation of charges in a disordered organic solid is studied by using a grid-based kinetic Monte Carlo (KMC) method to monitor the motion of charge-carriers as hopping events. The KMC simulations were done by employing an isotropic three-dimensional (3D) simulation box (100 × 100 × 100 lattice sites) with a lattice constant of 1.5 nm [27,28]. We consider both random- and spatially correlated energetic disorder. For the simulations with uncorrelated disorder, the lattice sites are assigned a random energy drawn from a Gaussian distribution g(ε) with a standard deviation σ_{DOS} centered at zero energy:

$$g(\varepsilon) = \frac{N}{\sigma\sqrt{2\pi}} \exp\left[-\frac{1}{2}\left(\frac{\varepsilon}{\sigma_{DOS}}\right)^2\right] \tag{3}$$

For systems with correlated disorder, the energy correlations between the lattice sites are modeled using the approach suggested by Bobbert *et al.* [29]. The energy at a site i is taken equal to the electrostatic energy resulting from permanent random dipoles $\vec{d}_j$ of equal magnitude d but random orientations on all the other organic sites $j \neq i$. The resulting DOS is a Gaussian, with a width σ_{DOS} proportional to d [10]. The on-site energy E_i is then evaluated by using the Ewald summation method:

$$E_i = -\sum_{j \neq i} \frac{e\vec{d}_j \cdot (\vec{r}_j - \vec{r}_i)}{\varepsilon_0 \varepsilon_r |\vec{r}_j - \vec{r}_i|^3} \tag{4}$$

with the sum over all sites j in a large cubic box of 30 lattice sites (in each direction) around site i, e the unit charge, ε_0 the vacuum permittivity, and ε_r the material's relative permittivity. In this report we have taken ε_r = 3 for all the simulations. The resulting disorder strength is then given by $\sigma_{DOS} \approx 2.35 \frac{e \cdot d}{\varepsilon \cdot \varepsilon_0 \cdot a^2}$. Figure 5a and b illustrate the impact of spatial correlations on the energy landscape in an arbitrary X-Y plane (2D cross section) of the simulation box. In the case of system with random disorder (Figure 5a), the position of energetic peaks and valleys is found to be completely uncorrelated. On the contrary, in the case of system with correlated disorder the sites of higher (lower) energy depicted with blue (red) color (Figure 5b), are found to be in the vicinity of other higher (lower) energy sites. The spatial correlation function $C(r_{ij})$ which quantifies the degree of correlation between sites at a separation of r_{ij} from each other can be expressed as:

$$C(r_{ij}) = \frac{\langle(E_i - \langle E\rangle)(E_j - \langle E\rangle)\rangle}{\langle(E_i - \langle E\rangle)^2\rangle} \tag{5}$$

where E_i and E_j are the energies of the sites i and j separated by a distance r_{ij} and, $<\cdots>$ represents the expectation value. $C(r_{ij})$ is 1 if E_i and E_j are fully correlated and 0 if they are uncorrelated. The spatial correlation function evaluated for the X-Y plane energy sites in Figure 5a and b is shown in Figure 5(c) and (d), respectively. While $C(r_{ij})$ is found to be 0 for the system with random disorder, it exhibits a $1/r_{ij}$ dependence for the system with randomly oriented site dipoles as expected from the interaction of a charge with the long-range dipole electrostatic potential of a three-dimensional ensemble of uncorrelated dipoles [10].
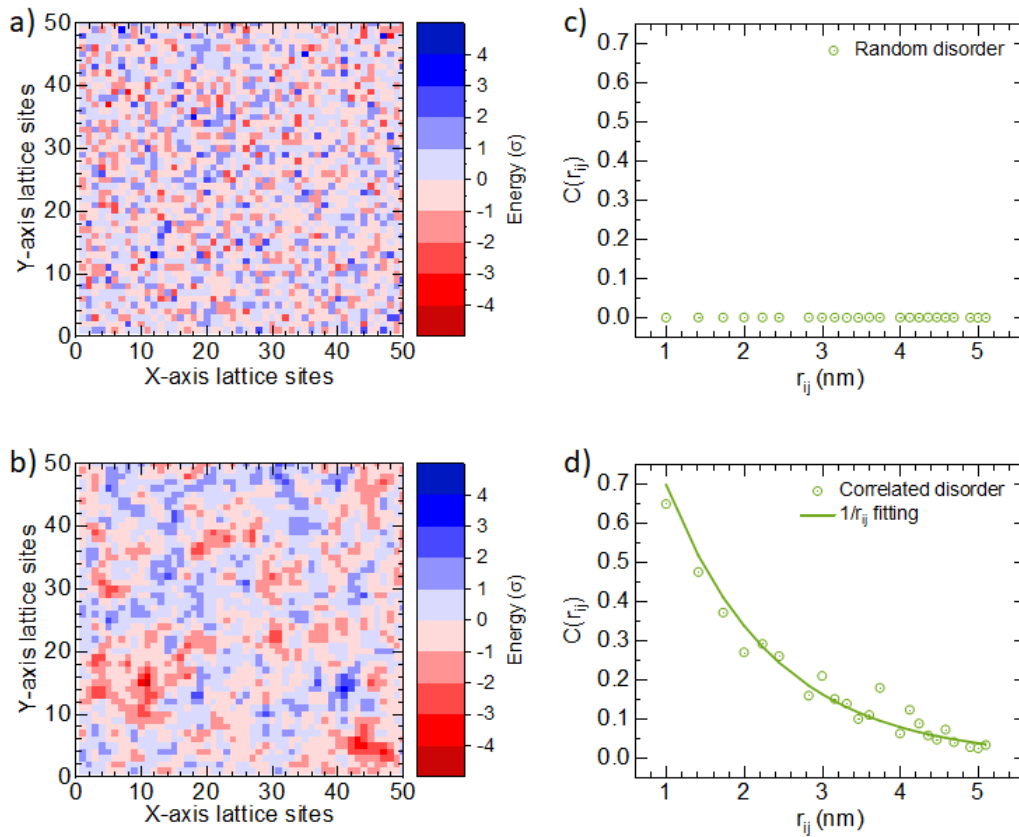
Figure 5: Heatmap of energetic landscape for a system with a) random disorder and b) correlated disorder. The variation of spatial energy correlation function, $C(r_{ij})$ (see Eq. (5)) with distance for c) random disorder system and d) correlated disorder system.

Both variable time step KMC (vt-KMC) and constant time step KMC (ct-KMC) approaches have been utilized to solve the master equation. For vt-KMC the following procedure was employed. At the beginning of the simulation, $t = 0$, a charge-carrier is generated randomly at one of the lattice sites. At each kinetic step, the charge can hop to any of the nearest-neighbor sites. In the case of KMC simulations in VRH regime, charge-carrier is also allowed to access non-nearest hopping sites. Every permissible hop is treated as an event and for each event i, the rate W_i is calculated. For the selection of an event, firstly, for each event i the partial sum $S_i = \sum_{j=1}^{i} W_{ij}$ is calculated. A random number φ is drawn from the interval $(0, 1]$ and from all possible events, the event i for which $S_{i-1} < \varphi W_T \leq S_i$ holds is selected, with $W_T = \sum_{j=1}^{N_{tot}} W_{ij}$, N_{tot} being the total number of events (permissible hops). The selected event is executed and the simulation time (t) is updated by the waiting time, $\tau_w = -ln(X)/W_T$ where X is a random number between 0 and 1.

In the ct-KMC simulations, total number of hopping neighbors N_{tot} are defined within a cube consisting of 5 x 5 x 5 lattice sites. A hopping event from state i to a generic state j $(i \neq j)$ is sampled uniformly from $N_{j \ldots tot}$ hopping neighbors, and the rate W_{ij} is calculated. The event is accepted if the associated hopping probability, $f_{ij} = \frac{W_{ij}}{v_0} > n$, where n is a uniform number between (0, 1], and v_0 (attempt-to-hop frequency) is the upper bound for hopping rate. Simulation time (t) is updated by $\Delta t = \frac{1}{v_0 N_{tot}}.ln(1/X)$, where X is a random number such that $X \in (0, 1]$. If event is accepted, event $i \rightarrow j$ is executed and charge-carrier coordinates are updated. The time scale is defined by $t_0 = 1/(v_0 N_{tot})$.

In the present paper, ct-KMC method is used to gain insight on the charge-carrier relaxation in short and intermediate time regimes. As the charge-carriers relax within the DOS, the hopping rates W_{ij} (and W_T) can decrease abruptly (by orders of magnitude), even if the number of hopping sites remains constant. Thus, a majority of ct-KMC trials are rejected leading to computationally intensive simulations. On the other hand, in vt-KMC the time step is evaluated as the inverse of W_T which leads to a non-linear increase in the time step as the charge-carriers relax in energy. As a result, we lose temporal resolution and hence the vt-KMC results will be parametrized in terms of the number of hops. However, this allows us to examine the long-time limit of the charge-carrier relaxation process at a reasonable computational cost using the vt-KMC method.

3.2. Simulation results

As it was mentioned in the experimental section, the TSL curve itself is expected to map a distribution of charge-carriers localized within the lower energy states of the DOS distribution, i.e., the ODOS distribution, formed because of the downward hopping of the charges within the DOS at 5 K. For comparison with the TSL experiments we are therefore interested in the long-time limit of the energetic relaxation of the charges and hence we consider vt-KMC simulation results. The selected simulation temperature (T = 5 K) corresponds to a "nonactivated relaxation" (NAR) mode [7], often termed the regime of purely downward hopping motion. In contrast, at a moderate degree of disorder (and large enough temperature) charge-carriers enter the regime of "activated relaxation" (AR) after a critical time (known as segregation time) [7] . Evolution of the distribution of charge-carriers in a system with random disorder of the DOS width, σ_{DOS} = 50 meV is depicted in Figure 6(a). The data illustrated are the Gaussian fit results of the energy distribution of charges obtained after a certain number of hops. With increasing number of hops, the energy distribution of charges moves to deeper localized states and narrows. The mean energy ($\langle\varepsilon\rangle$) and the width ($\sigma$) of the charge-carrier ensemble, both normalized by the DOS width (σ_{DOS}), are plotted in Figure 6(b) as a function of number of hops. A significant initial drop in the mean energy is observed, followed by a decrease in the relaxation rate. The largest shift in mean energy ($\langle\varepsilon\rangle \approx -2.5\ \sigma_{DOS}$) is observed within the first 20 hops (Figure 6(a) and 6(b)). This is because only the newly visited sites contribute to the shift in the mean energy $\langle\varepsilon\rangle$ [1,5,22], and as the charges relax to deeper localized states, the availability of suitable energy sites decreases. In other words, once a charge is captured by a deep trap, it oscillates infinitely and never leaves the local minima. This feature is also captured in the vt-KMC simulations. As shown in Figure S2, the number of newly visited sites increases significantly within the first 20 hops followed by a slow increase for higher number of hops. It is to be noted that even after 10^6 hops the number of newly visited sites remains less than 10, in agreement with previous reports [1,5,22].

Like mean energy, considerable initial narrowing of the energy distribution of the charges is followed by almost constant σ as the number of hops is increased further. Since dynamic equilibrium is unattainable at 5 K, the charge packet evolves infinitely with simulation time. However, a further increase in simulation time should not drastically affect the distribution of charges oscillating in the vicinity of local minima and hence the charge ensemble after 10^6 hops could be considered as the ODOS distribution of the charges. In particular, we are interested in ODOS distribution shape (Figure

S3a). One can notice that even after 10^6 hops, it is still asymmetric, i.e., while low energy part, being limited by the number of available neighbors, follows Gaussian distribution, high energy part follows a function steeper than Gaussian. Such behavior was predicted theoretically by Arkhipov and coworkers previously [16]. The ODOS width (σ_{ODOS}) could be used as a reference value on the real time scale and can be compared with the experimentally measured width of the TSL band σ_{TSL}. One can note that our simulation yields $\sigma_{ODOS} = 0.36 \times \sigma_{DOS}$, which does not represent the experimentally obtained width $\sigma_{TSL} = 2/3 \times \sigma_{DOS} \approx 0.67 \times \sigma_{DOS}$. The system with random disorder is thus unsuitable for correct quantitative explanation of the experimental results, motivating the exploration of an alternative approach.
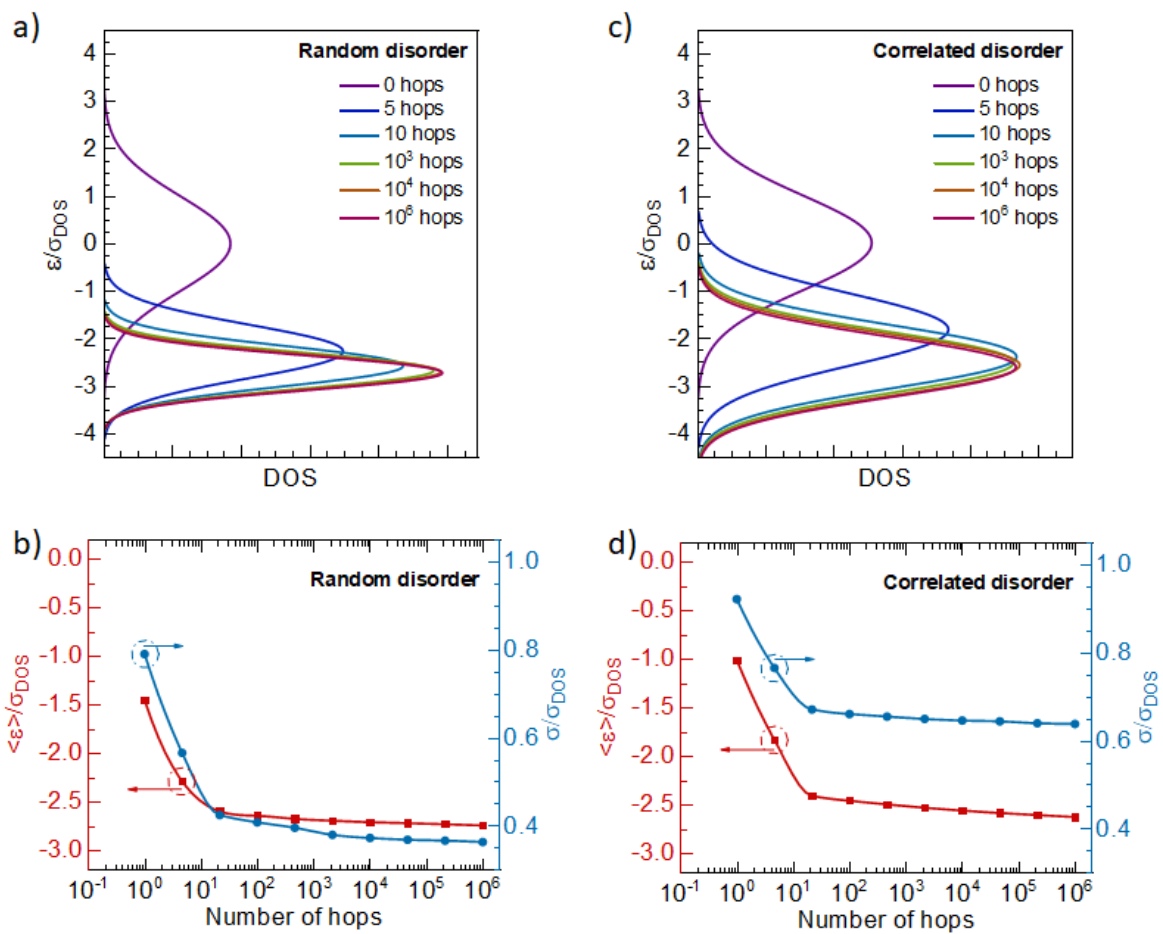
Figure 6: **vt-KMC simulation results** - Evolution of charge distribution with the number of hops for a system with a) random- and b) spatially correlated energetic disorder. The data illustrated are the Gaussian fit results of the energy distribution of charges obtained after the specified number of hops

at 5 K. Variation of mean energy ($\langle\varepsilon\rangle$) and width ($\sigma$) of the energy distribution (both normalized by the DOS width, σ_{DOS}) with the number of hops, for c) random and d) correlated disorder.

In the original Gaussian disorder model (GDM) by Bässler, any spatial correlations between the energies of the hopping sites were disregarded. The Correlated disorder model (CDM) has been crucial in predicting the Poole-Frenkel (PF) mobility field dependence over a broad field range [30-32]; however, it has never been considered in the context of the energetic relaxation of the charges. Since the materials used in this study are polar materials [12,17,33] and the TSL measurements are performed at zero fields, we now turn our attention to the results obtained for charge-carrier relaxation in an energy correlated medium. Like the system with random energetic disorder (Figure 6(a)), the charge ensemble shifts to lower energy and narrows in the case of correlated disorder system as well (Figure 6(c)). However, unlike the uncorrelated disorder system, narrowing effect is considerably weaker in the system with spatially correlated disorder. It can be seen from Figure 6(d) that within the span of first 20 hops the width of the energy distribution of the charges reduces to $0.42\sigma_{DOS}$ for random disorder *vs.* $0.67\sigma_{DOS}$ for correlated disorder leading eventually to a larger ODOS width of $\sigma_{ODOS} = 0.64 \times \sigma_{DOS}$ (Figure S3b). $\langle\varepsilon\rangle$ decreases significantly within the course of first 20 hops followed by a slow logarithmic dependence on the number of hops (Figure 6(d)). The shift in mean energy after 10^6 hops is almost equal for the system with correlated ($\langle\varepsilon\rangle \approx -2.6\ \sigma_{DOS}$) or random disorder ($\langle\varepsilon\rangle \approx -2.7\ \sigma_{DOS}$), the former showing slightly more frustrated behavior than the latter. In general, the nonactivated relaxation of carriers clearly takes place at such low temperatures and the average rate of distribution narrowing decreases with increasing number of hops. In the case of random disorder all hops to the new sites dominantly contribute to the narrowing, whereas hops amongst the correlated sites with almost the same energies are unlikely to affect the energy loss during relaxation and consequently the standard deviation of the relaxed charge ensemble. A key finding of this work is that the accounting for the spatial energy correlations, that are indeed present in organic media, allows reproducing experimentally obtained values for the ODOS width, i.e., the calculated σ_{ODOS} in a correlated system $\approx \sigma_{TSL}$ evaluated experimentally.

Temperature and time dependence

So far, we focused on the non-activated relaxation process, i.e., carrier jumps could only take place to lower energy sites. We next take thermal activation into account for both, system with random

and with correlated disorder (σ_{DOS} = 50 meV), as shown in Figure 7(a) and (b), respectively. We use the ct-KMC approach in order to obtain a dependence in the hopping time rather than in the number of hops. This allows for precise temporal tracking of charge carrier relaxation.

A significant drop of mean energy is observed for $t < 10^4 t_0$ indicating fast initial energy dissipation for all simulated temperatures. This is followed by a slower dissipation process at longer times. A particular notable feature of the charge-carrier relaxation is that the mean energy decreases upon cooling from 500 K to 150 K yet then increases when temperature is further reduced to 4 K. This phenomenon can be explained by the concept of frustrated spectral diffusion. The key idea is the following. The charges relax in the DOS by executing jumps to neighboring sites. These jumps may be downhill in energy or uphill, provided there is sufficient thermal energy for uphill jumps. As the temperature reduces, uphill jumps become less likely and are eventually frozen out. However, to get to lower energy sites via nearest-neighbor-jumps, occasional uphill jumps may be required. Their freezing out can therefore frustrate the overall relaxation process, so that the carriers remain in a local energy minimum. The occurrence of this frustrated spectral diffusion has been observed experimentally for triplet excitations [4]. KMC simulations by Athanasopoulos *et al.* demonstrated that the frustration can be lifted if more neighboring sites are available or if jumps can occur to sites further away [8]. The top panels of Figure 7a and b thus illustrate the impact that falling out of thermal equilibrium – here below 150 K (corresponding to a $k_B T / \sigma_{DOS} < 0.26$) - has on the mean energy of the charges. The bottom panels of Figure 7a and b, focus on the effect of energy relaxation on the ODOS width. For $t < 10^4 t_0$ the width reduces with increasing time. At longer times, this reduction continues for temperatures below 150 K. In contrast, for higher temperatures the width increases as time proceeds. This effect occurs in a similar manner for both random and correlated disorder, yet the overall reduction of the width is significantly reduced when correlated disorder is considered.
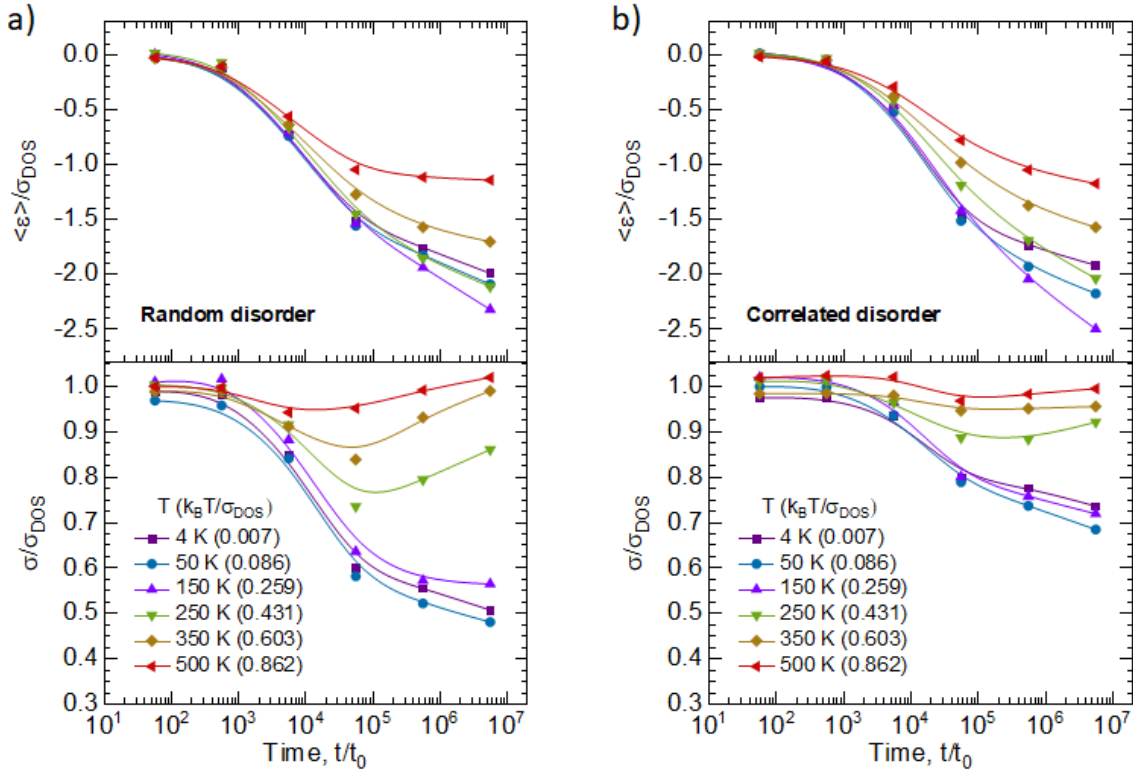
Figure 7: **ct-KMC simulation results** -The simulated normalized variation of mean energy ($< \varepsilon >/\sigma_{DOS}$, top panels) and the energetic width (σ/σ_{DOS}, bottom panels) of the distribution of charges as a function of simulation time at variable temperatures for a system with a) random disorder and b) correlated disorder. Results are shown for ct-KMC simulations performed for a DOS distribution of width, σ_{DOS} = 50 meV. Solid lines serve as a guide to the eye.

4. Discussion

In amorphous organic semiconductor films, energetic relaxation of excitations occurs by a sequence of random hops. The condition of finding a low energy hopping site is easily met in the center of the DOS so that downhill hops are fast. Yet, for the hopping sites in the tail of the DOS, suitable hopping sites are further apart, which slows down the transfer. As a result, the excitations generated in the center (or high-energy part) of the DOS distribution relax faster than the ones generated in the tail of the DOS. Figure 8a demonstrates temporal evolution of the energy distribution of the charge-carriers generated uniformly over the DOS at high temperatures (T) and/or low σ_{DOS}, i.e., in the regime of equilibrium transport. The distribution shows some narrowing at *earlier times* because of

the domination of downwards hops in such time domain. However, as the time progresses, the carriers' distribution starts to broaden, as the carriers in lower part of the DOS start relaxing at later times via executing upward hops. Such a non-monotonous temporal evolution of relaxed carriers' distribution (Figure 8a) is obtained because carrier's capture by local energetic minima is much faster than their release. Eventually, thermal equilibrium is established, and ODOS is formed around the equilibrium energy ($\varepsilon_{eq} = -\sigma_{DOS}^2/k_B T$) with a width σ_{ODOS} equal to the width of the DOS (σ_{DOS}) [1]. On the contrary, at low temperatures and consequently in the regime of non-equilibrium dispersive transport ($\sigma_{DOS}/k_B T \gg 1$; high σ_{DOS} or low T), the thermal equilibrium is unattainable. Therefore, at low temperatures, the photogenerated excitations hop towards the lower energy sites until they reach the DOS tail (Figure 8b). At any instance in time, irrespective of the mean energy of the relaxed charge carrier ensemble, the excitations at relatively higher energy sites within the DOS still relax faster than the excitations at relatively deeper energy sites. As a result, the width (σ_{ODOS}) of the relaxed charge-carrier ensemble decreases monotonously with increasing time (Figure 8b). These two scenarios are well reproduced in the ct-KMC results presented in Figure 7, which clearly demonstrate that ODOS narrowing is a consequence of non-equilibrium transport. This is also corroborated by previous reports, which suggest that in the regime of equilibrium transport such a narrowing is absent [1,5]. The observation that an ODOS smaller than the full DOS width is a result of the non-equilibrium nature of the transport has not been made before. It is a major result of our study.
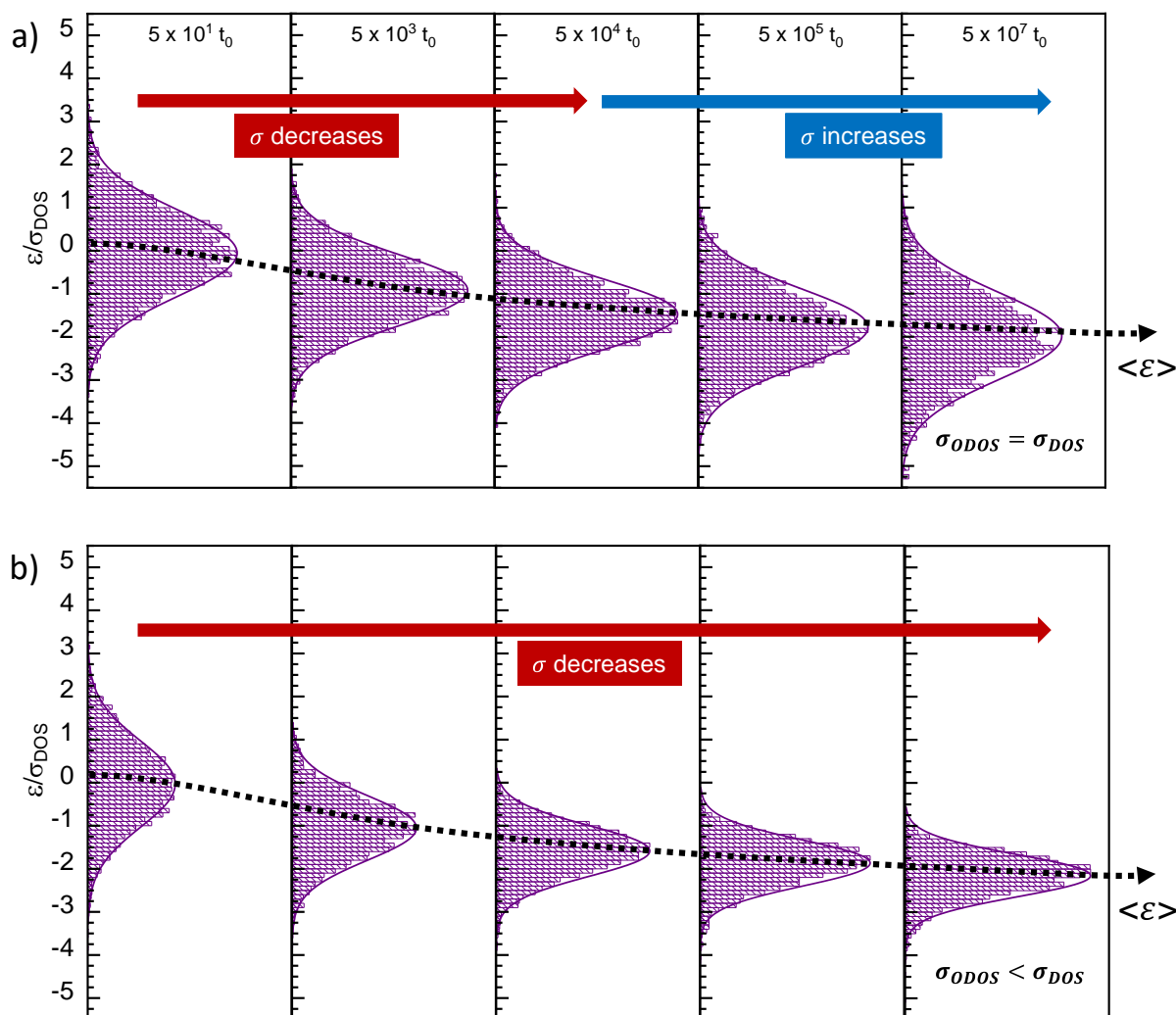
Figure 8: Schematic representation of the temporal evolution of the charge carrier ensemble for a) equilibrium transport b) non-equilibrium transport for selected time intervals.

As briefly mentioned in the previous sections, the energetic relaxation has already been extensively studied for singlet and triplet excitations and is manifested as spectral diffusion in this context [34]. Experimentally, spectral diffusion has been visualized as the bathochromic shift of fluorescence and phosphorescence with temperature for many conjugated systems such as poly(p-phenylenevinylene) [35], poly(p-phenylene) [4,8,36] and polyfluorenes [8,37], as well as for small molecular materials such as thermally activated delayed fluorescence emitters [38] and dendrimers [39]. It has also been crucial in analyzing the photocurrent and photoluminescence spectra of charge transfer (CT) states in donor-acceptor blends, commonly used as an active layer in organic solar cells [40-43]. Though a

lot of attention was attributed to the shift in mean energy of the relaxed excitation ensemble as the spectral diffusion progresses, the spectral narrowing was often not analyzed or discussed [8,37]. Recently, Kahle *et al.* [44] pointed out that the experimentally observed fluorescence linewidths are significantly lower than those of absorption. This implies that radiative decay of excitations occurs before the spectral diffusion has attained equilibrium and thus further illustrates the importance of spectral narrowing studies in the regime of non-equilibrium transport.

While the migration of singlet and triplet excitations can be examined spectroscopically, it is difficult to monitor the diffusion of charges. Though the charge carrier relaxation dynamics process cannot be probed with TSL, the latter technique allows us to investigate the ODOS distribution formed as a result of the charge-carrier relaxation process. As shown in the KMC results of Figure 6 and 7, relaxation never achieves equilibrium at low temperatures. Though, the rate of relaxation is fast at earlier times, it slows down as the time progresses. At large delay times after excitation, the mean energy and energetic width of the charge carrier ensemble virtually saturates. It is therefore important to point out that, since the process of photogeneration and relaxation of excitations take place at Helium temperature in TSL experiments, the TSL experiments probe a quasi-stationary ODOS distribution.

As theoretically illustrated by Arkhipov *et al.* [16] the ODOS spectra measured in TSL experiments also serve as a direct optical probe of energetic disorder of the organic semiconductor films. However, in such an analysis ("Method-1") only the high temperature wing of the TSL spectra is analyzed which could be of relatively low intensity in some organic materials. Therefore, as suggested in the present paper, the new experimental methodology, namely "Method-2" of determining the DOS width, where the full TSL signal rather than the just the high temperature wing of the TSL signal is analyzed, could be useful. Furthermore, "Method-2" relies on the general observation reported in this work, based on the study done on the neat organic semiconductor films of 18 commonly employed materials (used as hosts, emitters, hole/electron transport materials) in the fabrication of amorphous thin film OLEDs, that $\sigma_{TSL} = \sigma_{ODOS} = 2/3 \, \sigma_{DOS}$.

At last, we discuss the impact of spatial energy correlations on the energetic relaxation process in amorphous organic semiconductor films at low temperatures. The general observation ($\sigma_{ODOS} = 2/3 \, \sigma_{DOS}$) of the TSL experiments could only be reproduced after the introduction of energy

correlations. It is worth noting that in the initial studies the concept of correlation between the energies of spatially adjacent sites, known as the "correlated disorder model" (CDM) [10,11,45] was mostly utilized to justify an extended range of Poole-Frenkel-type field dependence of the charge mobility as obtained from time-of-flight measurements (i.e., in the low carrier concentration regime). Later, it was recognized that accounting for the carrier concentration dependence of mobility in the analysis of transport measurements of organic electronic devices (operating in space charge limiting current regime) is also crucial to establish the actual applicability of the GDM or CDM; and to resolve controversies concerning the presence and degree of spatial correlation of the site energies [31,32,46]. It has been theoretically demonstrated [32] that presence of the correlated disorder leads to a less pronounced carrier density dependence of charge mobility as compared to randomly disordered system, however the field dependence becomes more pronounced. Generally, energy correlations are not universally important for reproducing current-voltage (IV) characteristics in all organic materials. Coehoorn and coworkers [31,46] analyzed IV-characteristics, measured for different layer thicknesses and temperatures in sandwich-type devices based on amorphous small-molecule organic semiconductors, and concluded that site energies are spatially correlated in these materials. This was based on the observation that the site density, as obtained from the analysis of the IV-curves, is much lower than the experimentally determined molecular volume density in the case of CDM than for the case of GDM. On the other hand, the same group has also found [32] that site-energy correlations do not play an important role in poly(*p*-phenylenevinylene) based devices and much better fit of their current–voltage–temperature characteristics could be obtained by assuming a random disorder. In the present paper we suggest a much simpler approach of assessing the importance of energy correlations in the amorphous organic semiconductor films by using a purely spectroscopic TSL technique. In this regard, a key result of the present study is that energy correlations have a significant role in determining the "spectral narrowing", as observed in TSL experiments and hence on the energetic relaxation within the disordered energetic landscape at low temperatures. Evidently, in the case of random disorder all hops to the new sites contribute to the narrowing, whereas hops among the correlated sites with almost the same energies do not.

5. Conclusions

In summary, TSL technique is used to probe the distribution of relaxed charge-carriers trapped within the DOS, i.e., an occupied DOS (ODOS) distribution formed as a result of energetic relaxation of

charges within the DOS at low temperatures. The high-temperature wing of the TSL curve is an exact replica of the deeper portion of the DOS distribution and thus, it's Gaussian analysis (Method-1) yielded the effective DOS width, σ_{DOS}. Moreover, a Gaussian fit of the IR-cleaned TSL curve (σ_{TSL}) allowed us to determine the ODOS width (Method-2). TSL experiments conducted on pristine amorphous films of 18 low molecular weight organic materials commonly used in the fabrication of OLEDs led to a rather general observation that, the ODOS distribution formed at low temperatures is narrower as compared to the DOS; and that it leads to a universal ratio of $\sigma_{TSL}/\sigma_{DOS} = \sigma_{ODOS}/\sigma_{DOS} \approx 2/3$. To gain deeper insight into this effect, we performed KMC simulations of charge-carrier energetic relaxation process within the DOS. The KMC simulation-based study illustrated that the "spectral narrowing" effect as observed in TSL experiments, is a genuine property of the carrier relaxation within the Gaussian DOS at low temperature and that spatial correlations among the energy of the hopping sites have a significant effect on this narrowing effect. Moreover, though it was never considered important in the past, a key finding of this work is that the introduction of energy correlations, which are indeed present in organic media, allows reproducing experimentally obtained values for the ODOS width, i.e., σ_{ODOS} in a correlated system $\approx$ TSL σ_{ODOS}.

Acknowledgments

References

[1]   H. Bässler, Physica Status Solidi B **175**, 15 (1993).

[2]   H. Bässler, (Springer Berlin Heidelberg New York, 1994).

[3]   A. Köhler and H. Bässler, (Wiley-VCH Verlag, Weinheim, Germany, 2015).

[4]   S. T. Hoffmann, H. Bässler, J.-M. Koenen, M. Forster, U. Scherf, E. Scheler, P. Strohriegl, and A. Köhler, Physical Review B **81**, 115103 (2010).

[5]   B. Ries, H. Bässler, M. Grünewald, and B. Movaghar, Physical Review B **37**, 5508 (1988).

[6]   R. Richert and H. Bässler, Chemical physics letters **118**, 235 (1985).

[7]   P. Borsenberger, R. Richert, and H. Bässler, Physical Review B **47**, 4289 (1993).

[8]   S. Athanasopoulos, S. T. Hoffmann, H. Bässler, A. Köhler, and D. Beljonne, The Journal of Physical Chemistry Letters **4**, 1694 (2013).

[9]   D. H. Dunlap, P. E. Parris, and V. M. Kenkre, Physical review letters **77**, 542 (1996).

[10]   S. V. Novikov, D. H. Dunlap, V. M. Kenkre, P. E. Parris, and A. V. Vannikov, Physical Review Letters **81**, 4472 (1998).

[11]   S. Novikov and A. Vannikov, The Journal of Physical Chemistry C **113**, 2532 (2009).

[12]   A. Stankevych, A. Vakhnin, D. Andrienko, L. Paterson, J. Genoe, I. Fishchuk, H. Bässler, A. Köhler, and A. Kadashchuk, Physical Review Applied **15**, 044050 (2021).

[13]   A. Kadashchuk, N. Ostapenko, V. Zaika, and S. Nešpurek, Chemical physics **234**, 285 (1998).

[14]   A. Kadashchuk, Y. Skryshevski, Y. Piryatinski, A. Vakhnin, E. Emelianova, V. Arkhipov, H. Bässler, and J. Shinar, Journal of applied physics **91**, 5016 (2002).

[15]   A. Kadashchuk, D. Weiss, P. Borsenberger, S. Nešpurek, N. Ostapenko, and V. Zaika, Chemical physics **247**, 307 (1999).

[16]   V. Arkhipov, E. Emelianova, A. Kadashchuk, and H. Bässler, Chemical Physics **266**, 97 (2001).

[17]   A. Mondal, L. Paterson, J. Cho, K.-H. Lin, B. van der Zee, G.-J. A. Wetzelaer, A. Stankevych, A. Vakhnin, J.-J. Kim, and A. Kadashchuk, Chemical Physics Reviews **2**, 031304 (2021).

[18]   V. Arkhipov, E. Emelianova, R. Schmechel, and H. Von Seggern, Journal of non-crystalline solids **338**, 626 (2004).

[19]   B. Schweitzer, V. Arkhipov, U. Scherf, and H. Bässler, Chemical physics letters **313**, 57 (1999).

[20]   V. Nikitenko, D. Hertel, and H. Bässler, Chemical physics letters **348**, 89 (2001).

[21]   A. Kadashchuk, Y. Skryshevskii, A. Vakhnin, N. Ostapenko, V. Arkhipov, E. Emelianova, and H. Bässler, Physical Review B **63**, 115205 (2001).

[22]   B. Movaghar, B. Ries, and M. Grünewald, Physical Review B **34**, 5574 (1986).

[23]   M. Sakurai, R. Kabe, M. Fuki, Z. Lin, K. Jinnai, Y. Kobori, C. Adachi, and T. Tachikawa, Communications Materials **2**, 1 (2021).

[24]   P. de Silva and T. Van Voorhis, The journal of physical chemistry letters **9**, 1329 (2018).

[25]   A. Lukyanov and D. Andrienko, Physical Review B **82**, 193202 (2010).

[26]   D. Andrienko, 2020.

[27]   R. Saxena, T. Meier, S. Athanasopoulos, H. Bässler, and A. Köhler, Physical Review Applied **14**, 034050 (2020).

[28]   R. Saxena, V. Nikitenko, I. Fishchuk, Y. V. Burdakov, Y. V. Metel, J. Genoe, H. Bässler, A. Köhler, and A. Kadashchuk, Physical Review B **103**, 165202 (2021).

[29]   J. Van der Holst, F. Van Oost, R. Coehoorn, and P. Bobbert, Physical Review B **83**, 085206 (2011).

[30]   M. Bouhassoune, Org. Electron **10**, 437 (2009).

[31]   S. Van Mensfoort, V. Shabro, R. De Vries, R. Janssen, and R. Coehoorn, Journal of Applied Physics **107**, 113710 (2010).

[32]   M. Bouhassoune, S. Van Mensfoort, P. Bobbert, and R. Coehoorn, Organic Electronics **10**, 437 (2009).

[33]   X. De Vries and R. Coehoorn, Physical Review Materials **4**, 085602 (2020).

[34]   S. C. Meskers, J. Hübner, M. Oestreich, and H. Bässler, The Journal of Physical Chemistry B **105**, 9139 (2001).

[35]   S. T. Hoffmann, H. Bässler, and A. Köhler, The Journal of Physical Chemistry B **114**, 17037 (2010).

[36]   S. T. Hoffmann, E. Scheler, J.-M. Koenen, M. Forster, U. Scherf, P. Strohriegl, H. Bässler, and A. Köhler, Physical Review B **81**, 165208 (2010).

[37]   S. T. Hoffmann, S. Athanasopoulos, D. Beljonne, H. Bässler, and A. Köhler, The Journal of Physical Chemistry C **116**, 16371 (2012).

[38]   F. B. Dias, T. J. Penfold, and A. P. Monkman, Methods and applications in fluorescence **5**, 012001 (2017).

[39]   D. Sun, R. Saxena, X. Fan, S. Athanasopoulos, E. Duda, M. Zhang, S. Bagnich, X. Zhang, E. Zysman-Colman, and A. Köhler, Advanced Science, 2201470 (2022).

[40]   Y. Liu, K. Zojer, B. Lassen, J. Kjelstrup-Hansen, H.-G. n. Rubahn, and M. Madsen, The Journal of Physical Chemistry C **119**, 26588 (2015).

[41]   F.-J. Kahle, A. Rudnick, H. Bässler, and A. Köhler, Materials Horizons **5**, 837 (2018).

[42]   A. Melianas, N. Felekidis, Y. Puttisong, S. C. Meskers, O. Inganäs, W. M. Chen, and M. Kemerink, Proceedings of the National Academy of Sciences **116**, 23416 (2019).

[43]   T. Upreti, S. Wilken, H. Zhang, and M. Kemerink, The journal of physical chemistry letters **12**, 9874 (2021).

[44]   F. J. Kahle, A. Rudnick, S. Wedler, R. Saxena, R. Ammenhäuser, U. Scherf, S. Bagnich, H. Bässler, and A. Köhler, Advanced Energy Materials **12**, 2103063 (2022).

[45]   Y. N. Gartstein and E. Conwell, Chemical Physics Letters **245**, 351 (1995).

[46]   S. Van Mensfoort, R. De Vries, V. Shabro, H. Loebl, R. Janssen, and R. Coehoorn, Organic Electronics **11**, 1408 (2010).

Supplemental Material

Impact of energy correlations on narrowing of occupied density of state distribution for charge-carriers at low temperatures in disordered organic semiconductors

Andrei Stankevych,[1†] Rishabh Saxena,[2†] Alexander Vakhnin,[1] Christof Pflumm,[3] Jan Genoe,[4] Heinz Bässler,[5] Anna Köhler,[2,5*] and Andrey Kadashchuk[1,4*]

[1] Institute of Physics, National Academy of Sciences of Ukraine, Prospect Nauky 46, 03028 Kyiv, Ukraine

[2] Soft Matter Optoelectronics and Bavarian Polymer Institute (BPS), Universitätsstrasse 30, 95448 Bayreuth, Germany

[3] Merck KGaA, Display Solutions, Frankfurter Straße 250, 64293 Darmstadt, Germany.

[4] IMEC, Kapeldreef 75, B-3001 Leuven, Belgium

[5] Bayreuth Institute of Macromolecular Research (BIMF), Universitätsstrasse 30, 95448 Bayreuth, Germany

[†] Authors contributed equally to this work

*Corresponding author: kadash@iop.kiev.ua, anna.koehler@uni-bayreuth.de

Note S1: Full names of the compounds used in this study

The full names of the molecular structures presented in Figure 1 of the main text are as follows:

N,N'-Di(1-naphthyl) -N,N'-diphenyl-(1,1'-biphenyl)-4,4'-diamine (NPB), N,N'-Di(1-naphthyl)-N,N'-diphenyl-(1,1'-biphenyl)-4,4'-diamine (Spiro-TAD), N,N'-Bis(3-methylphenyl)-N,N'-diphenylbenzidine (TPD), 10-(4-(4,6-Diphenyl-1,3,5-triazin-2-yl)phenyl)-9,9-dimethyl-9,10-dihydroacridine (DMAC-TRZ), 4,4'-Bis(N-carbazolyl)-1,1'-biphenyl (CBP), 3,3'-(di(9H-carbazol-9-yl)-1,1'-biphenyl (mCBP), 1,3-Bis(N-carbazolyl)benzene (mCP), 10-(4-(4,6-Diphenyl-1,3,5-triazin-2-yl) pyridin-3-yl)-9,9-dimethyl-9,10-dihydroacridine (DMAC-py-TRZ), 3',5-di(9H-carbazol-9-yl)-[1,1'-biphenyl]-3- carbonitrile (mCBP-CN), 4,5-Bis(carbazol-9-yl)-1,2-dicyanobenzene (2CzPN), 2,9-Dinaphthalen-2-yl-4,7-diphenyl-1,10-phenanthroline (NBPhen), Tris(8-hydroxyquinoline)aluminum (Alq3), 9-(3-(9H-Carbazol-9-yl)phenyl)-9H-carbazole-3-carbonitrile (mCP-CN), 1,2,3,5-Tetrakis (carbazol-9-yl)-4,6-dicyanobenzene, 2,4,5,6-Tetrakis(9H-carbazol-9-yl) isophthalonitrile (4CzIPN) and 2,9-Dimethyl-4,7-diphenyl-1,10-phenanthroline (BCP).

Note S2: Fractional thermally stimulated luminescence (TSL) methodology

The main idea of fractional TSL technique is the following: during each heating cycle i, the sample is heated from an initial temperature $T_i = T_0 + (i-1)\Delta T_1$ (T_0 = 5 K, ΔT_1 = 5 K) to the final temperature $T_{f,i} = T_i + \Delta T_2$ (ΔT_2 = 20 K) using a constant heating rate β (for schematic illustration, see Figure S1a) and the emitted light intensity, $I_{TSL}(T)$, is recorded during the heating process, as shown in Figure S1b. Subsequently, as demonstrated in Figure S1c, the activation energy $\langle E_a \rangle$ for each heating cycle is calculated by performing an Arrhenius analysis of the fractional TSL data. The calculated activation energies can then be plotted against the mean temperature of the heating cycle for which a given $\langle E_a \rangle$ value was obtained. We found that, for the organic materials studied in the present work, $\langle E_a \rangle$ increases linearly with temperature (Figure 2, main text) and can be described reasonably well by the following empirical relation (Eq. (2), main text).
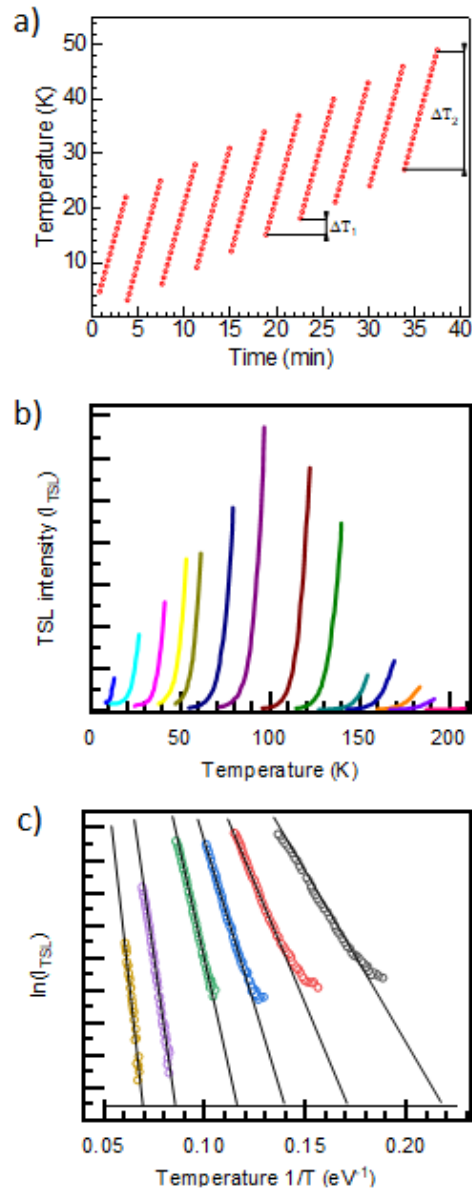
Figure S1: a) Schematic illustration of heating cycles used in fractional TSL method, b) TSL intensity (I_{TSL}) measured during each heating cycle and c) Arrhenius plot ($\ln{(I_{TSL})}\ vs.\ 1/T$) for each heating cycle for the calculation of activation energy ($\langle E_a \rangle$) during each heating cycle.
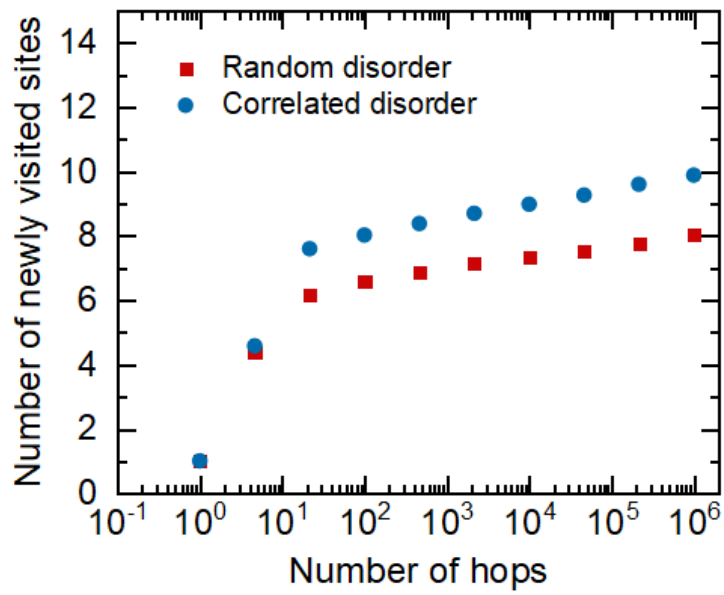
Figure S2: vt-KMC simulation results - comparison of the newly visited sites as a function of number of hops for system with random and correlated disorder.
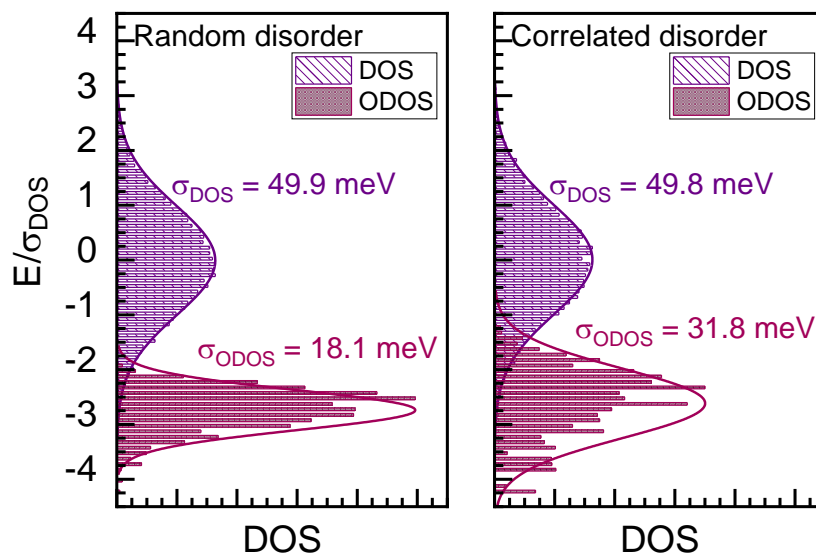
Figure S3: vt-KMC simulation results – comparison of ODOS distribution (after 10^6 hops) for system with random and correlated disorder.
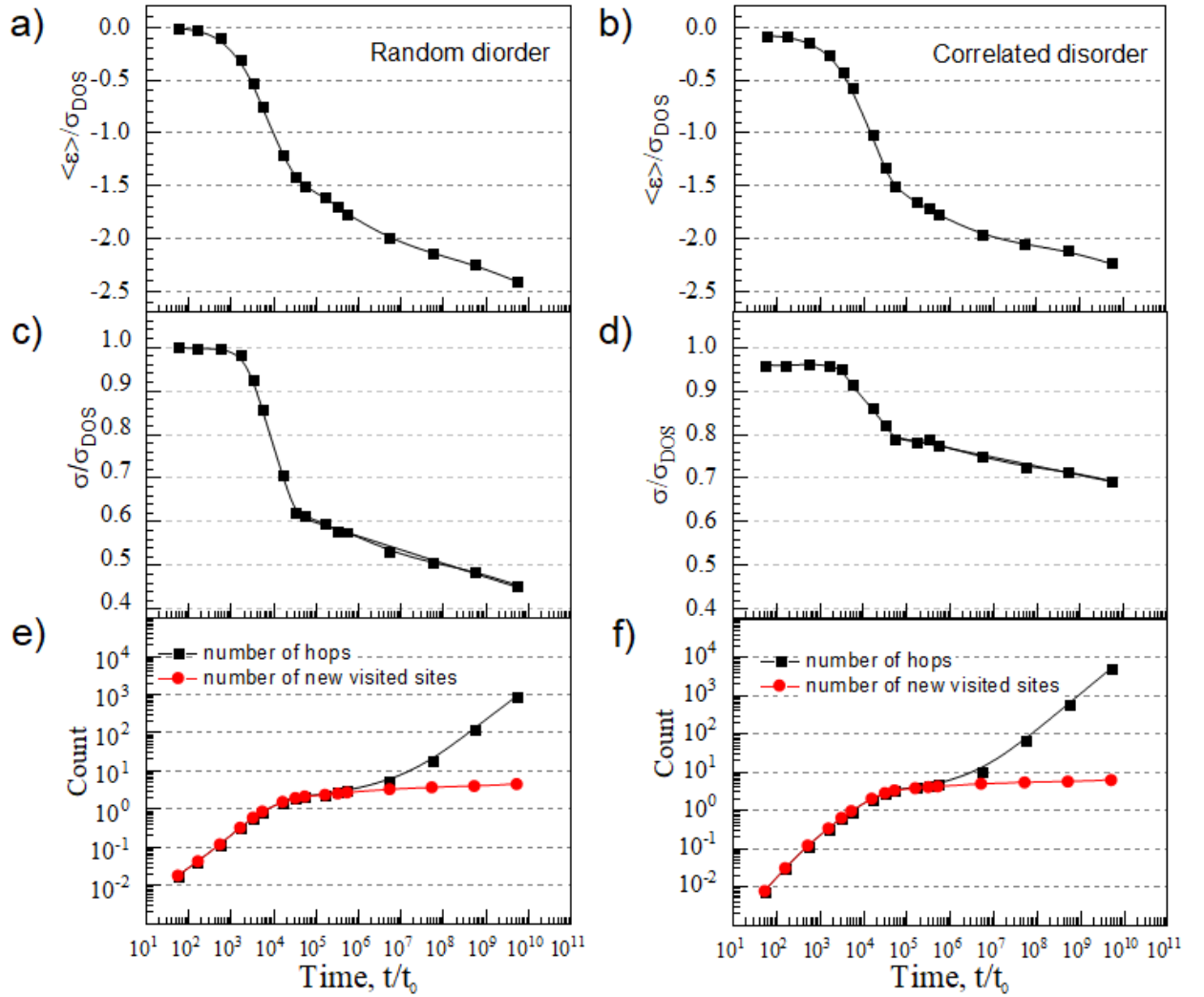
Figure S4: **ct-KMC simulation results** - mean energy of the distribution of hopping carriers normalized by the width of DOS ($< \varepsilon >/\sigma_{DOS}$) as a function of simulated time for a) random and b) correlated disorder system. Energetic width of the distribution of hopping carriers normalized by the width of DOS (σ/σ_{DOS}) as a function of simulated time for c) random and d) correlated disorder system. Number of new visited sites and number of hops as function of time for e) random and f) correlated disorder system.
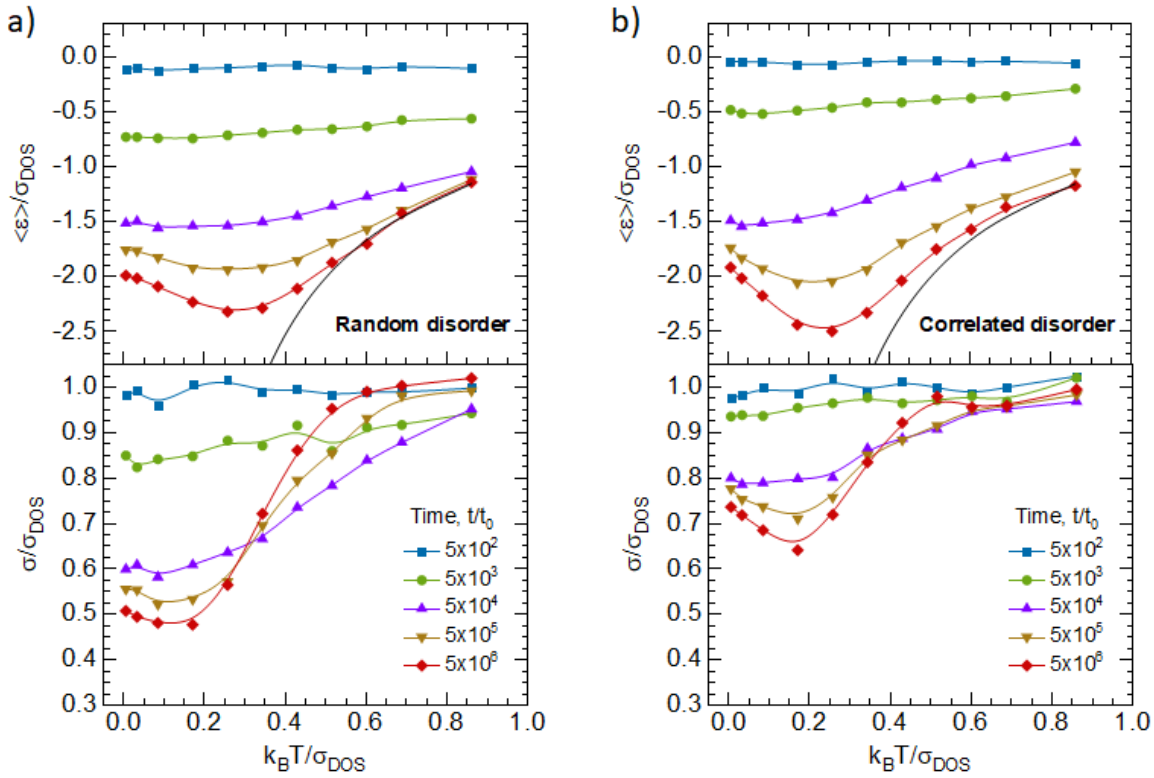
Figure S5: The simulated normalized variation of mean energy ($< \varepsilon >/\sigma_{DOS}$, top panels) and the energetic width (σ/σ_{DOS}, bottom panels) of the distribution of charges as a function of $k_B T/\sigma_{DOS}$ at variable simulation time for a system with a) random disorder and b) correlated disorder. Results are shown for ct-KMC simulations performed for a DOS distribution of width, σ_{DOS} = 50 meV. The black solid line in the top panels indicates the spectral relaxation expected for thermal equilibrium according to $< \varepsilon >/\sigma_{DOS} = -\sigma_{DOS}/k_B T$. Other solid lines guide the eye.

10 Kinetic Monte Carlo Study of Triplet-Triplet Annihilation in Conjugated Luminescent Materials

Rishabh Saxena, *Tobias Meier*, *Stavros Athanasopoulos*, *Heinz Bässler*, and *Anna Köhler*

Kinetic Monte Carlo Study of Triplet-Triplet Annihilation in Conjugated Luminescent Materials

Rishabh Saxena,[1] Tobias Meier,[1] Stavros Athanasopoulos,[2] Heinz Bässler,[3] and Anna Köhler[1,3,*]

[1] *Soft Matter Optoelectronics and Bavarian Polymer Institute (BPS), University of Bayreuth, Universitätsstr. 30, 95440 Bayreuth, Germany*

[2] *Departamento de Física, Universidad Carlos III de Madrid, Avenida Universidad 30, 28911 Leganés, Madrid, Spain*

[3] *Bayreuth Institute of Macromolecular Research (BIMF), University of Bayreuth, Universitätsstr. 30, 95440 Bayreuth, Germany*

It is well known that in organic solids the collision of two excitons can give rise to delayed fluorescence (DF). Revived interest in this topic is stimulated by the current endeavor towards the development of efficient organic optoelectronic devices such as organic light-emitting diodes (OLEDs) and solar cells, or sensitizers used in photodynamic therapy. In such devices, triplet excitations are ubiquitously present but their annihilations can be either detrimental, e.g., giving rise to a roll-off of intensity in an OLED, or mandatory, e.g., if the sensitizer relies on up-conversion of long-lived low-energy triplet excitations. Since the employed materials are usually noncrystalline, optical excitations migrate via incoherent hopping. Here, we employ kinetic Monte Carlo simulations (KMC) to study the complex interplay of triplet-triplet annihilation (TTA) and quenching of the triplet excitations by impurities in a single-component system featuring a Gaussian energy landscape and variable system parameters such as the length of the hopping sites, i.e., a conjugated oligomer, the morphology of the system, the degree of disorder (σ), the concentration of triplet excitations, and temperature. We also explore the effect of polaronic contributions to the hopping rates. A key conclusion is that the DF features a maximum at a temperature that scales with $\sigma/k_B T$. This is related to disorder-induced filamentary currents and thus locally enhanced triplet densities. We predict that a maximum for the TTA process near room temperature or above requires typically a disorder parameter of at least 70 meV.

I. INTRODUCTION

Triplet-triplet annihilation (TTA) plays an important role in controlling the operation of organic optoelectronic devices such as organic light-emitting diodes (OLEDs), organic solid-state lasers, and organic solar cells (OSCs) [1–5]. In OLEDs, TTA is devised as one of the efficient ways of converting the dark triplet excitons into emissive singlet excitons, which can decay radiatively to contribute to delayed fluorescence (DF) [6,7]. In solar cells, TTA can also be employed to improve efficiencies. The maximum theoretical power-conversion efficiency (PCE) of single-junction solar cells is dictated by the Shockley-Queisser limit, which depends on the bandgap of the light-absorbing material. TTA sensitized photon up-conversion can increase the PCE of OSCs by converting the low-energy photons into high-energy radiations that can be utilized by the absorber [8,9]. The same mechanism is used for sensitizing

semiconductor photocatalysts using the broad-spectrum sunlight [10,11]. TTA sensitized photon up-conversion is also advantageous in the fields of biomedical applications such as photoinduced drug delivery and photodynamic therapy [12,13]. In particular, up-conversion of red light with increased penetration in biological systems into blue light that is required for most photochemical reactions has been proved to be highly relevant [14].

TTA involves the collision of two triplets and thus depends on the diffusivity of triplet excitons [6,7,15–17]. Therefore, from a theoretical viewpoint, studying TTA in a model system also contributes to the fundamental understanding of triplet transport. The transport of neutral excitations through the inhomogenously disordered medium such as an amorphous organic semiconductor film proceeds via incoherent hopping between the localized sites [18]. In this scenario, the transport is controlled by the electronic coupling between the constituent molecular units and the static disorder present due to different possible configurations of the constituent molecules [19]. The electronic coupling for spin-triplet excitations in

*anna.koehler@uni-bayreuth.de

144

purely organic materials is dominated by exchange interaction (Dexter-type transfer), which depends on the wavefunction overlap [20]. Thus, the understanding developed in the process of investigating TTA can be utilized to control the triplet diffusion in order to optimize the efficiency of organic semiconductor devices extending from next-generation thermally activated delayed-fluorescence OLEDs [21] to phosphorescent-sensitizer-employed OSCs [22].

In phosphorescent OLEDs or TADF-based OLEDs made with host-guest systems, TTA is considered as one of the principle contributors towards the efficiency roll-off at high luminance [21,23,24]. Another main factor determining the efficiency roll-off in OLEDs is triplet-polaron quenching, which again depends on the diffusion of triplet excitons [25,26]. However, TTA does not necessarily need to be detrimental. It can also enhance the internal quantum efficiency of OLEDs when it contributes to delayed fluorescence via an up-conversion mechanism [27–29]. This requires efficient bimolecular recombination whereas monomolecular quenching of triplets at trap sites needs to be avoided [30,31]. Thus, in summary, TTA can be useful for solar energy conversion, photodynamic therapy, and understanding of triplet diffusivity and for the efficiency of OLEDs, and numerous studies have been devoted to improving these processes [9,13,32]. Nevertheless, a comprehensive study on how the bimolecular annihilation and monomolecular quenching processes compete with each other and the influence of material and film properties in controlling and modifying this competition is still lacking. We, therefore, intend to address this issue for a single-component system through our study.

We report an investigation of triplet hopping by means of kinetic Monte Carlo (KMC) simulations. In particular, we study the interplay between bimolecular TTA and monomolecular quenching processes (at trap sites) to eventually simulate the temperature dependence of quenching, delayed fluorescence, and phosphorescence (Ph) efficiency in conjugated polymers. Our simulation results are in agreement with the experimental observations of Hoffmann *et al.* [30]. In that paper, the authors studied the temperature dependence of Ph and DF in a series of poly(p-phenylene) derivatives and analyzed the findings on the basis of conventional rate equation for triplet excitons under steady-state conditions, yet only in the limit of low excitation intensities. KMC simulations provide the additional advantage of elucidating the temperature activation of the trap-induced quenching processes, which is difficult to do experimentally. When recording the phosphorescence intensity as a function of temperature, we can only observe that the Ph reduces, yet without direct indication of which fraction of this was caused by TTA, by trap-induced quenching, or by other thermally activated nonradiative decay channels. Moreover, with the

KMC simulations, we can disentangle the effect of each individual material parameter on the temperature dependence of various photophysical processes. Therefore, we use Monte Carlo simulations to determine which material properties need to be tuned to obtain minimum quenching and maximum DF at room temperature.

The simulation parameters are the degree of electronic coupling between the hopping sites, the static energetic disorder and the quencher ("trap") concentration. Conjugated segments are designed, and the delocalization effects associated with the conjugated polymers are studied in terms of the length of the conjugated chromophores and anisotropic triplet hopping rates. Athanasopoulos *et al.* [33] showed in a KMC study of the temperature dependence of spectral diffusion that triplet transport could be affected by the number of available energetic sites for hopping because of the short-range nature of the exchange coupling. In a realistic film, polymer chains may be more or less rigid and entangled or partially aligned, so that the resulting morphology is complex. Two limiting real morphologies is one where all chains are aligned and one where all chains cross each other heavily. We try to realize these two limiting cases in our model through two design morphologies, referred to as parallel and grid lattice. In both cases, the polymer chains are taken as a rigid one-dimensional sequence of lattice sites. For the parallel lattice, the chain orientation is the same in each layer, whereas for the grid lattice, the chain orientation is rotated by 90° between alternate layers. As detailed in the methods section, this results in a significantly higher number of nearest neighbors for the grid lattice. In this way, we investigate the role of morphology in controlling the interplay between bimolecular TTA and monomolecular quenching processes. Furthermore, Miller-Abrahams triplet hopping rates only include the disorder contribution to triplet diffusion. It does not take into consideration the polaronic effects associated with the conformational distortions upon energy transfer, described in terms of the geometric reorganization energy. These polaronic effects can be incorporated by including an activation energy in the triplet hopping rates through Marcus-type formalism [34,35]. We discuss in detail how the presence of reorganization energy effects does alter the temperature dependence of mono and bimolecular processes.

This paper is structured as follows. The details of the simulation technique are given in Sec. II. The results section, Sec. III, is concerned with analyzing the influence of morphology, defects, excitation density, wavefunction delocalization, energetic disorder, and geometric relaxation energy. We also focus on comparing our KMC results to what is expected from solving rate equations. In the concluding discussion, Sec. IV, we discuss how parameters need to be tuned to obtain a high TTA yield at room temperature while summarizing our key findings.

145

II. SIMULATION TECHNIQUE

The dynamic interplay of triplet-triplet annihilation and quenching of triplets at trap sites has been studied by employing a lattice-based kinetic Monte Carlo method to monitor the motion of excitons as hopping events. To describe the diffusion of triplet states through the disordered medium, we initially consider a Miller-Abrahams-(MA) type hopping between energetically uncorrelated sites of a point lattice [36]. This corresponds to a single-phonon-assisted tunneling between two sites of energy ε_i and ε_j with a rate

$$k_{ij,T} = \begin{cases} \nu_0 \, e^{-2\gamma R_{ij}}, & \varepsilon_i \geq \varepsilon_j, \\ \nu_0 \, e^{-2\gamma R_{ij}} \, e^{-(\varepsilon_j - \varepsilon_i)/k_B T}, & \varepsilon_i < \varepsilon_j. \end{cases} \quad (1)$$

ν_0 is the attempt-to-hop frequency, γ is the inverse localization length, R_{ij} is the hopping distance, and $k_B T$ the thermal energy. The absolute value of γ determines the localization of the triplet (or charge) wave function; small γ implies a large delocalization. The exponential decrease of the hopping rate with γR_{ij} incorporates the short-range nature of the MA rate. The MA model assumes that the Boltzmann factor is equal to 1 for a downward hop, whereas thermal activation is required for a hop to a higher-energy site. The attempt-to-hop frequency is typically of the order of a phonon mode, here we choose $\nu_0 = 10^{12}$ s^{-1}. The minimum hopping time is defined by $t_0 = (1/\nu_0)e^{2\gamma\alpha}$, where α is the lattice spacing (minimum hopping distance). The triplet lifetime (τ_T) is described as a multiple of t_0 and is defined in such a way that $(1/k_{\text{ISC}}\tau_{\text{Ph}}) \approx (\tau_T/t_0)$, where k_{ISC} and τ_{Ph} are the intersystem crossing (ISC) rate and phosphorescence lifetime, respectively.

While the triplets and charges are taken to diffuse only via exchange interaction [18,20,37], which depends upon the wave-function overlap, singlet excitons can also diffuse by long-range dipole interaction. Thus, to model singlet diffusion, we consider a MA + Förster-type rate:

$$k_{ij,S} = \begin{cases} \left[\nu_0 \, e^{-2\gamma R_{ij}} + \frac{1}{\tau_s} \left(\frac{R_F}{R_{ij}} \right)^6 \right], & \varepsilon_i \geq \varepsilon_j, \\ \left[\nu_0 \, e^{-2\gamma R_{ij}} + \frac{1}{\tau_s} \left(\frac{R_F}{R_{ij}} \right)^6 \right] e^{-(\varepsilon_j - \varepsilon_i)/k_B T}, & \varepsilon_i < \varepsilon_j. \end{cases} \quad (2)$$

τ_s is the intrinsic lifetime of singlet exciton and R_F is the Förster radius. γ is assumed to be the same for singlets and triplets. Here we consider $\tau_s = 1$ ns and $R_F = 3$ nm [38,39]. R_F depends on the spectral overlap of the absorption spectrum of the acceptor and emission spectrum of the donor and is defined such that at the Förster radius the energy-transfer rate is equal to the sum of radiative and nonradiative decay rates. Dipole coupling is usually dominant over exchange coupling but in the case where the long-range Coulombic rate is very small (large τ_s or small R_F),

as discussed below for the triplets, the Förster rate becomes less than the Dexter rate and the short-range exchange mechanism becomes the dominant diffusion mechanism for singlets as well.

For host-guest systems, the Eindhoven group have investigated the diffusion of triplets in detail by using transient PL measurements coupled with KMC simulations, and have analyzed the relative contribution of single-step Förster-type triplet-triplet interactions and the multi-step triplet diffusion processes to the mechanism of TTA in phosphorescent host-guest systems [1,32,40–43]. The results from the Eindhoven group stimulated us to consider the contribution of dipole-dipole-coupling-induced long-range Förster rate to the triplet hopping in addition to the short-range Dexter rate [1,40–42]. The impact of increasing the Förster contribution to triplet transport on the temperature dependence of quenching, DF and Ph events is shown in Fig. S1 (see the Supplemental Material [44]). The data are shown for purely Dexter-type rates and for increased contribution from the Coulombic interactions represented by the increase in Förster radius from 1 to 5 nm. No significant changes are observed with the incorporation of Förster rates. The reason lies in the comparatively long lifetime of the triplet states. The Förster-type transfer rate is inversely proportional to the lifetime of the state considered. Thus, for triplet states, the Förster-type energy rate is rather low, so that it cannot compete with the Dexter-type energy-transfer rate. As a result, the Dexter transfer dominates the energy-transfer process entirely here. This is different from the case of strongly phosphorescent emitters that are characterized by a much shorter triplet lifetime. We, therefore, subsequently only considered the Dexter-type MA rate for the triplet hopping process.

At time $t = 0$, random lattice sites in the simulation box ($100 \times 50 \times 50$ lattice sites) are initialized with a predefined number of triplets in accordance with an initial triplet density $[T_0]$. In our simulation, the lattice points have a spacing of 1.5 nm in direction of the x and z axis, while a spacing of 1.68 nm is adopted along the y axis. This anisotropic choice is based on matching experimental conditions in previous work [18,33]. By repeating some of the simulations for an isotropic lattice configuration, we confirm that our use of a slightly anisotropic lattice does not have a significant impact on our results and conclusion (see Fig. S2 within the Supplemental Material [44]). Generating 100 triplet excitations in this simulation box corresponds to a triplet density of about 10^{17} cm^{-3}.

In addition, some of the point sites are assigned as deep trap sites (sites of significantly lower energy) based upon a trap concentration (c_t). The triplet (singlet) energy is taken from a Gaussian distribution centered on energy E_T (E_S) with a variance of σ_T (σ_S) representing the static uncorrelated disorder in triplet (singlet) excited-state energies. At each Monte Carlo step each excitation can either diffuse to

146

a neighboring site with rate $k_{ij,T}$ ($k_{ij,S}$) or can decay radiatively with rate $k_{R,T}$ ($k_{R,S}$) or can decay nonradiatively with rate $k_{NR,T}$ ($k_{NR,S}$). Singlets can also undergo ISC (with rate k_{ISC}) thus leading to the generation of triplets. A schematic of all the radiative and nonradiative processes considered is shown in Fig. 1(a). Exciton-exciton annihilations and triplet quenching at the trap sites are considered as on-site and instantaneous processes, i.e., if two excitons reach the same lattice site, they annihilate. Similarly, if a triplet reaches a trap site, it is quenched. The quenching rate (k_Q) is represented as $k_Q = k_t c_Q$, where k_t is the triplet diffusion rate and c_Q is the effective quencher concentration, which here is simply the trap concentration (c_t) [30]. The trap depth is taken to be 300 meV, so that detrapping is negligible [45]. An interaction between two triplets can give rise to singlets, triplets, and quintets with a statistical probability of 1/9, 3/9, and 5/9, respectively. Therefore, if the formed singlets decay radiatively, they contribute to delayed fluorescence. Quintets are generally not formed because of the high energy associated with them; thus, this event can be simply described as the scattering of two triplets. This is how triplet-triplet annihilation is executed in this "computer experiment." Singlet-triplet annihilation (STA) and singlet-singlet annihilation (SSA) are included in the simulations, and are modeled as on-site and instantaneous processes, in a similar way as TTA. However, they eventually turn out to be negligible as compared to other emissive and exciton loss processes. There are two reasons for this: firstly, the short lifetime of singlets (in the range

of ns) prevents the buildup of a significant population that is needed for SSA or STA events. This is in contrast to triplets that live for milliseconds and so have enough lifetime to find each other as a sequence of hops. Second, the singlets (here) in the KMC simulation are generated from the TTA events, i.e., the initial singlet population is only a small fraction of the initial triplet population. Thus at low initial triplet density considered in the simulation ($[T_0] = 10^{16}$–10^{18} cm^{-3}), the number of singlets present at any given time is rather low. These two reasons combined, the chances of a singlet encountering a triplet or another singlet are insignificant and consequently STA and SSA events are less probable as compared to TTA. This might not be true for high $[T_0]$ (for example, $[T_0] \geq 5 \times 10^{18}$ cm^{-3}) and thus the STA and SSA events may no longer be negligible.

For each excitation, the rates of the processes described are determined. For computational efficiency reasons, hops to only a fixed number of nearest neighbors are considered, that is, we took sites up to the fourth-nearest neighbor into account. For each event i, the rate k_i is calculated. For the selection of an event, firstly, for each event i the partial sum $S_i = \sum_{\beta=1}^{i} k_\beta$ is calculated. A random number is drawn from the interval $(0, k_T]$, with $k_T = \sum_{\beta=1}^{N} k_\beta$, N being the total number of events. From all possible events, the event i for which $S_{i-1} < \varphi k_T \leq S_i$, $\varphi \in (0, 1]$ holds is selected. The selected event is executed for the corresponding excitation and the simulation time is updated by the waiting time, $\tau_w = -\ln(X)/k_T$, where X
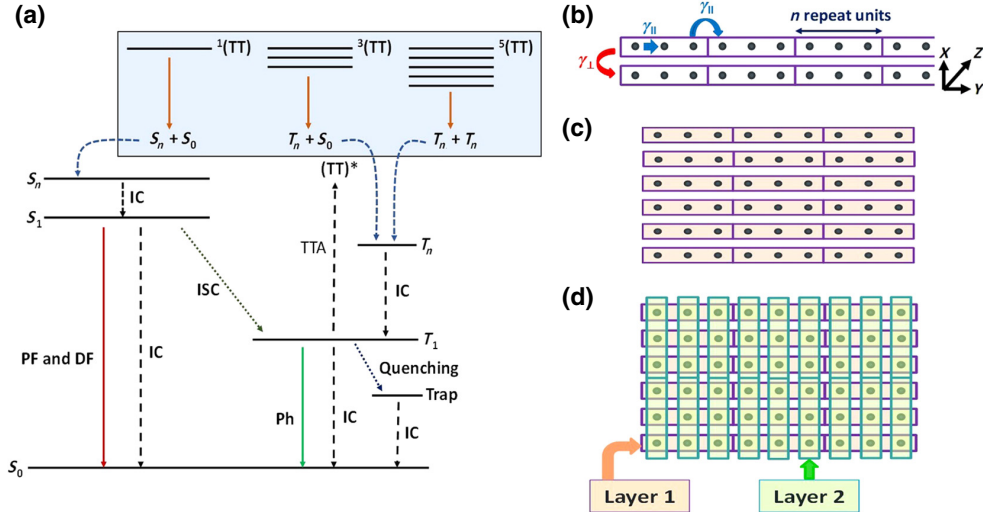
FIG. 1. (a) Schematic of all the radiative and nonradiative processes considered in the KMC simulation (PF, prompt fluorescence; DF, delayed fluorescence; IC, internal conversion; ISC, intersystem crossing; Ph, phosphorescence; TTA, triplet-triplet annihilation). The reaction of TTA can be given as $T_1 + T_1 \rightarrow (TT)^*$. (b) Pictorial representation of the design of a conjugated segment with "n" isoenergetic repeat units and separate inverse localization lengths for triplet transport parallel and perpendicular to the chain. (c) Top view of the parallel lattice with all the chains along y direction in all the layers. (d) Top view of the grid lattice with all the chains in layer 1 and layer 2 aligned along y and x direction, respectively.

147

is a random number between 0 and 1. The simulation stops when there is no excitation left in the simulation box. Results are obtained by averaging over a sufficiently high number of trials, e.g., 100 trials (for details, refer to Sec. S1 within the Supplemental Material [44]). The effects of morphology and material parameters such as conjugation length (n), inverse localization length along ($\gamma_\parallel$) and perpendicular ($\gamma_\perp$) to the chain, trap concentration (c_t) and energetic disorder (σ) on quenching, delayed fluorescence and phosphorescence processes are simulated. The resulting variation of quenching, DF and Ph events with temperature is expressed in terms of the percentage of the initial ($t = 0$) number of triplets in the simulation box.

By considering extended conjugated chromophores, our study explicitly includes the effect of conjugation length. Following the approach of Athanasopoulos *et al.* we implement the delocalization of an exciton over several repeat units by defining a conjugated chromophore as a segment with "n" isoenergetic lattice sites as illustrated in Fig. 1(b), that have strong electronic coupling between them [18,33]. The different electronic coupling for transport parallel and perpendicular to the conjugated chromophores is obtained by adopting different values for the inverse localization length γ if the sites i and j are in a direction parallel to the chain ($\gamma_\parallel$) or perpendicular to the chain ($\gamma_\perp$). Thus, the ratio $\gamma_\parallel : \gamma_\perp$ determines the anisotropy of the triplet transport. For example, $\gamma_\parallel = 1\,\mathrm{nm}^{-1}$ and $\gamma_\perp = 2\,\mathrm{nm}^{-1}$ ($\gamma_\parallel : \gamma_\perp = 0.5$) implies higher coupling in a direction parallel to the chain and lower coupling for hops perpendicular to the chain, thus making triplet hops parallel to the chain more probable than hops perpendicular to the chain. This applies to both, hops between conjugated segments of adjacent chains and hops between conjugated segments along the same chain. Moreover, since each conjugated segment is represented by a sequence of lattice points with identical energy, while the energies differ between the conjugated segments, the hops within a conjugated segment are inherently faster than the hops between the conjugated segments. This procedure allows us to treat the conjugation and delocalization effects in a stochastic manner.

When considering elongated chromophores, their mutual arrangement, i.e., the film morphology, becomes a key parameter. This is because the electronic coupling for the hopping of triplet excitons is provided by exchange interaction, which depends on the orbital overlap of the sites involved in the hopping process [Eq. (1)]. Thus, the number of accessible and adjacent neighboring sites is crucial for the transport of triplets, and for elongated chromophores, different film morphologies result in a different number of accessible neighbors. Consider, for example, a thin film consisting of elongated conjugated chromophores such as rigid oligomers that are all oriented along the same direction, e.g., along the y axis [Fig. 1(c)]. In the simplest case of such a parallel arrangement, hops are possible from

each chromophore to adjacent neighbors on either side as well as on the top and bottom and at the chromophore ends. In contrast, consider now the case where the oligomers are still all aligned along the y axis in one layer, yet they are all aligned orthogonally, e.g., along the x axis, in the layer above and below it [Fig. 1(d)]. This gridlike arrangement increases the number of contact points to next neighbors in the layer above and below from previously only two contacts in total to several contacts [for Fig. 1(d) that is two times three equal contacts in total, for the layers above and below, as illustrated in Fig. S3 within the Supplemental Material [44]]. As a consequence, more hops to sites of different energy are possible, and this significantly impacts on triplet diffusion.

The same approach was taken by Athanasopoulos *et al.* [33] who studied the temperature dependence of spectral relaxation for triplet states. They found that increasing the number of available lattice sites for hopping by changing from a parallel chromophore arrangement to a gridlike chromophore arrangement helps in overcoming local energy barriers that otherwise stop the relaxation prior to reaching lower-energy sites, in agreement with experimental results. This approach of chains in parallel or gridlike arrangement represent two extreme cases. Of course, real polymer films have far more complex morphologies and sophisticated approaches exist to represent them [46], yet our approach is sufficient to capture the essential physics with reasonable computational effort.

III. RESULTS AND ANALYSIS

A. General features

In KMC simulation, we monitor the interplay between intrinsic decay of triplet excitations, i.e., phosphorescence, quenching at nonradiative scavengers (Q), and delayed fluorescence as a function of temperature and a whole set of system parameters. Figure 2(a) shows the evolution of these quantities for two lattices and for two different values of initial triplet density, $[T_0] = 5 \times 10^{16}\,\mathrm{cm}^{-3}$ and $10^{18}\,\mathrm{cm}^{-3}$, equivalent to 50 and 1000 excitations, respectively. The resulting incidences are given as a percentage of the initial ($t = 0$) number of triplets in the simulation box. Results for a wider range of initial triplet densities $[T_0]$ can be found in Fig. S4 within the Supplemental Material [44]. The percentages of Ph, DF, and quenching do not add up to 100% due to the spin statistics inherent in the TTA process. Independent of the choice of lattice and excitation density, we obtain general trends that are in excellent agreement with the experimental observations of Hoffmann *et al.* [30], thus confirming our computational approach. The general evolution we observe is the following.

At very low temperature, there is phosphorescence as well as some delayed fluorescence. Upon increasing temperature, quenching turns on at the expense of Ph.

148
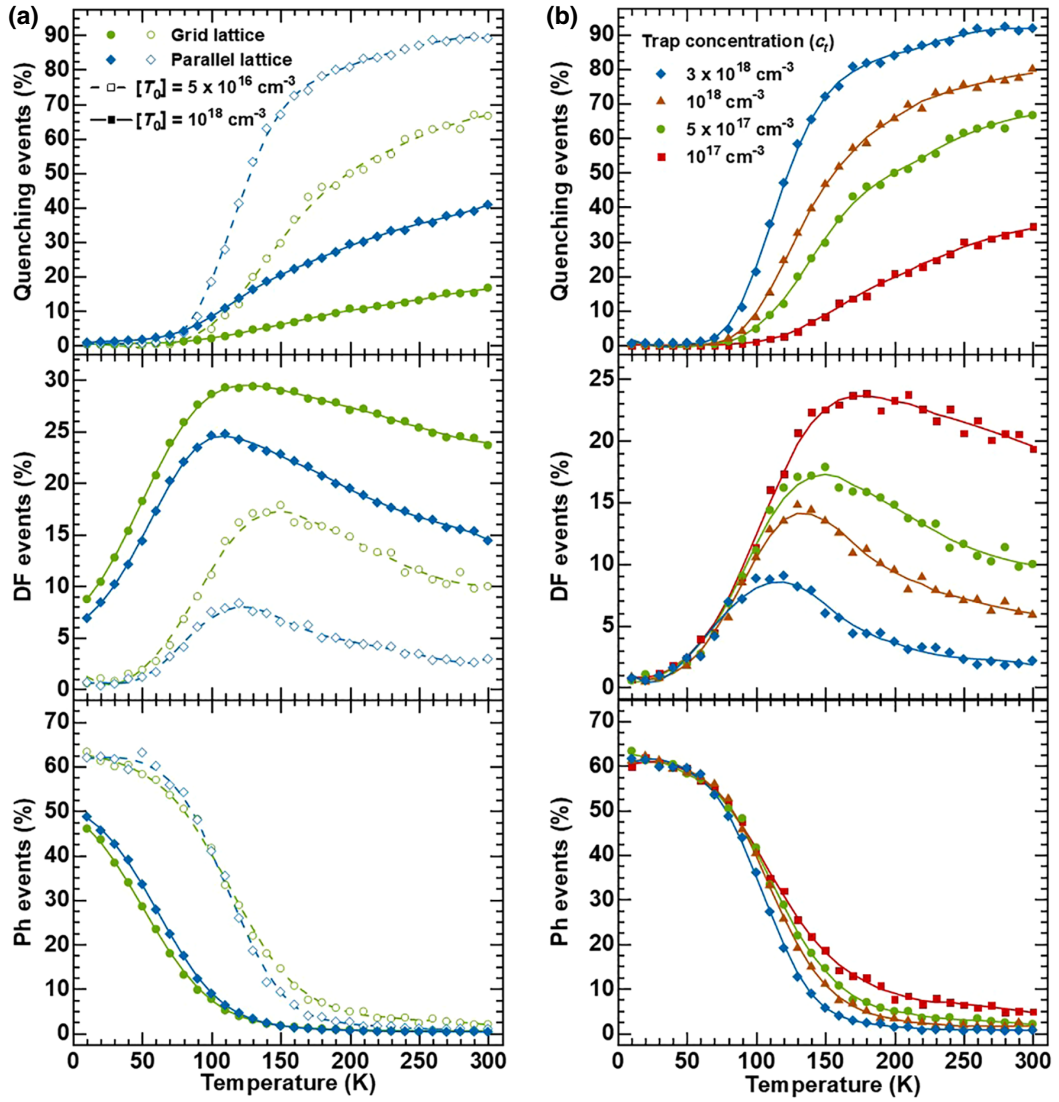
FIG. 2. Comparison of simulated quenching, DF, and Ph events (a) in the grid (green circles) and parallel lattice (blue diamonds) to study the influence of morphology on the temperature dependence of monomolecular and bimolecular recombination processes. Data are shown for two different values of initial triplet density, $[T_0] = 5 \times 10^{16}$ cm^{-3} (empty symbol, dashed line) and 10^{18} cm^{-3} (filled symbol, solid line). (b) With the triplet quenching rate parametrized in terms of the trap concentration (c_t). Data for $c_t = 10^{17}$ cm^{-3} (red squares), $c_t = 5 \times 10^{17}$ cm^{-3} (green circles), $c_t = 10^{18}$ cm^{-3} (brown triangles), and $c_t = 3 \times 10^{18}$ cm^{-3} (blue diamonds). A constant coupling along and perpendicular to the chain ($\gamma_{\parallel} = 1.5$ nm^{-1} and $\gamma_{\perp} = 2$ nm^{-1}) is used and a disorder of $\sigma = 35$ meV is used for the triplet energy distribution. For (a), $c_t = 5 \times 10^{17}$ cm^{-3} and for (b) grid lattice morphology with $n = 3$ is used. Solid lines serve as a guide to the eye.

Simultaneously DF increases such as to pass over a maximum. This behavior is a generic feature of hopping of excitations within a Gaussian density of states (DOS) distribution. At very low temperatures, most of the triplets that have been initially generated randomly within the DOS relax up to some point and subsequently emit phosphorescence [33]. At intermediate temperatures thermally activated dispersive transport leads to growing DF. At even higher temperatures, DF decreases because

the concentration of triplets needed for their bimolecular encounter is diminished due to progressive quenching at triplet scavengers.

B. Effect of lattice choice and excitation intensity

The KMC simulations allow us to explore how the DF intensity is affected by the film morphology and the excitation density, even for high illumination intensities.

When comparing the two lattices, we observe less quenching and more DF for the grid lattice (shown in green circles). This applies not only to the peak value but, also to the value at 300 K where devices typically operate. Furthermore, the temperature T_{max} at which the DF peaks, shifts to slightly higher values for the grid lattice. The fraction of phosphorescence events is not affected by the choice of lattice. We observe a similar trend, i.e., a reduced fraction of quenching events, more DF and, in contrast to the change of lattice, a reduction of Ph when the excitation density is increased.

The intensity dependence is straightforward to understand. For a given temperature, a higher excitation density increases the triplet population $[T]$, so that the bimolecular process, TTA, is favored over the monomolecular quenching process. In Fig. 2(a) we see that using a grid lattice has the same effect as increasing the excitation density, i.e., the bimolecular DF process is favored over the monomolecular quenching process. Evidently, using an arrangement with many contact points that allow for more isotropic hopping increases the chance of two triplets meeting each other, even if they have been generated at some distance and at different chains. This is consistent with the earlier results of Athanasopoulos *et al.* on spectral diffusion, where very low-energy sites in the DOS can only be reached for the grid lattice [33].

Since our primary aim is to establish guidelines for achieving high DF at room temperature, therefore we discuss the influence of all the other material parameters for the grid lattice with an initial triplet density $[T_0]$ of 5×10^{16} cm^{-3}. This value corresponds to the triplet density generated in an optical experiment with an excitation fluence of approximately 10 μJ/cm^2, incident photon wavelength of 355 nm (typical of a Nd : YAG laser), an absorption length of 100 nm with an underlying assumption of uniform absorption with a coefficient of about 10^5 cm^{-1} throughout the film thickness and considering a singlet-to-triplet yield of about 1%–2% typical for purely organic materials (with no heavy atoms and ISC rate of approximately 10^7 s^{-1}) [20].

C. Influence of trap concentration (c_t)

Even well synthesized and purified compounds contain some residual amount of structural or chemical defect sites where triplet states can be quenched. It is clear that their amount plays a key role in controlling the dynamic interplay between the bimolecular and monomolecular processes. Figure 2(b) illustrates quantitatively the impact of reducing the concentration of such quenching sites. In agreement with typical defect concentrations [47], we vary the trap concentration from 3×10^{18} cm^{-3} to 10^{17} cm^{-3} and observe a strong increase in the DF at room temperature as the defect concentration reduces, in addition to a slight shift of the DF peak (T_{max}) to higher temperatures.

Evidently, the purity of compounds is a key parameter to obtain high TTA rates.

D. Influence of delocalization

The present OLED technology is dominated by using molecules suitable for making devices through thermal evaporation in vacuum. Nevertheless, using solution-processed molecules such as oligomers or even polymers is still a possible avenue. Moreover, triplets move by means of wave-function overlap, so that transport along a conjugated backbone is usually faster than hopping to an adjacent chromophore [18]. Therefore, conjugation of the chromophore should affect the temperature evolution of bimolecular annihilation and monomolecular quenching processes. As described above and as depicted in Fig. 1(b), in our simulation, the length of a chromophore is defined through the number of adjacent isoenergetic sites (n) along the chain.

Figure 3(a) shows the effect of conjugation on quenching, DF and Ph events for the grid lattice. Quenching events decrease with increasing length of the conjugated segment and concomitantly, DF events increase with the peak in DF (represented by T_{max}) remaining at approximately similar temperature. The fraction of DF events at room temperature is also raised. This effect can be understood by the reasoning already brought forward to comprehend the increased DF for the grid morphology compared to the parallel lattice. As the length of the conjugated segment is increased, the number of crossing points to chromophores of different energies raises [cf. Fig. 1(d)]. In this way, an increasing conjugation length leads to an increased rate of successful hops to adjacent chromophores and, somewhat paradox, more isotropic diffusion. This, in turn, enhances the chance of two triplets meeting, i.e., the bimolecular recombination rate, and thus suppresses the relative number of quenching events.

The anisotropy of the excitation transport also becomes key when considering transport along the polymer chains. This anisotropy is studied by systematically varying the ratio $\gamma_\parallel : \gamma_\perp$ as, due to the Dexter-type nature of triplet transfer, this ratio controls the directionality and hence the anisotropy of triplet diffusion [18,33]. $\gamma_\parallel : \gamma_\perp = 1$ corresponds to isotropic diffusion, whereas $\gamma_\parallel : \gamma_\perp < 1$ ensures that coupling along the chain is stronger than perpendicular to it. Figure 3(b) summarizes this effect for a conjugated segment of length $n = 10$. As the hopping events perpendicular to the chain direction are increased by reducing $\gamma_\perp$ from 4 to 2, we observe an increase in DF events up to about 150 K, yet there is no effect at higher temperatures. This is in contrast to the effects obtained when using the grid over the parallel-chain arrangement or when increasing the conjugation length, and, at first sight, may seem counterintuitive since increasing the electronic coupling to adjacent chains should have a similar effect. A similar

150
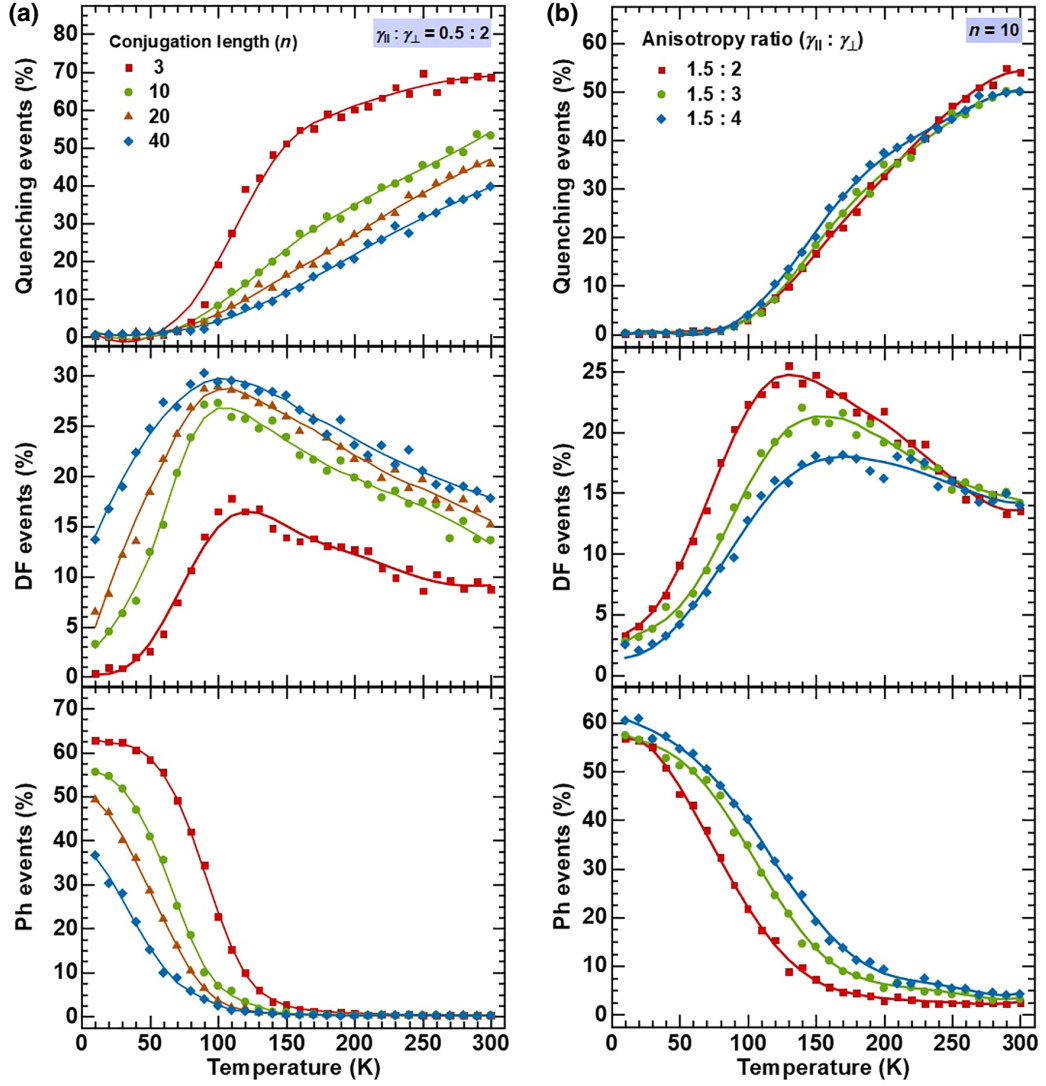
FIG. 3. Influence of delocalization is studied by simulating the number of quenching, DF, and Ph events by (a) varying the length of the conjugated segment (n) from 3 to 40 for the grid lattice morphology with $\gamma_\parallel = 0.5\,\mathrm{nm}^{-1}$ and $\gamma_\perp = 2\,\mathrm{nm}^{-1}$ and (b) for a fixed n ($n = 10$) by varying the anisotropy of coupling with a constant parallel to the chain inverse localization length of $\gamma_\parallel = 1.5\,\mathrm{nm}^{-1}$ and varying the one perpendicular to the chain ($\gamma_\perp$) from 4 to 2 nm^{-1}, thus increasing the interchain hopping transport. The results are obtained with a constant trap concentration $c_t = 5 \times 10^{17}\,\mathrm{cm}^{-3}$ and energetic disorder $\sigma = 35\,\mathrm{meV}$. Solid lines serve as a guide to the eye.

result is obtained when keeping $\gamma_\perp$ constant and reducing $\gamma_\parallel$ such as to increase the conjugation along the chain, see Fig. S5 within the Supplemental Material [44].

It can be easily understood by recalling that the MA rate [Eq. (1)], consists of two exponential terms, that is the strength of the electronic coupling, $e^{-2\gamma R_{ij}}$, and the Boltzmann factor for upward jumps. Increasing the coupling perpendicular to the chain increases the off-chain hopping rate. While this dominates from low temperatures up to about 150 K, from 150 K onwards the Boltzmann term controls the total rate, irrespective of the enhancement in

the coupling. We note that going to even smaller values than 2 for $\gamma_\perp$ is unrealistic. This strong influence of the Boltzmann factor calls for a closer inspection on the impact of energetic disorder.

E. Influence of energetic disorder (σ)

Figure 4(a) shows the variation of Ph, DF, and quenching events for different energetic disorder values for the triplets, using the same parameters and the MA rate employed so far. As the energetic disorder increases from

151
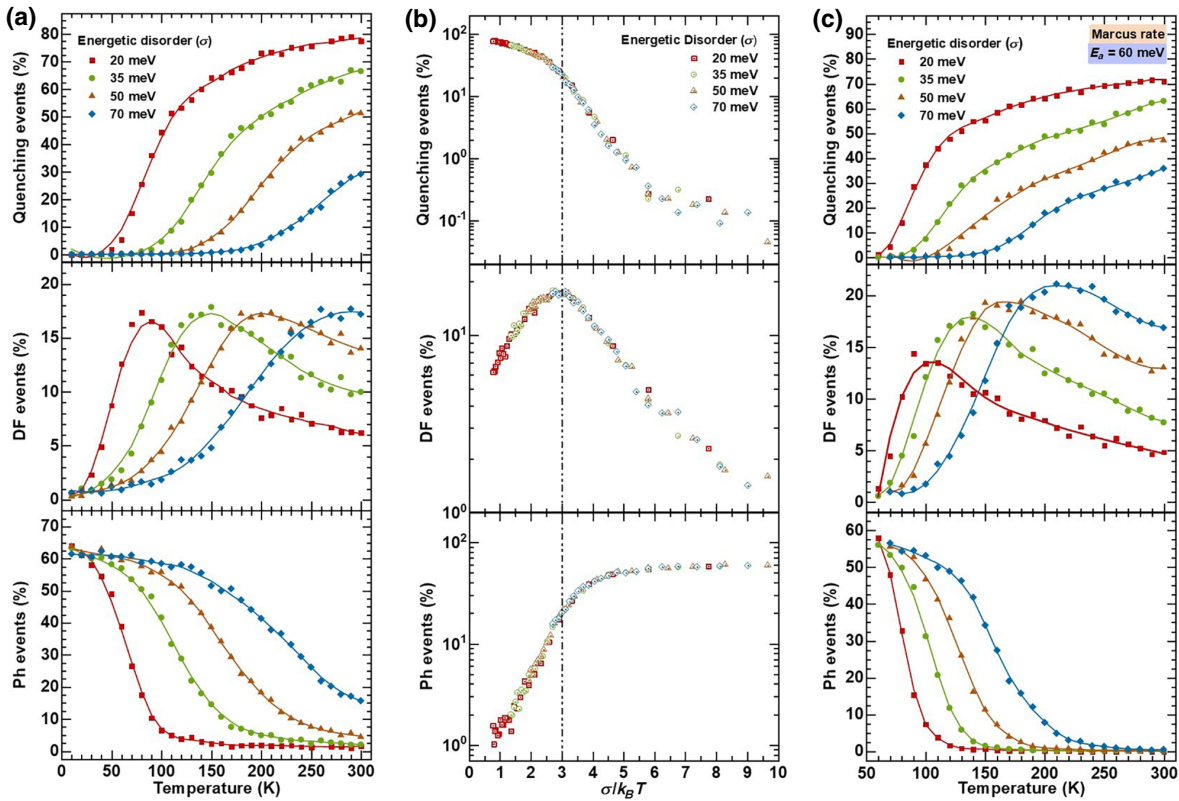
FIG. 4.   Effect of static disorder (σ) is investigated on the temperature dependence of quenching, DF, and Ph events for (a) and (b) Miller-Abrahams rate and (c) for a Marcus rate with $E_a = 60$ meV. (b) shows data in (a) represented with respect to thermal energy normalized disorder (σ) values instead of temperature on a semilog scale. A grid morphology with the length of the conjugated segment $n = 3$ and a constant coupling along and perpendicular to the chain ($\gamma_\parallel = 1.5$ nm^{-1} and $\gamma_\perp = 2$ nm^{-1}) is used. Trap concentration $c_t = 5 \times 10^{17}$ cm^{-3} is used for obtaining the simulation results. Solid lines serve as a guide to the eye.

20 to 70 meV, both TTA and quenching rates slow down and the DF peak (T_{max}) shifts to room temperature for a disorder of 70 meV, while remaining at the same value throughout. It appears that the same curves are just stretched towards higher temperature values.

In fact, for a Gaussian DOS with a MA hopping rate, there is an inherent scalability between disorder and temperature [19,39,48,49]. This is illustrated in Fig. 4(b), where the same data are displayed on a semilogarithmic scale as a function of $\sigma/k_B T$ instead of temperature. As shown, the quenching, DF, and Ph events for all the disorder values superimpose on each other for identical $\sigma/k_B T$ values. In particular, the DF events peak at around $\sigma/k_B T \approx 3$ for all the disorder values. Thus, to obtain maximum DF at room temperature (with $k_B T \approx 25$ meV), an energetic disorder of $\sigma \approx 75$ meV is required (for values of γ and trap concentration as given in the caption to Fig. 4).

F. Influence of geometric relaxation energy (λ)

The MA rate is very easy to implement in a simulation, and it is thus widely used to model excitation transport in disordered materials. However, it neglects that the transfer of an excitation from one site to another is generally associated with some change in molecular configuration. The energetic changes associated with these molecular distortions are expressed in terms of the geometric relaxation energy (λ) [50]. When λ is small compared to the site disorder parametrized through σ, the MA rate still gives a very good description [34,37]. We estimate this is often the case for charges, yet not for triplets, where geometric relaxation energies can be large compared to σ, so that they dominate the transport at room temperature [37,51]. When such electron-phonon coupling cannot be neglected, relaxation energy must also enter the expression of triplet hopping rate as an additional activation term and the transport at high temperatures can be modeled within

the Marcus formalism [35].

$$k_{ij} = \frac{J_{ij}^2}{\hbar}\sqrt{\frac{\pi}{4E_a k_B T}}\exp\left\{-\frac{(\Delta G + 4E_a)^2}{16E_a k_B T}\right\}, \quad (3)$$

where $J_{ij} = J_0 e^{-\gamma R_{ij}}$ represents the electronic coupling. J_0 is the nearest-neighbor coupling constant. E_a represents the additional activation energy due to the geometric reorganization and relates to the reorganization energy (λ) as $E_a = \lambda/4$. $\Delta G = (\varepsilon_j - \varepsilon_i)$ represents the free-energy difference between the two hopping sites and thus incorporates the effect of energetic disorder (σ).

We compare the influence of material parameters on TTA and quenching rate when the Marcus rate, Eq. (3), is used for triplet diffusion and summarize the differences as compared with the MA approach. We find that the influence of trap concentration (c_t), conjugation length (n), and anisotropy ratio ($\gamma_\parallel : \gamma_\perp$) are qualitatively and quantitatively very similar to the results obtained by using Miller-Abrahams rate, as shown in Figs. S6, S7, and S8 within the Supplemental Material [44]. A quantitative difference occurs when considering the effect of energetic disorder on the temperature dependence of quenching, DF, and Ph events in the presence of geometric reorganization [Fig. 4(c)]. The activation energy is fixed at $E_a = 60$ meV and σ is varied from 20 to 70 meV. Similar to the scenario when the MA rate is used, the relative influence of quenching compared to TTA is suppressed with increasing disorder so that the peak of the DF shifts to higher temperature. However, this peak shift is now accompanied by an increase in overall intensity for high disorder values, and a decrease for low disorder values. For σ of about 35 meV, the temperature and intensity of the DF peak are identical for the MA and the Marcus rate.

To understand the origin of this difference, we compare the effect of disorder for both the approaches (Fig. S9 within the Supplemental Material [44]). We find that the percentage of quenching events at the DF peak temperature, $T_{\max}$, is constant when MA rates are used, yet it reduces with increasing disorder when Marcus rates are used. More precisely, the quenching events in the Marcus case fall from values above the one for the MA case to values below it. The reason for this is related to the way how an additional activation energy impacts on the overall hopping rates given by Eqs. (1) and (3). For a MA rate, an increase in disorder can be compensated by an increase in temperature, so that the average hopping rate remains unchanged. For higher disorder, the DF peak occurs at correspondingly higher temperature, yet the ratio of quenching events to DF events at $T_{\max}$ remains unaffected. In contrast, in the Marcus rate, Eq. (3), a constant term is added. How this impact on the rate depends on σ relative to E_a [34,52]. A detailed analysis is complex and requires going beyond the rate equation for two individual sites, rather, the statistical mean value for the mobility

of the triplet exciton needs to be considered, as detailed in Sec. S2 within the Supplemental Material [44]. The effect is that in the Marcus case, the mobility of triplets decreases faster with temperature when the disorder is large, compared to the MA case. As a result, at higher temperatures, quenching is more suppressed than in the MA case. Less quenching implies a higher triplet concentration [T], and thus the bimolecular TTA process is favored. Overall, this shifts $T_{\max}$ to lower temperatures compared to the MA case [Fig. 4(a)] and leads to higher peak values.

While variation of the disorder has a strong impact on the fraction of TTA events that occur, changes in the geometric reorganization energy do not affect the intensity of the room-temperature DF (Fig. 5). Similar to the case of varying the off-chain coupling [Fig. 3(b)], the additional activation energy due to molecular reorganization effects only modifies the low-temperature part of the curve, while the behavior at room temperature is entirely dominated by the disorder contribution.

G. The role of disorder in the TTA process

The role of disorder is twofold. First, it changes the hopping rate, i.e., Eq. (1) or (3). Second, and perhaps less appreciated though relevant, is the fact that by changing the energy landscape, it modifies the spatial distribution of the triplet states. This is illustrated in Fig. 6 for MA rates for two cases, $\sigma/k_B T < 1$ and $\sigma/k_B T > 1$. Taking $k_B T$ at room temperature, this corresponds to σ values of 20 and 70 meV, respectively. Analogous figures for 35 and 50 meV can be found within the Supplemental Material [44] (Fig. S10). The color plot in Fig. 6 (heat map) indicates an exemplary cut through the X-Z plane. In the top panel, the color indicates the number of annihilations that occur at any lattice site in that plane. They are normalized relative to the maximum number of annihilations observed at a lattice site in that plane. In the bottom panel, any lattice sites with energies that are more than 1.5σ below the center of the DOS are indicated in red color. Grid lines are shown to ease visual comparison between the top and bottom panel. In addition, an enlarged view is shown in Fig. S11 within the Supplemental Material [44]. Evidently, there is little correlation between the fraction of TTA events in a lattice plane and the lower-energy sites when the disorder is smaller than the mean thermal energy. However, when the energetic landscape has valleys deeper than the mean available thermal energy, the TTA events are observed mostly in the energetic valleys. To allow for a more quantitative assessment, we calculate Pearson linear correlation function (ρ). Essentially, this function corresponds to the covariance of the energy of the lattice sites and the number of annihilations happening at those lattice sites within a particular plane normalized by the product of their standard deviations (for expression refer to Sec. S3 within the Supplemental Material [44]). We find $\rho = -0.12$ for a
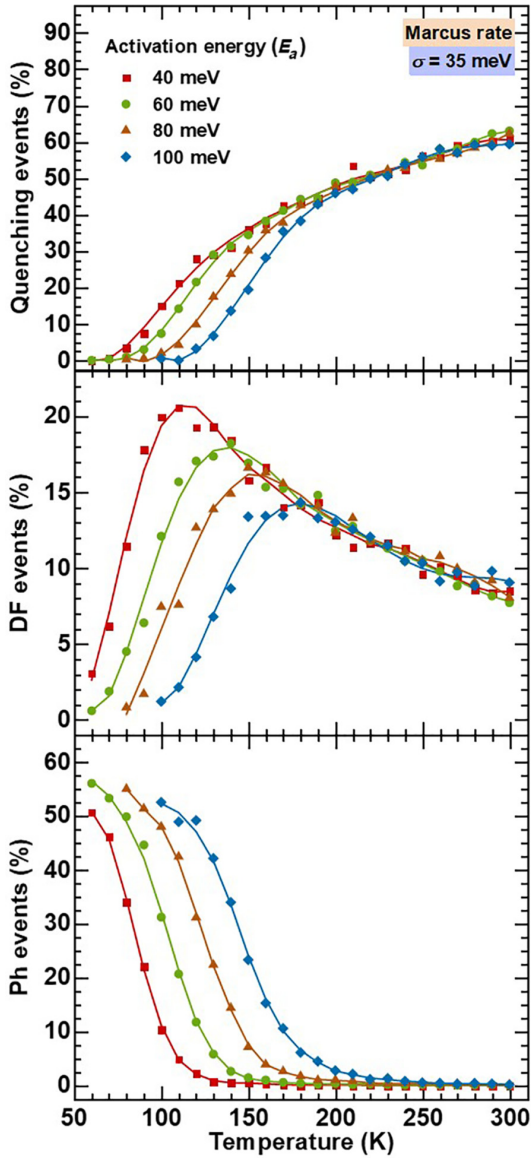
FIG. 5. Simulated dependence of quenching, DF, and Ph events with Marcus rate in the presence of both energetic disorder and reorganization induced polaronic disorder. Simulated data for energetic disorder $\sigma = 35$ meV and $E_a = 40, 60, 80$, and 100 meV. Solid lines serve as a guide to the eye.

disorder parameter of $\sigma = 20$ meV, yet $\rho = -0.21, -0.23$ and -0.22 for $\sigma = 35, 50$, and 70 meV. These ρ values are obtained by averaging over all the planes in the simulation box. It is negative because there is negative covariance (low energy implies a high number of annihilations).

This is straightforward to understand and can be explained in the framework of the transport energy developed for charge carriers [53]. For $\sigma/k_B T > 1$, the triplets relax energetically and hop predominantly through the valleys, so that a nonuniform distribution results. Such a filamentary nature of excitation transport has previously been observed for charges in disordered materials [54,55]. As the bimolecular TTA process depends quadratically on the triplet density, the TTA events also take place predominantly in the valleys. This implies a higher effective TTA rate than is expected on the basis of the spatially averaged triplet density. Evidently, a high $\sigma/k_B T$ value is required for a high TTA yield.

H. Comparison to analytical calculation

It is instructive to compare the results of the MC simulation to experimental data and to analytical calculations. In earlier work, we along with others were already able to demonstrate that kinetic MC simulations can accurately reproduce the spectral signatures of triplet diffusion in conjugated materials [1,18]. Nearly a decade ago, Hoffmann et al. published a detailed investigation of the temperature dependence of delayed fluorescence and phosphorescence for poly- and oligofluorenes [30]. As mentioned earlier, the results of our MC simulation are in very good agreement with the experimental data by Hoffmann et al. In this work, Hoffmann et al. also formulated an analytical theory for the limit of low excitation density that could describe the experimental results, albeit only when the conjugation length was not too long. Here we extend the approach by Hoffmann et al. to apply to any excitation density and compare the analytical result to our KMC data.

Bimolecular recombination with an annihilation rate constant γ_{TTA} (not to be confused with the symbol for inverse conjugation length) gives rise to DF with an intensity

$$I_{\text{DF}} = c\gamma_{\text{TTA}}[T]^2, \quad (4)$$

where c is a constant equal to the fraction of triplet-triplet encounters that generate a singlet state times the rate constant for the radiative singlet decay. $[T]$ denotes the concentration of triplet excitons. Under steady-state conditions

$$\frac{d[T]}{dt} = 0 = G - (k_R + k_{NR} + k_Q)[T] - \gamma_{\text{TTA}}[T]^2, \quad (5)$$

where G is the formation rate of triplet excitons, k_R and k_{NR} are radiative and nonradiative decay rates, and k_Q is the monomolecular quenching rate. Solving the quadratic Eq. (5) for triplet exciton concentration and neglecting the negative solution for $[T]$ yields

$$[T] = \frac{-(k_R + k_{NR} + k_Q) + \sqrt{(k_R + k_{NR} + k_Q)^2 + 4\gamma_{\text{TTA}}G}}{2\gamma_{\text{TTA}}}.$$
$$(6)$$

154

(a)

(b)
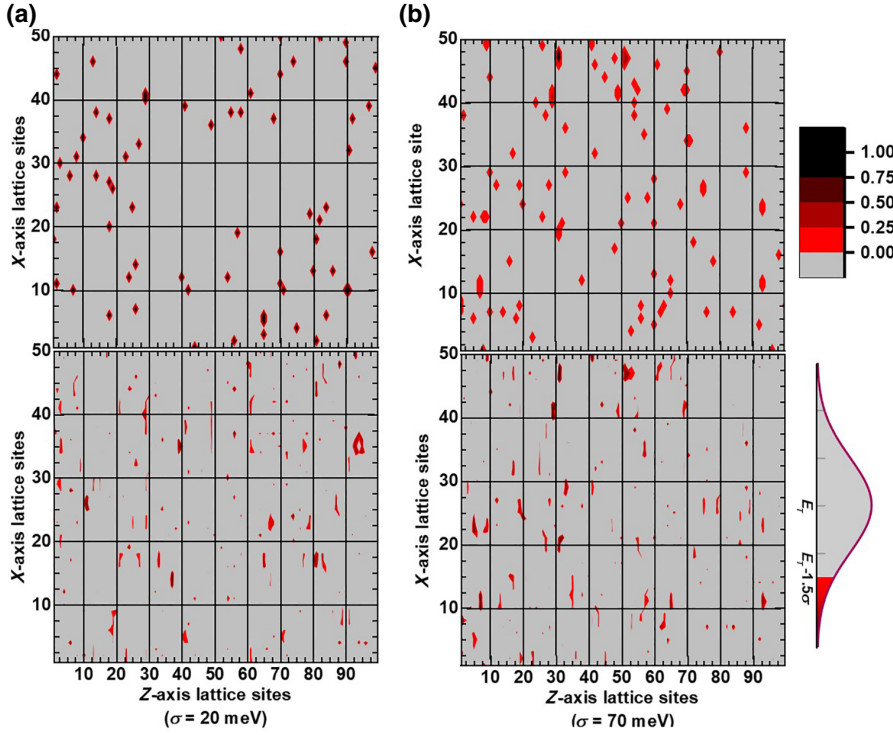
FIG. 6. Color maps showing (top panels) the relative number of annihilations per lattice site in the X-Z plane (with gray indicating zero annihilations and black implying the maximum number of annihilation events found in that plane at a site), and (bottom panels) the triplet state energies for each site in that plane. Sites with energies below 1.5σ of the mean triplet energy (E_T) are colored in red. This is shown for 300 K for (a) $\sigma = 20$ meV (i.e., $\sigma/k_BT < 1$) and (b) $\sigma = 70$ meV (i.e., $\sigma/k_BT > 1$).

The condition to derive $T_{\max}$, the temperature at which DF exhibits a maximum.

$$\frac{\partial I_{\mathrm{DF}}}{\partial T} = 0. \tag{7}$$

To carry out the derivative, we need to assume a temperature dependence for the different parameters involved. We take G, k_{R}, and k_{NR} to be independent of temperature in agreement with usual experimental findings, while we consider k_Q and γ_{TTA} to vary with temperature. For simplicity, we assume an Arrheniuslike temperature dependence of k_Q and γ_{TTA} with constant activation energy E_{act}, viz.

$$k_Q = k_{Q0} + k_{Q1} \exp\left(\frac{-E_{\mathrm{act}}}{k_BT}\right), \tag{8}$$

$$\gamma_{\mathrm{TTA}} = \gamma_0 + \gamma_1 \exp\left(\frac{-E_{\mathrm{act}}}{k_BT}\right). \tag{9}$$

Inserting Eqs. (8) and (9) into Eq. (6), Eq. (6) in Eq. (4) and then using I_{DF} from Eq. (4) into Eq. (7) and solving it, we obtain

$$T_{\max,1} = \frac{E_{\mathrm{act}}}{k_B} \left\{ \ln\left[\frac{\gamma_1 k_{Q1}}{\gamma_1 (k_{\mathrm{R}} + k_{\mathrm{NR}} + k_{Q0}) - 2k_{Q1}\gamma_0}\right] \right\}^{-1}, \tag{10}$$

$$T_{\max,2} = \frac{E_{\mathrm{act}}}{k_B} \left[\ln\left(\frac{-\gamma_1}{\gamma_0}\right) \right]^{-1}. \tag{11}$$

In Eq. (9) γ_0 and $\gamma_1 > 0$, so that $T_{\max,2}$ is not a proper solution in this context. Thus $T_{\max} = T_{\max,1}$. This is, exactly the same expression that was obtained by Hoffmann *et al.* in the limit of low exciton concentration by neglecting the quadratic triplet-triplet annihilation term in Eq. (5). As shown by Hoffmann for the low-intensity case, a similar expression results when the argument (E_{act}/k_BT) in the exponential of Eqs. (5) and (6) is replaced by $(\sigma/k_BT)^2$, that is

$$T_{\max,1} = \frac{\sigma}{k_B} \left\{ \ln\left[\frac{\gamma_1 k_{Q1}}{\gamma_1 (k_{\mathrm{R}} + k_{\mathrm{NR}} + k_{Q0}) - 2k_{Q1}\gamma_0}\right] \right\}^{-1/2}. \tag{12}$$

Equations (10) and (12) reflect the dependence of $T_{\max}$ on key parameters such as the sample purity and on the energetic disorder. The central observation is, however, that $T_{\max}$ does not contain any dependence on the generation rate G. This is at variance with the simulation results (cf. Fig. 1 and S4) as well as with the experimental observations. Both indicate a dependence of DF peak position on the excitation intensity. Thus, we reach the conclusion that the constants k_{Q0}, k_{Q1}, γ_0, and γ_1 as described in Eqs. (8) and (9) must, in some way, be dependent on the generation intensity.

This information is key and needs to be included to correctly predict the dependence of DF on the excitation intensity. In contrast to analytical calculations, MC simulations inherently consider the excitation intensity dependence of different emissive processes and exciton-loss processes. In addition, any time dependence of the diffusion and annihilation processes is inherently included, while analytical calculations (described above) represent the steady-state condition [56]. The energetic relaxation and subsequent diffusion of excitations into the valleys of the energy landscape is well known [54,57]. This enhances the local triplet density there over the average value. We consider this nonuniform triplet density to be the reason for the dependence of the above constants on the generation rate G. [Comparison to the MC simulations in Figs. 3 and 4 with Eq. (10) further show that the dependence of $T_{\max}$ on conjugation length and transport anisotropy is also not captured by Eq. (10), unless the impact of conjugation length and transport anisotropy on the constants k_{Q0}, k_{Q1}, γ_0 and γ_1 are explicitly taken into account. This is, though, of lesser relevance since this dependence is comparatively weak, as evident in Figs. 3 and 4.]

IV. CONCLUDING DISCUSSION

One of the advantages of kinetic MC simulations is that it allows to decouple the effects caused from different material parameters by systematically varying only one of them. In this way, our study allowed us to identify and highlight the strong role of detrimental triplet quenching by impurities. Further, we find that the film morphology plays a key role in determining the relative extent of bimolecular and monomolecular recombination. A morphology of mostly parallel chains, conducive for directional transport, favors quenching at the trap sites whereas a gridlike morphology of many crossing chains that allows for more isotropic hopping enhances the fraction of TTA events. Our study of delocalization effects suggests that increasing the length of conjugated segments improves DF by raising the number of readily accessible crossing points to other chains, thus increasing the isotropy of transport.

The role of energetic disorder is twofold. First, an increased disorder reduces the triplet diffusivity [19,39, 48]. A high diffusivity enables triplet motion to impurity sites where their concentration is reduced. Since TTA depends quadratically on the triplet concentration, the fraction of TTA events eventually reduces. Thus, a moderately low triplet diffusivity is desirable. In fact, in our earlier study we found that the reason why the number of TTA events peaks at a certain temperature is simply that the temperature activated diffusivity becomes too high [30]. This is consistent with the results of Blom and co-workers on singlet diffusion in poly-(p-phenylene vinylene) (PPV) derivatives [58]. They found that the more disordered super-yellow-PPV had a lower diffusivity at

room temperature and thus a longer exciton lifetime. This gives rise to a higher photoluminescence quantum yield due to the slower exciton diffusion towards quenching sites [59].

The second role of energetic disorder, however, is that it causes filamentary transport, thus enhancing the probability of two triplets to encounter each other rather than an impurity. A key result of our study is that energetic disorder is crucial for obtaining a high yield of TTA events at room temperature. For typical values of the remaining parameters, a disorder in the order of $\sigma/k_B T \approx 3$ is required to obtain a DF peak at room temperature. Using values such as $\sigma \approx 70$ meV, a trap concentration of approximately 10^{17} cm^{-3}, $\gamma_\parallel = 0.5$ nm^{-1}, $\gamma_\perp = 2$ nm^{-1} and a conjugation length of 20 repeat units, we obtain a yield of TTA events of 140%, i.e., about 30% DF events for an excitation intensity of 5×10^{16} cm^{-3} (Fig. S12 within the Supplemental Material [44]). We note that the yield of TTA events exceeds 100% of the initial number of triplets present. This is because through the spin statistics, we consider secondary processes, i.e., that two triplets may collide to form one TTA event, then separate (e.g., because they formed a quintet state), and collide again with a certain probability.

We finally address the question of modeling excitation transport via the energetic-disorder-controlled Miller-Abrahams or polaronic-activation-controlled Marcus approach, which has always been a topic of debate in the community [60]. Coehoorn and co-workers have been able to successfully model charge transport and exciton dynamics in OLEDs by simply incorporating the Miller-Abrahams transport rates [1,32,40–42]. The recent full quantum treatment of charge-carrier dynamics in amorphous organic semiconductors indeed confirms that the MA approach captures the salient features of transport, albeit at low temperatures [61]. In our earlier studies we observed that the reorganization energy can have a substantial influence on the rates for triplet processes, notably at higher temperatures (>100 K), which requires the use of the Marcus rate to describe the hopping process [18]. Therefore, we use the MA approach to first address the current problem and subsequently only highlighted the key differences that can be expected if the reorganization energy effects are explicitly considered in these energetically disordered materials. We observe that delocalization effects and the effects due to trap concentration do not change. Disorder effects are also more or less similar except for an increase in DF intensity for higher energetic disorders. Decreased reorganization energy increases the DF at low temperatures but does not have any effect on room-temperature DF. We attribute the comparatively low sensitivity of the result to the specific hopping rate chosen to the fact that this study is concerned with determining yields for triplet processes rather than rates.

156

In brief, we develop a kinetic Monte Carlo study that describes how TTA, triplet quenching and phosphorescence evolve as a function of temperature when a wide range of experimental and material parameters are varied. Our results are qualitatively consistent over a whole range of parameters with the experiments performed on a series of poly(p-polyfluorenes), confirming the suitability of the model [33]. We find that the choice of hopping rate is not critical when considering the yield of TTA events, and that analytical studies need to include the intensity and time dependence of quenching and annihilation constants to come to a description that reflects experiments. Optimizing the TTA process, and concomitantly the yield of DF, to peak at room temperature is possible. It requires (i) a high disorder and therefore dispersive transport (in the range of $\sigma/k_B T \approx 3$), (ii) a high sample purity (about 10^{17} quenching sites per cm^3), and (iii) a morphology and conjugation length with many contact points that enables isotropic hopping.

[1] H. van Eersel, P. A. Bobbert, and R. Coehoorn, Kinetic Monte Carlo study of triplet-triplet annihilation in organic phosphorescent emitters, J. Appl. Phys. **117,** 115502 (2015).

[2] C. Gärtner, C. Karnutsch, U. Lemmer, and C. Pflumm, The influence of annihilation processes on the threshold current density of organic laser diodes, J. Appl. Phys. **101,** 023107 (2007).

[3] A. Monguzzi and J. Pedrini, Recent advances in the application triplet–triplet annihilation-based photon upconversion systems to solar technologies, J. Photonics Energy **8,** 1 (2017).

[4] D. W. Gehrig, I. A. Howard, and F. Laquai, Charge carrier generation followed by triplet state formation, annihilation, and carrier recreation in PBDTTT-C/PC60BM photovoltaic blends, J. Phys. Chem. C **119,** 13509 (2015).

[5] P. C. Chow, S. Gelinas, A. Rao, and R. H. Friend, Quantitative bimolecular recombination in organic photovoltaics

[6] through triplet exciton formation, J. Am. Chem. Soc. **136,** 3424 (2014).

[6] S. Baluschev, T. Miteva, V. Yakutkin, G. Nelles, A. Yasuda, and G. Wegner, Up-conversion Fluorescence: Noncoherent Excitation by Sunlight, Phys. Rev. Lett. **97,** 143903 (2006).

[7] F. Laquai, G. Wegner, C. Im, A. Busing, and S. Heun, Efficient upconversion fluorescence in a blue-emitting spirobifluorene-anthracene copolymer doped with low concentrations of Pt(II)octaethylporphyrin, J. Chem. Phys. **123,** 074902 (2005).

[8] V. Gray, D. Dzebo, M. Abrahamsson, B. Albinsson, and K. Moth-Poulsen, Triplet-triplet annihilation photon-upconversion: Towards solar energy applications, Phys. Chem. Chem. Phys. **16,** 10345 (2014).

[9] N. Nishimura, V. Gray, J. R. Allardice, Z. Zhang, A. Pershin, D. Beljonne, and A. Rao, Photon upconversion from near-infrared to blue light with TIPS-anthracene as an efficient triplet–triplet annihilator, ACS Mater. Lett. **1,** 660 (2019).

[10] T. F. Schulze and T. W. Schmidt, Photochemical upconversion: Present status and prospects for its application to solar energy conversion, Energy Environ. Sci. **8,** 103 (2015).

[11] B. D. Ravetz, A. B. Pun, E. M. Churchill, D. N. Congreve, T. Rovis, and L. M. Campos, Photoredox catalysis using infrared light via triplet fusion upconversion, Nature **565,** 343 (2019).

[12] M. P. Rauch and R. R. Knowles, Applications and prospects for triplet-triplet annihilation photon upconversion, Chimia **72,** 501 (2018).

[13] S. H. Askes, A. Bahreman, and S. Bonnet, Activation of a photodissociative ruthenium complex by triplet-triplet annihilation upconversion in liposomes, Angew. Chem. Int. Ed. **53,** 1029 (2014).

[14] Y. Sasaki, S. Amemori, H. Kouno, N. Yanai, and N. Kimizuka, Near infrared-to-blue photon upconversion by exploiting direct S–T absorption of a molecular sensitizer, J. Mater. Chem. C **5,** 5063 (2017).

[15] M. Lebental, H. Choukri, S. Chénais, S. Forget, A. Siove, B. Geffroy, and E. Tutiš, Diffusion of triplet excitons in an operational organic light-emitting diode, Phys. Rev. B. **79,** 165318 (2009).

[16] S. A. Bagnich and H. Bässler, Origin of delayed fluorescence of a ladder-type methyl-poly(para-phenylene) doped with Pt(II)octaethylporphyrin, Chem. Phys. Lett. **381,** 464 (2003).

[17] Y. Zhang and S. R. Forrest, Triplet diffusion leads to triplet–triplet annihilation in organic phosphorescent emitters, Chem. Phys. Lett. **590,** 106 (2013).

[18] S. T. Hoffmann, S. Athanasopoulos, D. Beljonne, H. Bässler, and A. Köhler, How do triplets and charges move in disordered organic semiconductors? A Monte Carlo study comprising the equilibrium and nonequilibrium regime, J. Phys. Chem. C **116,** 16371 (2012).

[19] H. Bässler, Charge transport in disordered organic photoconductors a Monte Carlo simulation study, Phys. Status Solidi B **175,** 15 (1993).

[20] A. Köhler and H. Bässler, Triplet states in organic semiconductors, Mater. Sci. Eng., R **66,** 71 (2009).

[21] K. Masui, H. Nakanotani, and C. Adachi, Analysis of exciton annihilation in high-efficiency sky-blue organic

light-emitting diodes with thermally activated delayed fluorescence, Org. Electron. **14,** 2721 (2013).

[22] J. Popp, W. Kaiser, and A. Gagliardi, Impact of phosphorescent sensitizers and morphology on the photovoltaic performance in organic solar cells, Adv. Theor. Simul. **2,** 1800114 (2019).

[23] C. Adachi and S. R. Forrest, Transient analysis of organic electrophosphorescence. II. Transient analysis of triplet-triplet annihilation, Phys. Rev. B. **62,** 10967 (2000).

[24] N. C. Giebink and S. R. Forrest, Quantum efficiency roll-off at high brightness in fluorescent and phosphorescent organic light emitting diodes, Phys. Rev. B. **77,** 235215 (2008).

[25] S. Reineke, K. Walzer, and K. Leo, Triplet-exciton quenching in organic phosphorescent light-emitting diodes with Ir-based emitters, Phys. Rev. B. **75,** 125328 (2007).

[26] F. X. Zang, T. C. Sum, A. C. H. Huan, T. L. Li, W. L. Li, and F. Zhu, Reduced efficiency roll-off in phosphorescent organic light emitting diodes at ultrahigh current densities by suppression of triplet-polaron quenching, Appl. Phys. Lett. **93,** 023309 (2008).

[27] S. M. Suresh, E. Duda, D. Hall, Z. Yao, S. Bagnich, A. M. Z. Slawin, H. Bassler, D. Beljonne, M. Buck, Y. Olivier, et al., A deep blue B,N-doped heptacene emitter that shows both thermally activated delayed fluorescence and delayed fluorescence by triplet-triplet annihilation, J. Am. Chem. Soc. **142,** 6588 (2020).

[28] P. Y. Chou, H. H. Chou, Y. H. Chen, T. H. Su, C. Y. Liao, H. W. Lin, W. C. Lin, H. Y. Yen, I. C. Chen, and C. H. Cheng, Efficient delayed fluorescence via triplet-triplet annihilation for deep-blue electroluminescence, Chem. Commun. **50,** 6869 (2014).

[29] F. B. Dias, Kinetics of thermal-assisted delayed fluorescence in blue organic emitters with large singlet-triplet energy gap, Philos. Trans. R. Soc. London, Ser. A **373,** 20140447 (2015).

[30] S. T. Hoffmann, J. M. Koenen, U. Scherf, I. Bauer, P. Strohriegl, H. Bassler, and A. Kohler, Triplet-triplet annihilation in a series of poly(p-phenylene) derivatives, J. Phys. Chem. B **115,** 8417 (2011).

[31] H. Goudarzi and P. E. Keivanidis, Triplet–triplet annihilation-induced up-converted delayed luminescence in solid-state organic composites: Monitoring low-energy photon up-conversion at low temperatures, J. Phys. Chem. C **118,** 14256 (2014).

[32] A. Ligthart, X. de Vries, L. Zhang, M. C. W. M. Pols, P. A. Bobbert, H. van Eersel, and R. Coehoorn, Effect of triplet confinement on triplet-triplet annihilation in organic phosphorescent host-guest systems, Adv. Funct. Mater. **28,** 1804618 (2018).

[33] S. Athanasopoulos, S. T. Hoffmann, H. Bassler, A. Kohler, and D. Beljonne, To hop or not to hop? understanding the temperature dependence of spectral diffusion in organic semiconductors, J. Phys. Chem. Lett. **4,** 1694 (2013).

[34] I. I. Fishchuk, A. Kadashchuk, S. T. Hoffmann, S. Athanasopoulos, J. Genoe, H. Bässler, and A. Köhler, Unified description for hopping transport in organic semiconductors including both energetic disorder and polaronic contributions, Phys. Rev. B. **88,** 125202 (2013).

[35] R. A. Marcus, Electron transfer reactions in chemistry. Theory and experiment, Rev. Mod. Phys. **65,** 599 (1993).

[36] A. Miller and E. Abrahams, Impurity conduction at low concentrations, Physical Review **120,** 745 (1960).

[37] A. Köhler and H. Bässler, What controls triplet exciton transfer in organic semiconductors?, J. Mater. Chem. **21,** 4003 (2011).

[38] S. Athanasopoulos, E. Emelianova, A. B. Walker, and D. Beljonne, Modelling exciton diffusion in disordered conjugated polymers, Proc. SPIE **7722,** 772214 (2010).

[39] S. Athanasopoulos, E. V. Emelianova, A. B. Walker, and D. Beljonne, Exciton diffusion in energetically disordered organic materials, Phys. Rev. B. **80,** 195209 (2009).

[40] L. Zhang, H. van Eersel, P. A. Bobbert, and R. Coehoorn, Analysis of the phosphorescent dye concentration dependence of triplet-triplet annihilation in organic host-guest systems, Chem. Phys. Lett. **662,** 221 (2016).

[41] L. Zhang, H. van Eersel, P. A. Bobbert, and R. Coehoorn, Clarifying the mechanism of triplet–triplet annihilation in phosphorescent organic host–guest systems: A combined experimental and simulation study, Chem. Phys. Lett. **652,** 142 (2016).

[42] R. Coehoorn, P. A. Bobbert, and H. van Eersel, Effect of exciton diffusion on the triplet-triplet annihilation rate in organic semiconductor host-guest systems, Phys. Rev. B. **99,** 024201 (2019).

[43] X. de Vries, P. Friederich, W. Wenzel, R. Coehoorn, and P. A. Bobbert, Triplet exciton diffusion in metalorganic phosphorescent host-guest systems from first principles, Phys. Rev. B. **99,** 205201 (2019).

[44] See Supplemental Material at http://link.aps.org/supplemental/10.1103/PhysRevApplied.14.034050 for additional simulation results, description of the effect of disorder on MA, and Marcus rates and expression of Pearson correlation function.

[45] S. Athanasopoulos, E. Hennebicq, D. Beljonne, and A. B. Walker, Trap limited exciton transport conjugated polymers, J. Phys. Chem. C **112,** 11532 (2008).

[46] P. Kordt, J. J. van der Holst, M. Al Helwi, W. Kowalsky, F. May, A. Badinski, C. Lennartz, and D. Andrienko, Modeling of organic light emitting diodes: From molecular to device properties, Adv. Funct. Mater. **25,** 1955 (2015).

[47] H. T. Nicolai, M. Kuik, G. A. Wetzelaer, B. de Boer, C. Campbell, C. Risko, J. L. Bredas, and P. W. Blom, Unification of trap-limited electron transport in semiconducting polymers, Nat. Mater. **11,** 882 (2012).

[48] B. Movaghar, M. Grunewald, B. Ries, H. Bassler, and D. Wurtz, Diffusion and relaxation of energy in disordered organic and inorganic materials, Phys. Rev. B: Condens. Matter **33,** 5545 (1986).

[49] M. Ansari-Rad and S. Athanasopoulos, Theoretical study of equilibrium and nonequilibrium exciton dynamics in disordered semiconductors, Phys. Rev. B. **98,** 085204 (2018).

[50] I. I. Fishchuk, A. Kadashchuk, L. Sudha Devi, P. Heremans, H. Bässler, and A. Köhler, Triplet energy transfer in conjugated polymers. II. A polaron theory description addressing the influence of disorder, Phys. Rev. B. **78,** 045211 (2008).

[51] L. Grisanti, Y. Olivier, L. Wang, S. Athanasopoulos, J. Cornil, and D. Beljonne, Roles of local and nonlocal

158

electron-phonon couplings in triplet exciton diffusion in the anthracene crystal, Phys. Rev. B. **88,** 035450 (2013).

[52] I. I. Fishchuk, A. Kadashchuk, S. T. Hoffmann, S. Athanasopoulos, J. Genoe, H. Bässler, and A. Köhler, Analytic model of hopping transport in organic semiconductors including both energetic disorder and polaronic contributions, AIP Conf. Proc. **1610,** 47 (2014).

[53] V. Arkhipov, E. Emelianova, G. Adriaenssens, and H. Bässler, Equilibrium carrier mobility in disordered organic semiconductors, J. Non-Cryst. Solids **299,** 1047 (2002).

[54] J. J. M. van der Holst, M. A. Uijttewaal, B. Ramachandhran, R. Coehoorn, P. A. Bobbert, G. A. de Wijs, and R. A. de Groot, Modeling and analysis of the three-dimensional current density in sandwich-type single-carrier devices of disordered organic semiconductors, Phys. Rev. B. **79,** 085203 (2009).

[55] Y. Shen and N. C. Giebink, Monte Carlo Simulations of Nanoscale Electrical Inhomogeneity in Organic Light-Emitting Diodes and its Impact on Their Efficiency and Lifetime, Phys. Rev. Appl. **4,** 054017 (2015).

[56] D. T. Gillespie, A general method for numerically simulating the stochastic time evolution of coupled chemical reactions, J. Comput. Phys. **22,** 403 (1976).

[57] R. Coehoorn and P. A. Bobbert, Effects of Gaussian disorder on charge carrier transport and recombination in organic semiconductors, Phys. Status Solidi A **209,** 2354 (2012).

[58] I. Rörich, A.-K. Schönbein, D. K. Mangalore, A. Halda Ribeiro, C. Kasparek, C. Bauer, N. I. Crǎciun, P. W. M. Blom, and C. Ramanan, Temperature dependence of the photo- and electroluminescence of poly(p-phenylene vinylene) based polymers, J. Mater. Chem. C **6,** 10569 (2018).

[59] I. Rorich, O. V. Mikhnenko, D. Gehrig, P. W. Blom, and N. I. Craciun, Influence of energetic disorder on exciton lifetime and photoluminescence efficiency in conjugated polymers, J. Phys. Chem. B **121,** 1405 (2017).

[60] S. T. Hoffmann, E. Scheler, J.-M. Koenen, M. Forster, U. Scherf, P. Strohriegl, H. Bässler, and A. Köhler, Triplet energy transfer in conjugated polymers. III. An experimental assessment regarding the influence of disorder on polaronic transport, Phys. Rev. B. **81,** 165208 (2010).

[61] X. de Vries, P. Friederich, W. Wenzel, R. Coehoorn, and P. A. Bobbert, Full quantum treatment of charge dynamics in amorphous molecular semiconductors, Phys. Rev. B. **97,** 075203 (2018).

A kinetic Monte Carlo study of triplet-triplet annihilation in conjugated luminescent materials

(Supplemental Material)

Rishabh Saxena[1], Tobias Meier,[1] Stavros Athanasopoulos,[2] Heinz Bässler[3], Anna Köhler[1,3*]

[1] Soft Matter Optoelectronics and Bavarian Polymer Institute (BPS), University of Bayreuth, Universitätsstr. 30, 95440 Bayreuth, Germany

[2] Departamento de Física, Universidad Carlos III de Madrid, Avenida Universidad 30, 28911 Leganés, Madrid, Spain

[3] Bayreuth Institute of Macromolecular Research (BIMF), University of Bayreuth, Universitätsstr. 30, 95440 Bayreuth, Germany

* e-mail: anna.koehler@uni-bayreuth.de
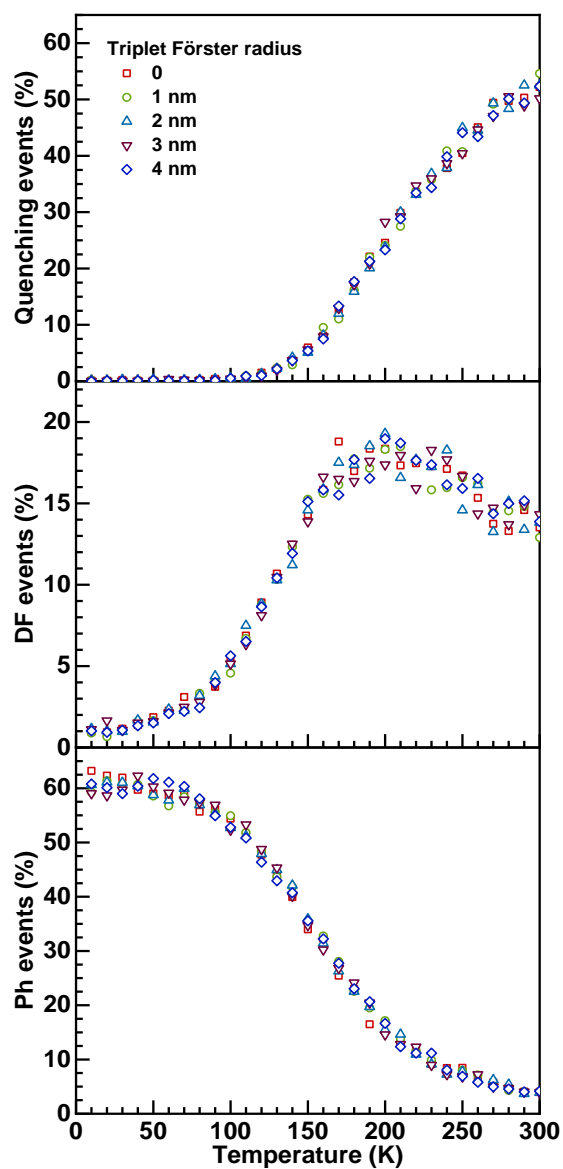
Figure S1: Systematic study of increasing Förster contribution to triplet diffusion rate represented in terms of the triplet Förster radius.
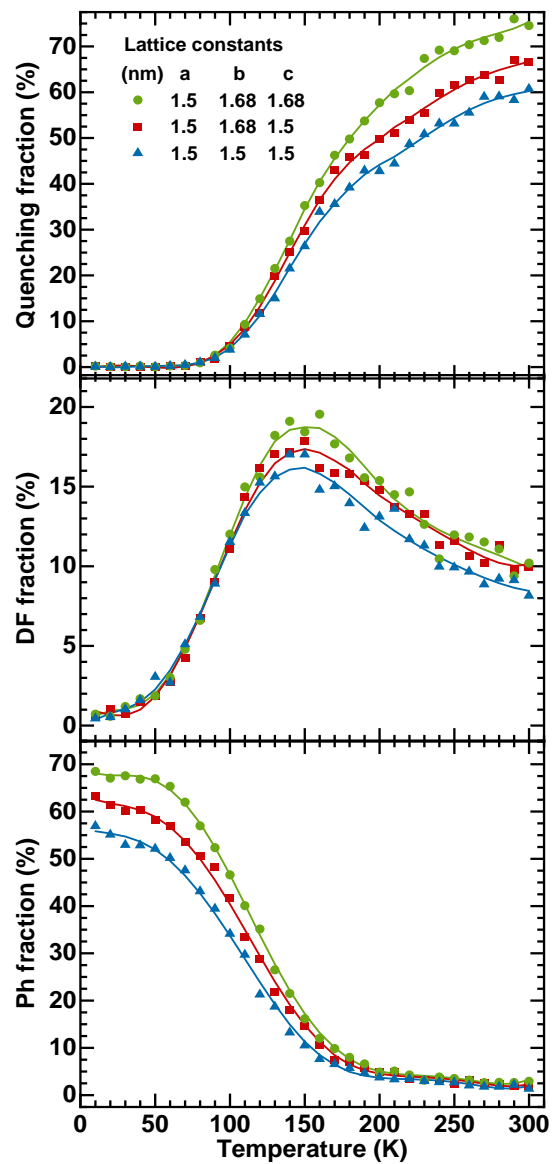
Figure S2: The effect of deviating from a perfectly isotropic lattice (lattice constant 1.5 nm) to an anisotropic lattice.

Section S1- Technical detail:

The number of necessary trials is determined by considering the noise level. Because of the energetic disorder, a proper statistics can only be obtained if the results are averaged over the trajectory of several thousand of excitons traversing different disordered landscapes. Generally, anything above 1000 excitons is sufficient to produce good statistically averaged results; we have considered this number to be around 5000 for the present study. Thus, the 'sufficient number of trials' required to obtain a good statistics depends on the initial triplet density. For example, for 100 excitons in the simulation box, corresponding to an initial triplet density of around 10^{17} cm^{-3}, we have used 50 trials; for 50 excitons at $t = 0$ we have used 100 trials and so on.
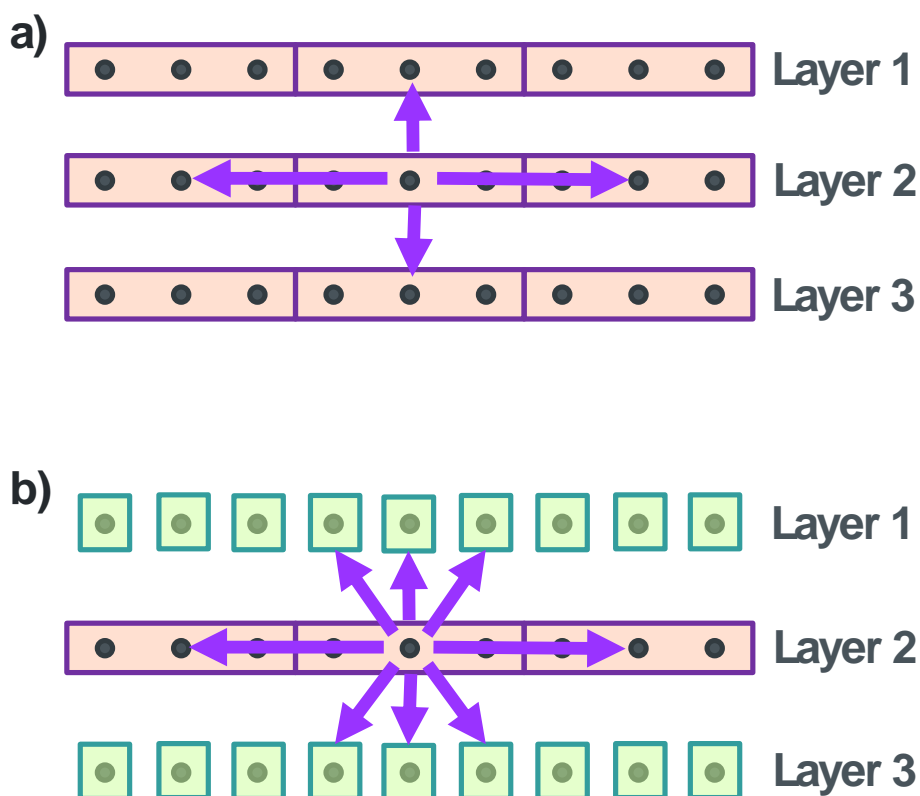
Figure S3: The side view for a) parallel chain lattice (Fig. 1c) and b) grid chain lattice (Fig. 1d) of the manuscript for the case of a polymer chain with conjugation length 3. We recall that within each conjugated segment, the lattice points have the same energy implying that hops within a conjugated segment are very fast. We have therefore indicated possible hops to nearest neighbors only from the center point of each conjugated segment. It is evident that the lattice grid, in the 2D YZ-plane, has only 4 nearest neighbors (i.e. sites with different energies) to which hops are possible. In contrast, for the grid lattice, 8 nearest neighbors with different energies are accessible within the YZ plane. This then multiplies when considering the full 3D arrangement.
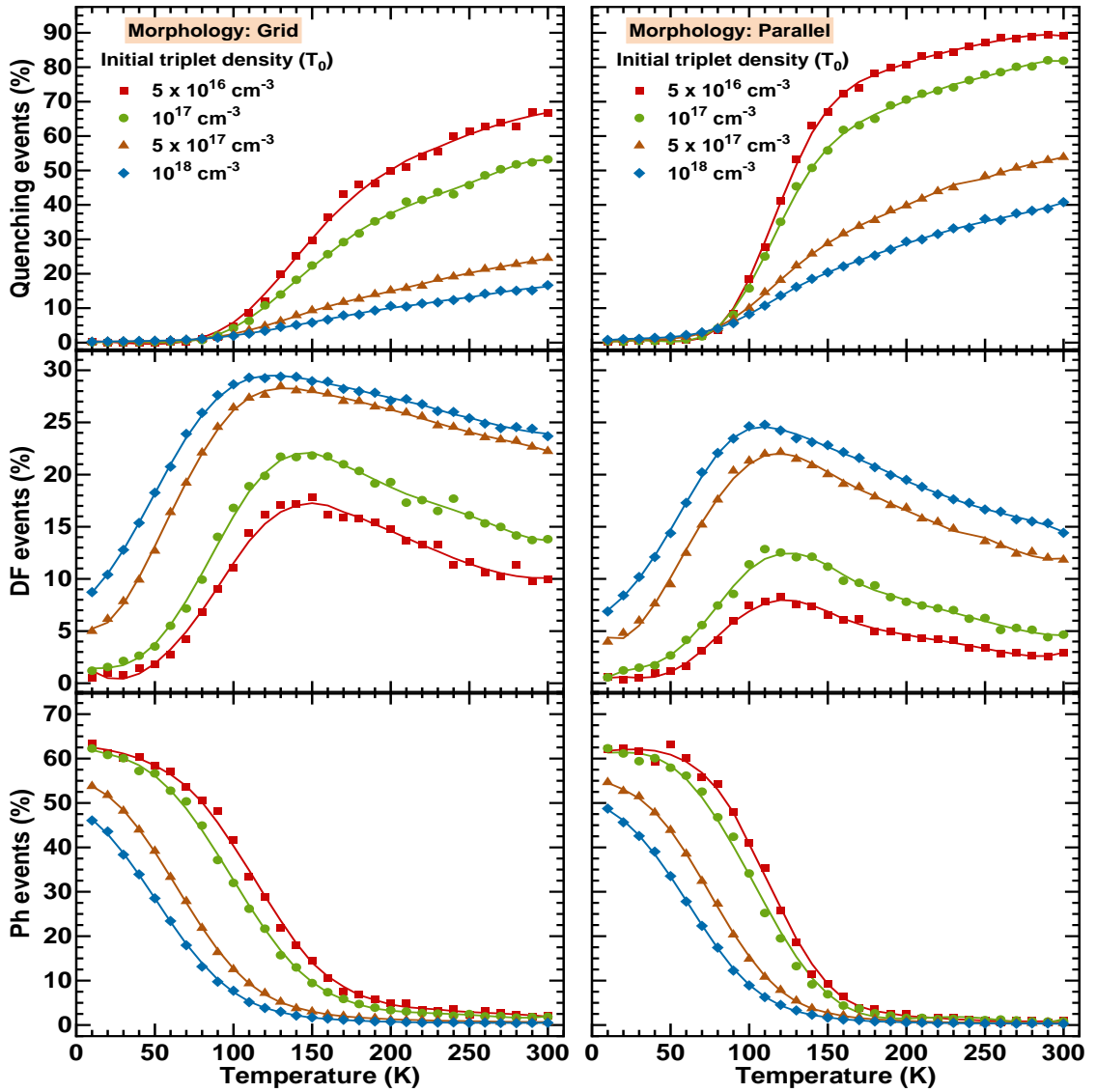
Figure S4: Influence of initial triplet density (T_0) is studied by simulating the number of quenching, DF and Ph events for grid (left panel) and parallel (right panel) lattice with $\gamma_{\parallel} = 1.5$ nm^{-1} and $\gamma_{\perp} = 2$ nm^{-1}. Data for $T_0 = 5 \times 10^{16}$ cm^{-3} (red squares), $T_0 = 10^{17}$ cm^{-3} (green circles), $T_0 = 5 \times 10^{17}$ cm^{-3} (brown triangles) and $T_0 = 10^{18}$ cm^{-3} (blue diamonds). The results are obtained with a constant length of the conjugated segment, $n = 3$, trap concentration $c_t = 5 \times 10^{17}$ cm^{-3} and energetic disorder $\sigma = 35$ meV. Solid lines serve as a guide-to-the-eye.
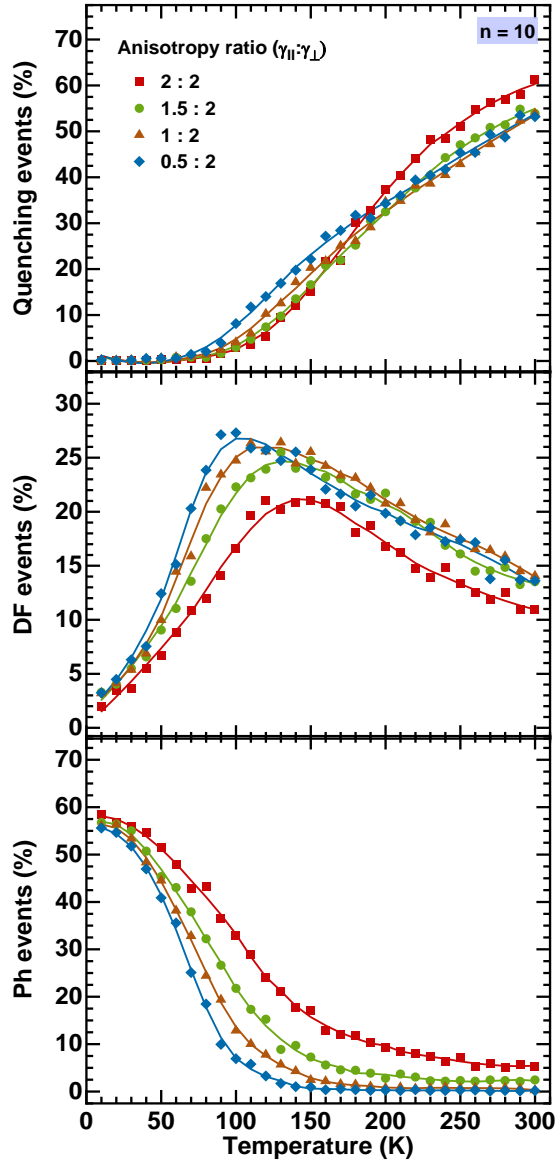
Figure S5: Influence of delocalization is studied by simulating the number of quenching, DF and Ph events for a fixed n (n = 10) by varying the anisotropy of coupling with a constant perpendicular to the chain inverse localization length of $\gamma_\perp = 1.5$ nm^{-1} and varying the one parallel to the chain ($\gamma_\parallel$) from 2 to 0.5 nm^{-1}, thus increasing the interchain hopping transport. The results are obtained with a constant trap concentration $c_t = 5 \times 10^{17}$ cm^{-3} and energetic disorder $\sigma = 35$ meV. Solid lines serve as a guide-to-the-eye.
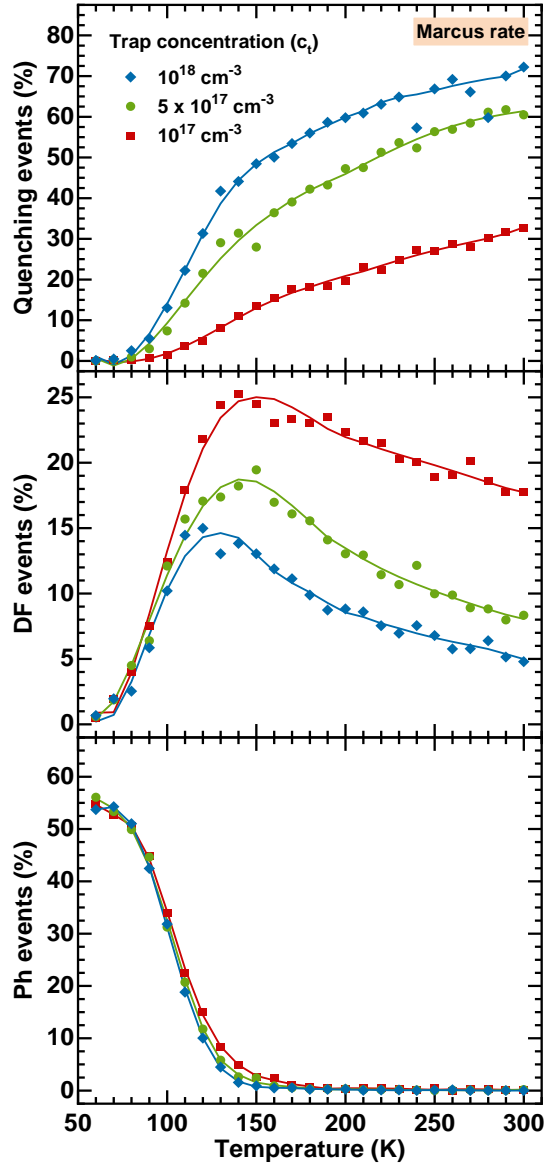
Figure S6: Effect of trap concentration (c_t) on the temperature dependence of quenching, DF and Ph events is investigated using **Marcus rate** for triplet hopping. Data for $c_t = 10^{17}$ cm^{-3} (red squares), $c_t = 5 \times 10^{17}$ cm^{-3} (green circles) and $c_t = 10^{18}$ cm^{-3} (blue diamonds). Grid lattice morphology with the length of the conjugated segment $n = 3$ and a constant coupling along and perpendicular to the chain ($\gamma_{\parallel} = 1.5$ nm^{-1} and $\gamma_{\perp} = 2$ nm^{-1}) is used. A disorder of $\sigma = 35$ meV is used for the triplet energy distribution. Solid lines serve as a guide-to-the-eye.
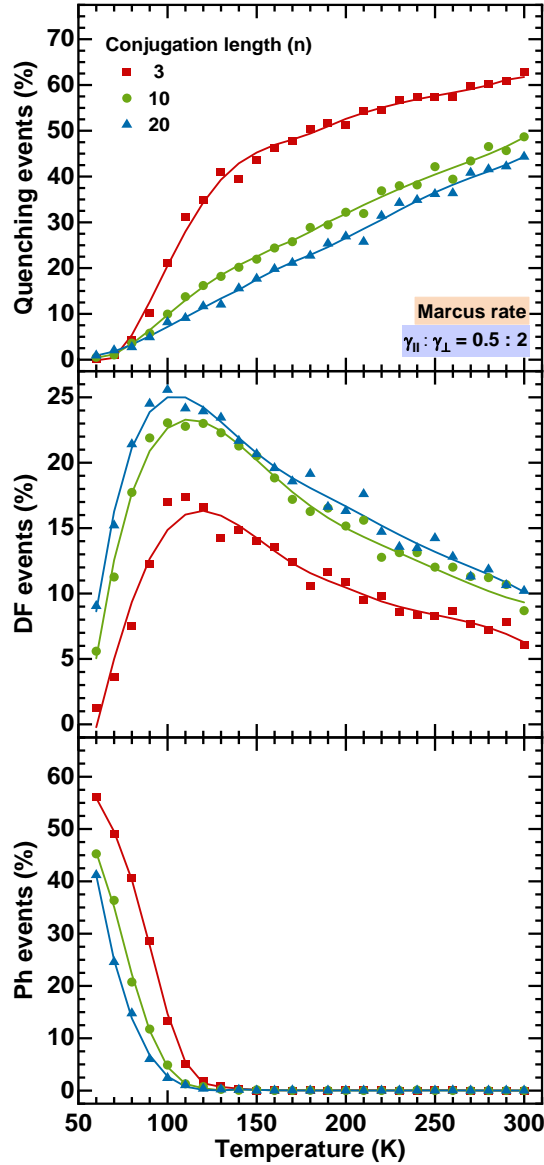
Figure S7: Effect of length of the conjugated segment (*n*) on the temperature dependence of quenching, DF and Ph events is investigated using **Marcus rate** for triplet hopping. Data for *n* = 3 (red squares), *n* = 10 (green circles) and *n* = 20 (blue diamonds). Grid lattice morphology with the length of the conjugated segment *n* = 3 and a constant coupling along and perpendicular to the chain ($\gamma_{\parallel}$ = 0.5 nm^{-1} and $\gamma_{\perp}$ = 2 nm^{-1}) is used. A trap concentration of c_t = 5 x 10^{17} cm^{-3} and a disorder of σ = 35 meV is used for the triplet energy distribution. Solid lines serve as a guide-to-the-eye.
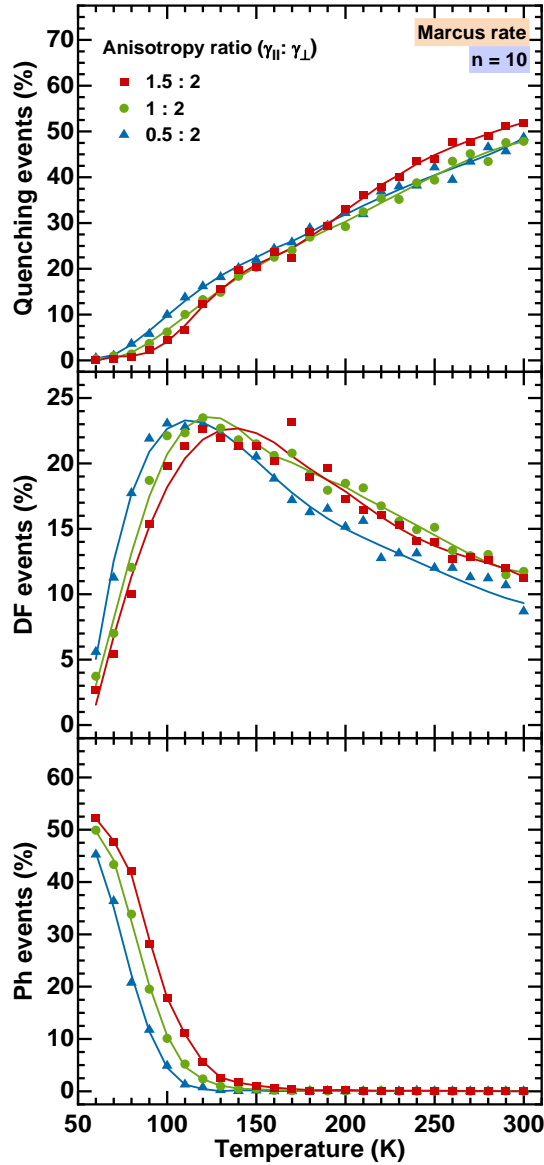
Figure S8: Effect of the anisotropy of coupling on the temperature dependence of quenching, DF and Ph events is simulated with a constant perpendicular to the chain inverse localization length of $\gamma_\perp = 2$ nm^{-1} and varying the same for parallel to the chain transport ($\gamma_{||}$) from 1.5 to 0.5 nm^{-1}, thus increasing the intrachain hopping transport. Simulations are performed for a grid lattice morphology with the length of the conjugated segment $n = 10$, trap concentration $c_t = 5$ x 10^{17} cm^{-3} and energetic disorder $\sigma = 35$ meV. Solid lines serve as a guide-to-the-eye. The simulations are done using **Marcus rate** for triplet hopping.
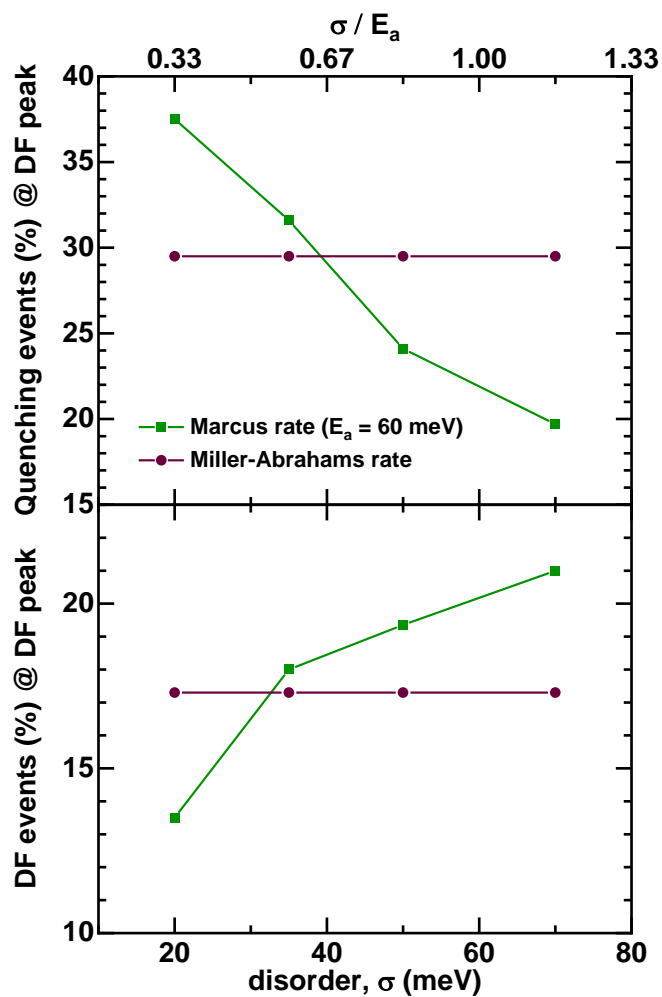
Figure S9: Quenching and DF events at the DF peak remain same for Miller-Abrahams rate remain the same for all disorder values whereas for Marcus rate, the quenching events at the DF event peak decrease with the disorder and as a result DF events increase at the DF event peak with increasing disorder.

Section S2 - Effect of disorder: Marcus vs Miller-Abrahams rate:

The statistically averaged mobility expression within the disorder dominated Miller-Abrahams (MA) formalism:[1]

$$\mu(\sigma, T) \propto exp\left[-C\left(\frac{\sigma}{KT}\right)^2\right] \tag{S1}$$

C is a scaling parameter and equals 0.44 ($\approx (2/3)^2$) for a 3-dimensional isotropic transport.

In the presence of geometric distortions, the expression for mobility should be modified. Bässler *et. al.*[1] suggested that the interplay between disorder and polaronic effects could be quantified as:

$$\mu(\sigma, E_a, T) \propto exp\left[-\frac{E_a}{KT} - C\left(\frac{\sigma}{KT}\right)^2\right] \tag{S2}$$

with a variable parameter C. Fishchuk *et. al.*[2] applied effective mass approximation (EMA) theory and suggested that C increases with the ratio between the energetic disorder and polaronic activation energy viz. σ/E_a. In addition, confirming that C approaches 0.44 for high σ/E_a values as expected for Miller-Abrahams rates applicable for negligible (or no) polaronic transport. [2]

Analyzing the effect of disorder for both the approaches (**Figure S8**), we find that the quenching at T_{max} is similar for all the disorder values when MA rates are used whereas the quenching decreases for increasing disorder when Marcus rates are used. **For MA rates**: when the disorder increases, mobility decreases, TTA slows down, quenching at the trap sites slows down and the peak in DF events can be perfectly shifted to room temperature for a disorder of 70 meV. **While for Marcus rates**: as disorder (σ) increases (the ratio σ/E_a increases), C in eq. S2 increases,[2] and thus mobility of triplets decreases at a faster rate as compared to small disorder values. This results in the decrease of quenching events at T_{max} and thus increase in DF events at T_{max}, unlike the case when reorganization effects can be completely neglected.
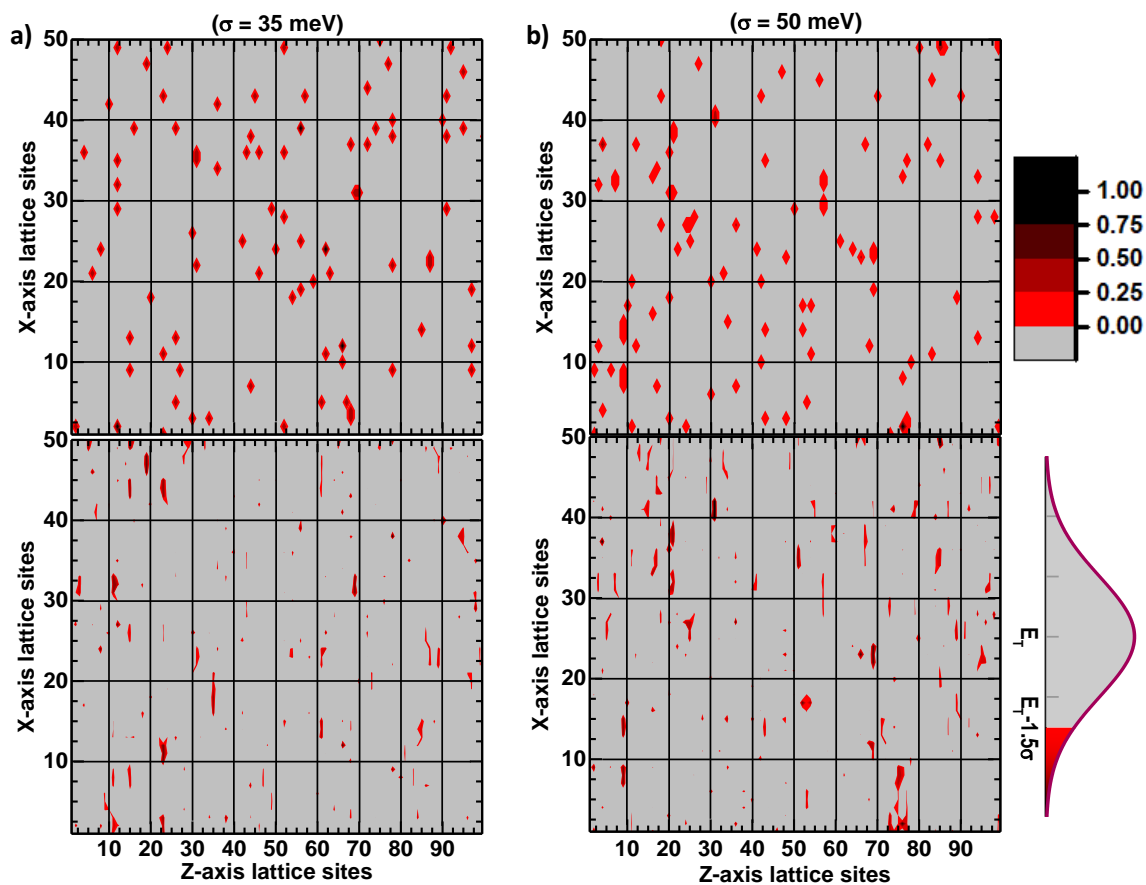
Figure S10: Heatmaps showing normalized annihilations in the X-Z plane (top panels) and the triplet energies below 1.5σ of the mean triplet energy (E_T) for (a) 35 meV and (b) 50 meV (Temperature: 300 K).
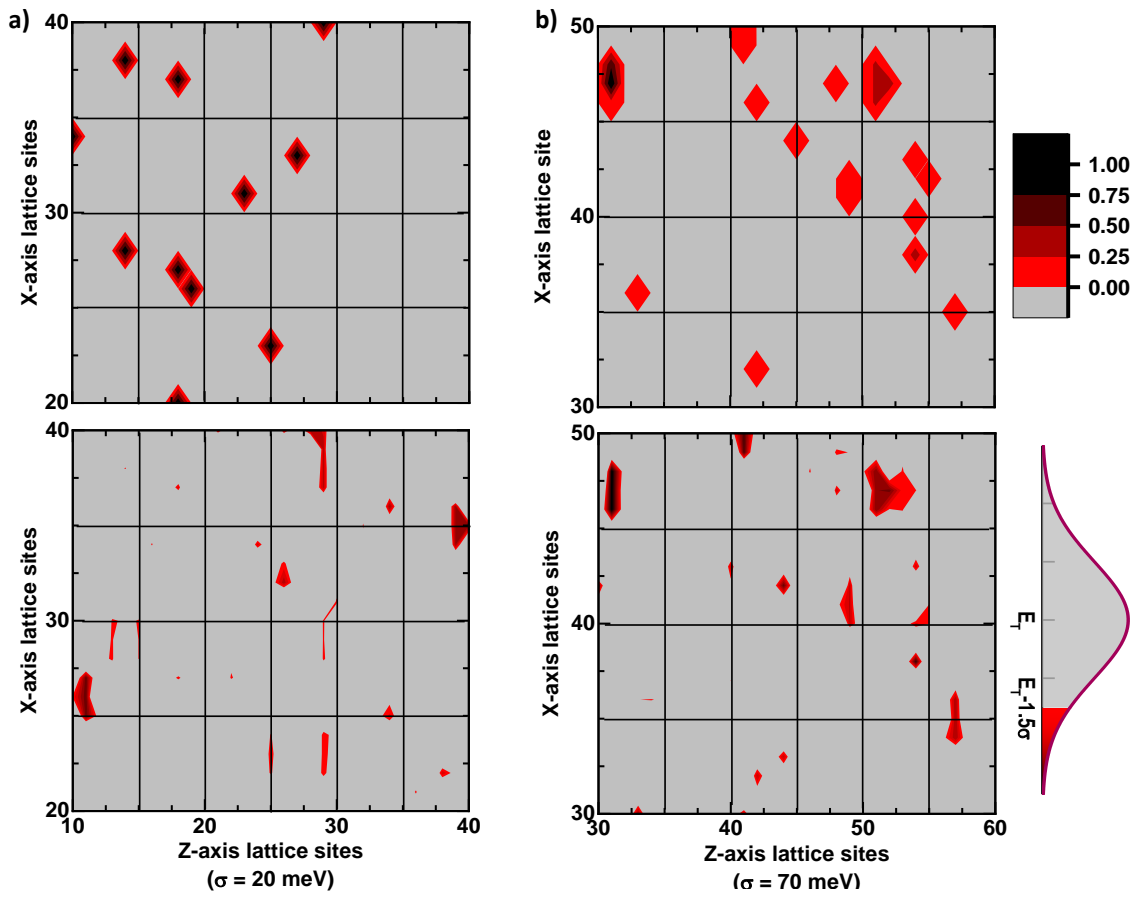
Figure S11: Certain sections of **Figure 6** of the main text are enlarged here to aid the correlation between the number of annihilations and energetic valleys. Heatmaps showing normalized annihilations in the X-Z plane (top panels) and the triplet energies below 1.5σ of the mean triplet energy (E_T) for (a) 20 meV and (b) 70 meV (Temperature: 300 K).

Section S3 - Pearson linear correlation function:

Pearson linear correlation function is given by the covariance of number of annihilations and energy of the lattice in a given plane normalized by the product of their standard deviations.

$$\rho_{A,E} = \frac{<A(x,z)E(x,z)> \; - <A(x,z)><E(x,z)>}{\sqrt{<A^2(x,z)> \; - <A(x,z)>^2}\sqrt{<E^2(x,z)> \; - <E(x,z)>^2}}$$

$A \equiv$ no. of annihilations at a lattice site in the X-Z plane.

$E \equiv$ energy of the lattice site in the X-Z plane.

$\rho_{A,E}$ is obtained by averaging over all the X-Z planes in the simulation box.

174
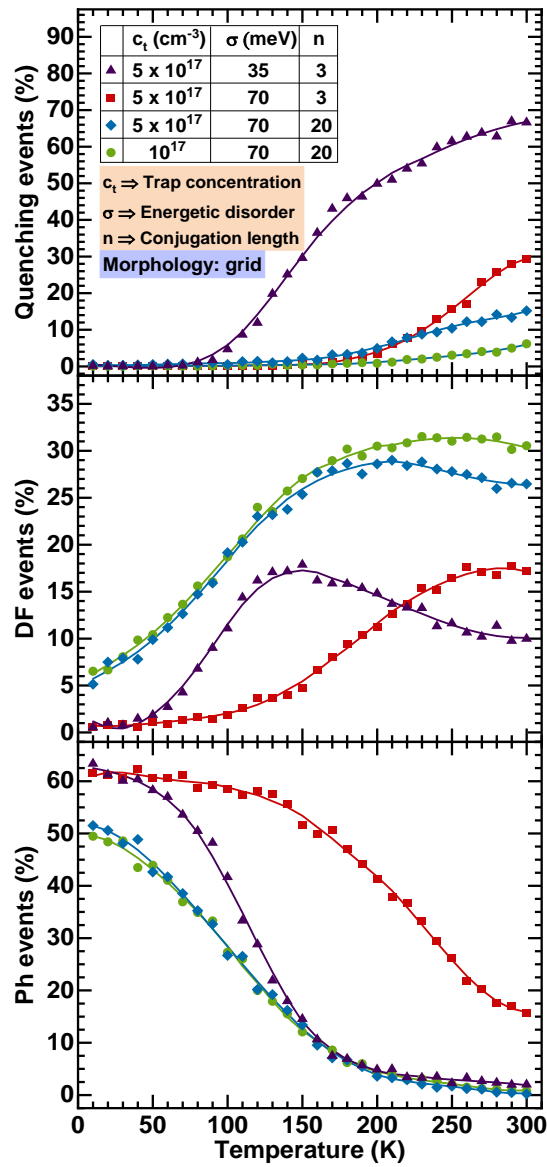
Figure S12: Observing the coupled effect of all the tuned material parameters required for maximum DF at room temperature.

References:

[1]   H. Bässler, Charge transport in disordered organic photoconductors a Monte Carlo simulation study, Phys. Status Solidi B **175**, 15 (1993).

[2]   I. I. Fishchuk, A. Kadashchuk, S. T. Hoffmann, S. Athanasopoulos, J. Genoe, H. Bässler, and A. Köhler, Unified description for hopping transport in organic semiconductors including both energetic disorder and polaronic contributions, Phys. Rev. B. **88**, 125202 (2013).

11 Regiochemistry of Donor Dendrons Controls the Performance of Thermally Activated Delayed Fluorescence Dendrimer Emitters Translating in Their Use in High Efficiency Solution-Processed Organic Light-Emitting Diodes
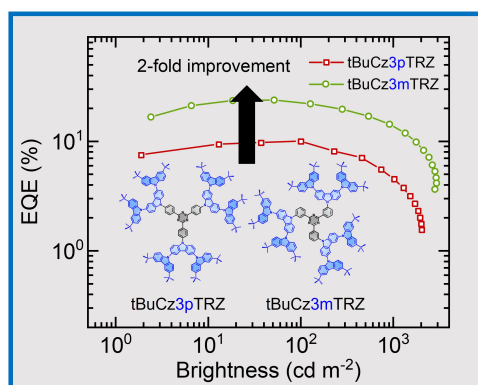
Dianming Sun,[‡] **Rishabh Saxena**,[‡] Xiaochun Fan, Stavros Athanasopoulos,
Eimantas Duda, Ming Zhang, Sergey Bagnich, Xiaohong Zhang,
Eli Zysman-Colman, and Anna Köhler

[‡] Authors contributed equally

Regiochemistry of Donor Dendrons Controls the Performance of Thermally Activated Delayed Fluorescence Dendrimer Emitters for High Efficiency Solution-Processed Organic Light-Emitting Diodes

Dianming Sun,* Rishabh Saxena, Xiaochun Fan, Stavros Athanasopoulos, Eimantas Duda, Ming Zhang, Sergey Bagnich, Xiaohong Zhang,* Eli Zysman-Colman,* and Anna Köhler*

The potential of dendrimers exhibiting thermally activated delayed fluorescence (TADF) as emitters in solution-processed organic light-emitting diodes (OLEDs) has to date not yet been realized. This in part is due to a poor understanding of the structure–property relationship in dendrimers where reports of detailed photophysical characterization and mechanism studies are lacking. In this report, using absorption and solvatochromic photoluminescence studies in solution, the origin and character of the lowest excited electronic states in dendrimers with multiple dendritic electron-donating moieties connected to a central electron-withdrawing core via a *para*- or a *meta*-phenylene bridge is probed. Characterization of host-free OLEDs reveals the superiority of *meta*-linked dendrimers as compared to the already reported *para*-analogue. Comparative temperature-dependent time-resolved solid-state photoluminescence measurements and quantum chemical studies explore the effect of the substitution mode on the TADF properties and the reverse intersystem crossing (RISC) mechanism, respectively. For TADF dendrimers with similarly small ΔE_{ST}, it is observed that RISC can be enhanced by the regiochemistry of the donor dendrons due to control of the reorganization energies, which is a heretofore unexploited strategy that is distinct from the involvement of intermediate triplet states through a nonadiabatic (vibronic) coupling with the lowest singlet charge transfer state.

1. Introduction

Since 2012, organic compounds showing thermally activated delayed fluorescence (TADF) have generated intense interest as replacement emitter materials for noble-metal based phosphorescent complexes in organic light emitting diodes (OLEDs)[1] as TADF-based materials are sustainable and less expensive to synthesize while also allowing for 100% internal quantum efficiency (IQE) by recruiting both singlet and triplet excitons for light emission. Since the first organic TADF OLED was reported in 2009,[2] the design of purely organic TADF-based emitters has evolved rapidly, and vacuum-deposited OLEDs have demonstrated impressive maximum external quantum efficiencies (EQE_max) exceeding 20% for each of the three primary colors. Further, low molecular weight small molecule TADF OLEDs have satisfied critical industry requirements in terms of color, efficiency, and device lifetime, and so can be envisioned to replace phosphorescent emitters in commercial display panels.

D. Sun, X. Fan, M. Zhang, X. Zhang
Institute of Functional Nano & Soft Materials (FUNSOM) and Jiangsu
Key Laboratory for Carbon-Based Functional Materials & Devices
Joint International Research Laboratory of Carbon-Based Functional
Materials and Devices
Soochow University
Suzhou, Jiangsu 215123, P. R. China
E-mail: sd235@st-andrews.ac.uk; xiaohong_zhang@suda.edu.cn

D. Sun, E. Zysman-Colman
Organic Semiconductor Centre
EaStCHEM School of Chemistry
University of St Andrews
St Andrews KY16 9ST, UK
E-mail: eli.zysman-colman@st-andrews.ac.uk

R. Saxena, E. Duda, S. Bagnich, A. Köhler
Soft Matter Optoelectronics
Soft Matter Optoelectronics and Bavarian Polymer Institute (BPI)
University of Bayreuth
Universitätsstraße 30, 95447 Bayreuth, Germany
E-mail: anna.koehler@uni-bayreuth.de

S. Athanasopoulos
Departamento de Física
Universidad Carlos III de Madrid
Avenida Universidad 30, 28911 Leganés, Madrid, Spain

Though generally OLEDs are fabricated by vacuum deposition, the cost of fabrication coupled with the inefficient use of materials and limitations on the size of pixel are all detracting features of this technology. An alternative fabrication process that is cost- and materials-efficient is solution-processing. Solution-processing OLED fabrication techniques such as spin-coating[3] and ink-jet printing[4] are advantageous as the device architecture is simpler, less material is lost during film formation and large-area display fabrication becomes much more feasible. What is required are devices that exhibit comparable performance metrics as vacuum-deposited devices, and this is underpinned by high-performance solution-processable emitter materials. Unlike small molecules, dendrimers and polymers allow for easy solution-processed manufacture of large-area devices because of their superior film-forming ability, excellent thermal and morphological stability, and high affinity for substrates.[5] The molecular weight distribution of polymers, however, normally leads to batch-to-batch deviation of their (photo)physical properties. Unlike polymers, dendrimers have a defined molecular weight. Moreover, in general, most TADF dendrimers do not need to be dispersed into host matrices to suppress concentration or aggregation-caused quenching of the emission and/or exciton annihilation. Thus, nondoped OLEDs can be fabricated resulting in a simplified device architecture.

To date, there have been only a handful of reports using TADF dendrimers,[6] most of which disclose devices that possess efficiencies that are far from the state-of-the-art (Table S1, Supporting Information) of small molecule TADF OLEDs. Slow progress due to a paucity of examples of TADF dendrimers and a poor understanding of their photophysics have hampered the development of dendrimer TADF OLEDs. Most of the reported TADF dendrimers adopt multiple dendritic electron-donating moieties that are connected to a central electron-withdrawing core structure through either conjugated or nonconjugated linkers. Delocalization of the distribution of the electron density of the highest occupied molecular orbital (HOMO) over the donor dendrons, combined with confinement of the electron density in the lowest unoccupied molecular orbital (LUMO) within the acceptor core results in a small exchange integral and an efficient reverse intersystem crossing (RISC) rate. Furthermore, the presence of many donors results in a closer packing of dendrons around acceptor core that helps to improve the charge injection ability of the material and reduce the probability of triplet-triplet annihilation (TTA) in the neat film.[7] As well, the presence of a large number of donor dendrons around the central acceptor can effectively increase the transition integral for large radiative decay rate.[8]

The first TADF dendrimers devised were based on trisubstituted dendronized carbazole donors distributed about a central triphenyltriazine (**TRZ**) unit.[6a] Yamamoto et al.[6e] reported that the performance of the "host-free" devices could be improved by decorating each of the peripheral carbazoles with *tert*-butyl groups (**tBuG2TAZ**). The chemical structure of one of this second generation carbazole-triazine dendrimer, **tBuCz3pTRZ**, is

A. Köhler
Bayreuth Institute of Macromolecular Research (BIMF)
University of Bayreuth
Universitätstraße 30, 95447 Bayreuth, Germany

shown in **Figure 1**a. It consists of a **TRZ** acceptor linked to the 3,3′′,6,6′′-tetrakis(*tert*-butyl-9′H-9,3′:6′,9′′-tercarbazole) (**2Gt-BuCz**) donors via a *para*-phenylene bridge. **tBuCz3pTRZ** shows 100% photoluminescence quantum yield (PLQY) in toluene solution but suffers significant quenching in the solid state, especially in nondoped films. Most TADF dendrimers adopt donor-*para*-π-acceptor architectures where the donor and acceptor units are *para*-connected about a phenylene bridging moiety. Despite the small ΔE_{ST} values that emanate from this design, the performance of the OLEDs is not comparable to those based on small-molecule TADF OLEDs. Consequently, there is a disconnect between this key parameter and the performance of the device and thus, it is important to understand more fundamentally the photophysics of TADF dendrimers and their relationship to both the structure and the device performance.

In general, the relative position of donors and acceptor has a significant effect on the TADF properties.[9] Different substitution modes influence the spatial overlap of the HOMO hole density and the lowest unoccupied molecular orbital (LUMO) electron density distributions. This leads to different ΔE_{ST} values, thus affecting the efficiency and nature of the RISC process of the TADF materials. This motivated us to compare the *para*-bridged dendrimer with its *meta*-based analogues to assess the influence of the *para*- versus *meta*-linked dendrons. This information is important because the correlation of the photophysical and device properties with the molecular structure is crucial for the design of highly efficient TADF dendrimers. In the present work, we synthesized a series of TADF dendrimers with a *meta*-phenylene bridge and investigated their photophysics in detail to build a fundamental understanding of the origin and nature of the lowest energy excited states.

2. Results

2.1. Device Characterization for *para*- versus *meta*-Linked Dendrimers

To assess the effect of substitution position of the donor dendrons on the dendrimer emitter on the OLED metrics, firstly we synthesized the previously reported **tBuCz3pTRZ** and its *meta*-analog **tBuCz3mTRZ** (Figure 1a) (see the Supporting Information for synthesis). The electrochemical properties were determined to evaluate the HOMO and LUMO levels. Both dendrimers possess similar electrochemical properties that translate into similar energy HOMOs of −5.41 and −5.40 eV while the LUMO levels are −2.84 and −2.82 eV for **tBuCz3pTRZ** and **tBuCz3mTRZ**, respectively (Table S2, Supporting Information). The high-lying HOMO level should facilitate the injection of holes from the PEDOT:PSS hole-injection layer. Simple nondoped (i.e., host-free) devices were fabricated with a device configuration of ITO/PEDOT:PSS (35 nm)/dendrimer (40 nm)/TmPyB (40 nm)/LiF (1 nm)/Al (100 nm). A schematic diagram illustrating the device structure is also presented in Figure 1b. Figure 1c shows the current density–voltage–luminance (*J*–*V*–*L*) curves for the devices employing **tBuCz3pTRZ** and **tBuCz3mTRZ** within the emissive layer. Devices based on these dendrimers have the same turn-on voltage of around 3.3 V. The EQE versus brightness curves for the two devices are shown in Figure 1d. The **tBuCz3mTRZ**-based device exhibited a maximum external quantum efficiency

ADVANCED
SCIENCE NEWS

www.advancedsciencenews.com

ADVANCED
SCIENCE
Open Access

www.advancedscience.com
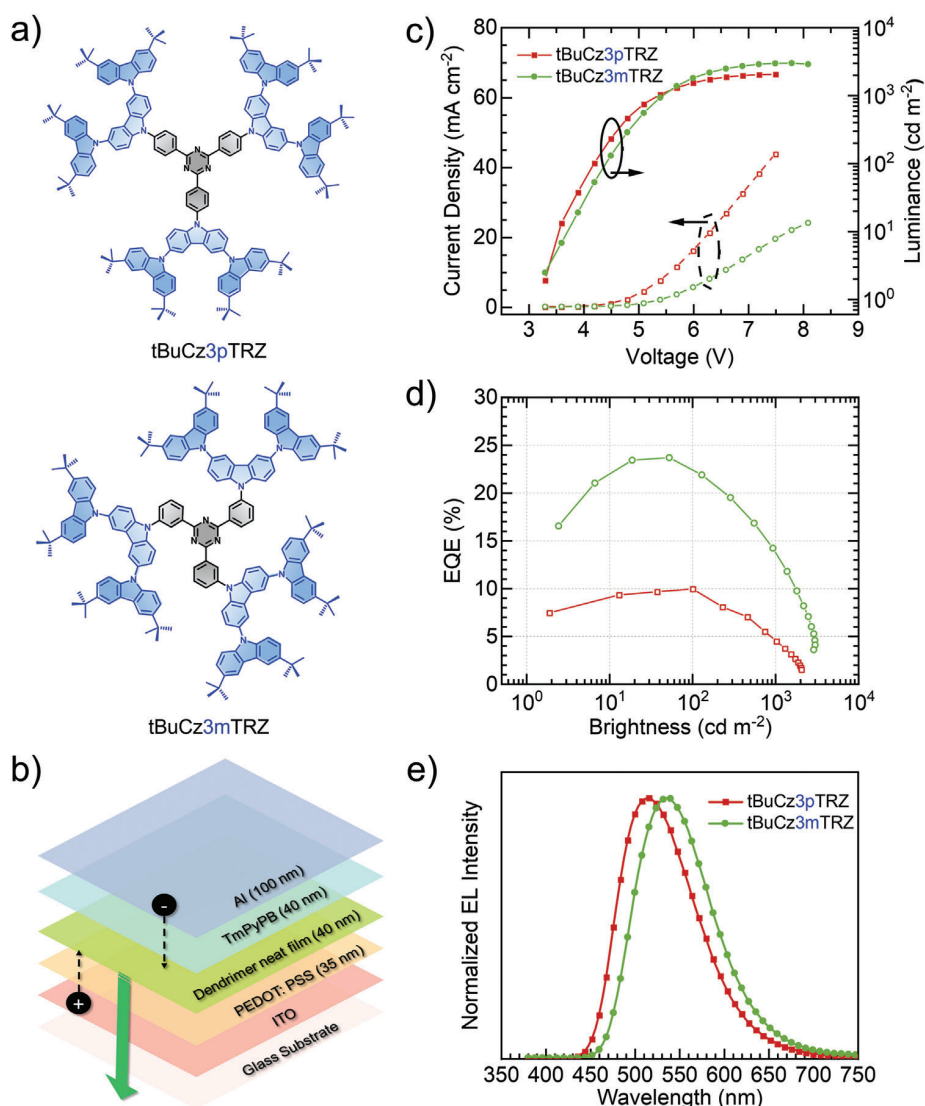
Figure 1. a) Molecular structures of **tBuCz3pTRZ** and **tBuCz3mTRZ**. b) Device configuration of the nondoped solution processed OLEDs. c) Current density–voltage–luminance plot, d) EQE versus brightness curve, and e) electroluminescence (EL) spectra for the nondoped OLEDs based on **tBuCz3pTRZ** and **tBuCz3mTRZ**.

(EQE$_{max}$) of 23.8% (EQE at 100 cd m^{-2}, EQE$_{100}$ = 22.2%), while the tBuCz3pTRZ-based device showed a much more moderate EQE$_{max}$ of 10% (which was obtained at 100 cd m^{-2}), which is consistent with the reported value of 9.5%, albeit the device was fabricated with a different architecture.[6e] This two-fold improvement in the EQE$_{max}$ increases to a factor of 3 at higher luminance where an EQE at 1000 cd m^{-2} of 15% was obtained for the **tBuCz3mTRZ**-based device compared to 5% for **tBuCz3pTRZ**-based device. The EL spectra of these two devices, shown in Figure 1e, have similar spectral shape with the peak, λ_{EL}, at 516 nm for the **tBuCz3pTRZ**-based device and 536 nm for the **tBuCz3mTRZ**-based device.

To understand whether this enhanced performance can really be associated with the change in regiochemistry of the donor dendrons linked to the acceptor core, two more *meta*-bridged

dendrimers, **tBuCz2mTRZ** and **tBuCz4mTRZ**, were prepared by connecting carbazole dendron units to the acceptor TRZ core. **tBuCz2mTRZ** and **tBuCz4mTRZ** (**Figure 2**) contain two and four dendrons, respectively, within their chemical structure and possess different symmetry compared to **tBuCz3mTRZ**. The devices were prepared using the same architecture and the OLED performance is shown in Figure S3 (Supporting Information). Intriguingly, the **tBuCz2mTRZ**-based device (EQE$_{max}$ = 19.9% at 23 cd m^{-2}; EQE$_{100}$ = 12.0%) as well as the **tBuCz4mTRZ**-based device (EQE$_{max}$ = 23.8% at 100 cd m^{-2}) are also found to have higher EQEs than that of the OLED with **tBuCz3pTRZ** (Figure S3b, Supporting Information). The EQE$_{max}$ reported here (Table S3, Supporting Information) for the *meta*-linked dendrimers are amongst the highest values reported for solution-processed TADF OLEDs (see Table S1 in the Supporting Information). The
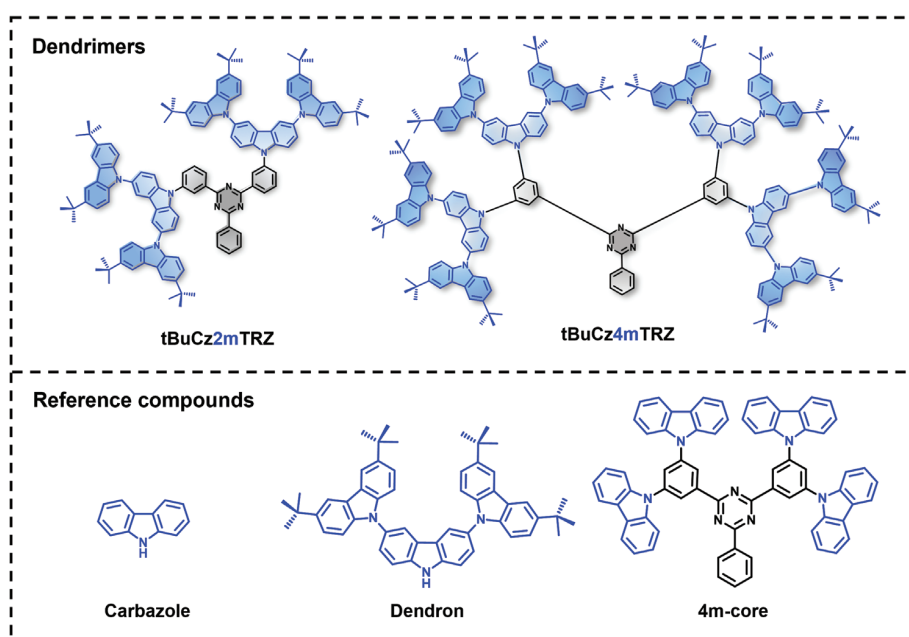
Figure 2. The molecular structures of the *meta*-connected dendrimers, **tBuCz2mTRZ** and **tBuCz4mTRZ** as well as the three reference compounds, carbazole, dendron, and **4m-core** (**tBuCz4mTRZ** without the outer tBuCz units).

results establish that, for the same device architecture, these *meta*-dendrimer-based OLEDs show significantly better EL performance than the *para*-dendrimer analogue, which in turn, confirms the importance of the substitution mode between the donor dendrons and the acceptor moiety in the molecular design of TADF dendrimers. However, a detailed photophysical and quantum chemical analysis is needed to understand the correlation between the OLED performance with the dendrimer structure, which is the object of this study. A separate publication is dedicated to the exploitation of this insight in the design of an optimized chemical structure that involves both, *meta*-connected and *para*-connected donor dendrons leading to OLEDs with EQE$_{max}$ of 28.7%.[10]

2.2. Photophysics of the Singlet Excited States

Room temperature (RT) absorption and emission spectra of the dendrimers in toluene solution at low concentration are shown in **Figure 3**a (for a linear plot) and in Figures 3b,c (for semilogarithmic plots). For reference, the absorption and emission spectra of reference compounds (see Figure 2 for chemical structures), **carbazole**, **dendron**, and **4m-core**, are shown in Figure 3d. Two distinct bands characterize the absorption of each dendrimer. The broad band below 3.5 eV with weak-to-moderate intensity (Figures 3a,b) is assigned to a CT transition, while the strongly absorbing band with structured features above 3.5 eV arises from locally excited (LE) transitions on the carbazole units.

The nature of the LE band becomes evident when comparing it to the absorption spectra of the reference compounds (Figure 3d). The absorption spectra of **carbazole** shows vibrational features with peaks at 3.83 eV (324 nm) and 3.66 eV (339 nm) and the

Stokes shift between the 0–0 peaks of absorption and emission is small.[11] The structured features of the absorption spectrum of **4m-core** match well in energy and spectral shape with the **carbazole** *π–π** transition. In contrast to **carbazole** (Figure 3d, top panel), **4m-core** exhibits a broad and weak absorption band below 3.5 eV that we attribute to absorption from a CT state between the carbazoles and the central triazine acceptor (Figure 3d, bottom panel). The emission of **4m-core** arises from this CT state as the emission is symmetric to the CT absorption. In comparison with **carbazole** absorption, the dendron absorption is slightly red shifted with two structured peaks at 3.70 eV (335 nm) and 3.55 eV (350 nm), and a weak shoulder at 3.84 (323 nm). In addition, the relative intensity of the vibrational peak at 3.70 eV (335 nm) with respect to the 0–0 vibration peak at 3.55 eV is different from that of the **carbazole** absorption. Thus, we can conclude that the dendron absorption is comprised of two vertical excitation processes corresponding to: i) a lower energy absorption from an excitation that is localized on the central carbazole (denoted as LE$_1$ and indicated here by the black arrow); and ii) a higher energy absorption from the excitation localized on the outer, individual carbazoles (referred to as LE$_2$ and indicated here by the green arrows). Due to the prevailing substitution pattern of the donor dendron we expect the central carbazole to be more electron-rich than the peripheral carbazoles, so that its excited state is slightly lower in energy. From the absorption spectra, each of the dendrimers, **tBuCz3pTRZ**, **tBuCz3mTRZ**, **tBuCz2mTRZ**, and **tBuCz4mTRZ**, exhibits similar structured features that resemble those of the dendron. Therefore, it is affirmed that their absorption spectra are dominated by the same LE$_1$ and LE$_2$ states as from the dendron. For clarity, they are indicated in Figure 3b. Furthermore, as shown in Figure 3b, the molar absorptivity of the bands in the range 3.5–3.8 eV increases from **tBuCz2mTRZ** to

**ADVANCED
SCIENCE NEWS**

www.advancedsciencenews.com

**ADVANCED
SCIENCE**
Open Access

www.advancedscience.com
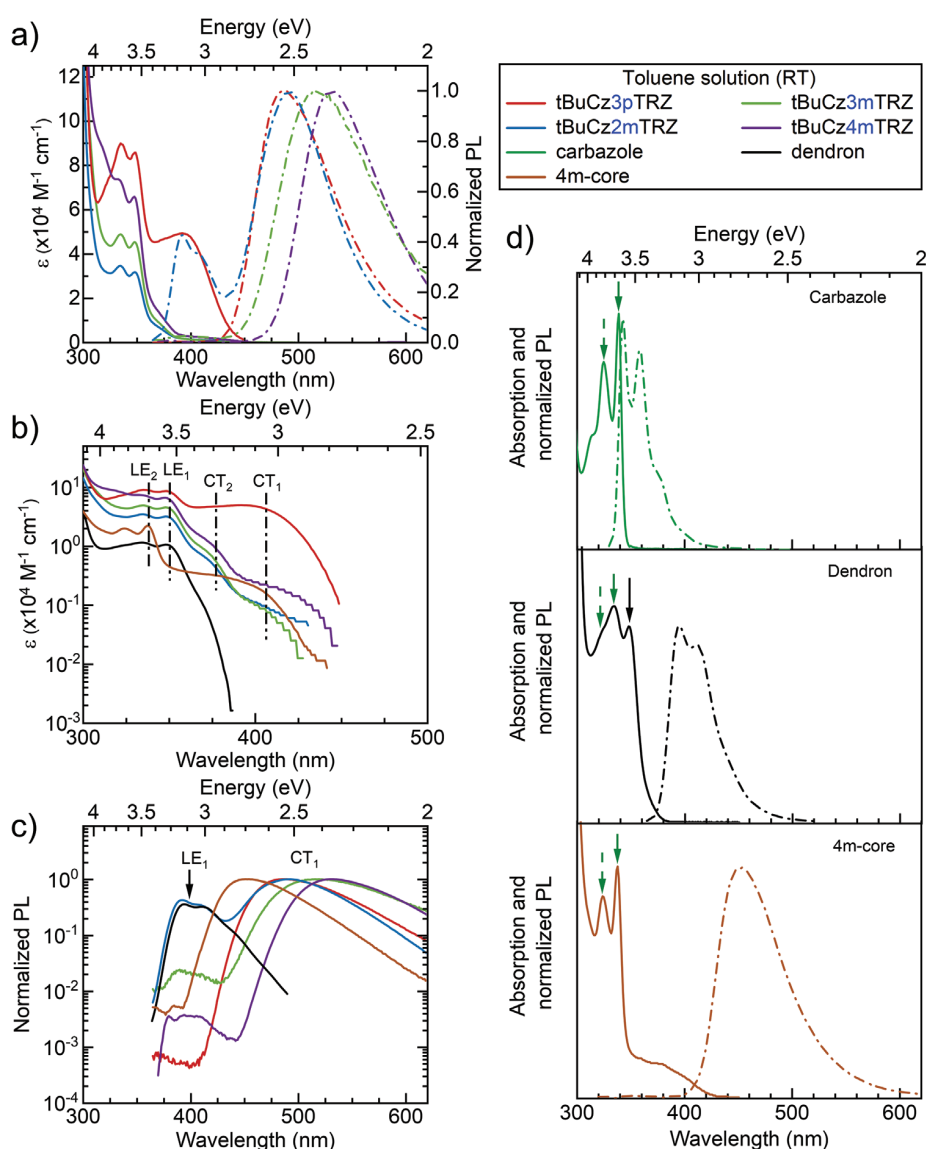
Figure 3. RT solution photophysics of the dendrimer and model compounds (λ_{exc} = 300 nm): a) Molar absorptivity and normalized emission spectra in toluene on a linear scale. b) Molar absorptivity and c) emission spectra on a log scale along with the molar absorptivity/emission spectra. d) Absorption and emission spectra (on a linear scale) of the carbazole, dendron and **4m-core**. LE$_1$, LE$_2$, CT$_1$, CT$_2$ refer to the lower and higher energy singlet LE and CT states as described in the text. Arrows in d) refer to the 0-0 transition (solid green) and 0–1 transition (dotted green) of the LE$_2$ and the LE$_1$ absorption (solid black).

tBuCz3mTRZ to **tBuCz4mTRZ**. This is consistent with the presence of an increasing number of donor dendron units in their chemical structure. Similar behavior in the absorption spectra have been reported in the literature;[6a,b,e] however, the spectral features around 300–400 nm have either not been discussed or have been ascribed to intramolecular CT absorption.[6b]

In addition to the structured dendron emission, **tBuCz3pTRZ** is characterized by the presence of a strong, broad absorption band in the range of 2.8–3.4 eV, which we ascribe to a CT transition (and refer to as CT$_1$) from the dendron donors to the triazine (TRZ) acceptor. However, when the *para*-connected donor dendron is replaced by the *meta*-connected donor dendron this

broad feature remains approximately at the same energy (centered roughly at 3.05 eV), but the extinction coefficient is reduced by over an order of magnitude. The *meta*-connection compounds are also characterized by a higher energy broad, unstructured absorption band centered at 3.3 eV (labelled CT$_2$) with a larger molar extinction coefficient than the lower energy CT$_1$ band. The comparable extinction coefficient of CT$_1$ band and the LE absorption features in **tBuCz3pTRZ** indicates a significant overlap of electron and hole wavefunctions, and consequently some admixture of transitions with both π–π* and CT$_1$ character. By comparison with the absorption features of the *meta*-connection dendrimers, it is evident that a CT$_2$ state is present in **tBuCz3pTRZ**

ADVANCED
SCIENCE NEWS

www.advancedsciencenews.com

ADVANCED SCIENCE
Open Access

www.advancedscience.com
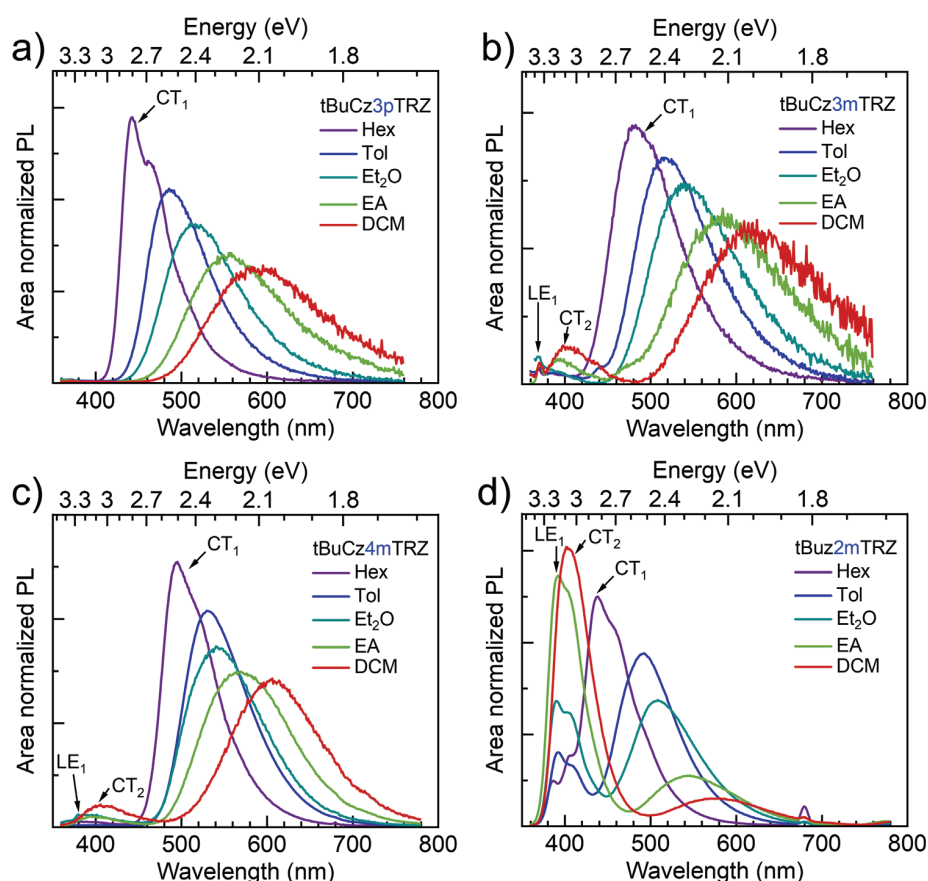
Figure 4. Solvatochromic PL spectra, normalized according to the integrated area (λ_{exc} = 340 nm; 3 × 10^{-5} M), of the dendrimers in hexane (Hex), toluene (Tol), diethyl ether (Et$_2$O), ethyl acetate (EA) and dichloromethane (DCM). LE$_1$ and CT$_1$ refer to the lowest energy singlet LE and CT states and LE$_X$ refers to the exciplex LE state as described in the text.

as well; however, the strong extinction coefficient of the CT$_1$ state prevents the corresponding feature from being distinctly visible in the absorption spectrum of **tBuCz3pTRZ**.

A simpler set of spectral features is observed in the emission spectra in toluene solution. All dendrimers exhibit a broad structureless CT$_1$ emission (Figure 3a) and, in addition, the *meta*-connection-based dendrimers also show a high-energy emission band, which is evident on a linear scale for **tBuCz2mTRZ** (Figure 3a) and on a logarithmic scale for the other *meta*-connection dendrimers (Figure 3c). We attribute the broad CT emission to the CT$_1$ state, as this band is symmetric to the CT$_1$ absorption of all the dendrimers (Figure S4, Supporting Information). The CT$_1$ emission spectra peak at (λ_{PL}) 489 nm (2.54 eV), 493 nm (2.52 eV), 520 nm (2.38 eV), and 532 nm (2.33 eV) for **tBuCz3pTRZ**, **tBuCz3mTRZ**, **tBuCz2mTRZ**, and **tBuCz4mTRZ**, respectively. The emission spectrum of **tBuCz3pTRZ** matches with the one reported by Yamamoto et al.[6e] The structured higher energy emission band is attributed to originating from the LE$_1$ state, as it closely matches the dendron emission in energy and spectral shape (Figures 3c,d).

Solvatochromic PL measurements further confirm the nature of these states and explain the reason behind the observation of concomitant emission from different states. While only a sin-

gle band is observed in **tBuCz3pTRZ**, three distinct bands can be identified in the emission spectra of the *meta*-connection dendrimers in low polarity solvents (**Figure 4**). Since the position of the high-energy band (at around 380 nm/3.26 eV) in the *meta*-connection dendrimers is insensitive to the solvent polarity it is readily assigned to a LE state, presumably LE$_1$. The intensity of this LE band is extremely low in **tBuCz3mTRZ** and **tBuCz4mTRZ**; however, a strong LE signal is obtained in the emission spectra of **tBuCz2mTRZ**, even for high polarity solvents. The second band that changes only a little (about 120 meV) with solvent polarity is centered around 3 eV (400 nm). It is visible in Et$_2$O, EtOAc, and CH$_2$Cl$_2$ (DCM) for **tBuCz3mTRZ** and **tBuCz4mTRZ**, and only in DCM for **tBuCz2mTRZ**. The lack of a pronounced solvatochromism also identifies it as a LE state. The position and the broad spectral shape are identical to the emission from a partial overlap excimer from a carbazole moiety,[12] and an increased tendency to such excimer formation for more polar solvents is plausible. Thus, the features above 2.9 eV (420 nm) are attributed to an emission localized on the donor dendron and associated partial overlap excimers. In contrast to these LE features, with increasing solvent polarity we observe a bathochromic shift and a broadening of both the emission in **tBuCz3pTRZ** and the dominant low-energy band in the

ADVANCED
SCIENCE NEWS

www.advancedsciencenews.com

ADVANCED SCIENCE
Open Access

www.advancedscience.com

meta-connection dendrimers. We take this to confirm the charge-transfer character of the low energy band already assigned to CT$_1$.

Simultaneous emission from states of different energy can only be observed when the rate of internal conversion from the higher energy states to the lower energy states is sufficiently slow to compete with the rate of radiative decay of the higher energy states. Internal conversion from LE to CT state requires an electron transfer to the acceptor moiety, which occurs via an exchange mechanism (Dexter transfer) and thus depends strongly on the wavefunction overlap. Because of the more conjugated structure of **tBuCz3pTRZ**, this is expected to be fast in this case so that the only radiative contribution to the steady-state emission spectrum comes from the lowest energy CT$_1$ state, while the transfer rate is slowed down for the poorly conjugated *meta*-connection dendrimers. The charge transfer rate decreases further with an increasing energy gap between the LE states (above 2.9 eV) and CT states (moving from about 2.8 eV down to about 2.1 eV with increasing solvent polarity) involved in these transitions. As a result, the rate of emission from the LE$_1$ state and the associated excimer becomes comparable to the rate of internal conversion from LE$_1$ to CT$_1$, and thus, LE$_1$ emission *and* CT$_1$ emission can both be observed in the meta-connection compounds.

2.3. Photophysics of Triplet Excited States and TADF

Having clarified the nature of the lowest singlet excited states, next we address the triplet states and the associated TADF properties of these dendrimers. For TADF materials, the energy difference between the lowest singlet (S$_1$) and triplet excited states (T$_1$), ΔE_{ST}, is one of the key parameters used to assess the potential of the emitter to be used in OLEDs. We first investigated the solid-state emission in a host matrix to reduce any impact of possible excimers (or aggregates) as well as the impact of bimolecular annihilation processes on the analysis of the monomolecular dendrimer properties such as quantum efficiencies and decay rate constants. **Figure 5**a shows the spectra for the prompt fluorescence, PF (delay time: 10 ns, gating time: 7 ns) and phosphorescence, Ph (delay time: 10 ms, gating time: 1 ms) acquired in the doped films (10 wt% dendrimer in mCP) at 5 K. mCP was identified as a suitable host material because of its high-triplet energy and good miscibility with various dopants. The characteristically broad and unstructured prompt fluorescence (phosphorescence) in the doped films indicates the dominant CT nature of the S$_1$ (T$_1$) state for each dendrimer as supported by our RT absorption and emission investigation probing the nature of the singlet state. The S$_1$ and T$_1$ energies are then taken from the onsets of PF and Ph, respectively, and are summarized in **Table 1**. Accordingly, the ΔE_{ST} values are in the range of 50–100 meV. Similar S$_1$, T$_1$, and ΔE_{ST} values are also obtained for all the dendrimers in toluene glass at 5 K (Figure S5, Supporting Information). Such small differences between the lowest singlet and triplet excited states will facilitate a rapid RISC in these dendrimers, especially in the *meta*-connection dendrimers where the ΔE_{ST} is smallest.

Figure 5b shows the photoluminescence (PL) decays of the 10 wt% doped dendrimer films in mCP. The PL decays are typical for a TADF emitter, i.e., they are characterized by two different regimes that correspond to prompt fluorescence and delayed flu-

orescence, and the intensity of DF increases with the increasing temperature. Notably, for **tBuCz3mTRZ** and **tBuCz4mTRZ**, much stronger thermal activation is observed between 5 K and 25 K as compared to the thermal activation at higher temperatures, implying extremely efficient RISC as it is an endothermic process. To calculate the effective activation energy barrier (E_{act}) for the RISC process, the intensity of the DF (at a delay time of 1 µs) is plotted logarithmically against $1000/T$, as shown in **Figure 6**a. A linear relationship of this Arrhenius plot above 200 K indicates the absence of phosphorescence within this temperature range. The E_{act} values (Table 1) thus obtained are approximately half the corresponding ΔE_{ST} values. For comparison, the PL decays at 300 K are plotted in Figure 6b. The PF decay lifetime of **tBuCz3pTRZ** is shorter than those of the *meta*-connection dendrimers owing to the greater hole-electron overlap of the lowest ^{1}CT state, while the DF/PF ratio is higher for the *meta*-connection dendrimers. The PL decays at 300 K along with the photoluminescence quantum yield (PLQY) values were used to calculate the quantum efficiencies and rate constants associated with different kinetics processes resulting in the excited state of the 10 wt% doped films in mCP. The parameters were determined according to the procedure described in the Supporting Information and are summarized in **Table 2**. Of particular interest are the total PLQY values (φ_{PL}), the quantum efficiency for DF (φ_{DF}), and the RISC rates (k_{RISC}). Under N$_2$, the **tBuCz3pTRZ** film has the highest PLQY of 89% while **tBuCz3mTRZ** and **tBuCz4mTRZ** have similar φ_{PL} of about 80% and **tBuCz2mTRZ** has the lowest φ_{PL} of 65%. Interestingly, φ_{DF} is significantly lower for **tBuCz3pTRZ** (0.19) when compared to the *meta*-connection dendrimers (0.63, 0.45, and 0.50 for **tBuCz3mTRZ**, **tBuCz2mTRZ**, and **tBuCz4mTRZ**, respectively). This illustrates that although the φ_{PL} of **tBuCz3pTRZ** is the highest, most of the contribution to the PL comes from PF and not from DF, i.e., from the photoexcited singlets and not the RISC-activated singlets. Furthermore, the RISC efficiency (φ_{RISC}) and RISC rate (k_{RISC}) of **tBuCz3pTRZ** are also significantly lower when compared to the *meta*-connection dendrimers (for values, refer Table 2). These parameters are of crucial importance to the device performance because they govern to population of triplet excitons because of electrical excitation. In view of the device application, we note the remarkable efficiency of **tBuCz3mTRZ** for RISC of 95% in the doped film, which remains high at 89% in the neat film.

For the photophysical character in neat films under N$_2$, a significant decrease in φ_{PL} is observed for **tBuCz3pTRZ** (51% in neat film compared with 89% in doped film), while in contrast, the concentration quenching of **tBuCz3mTRZ** (62% in neat film compared with 81% in doped film), **tBuCz2mTRZ** (59% in neat film compared with 65% in doped film) and **tBuCz4mTRZ** (67% in neat film compared with 79% in doped film) is suppressed. The PL decays of the neat films also reveal the temperature dependence of the DF as low as 25 K, implying that efficient RISC behavior is preserved in neat films (Figure S7, Supporting Information). Rate constants determined from the RT PL decays (Table 2), though affected by the presence of bimolecular processes (not considered in the analysis described in the Supporting Information), resemble qualitatively to the ones derived for the 10 wt% doped dendrimer films. This implies that the conclusions derived for the devices based on doped OLEDs, based on the

184

ADVANCED
SCIENCE NEWS

www.advancedsciencenews.com

ADVANCED SCIENCE
Open Access

www.advancedscience.com
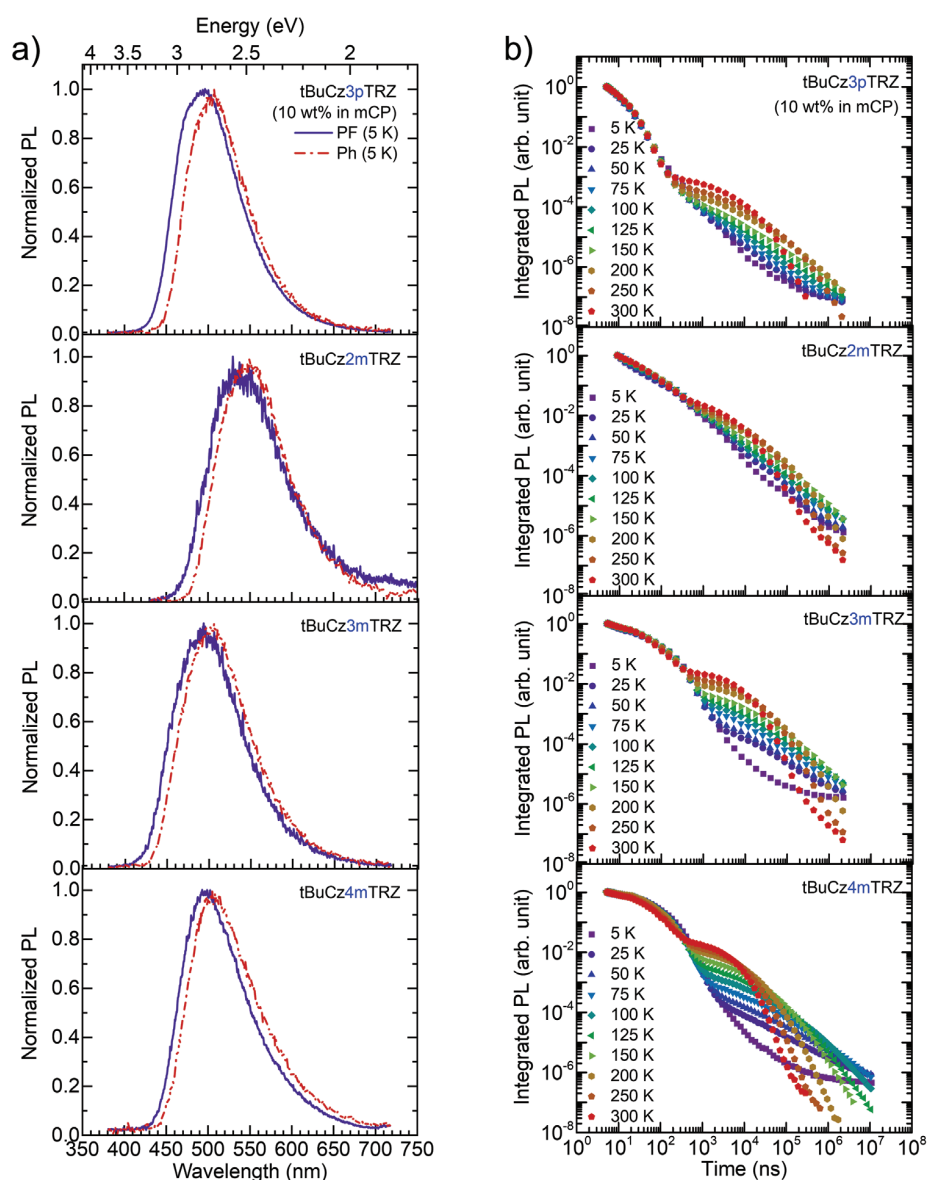
Figure 5. a) 5 K prompt fluorescence (delay time: 10 ns, blue solid line) and 5 K phosphorescence (delay time: 10 ms, red dashed-dotted line) of the and b) temperature dependent PL decay curves for 10 wt% dendrimer films doped in mCP (λ_{exc} = 355 nm).

photophysical parameters (φ_{DF}, φ_{RISC}, and k_{RISC}), remain valid for neat film OLEDs as well.

3. Quantum Chemical Calculations

The photophysical study reveals that the substitution pattern of the donor dendrons has a significant impact on the photophysics of the dendrimers. The *meta*-connection dendrimers possess the smaller ΔE_{ST}, show more efficient TADF with faster RISC, and thus the corresponding OLEDs exhibit improved performance. However, to understand the factors governing the differences in TADF properties and how these correlates with the

donor dendron substitution pattern, we first must understand both the nature and degree of mixing of the low-lying excited states.

It has been advanced that the vibrational coupling between closely lying triplet excited states can assist the RISC process via a second order perturbation effect.[13] To verify the implication of higher lying triplet states in the RISC process, we performed excited state geometry optimizations for the model dendrimers **tBuCz1pTRZ** and **tBuCz1mTRZ** (Figures S14 and S15, Supporting Information) that contain only one donor dendron connected to the triphenyl triazine unit instead of three. We found that the optimized T_2 state lies considerably higher in energy than the T_1 state ($\Delta E_{T_2-T_1}$ = 370 meV for **tBuCz1pTRZ** and 220 meV

Table 1. Comparison of photophysical properties for 10 wt% dendrimer films doped in mCP.

	S_1 [a] [nm eV]	T_1 [b] [nm eV]	ΔE_{ST} [c] [meV]	E_{act} [d] [meV]
tBuCz3pTRZ	436 (2.84)	452 (2.74)	100	52 ± 2
tBuCz3mTRZ	425 (2.92)	437 (2.84)	80	44 ± 3
tBuCz2mTRZ	470 (2.64)	482 (2.57)	70	22 ± 3
tBuCz4mTRZ	442 (2.81)	450 (2.76)	50	27 ± 2

[a] Lowest singlet energy determined from the onset of the PF (5 K; delay time 10 ns, gating time 7 ns); [b] Lowest triplet energy determined from the onset of the Ph (5 K; delay time 10 ms, gating time 10 ms); [c] Energy difference between S_1 and T_1; [d] Activation energy determined from the Arrhenius plot of the DF intensity versus $1/T$.

for **tBuCz1mTRZ**). We note that the additional dendrons in **tBuCz3pTRZ** and **tBuCz3mTRZ** can lead to the introduction of additional degenerate triplet states; however, this will not affect our conclusion that T_2 (or indeed any other higher lying triplet state) is expected to be only minimally involved in the RISC process. Thus, the explanation of the observed difference in the RISC rates warrants consideration within the limit of first order perturbation theory.

k_{RISC} can be computed in the framework of Fermi's Golden rule[14]

$$k_{RISC} = \frac{2\pi}{\hbar} \rho_{FC} \left| \langle S_1 | \hat{H}_{SO} | T_1 \rangle \right|^2 \qquad (1)$$

where $\langle S_1 | \hat{H}_{SO} | T_1 \rangle$ is the spin orbit coupling (SOC) matrix element from T_1 to S_1 and ρ_{FC} denotes the Franck–Condon-weighted density of states term, which can be evaluated according to the semi-classical Marcus–Hush formulation[15]

$$\rho_{FC} = \frac{1}{\sqrt{4\pi \lambda k_B T}} \exp \left[-\frac{(\Delta E_{ST} + \lambda)^2}{4\lambda k_B T} \right] \qquad (2)$$

$\lambda = \lambda_{inter} + \lambda_{intra}$ is the Marcus reorganization energy (Figure S16, Supporting Information) associated with the vibrational coupling to intermolecular and intramolecular low frequency vibrational modes. Equation (2) assumes that the quantum nature of the low frequency modes (with energies, $\hbar\omega$, of a few meV) does not need to be considered explicitly, i.e., $k_B T \gg \hbar\omega$, and can be treated classically.[15,16] Thus, k_{RISC} depends on the adiabatic ΔE_{ST}, the SOC matrix element in the geometry of the relaxed T_1 state and the coupling to the low frequency modes associated with the RISC from T_1 to S_1. We have used **Cz3pTRZ** and **Cz3mTRZ** as model compounds to evaluate these quantities at the TDA-DFT M06-2X/6-31G(d,p) level. The *tert*-butyl (tBu) groups were replaced with hydrogen atoms in order to reduce the computational cost.

In the S_1 state equilibrium geometry of **Cz3pTRZ** (**Figure 7**) the hole and electron natural transition orbitals (NTOs) are localized on the donor dendron and phenyltriazine, respectively. Additionally, the donor dendron adopts a highly twisted conformation with respect to the TRZ with a dihedral angle of 79°. This indicates that the S_1 state possesses intramolecular CT character, which is also confirmed by a charge transfer number (ω_{CT}) value of 0.87; ω_{CT} (see the Experimental Section for the defini-

tion) takes values between 0 (for a Frenkel exciton) and 1 (for a pure CT exciton). The S_1 state of **Cz3mTRZ** possesses a similar CT character ($\omega_{CT} = 0.91$) but adopts a less twisted conformation with a much smaller dihedral angle, $\theta = 57°$ as compared to that of **Cz3pTRZ** in its ^{1}CT state. While the electron NTO in the T_1 state of **Cz3mTRZ** is localized on the phenyltriazine (while some delocalization to the carbazole is found for **Cz3pTRZ**), the hole NTO extends from the central carbazole of the donor dendron to the bridging phenylene and to a smaller extent to the triazine unit (unlike **Cz3pTRZ** where there is a larger amount of hole density on the triazine unit). This leads to a greater CT character in the T_1 state of **Cz3mTRZ** ($\omega_{CT} = 0.54$) as compared to **Cz3pTRZ** ($\omega_{CT} = 0.38$), even though θ remains the same (42°–43°). It is worth emphasizing at this point that while the RISC process in **Cz3pTRZ** involves a relatively large dihedral angle change ($\Delta\theta$) of about 37°, there is a much more moderate change of 13° in **Cz3mTRZ**. The adiabatic ΔE_{ST} for **Cz3pTRZ** ($\Delta E_{ST} = 290$ meV; $S_1 = 2.96$ eV, $T_1 = 2.67$ eV) is thus larger than that for **Cz3mTRZ**
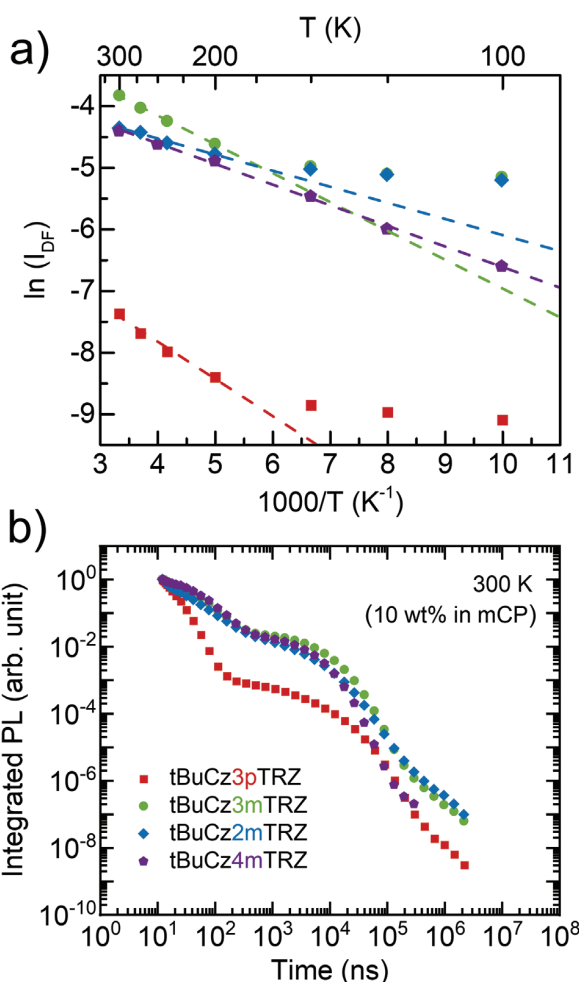
Figure 6. a) Arrhenius plot showing the variation of $\ln(I_{DF})$ with $1/T$ used to calculate E_{act} for the RISC process and b) 300 K PL decay curve for **tBuCz3pTRZ**, **tBuCz3mTRZ**, **tBuCz2mTRZ**, and **tBuCz4mTRZ** doped films (10 wt% in mCP).

Table 2. Comparison of photophysical properties in 10 wt% dendrimer films doped in mCP and neat dendrimer films.

	τ_{PF}[a] [ns]	τ_{DF}[b] [μs]	φ_{PL}[c] [%]	$\varphi_{DF}/\varphi_{PF}$[d]	φ_{PF}[e]	φ_{DF}[f]	φ_{ISC}[g]	φ_{RISC}[h]	k_F[i] [×10^7 s^{-1}]	k_{ISC}[j] [×10^7 s^{-1}]	k_{RISC}[k] [×10^5 s^{-1}]	k_{NR}^T[l] [×10^5 s^{-1}]
					Doped film (10 wt% dendrimer in mCP)							
tBuCz3pTRZ	9.8	3.1	89	0.27	0.70	0.19	0.71	0.71	7.19	3.05	0.5	0.2
tBuCz3mTRZ	50.2	5.5	81	3.51	0.18	0.63	0.95	0.95	0.36	1.63	3.7	0.2
tBuCz2mTRZ	40.3	4.0	65	2.31	0.20	0.45	0.80	0.87	0.49	1.99	2.2	0.3
tBuCz4mTRZ	52.2	3.4	79	1.68	0.29	0.50	0.71	0.89	0.57	1.35	3.5	0.4
					Neat dendrimer film							
tBuCz3pTRZ	13.4	1.4	51	0.56	0.33	0.18	0.67	0.53	2.44	5.04	0.7	1.4
tBuCz3mTRZ	54.2	2.2	62	3.04	0.15	0.47	0.85	0.89	0.28	1.56	6.5	0.7
tBuCz2mTRZ	96.7	1.1	59	0.85	0.32	0.27	0.68	0.67	0.33	0.70	5.4	1.9
tBuCz4mTRZ	62.7	1.7	67	1.2	0.31	0.37	0.70	0.78	0.49	1.11	4.3	0.9

[a] Lifetime of prompt emission (obtained by single exponential fitting of prompt emission decay regime at RT) λ_{exc} = 355 nm; [b] Average lifetime of delayed emission, $\tau_{DF} = \frac{\int t \, I_{DF} \, dt}{\int I_{DF} \, dt}$; [c] Photoluminescence quantum yield, under N_2; [d] DF/PF = $\int \frac{I_{DF(t)}}{I_{PF(t)}} dt$; [e] PF quantum efficiency; [f] DF quantum efficiency; [g] ISC quantum efficiency; [h] RISC quantum efficiency; [i] Radiative decay rate of singlet excitons; [j] ISC rate; [k] RISC rate; [l] Nonradiative rate of triplet excitons. The procedure of determining all the photophysical parameters is described in Section S1 of the Supporting Information.
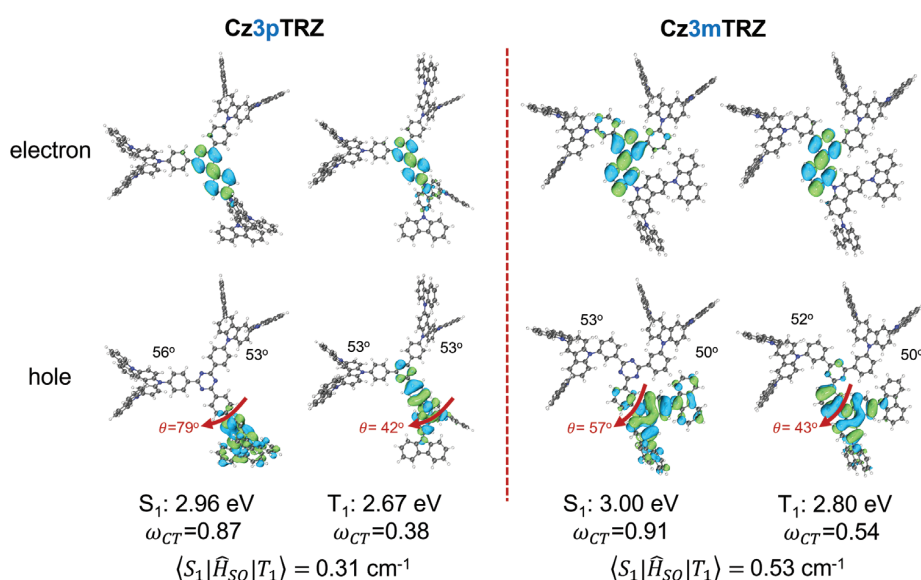
Figure 7. Natural transition orbital (NTO) pairs for the S_1 and T_1 states of **Cz3pTRZ** and **Cz3mTRZ**. The spin–orbit coupling (SOC) matrix elements are also provided.

(ΔE_{ST} = 200 meV; S_1 = 3.00 eV, T_1 = 2.80 eV), in qualitative agreement with the experimentally determined singlet–triplet gaps; however, the computed ΔE_{ST} values are larger than the experimental values due to the fact that the M06-2X functional overestimates the singlet state energies.

Experimentally, it was found that the adiabatic ΔE_{ST} for **tBuCz3mTRZ** (80 meV) is smaller than that of **tBuCz3pTRZ** (100 meV). According to the Boltzmann distribution, this ΔE_{ST} difference can lead to a 40% (1.4 times) enhancement of RISC in **tBuCz3mTRZ** as compared to **tBuCz3pTRZ** and thus, the ΔE_{ST} difference alone is not sufficient to explain the observed differences in k_{RISC} for *meta-* versus *para*-linked dendrimers. However, when the ΔE_{ST} values are similar, even a few tenths of cm^{-1} in-crease in the SOC matrix element can lead to a considerable enhancement of the RISC rate.[14] We thus calculated the SOC matrix element for the RISC process ($\langle S_1|\hat{H}_{SO}|T_1\rangle$) at the T_1 state geometry, since the initial state for the RISC process is the T_1 state. The calculated SOC matrix element was found to be higher for **Cz3mTRZ** (0.53 cm^{-1}) as compared to **Cz3pTRZ** (0.31 cm^{-1}). Closer consideration of the NTOs at the optimized triplet excited state geometries reveals that for **Cz3mTRZ** there is a change in the orbital character only for the HOMO NTO between S_1 and T_1 due to the reduced conjugation present in **Cz3mTRZ** (while for **Cz3pTRZ** there is a change for both the HOMO and LUMO NTOs), and according to El-Sayed's rule this will lead to larger SOC in **Cz3mTRZ**.

The coupling to the vibrational modes approximated in terms of the Marcus reorganization energy is also an important parameter, as it controls the Franck–Condon-weighted density of states (Equation (2)) and hence the k_{RISC} (Equation (1)). The calculated intramolecular (λ_{intra}) reorganization energy for **Cz3pTRZ** (275 meV) was found to be higher as compared to **Cz3mTRZ** (155 meV). We recall that the S_1 state for both *para-* and *meta-*linked dendrimers is strongly CT in nature and that there is a nearly orthogonal (i.e., $\theta = 79°$) conformation adopted between the donor dendron and the phenylenes. While geometric relaxation from this is restricted in **Cz3mTRZ** because of steric constraints, it is possible for there to be significantly larger changes in dihedral angles in **Cz3pTRZ**. This implies a larger reorganization energy for the $T_1 \rightarrow S_1$ transition in **Cz3pTRZ** as compared to **Cz3mTRZ**.

As a final check, the RISC rates can be calculated within the framework of Equations (1) and (2) using the computed reorganization energies and SOC values along with the experimentally determined ΔE_{ST} values (see Table S5 in the Supporting Information). Ignoring the outer sphere contribution of the surrounding medium to the reorganization energy, the k_{RISC} values are 5.1×10^5 s^{-1} for **Cz3pTRZ** and 9.4×10^6 s^{-1} for **Cz3mTRZ**. By considering an intermolecular reorganization energy (λ_{inter}) value of 300 meV for both **Cz3pTRZ** and **Cz3mTRZ**, this reduces k_{RISC} to 0.2×10^5 s^{-1} for **Cz3pTRZ** and 3.6×10^6 s^{-1} for **Cz3mTRZ**, values that are in excellent agreement with those experimentally determined for **tBuCz3pTRZ** and **tBuCz3mTRZ**. Thus, the smaller ΔE_{ST}, greater SOC and smaller reorganization energy combine to lead to a faster k_{RISC} in **tBuCz3mTRZ** compared to **tBuCz3pTRZ**.

4. Discussion

Based on the photophysical analysis we can conclude that all dendrimers in the doped and neat films exhibit high PLQY. However, the contribution of delayed emission to the total emission and the RISC rate, both being the characteristic of an efficient RISC process and of key importance to OLED operation, are much greater/faster in the case of the *meta*-connected dendrimers. This is consistent with the improved EL performance of the *meta*-dendrimer OLEDs. The ISC rate constant (k_{ISC}) is approximately similar across the series of dendrimers, with slightly lower values for *meta*-connected dendrimers; however, k_{RISC} is several times faster for the *meta*-connected dendrimers. Though this is the first report where *meta*-connected dendrimers have been reported, the impact of the substitution pattern of donors with respect to the acceptor on the TADF properties has been studied extensively for small molecules.[9] The OLEDs employing the *meta*-isomers often exhibit higher EQEs than the devices with the *para*-isomer.[17] This improvement has been ascribed to the reduced conjugation between donor and acceptor units and thus reduced ΔE_{ST}. Recently, we also underlined the role of *meta*-linkage in reducing the conjugation between the donor and acceptor units.[18]

In the present work as well, the extinction coefficient of the ^{1}CT state decreases by an order of magnitude when the more conjugated *para*-connection is replaced by the less conjugated *meta*-connection (Figure 3b). This is also evident from the anti-Kasha emission in *meta*-dendrimers (Figure 3c) arising from the slow charge transfer from the ^{1}LE to the ^{1}CT state owing to the weaker conjugation in *meta*-connected dendrimers as compared to the
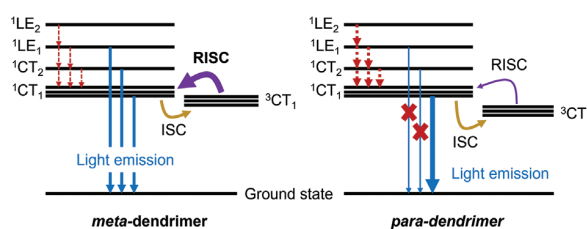
Figure 8. Jablonski diagram describing the dual CT/LE emission (blue solid), internal conversion (red dot), intersystem crossing (yellow solid), reverse intersystem crossing (purple solid) processes for *meta-/para-*dendrimers. The thicker arrow lines indicate a faster rate of corresponding process while thinner arrow lines indicate a slower rate of the corresponding process.

para-connected dendrimer. However, the reduction in conjugation and the associated decrease in ΔE_{ST} alone cannot explain the increase in k_{RISC} rate in going from *para*- to *meta*-connected dendrimers. Penfold, Monkman and coworkers advanced that the nonadiabatic (vibronic) coupling between a ^{3}CT state and a higher-lying ^{3}LE state can promote RISC to the ^{1}CT state.[13] However, this mechanism is not operational in the dendrimers in this study as these LE T_n states are too destabilized to be implicated in any significant fashion to the RISC process.

Nevertheless, it is worth recalling that there are other factors within the first order perturbation theory (Equations (1) and (2)) that can be considered in the chemical design other than ΔE_{ST}, these include the SOC matrix element for the RISC process ($\langle S_1 | \hat{H}_{SO} | T_1 \rangle$) and the reorganization energy (λ). Though the molecular design of donor-acceptor TADF emitters has most often focused on either the minimization the ΔE_{ST} or the enhancement of the SOC for the $T_1 \rightarrow S_1$ transition, the role of λ has been frequently overlooked. Furthermore, from a chemical design perspective, optimizing these parameters (ΔE_{ST}, SOC, and λ) should be easier than optimizing the $T_n - T_1$ gap. Increasing RISC is the central issue for TADF emitters and, as discussed above, *meta*-connection dendrimers possess several design advantages over *para*-connection dendrimer with respect to enhancing RISC. We emphasize that the change in geometry between T_1 and S_1 is an important parameter, especially in the case of bulky dendrimer systems and can be used as a general design principle.

The results inspired us to further improve the design of TADF dendrimers in related study[10] by combining the advantages of *para*- and *meta*-connected dendrimers as illustrated in **Figure 8**. Through the introduction of both *para*- and *meta*-connected donor dendrons about the triazine acceptor, the dendrimer **tBuCz2m2pTRZ** was then found to not only inherit a high RISC rate, large oscillator strength, but also shows a desired suppressed concentration quenching as evident by the improved OLED performance.[10]

5. Conclusions

In summary, highly efficient TADF dendrimers were developed with a strategy of weak conjugation between the multiple donor dendrons and the TRZ acceptor. This design affords an extremely efficient utilization of triplet excitons because of a vanishing singlet–triplet splitting energy, which is critical to determine the efficiency of TADF materials. From our thorough investigation

**ADVANCED
SCIENCE NEWS**

www.advancedsciencenews.com

**ADVANCED
SCIENCE**
Open Access

www.advancedscience.com

of the dendrimer photophysical properties in toluene solution, we were able to reveal the origin and nature of the lowest excited states. Investigations in the solid state revealed that better TADF properties are obtained for the *meta*-linked dendrimers when compared to the *para*-linked dendrimers, thus demonstrating the validity of this design strategy for a highly efficient TADF dendrimer by combining the feature of multiple donors, weak conjugated connection, and dendritic structure. Although both *meta*- and *para*-linked dendrimers possess small ΔE_{ST} values, normally implying similar k_{RISC} given the similar molecular structures, what the present study reveals is that the reorganization energy can play an important role in enhancing k_{RISC}, and that this can be modulated as a function of the donor dendron substitution pattern about the central triazine acceptor.

6. Experimental Section

Synthesis: The procedures for the synthesis of the TADF dendrimer and the corresponding characterization are reported in the Supporting Information.

Theoretical Calculations: The ground state geometries of the para and meta-connected compounds were optimized in the gas phase using density functional theory at the M06-2X/6-31G(d,p) level of theory.[19] Subsequently, the first singlet and triplet excited state geometries were optimized through linear response time-dependent density functional theory at the M06-2X/6-31G(d,p) level within the Tamm–Dancoff approximation (TDA).[20] It was found previously that the M06-2X exchange-correlation functional provides a good description of the excited states in carbazole-triazine bipolar host compounds.[18] Calculations were performed using the Gaussian 09 software.[21] Electron–hole natural transition orbitals were computed using the Multiwfn software.[22] The nature of the charge-transfer character of the transitions was further quantified in terms of charge transfer numbers ω_{CT} computed by a transition density matrix analysis[23] based on a defragmentation of the molecules in donor and acceptor units. Internal, structural reorganization energies λ of the compounds for the reverse intersystem crossing $T_1 \rightarrow S_1$ were computed by evaluating the total energy difference between the singlet state at the optimized T_1 geometry and the singlet state at the optimized S_1 geometry, i.e., $\lambda = E_{S1}(T_1) - E_{S1}(S_1)$.

The spin–orbit coupling elements for reverse intersystem crossing between the lowest triplet (T_1) and singlet (S_1) electronic states were computed at the relaxed T_1 geometries within the TDA by employing the one-electron Breit Pauli Hamiltonian. Spin–orbit coupling calculations were performed using the Q-Chem 5.2 software.[24]

Photophysical Characterization: For steady-state emission studies, degassed solutions were prepared via three freeze–pump–thaw cycles and spectra were taken using home-made Schlenk quartz cuvette. Steady-state spectra were recorded at room temperature using an Edinburgh Instruments F980 fluorimeter. Samples were excited at 340 nm for steady-state measurements.

For time-resolved PL measurements, the solution was prepared by dissolving the dendrimers into toluene at a concentration of 3×10^{-5} M, then heated and sonicated the solution before measurement. Thin film was prepared by spin-coating a solution of 10 wt% dendrimer in mCP at 2000 rpm on a quartz substrate. The solution for spin-coating was prepared by dissolving the dendrimer and mCP in chloroform, and then filtered using a syringe filter. The time-resolved PL measurements of the thin films and solutions were carried out using an iCCD camera by exponentially increasing delay and gating times where gating time is kept lower by 10 times compared to the delay time. The samples and cuvettes were kept in a continuous flow He-cryostat with temperature controller. They were excited at 355 nm by a lamp-pumped Nd:YAG laser (Innolas SpitLight 600). Emission from the samples was focused onto a spectrograph (Oriel MS257) and detected on a gated iCCD camera (iStar A-DH334T-18F-03). The mea-surements were recorded under He exchange gas unless otherwise stated. Solution PLQY measurements were obtained using a Jasco FP-8600 spectrofluorometer for excitation at 325 nm.

OLED Fabrication: The OLED devices were fabricated in bottom-emitting architecture. A prepatterned indium tin oxide (ITO) glass substrate was used as the anode. PEDOT: PSS8000 was spin-coated on the clean ITO substrate as the hole-injection layer and then thermally annealed at 140 °C for 1 h before transferred to a glovebox. The emitting layer (EML) was formed by spin-coating the dendrimer from chlorobenzene solution with a concentration of 10 mg mL^{-1}. TmPyPB, LiF and Al were then vacuum-deposited on EML subsequently in a vacuum chamber. Detailed operation and characterization are reported in the Supporting Information.

Supporting Information

Supporting Information is available from the Wiley Online Library or from the author.

Conflict of Interest

Dr. Dianming Sun and Prof. Eli Zysman-Colman are the co-inventors of a patent, PCT/GB2021/052844, based on the materials in this manuscript.

Data Availability Statement

The research data supporting this publication can be accessed at https://doi.org/10.17630/1c0258ff-02d5-4332-a0a3-6acdc0892eb2.

**ADVANCED
SCIENCE NEWS**

www.advancedsciencenews.com

**ADVANCED
SCIENCE**
Open Access

www.advancedscience.com

[1] a) Y. Tao, K. Yuan, T. Chen, P. Xu, H. Li, R. Chen, C. Zheng, L. Zhang, W. Huang, *Adv. Mater.* **2014**, *26*, 7931; b) Y. Im, M. Kim, Y. J. Cho, J.-A. Seo, K. S. Yook, J. Y. Lee, *Chem. Mater.* **2017**, *29*, 1946; c) M. Y. Wong, E. Zysman-Colman, *Adv. Mater.* **2017**, *29*, 1605444; d) Y. Xie, Z. Li, *J. Polym. Sci. A: Polym. Chem.* **2017**, *55*, 575; e) Z. Yang, Z. Mao, Z. Xie, Y. Zhang, S. Liu, J. Zhao, J. Xu, Z. Chi, M. P. Aldred, *Chem. Soc. Rev.* **2017**, *46*, 915; f) X. Cai, S. J. Su, *Adv. Funct. Mater.* **2018**, *28*, 1802558; g) X.-K. Chen, D. Kim, J.-L. Brédas, *Acc. Chem. Res.* **2018**, *51*, 2215; h) Y. Liu, C. Li, Z. Ren, S. Yan, M. R. Bryce, *Nat. Rev. Mater.* **2018**, *3*, 18020; i) Y. Zou, S. Gong, G. Xie, C. Yang, *Adv. Opt. Mater.* **2018**, *6*, 1800568; j) S. K. Jeon, H. L. Lee, K. S. Yook, J. Y. Lee, *Adv. Mater.* **2019**, *31*, 1803524; k) S. Y. Byeon, D. R. Lee, K. S. Yook, J. Y. Lee, *Adv. Mater.* **2019**, *31*, 1803714.

[2] A. Endo, M. Ogasawara, A. Takahashi, D. Yokoyama, Y. Kato, C. Adachi, *Adv. Mater.* **2009**, *21*, 4802.

[3] a) Y. Yuan, G. Giri, A. L. Ayzner, A. P. Zoombelt, S. C. Mannsfeld, J. Chen, D. Nordlund, M. F. Toney, J. Huang, Z. Bao, *Nat. Commun.* **2014**, *5*, 3005; b) D. B. Mitzi, L. L. Kosbar, C. E. Murray, M. Copel, A. Afzali, *Nature* **2004**, *428*, 299.

[4] J. Heinzl, C. Hertz, *Advances in Electronics and Electron Physics*, Vol. 65, Elsevier, Amsterdam **1985**, p. 91.

[5] a) C. R. McNeill, N. C. Greenham, *Adv. Mater.* **2009**, *21*, 3840; b) J. L. Brédas, R. R. Chance, *Conjugated Polymeric Materials: Opportunities in Electronics, Optoelectronics, and Molecular Electronics*, Springer Science & Business Media, Berlin, Germany **2012**; c) S.-C. Lo, P. L. Burn, *Chem. Rev.* **2007**, *107*, 1097; d) P. L. Burn, S. C. Lo, I. D. Samuel, *Adv. Mater.* **2007**, *19*, 1675.

[6] a) K. Albrecht, K. Matsuoka, K. Fujita, K. Yamamoto, *Angew. Chem., Int. Ed.* **2015**, *54*, 5677; b) X. Ban, W. Jiang, T. Lu, X. Jing, Q. Tang, S. Huang, K. Sun, B. Huang, B. Lin, Y. Sun, *J. Mater. Chem. C* **2016**, *4*, 8810; c) Y. Li, G. Xie, S. Gong, K. Wu, C. Yang, *Chem. Sci.* **2016**, *7*, 5441; d) J. Luo, S. Gong, Y. Gu, T. Chen, Y. Li, C. Zhong, G. Xie, C. Yang, *J. Mater. Chem. C* **2016**, *4*, 2442; e) K. Albrecht, K. Matsuoka, D. Yokoyama, Y. Sakai, A. Nakayama, K. Fujita, K. Yamamoto, *Chem. Commun.* **2017**, *53*, 2439; f) X. Ban, W. Jiang, K. Sun, B. Lin, Y. Sun, *ACS Appl. Mater. Interfaces* **2017**, *9*, 7339; g) J. Li, X. Liao, H. Xu, L. Li, J. Zhang, H. Wang, B. Xu, *Dyes Pigm.* **2017**, *140*, 79; h) Y. Li, T. Chen, M. Huang, Y. Gu, S. Gong, G. Xie, C. Yang, *J. Mater. Chem. C* **2017**, *5*, 3480; i) K. Matsuoka, K. Albrecht, K. Yamamoto, K. Fujita, *Sci. Rep.* **2017**, *7*, 1; j) K. Sun, D. Chu, Y. Cui, W. Tian, Y. Sun, W. Jiang, *Org. Electron.* **2017**, *48*, 389; k) K. Sun, Y. Sun, T. Huang, J. Luo, W. Jiang, Y. Sun, *Org. Electron.* **2017**, *42*, 123; l) K. Albrecht, K. Matsuoka, K. Fujita, K. Yamamoto, *Mater. Chem. Front.* **2018**, *2*, 1097; m) M. Godumala, S. Choi, H. J. Kim, C. Lee, S. Park, J. S. Moon, K. S.i Woo, J. H. Kwon, M. J. Cho, D. H. Choi, *J. Mater. Chem. C* **2018**, *6*, 1160; n) K. Matsuoka, K. Albrecht, A. Nakayama, K. Yamamoto, K. Fujita, *ACS Appl. Mater. Interfaces* **2018**, *10*, 33343; o) D. Liu, W. Tian, Y. Feng, X. Zhang, X. Ban, W. Jiang, Y. Sun, *ACS Appl. Mater. Interfaces* **2019**, *11*, 16737; p) X. Wang, S. Wang, J. Lv, S. Shao, L. Wang, X. Jing, F. Wang, *Chem. Sci.* **2019**, *10*, 2915.

[7] a) R. Saxena, T. Meier, S. Athanasopoulos, H. Bässler, A. Köhler, *Phys. Rev. Appl.* **2020**, *14*, 034050; b) M. Jakoby, S. Heidrich, L. Graf von Reventlow, C. Degitz, S. M. Suresh, E. Zysman-Colman, W. Wenzel, B. S. Richards, I. A. Howard, *Chem. Sci.* **2021**, *12*, 1121.

[8] X. Cai, D. Chen, K. Gao, L. Gan, Q. Yin, Z. Qiao, Z. Chen, X. Jiang, S. J. Su, *Adv. Funct. Mater.* **2017**, *28*, 1704927.

[9] F.-M. Xie, J.-X. Zhou, Y.-Q. Li, J.-X. Tang, *J. Mater. Chem. C* **2020**, *8*, 9476.

[10] D. Sun, E. Duda, X. Fan, R. Saxena, M. Zhang, S. Bagnich, X. Zhang, A. Köhler, E. Zysman-Colman, *Adv. Mater.* **2022**, http://doi.org/10.1002/adma.202110344.

[11] S. A. Bagnich, A. Rudnick, P. Schroegel, P. Strohriegl, A. Köhler, *Philos. Trans. R. Soc. A* **2015**, *373*, 20140446.

[12] K. Tani, Y. Tohda, H. Takemura, H. Ohkita, S. Ito, M. Yamamoto, *Chem. Commun.* **2001**, 1914.

[13] a) J. Gibson, T. J. Penfold, *Phys. Chem. Chem. Phys.* **2017**, *19*, 8428; b) F. B. Dias, J. Santos, D. R. Graves, P. Data, R. S. Nobuyasu, M. A. Fox, A. S. Batsanov, T. Palmeira, M. N. Berberan-Santos, M. R. Bryce, A. P. Monkman, *Adv. Sci.* **2016**, *3*, 1600080; c) J. Gibson, A. P. Monkman, T. J. Penfold, *ChemPhysChem* **2016**, *17*, 2956; d) X.-K. Chen, S.-F. Zhang, J.-X. Fan, A.-M. Ren, *J. Phys. Chem. C* **2015**, *119*, 9728; e) M. K. Etherington, J. Gibson, H. F. Higginbotham, T. J. Penfold, A. P. Monkman, *Nat. Commun.* **2016**, *7*, 13680.

[14] P. K. Samanta, D. Kim, V. Coropceanu, J.-L. Brédas, *J. Am. Chem. Soc.* **2017**, *139*, 4042.

[15] a) L. Wang, Q. Ou, Q. Peng, Z. Shuai, *J. Phys. Chem. A* **2021**, *125*, 1468; b) I. E. Serdiuk, M. Mońka, K. Kozakiewicz, B. Liberek, P. Bojarski, S. Y. Park, *J. Phys. Chem. B* **2021**, *125*, 2696.

[16] J. Jortner, *J. Chem. Phys.* **1976**, *64*, 4860.

[17] a) X. Lv, W. Zhang, D. Ding, C. Han, Z. Huang, S. Xiang, Q. Zhang, H. Xu, L. Wang, *Adv. Opt. Mater.* **2018**, *6*, 1800165; b) T. Matulaitis, P. Imbrasas, N. A. Kukhta, P. Baronas, T. Bučiūnas, D. Banevičius, K. Kazlauskas, J. V. Gražulevičius, S. Juršėnas, *J. Phys. Chem. C* **2017**, *121*, 23618; c) D. Karthik, S. Y. Lee, D. H. Ahn, H. Lee, J. Y. Lee, J. H. Kwon, J. H. Park, *Org. Electron.* **2019**, *74*, 282.

[18] F. Rodella, S. Bagnich, E. Duda, T. Meier, J. Kahle, S. Athanasopoulos, A. Köhler, P. Strohriegl, *Front. Chem.* **2020**, *8*, 657.

[19] a) Y. Zhao, D. G. Truhlar, *Theor. Chem. Acc.* **2008**, *120*, 215; b) W. J. Hehre, R. Ditchfield, J. A. Pople, *J. Chem. Phys.* **1972**, *56*, 2257; c) P. C. Hariharan, J. A. Pople, *Theor. Chim. Acta* **1973**, *28*, 213; d) R. Ditchfield, W. J. Hehre, J. A. Pople, *J. Chem. Phys.* **1971**, *54*, 724.

[20] S. Hirata, M. Head-Gordon, *Chem. Phys. Lett.* **1999**, *314*, 291.

[21] M. J. Frisch, G. W. Trucks, H. B. Schlegel, G. E. Scuseria, M. A. Robb, J. R. Cheeseman, G. Scalmani, V. Barone, B. Mennucci, G. A. Petersson, H. Nakatsuji, M. Caricato, X. Li, H. P. Hratchian, A. F. Izmaylov, J. Bloino, G. Zheng, J. L. Sonnenberg, M. Hada, M. Ehara, K. Toyota, R. Fukuda, J. Hasegawa, M. Ishida, T. Nakajima, Y. Honda, O. Kitao, H. Nakai, T. Vreven, J. J. A. Montgomery, et al., *Gaussian 09, Revision D.01*, Gaussian, Inc, Wallingford, CT **2013**.

[22] T. Lu, F. Chen, *J. Comput. Chem.* **2012**, *33*, 580.

[23] F. Plasser, *J. Chem. Phys.* **2020**, *152*, 084108.

[24] Y. Shao, Z. Gan, E. Epifanovsky, A. T. B. Gilbert, M. Wormit, J. Kussmann, A. W. Lange, A. Behn, J. Deng, X. Feng, D. Ghosh, M. Goldey, P. R. Horn, L. D. Jacobson, I. Kaliman, R. Z. Khaliullin, T. Kuś, A. Landau, J. Liu, E. I. Proynov, Y. M. Rhee, R. M. Richard, M. A. Rohrdanz, R. P. Steele, E. J. Sundstrom, H. L. Woodcock, P. M. Zimmerman, D. Zuev, B. Albrecht, E. Alguire, et al., *Mol. Phys.* **2015**, *113*, 184.

ADVANCED SCIENCE

Open Access

Supporting Information

Regiochemistry of Donor Dendrons Controls the Performance of Thermally Activated Delayed Fluorescence Dendrimer Emitters for High Efficiency Solution-Processed Organic Light-Emitting Diodes

Dianming Sun*, Rishabh Saxena, Xiaochun Fan, Stavros Athanasopoulos, Eimantas Duda, Ming Zhang, Sergey Bagnich, Xiaohong Zhang*, Eli Zysman-Colman* and Anna Köhler*

Supplementary Information

Regiochemistry of Donor Dendrons Controls the Performance of Thermally Activated Delayed Fluorescence Dendrimer Emitters Translating in Their Use in High Efficiency Solution-Processed Organic Light-Emitting Diodes

Dianming Sun[1,2†], Rishabh Saxena[3†], Xiaochun Fan[1], Stavros Athanasopoulos[5], Eimantas Duda[3], Ming Zhang[1], Sergey Bagnich[3], Xiaohong Zhang[1*], Eli Zysman-Colman[2*] and Anna Köhler[3,4*]*

Table of Contents

Synthesis and Characterization

The starting material, **G2tBuCzH** and 2,4,6-tris(3-bromophenyl)-1,3,5-triazine, were synthesized according to literature procedures.[1] All solvents and reagents were obtained from commercial sources and used as received. Air-sensitive reactions were performed under a nitrogen atmosphere using Schlenk techniques, no special precautions were taken to exclude air or moisture during work-up. Anhydrous THF was obtained from a Pure Solv™ solvent purification system (Innovative Technologies). Flash column chromatography was carried out using silica gel (Silia-P from Silicycle, 60 Å, 40-63 μm). Analytical thin-layer-chromatography (TLC) was performed with silica plates with aluminium backings (250 μm with F-254 indicator). TLC visualization was accomplished by 254/365 nm UV lamp. ^{1}H, ^{13}C, ^{19}F and 2D NMR spectra were recorded on a Bruker Advance spectrometer. ^{19}F NMR spectrum was recorded with proton decoupling. ^{1}H and ^{13}C NMR spectra were referenced residual solvent peaks with respect to TMS (δ = 0 ppm). The following abbreviations have been used for multiplicity assignments: "s" for singlet, "d" for doublet, "t" for triplet, "m" for multiplet, and "brs" for broad singlet. Melting points were measured using open-ended capillaries on an Electrothermal melting point apparatus IA9200 and are uncorrected. Matrix Assisted Laser Desorption/Ionization-Time of Flight-Mass Spectrometry (MALDI-TOF-MS) was performed by EPSRC National Mass Spectrometry Service Centre (NMSSC), Swansea. Elemental analyses were performed by Mr. Stephen Boyer, London Metropolitan University. tBuCz3pTRZ was synthesized according to the procedure in the literature.[1a]

Detailed synthetic routes and procedures of the target compounds are outlined as below.
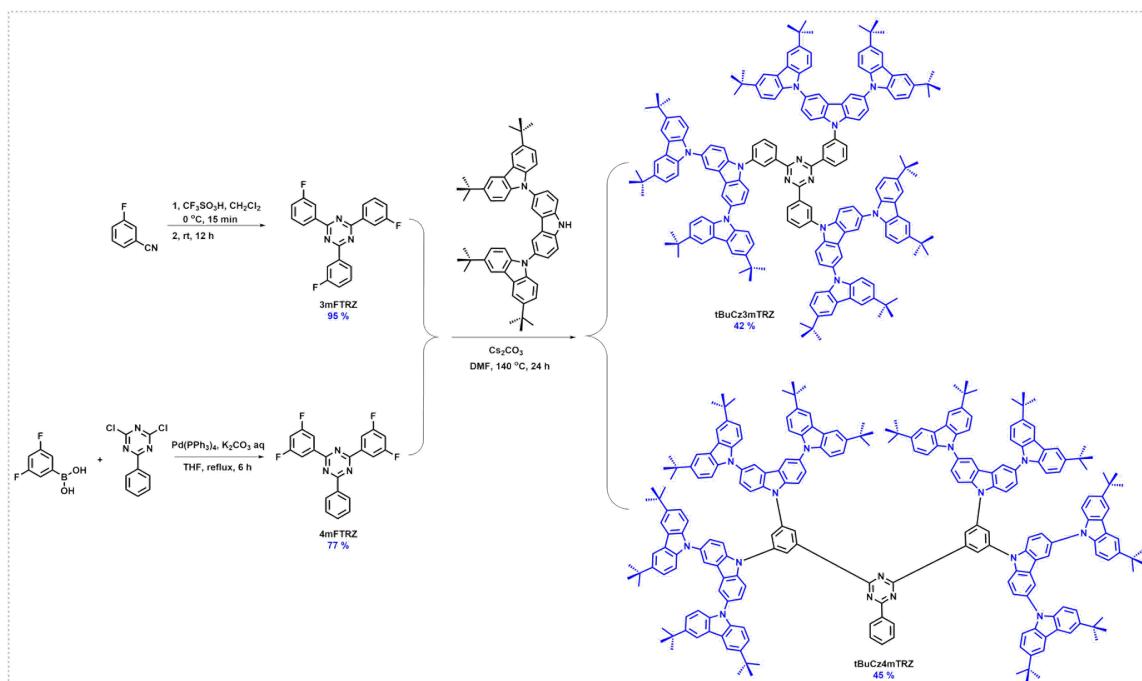
Scheme S1. Synthetic route for **tBuCz3mTRZ** and **tBuCz4mTRZ**.

Synthesis of *2,4-bis(3,5-difluorophenyl)-6-phenyl-1,3,5-triazine* (**4mFTRZ**).

A mixture of (3,5-difluorophenyl)boronic acid (632 mg, 4 mmol，2 equiv.), 2,4-dichloro-6-phenyl-1,3,5-triazine (452 mg, 2 mmol, 1 equiv.) and tetrakis(triphenylphosphine)palladium(0) (115 mg, 0.1 mmol, 0.25 equiv.) in degassed THF (20 mL), and 2M K_2CO_3 (5 mL) aqueous solution was refluxed for 12 h. After cooling to room temperature, the resulting precipitate was filtered and washed with both THF and DCM (each 3×20 mL). Then the collected precipitate was dried in a desiccator to afford a white solid (590 mg). **Yield**: 77%. **R_f**: 0.45 (Hexane: DCM=2:1 on silica plate). **Mp**: decomposes before melting. **^{1}H NMR (400 MHz, d_6-DMSO) δ (ppm)**: 8.84 (d, J=7 Hz, 2H), 8.49 (d, J=8 Hz, 4H), 7.76 (t, J=7 Hz, 1H), 7.68 (t, J=8 Hz, 4H). **^{19}F NMR (376 MHz, d_6-DMSO) δ (ppm)**: -108.46. **Anal. Calcd. For $C_{21}H_{11}F_4N_3$ (%)**: C 66.14, H 2.91, N 11.02; **Found**: C 66.32, H 2.88, N 10.76.

Synthesis of *2,4,6-tris(3-(3,3'',6,6''-tetra-tert-butyl-9'H-[9,3':6',9''-tercarbazol]-9'-yl)phenyl)-1,3,5-triazine* (**tBuCz3mTRZ**).

A mixture of 3,3'',6,6''-tetrakis(*tert*-butyl-9'H-9,3':6',9''-tercarbazole) (**G2tBuCzH**) (1.19 g, 1.65 mmol, 3.3 equiv.), 2,4,6-tris(3-bromophenyl)-1,3,5-triazine (273 mg, 0.5 mmol, 1 equiv.), tetrakis(triphenylphosphine)palladium(0) (67 mg, 0.075 mmol, 0.15 equiv.), Xphos (72 mg, 0.15 mmol, 0.3 equiv.) and sodium *tert*-butoxide (432 mg, 4.5 mmol, 9 equiv.) in degassed anhydrous toluene (40 mL) was refluxed for 24 h. After cooling to room temperature, the mixture was filtered and washed with both brine and DCM (each 3×20 mL). The combined organic layers were dried with anhydrous sodium sulphate and concentrated under reduced pressure. The crude mixture was purified by silica gel flash column chromatography using hexane: DCM = 20: 1 as eluent to afford the desired compound as a green solid (950 mg). **Yield**: 77%. **R$_f$:** 0.4 (hexane: DCM = 2:1 on silica plate). **Mp**: no melting point was observed within the temperature range of 20 °C to 350 °C. **^{1}H NMR (400 MHz, Chloroform-*d*)**: δ 9.22 (t, J = 1.9 Hz, 3H), 9.00 (dt, J = 7.8, 1.4 Hz, 3H), 8.36 – 8.27 (m, 6H), 8.22 – 8.14 (m, 12H), 8.04 (ddd, J = 7.9, 2.2, 1.3 Hz, 3H), 7.97 (t, J = 7.8 Hz, 3H), 7.78 – 7.71 (m, 6H), 7.68 (dd, J = 8.7, 2.0 Hz, 6H), 7.47 (dd, J = 8.7, 1.9 Hz, 12H), 7.38 (dd, J = 8.5, 0.7 Hz, 12H), 1.48 (s, 108H). **^{13}C NMR (101 MHz, CDCl3)**: δ 171.62, 142.63, 140.10, 138.07, 131.76, 131.21, 130.94, 128.90, 127.91, 126.17, 124.14, 123.61, 123.17, 119.43, 116.28, 111.09, 109.07, 79.27, 76.91, 76.72, 34.75, 32.06. **MALDI-TOF-MS** (m/z): [M]$^+$ Calculated: 2468.40, Found: 2468.36. **Anal. Calcd. For C$_{177}$H$_{174}$N$_{12}$ (%)**: C, 86.09; H, 7.10; N, 6.81; **Found**: C, 86.01; H, 7.03; N, 6.81.

Synthesis of *9',9'''',9'''''''',9''''''''''''-((6-phenyl-1,3,5-triazine-2,4-diyl)bis(benzene-5,1,3-triyl))tetrakis(3,3'',6,6''-tetra-tert-butyl-9'H-9,3':6',9''-tercarbazole)* (**tBuCz4mTRZ**).

Under nitrogen, a mixture of 3,3'',6,6''-tetrakis(*tert*-butyl-9'H-9,3':6',9''-tercarbazole) (**G2tBuCzH**) (794 mg, 1.1 mmol, 4.4 equiv.), 2,4-bis(3,5-difluorophenyl)-6-phenyl-1,3,5-triazine (95 mg, 0.25 mmol, 1 equiv.) and cesium carbonate (652 mg, 2 mmol, 8 equiv.) in dry DMF (20 ml) was reflux for 24 h. After cooling to room temperature, the reaction was extracted with chloroform and washed with water (3×30 mL). The organic phase was dried over Na_2SO_4 and concentrated under reduced pressure. The crude product was purified by column chromatography on silica gel using 1:10 dichloromethane/hexane as eluent and then further purification was performed with preparative GPC column using THF as eluent to afford a yellow solid (360 mg). **Yield**: 45%. **R$_f$**: 0.35 (Hexane: DCM=2:1 on silica plate). **Mp**: no melting point was observed within the temperature range of 20 ºC to 350 ºC. **^{1}H NMR (400 MHz, Chloroform-*d*)**: δ 9.35 (d, J = 2.0 Hz, 4H), 8.93 – 8.87 (m, 2H), 8.44 (t, J = 2.0 Hz, 2H), 8.35 – 8.28 (m, 8H), 8.16 (dd, J = 1.9, 0.7 Hz, 16H), 7.96 – 7.87 (m, 8H), 7.72 (dd, J = 8.7, 2.0 Hz, 9H), 7.69 – 7.61 (m, 2H), 7.41 (dd, J = 8.7, 1.9 Hz, 16H), 7.34 (dd, J = 8.6, 0.6 Hz, 16H), 1.44 (s, 144H). **^{13}C NMR (101 MHz, CDCl$_3$)**: δ 142.71, 140.09, 139.97, 131.77, 126.37, 124.51, 123.62, 123.21, 119.58, 116.29, 111.00, 108.99, 77.35, 77.04, 76.72, 34.72, 32.02. **MALDI-TOF-MS** (m/z): [M]$^+$ Calculated: 3189.44, Found: 3189.43. **Anal. Calcd. For C$_{229}$H$_{227}$N$_{15}$ (%)**: C, 86.24; H, 7.17; N, 6.59; **Found**: C, 86.11; H, 7.04; N, 6.57.

Electrochemistry measurements

Cyclic Voltammetry (CV) analysis was performed on an Electrochemical Analyzer potentiostat model 620E from CH Instruments at a sweep rate of 100 mV/s. Differential pulse voltammetry (DPV) was conducted with an increment potential of 0.004 V and a pulse amplitude, width, and period of 50 mV, 0.05, and 0.5 s, respectively. Samples were prepared as dimethylformamide (DMF) solutions, which were degassed by sparging with DMF-saturated argon gas for 5 minutes prior to measurements. All measurements were performed using 0.1 M DMF solution of tetra-*n*-butylammonium hexafluorophosphate, [*n*Bu$_4$N]PF$_6$]. An Ag/Ag$^+$ electrode was used as the reference electrode while a glassy carbon electrode and a platinum wire were used as the working electrode and counter electrode, respectively. The redox potentials are reported relative to a saturated calomel electrode (SCE) with a ferrocenium/ferrocene (Fc/Fc$^+$) redox couple as the internal standard (0.45 V vs SCE).[2]
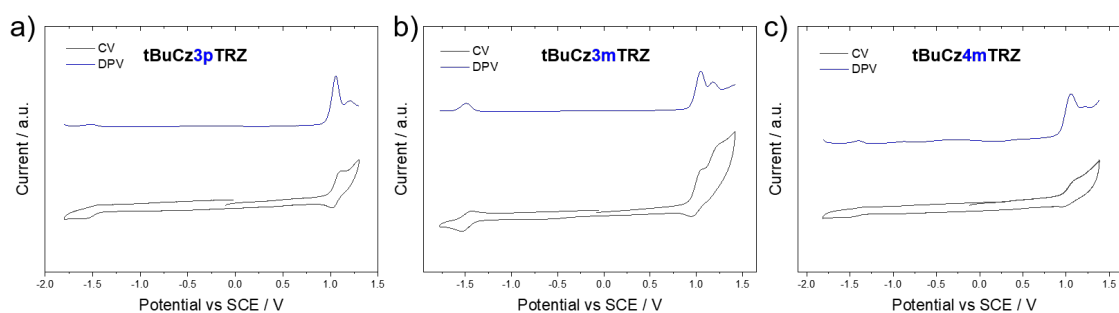
Figure S1. Cyclic voltammogram (CV) and differential pulse voltammetry (DPV) of **tBuCz3pTRZ**, **tBuCz3mTRZ** and **tBuCz4mTRZ** in degassed DMF with 0.1 M [*n*Bu$_4$N]PF$_6$ as the supporting electrolyte and Fc/Fc$^+$ as the internal reference (0.45 V vs SCE).[2]

198

Table S1. Summary of literature-reported solution-processed non-doped OLED performance with TADF dendrimers as emitters.

Emitting layer	Peak [nm]	FWHM [nm]	V_{on} [a] [V]	CE [cd A^{-1}]	PE [lm W^{-1}]	EQE$_{max}$ [%]	EQE$_{100}$ [%]	CIE (x,y)	Max. Luminance [cd m^{-2}]	Ref
G2TAZ	500/-	-/-	3.3/3.7	-/15.6	6/11.5	2.4/6.3	-/6.2	(0.251,0.493)/-	~1000/1243	[3]/[1a]
G3TAZ	515	-	3.5	-	8.5	3.4	-	(0.266,0.485)	~1000	[3]
G4TAZ	510	-	3.5	-	3.1	1.5	-	(0.232,0.368)	~200	[3]
tBuG2TAZ	500	-	3.5	25.4	16.1	9.5	9.4	-	2423	[1a]
PhG2TAZ	500	-	3.2	23.1	17.3	8.2	8.0	-	2316	[1a]
MeG2TAZ	500	-	3.0	26.5	21.5	9.4	9.4	-	2235	[1a]
G2B	500	-	3.4	14.0	11.5	5.7	-	(0.26, 0.48)	~1000	[4]
G3B	516	-	3.7	7.7	5.7	2.9	-	(0.31, 0.50)	~500	[4]
CzDMAC-DPS	502	-	3.6	30.6	24.0	12.2	6.9	(0.22, 0.44)	~2000	[5]
DCzDMAC-DPS	480	-	5.2	3.8	2.0	2.2	1.5	(0.18, 0.27)	~500	[5]
CDE1	552	114	4.4	38.9	17.3	13.8	-	(0.40, 0.54)	~10 000	[6]
CDE2	522	118	7.7	-	-	5.2	-	(0.32, 0.51)	2512	[6]
TZ-Cz	520	-	4.0	20.0	-	6.5	-	(0.24, 0.51)	18 200	[7]
TZ-3Cz	520	-	3.6	30.5	-	10.1	-	(0.24, 0.51)	22 950	[7]
POCz-DPS	480	-	5.4	12.6	-	7.3	-	(0.18, 0.30)	2700	[8]
G-TCTA	550	-	4.4	1.40	0.93	0.50	0.26	(0.46, 0.52)	1200	[9]
G-mCP	550	-	2.7	44.5	46.6	16.5	14.6	(0.42, 0.55)	18 800	[9]
2CzSO	516	96	4.7	-	-	10.7	-	(0.24, 0.49)	4706	[10]
3CzSO	510	90	4.3	-	-	6.3	-	(0.29, 0.52)	3531	[10]
TB2CZ-ACTRZ	520	-	4	30.8	24.2	9.5	-	(0.32, 0.57)	2336	[11]
TB14CZ-ACTRZ	496	-	4.5	20.7	14.5	8.1	-	(0.22, 0.43)	2770	[11]
G2	~430	-	4.8	4.1	1.6	-	-	(0.15, 0.12)	<1000	[12]
G3	~440	-	5.2	1.07	0.49	-	-	(0.19, 0.15)	<1000	[12]
MPPA-Cz	728	-	6.4	-	-	0.064	-	(0.70, 0.29)	24	[13]
MPPA-3Cz	715	-	6.2	-	-	0.254	-	(0.69, 0.30)	135	[13]

Table S2. Electrochemical data and theoretical properties of **tBuCz3pTRZ**, **tBuCz3mTRZ** and **tBuCz4mTRZ**

	Electrochemical potential [a]			Theoretical [e]					
	E_{ox} [b] / V	E_{red} [c] / V	ΔE_{H-L} [d] / V	HOMO / eV	LUMO / eV	f [f]	S_1 / eV	T_1 / eV	ΔE_{ST} / eV
tBuCz3pTRZ	1.06	-1.51	2.57	-5.32	-2.34	0.2533	2.60	2.53	0.07
tBuCz3mTRZ	1.05	-1.49	2.54	-5.29	-2.37	0.0125	2.51	2.46	0.05
tBuCz4mTRZ	1.06	-1.40	2.46	-5.29	-2.52	0.0055	2.38	2.35	0.03

[a] Potential values were obtained from the DPV peak values and referenced with respect to SCE (Fc/Fc$^+$ = 0.45 eV), the measurement was performed in DMF; [b] Oxidation potential calculated from the DPV peak value; [c] Reduction potential calculated from the DPV peak value; [d] $\Delta E_{H-L} = E_{ox}-E_{red}$; [e] Calculated in the gas phase at PBE0/6-31G(d, p) level; [f] Calculated oscillator strength of S_1.

The electrochemical properties of **tBuCz3pTRZ**, **tBuCz3mTRZ** and **tBuCz4mTRZ** were investigated by cyclic voltammetry (CV) and differential pulse voltammetry (DPV) in dimethylformamide (DMF). As shown in **Figure S1**, all dendrimers show two similar irreversible oxidation waves (1.06, 1.21 V for **tBuCz3pTRZ**; 1.05, 1.18 V for **tBuCz3mTRZ**; 1.06, 1.21 V for **tBuCz4mTRZ** according to DPV peak values), which can be ascribed to the hole delocalization over the inner and peripheral carbazoles of the tercarbzole donor dendron unit. The calculated HOMO levels for **tBuCz3pTRZ**, **tBuCz3mTRZ**, and **tBuCz4mTRZ** are -5.41 eV, -5.40 eV and -5.41 eV, respectively, which are very close to the simulated HOMO levels (**Table S2**). The reduction was found to be irreversible as well for all the dendrimers and the LUMOs for **tBuCz3pTRZ**, **tBuCz3mTRZ**, and **tBuCz4mTRZ** were calculated to be -2.84 eV, -2.86 eV, and -2.95 eV respectively, according to the peak value of the DPV.

OLED fabrication and characterization

The OLED devices were fabricated using a bottom-emitting architecture. A pre-patterned indium tin oxide (ITO) glass substrate with a sheet resistance of 15 Ω square^{-1} was pre-cleaned carefully with detergent and deionized water and then exposed to UV-ozone for 15 min. PEDOT:PSS was spin-coated onto the clean ITO substrate as the hole-injection layer, followed by thermal treatment under 120 °C for 30 min. Then a 10 mg/mL chlorobenzene solution of our dendrimers was spin-coated to form a 35-45 nm thick emissive layer (EML) and annealed at 120 °C for 10 min to remove residual solvent before transfer to the vacuum chamber. A 40 nm-thick electron-transporting layer (ETL) of Tm3PyPB was then vacuum deposited at a rate of 1 Å/s, which was controlled *in situ* using quartz crystal monitors. The electron injection layer LiF was deposited at a rate of 0.1 Å/s while the Al cathode was deposited at a rate of 10 Å/s through the shadow mask defining the top electrode. The spatial overlap of the anode and cathode electrodes determined the active area of the OLED, which was estimated to be 4 mm^2. Electroluminescence (EL), CIE color coordinates, and spectra were obtained via a Spectrascan PR655 photometer, and the luminance-current-voltage characteristics were determined with a computer-controlled Keithley 2400 Source meter. EQE was calculated from the current density, luminance, and EL spectrum, assuming Lambertian emission distribution.

Figure S2. Current and power efficiency versus current density curves for **tBuCz3pTRZ** and **tBuCz3pTRZ**.
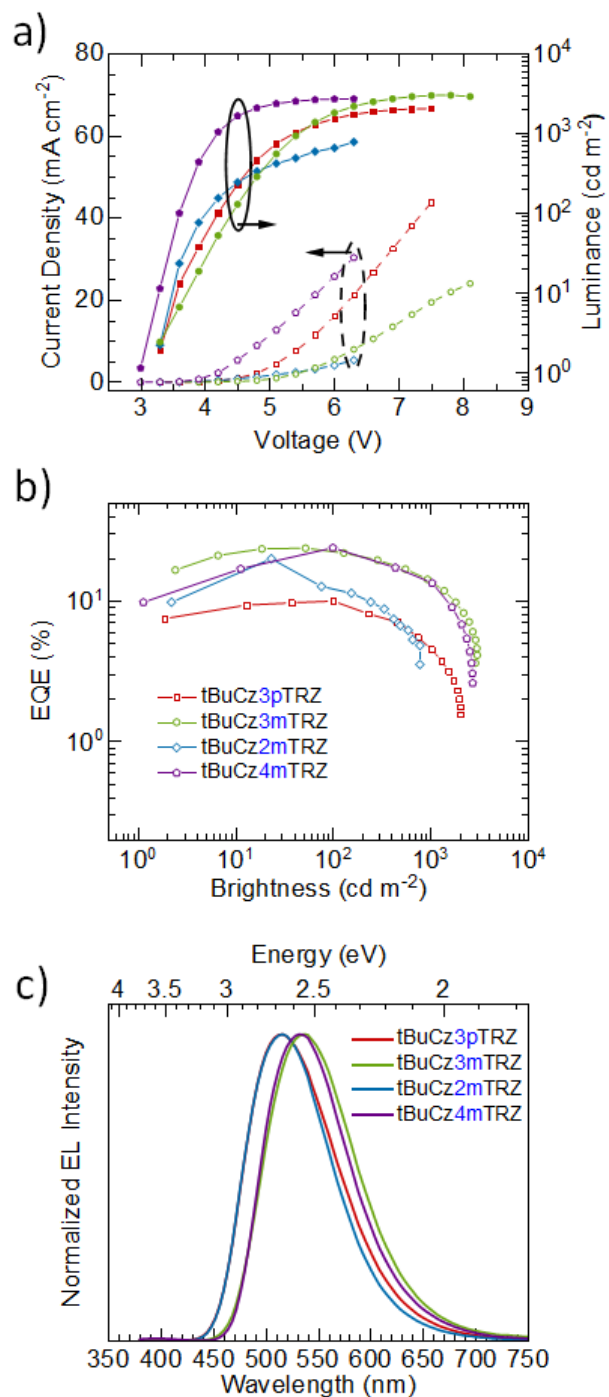
Figure S3. a) Current density-voltage-luminance (J-V-L) curves, b) EQE vs brightness curve and c) electroluminescence (EL) spectra for **tBuCz3pTRZ**, **tBuCz3mTRZ**, **tBuCz2mTRZ** and **tBuCz4mTRZ**.

Table S3. Summary of device performance

Emitting layer [a]	λ_{EL} [b] / nm	FWHM [c] / nm	V_{on} [d] / V	CE [e] / cd A^{-1}	PE [f] / lm W^{-1}	EQE$_{max}$ [g] / %	EQE$_{100}$ [h] / %	EQE$_{500}$ / %	CIE [i] / (x,y)	L$_{max}$ [j] / cd m^{-2}
tBuCz3pTRZ	516	100	3.3	30.0	24.5	10.0	10.0	6.9	0.27, 0.52	2039
tBuCz2mTRZ	516	95	3.3	59.9	52.2	19.9	12.0	6.4	0.27, 0.53	777
tBuCz3mTRZ	536	100	3.3	78.7	61.0	23.7	22.2	17.5	0.35, 0.57	2994
tBuCz4mTRZ	536	93	3.0	81.5	71.1	23.8	23.8	17.0	0.36, 0.58	2691

a) The device structure is: ITO/PEDOT:PSS (35 nm)/ dendrimer (40 nm)/TmPyPB (40 nm)/LiF (1 nm)/ Al (100 nm); b) Emission maximum; c) Full width at half maximum, FWHM; d) turn-on voltage at the luminance of 1 cd m^{-2}; e) Maximum current efficiency; f) Maximum power efficiency; g) Maximum external quantum efficiency; h) At the luminance of 100 cd m^{-2}; i) Commission Internationale de l'Éclairage; j) Maximum luminance.

Photophysical characterization
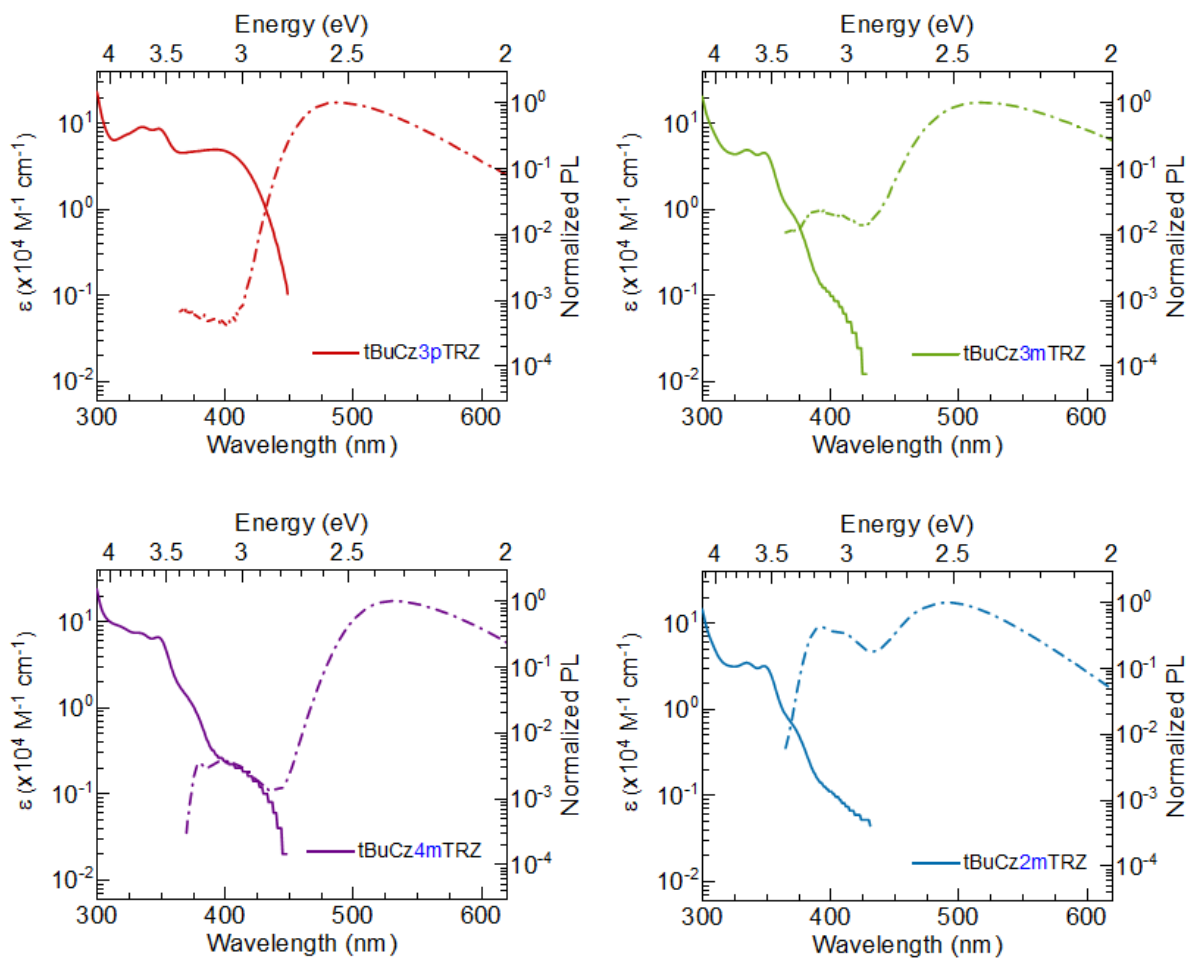
Figure S4. RT molar absorption and emission (λ_{exc} = 300 nm) for the dendrimers under investigation in toluene solution (concentration = 0.05 mg/mL).

Table S4. Summary of PL maxima in solvatochromic study of **tBuCz3pTRZ**, **tBuCz2mTRZ**, **tBuCz3mTRZ** and **tBuCz4mTRZ**

Solvent	λ_{PL} [a] / nm			
	tBuCz3pTRZ	**tBuCz2mTRZ**	**tBuCz3mTRZ**	**tBuCz4mTRZ**
Hexane (Hex)	442	439	483	496
Toluene (Tol)	486	492	517	532
Diethyl ether (Et$_2$O)	517	509	543	541
Ethyl acetate (EA)	558	546	584	569
CH$_2$Cl$_2$	590	574	619	606

[a] Peak value of PL spectra obtained under aerated conditions at 300 K, concentration of 3×10^{-5} M, λ_{exc} = 300 nm.
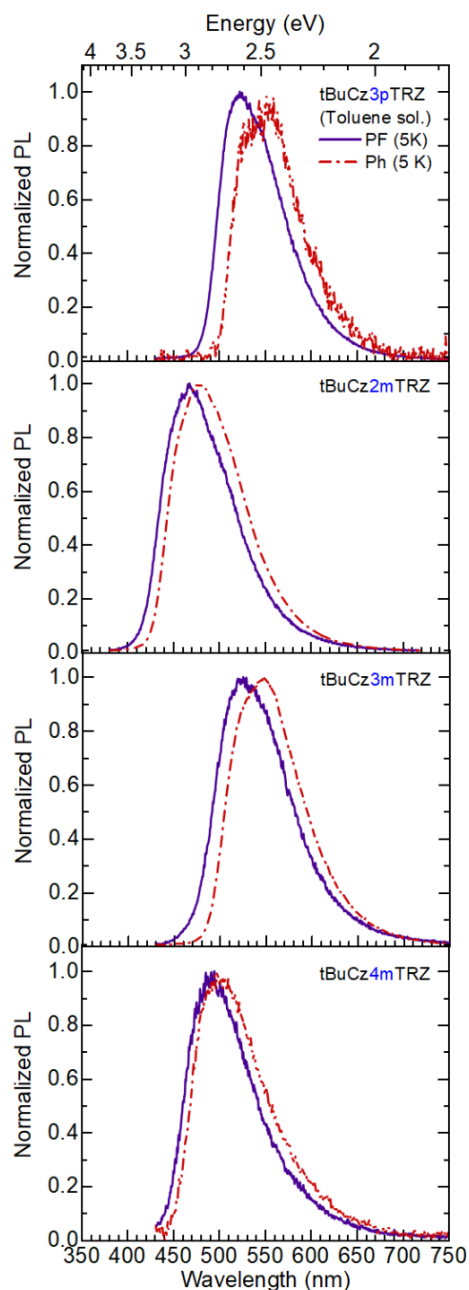
Figure S5. Prompt fluorescence (delay time: 10 ns, gating time: 7 ns) and phosphorescence (delay time: 10 ms, gating time: 1 ms) acquired in toluene glass at 5 K (λ_{exc} = 355 nm). The singlet (triplet) energies at 5 K are determined to be 2.57 eV (2.47 eV), 2.62 eV (2.54 eV), 2.94 eV (2.88 eV) and 2.81 eV (2.76 eV) and, the ΔE_{ST} values are estimated to be 100 meV, 80 meV, 60 meV and 50 meV for **tBuCz3pTRZ**, **tBuCz3mTRZ**, **tBuCz2mTRZ** and **tBuCz4mTRZ**, respectively.

206
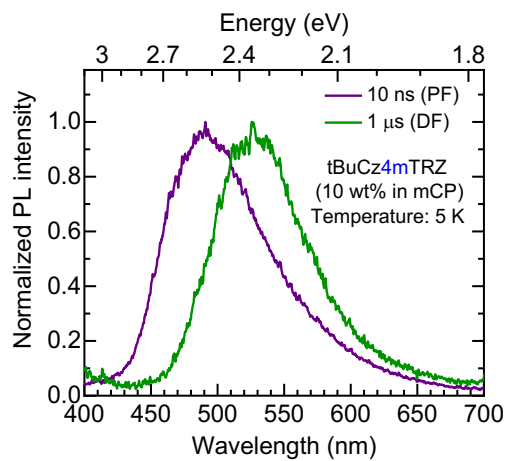
Figure S6. Comparison of prompt fluorescence (PF) and delayed fluorescence (DF) spectra for 10 wt% doped dendrimer films in mCP.
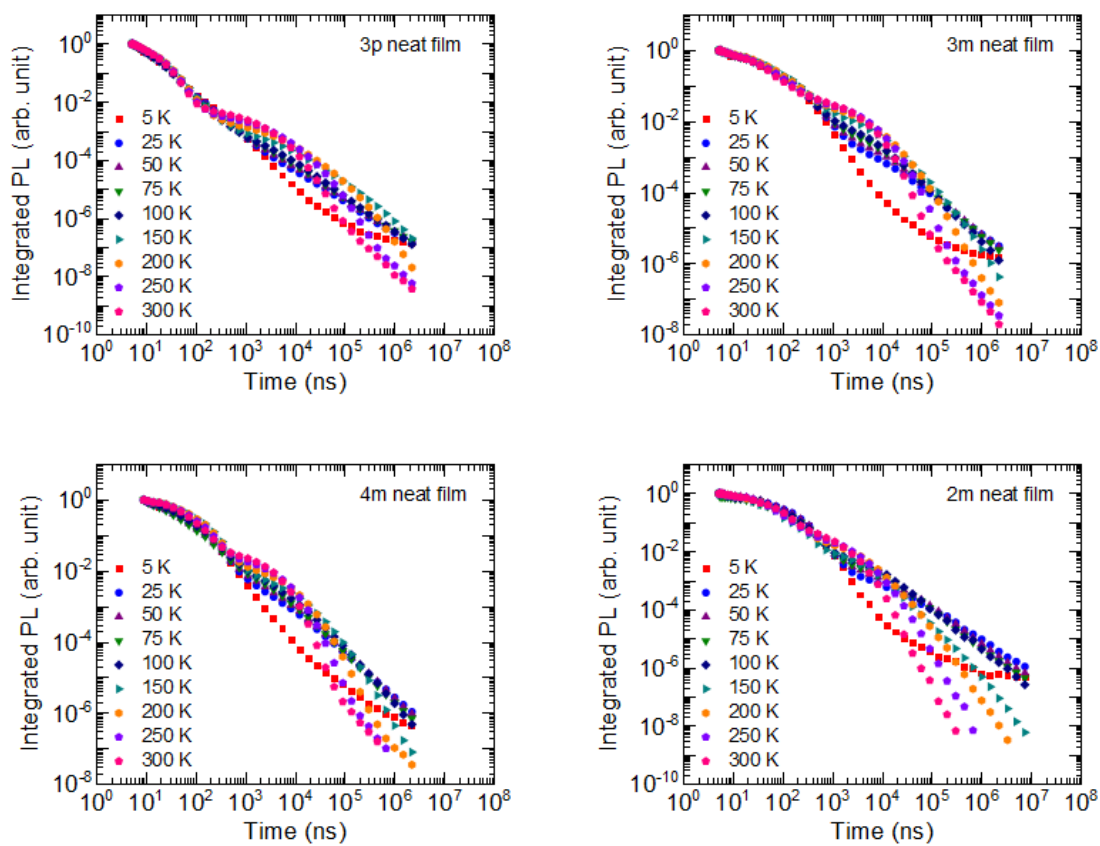
Figure S7. Temperature dependent PL decays of dendrimer neat films.

Determination of photophysical rate constants

- The rate constants were determined according to the method described in literature. [14]

- Prompt lifetime (τ_{PF}) and delayed lifetime (τ_{DF}) were determined from the monoexponential fits of the prompt and delayed components of the PL decay at RT. Photoluminescence quantum efficiency (ϕ_{PL}) was determined under N_2 atmosphere. ϕ_{DF}/ϕ_{PF} was determined from the ratio of the corresponding integrals in the PL decay curves.

- Since, $\phi_{PL} = \phi_{PF} + \phi_{DF} \Rightarrow \phi_{PF} = \dfrac{\phi_{PL}}{1+\phi_{DF}/\phi_{PF}}$ and $\phi_{DF} = \phi_{PL} - \phi_{PF}$.

- Assuming negligible nonradiative singlet decay rate, ISC quantum efficiency, $\phi_{ISC} = 1 - \phi_{PF}$.

- RISC quantum efficiency is then determined as: $\phi_{rISC} = \dfrac{\phi_{DF}}{\phi_{ISC}\,\phi_{PL}}$

- Radiative singlet decay rate, $k_F = \dfrac{\phi_{PF}}{\tau_{PF}}$.

- Intersystem crossing rate, $k_{ISC} = \dfrac{\phi_{ISC}}{\tau_{PF}}$.

- Reverse intersystem crossing rate, $k_{RISC} = \dfrac{1}{\phi_{ISC}\,\tau_{DF}}\left(\dfrac{\phi_{DF}}{\phi_{PF}}\right)$.

- Nonradiative triplet decay rate, $k_{NR}^{T} = \dfrac{k_{rISC}}{\phi_{rISC}} - k_{rISC}$.

Theoretical calculations
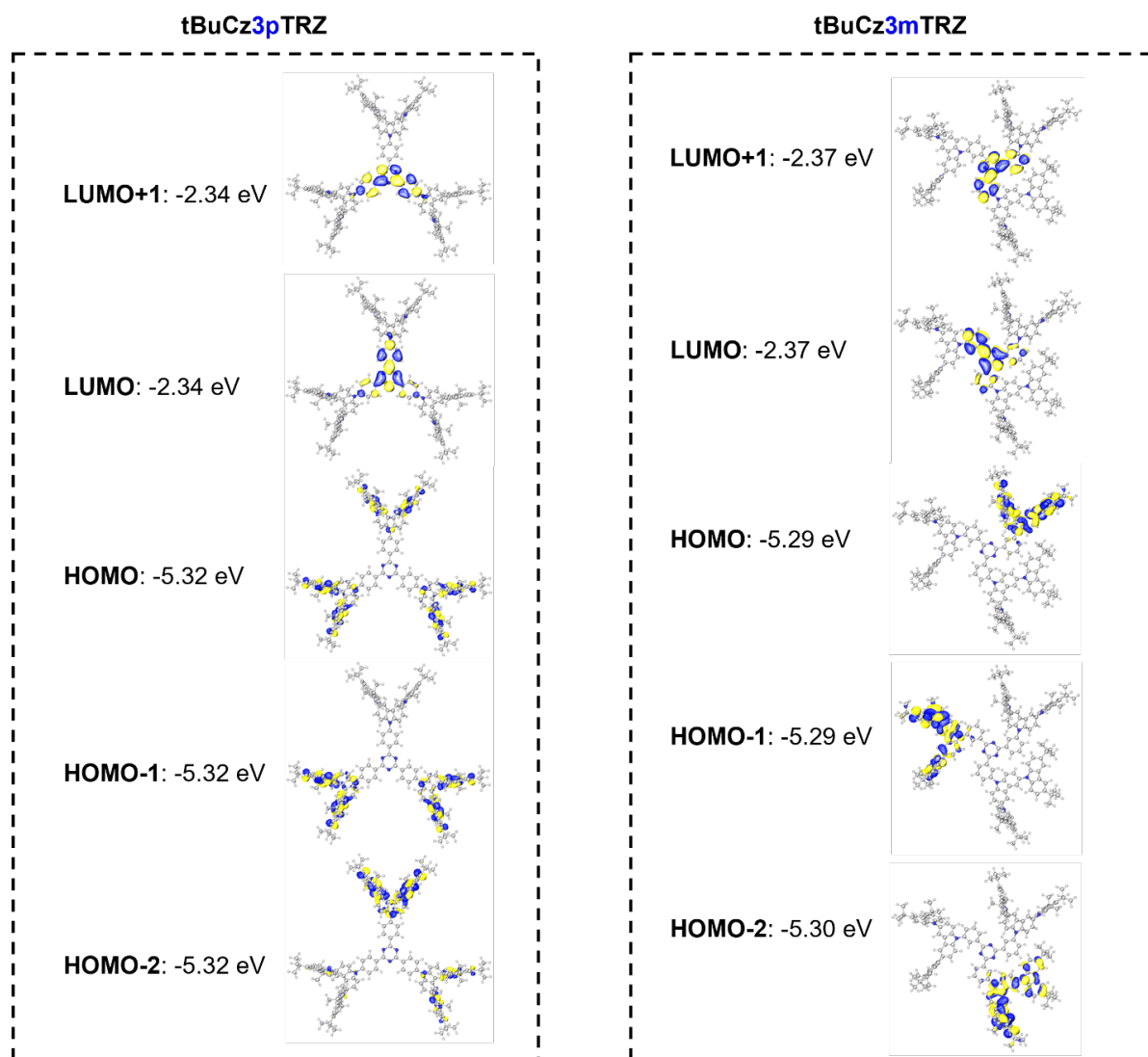
Figure S8. Calculated distribution of molecular orbitals for **tBuCz3pTRZ** and **tBuCz3mTRZ**. (isovalue= 0.02)
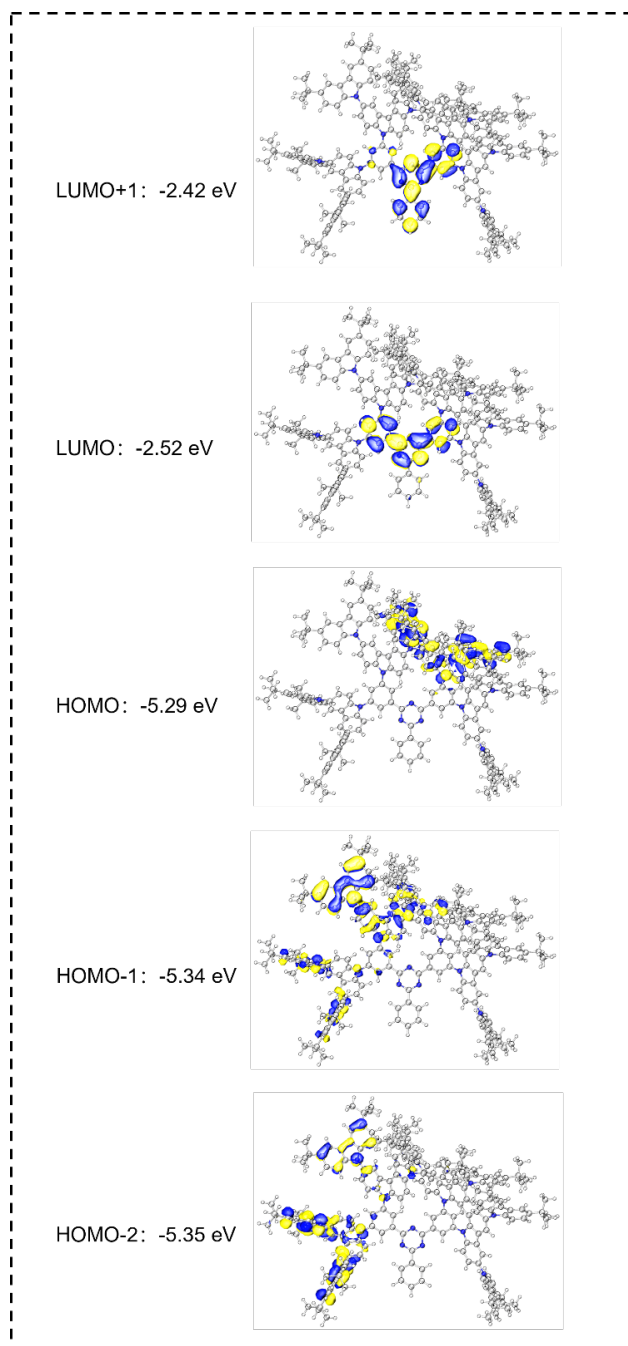
Figure S9. Calculated distribution of molecular orbitals for **tBuCz4mTRZ**. (isovalue= 0.02)
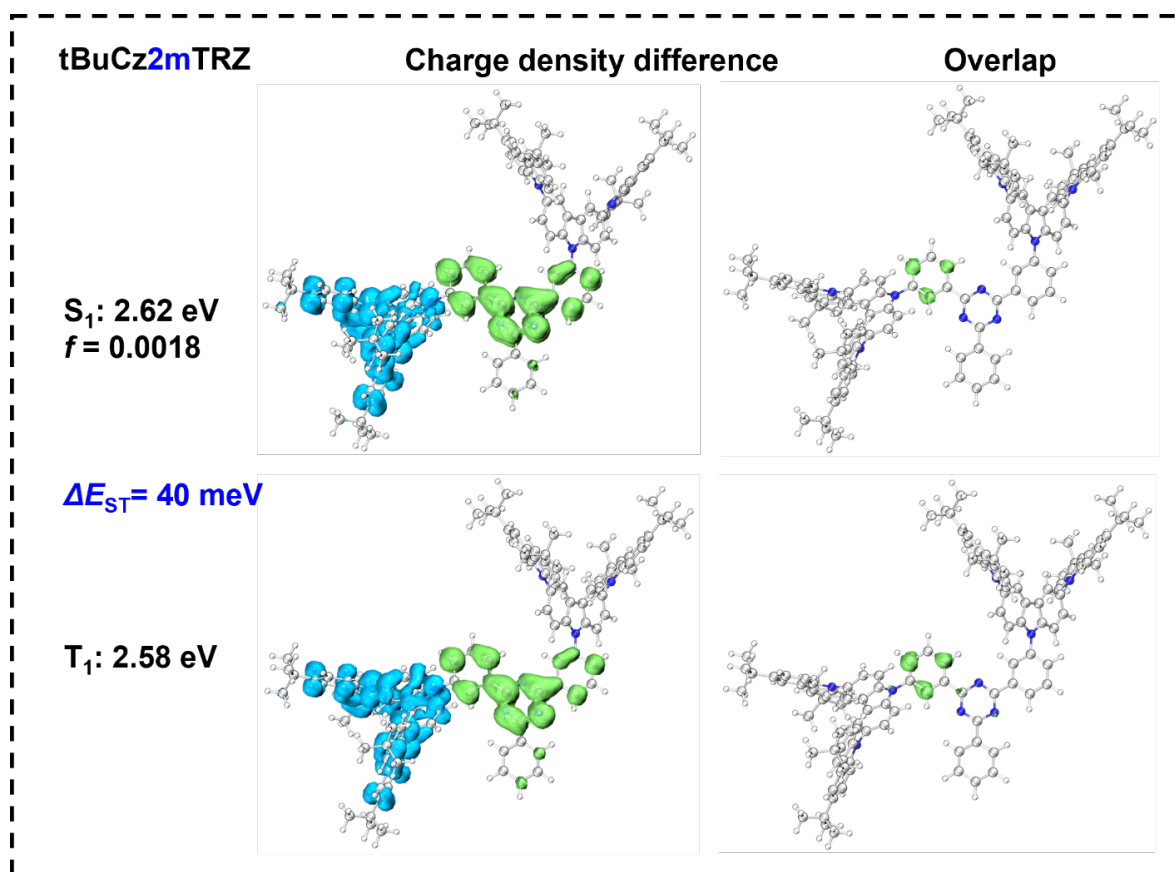
Figure S10. Pictorial representation of charge density difference and overlap of hole and electron for **tBuCz2mTRZ**. *f* indicates the oscillator strength and S_1/ T_1 are the calculated first singlet/ triplet energy. ΔE_{ST} refers to the energy difference between S_1 and T_1. (isovalue= 0.02)

212
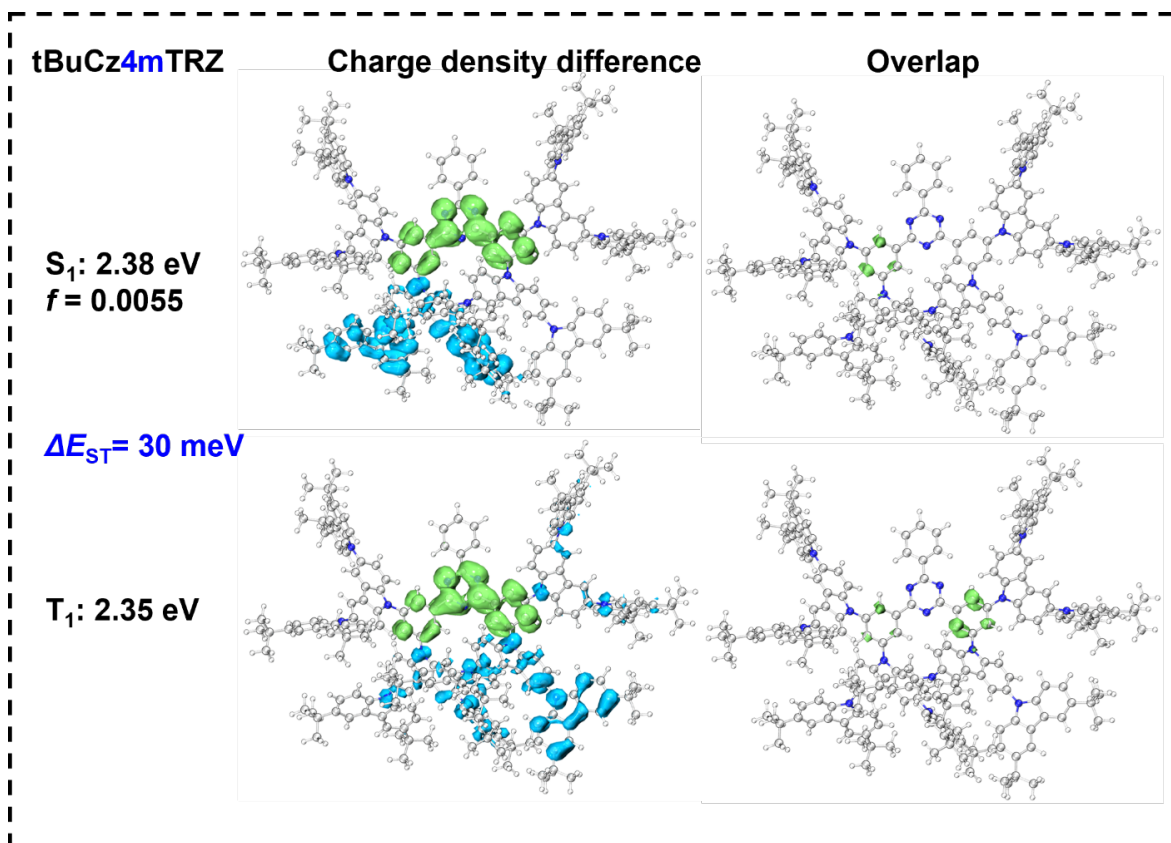
Figure S11. Pictorial representation of charge density difference and overlap of hole and electron for **tBuCz4mTRZ**. f indicates the oscillator strength and S_1/ T_1 are the calculated first singlet/ triplet energy. ΔE_{ST} refers to the energy difference between S_1 and T_1. (isovalue= 0.02)
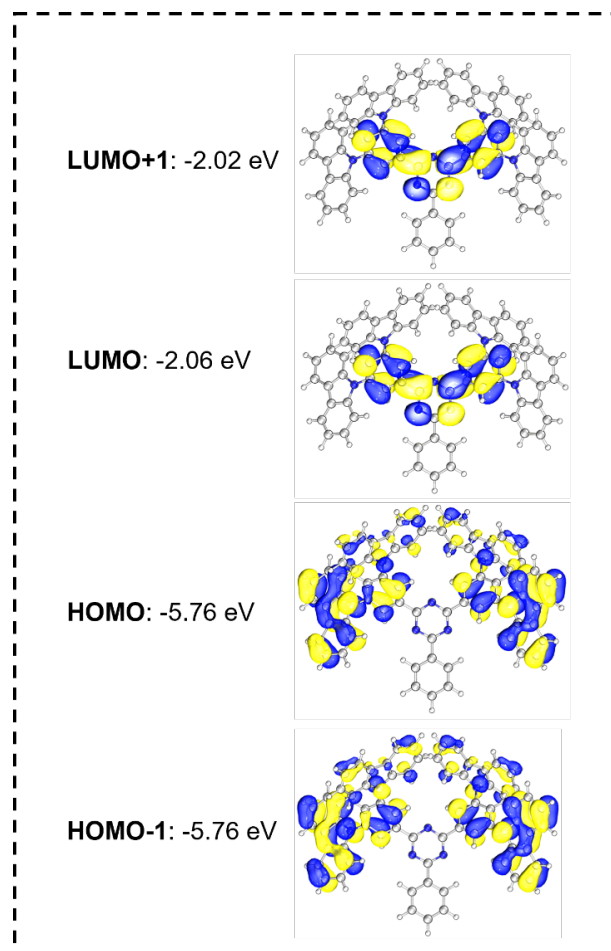
Figure S12. Calculated distribution of molecular orbitals for **4m-core**. (isovalue= 0.02)

214
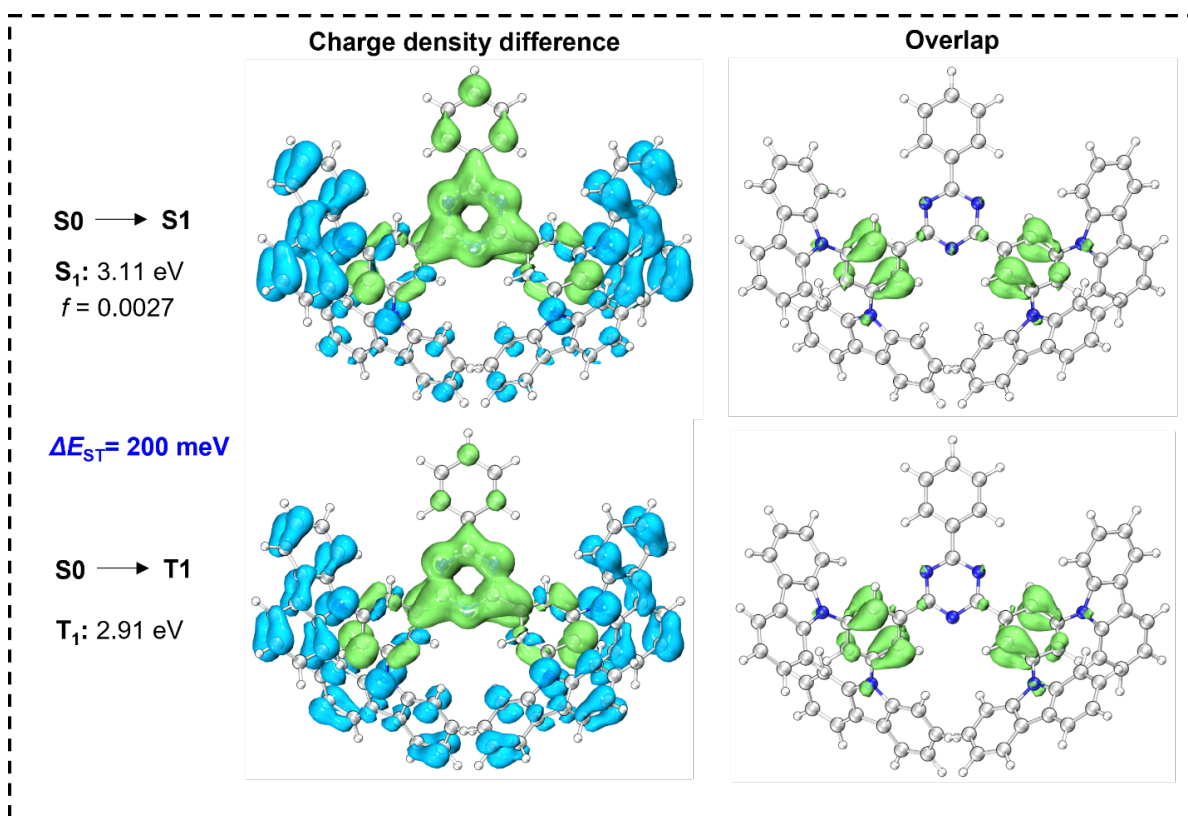
Figure S13. Pictorial representation of charge density difference and overlap of hole and electron for **4m-core**. f indicates the oscillator strength and S_1/ T_1 are the calculated first singlet/ triplet energy. ΔE_{ST} refers to the energy difference between S_1 and T_1. (isovalue= 0.02)

hole   electron

49.57°

S_1: 3.19 eV
$f = 0.17$

$\Delta E_{S1\text{-}T1}$ = 460 meV

69.33°

LUMO

^{3}LE

T_2: 3.10 eV

51.31°

$\Delta E_{T2\text{-}T1}$ = 370 meV

^{3}LE+ ^{3}CT

T_1: 2.73 eV

41.73°

HOMO

S_0 geometry
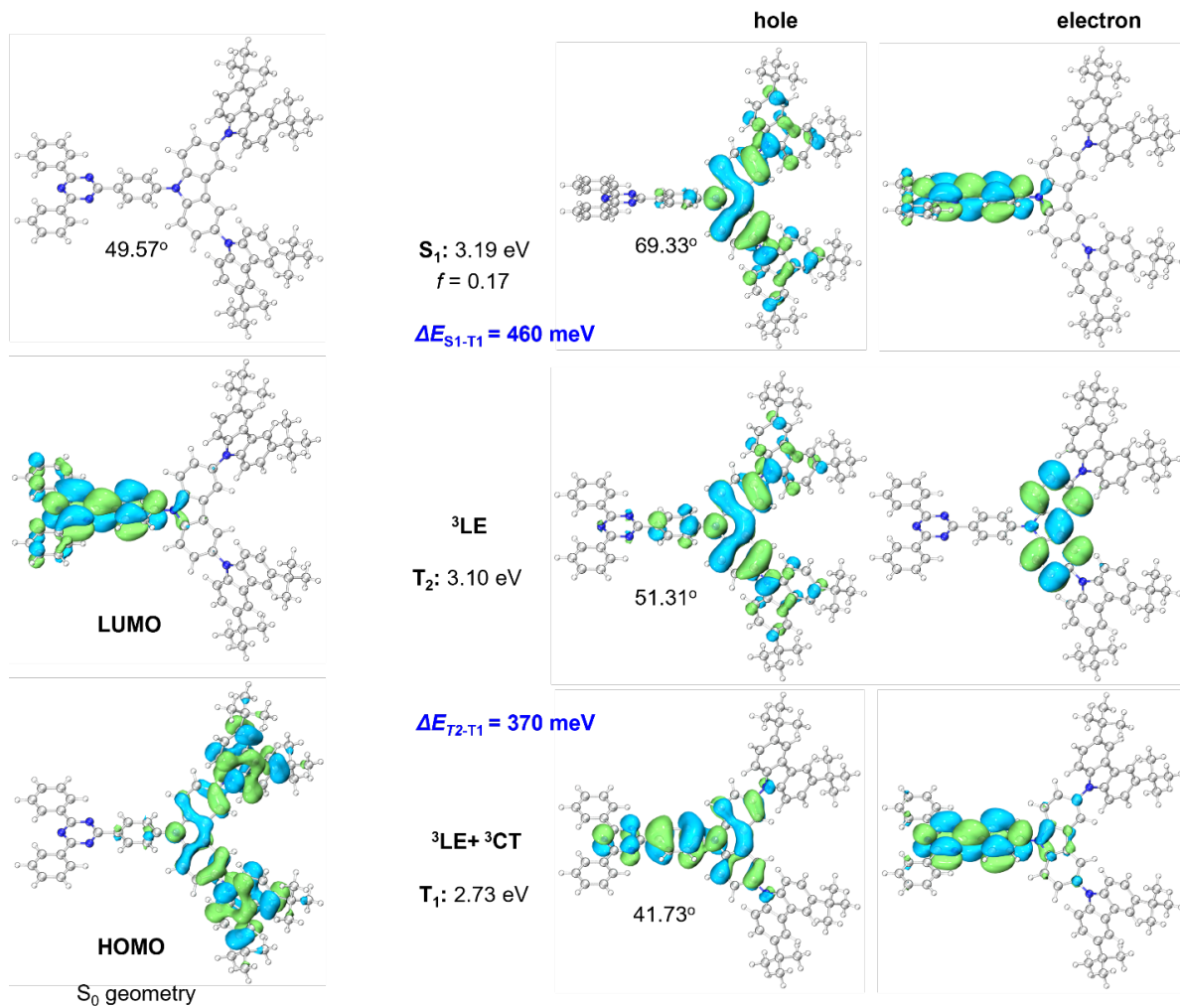
Figure S14. Natural transition orbital (NTO) pairs for the S1 and T1 states of **tBuCz1pTRZ**.

S25

216
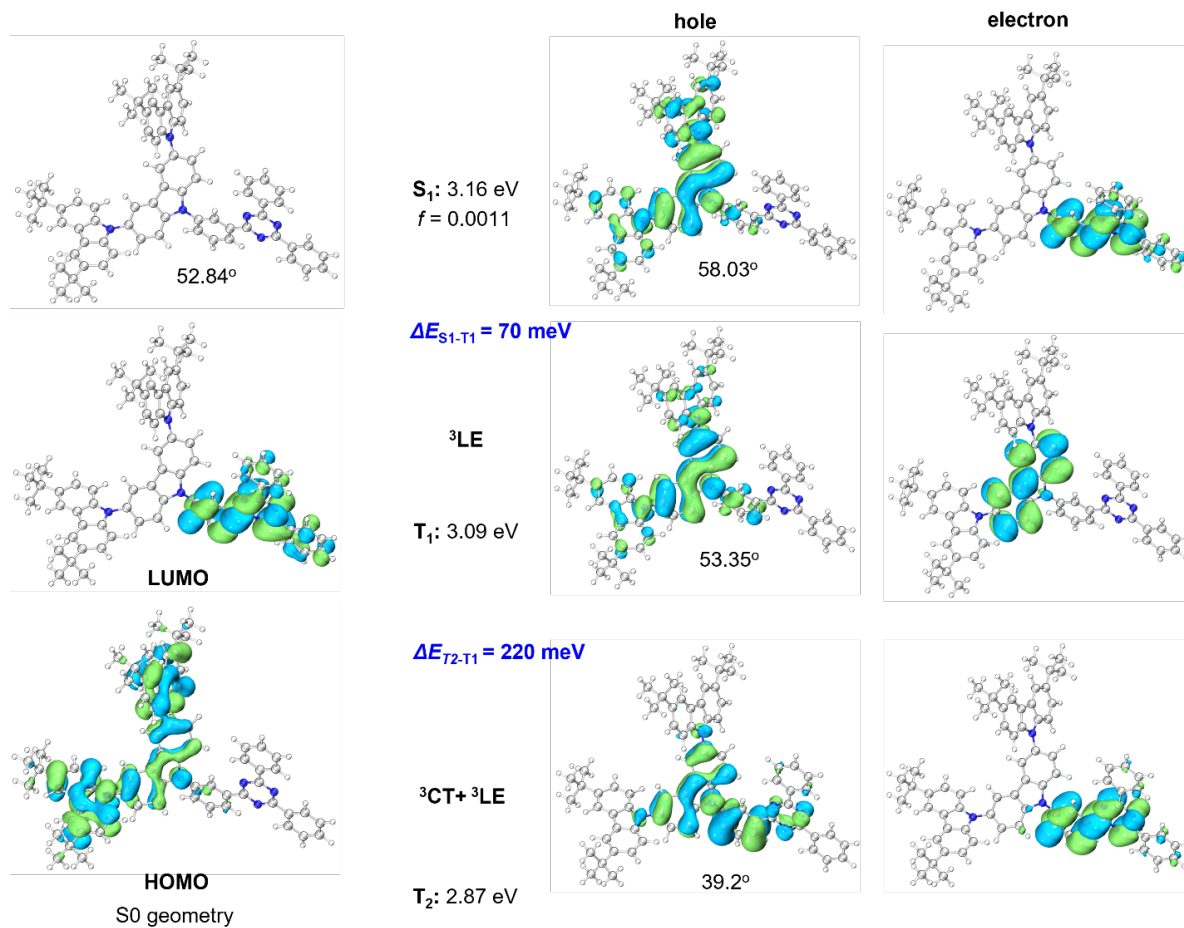
Figure S15. Natural transition orbital (NTO) pairs for the S1 and T1 states of **tBuCz1mTRZ**.
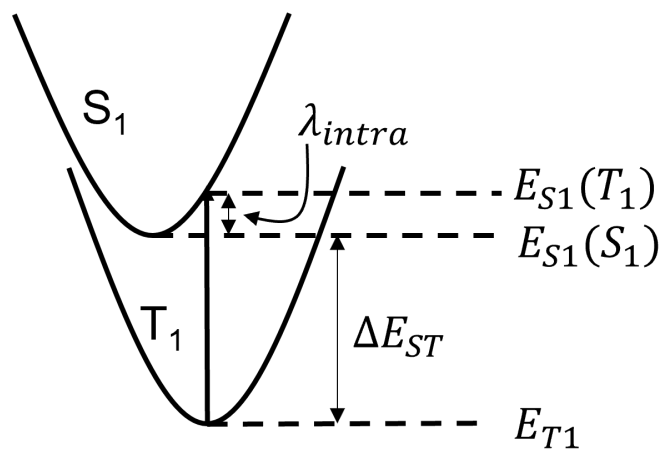
Figure S16. Marcus' parabolic free energy curves for the description of the reorganization energy.

Table S5. Reverse intersystem crossing rates determined from experiment and computation.

Parameter	tBuCz3pTRZ	tBuCz3mTRZ	Method	λ_{inter} (meV)
E_{ST} (meV)	100	80	Experiment	---
SOCME (cm^{-1})	0.31	0.53	Quantum chemical analysis	---
λ_{intra} (meV)	275	155		
k_{RISC} (s^{-1})	5×10^5	9×10^6	Eq. 1 and 2	0
k_{RISC} (s^{-1})	5×10^4	4×10^5	Experiment	---
k_{RISC} (s^{-1})	2.1×10^4	3.6×10^5	Eq. 1 and 2	300

Reference

[1]   a) K. Albrecht, K. Matsuoka, D. Yokoyama, Y. Sakai, A. Nakayama, K. Fujita, K. Yamamoto, *Chem. Comm.* **2017**, 53, 2439; b) A. Sørensen, A. M. Castilla, T. K. Ronson, M. Pittelkow, J. R. Nitschke, *Angew. Chem. Int. Ed.* **2013**, 52, 11273.

[2]   N. G. Connelly, W. E. Geiger, *Chem. Rev.* **1996**, 96, 877.

[3]   K. Albrecht, K. Matsuoka, K. Fujita, K. Yamamoto, *Angew. Chem. Int. Ed.* **2015**, 54, 5677.

[4]   K. Matsuoka, K. Albrecht, K. Yamamoto, K. Fujita, *Sci. Rep.* **2017**, 7, 1.

[5]   J. Luo, S. Gong, Y. Gu, T. Chen, Y. Li, C. Zhong, G. Xie, C. Yang, *J. Mater. Chem. C* **2016**, 4, 2442.

[6]   Y. Li, G. Xie, S. Gong, K. Wu, C. Yang, *Chem. Sci.* **2016**, 7, 5441.

[7]   X. Ban, W. Jiang, T. Lu, X. Jing, Q. Tang, S. Huang, K. Sun, B. Huang, B. Lin, Y. Sun, *J. Mater. Chem. C* **2016**, 4, 8810.

[8]   X. Ban, W. Jiang, K. Sun, B. Lin, Y. Sun, *ACS Appl. Mater. Interfaces* **2017**, 9, 7339.

[9]   K. Sun, Y. Sun, W. Tian, D. Liu, Y. Feng, Y. Sun, W. Jiang, *J. Mater. Chem. C* **2018**, 6, 43.

[10]   Y. Li, T. Chen, M. Huang, Y. Gu, S. Gong, G. Xie, C. Yang, *J. Mater. Chem. C* **2017**, 5, 3480.

[11]   M. Godumala, S. Choi, H. J. Kim, C. Lee, S. Park, J. S. Moon, K. Si Woo, J. H. Kwon, M. J. Cho, D. H. Choi, *J. Mater. Chem. C* **2018**, 6, 1160.

[12]   J. Li, X. Liao, H. Xu, L. Li, J. Zhang, H. Wang, B. Xu, *Dyes Pigm.* **2017**, 140, 79.

[13]   K. Sun, D. Chu, Y. Cui, W. Tian, Y. Sun, W. Jiang, *Org. Electron.* **2017**, 48, 389.

[14]   a) G. Kreiza, D. Banevičius, J. Jovaišaitė, K. Maleckaitė, D. Gudeika, D. Volyniuk, J. V. Gražulevičius, S. Juršėnas, K. Kazlauskas, *J. Mater. Chem. C* **2019**, 7, 11522; b) F. B. Dias, T. J. Penfold, A. P. Monkman, *Methods Appl. Fluoresc.* **2017**, 5, 012001.

220

12 Thermally Activated Delayed Fluorescent Dendrimers that Underpin High-efficiency Host-Free Solution-Processed Organic Light Emitting Diodes
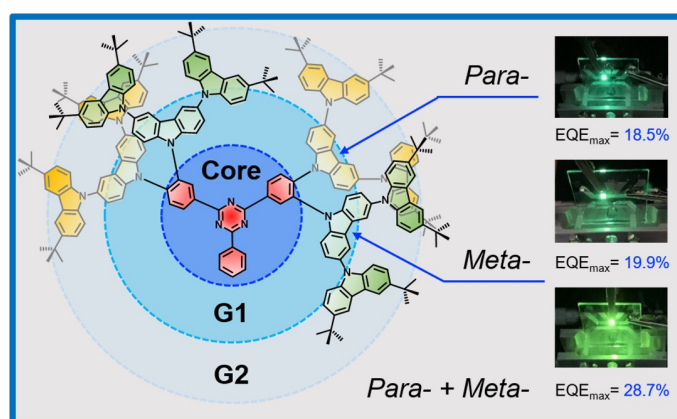
Dianming Sun,[‡] Eimantas Duda,[‡] Xiaochun Fan, **Rishabh Saxena**,
Ming Zhang, Sergey Bagnich, Xiaohong Zhang, Anna Köhler, and *Eli Zysman-Colman*
[‡] Authors contributed equally

Thermally Activated Delayed Fluorescent Dendrimers that Underpin High-Efficiency Host-Free Solution-Processed Organic Light-Emitting Diodes

Dianming Sun,* Eimantas Duda, Xiaochun Fan, Rishabh Saxena, Ming Zhang, Sergey Bagnich, Xiaohong Zhang,* Anna Köhler,* and Eli Zysman-Colman*

The development of high-performance solution-processed organic light-emitting diodes (OLEDs) remains a challenge. An effective solution, highlighted in this work, is to use highly efficient thermally activated delayed fluorescence (TADF) dendrimers as emitters. Here, the design, synthesis, density functional theory (DFT) modeling, and photophysics of three triazine-based dendrimers, tBuCz2pTRZ, tBuCz2mTRZ, and tBuCz2m2pTRZ, is reported, which resolve the conflicting requirements of achieving simultaneously a small ΔE_{ST} and a large oscillator strength by incorporating both *meta-* and *para-*connected donor dendrons about a central triazine acceptor. The solution-processed OLED containing a host-free emitting layer exhibits an excellent maximum external quantum efficiency (EQE_max) of 28.7%, a current efficiency of 98.8 cd A^{-1}, and a power efficiency of 91.3 lm W^{-1}. The device emits with an electroluminescence maximum, λ_{EL}, of 540 nm and Commission International de l'Éclairage (CIE) color coordinates of (0.37, 0.57). This represents the most efficient host-free solution-processed OLED reported to date. Further optimization directed at improving the charge balance within the device results in an emissive layer containing 30 wt% OXD-7, which leads to an OLED with the similar EQE_max of 28.4% but showing a significantly improved efficiency rolloff where the EQE remains high at 22.7% at a luminance of 500 cd m^{-2}.

1. Introduction

Small-molecule-based thermally activated delayed fluorescence (TADF) materials[1] have proliferated since their first successful demonstration in high-efficiency organic light-emitting diodes (OLEDs).[2] A number of benchmark red,[3] green,[4] and blue[5] emitters have already been developed exhibiting more than 20% maximum external quantum efficiency, EQE_max, highlighting the significant and rapid advances in TADF materials' design and demonstrating their viability as replacement materials for state-of-the-art phosphorescent (for red and green) and fluorescent (blue) emitters in commercial OLEDs. However, the aforementioned high efficiency of the OLEDs relies not only on the intrinsic photophysical properties of the emitter but also on the rather complicated multilayered device architecture typically used in vacuum-deposited devices, which increases the cost of device fabrication. An alternative strategy would be to fabricate the OLED using lower-cost solution-processing techniques such as ink-jet printing.[6] TADF dendrimers are perfect candidates for solution-processed host-free OLEDs for the following reasons: 1) the singlet–triplet gap, ΔE_{ST}, can be easily adjusted within the modular molecular design using dendronized donors or acceptors; 2) intermolecular quenching can be largely avoided by careful design of the dendron motif; and 3) intersystem crossing (ISC) or reverse intersystem crossing

D. Sun, X. Fan, M. Zhang, X. Zhang
Institute of Functional Nano & Soft Materials (FUNSOM) and Jiangsu
Key Laboratory for Carbon-Based Functional Materials & Devices
Joint International Research Laboratory of Carbon-Based Functional
Materials and Devices
Soochow University
Suzhou, Jiangsu 215123, P. R. China
E-mail: xiaohong_zhang@suda.edu.cn

D. Sun, E. Zysman-Colman
Organic Semiconductor Centre
EaStCHEM School of Chemistry
University of St Andrews
St Andrews KY16 9ST, UK
E-mail: sd235@st-andrews.ac.uk; eli.zysman-colman@st-andrews.ac.uk

E. Duda, R. Saxena, S. Bagnich, A. Köhler
Soft Matter Optoelectronics
BIMF & BPI
University of Bayreuth
Universitätsstraße 30, 95447 Bayreuth, Germany
E-mail: anna.koehler@uni-bayreuth.de

222

**ADVANCED
SCIENCE NEWS**

www.advancedsciencenews.com

**ADVANCED
MATERIALS**

www.advmat.de

(RISC) rates can both be enhanced due to the large density of excited states.[7] Despite these identified advantages, to the best of our knowledge, only a handful dendrimer-based OLEDs have been reported. An overview of the history of the development of emissive dendrimers (pioneering work and state-of-the-art work for fluorescent, phosphorescent, and TADF dendrimers) is schematically outlined in **Figure 1**. The OLEDs using these dendrimers mostly show only moderate performance, with EQE_{max} ranging from 3% to 20%.[8]

The most widely used approach to construct a TADF dendrimer is to adopt a donor–acceptor design, one that is frequently used in small molecule TADF emitters, in which several donor dendrons (second, third, and fourth generations) are attached to a central acceptor by *para*-connected phenylene bridges.[8a] Efficient TADF can be achieved through delocalization of the highest occupied molecular orbital (HOMO) across increasing generations of donor dendrons.[9] However, the TADF performance of these dendrimers worsens because the electron coupling between dendrons and acceptor cores decreases with increasing dendrimer size beyond the second generation, resulting in significantly reduced oscillator strength, thus leading to a poorer photoluminescence quantum yield (PLQY). In order to mitigate aggregation-caused quenching (ACQ), the dendrimers must be dispersed at low concentrations within a suitable host matrix.[10] Another strategy is to decorate benchmark small TADF molecules with commonly used host units (e.g., mCP: 1,3-bis(*N*-carbazolyl)benzene, CBP: 4,4′-bis(*N*-carbazolyl)-1,1′-biphenyl, and TCTA: tris(4-carbazoyl-9-ylphenyl) amine) linked together by unconjugated alkyl chains.[8b,11] The performance of these dendrimers is directly dependent on the inherent properties of the TADF small-molecule-based core structures. The peripheral host dendrons are used to suppress concentration quenching and triplet–triplet annihilation (TTA) in pristine films. However, the device efficiencies employing these dendrimers remain generally inferior to those employing only the core small molecule TADF emitter when doped into a host matrix. There, thus, remains an outstanding challenge to design dendrimer-based emitters that show comparable efficiencies to their small molecule brethren.

Triphenyltriazine (TRZ) is one of the most common electron acceptors used in TADF emitter design. The D_3-symmetric structure permits up to three symmetric or asymmetric donor groups, or dendrons, to be attached to one TRZ moiety.[12] The first TADF dendrimers were designed based on trisubstituted second-to-fourth-generation carbazole-based donor dendrons grafted onto a central TRZ acceptor.[8a] Despite this design leading to extremely small ΔE_{ST} values (0.03–0.06 eV) due to a HOMO delocalized across the donor dendrons, the host-free OLEDs achieved an EQE_{max} of less than 5%. The performance of the "host-free" devices ($EQE_{max} = 9.5\%$) could be improved by decorating each of the peripheral carbazoles with *tert*-butyl groups (tBuG2TAZ, cf., Figure 1).[8e] When this dendrimer was dispersed into a suitable host matrix, the EQE_{max} improved further to 16.1%. Overall, there is to date only a small number of examples of TADF emitters used in host-free OLEDs; of these, only a few reports document OLEDs with EQE_{max} superior to 20%, such as devices with **DMAC-TRZ**[13] ($EQE_{max} = 20\%$, $\lambda_{EL} = 500$ nm), **DCB-BP-PXZ**[14] ($EQE_{max} = 22.6\%$, $\lambda_{EL} = 548$ nm), and **DMAC-BPI**[15] ($EQE_{max} = 24.7\%$, $\lambda_{EL} = 508$ nm). To date, the

only dendrimer-based host-free solution-processed OLED with an EQE_{max} greater than 20% is that using **5CzBN-2Cz** as the emitter ($EQE_{max} = 20.4\%$)[16] a hole-barrier layer of PO-T2T was, however, introduced into the device. These results illustrate the challenge of designing dendrimer emitters that can be used in high-performance host-free OLEDs.

2. Design of TADF Dendrimers

We initially designed two dendrimers, **tBuCz2pTRZ** and **tBuCz2mTRZ**, as reference molecules (Figure 1). These two dendrimers contain 3,3″″,6,6″″-tetrakis(*tert*-butyl-9″*H*-9,3″:6′,9″-tercarbazole) (**tBuCz2G**) donors surrounding a triazine (TRZ) acceptor, linked either via a *para*-phenylene or a *meta*-phenylene bridge, respectively. We compared the optoelectronic properties of these model systems to the targeted emitter **tBuCz2m2pTRZ** (Figure 1), which is based on a design that combines facets of both **tBuCz2pTRZ** and **tBuCz2mTRZ**. We surmised that this design would inherit key properties from both dendrimers, with the excited-state behavior being modulated as a result of the interactions between the two adjacent donor dendrons. Our design follows three considerations: i) the *para*-connection of **tBuCz2pTRZ** leads to strong electronic coupling between the donor and the acceptor, which results in a high oscillator strength for the intramolecular charge-transfer (ICT) transition, while the *meta*-connection of **tBuCz2mTRZ** provides an avenue for an emitter possessing a small ΔE_{ST}, as the *meta*-disposed donor and acceptor groups are electronically decoupled. ii) The increasing number of peripheral dendritic moieties, the nature of how and the density with which they are packed together are expected to suppress quenching of the emission caused by intermolecular interactions. iii) The presence of many dendritic dendrons surrounding the central acceptor should lead to an increase in the density of triplet excited states that will enhance the nonadiabatic coupling to the singlet state thereby leading to more efficient RISC between T_1 and S_1.
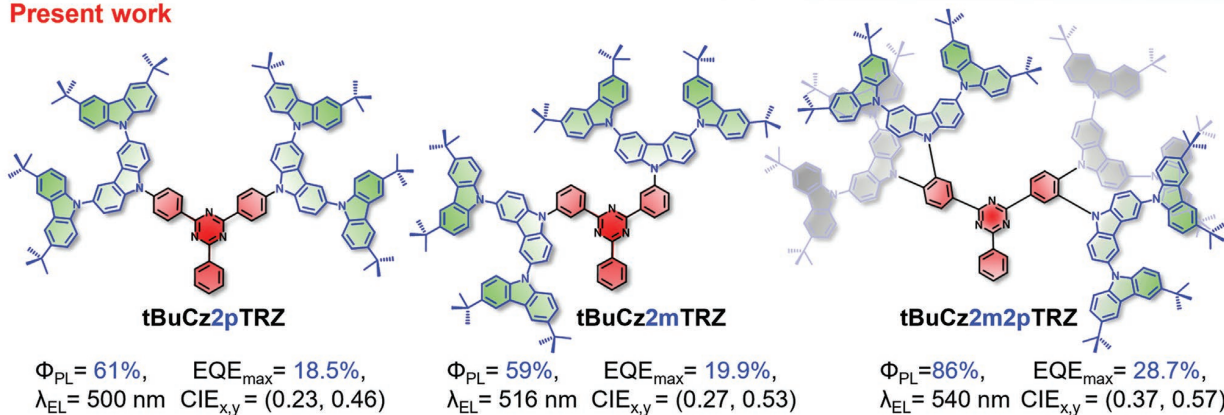
We decided to focus only on a second-generation *tert*-butylcarbazole-based donor dendron as for most reported OLEDs using TADF dendrimers; the ones employing a second-generation donor dendron showed the highest EQE_{max}.[17] This observation is substantiated in our dendrimer design by density functional theory (DFT) calculations, which show that the oscillator strength decreases further due to the increased delocalization of HOMO when employing higher generations of donor dendrons (Figure S11, Supporting Information), implying reduced PLQY of higher generation dendrimers in our case.

Employing this strategy, a very small ΔE_{ST} (40 meV) coupled with a significant PLQY of 90% in solution has been realized simultaneously. Importantly, even as a pristine film, these excellent optoelectronic properties are conserved ($\Delta E_{ST} = 40$ meV, PLQY = 86%). While the role of the *meta*- versus *para*-connection in the improvement of the electronic structure relevant to TADF is addressed in a related publication,[18] we focus here on the performance of the actual TADF devices. A host-free solution-processed OLED using a simple device configuration without exciton barrier layers and containing **tBuCz2m2pTRZ** as the emitter exhibited a record high EQE_{max} of 28.7%.

ADVANCED
SCIENCE NEWS
www.advancedsciencenews.com

ADVANCED
MATERIALS
www.advmat.de

Previous work – Top: Pioneering work; Middle: State-of-the-art work.

Φ_{PL} = 52%
λ_{EL} = 500 nm

G2TAZ

EQE_{max} = 8.0%, $CIE_{x,y}$ = (0.25, 0.49)
Angew. Chem. Int. Ed. **2015**, *54*, 5677.

Fl dendrimer   **Phos** dendrimer   **TADF** dendrimer

1996   2001   2014   2015   2017   2019

Fl dendrimer   **Phos** dendrimer   **TADF** dendrimer

HFB-diF-Dpa

5CzBN-2Cz
Φ_{PL} = 80%, λ_{EL} = 515 nm
EQE_{max} = 20.4%,
$CIE_{x,y}$ = (0.25, 0.52)

Φ_{PL} = 77%, λ_{EL} = 429, 452 nm
EQE_{max} = 5.5%, $CIE_{x,y}$ = (0.15, 0.14)

Φ_{PL} = 45%, λ_{EL} = 540 nm
EQE_{max} = 21.2%, $CIE_{x,y}$ = (0.42, 0.56)

Chem. Mater., **2014**, *26*, 3074.   *Chem. Commun.*, **2017**, *53*, 5128.   *ACS Appl. Mater. Interfaces*, **2019**, *11*, 16737.

Present work

tBuCz2pTRZ

Φ_{PL} = 61%, EQE_{max} = 18.5%,
λ_{EL} = 500 nm $CIE_{x,y}$ = (0.23, 0.46)

tBuCz2mTRZ

Φ_{PL} = 59%, EQE_{max} = 19.9%,
λ_{EL} = 516 nm $CIE_{x,y}$ = (0.27, 0.53)

tBuCz2m2pTRZ

Φ_{PL} = 86%, EQE_{max} = 28.7%,
λ_{EL} = 540 nm $CIE_{x,y}$ = (0.37, 0.57)

Figure 1. Molecular structures of pioneering work (top) and state-of-the-art work (middle) for fluorescent (Fl), phosphorescent (Phos), and TADF dendrimers used as emitters in OLEDs and structures of the dendrimers **tBuCz2pTRZ**, **tBuCz2mTRZ**, and **tBuCz2m2pTRZ** reported in this study (bottom) based on bespoke second-generation *tert*-butylcarbazole donor (**tBuCz2G**) and triphenyltriazine acceptor (TRZ) linked through *para*- and *meta*-connections.

Importantly, the efficiency roll-off of the OLED is significantly improved by doping 30 wt% OXD-7, an electron-transporting material, into the emissive layer. As a result of the improved charge balance, the EQE of the optimized device not only

ADVANCED
SCIENCE NEWS
www.advancedsciencenews.com

ADVANCED
MATERIALS
www.advmat.de

reached a similar maximum EQE of 28.4%, but also maintained its efficiency of 22.7% at a luminance of 500 cd m^{-2}.

3. Theoretical Calculations

We started our investigation by employing quantum-chemical calculations to estimate the influence of the molecular design on both ΔE_{ST} and the oscillator strength, f, as well as to identify the hole and electron distributions in the lowest-lying excited singlet (S_1) and triplet states (T_1). **Figure 2**a displays the natural transition orbitals (NTOs) for S_1 and T_1. For all compounds, the hole and electron densities are clearly separated. Complemented by a solvatochromic study (Figure 2b), and

as discussed further in the following sections, all spectra can be ascribed to charge-transfer (CT) transitions. Even though all three compounds show the same negligible wavefunction overlap, significant differences in the calculated oscillator strength exist. While **tBuCz2pTRZ** has the largest calculated oscillator strength ($f = 0.26$), it is negligible for **tBuCz2mTRZ** ($f = 0.002$). The significantly higher oscillator strength calculated for **tBuCz2pTRZ** in the gas phase is expected due to a stronger electronic coupling between donor dendrons and the TRZ acceptor through the *para*-connection compared to the *meta*-connection in **tBuCz2mTRZ**. In the case of **tBuCz2m2pTRZ** ($f = 0.10$), the oscillator strength is of an intermediate intensity to those of **tBuCz2pTRZ** and **tBuCz2mTRZ**. The calculations show that the ΔE_{ST} values are about equal
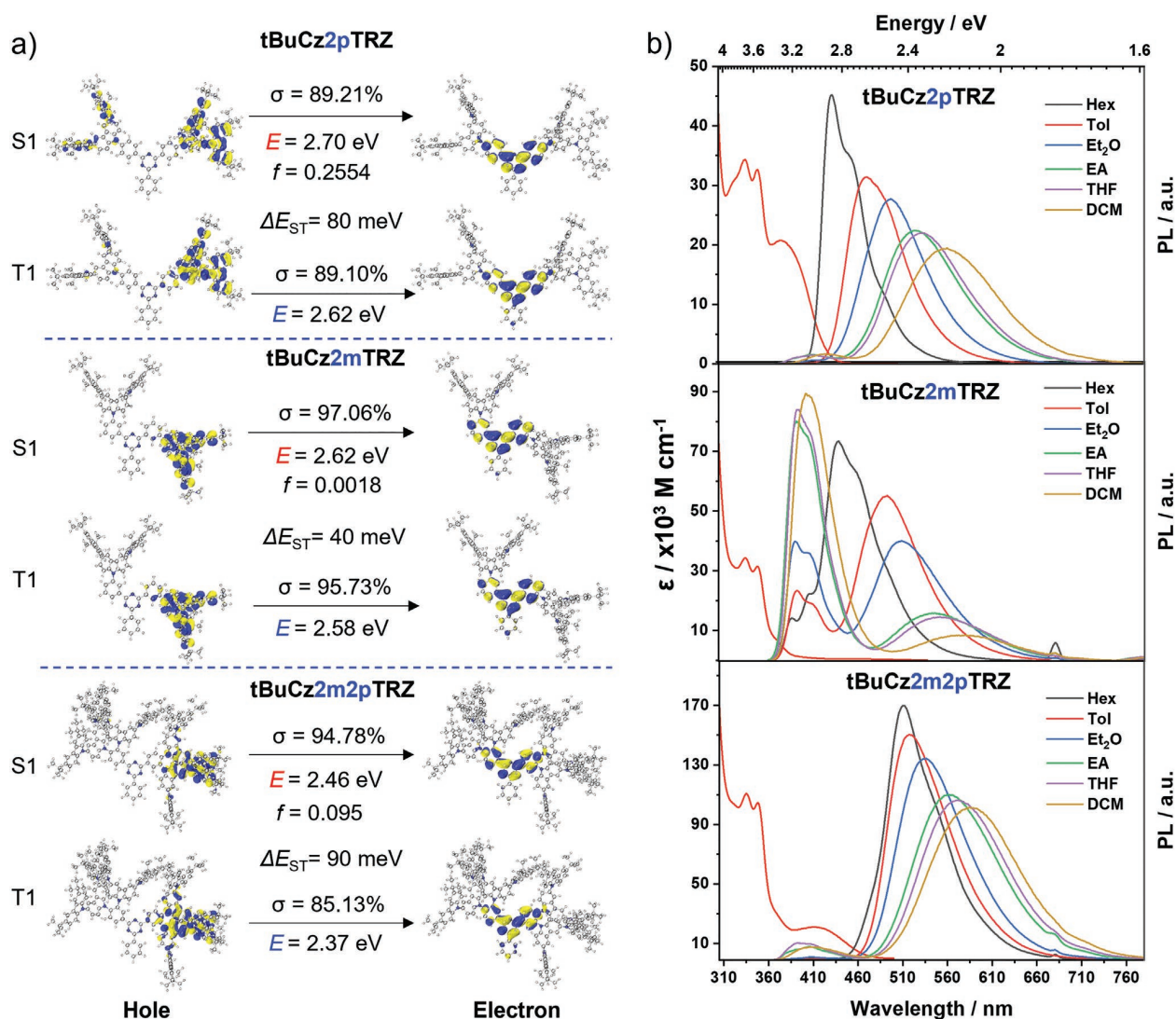
Figure 2. Theoretical and photophysical properties of **tBuCz2pTRZ** (top), **tBuCz2mTRZ** (middle), and **tBuCz2m2pTRZ** (bottom). a) Pictorial representation of the natural transition orbitals (NTO) describing the S_1 and T_1 states for **tBuCz2m2pTRZ**, as calculated at the TDA-PBE0/6-31G(d,p) level (isovalue = 0.02) where σ refers to the weight of the illustrated hole–electron contribution to the excitation, and f indicates the oscillator strength, and E_{S1} and E_{T1} are the calculated lowest singlet and triplet excited states, respectively. b) Molar absorptivity measured in toluene and solvatochromic PL spectra normalized by the integrated area ($\lambda_{exc} = 340$ nm; 3×10^{-5} M). (The emission at 680 nm arises from the second harmonic of the laser source.)

225

**ADVANCED
SCIENCE NEWS**

www.advancedsciencenews.com

**ADVANCED
MATERIALS**

www.advmat.de

(80 and 90 meV) for **tBuCz2pTRZ** and **tBuCz2m2pTRZ**, but half as large as 40 meV for **tBuCz2mTRZ**.

The optimized structures in the ground state and the electron density distributions of the HOMO and lowest unoccupied molecular orbital (LUMO) of **tBuCz2pTRZ**, **tBuCz2mTRZ**, and **tBuCz2m2pTRZ** are shown in Figures S3 and S4 (Supporting Information) (calculated at the PBE0/6-31G(d,p) level). The TRZ acceptor within each dendrimer adopts a nearly planar conformation. The dihedral angle between the planes of the inner carbazoles, and the TRZ values are similar at around 55° and 53° for **tBuCz2pTRZ** and **tBuCz2mTRZ**, respectively. Interestingly, although large steric repulsion exists between *para*- and *meta*-connected donor dendrons in **tBuCz2m2pTRZ**, the conformations of the donor dendrons in the model dendrimers are conserved, with dihedral angles (54° for *para*-connections and 55° for *meta*-connections) that are similar to those in **tBuCz2pTRZ** and **tBuCz2mTRZ**. This indicates that the degree of conjugation observed in **tBuCz2pTRZ** and **tBuCz2mTRZ** will be maintained in **tBuCz2m2pTRZ**.

Furthermore, calculations show that there are corresponding degenerate S_2 and T_2 states due to the symmetry of the molecular structures. The DFT calculations also reveal the presence of multiple excited states arising from CT transition of donor dendron (D) to the TRZ acceptor (A) for **tBuCz2pTRZ**, **tBuCz2mTRZ**, and **tBuCz2m2pTRZ** (see Tables S2–S4 in the Supporting Information). We expect that these higher-lying CT states will show substantial mixing with the lowest ^{1,3}CT states by both spin–orbit coupling (SOC) and spin–vibronic coupling. The large number of closely lying excited states should directly translate into faster ISC and RISC rates in an analogous fashion to how D–A–D TADF emitters show more efficient TADF and higher PLQY compared to their D–A analogs.[7a,19] This aspect is addressed in more detail in a study on the difference between the electronic structure of the *meta*- and *para*-connected compounds.[18]

4. Electrochemistry

For solution-processed OLEDs, an emitting layer (EML) is generally spin-coated onto a wet-processed poly(3,4-ethylenedioxythiophene):poly(styrenesulfonate) (PEDOT:PSS) hole injection layer without any additional hole-transporting material, in part because spin-coating of the EML may dissolve/disturb the underlying hole-transporting layer. A relatively high-lying HOMO energy level is required for the emitters to match the HOMO level of PEDOT:PSS (−5.1 eV)[20] and thus ensure efficient hole injection. As shown in Figure S4 (Supporting Information), all three dendrimers possess similar electrochemical properties, with two resolvable quasireversible oxidation waves with E_{ox} at 1.07 and 1.19 eV versus saturated calomel electrode (SCE) (measured from the peak value of the differential pulse voltammetry (DPV) scan), which correspond to the oxidation of the inner carbazole and the peripheral *tert*-butylcarbazole, respectively.[21] Scanning to negative potentials, the E_{red} (measured from the peak value of the DPV scan) of −1.54 V versus SCE for **tBuCz2m2pTRZ** is anodically shifted by 0.13 V compared to those of **tBuCz2pTRZ** and **tBuCz2mTRZ**, both of which show the same E_{red} of −1.67 V versus SCE. This shift is consistent

with a slightly greater conjugation between the acceptor and two additional **tBuCz2G** dendrons in **tBuCz2m2pTRZ** as evidenced by the DFT calculations (see Figure 2a). Thus, in summary, the HOMO levels are −5.41 eV for all three dendrimers while the LUMO levels are −2.67, −2.67, and −2.8 eV for **tBuCz2pTRZ**, **tBuCz2mTRZ**, and **tBuCz2m2pTRZ**, respectively.

5. Photophysical Properties

To exclude bimolecular interactions and to assess the properties of monomolecular species, we started the photophysical investigation with absorption and photoluminescence measurements in dilute solution. In Figure 2b, the absorption spectra for all three compounds in toluene show very similar profiles. Peaks at λ_{abs} = 337 and 342 nm can be ascribed to the π–π^* transitions on the carbazole.[22] The broad band at 385 nm for **tBuCz2pTRZ** is assigned to an ICT transition from the *para*-connected donor dendron to the TRZ acceptor with a molar extinction coefficient, ε = 3500 M^{-1} cm^{-1}; a weak ICT absorption (ε = 300 M^{-1} cm^{-1}) is barely visible for **tBuCz2mTRZ**. In contrast, as shown in Figure 2b (top and bottom), the ICT absorption for **tBuCz2m2pTRZ** at 415 nm (ε = 1500 M^{-1} cm^{-1}) is comparable to that of **tBuCz2pTRZ**, consistent with the *para*-connected donor dendrons that contribute to the large oscillator strength; further, it is redshifted, in line with the trends in the electrochemical gaps observed by DPV (Figure S4, Supporting Information). While the gas phase calculations suggest an increase of factors of 100 and 50, respectively, for the oscillator strength when going from the *meta*-connected compound **tBuCz2mTRZ** to the compounds with *para*-connected carbazoles, **tBuCz2pTRZ** and **tBuCz2m2pTRZ**, the solution measurements yield a much weaker increase of only factors of 7 and 3, respectively. We attribute this to conformational deviations from the perfect gas phase geometry in solution due to the presence of the solvent molecules that reduce the maximal possible excited state delocalization.

Figure 2b shows the photoluminescence spectra of the three compounds in a range of solvents of increasing polarity ($f(\varepsilon,n)$ = 0, 0.013, 0.167, 0.200, 0.210, and 0.217 for hexane, toluene, diethyl ether, EtOAc, tetrahydrofuran (THF), and dichloromethane (DCM), respectively;[23] $f(\varepsilon,n)$ is a solvent polarity function). Two emission bands can be identified. With increasing solvent polarity, the emission peak of the high-energy band retains its spectral position around 400 nm while the low-energy band redshifts to longer wavelength and the emission band broadens. This positive solvatochromism of the low-energy band is typical for an ICT state. Due to the absence of spectral shift with increasing solvent polarity, the high-energy band can be associated with a locally excited (LE) state. The relative intensity of this LE band is low when a *para*-connection is present, i.e., for **tBuCz2pTRZ** and **tBuCz2m2pTRZ** (see Figure S14 in the Supporting Information for the log scale). For **tBuCz2mTRZ**, where only a *meta*-connection exists, the relative intensity of the LE band increases with increasing solvent polarity and, thus, energetic separation from the CT state. This is straightforward to understand. Simultaneous emission from an LE and a CT state can be observed when internal conversion from the LE to the CT state is slower than radiative decay from the LE state.
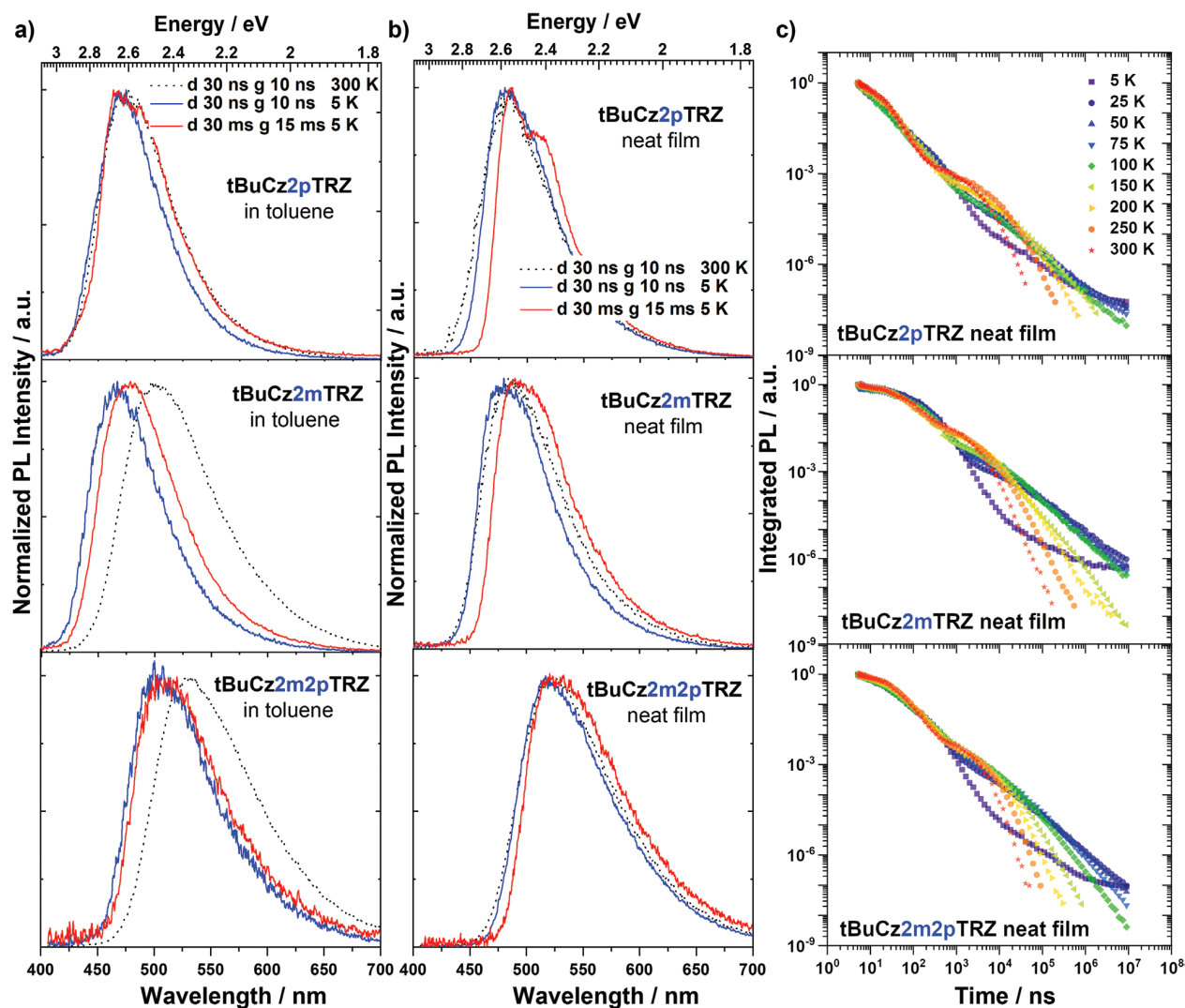
Figure 3. Prompt fluorescence ($d = 30$ ns g^{-1}: 10 ns) at 300 K (black dotted line) and at 5 K (blue solid line). a,b) Phosphorescence with detection in the millisecond range ($d = 30$ ms g^{-1}: 15 ms) at 5 K (red solid line) of **tBuCz2pTRZ** (top), **tBuCz2mTRZ** (middle), and **tBuCz2m2pTRZ** (bottom) in 3×10^{-5} M toluene solution (a) and neat film (b). In the legend, d refers to delay time and g refers to gate time. c) Temperature-dependent time-resolved PL decay of neat films. The decays were obtained by integrating each time-resolved spectrum across the full spectral range ($\lambda_{exc} = 355$ nm).

The conversion from an LE to a CT state implies an electron transfer, which depends strongly on the wavefunction overlap. This should, therefore, be faster for the compounds with *para*-connected donor dendrons than with *meta*-connected donor dendrons, consistent with a greater relative CT emission. There are two further factors that contribute to the ratio of LE:CT emission. First, with increasing polarity, the CT character in the CT state increases and this reduces its emission intensity, so that the relative contribution from the LE state emission gains weight. Further, the internal conversion rate slows with an increasing gap between the two states, known as the energy gap law, implying more LE emission in the more polar solvents, where the gap between LE and CT states is larger. Overall, the simultaneous LE and CT state emission indicates that, for some of the donor dendrons, the rate of ICT is slow compared to the radiative emission rate from the LE state. These groups could

therefore act as hole-transporting units or host moieties, given their suitably higher triplet energies for the ICT-based emission of the dendrimers.

Prompt and delayed emissions were measured after pulsed excitation in order to gain deeper insight into the nature of the excited states of the emitters in solution and film. **Figure 3**a shows the prompt spectra of the three dendrimers in 3×10^{-5} M toluene solution with a delay time of 30 ns and a gating time of 10 ns. The characteristically broad and unstructured prompt emission in toluene, corroborated by quantum-chemical calculations (Figure 2; Figures S8–S10, Supporting Information), indicate strong CT character for all three dendrimers. The prompt emission at both 300 and 5 K is almost identical for **tBuCz2pTRZ**, while in contrast, there exists a significant blueshift upon cooling from 300 to 5 K for **tBuCz2mTRZ** and **tBuCz2m2pTRZ**, both of which contain electronically

227

**ADVANCED
SCIENCE NEWS**

www.advancedsciencenews.com

**ADVANCED
MATERIALS**

www.advmat.de

decoupled donor dendrons. The blueshift is due to reduced geometric reorganization after excitation at 5 K because of the rigid matrix. The singlet energies were then measured from the onset of the prompt emission spectra at 5 K to be 2.92, 2.94, and 2.73 eV for **tBuCz2pTRZ**, **tBuCz2mTRZ**, and **tBuCz2m2pTRZ**, respectively (see Figure S15 in the Supporting Information); if the central peak positions are taken, the respective values are 2.64, 2.66, and 2.48 eV. The singlet energies of **tBuCz2pTRZ** are nearly isoenergetic to those of **tBuCz2mTRZ**, indicating similar energies of their lowest singlet (^{1}CT) states regardless of the electronic coupling between the donor and acceptor. The spectra determined at 5 K using a long delay time of 30 ms (gate time = 15 ms) are ascribed to phosphorescence. Similar to the prompt emission, the phosphorescence spectra are also broad and structureless, indicating emission from ^{3}CT states, assignments that are also supported by quantum-chemical calculations (Figures S8–S10, Supporting Information). The phosphorescence spectrum of **tBuCz2mTRZ** closely resembles that of **tBuCz2pTRZ**, resulting in close-lying triplet states at 2.83 and 2.88 eV, for **tBuCz2pTRZ** and **tBuCz2mTRZ**, respectively, measured from the onset of these spectra. Taking the offset between the prompt emission and phosphorescence spectra, ΔE_{ST} values of 90 and 60 meV were estimated for **tBuCz2pTRZ** and **tBuCz2mTRZ**, respectively. The T$_1$ state of **tBuCz2m2pTRZ** has its onset at 2.69 eV, leading to a ΔE_{ST} value of 40 meV. The presence of the smaller gap between the singlet and triplet states should lead to faster RISC in this dendrimer. The estimated ΔE_{ST} values agree largely with the quantum-chemical calculations.

For electroluminescent devices, it is essential to understand how the photophysical properties in solution translate into neat films. In the context of host-free devices, we therefore next investigated the neat thin-film photophysics of **tBuCz2pTRZ**, **tBuCz2mTRZ**, and **tBuCz2m2pTRZ** at 300 and at 5 K (Figure 3b). Similar to the features observed in toluene, the prompt emission at both 300 and 5 K in neat films is also broad and unstructured. However, in neat films, the prompt emission at 300 K resembles that at 5 K for each dendrimer, unlike that observed for the prompt emission behavior of **tBuCz2mTRZ** and **tBuCz2pTRZ** in toluene. This implies that there is little reorganization after excitation within the thin film even at room temperature (RT) due to the packing of the emitters within the film. The prompt emission of **tBuCz2pTRZ**

still closely resembles that of **tBuCz2mTRZ**. The energy levels of the ^{1}CT states determined from the onsets of the corresponding prompt fluorescence (PF) spectra at 5 K are calculated to be 2.78, 2.81, and 2.63 eV for **tBuCz2pTRZ**, **tBuCz2mTRZ**, and **tBuCz2m2pTRZ**, respectively, values that are stabilized by 140–160 meV compared to those in toluene glass. The spectra obtained at 5 K after a time delay of 30 ms are, again, ascribed to phosphorescence. The phosphorescence spectrum for **tBuCz2pTRZ** is structured with a major peak at 486 nm (2.55 eV) and a low energy feature around 510 nm (2.43 eV) that we ascribe to unresolved vibrational transition. The phosphorescence spectra of **tBuCz2mTRZ** and **tBuCz2m2pTRZ** remain unstructured and broader than the phosphorescence spectrum of **tBuCz2pTRZ**, which we ascribe to a more significant structural disorder due to the presence of the *meta*-connected donor dendron, and, for **tBuCz2m2pTRZ**, a greater number of dendrons. The energies of the T$_1$ states of **tBuCz2pTRZ** and **tBuCz2mTRZ** measured from the onsets are 2.69 and 2.72 eV, respectively, leading to the same ΔE_{ST} value of 90 meV. The similar energies of their respective S$_1$ and T$_1$ states indicate that the presence of *para*- or *meta*-connections between the donor and acceptor has only a small effect on the nature of the excited states. The energy of the T$_1$ state of **tBuCz2m2pTRZ** is located at 2.59 eV, leading to the smallest ΔE_{ST} value of 40 meV, which is also the same value as that determined in toluene glass.

Figure 3c shows the PL decay curves of neat films. All decays at 300 K show two regimes, a PF regime followed by a delayed fluorescence (DF) component from about 500 ns onward. The intensity of DF decreases upon cooling and vanishes at 5 K, yet, for **tBuCz2mTRZ** and **tBuCz2m2pTRZ**, most thermal activation occurs between 5 and 25 K (Figures S18 and S19, Supporting Information), implying a very efficient RISC even at low temperature. The corresponding activation energies for **tBuCz2mTRZ** and **tBuCz2m2pTRZ** are likely to be smaller than the optical ΔE_{ST} determined from the difference in offsets of the prompt fluorescence and phosphorescence spectra at 5 K. Part of the fast RISC rate can be accounted for by the large number of higher-lying excited states, as predicted by quantum-chemical calculations.[7a,24]

The PLQY values of the neat films as well as other photophysical parameters are collated in **Table 1**. Under N$_2$, **tBuCz2pTRZ** and **tBuCz2mTRZ** have similar PLQY values of 61% and 59%, respectively. For **tBuCz2m2pTRZ**, the PLQY in

Table 1. Comparison of photophysical properties in neat films at 300 K.

Neat film	λ_{PL}[a]	S$_1$[b]	T$_1$[c]	ΔE_{ST}[d]	Φ_{PL} N$_2$[e]	τ_{PF}[f]	τ_{DF}[g]	DF/PF[h]	k_{PF}[i]	k_{DF}[j]	k_r^{S}[k]	k_{nr}[l]
	[nm]	[eV]	[eV]	[eV]	[%]	[ns]	[µs]		[× 10^7 s^{-1}]	[× 10^5 s^{-1}]	[× 10^7 s^{-1}]	[× 10^7 s^{-1}]
tBuCz2pTRZ	481	2.78	2.69	0.09	61	11	1.2	0.15	9.1	8.3	4.8	4.3
tBuCz2mTRZ	483	2.81	2.72	0.09	59	52	1.3	1.3	1.9	9.1	0.5	1.4
tBuCz2m2pTRZ	520	2.63	2.59	0.04	86	31	1.1	0.4	3.2	9.1	2.0	1.2

[a]PL in neat film at 300 K; [b]Lowest singlet energy; [c]Lowest triplet energy; [d]Energy difference between S$_1$ and T$_1$; [e]Photoluminescence quantum yield; [f]Lifetime of prompt emission (obtained by single exponential fitting of prompt emission decay regime at RT as shown in Figure S20 (Supporting Information)) λ_{exc} = 355 nm; [g]Lifetime of delayed emission (obtained by single exponential fitting of delayed emission decay regime at RT as shown in Figure S20 (Supporting Information)) λ_{exc} = 355 nm; [h]DF/PF $= \int \frac{I_{DF(t)}}{I_{PF(t)}} dt$; [i]Decay rate of prompt emission; [j]Decay rate of delayed emission; [k]Radiative decay rate of singlet excitons; [l]Nonradiative decay rate determined by $\Phi_{PF} = \frac{k_r^S}{k_r^S + k_{nr}}$.

**ADVANCED
SCIENCE NEWS**

www.advancedsciencenews.com

**ADVANCED
MATERIALS**

www.advmat.de

N_2 is the highest among three dendrimers at 86%. To evaluate this in view of the TADF performance, the respective rates should be considered. First, the nonradiative rate reduces by a factor of 3 in the *meta*-connected compounds, **tBuCz2mTRZ** and **tBuCz2m2pTRZ**. The dominant nonradiative decay channel will be intersystem crossing; since we are in the blue-green spectral range, internal conversion is negligible, and the similar photoluminescence quantum yields in solution and neat film indicate that intermolecular interactions leading to concentration quenching are small. Further, even though the ISC rate is three times reduced, the RISC rate is 3–5 times faster in the two compounds with *meta*-connection (Table S7, Supporting Information). In an OLED structure, the triplet states are populated directly by hole–electron recombination, so that the ISC from S_1 to T_1 is not relevant, yet the RISC from T_1 to S_1 is decisive. This clearly places the compounds with *meta*-connections ahead of the *para*-connected one. For **tBuCz2m2pTRZ**, the radiative decay rate is about half that of the *para*-connected **tBuCz2pTRZ**, yet still four times greater than that of the purely *meta*-connected **tBuCz2mTRZ**. It seems that **tBuCz2m2pTRZ** embodies the best of both RISC and radiative decay rates from the *meta*- and the *para*-connected compounds. Notably, the lifetime of the delayed emission is very short for all three compounds, as desired for an emitter in an OLED (Table 1).

6. OLEDs

Motivated by the promising photophysical properties, we next fabricated devices. First, single carrier devices containing neat EMLs with **tBuCz2pTRZ**, **tBuCz2mTRZ**, and **tBuCz2m2pTRZ** were fabricated with the configuration of indium tin oxide (ITO)/PEDOT:PSS (35 nm)/dendrimer (40 nm)/MoO$_3$ (40 nm)/Al (100 nm) for hole-only devices and ITO/Al (40 nm)/dendrimer (40 nm)/TmPyPB (40 nm)/LiF (1 nm)/Al (100 nm) for electron-only devices, where TmPyPB is 1,3,5-tri(*m*-pyrid-3-yl-phenyl)benzene and acts as an electron-transporting layer. Their current density–voltage (*J–V*) characteristics are shown in Figure S22 (Supporting Information). The hole current starts to rise at a low threshold voltage of 3 V whereas electron current grows rapidly at around 5 V for all three devices, indicative of similar hole/electron injection barriers and efficient hole injection character of the three dendrimers. For hole-only devices with Ohmic electrodes, a higher hole current density at the same driving voltage indicates a better hole mobility. Thus, the hole-transporting ability follows the order of **tBuCz2pTRZ** < **tBuCz2mTRZ** < **tBuCz2m2pTRZ**. By contrast, similar electron-transporting/injection ability is observed for all three dendrimer devices as evidenced by the nearly identical electron current density curves. This is not unexpected given that all three dendrimers possess the same TRZ acceptor unit. Importantly, at the same effective driving voltage for both hole-only and electron-only devices, the electron currents in the electron-only devices are higher than the hole currents in the hole-only devices, indicating improved electron-transporting properties within the EML. We surmise that this is due to the presence of a similarly exposed TRZ in each dendrimer that provides an efficient pathway for electron transport.

We next fabricated simple bilayer devices consisting of ITO/PEDOT:PSS (35 nm)/dendrimer (40 nm)/TmPyPB (40 nm)/LiF (1 nm)/Al (100 nm). The emissive layer is composed of a neat film of one of **tBuCz2pTRZ**, **tBuCz2mTRZ**, and **tBuCz2m2pTRZ** for devices 1–3, respectively. The schematic diagram of the device structure together with energy level of each layer is shown in **Figure 4**a. The device performance is summarized in **Table 2**. The electroluminescence (EL) spectra of the devices are presented in Figure 4b. The EL spectra gradually redshift from devices 1 to 3, which is consistent with the trends observed for the PL spectra in toluene and as neat films. Device 3 is green emissive with a λ_{EL} of 540 nm and Commission Internationale de L'Éclairage (CIE) coordinates of (0.37, 0.57).

Figure 4c shows the current density–voltage–luminance (*J–V–L*) curves for these devices, all of which exhibit low turn on voltages between 3.1 and 3.3 V that are among the lowest values reported for solution-processed TADF OLEDs (see Table S8 in the Supporting Information). As a result, excellent power efficiencies, as high as 91.3 lm W^{-1} for the host-free device based on **tBuCz2m2pTRZ**, were reached. Among all these devices, the **tBuCz2m2pTRZ**-based device 3 shows the highest luminance of 6029 cd m^{-2} at 6.3 V, whereas device 1 achieved only half of that value and device 2 achieved only 777 cd m^{-2}.

Figure 4d shows the EQE versus current density for these devices. The EQE$_{max}$ of the best-performing examples of devices 1–3 are 18.5%, 19.9%, and 28.7%, respectively. The EQE$_{max}$ of device 3 is obtained at a luminance of 40 cd m^{-2}. The performance of device 3 is significantly improved compared to those of the other two OLEDs. Notably, the average EQE$_{max}$ values across 20 fabricated devices are 16.8%, 15.8%, and 26.3% for devices 1–3, respectively, according to the histogram of EQE$_{max}$ values (Figure 4e). The average EQE$_{max}$ of 26.3% for **tBuCz2m2pTRZ** is close to the highest obtained EQE$_{max}$ (28.7%), indicating high batch-to-batch reproducibility.

However, we do note the severe efficiency roll-off for device 3, which shows an EQE of 14.3% at 500 cd m^{-2}, which we ascribe to the imbalanced charge mobility within the **tBuCz2m2pTRZ** neat film. To address this issue, we doped into the emissive layer OXD-7 at 30 wt%, which serves as an electron-transporting material (**Figure 5**). Device 4, containing the OXD-7, shows the same low turn-on voltage at 3.1 V and the EL spectrum also remains the same. Device 4 shows a comparable EQE$_{max}$ of 28.4% to device 3. Importantly, a significant improvement in efficiency roll-off is observed for device 4 where the EQE reaches 22.7% at a luminance of 500 cd m^{-2} (Figure 5d). These champion values imply very effective exciton harvesting of **tBuCz2m2pTRZ** in the OLEDs, and concentration quenching that is largely suppressed in both devices 3 and 4. The extremely small ΔE_{ST}, very fast RISC, and the intermolecular packing of the dendrimers account for the significant improvement in performance compared to OLEDs using previously reported TADF dendrimers.

7. Conclusions

By taking advantage of the molecular design features embedded within **tBuCz2m2pTRZ**, we have rationalized the remarkable improvement in photophysical properties and device

229

**ADVANCED
SCIENCE NEWS**

www.advancedsciencenews.com

**ADVANCED
MATERIALS**

www.advmat.de
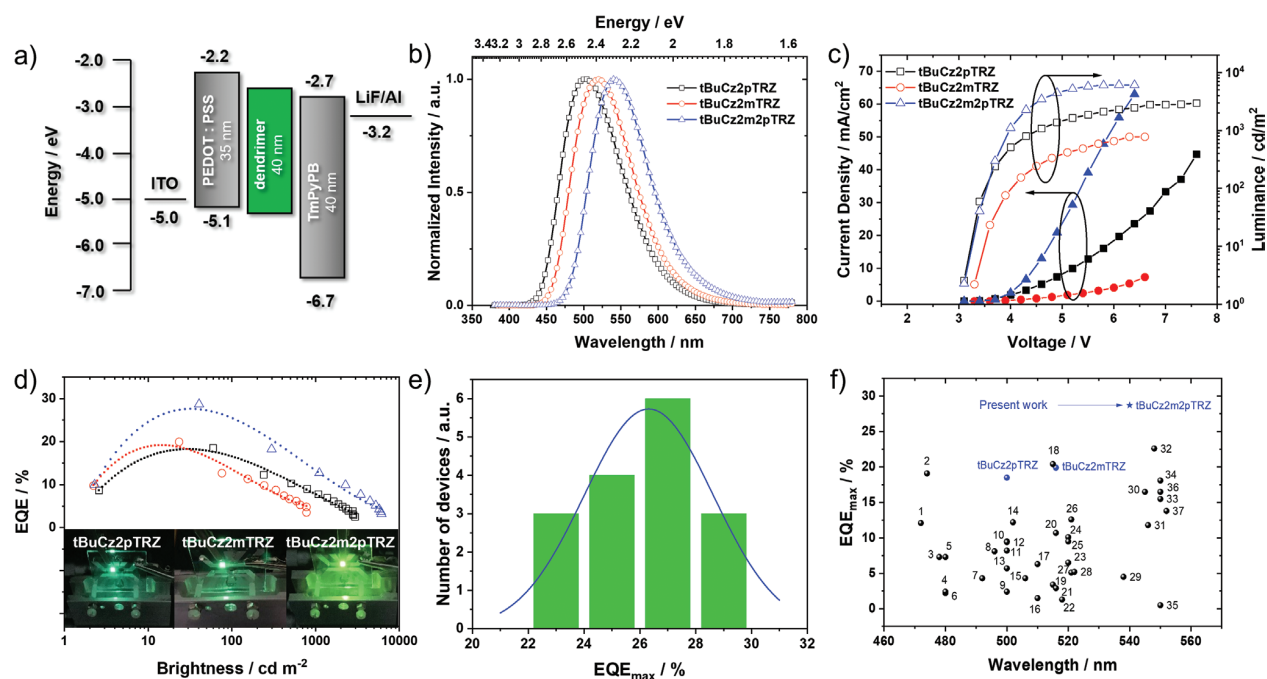
Figure 4. Electroluminescence characteristics of host-free OLEDs using **tBuCz2pTRZ**, **tBuCz2mTRZ**, and **tBuCz2m2pTRZ** as emitters. a) Device configuration. b) Normalized electroluminescence spectra. c) Current density and luminance versus driving voltage characteristics. d) EQE versus brightness for **tBuCz2pTRZ**-based (black), **tBuCz2mTRZ**-based (red), and **tBuCz2m2pTRZ** (blue)-based devices (the photos shown from bottom left to right are for **tBuCz2pTRZ-**, **tBuCz2mTRZ-**, and **tBuCz2m2pTRZ**-based devices, respectively). e) Statistical histogram of EQE$_{max}$ for **tBuCz2m2pTRZ**-based OLEDs. f) The EQE$_{max}$ of all reported solution-processed host-free TADF OLEDs as a function of wavelength. All the data for devices are summarized in Table S8 (Supporting Information).

performance through the synergistic effects of *meta*- and *para*-connected donor dendrons to the central triazine acceptor core. Importantly, there are a large number of low-lying excited states in **tBuCz2m2pTRZ** that facilitates reverse intersystem crossing, and the distribution of donor dendrons can effectively suppress concentration quenching. The photophysical investigation in solution also indicates that some dendrons, which have very slow internal charge transfer, may be able to function as host moieties. The extremely small ΔE_{ST} and large oscillator strength in both solution and neat film are evidence of the qualities that make **tBuCz2m2pTRZ** a high-performance emitter in efficient solution-processed OLEDs. We believe that the dendrimer design strategy disclosed in our study provides a route to high-performance solution-processed TADF OLEDs and evidences the full potential of dendrimers as emissive materials.

8. Experimental Section

Synthesis: The procedures for the synthesis of the TADF dendrimer and the corresponding characterization are reported in the Supporting Information.

Sample Preparation and Photophysical Characterization: All solution samples were prepared in high-performance liquid chromatography (HPLC) grade solvents with varying concentrations on the order of 10^{-5} or 10^{-6} M for absorption and emission studies. Films were prepared by spin-coating 10 mg mL^{-1} of chloroform solutions of dendrimers. Absorption spectra were recorded at RT using a Shimadzu UV1800 double-beam spectrophotometer. Steady-state emission spectra and phosphorescence spectra were obtained using a Jasco FP-8600 spectrofluorometer. The time-resolved emission measurements were obtained using the iCCD camera by exponentially increasing delay and gating times where the gating time was kept lower by ten times compared to the delay time. All measurements were recorded under vacuum unless otherwise stated. Full details are presented in the Supporting Information.

Table 2. Summary of device performance.

Device No.[a]	Emitting layer	λ_{EL} [nm]	FWHM[b] [nm]	V_{on}[c] [V]	CE$_{max}$ [cd A^{-1}]	PE$_{max}$ [lm W^{-1}]	EQE$_{max}$ [%]	EQE$_{100}$ [%]	EQE$_{500}$ [%]	CIE (x,y)
1	**tBuCz2pTRZ**	500	95	3.1	49.4	45.7	18.5	16.1	10.3	0.23, 0.46
2	**tBuCz2mTRZ**	516	95	3.3	59.9	52.2	19.9	12.0	6.4	0.27, 0.53
3	**tBuCz2m2pTRZ**	540	97	3.1	98.8	91.3	28.7	21.2	14.3	0.37, 0.57
4	**tBuCz2m2pTRZ**+ 30 wt% OXD-7	540	97	3.1	95.4	88.1	28.4	26.4	22.7	0.37, 0.57

[a]The device structure is ITO/PEDOT:PSS (35 nm)/dendrimer (40 nm)/TmPyPB (40 nm)/LiF (1 nm)/Al (100 nm); [b]Full wavelength at highest maximum; [c]At the luminance of 1 cd m^{-2}.

**ADVANCED
SCIENCE NEWS**

www.advancedsciencenews.com

**ADVANCED
MATERIALS**

www.advmat.de
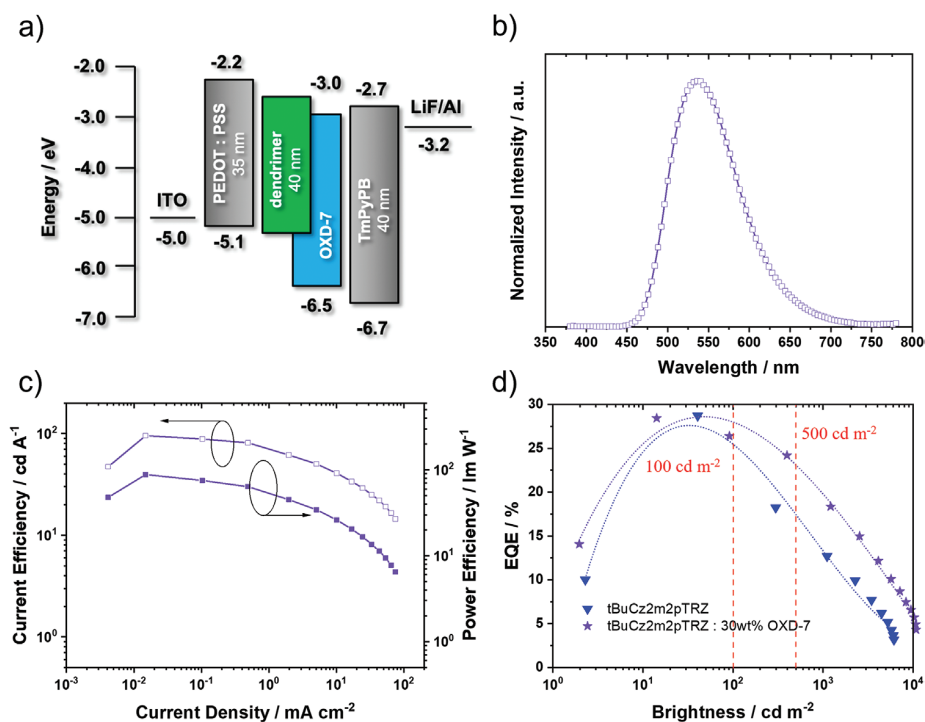
Figure 5. Electroluminescence characteristics of the OLED based on a **tBuCz2m2pTRZ**:30 wt% OXD-7 EML. a) Device configuration. b) Normalized electroluminescence spectra. c) Current efficiency and power efficiency versus current density. d) EQE versus brightness (comparison with the device without doping OXD-7 in the EML).

OLED Fabrication: The OLED devices were fabricated using a bottom-emitting architecture. A prepatterned ITO glass substrate was used as the anode. PEDOT:PSS8000 was spin-coated onto the clean ITO substrate as a hole-injection layer, then the 10 mg mL^{-1} dendrimers in chlorobenzene solution were spin-coated to form the EML. TmPyPB, LiF, and Al were each subsequently vacuum-deposited onto EML. More details are shown in the Supporting Information.

Supporting Information

Supporting Information is available from the Wiley Online Library or from the author.

Acknowledgements

Conflict of Interest

Dr. Dianming Sun and Prof. Eli Zysman-Colman are the co-inventors of a patent, PCT/GB2021/052844, based on the materials in this manuscript.

Data Availability Statement

The research data supporting this publication can be accessed at the University of St Andrews' Research Portal at https://doi.org/10.17630/e24f7f28-a9b4-426d-a74ff37334f08a0b.

Keywords

**ADVANCED
SCIENCE NEWS**

www.advancedsciencenews.com

**ADVANCED
MATERIALS**

www.advmat.de

[1] a) Y. Tao, K. Yuan, T. Chen, P. Xu, H. Li, R. Chen, C. Zheng, L. Zhang, W. Huang, *Adv. Mater.* **2014**, *26*, 7931; b) Y. Im, M. Kim, Y. J. Cho, J.-A. Seo, K. S. Yook, J. Y. Lee, *Chem. Mater.* **2017**, *29*, 1946; c) M. Y. Wong, E. Zysman-Colman, *Adv. Mater.* **2017**, *29*, 1605444; d) Z. Yang, Z. Mao, Z. Xie, Y. Zhang, S. Liu, J. Zhao, J. Xu, Z. Chi, M. P. Aldred, *Chem. Soc. Rev.* **2017**, *46*, 915; e) X. Cai, S. J. Su, *Adv. Funct. Mater.* **2018**, *28*, 1802558; f) Y. Liu, C. Li, Z. Ren, S. Yan, M. R. Bryce, *Nat. Rev. Mater.* **2018**, *3*, 18020; g) Y. Zou, S. Gong, G. Xie, C. Yang, *Adv. Opt. Mater.* **2018**, *6*, 1800568; h) X. Liang, Z.-L. Tu, Y.-X. Zheng, *Chem. - Eur. J.* **2019**, *25*, 5623.

[2] H. Uoyama, K. Goushi, K. Shizu, H. Nomura, C. Adachi, *Nature* **2012**, *492*, 234.

[3] a) W. Zeng, H. Y. Lai, W. K. Lee, M. Jiao, Y. J. Shiu, C. Zhong, S. Gong, T. Zhou, G. Xie, M. Sarma, K. T. Wong, C. C. Wu, C. Yang, *Adv. Mater.* **2017**, *30*, 1704961; b) Y. Yuan, Y. Hu, Y.-X. Zhang, J.-D. Lin, Y.-K. Wang, Z.-Q. Jiang, L.-S. Liao, S.-T. Lee, *Adv. Funct. Mater.* **2017**, *27*, 1700986; c) J.-X. Chen, K. Wang, C.-J. Zheng, M. Zhang, Y.-Z. Shi, S.-L. Tao, H. Lin, W. Liu, W.-W. Tao, X.-M. Ou, X.-H. Zhang, *Adv. Sci.* **2018**, *5*, 1800436; d) J.-X. Chen, W.-W. Tao, W.-C. Chen, Y.-F. Xiao, K. Wang, C. Cao, J. Yu, S. Li, F.-X. Geng, C. Adachi, C.-S. Lee, X.-H. Zhang, *Angew. Chem., Int. Ed.* **2019**, *58*, 14660; e) Y. Zhang, D. Zhang, T. Huang, A. J. Gillett, Y. Liu, D. Hu, L. Cui, Z. Bin, G. Li, J. Wei, *Angew. Chem., Int. Ed.* **2021**, *60*, 20498.

[4] a) T.-L. Wu, M.-J. Huang, C.-C. Lin, P.-Y. Huang, T.-Y. Chou, R.-W. Chen-Cheng, H.-W. Lin, R.-S. Liu, C.-H. Cheng, *Nat. Photonics* **2018**, *12*, 235; b) Y. Im, J. Y. Lee, *J. Inf. Disp.* **2017**, *18*, 101; c) Y. Zhang, D. Zhang, J. Wei, X. Hong, Y. Lu, D. Hu, G. Li, Z. Liu, Y. Chen, L. Duan, *Angew. Chem., Int. Ed.* **2020**, *132*, 17652.

[5] a) D. H. Ahn, S. W. Kim, H. Lee, I. J. Ko, D. Karthik, J. Y. Lee, J. H. Kwon, *Nat. Photonics* **2019**, *13*, 540; b) Y. Kondo, K. Yoshiura, S. Kitera, H. Nishi, S. Oda, H. Gotoh, Y. Sasada, M. Yanai, T. Hatakeyama, *Nat. Photonics* **2019**, *13*, 678; c) Q. Zhang, B. Li, S. Huang, H. Nomura, H. Tanaka, C. Adachi, *Nat. Photonics* **2014**, *8*, 326.

[6] Y. Xie, Z. Li, *J. Polym. Sci., Part A: Polym. Chem.* **2017**, *55*, 575.

[7] a) X.-K. Chen, S.-F. Zhang, J.-X. Fan, A.-M. Ren, *J. Phys. Chem. C* **2015**, *119*, 9728; b) J. Gibson, A. P. Monkman, T. J. Penfold, *ChemPhysChem* **2016**, *17*, 2956; c) J. Eng, J. Hagon, T. J. Penfold, *J. Mater. Chem. C* **2019**, *7*, 12942.

[8] a) K. Albrecht, K. Matsuoka, K. Fujita, K. Yamamoto, *Angew. Chem., Int. Ed.* **2015**, *54*, 5677; b) X. Ban, W. Jiang, T. Lu, X. Jing, Q. Tang, S. Huang, K. Sun, B. Huang, B. Lin, Y. Sun, *J. Mater. Chem. C* **2016**, *4*, 8810; c) Y. Li, G. Xie, S. Gong, K. Wu, C. Yang, *Chem. Sci.* **2016**, *7*, 5441; d) J. Luo, S. Gong, Y. Gu, T. Chen, Y. Li, C. Zhong, G. Xie, C. Yang, *J. Mater. Chem. C* **2016**, *4*, 2442; e) K. Albrecht, K. Matsuoka, D. Yokoyama, Y. Sakai, A. Nakayama, K. Fujita, K. Yamamoto, *Chem. Commun.* **2017**, *53*, 2439; f) X. Ban, W. Jiang, K. Sun, B. Lin,

Y. Sun, *ACS Appl. Mater. Interfaces* **2017**, *9*, 7339; g) Y. Li, T. Chen, M. Huang, Y. Gu, S. Gong, G. Xie, C. Yang, *J. Mater. Chem. C* **2017**, *5*, 3480; h) M. Godumala, S. Choi, H. J. Kim, C. Lee, S. Park, J. S. Moon, K. S. Woo, J. H. Kwon, M. J. Cho, D. H. Choi, *J. Mater. Chem. C* **2018**, *6*, 1160; i) K. Matsuoka, K. Albrecht, A. Nakayama, K. Yamamoto, K. Fujita, *ACS Appl. Mater. Interfaces* **2018**, *10*, 33343.

[9] S. Hirata, Y. Sakai, K. Masui, H. Tanaka, S. Y. Lee, H. Nomura, N. Nakamura, M. Yasumatsu, H. Nakanotani, Q. Zhang, K. Shizu, H. Miyazaki, C. Adachi, *Nat. Mater.* **2015**, *14*, 330.

[10] K. Albrecht, K. Matsuoka, K. Fujita, K. Yamamoto, *Mater. Chem. Front.* **2018**, *2*, 1097.

[11] a) K. Sun, Y. Sun, D. Liu, Y. Feng, X. Zhang, Y. Sun, W. Jiang, *Dyes Pigm.* **2017**, *147*, 436; b) K. Sun, Y. Sun, W. Tian, D. Liu, Y. Feng, Y. Sun, W. Jiang, *J. Mater. Chem. C* **2018**, *6*, 43.

[12] a) T. Matulaitis, P. Imbrasas, N. A. Kukhta, P. Baronas, T. Bučiūnas, D. Banevičius, K. Kazlauskas, J. V. Gražulevičius, S. Juršėnas, *J. Phys. Chem. C* **2017**, *121*, 23618; b) R. Braveenth, K. Y. Chai, *Materials* **2019**, *12*, 2646.

[13] W.-L. Tsai, M.-H. Huang, W.-K. Lee, Y.-J. Hsu, K.-C. Pan, Y.-H. Huang, H.-C. Ting, M. Sarma, Y.-Y. Ho, H.-C. Hu, C.-C. Chen, M.-T. Lee, K.-T. Wong, C.-C. Wu, *Chem. Commun.* **2015**, *51*, 13662.

[14] H. Liu, J. Zeng, J. Guo, H. Nie, Z. Zhao, B. Z. Tang, *Angew. Chem., Int. Ed.* **2018**, *57*, 9290.

[15] Z. Huang, Z. Bin, R. Su, F. Yang, J. Lan, J. You, *Angew. Chem., Int. Ed.* **2020**, *59*, 9992.

[16] D. Liu, W. Tian, Y. Feng, X. Zhang, X. Ban, W. Jiang, Y. Sun, *ACS Appl. Mater. Interfaces* **2019**, *11*, 16737.

[17] T. Huang, W. Jiang, L. Duan, *J. Mater. Chem. C* **2018**, *6*, 5577.

[18] D. Sun, R. Saxena, X. Fan, S. Athanasopoulos, E. Duda, M. Zhang, S. Bagnich, X. Zhang, A. Köhler, E. Zysman-Colman, *Adv. Sci.* **2022**, https://doi.org/10.1002/advs.202201470.

[19] J. Gibson, T. Penfold, *Phys. Chem. Chem. Phys.* **2017**, *19*, 8428.

[20] A. M. Nardes, M. Kemerink, M. M. de Kok, E. Vinken, K. Maturova, R. A. J. Janssen, *Org. Electron.* **2008**, *9*, 727.

[21] E. Duda, D. Hall, S. Bagnich, C. L. Carpenter-Warren, R. Saxena, M. Y. Wong, D. B. Cordes, A. M. Z. Slawin, D. Beljonne, Y. Olivier, E. Zysman-Colman, A. Köhler, *J. Phys. Chem. B* **2022**, *126*, 552.

[22] P.-I. Shih, C.-L. Chiang, A. K. Dixit, C.-K. Chen, M.-C. Yuan, R.-Y. Lee, C.-T. Chen, E. W.-G. Diau, C.-F. Shu, *Org. Lett.* **2006**, *8*, 2799.

[23] G. Wypych, *Handbook of Solvents*, ChemTec Publishing, Toronto, Canada **2001**.

[24] a) H. Noda, X.-K. Chen, H. Nakanotani, T. Hosokai, M. Miyajima, N. Notsuka, Y. Kashima, J.-L. Brédas, C. Adachi, *Nat. Mater.* **2019**, *18*, 1084; b) L.-S. Cui, A. J. Gillett, S.-F. Zhang, H. Ye, Y. Liu, X.-K. Chen, Z.-S. Lin, E. W. Evans, W. K. Myers, T. K. Ronson, H. Nakanotani, S. Reineke, J.-L. Bredas, C. Adachi, R. H. Friend, *Nat. Photonics* **2020**, *14*, 636.

ADVANCED MATERIALS

Supporting Information

Thermally Activated Delayed Fluorescent Dendrimers that Underpin High-Efficiency Host-Free Solution-Processed Organic Light-Emitting Diodes

Dianming Sun,* Eimantas Duda, Xiaochun Fan, Rishabh Saxena, Ming Zhang, Sergey Bagnich, Xiaohong Zhang,* Anna Köhler,* and Eli Zysman-Colman*

Supporting Information

Thermally Activated Delayed Fluorescent Dendrimers that Underpin High-Efficiency Host-Free Solution-Processed Organic Light-Emitting Diodes

Dianming Sun[1,2†*], Eimantas Duda[3†], Xiaochun Fan[1], Rishabh Saxena[3], Ming Zhang[1], Sergey Bagnich[3], Xiaohong Zhang[1*], Anna Köhler[3*] and Eli Zysman-Colman[2*]

[1]Institute of Functional Nano & Soft Materials (FUNSOM) and Jiangsu Key Laboratory for Carbon-Based Functional Materials & Devices, Joint International Research Laboratory of Carbon-Based Functional Materials and Devices, Soochow University, Suzhou, Jiangsu 215123, P.R. China. *E-mail: xiaohong_zhang@suda.edu.cn

[2]Organic Semiconductor Centre, EaStCHEM School of Chemistry, University of St Andrews, St Andrews KY16 9ST, UK. *E-mail: sd235@st-andrews.ac.uk, eli.zysman-colman@st-andrews.ac.uk

[3]Soft Matter Optoelectronics, BIMF & BPI, University of Bayreuth, Universitätsstraße 30, 95447 Bayreuth, Germany. *E-mail: anna.koehler@uni-bayreuth.de

[†]These two authors contributed equally to this work.

234

Table of Contents

Synthesis and characterization

All solvents and reagents were purchased and used as received. Air-sensitive reactions were performed under a nitrogen atmosphere using Schlenk techniques. Flash column chromatography was carried out using silica gel (Silia-P from Silicycle, 60 Å, 40-63 μm). Analytical thin-layer-chromatography (TLC) was performed with silica plates with aluminum backings (250 μm with F-254 indicator). Bio-Beads® SX3 resin was used to fill a 1.4 meter-length GPC column for the further purification of the target dendrimers. TLC visualization was accomplished by 254/365 nm UV lamp. ^{1}H, ^{13}C, ^{19}F and 2D NMR spectra were recorded on a Bruker Advance spectrometer. The following abbreviations have been used for multiplicity assignments: "s" for singlet, "d" for doublet, "dd" for doublet of doublets, "t" for triplet, "m" for multiplet, and "brs" for broad singlet. Deuterated chloroform (CDCl$_3$) was used as the solvent of record. Matrix Assisted Laser Desorption/Ionization-Time of Flight-Mass Spectrometry (MALDI-TOF-MS) was performed by Bruker autoflex MALDI-TOF mass spectrometer. High-resolution mass spectrometry (HRMS) was performed by BSRC Mass Spectrometry Facility, St Andrews. Elemental analyses were performed by Mr. Stephen Boyer, London Metropolitan University. Melting points were measured using open-ended capillaries on an Electrothermal 1101D Mel-Temp apparatus.

Detailed synthetic routes and procedures of the target compounds are outlined as below.
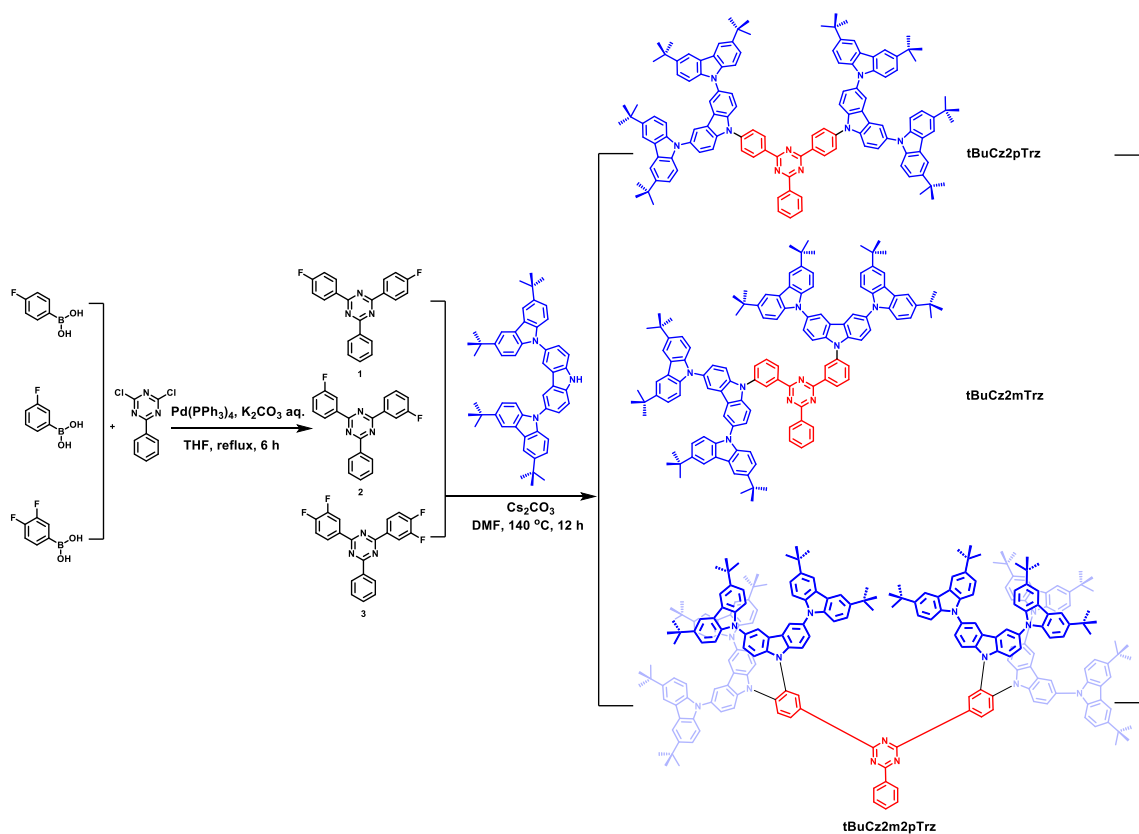
Scheme S1. Synthetic route for **tBuCz2pTRZ**, **tBuCz2mTRZ** and **tBuCz2m2pTRZ**.

Synthesis of *2,4-bis(4-fluorophenyl)-6-phenyl-1,3,5-triazine (1)*.

A mixture of (4-fluorophenyl)boronic acid (559 mg, 4 mmol, 2 equiv.), 2,4-dichloro-6-phenyl-1,3,5-triazine (452 mg, 2 mmol, 1 equiv.) and tetrakis(triphenylphosphine)palladium(0) (115 mg, 0.1 mmol, 0.25 equiv.) in degassed THF (20 mL), and 2M K_2CO_3 (5 mL) aqueous solution was refluxed for 12 h. After cooling to room temperature, the resulting precipitate was filtered and washed with both water and THF (each 3×20 mL). Then the collected precipitate was dried in a desiccator to afford a white solid (420 mg). **Yield**: 61%. **R$_f$:** 0.6 (Hexane: DCM=2:1). **Mp**: 254-255 °C; **Litt**:[1] 253-255 °C. **¹H NMR (400 MHz, CDCl₃) δ (ppm)**: 8.82 (m, 6H), 7.65 (m, 3H), 7.29 (m, 4H). **¹⁹F NMR (376 MHz, CDCl₃) δ (ppm)**: -106.93. **¹³C NMR (100 MHz, CDCl₃) δ (ppm)**: 171.66, 170.67, 167.12, 164.60, 135.99, 132.69, 132.29, 131.35, 128.95, 115.87. **HRMS-ESI (m/z)**: [M+H]$^+$ Calcd. for **C$_{21}$H$_{14}$F$_2$N$_3$**: 346.1156, **Found**: 346.1149. **Anal.**

Calcd. For C$_{21}$H$_{13}$F$_2$N$_3$ (%): C 73.04, H 3.79, N 12.17; **Found**: C 73.28, H 3.67, N 12.10. The characterization matches well with that reported in the literature.[1-2]

Synthesis of *2,4-bis(3-fluorophenyl)-6-phenyl-1,3,5-triazine (2)*.

A similar procedure to compound **1** was employed to afford a white solid (390 mg). **Yield**: 57%. **R$_f$**: 0.6 (Hexane: DCM=2:1). **Mp**: 256-257 ^{o}C. **^{1}H NMR (400 MHz, CDCl$_3$) δ (ppm)**: 8.80 (dt, J$_1$=6.7 Hz, J$_2$=1.5 Hz, 2H), 8.61 (dt, J$_1$=8 Hz, J$_2$=1.3 Hz, 2H), 8.49 (dq, J$_1$=10 Hz, J$_2$=1.5 Hz, 2H), 7.67 (m, 5H), 7.37 (t, J=8.3 Hz, 2H). **^{19}F NMR (376 MHz, CDCl$_3$) δ (ppm)**: -112.56. **^{13}C NMR (100 MHz, CDCl$_3$) δ (ppm)**: 171.95, 170.78, 164.38, 161.94, 138.42, 135.69, 132.90, 130.28, 129.04, 124.67, 119.70, 115.84. **HRMS-ESI (m/z)**: [M+H]$^+$ Calcd. for C$_{21}$H$_{14}$F$_2$N$_3$: 346.1156, **Found**: 346.1149. **Anal. Calcd. For C$_{21}$H$_{13}$F$_2$N$_3$ (%)**: C 73.04, H 3.79, N 12.17; **Found**: C 73.69, H 3.61, N 12.17.

Synthesis of *2,4-bis(3,4-difluorophenyl)-6-phenyl-1,3,5-triazine (3)*.

A similar procedure to compound **1** was employed to afford a white solid (630 mg). **Yield**: 83%. **R$_f$**: 0.65 (Hexane: DCM=2:1). **Mp**: decomposes at 305 ^{o}C before melting. **^{1}H NMR (400 MHz, CDCl$_3$) δ (ppm)**: 8.76 (d, J=7.6 Hz, 2H), 8.62 (t, J=10.7 Hz, 4H), 7.67 (m, 3H), 7.42 (q, J=8.6 Hz, 2H). **^{19}F NMR (376 MHz, CDCl$_3$) δ (ppm)**: -131.00 (d), -136.61 (d). **Anal. Calcd. For C$_{21}$H$_{11}$F$_4$N$_3$ (%)**: C 66.14, H 2.91, N 11.02; **Found**: C 66.16, H 2.83, N 10.84.

Synthesis of *9',9''''-((6-phenyl-1,3,5-triazine-2,4-diyl)bis(4,1-phenylene))bis(3,3'',6,6''-tetra-tert-butyl-9'H-9,3':6',9''-tercarbazole) (tBuCz2pTRZ)*.

Under nitrogen, a mixture of 3,3'',6,6''-tetrakis(*tert*-butyl-9'H-9,3':6',9''-tercarbazole) (794 mg, 1.1 mmol, 4.4 equiv.), 2,4-bis(3,4-difluorophenyl)-6-phenyl-1,3,5-triazine (95 mg, 0.25 mmol, 1 equiv.) and cesium carbonate (652 mg, 2 mmol, 8 equiv.) in dry DMF (20 ml) was reflux for

24 h. After cooling to room temperature, the reaction was extracted with chloroform and washed with water (3 × 30 mL). The organic phase was dried over Na_2SO_4 and concentrated under reduced pressure. The crude product was purified by column chromatography on silica gel using 1:20 dichloromethane/hexane as eluent and then further purification was performed with preparative GPC column using THF as eluent to afford a yellow solid (251 mg). **Yield**: 58%. **R$_f$:** 0.5 (Hexane: DCM=2:1). **^{1}H NMR (400 MHz, CDCl$_3$) δ (ppm)**: 9.23 (d, J=8.6 Hz, 4H), 8.95 (dd, J$_1$=6.4 Hz, J$_2$=1.5 Hz, 2H), 8.31 (d, J=2Hz, 4H), 8.20 (d, J=1.7Hz, 8H), 8.07 (d, J=8.7 Hz, 4H), 7.85 (d, J=8.6Hz, 4H), 7.72 (dd, J$_1$=6.8 Hz, J$_2$=2Hz, 7H), 7.52 (dd, J$_1$=6.9 Hz, J$_2$=1.9Hz, 8H), 7.41 (d, J=8.6Hz, 8H), 1.50 (s, 72H). **^{13}C NMR (100 MHz, CDCl$_3$) δ (ppm)**: 172.16, 171.08, 142.66, 141.32, 140.10, 139.94, 135.96, 135.48, 131.39, 131.05, 129.16, 128.90, 126.94, 126.19, 124.46, 123.64, 123.18, 119.45, 116.28, 111.31, 109.09, 34.77, 32.08. **MALDI-TOF-MS** (m/z): [M]$^+$ Calculated: 1749.41, **Found**: 1749.30. **Anal. Calcd. For C$_{125}$H$_{121}$N$_9$ (%)**: C, 85.82; H, 6.97; N, 7.21; **Found**: C, 85.76; H, 7.05; N, 7.19.

Synthesis of ***9',9''''-((6-phenyl-1,3,5-triazine-2,4-diyl)bis(3,1-phenylene))bis(3,3'',6,6''-tetra-tert-butyl-9'H-9,3':6',9''-tercarbazole) (tBuCz2mTRZ)***.

A similar procedure to ***tBuCz2mTRZ*** was employed but using **2** and 3,3'',6,6''-tetrakis(*tert*-butyl-9'H-9,3':6',9''-tercarbazole). **Yield**: 17% (120 mg). **R$_f$:** 0.4 (Hexane: DCM=2:1). **^{1}H NMR (400 MHz, CDCl$_3$) δ (ppm)**: 9.17 (s, 2H), 9.01 (d, J=7.7Hz, 2H), 8.80 (d, J=7.7Hz, 2H), 8.31 (s, 4H), 8.17 (s, 8H), 8.00 (d, J=7.7Hz, 2H), 7.94 (t, J=7.7Hz, 2H), 7.71 (d, J=7.7Hz, 4H), 7.67 (d, J=7.7Hz, 5H), 7.58 (t, J=7.7Hz, 2H), 7.46 (d, J=7.7Hz, 8H), 7.38 (d, J=7.7Hz, 8H), 1.47 (s, 72H). **^{13}C NMR (100 MHz, CDCl$_3$) δ (ppm)**: 172.3, 171.22, 142.63, 140.53, 140.14, 138.59, 137.99, 135.61, 131.48, 131.16, 130.78, 129.18, 128.89, 128.78, 127.85, 126.17, 124.14, 123.61, 123.17, 119.41, 116.27, 111.15, 109.10, 34.76, 32.07. **MALDI-TOF-MS**

(m/z): [M]$^+$ Calculated: 1749.41, **Found**: 1749.28. **Anal. Calcd. For C$_{125}$H$_{121}$N$_9$ (%)**: C, 85.82; H, 6.97; N, 7.21; **Found**: C, 85.71; H, 7.09; N, 7.20.

Synthesis of ***9',9'''',9'''''''',9''''''''''''-((6-phenyl-1,3,5-triazine-2,4-diyl)bis(benzene-4,1,2-triyl))tetrakis(3,3'',6,6''-tetra-tert-butyl-9'H-9,3':6',9''-tercarbazole) (tBuCz2m2pTRZ)***.

A similar procedure to ***tBuCz2mTRZ*** but using **3** and 3,3'',6,6''-tetrakis(*tert*-butyl-9'H-9,3':6',9''-tercarbazole). **Yield**: 82% (695 mg). **R$_f$:** 0.4 (Hexane: DCM=2:1). **^{1}H NMR (500 MHz, CDCl$_3$) δ (ppm)**: 9.72 (d, J = 2.0 Hz, 2H), 9.50 (dd, J = 8.3, 2.0 Hz, 2H), 9.03 – 8.97 (m, 2H), 8.52 (d, J = 8.3 Hz, 2H), 8.11 (s, 16H), 8.04 (dd, J = 14.1, 2.0 Hz, 8H), 7.77 (d, J = 7.1 Hz, 1H), 7.73 (t, J = 7.3 Hz, 2H), 7.48 (d, J = 8.6 Hz, 4H), 7.44 (d, J = 8.6 Hz, 4H), 7.34 (ddd, J = 10.2, 8.5, 2.0 Hz, 8H), 7.10 (s, 32H), 1.36 (s, 144H). **^{13}C NMR (126 MHz, CDCl$_3$) δ (ppm)**: 172.86, 170.85, 142.51, 139.77, 139.20, 139.01, 137.77, 135.42, 134.67, 133.58, 131.75, 131.49, 130.36, 129.42, 129.13, 125.26, 124.48, 124.32, 123.05, 118.91, 116.12, 111.31, 111.20, 108.71, 77.23, 34.62, 31.98. **MALDI-TOF-MS** (m/z): [M]$^+$ Calculated: 3189.44, Found: 3189.43. **Anal. Calcd. For C$_{229}$H$_{227}$N$_{15}$ (%)**: C, 86.24; H, 7.17; N, 6.59; **Found**: C, 86.21; H, 7.19; N, 6.60.

Morphology

Atomic force microscopy (AFM) height map of **tBuCz2pTRZ**, **tBuCz2mTRZ** and **tBuCz2m2pTRZ** with a topographic image area of 5 × 5 μm were carried out on a Bruker Dimension Icon AFM equipped with Scanasyst-Air peak force tapping mode AFM tips from Bruker.
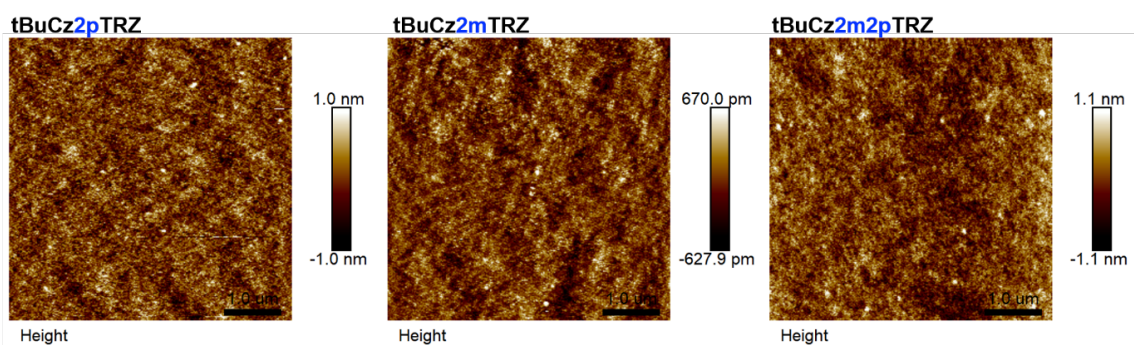
Figure S1. AFM height images of **tBuCz2pTRZ**, **tBuCz2mTRZ** and **tBuCz2m2pTRZ** spin-coated films.

Thermal properties

Thermogravimetric analysis (TGA) was undertaken with a METTLER TOLEDO TGA/DSC 1/1100SF instrument. The thermal stability of the samples under a nitrogen atmosphere was determined by measuring their weight loss while heating at a rate of 10 °C min^{-1} from ambient temperature to 650 °C. Differential scanning calorimetry (DSC) was performed on a TA DSC 2010 differential scanning calorimeter at a heating rate of 10 °C min^{-1} from 0 to 350 °C under nitrogen atmosphere. The glass transition temperature (T_g) was not observed from the second heating scan.
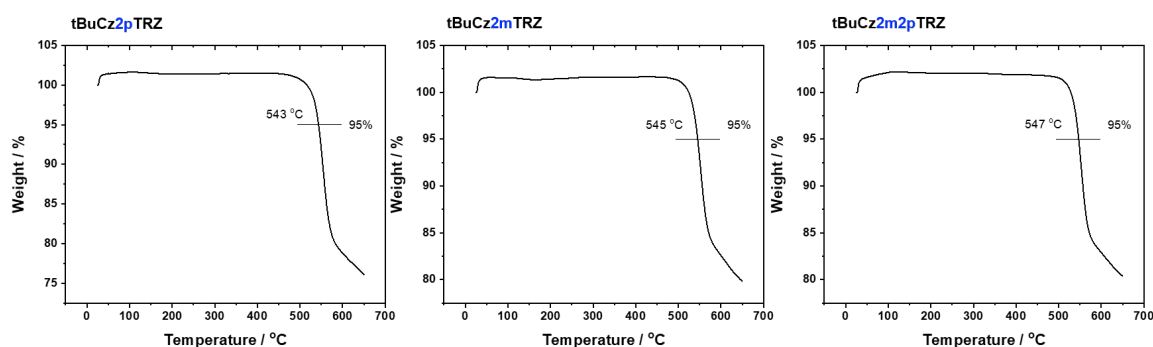
Figure S2. TGA curves of **tBuCz2pTRZ**, **tBuCz2mTRZ** and **tBuCz2m2pTRZ** recorded at a heating rate of 10 °C/min under nitrogen atmosphere.

S8
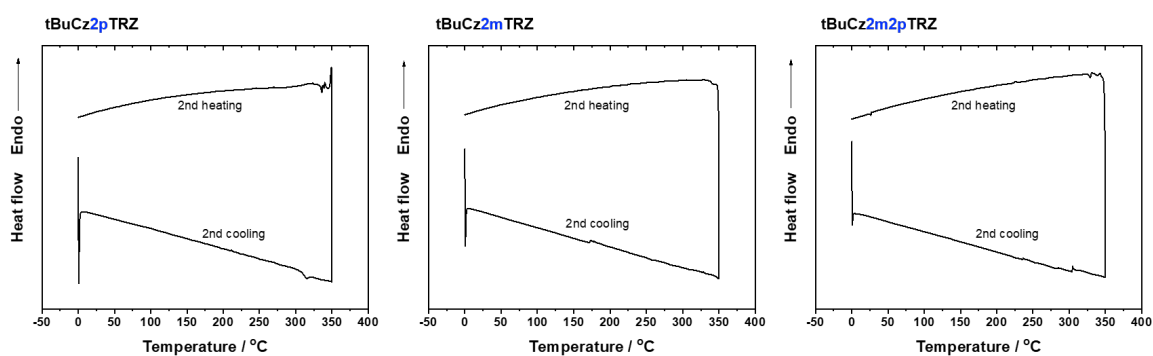
Figure S3. DSC traces of **tBuCz2pTRZ**, **tBuCz2mTRZ** and **tBuCz2m2pTRZ** recorded at a heating rate of 10 ºC/min under nitrogen atmosphere.

Electrochemistry measurements

Cyclic Voltammetry (CV) analysis and Differential pulse voltammetry (DPV) were performed on an Electrochemical Analyzer potentiostat model 620 D from CH Instruments. Samples were prepared by dissolving 5 mg of each dendrimer in dichloromethane (DCM) solution, which were degassed by sparging with DCM-saturated nitrogen gas for 5 minutes prior to measurements. All measurements were performed using 0.1 M DCM solution of tetra-*n*-butylammonium hexafluorophosphate [*n*Bu$_4$N]PF$_6$ as the electrolyte. An Ag/Ag$^+$ electrode was used as the reference electrode while a glassy carbon electrode and a platinum wire were used as the working electrode and counter electrode, respectively. The redox potentials are reported relative to a saturated calomel electrode (SCE) with a ferrocenium/ferrocene (Fc/Fc$^+$) redox couple as the internal standard (0.46 V vs SCE).[3] The HOMO and LUMO energies were determined using the relation $E_{HOMO/LUMO} = -(E_{ox}/E_{red} + 4.8)$ eV, where E_{ox} and E_{red} are the peak values of anodic and cathodic potentials, respectively calculated from DPV relative to Fc/Fc$^+$.[4]

242
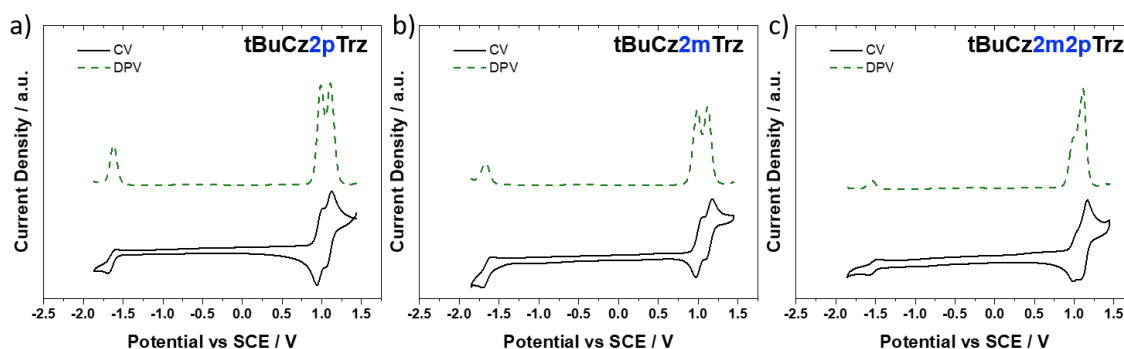
Figure S4. Cyclic voltammogram (CV) and differential pulse voltammetry (DPV) of **tBuCz2pTRZ**, **tBuCz2mTRZ** and **tBuCz2m2pTRZ** in degassed DCM with 0.1 M [nBu$_4$N]PF$_6$ as the supporting electrolyte and Fc/Fc$^+$ as the internal reference (0.46 V vs SCE [3]).

Table S1. Electrochemical data and theoretical properties of **tBuCz2pTRZ**, **tBuCz2mTRZ** and **tBuCz2m2pTRZ**

	Electrochemical potential [a]			Theoretical [e]					
	E_{ox} [b] / V	E_{red} [c] / V	ΔE_{H-L} [d] / V	HOMO / eV	LUMO / eV	f [f]	S_1	T_1	ΔE_{ST} / eV
tBuCz2pTRZ	1.07	1.67	2.74	-5.28	-2.20	0.26	2.70	2.62	0.08
tBuCz2mTRZ	1.07	1.67	2.74	-5.25	-2.25	0.00	2.62	2.58	0.04
tBuCz2m2pTRZ	1.07	1.54	2.61	-5.15	-2.33	0.10	2.46	2.37	0.09

[a] Potential values were obtained from the DPV peak values and referenced with respect to SCE (Fc/Fc$^+$ = 0.46 eV [3]), the measurement was performed in DCM; [b] Oxidation potential calculated from the DPV peak value; [c] Reduction potential calculated from the DPV peak value; [d] ΔE_{H-L} = E_{ox}-E_{red}; [e] Calculated in the gas phase at PBE0/6-31G(d,p) level; [f] Calculated oscillator strength of S_1.

Theoretical calculations

The ground state optimization was carried out at the Density Functional Theory (DFT) level with Gaussian 09[3] using the PBE0 functional[5] and the 6-31G(d,p) basis set[6] under vacuum. Excited state calculations have been performed at Time-Dependent DFT (TD-DFT) within the Tamm-Dancoff approximation (TDA)[7] using the same functional and basis set as for ground

S10

state geometry optimization. This methodology has been proven to show quantitative estimate of ΔE_{ST} in comparison to experiments.[8]
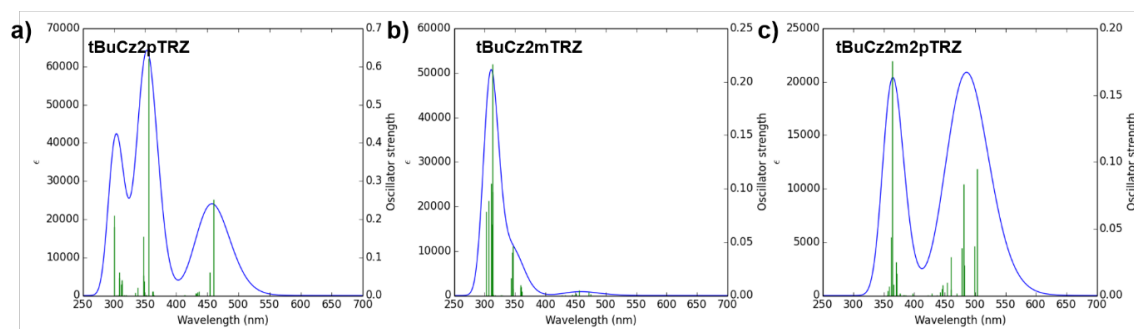
Figure S5. Simulated absorption spectra of a) **tBuCz2pTRZ**, b) **tBuCz2mTRZ** and c) **tBuCz2m2pTRZ** as calculated at the TDA-PBE0/6-31G(d,p) level in the gas phase.
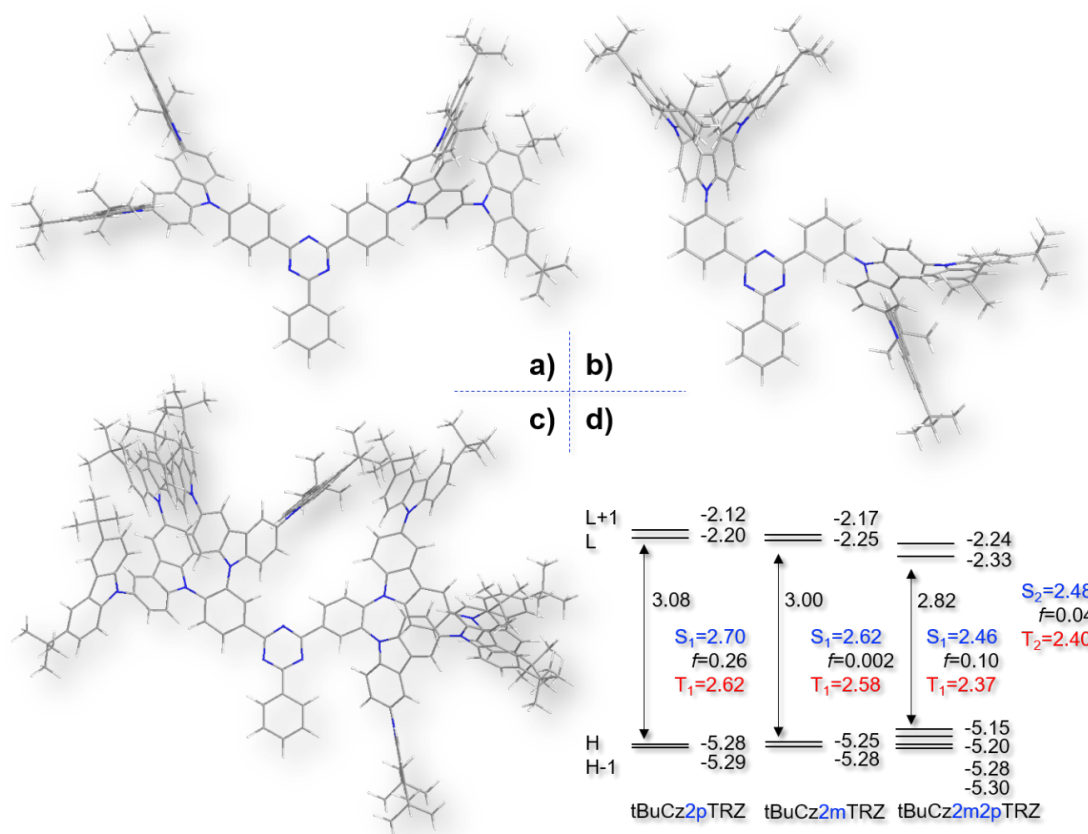
Figure S6. Optimized molecular structures of a) **tBuCz2pTRZ**, b) **tBuCz2mTRZ** and c) **tBuCz2m2pTRZ** in the ground state and d) energy level diagram for HOMO (H), HOMO-1 (H-1), LUMO (L), LUMO+1 (L+1), singlet (S_1, S_2), triplet energy (T_1, T_2) and oscillator strength (*f*).
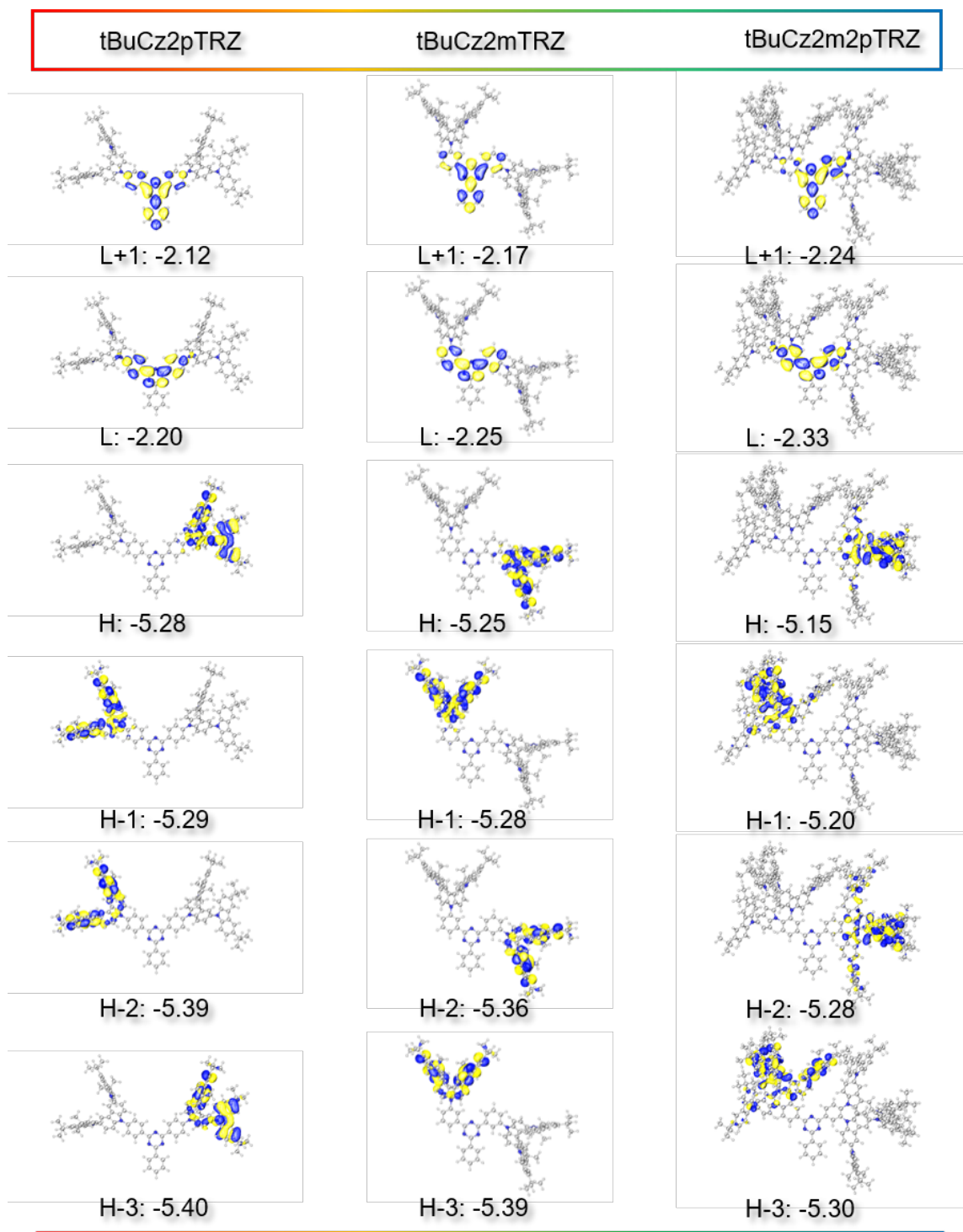
Figure S7. Calculated distribution of molecular orbitals for **tBuCz2pTRZ**, **tBuCz2mTRZ** and

tBuCz2m2pTRZ. (isovalue= 0.02)
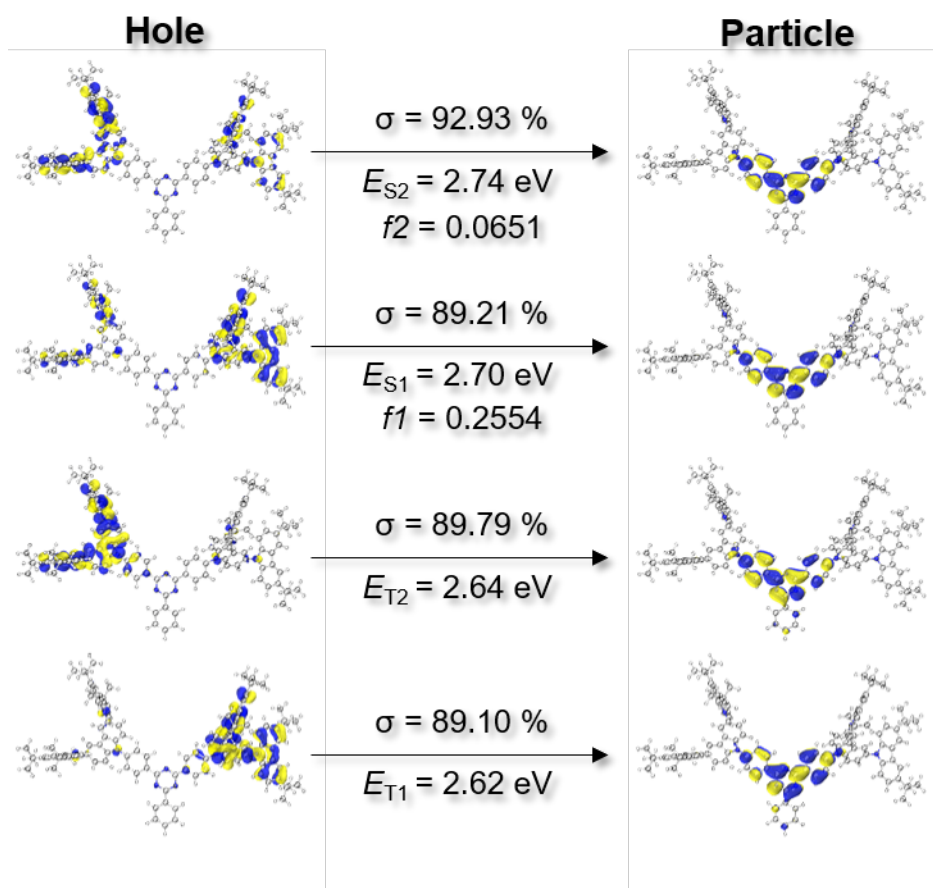
Figure S8. Pictorial representation of the natural transition orbitals (NTO) describing the S1 / T1 states for **tBuCz2pTRZ**, as calculated at the TDA-PBE0/6-31G(d,p) level. σ refers to the weight of the illustrated hole-particle contribution to the excitation. f indicates the oscillator strength and E_S/ E_T are the calculated first singlet/ triplet energy.
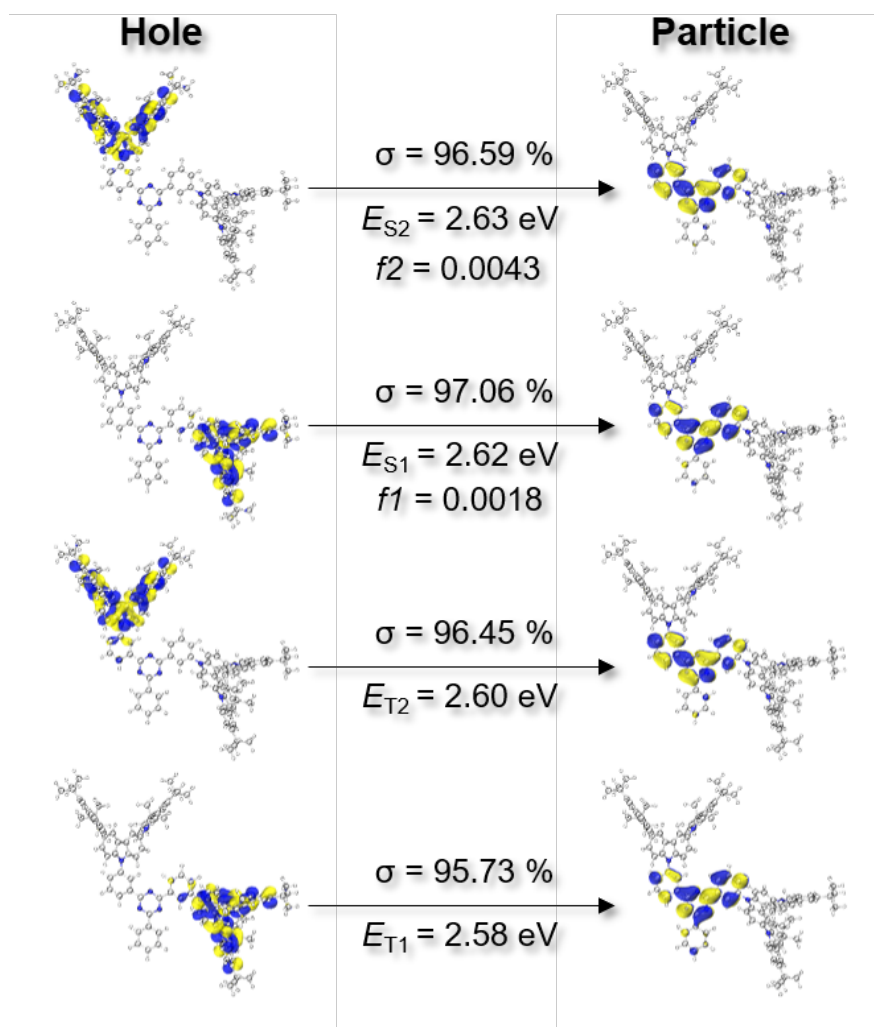
Figure S9. Pictorial representation of the natural transition orbitals (NTO) describing the S1 / T1 states for **tBuCz2mTRZ**, as calculated at the TDA-PBE0/6-31G(d,p) level. σ refers to the weight of the illustrated hole-particle contribution to the excitation. f indicates the oscillator strength and E_S/ E_T are the calculated first singlet/ triplet energy.
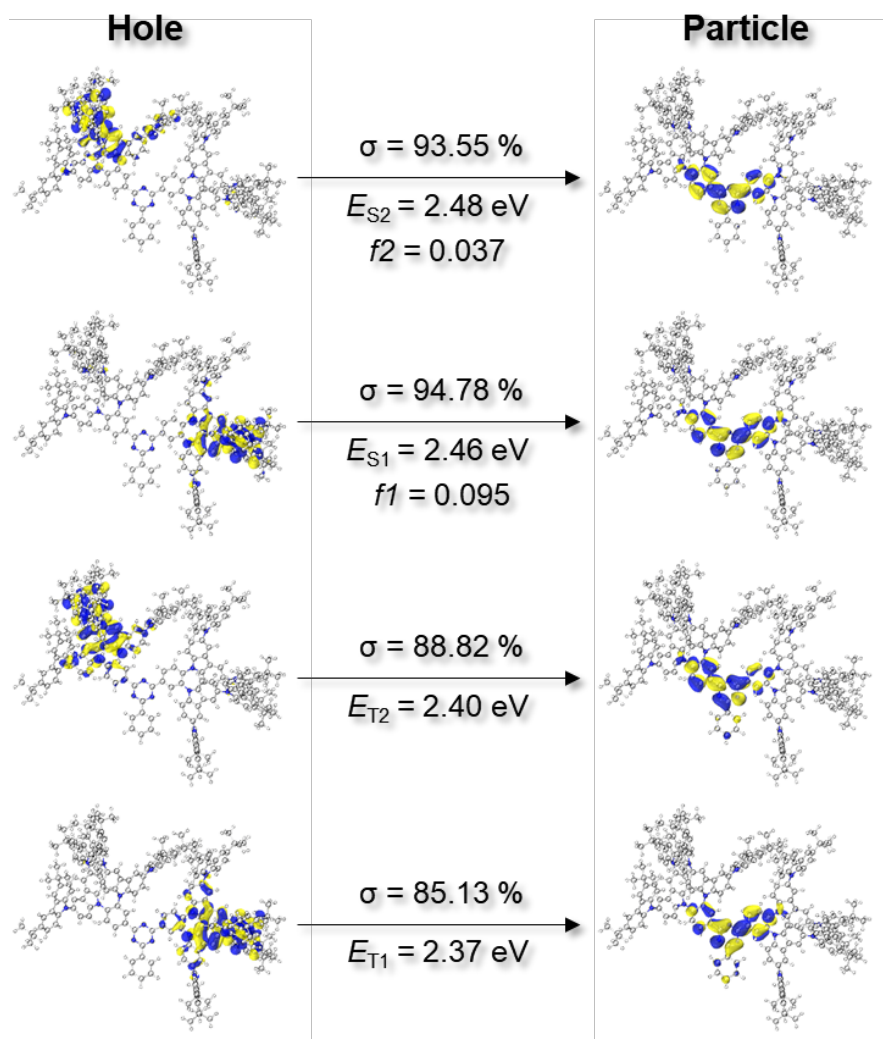
Figure S10. Pictorial representation of the natural transition orbitals (NTO) describing the S1 / T1 states for **tBuCz2m2pTRZ**, as calculated at the TDA-PBE0/6-31G(d,p) level. σ refers to the weight of the illustrated hole-particle contribution to the excitation. f indicates the oscillator strength and E_S/ E_T are the calculated first singlet/ triplet energy.

Table S2. Selected low energy vertical transitions with corresponding oscillator strengths (*f*) and character assignments for compound **tBuCz2pTRZ** calculated at the PBE0/6-31G(d,p) theory level.

State	E / eV	*f*	Main contribution
T_1	2.62	0	H-1->LUMO (16%), HOMO->LUMO (58%), HOMO->L+1 (12%)
T_2	2.64	0	H-1->LUMO (57%), H-1->L+1 (13%), HOMO->LUMO (17%)
S_1	2.70	0.2554	H-1->LUMO (20%), HOMO->LUMO (69%)
S_2	2.74	0.0651	H-1->LUMO (71%), HOMO->LUMO (21%)
T_3	2.83	0	HOMO->LUMO (15%), HOMO->L+1 (81%)
T_4	2.84	0	H-1->LUMO (16%), H-1->L+1 (78%)
S_3	2.84	0.0117	HOMO->L+1 (82%)
T_5	2.85	0	H-2->LUMO (87%)
S_4	2.85	0.0103	H-1->L+1 (79%)
T_6	2.86	0	H-3->LUMO (89%)
S_5	2.86	0.0060	H-2->LUMO (89%)
S_6	2.87	0.0057	H-3->LUMO (92%)
T_7	2.99	0	H-2->L+1 (90%)
S_7	2.99	0.0006	H-2->L+1 (92%)
T_8	3.00	0	H-3->L+1 (91%)
S_8	3.00	0.0004	H-3->L+1 (93%)

Table S3. Selected low energy vertical transitions with corresponding oscillator strengths (*f*) and character assignments for compound **tBuCz2mTRZ** calculated at the PBE0/6-31G(d,p) theory level.

State	E / eV	*f*	Main contribution
T_1	2.58	0	HOMO->LUMO (76%), HOMO->L+1 (17%)
T_2	2.60	0	H-1->LUMO (88%)
S_1	2.62	0.0018	HOMO->LUMO (85%), HOMO->L+1 (12%)
S_2	2.63	0.0043	H-1->LUMO (94%)
T_3	2.71	0	HOMO->LUMO (19%), HOMO->L+1 (77%)
S_3	2.72	0.0052	HOMO->LUMO (12%), HOMO->L+1 (84%)
T_4	2.75	0	H-1->L+1 (87%)
S_4	2.75	0.0022	H-1->L+1 (91%)
T_5	2.77	0	H-2->LUMO (89%), H-2->L+1 (10%)
S_5	2.77	0.0001	H-2->LUMO (89%)
T_6	2.79	0	H-3->LUMO (92%)
S_6	2.79	0.0009	H-3->LUMO (92%)
T_7	2.86	0	H-2->L+1 (88%)
S_7	2.86	0.0006	H-2->L+1 (88%)
T_8	2.90	0	H-3->L+1 (96%)
S_8	2.90	0.0002	H-3->L+1 (95%)

Table S4. Selected low energy vertical transitions with corresponding oscillator strengths (*f*) and character assignments for compound **tBuCz2m2pTRZ** calculated at the PBE0/6-31G(d,p) theory level.

State	E / eV	*f*	Main contribution
T_1	2.37	0	HOMO->LUMO (50%), HOMO->L+1 (26%)
T_2	2.40	0	H-1->LUMO (76%)
S_1	2.46	0.0950	HOMO->LUMO (71%), HOMO->L+1 (17%)
S_2	2.48	0.0370	H-1->LUMO (83%)
T_3	2.53	0	H-3->LUMO (89%)
T_4	2.54	0	H-2->LUMO (62%), H-2->L+1 (21%)
T_5	2.56	0	HOMO->LUMO (30%), HOMO->L+1 (59%)
S_3	2.57	0.0225	H-3->LUMO (12%), HOMO->LUMO (16%), HOMO->L+1 (62%)
S_4	2.57	0.0834	H-3->LUMO (59%), H-2->LUMO (12%), HOMO->L+1 (15%)
S_5	2.60	0.0354	H-3->LUMO (19%), H-2->LUMO (62%), H-2->L+1 (13%)
T_6	2.63	0	H-1->L+1 (83%)
S_6	2.64	0.0016	H-1->L+1 (84%)
T_7	2.68	0	H-4->LUMO (80%)
T_8	2.69	0	H-2->LUMO (26%), H-2->L+1 (65%)
S_7	2.69	0.0290	H-4->LUMO (54%), H-2->L+1 (23%)
S_8	2.70	0.0045	H-4->LUMO (26%), H-2->LUMO (10%), H-2->L+1 (52%)
T_9	2.71	0	H-5->LUMO (71%), H-5->L+1 (17%)
T_{10}	2.72	0	H-3->L+1 (71%)
S_9	2.73	0.0096	H-5->LUMO (74%), H-5->L+1 (10%)
S_{10}	2.73	0.0003	H-4->LUMO (11%), H-3->L+1 (69%)
T_{11}	2.75	0	H-7->LUMO (85%)
T_{12}	2.76	0	H-6->LUMO (75%), H-6->L+1 (16%)
S_{11}	2.78	0.0079	H-7->LUMO (57%), H-6->LUMO (32%)
S_{12}	2.78	0.0049	H-7->LUMO (37%), H-6->LUMO (46%)
T_{13}	2.80	0	H-6->L+1 (19%), H-5->LUMO (15%), H-5->L+1 (53%)
S_{13}	2.80	0.0028	H-6->L+1 (19%), H-5->LUMO (10%), H-5->L+1 (58%)
T_{14}	2.83	0	H-4->L+1 (83%)
S_{14}	2.83	0.0001	H-4->L+1 (82%)
T_{15}	2.88	0	H-6->LUMO (19%), H-6->L+1 (52%), H-5->L+1 (12%)
S_{15}	2.89	0.0018	H-6->LUMO (10%), H-6->L+1 (64%), H-5->L+1 (20%)

Calculations of four generations of *tert*-butylcarbazole-TRZ based derivatives
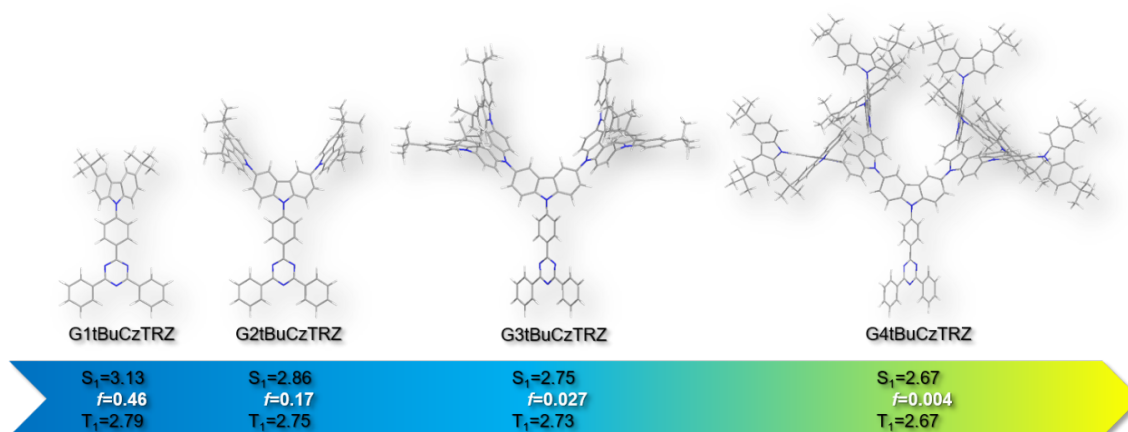
Figure S11. Optimized molecular structures and excited state energy levels for *tert*-butylcarbazole-triphenyltriazine derivatives: **G1tBuCzTRZ**, **G2tBuCzTRZ**, **G3tBuCzTRZ** and **G4tBuCzTRZ**.
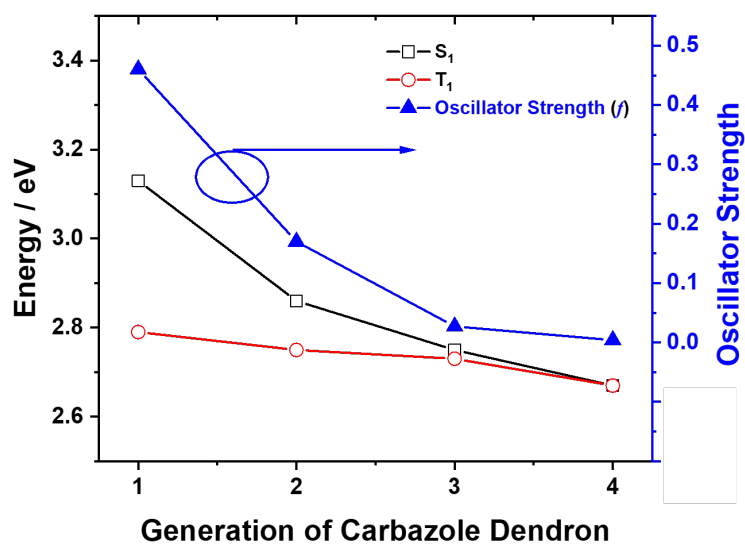
Figure S12. Calculated S_1 and T_1, oscillator strength (*f*) for the four model compounds: **G1tBuCzTRZ**, **G2tBuCzTRZ**, **G3tBuCzTRZ** and **G4tBuCzTRZ**.

252
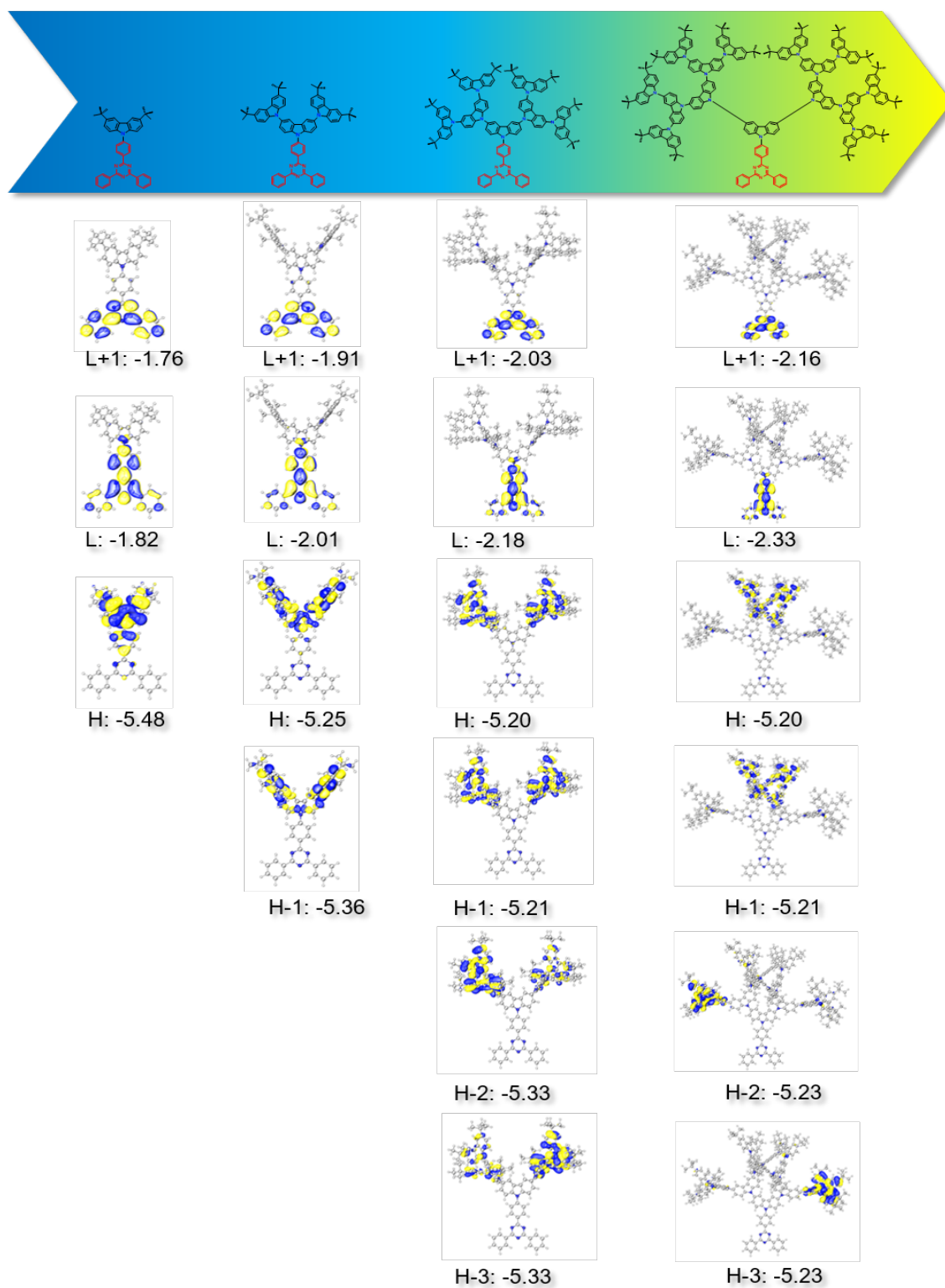
Figure S13. Calculated distribution of molecular orbitals for the four model compounds, which are based on increasing generations of *tert*-butylcarbazole dendrons from G1 to G4. **G1tBuCzTRZ**, **G2tBuCzTRZ**, **G3tBuCzTRZ** and **G4tBuCzTRZ** from left to right.

S20

Photophysical measurements

Absorption spectra were recorded at RT using a Shimadzu UV1800 double beam spectrophotometer. Molar absorptivity determination was verified by linear least-squares fit of values obtained from at least five independent solutions at varying concentrations on the order of 10^{-4} to 10^{-6} M. Steady-state emission spectra and phosphorescence spectra were obtained using a Jasco FP-8600 spectrofluorometer. The time-resolved emission measurements were obtained using the iCCD camera by exponentially increasing delay and gating times where the gating time is kept lower by 10 times compared to the delay time. Samples were excited at 355 nm by a q-switched laser from QS Lasers (MPL15100-DP). Emission from the samples was focused onto a spectrograph (Oriel MS257) and detected on a gated iCCD camera (iStar A-DH334T-18F-03). The measurements were recorded under vacuum unless otherwise stated. Thin film PLQY measurements were performed using an integrating sphere in a Hamamatsu C9920-02 system. Samples were excited by a xenon lamp coupled to a monochromator. The output was then fed into the integrating sphere via a fiber, exciting the sample. PL was collected with a multimode fiber and detected with a back-thinned CCD. The thin film PLQY were measured under N_2 using an integrating sphere.
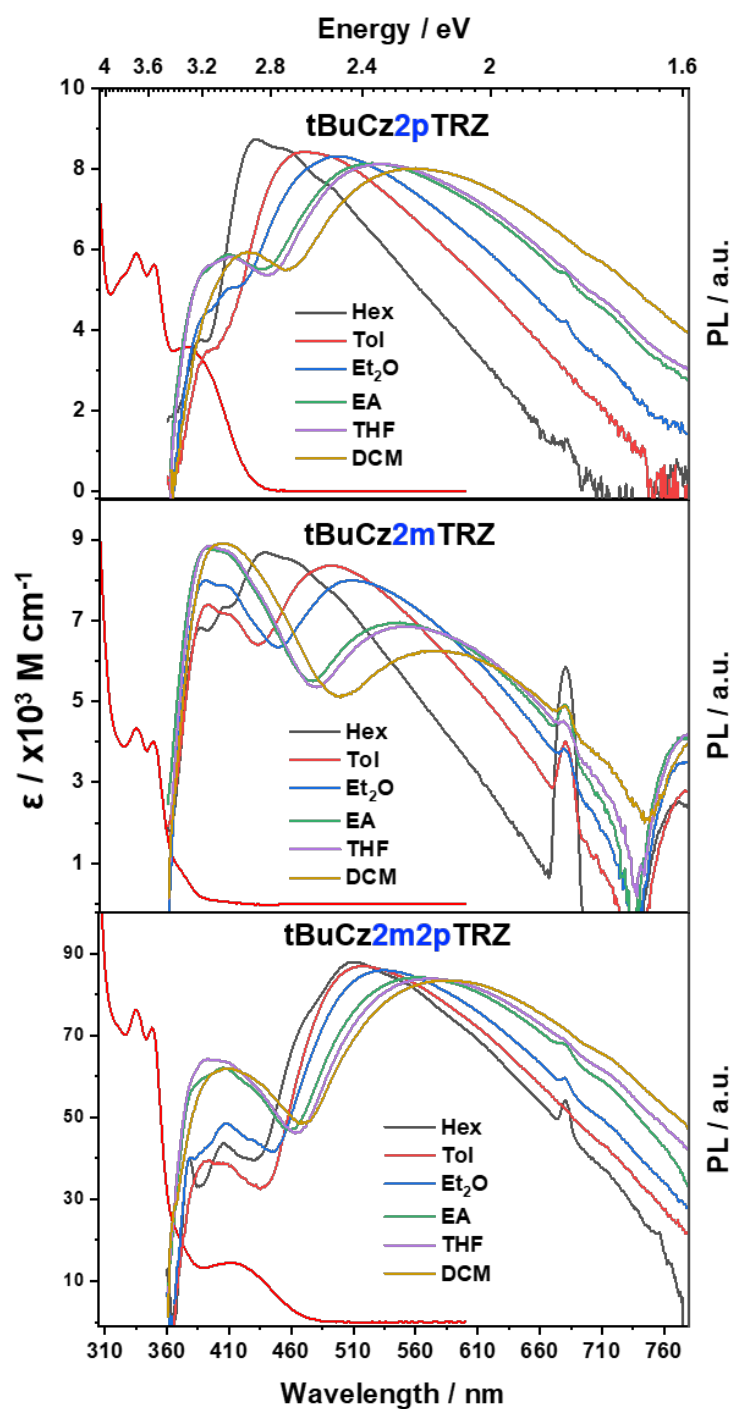
Figure S14. Molar absorptivity measured in toluene and solvatochromism PL study with spectra normalized by the integrated area (λ_{exc} = 340 nm; 3×10^{-5} M) presented using a log scale. (The emission at 680 nm arises from the second harmonic of the laser source.)
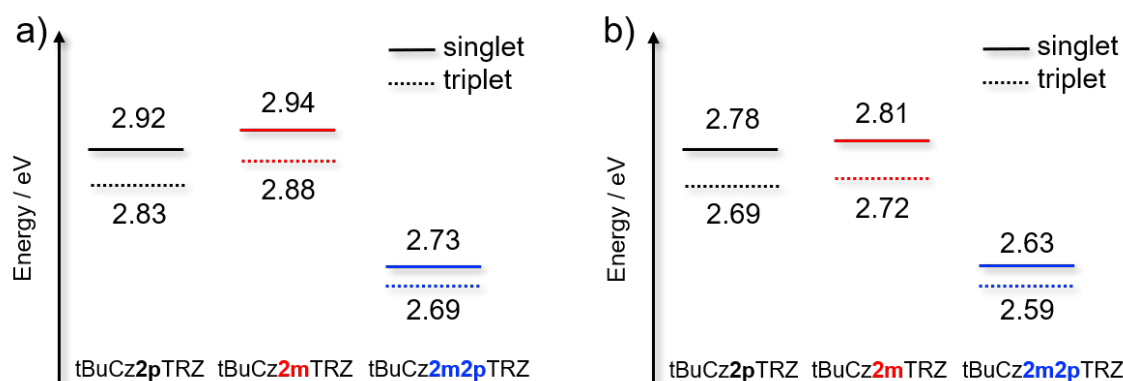
Figure S15. Energy diagrams of excited states. a) In toluene; b) In neat film. Black, **tBuCz2pTRZ**; red, **tBuCz2mTRZ**; blue, **tBuCz2m2pTRZ**.

Table S5. Summary of PL maxima in solvatochromic study of **tBuCz2pTRZ**, **tBuCz2mTRZ** and **tBuCz2m2pTRZ**

Solvent	λ_{PL} [a]		
	/ nm		
	tBuCz2pTRZ	**tBuCz2mTRZ**	**tBuCz2m2pTRZ**
Hexane (Hex)	432	439	511
Toluene (Tol)	471	492	517
Diethyl ether (Et$_2$O)	497	509	535
Ethyl acetate (EA)	524	546	560
THF	531	550	570
CHCl$_3$	559	574	586

[a] Peak value of PL spectra obtained under aerated conditions at 300 K, concentration of 3×10^{-5} M, λ_{exc} = 330 nm.

Table S6. Optoelectronic properties of **tBuCz2pTRZ**, **tBuCz2mTRZ** and **tBuCz2m2pTRZ** in toluene

	λ_{abs} [a]	ε	λ_{PL} [b]	Φ_{PL} [c]	Φ_{PL} [d]	ΔE_{ST} [e]
	/ nm	/ $\times10^3$ M^{-1} cm^{-1}	/ nm	/ %	/ %	/ eV
tBuCz2pTRZ	334/349/377	5.9/5.6/3.6	471	88	65	0.09
tBuCz2mTRZ	335/349/374	4.3/4.0/0.7	492	33	9	0.06
tBuCz2m2pTRZ	335/348/373/412	76.4/71.9/18.7/14.4	517	62	37	0.04

[a] UV–vis absorption; [b] PL in toluene degassing with N$_2$; [c] Photoluminescence quantum yield in toluene degassing with N$_2$ by integrating sphere; [d] Photoluminescence quantum yield in air by integrating sphere; [e] Energy gap between S$_1$ and T$_1$ calculated from the difference of the onsets of the fluorescence and phosphorescence spectra in toluene glass at 5 K.

256
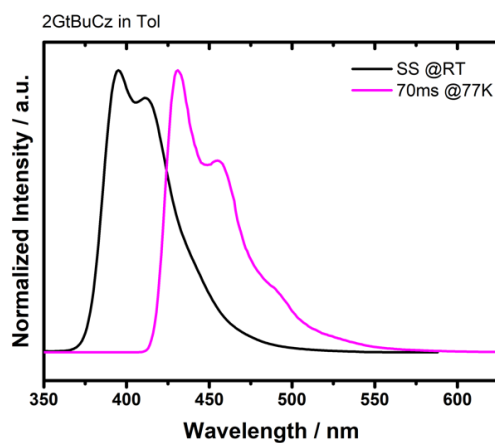
Figure S16. Steady-state emission and phosphorescence spectrum with 70 ms delay at 77 K of **2GtBuCz** in toluene. (λ_{exc}=340 nm)
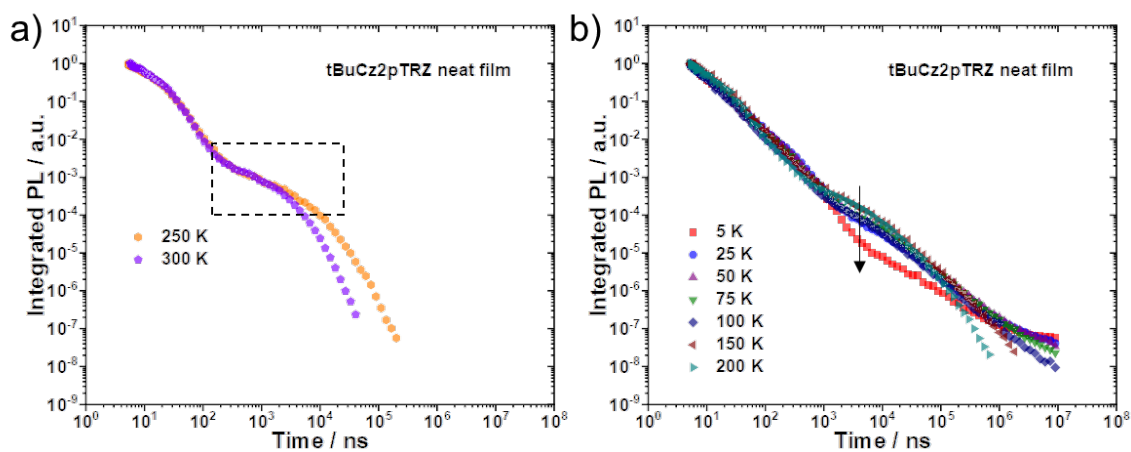
Figure S17. Temperature-dependent time-resolved PL decay of **tBuCz2pTRZ** in neat film. a) The intensity of delayed emission doesn't show any change; b) The intensity of delayed emission decreases slightly upon cooling. The decays were obtained by integrating each time-resolved spectrum across the full spectral range. (λ_{exc} = 355 nm; Q-switched Nd:YAG laser)

S24
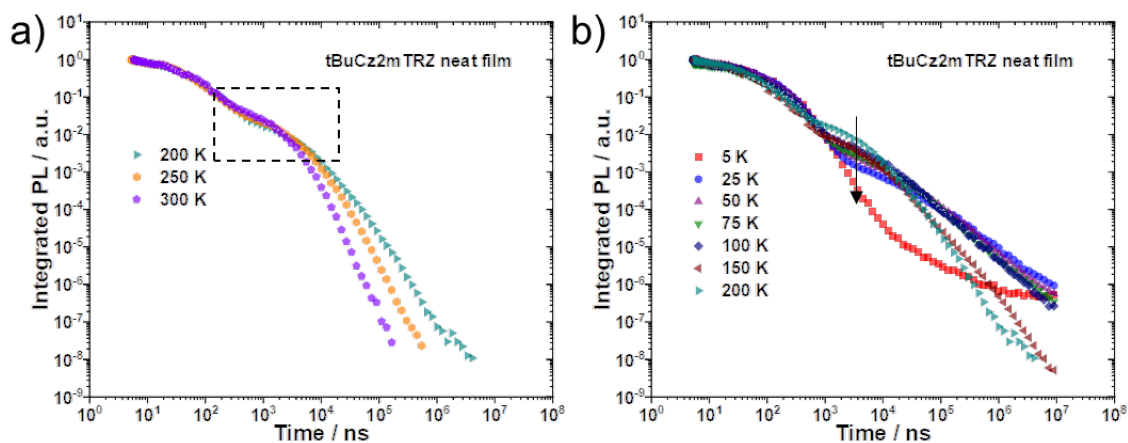
Figure S18. Temperature-dependent time-resolved PL decay of **tBuCz2mTRZ** in neat film. a) The intensity of delayed emission is almost independent of temperature; b) The intensity of delayed emission decreases upon cooling. The decays were obtained by integrating each time-resolved spectrum across the full spectral range. (λ_{exc} = 355 nm; Q-switched Nd:YAG laser)
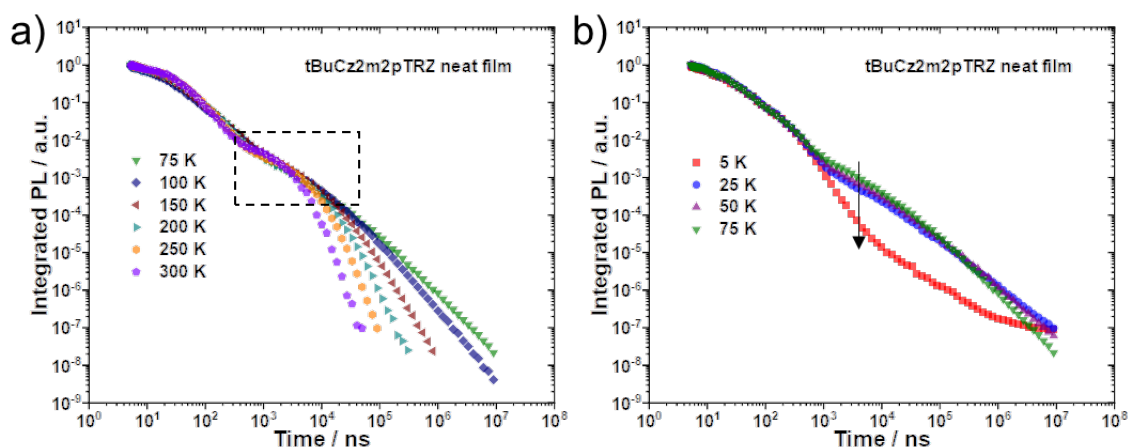
Figure S19. Temperature-dependent time-resolved PL decay of **tBuCz2m2pTRZ** in neat film. a) The intensity of delayed emission is almost independent of temperature; b) The intensity of delayed emission decreases slightly upon cooling. The decays were obtained by integrating each time-resolved spectrum across the full spectral range. (λ_{exc} = 355 nm; Q-switched Nd:YAG laser)

S25

258
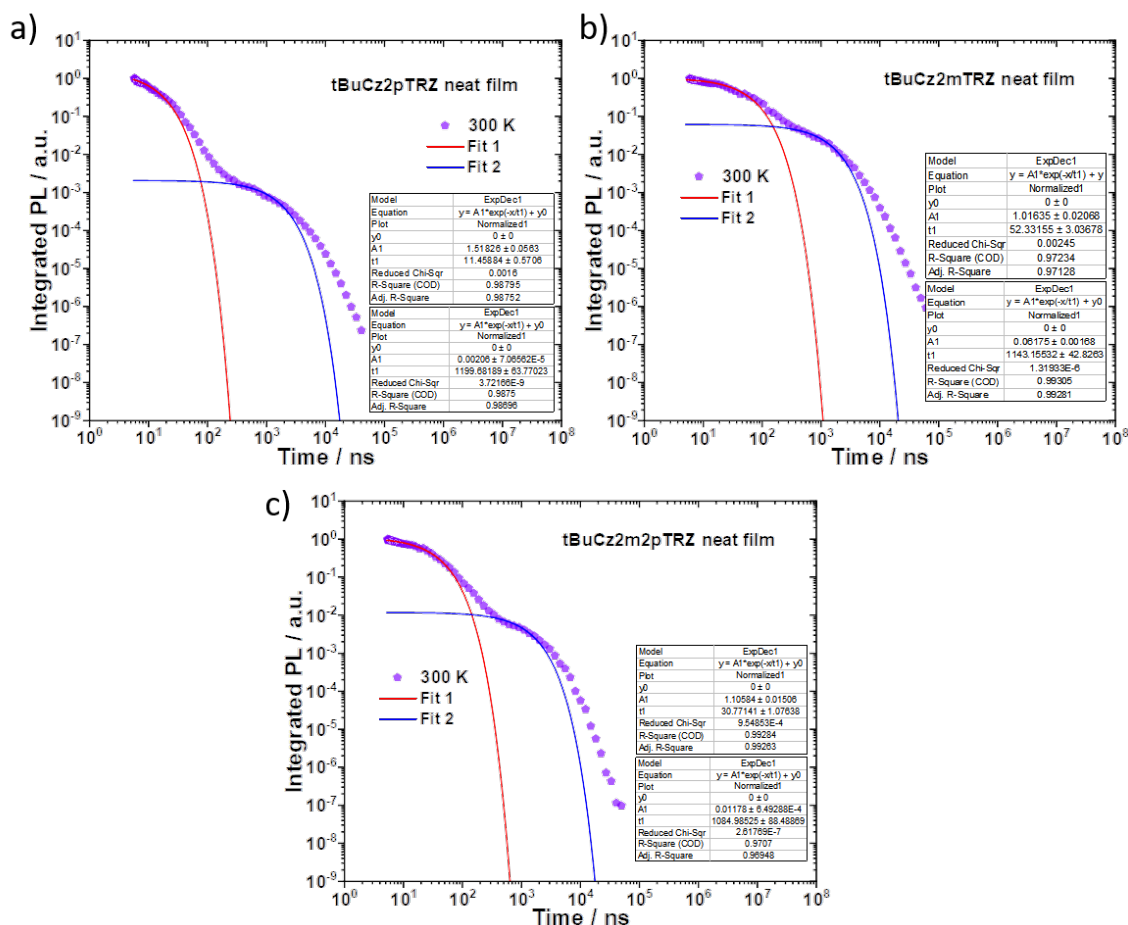
Figure S20. Temperature-dependent time-resolved PL decay and single exponential fitting of prompt and delayed emission regime for **tBuCz2pTRZ**, **tBuCz2mTRZ** and **tBuCz2m2pTRZ** in neat film at 300K.

Table S7. RISC-related parameters of **tBuCz2pTrz**, **tBuCz2mTrz** and **tBuCz2m2pTrz** in neat films.

	Φ_{PL}[a]	Φ_{DF}/Φ_{PF}[b]	τ_{PF}[c]	τ_{DF}[d]	Φ_{ISC}[e]	k_{ISC}[f]	k_{rISC}[g]
	/ %		/ ns	/ μs		/ ×10⁷, s⁻¹	/ ×10⁶, s⁻¹
tBuCz2pTRZ	61	0.15	11	1.2	0.47	4.3	0.3
tBuCz2mTRZ	59	1.3	52	1.1	0.74	1.4	1.6
tBuCz2m2pTRZ	86	0.4	31	1.1	0.39	1.2	0.9

[a] total PLQY (λ_{exc} = 340 nm); [b] ratio of the integrated areas of delayed and prompt emission; [c] lifetime of prompt emission estimated using a mono-exponential fit at 300 K; [d] average lifetime of delayed emission at 300 K; [e] intersystem crossing yield; [f] rate constant of intersystem crossing; [g] rate constant of reverse intersystem crossing.

S26

As bimolecular interactions cannot be safely excluded in neat films, we do not discuss RISC rates explicitly. But for reference, the Φ_{ISC}, k_{ISC} and k_{rISC} were calculated using the following methods. Prompt (τ_{PF}) and delayed (τ_{DF}) PL emission lifetimes were determined from mono-exponential fits of the prompt and delayed components of the transient PL decay at 300 K (**Figure S20**). Photoluminescence quantum yields (ϕ_{PL}) were determined using the integrating sphere under N_2 atmosphere. We assumed the internal conversion in the neat film to be negligible. This allows to approximate Φ_{ISC} as $\phi_{ISC} = 1 - \phi_{PF}$. We then calculated the intersystem crossing rate using $k_{ISC} = \frac{\Phi_{ISC}}{\tau_{PF}}$. Finally, the reverse intersystem crossing rate was obtained using $k_{rISC} = \frac{1}{\Phi_{ISC}\tau_{DF}}\left(\frac{\Phi_{DF}}{\Phi_{PF}}\right)$.

260
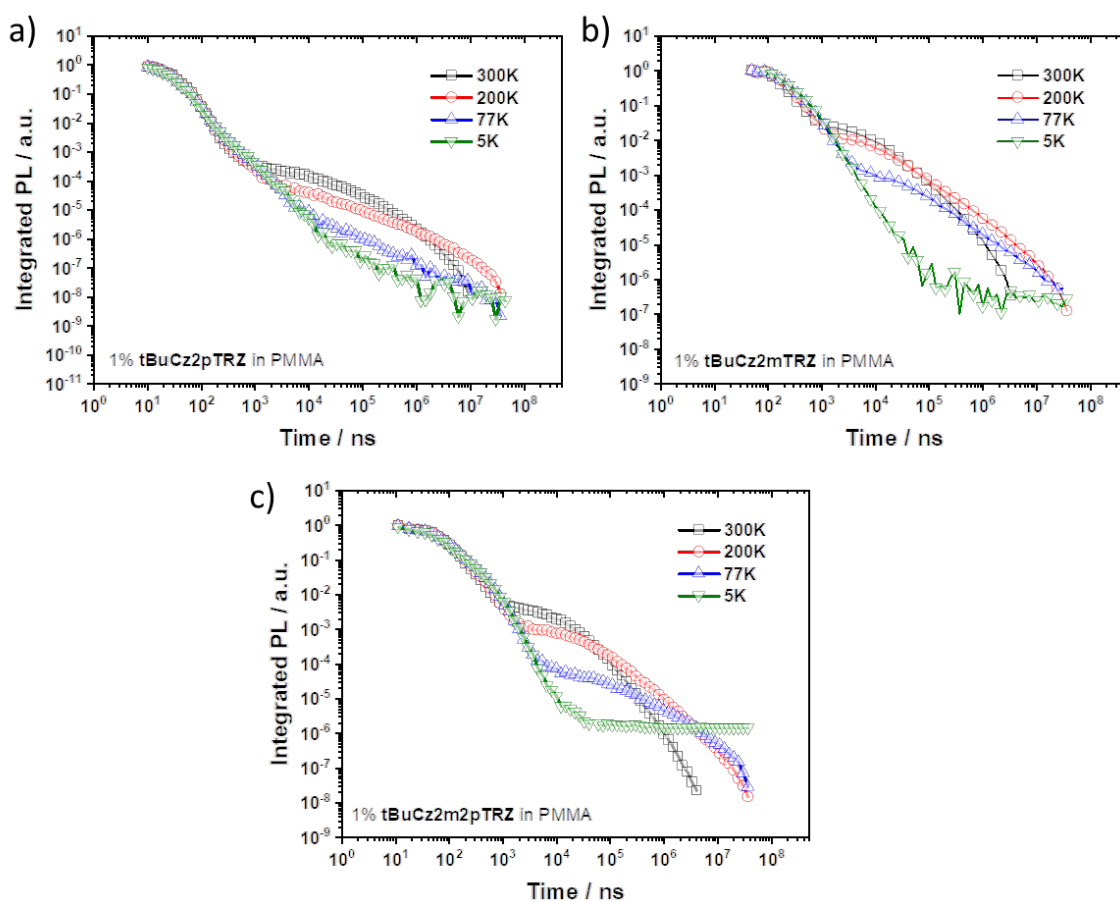
Figure S21. Time resolved decay of 1 wt% (a) **tBuCz2pTRZ**, (b) **tBuCz2mTRZ** and (c) **tBuCz2m2pTRZ** doped films in PMMA matrix at different temperatures. The decays were obtained by integrating each time-resolved spectrum across the full spectral range. (λ_{exc} = 355 nm; Q-switched Nd:YAG laser) (PMMA with average Mw ~350,000 g/mol was purchased from Sigma-Aldrich)

OLED fabrication and characterization

The OLED devices were fabricated using a bottom-emitting architecture. A pre-patterned indium tin oxide (ITO) glass substrate with a sheet resistance of 15 Ω square^{-1} was pre-cleaned carefully with detergent and deionized water and then exposed to UV-ozone for 15 min. PEDOT:PSS was spin-coated onto the clean ITO substrate as the hole-injection layer, followed by thermal treatment under 120 °C for 30 min. Then a 10 mg/mL chlorobenzene solution of our dendrimers was spin-coated to form a 35-45 nm thick emissive layer (EML) and annealed at 120 °C for 10 min to remove residual solvent before transfer to the vacuum chamber. A 40 nm-thick electron-transporting layer (ETL) of Tm3PyPB was then vacuum deposited at a rate of 1 Å/s, which was controlled *in situ* using quartz crystal monitors. The electron injection layer LiF was deposited at a rate of 0.1 Å/s while the Al cathode was deposited at a rate of 10 Å/s through the shadow mask defining the top electrode. The spatial overlap of the anode and cathode electrodes determined the active area of the OLED, which was estimated to be 4 mm^2. Electroluminescence (EL), CIE color coordinates, and spectra were obtained via a Spectrascan PR655 photometer, and the luminance-current-voltage characteristics were determined with a computer-controlled Keithley 2400 Source meter. EQE was calculated from the current density, luminance, and EL spectrum, assuming Lambertian emission distribution.

Figure S22. (a) Hole-only device with the configuration of ITO/PEDOT:PSS (35 nm)/Dendrimer (40 nm)/MoO$_3$ (40 nm)/Al (100 nm) and (b) Electron-only device with the configuration of ITO/Al (40 nm)/Dendrimer (40 nm)/TmPyPB (40 nm)/LiF (1 nm)/Al (100 nm), All devices have positive bias on the ITO.

Brief summary of TADF dendrimers
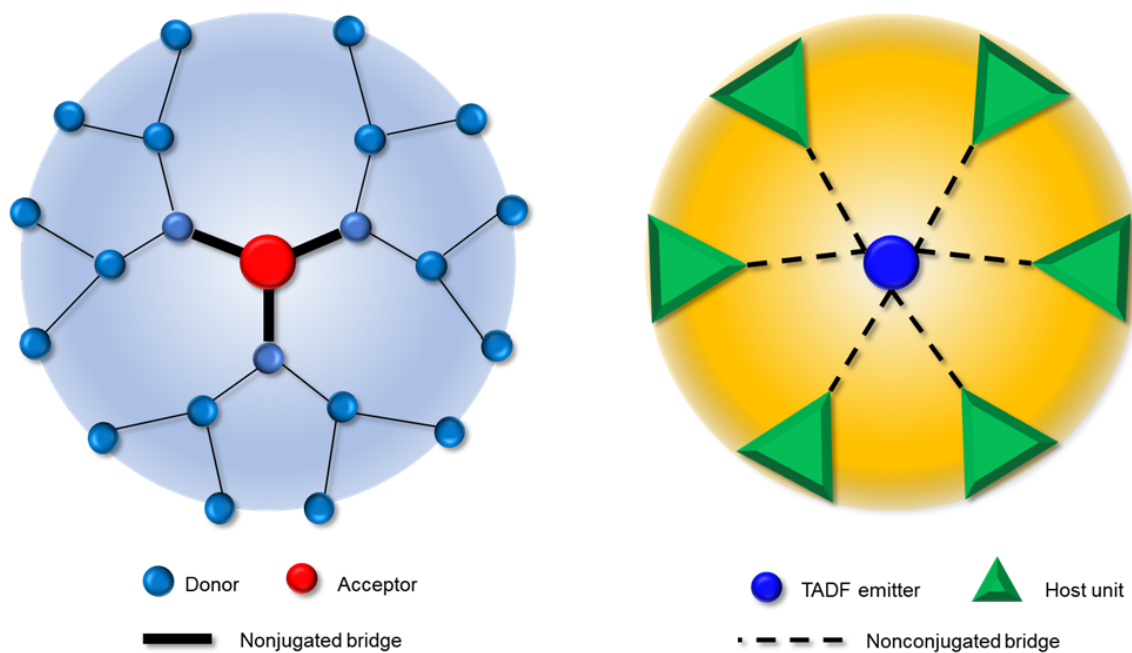
Figure S23. Illustrative scheme of two commonly used design strategies for TADF dendrimers.

Table S8. Summary of non-doped OLED performance from this work and reported small molecules, dendrimers and polymers.

	Emitting layer (neat film)	Peak / nm	FWHM / nm	V_{on} [a)] / V	CE / cd A^{-1}	PE / lm W^{-1}	EQE$_{max}$ / %	EQE$_{100}$ / %	CIE (x,y)	Lum$_{max}$ / cd m^{-2}	Ref
	tBuCz2pTRZ	500	95	3.1	49.4	45.7	18.5	16.1	0.23, 0.46	2956	**this work**
	tBuCz2mTRZ	516	95	3.3	59.9	52.2	19.9	12.0	0.27, 0.53	777	**this work**
	tBuCz2m2pTRZ	540	97	3.1	98.8	91.3	28.7	21.2	0.37, 0.57	6029	**this work**
1	G2	~430	-	4.8	4.1	1.6	-	-	0.15, 0.12	<1000	[9]
2	G3	~440	-	5.2	1.07	0.49	-	-	0.19, 0.15	<1000	[9-10]
3	P-Ac95-TRZ05	472	-	3.2	24.8	-	12.1	12.0	0.18, 0.27	6150	[10]
4	B-oTC	474	64	3.9	37.3	27.6	19.1	17.0	0.15, 0.26	4351	[11]
5	PBD-10	478	-	3.8	13.5	-	7.3	4.0	0.20, 0.29	~200	[12]
6	DCzDMAC-DPS	480	-	5.2	3.8	2.0	2.2	1.5	0.18, 0.27	~500	[13]
7	POCz-DPS	480	-	5.4	12.6	-	7.3	-	0.18, 0.30	2700	[14]
8	m-DTPACO	480	-	3.9	4.8	2.7	2.4	2.3	0.15, 0.28	10,005	[15]
9	P12	492	-	3.1	11.2	10.7	4.3	2.4	0.24, 0.43	~4000	[16]
10	TB14CZ-ACTRZ	496	-	4.5	20.7	14.5	8.1	-	0.22, 0.43	2770	[17]
11	G2TAZ	500/-	-/-	3.3/3.7	-/15.6	6/11.5	2.4/6.3	-/6.2	0.25, 0.49/-	~1000/1243	[18]/[19]
12	tBuG2TAZ	500	-	3.5	25.4	16.1	9.5	9.4	-	2423	[19]
13	PhG2TAZ	500	-	3.2	23.1	17.3	8.2	8.0	-	2316	[19]

S30

14	MeG2TAZ	500	-	3.0	26.5	21.5	9.4	9.4	-	2235	[19]
15	G2B	500	-	3.4	14.0	11.5	5.7	-	0.26, 0.48	~1000	[20]
16	CzDMAC-DPS	502	-	3.6	30.6	24.0	12.2	6.9	0.22, 0.44	~2000	[13]
17	tBuTCz2BP	506	-	4.5	9.2	-	4.3	-	0.26, 0.46	4200	[21]
18	G4TAZ	510	-	3.5	-	3.1	1.5	-	0.23, 0.37	~200	[18]
19	3CzSO	510	90	4.3	-	-	6.3	-	0.29, 0.52	3531	[22]
20	5CzBN-2Cz	515	-	3.6	63.0	48.7	20.4	-	0.25, 0.52	25,190	[23]
21	G3TAZ	515	-	3.5	-	8.5	3.4	-	0.27, 0.49	~1000	[18]
22	2CzSO	516	96	4.7	-	-	10.7	-	0.24, 0.49	4706	[22]
23	G3B	516	-	3.7	7.7	5.7	2.9	-	0.31, 0.50	~500	[20]
24	DBSOCz	518	-	4.5	1.6	-	1.3	-	0.24, 0.52	5325	[24]
25	TZ-Cz	520	-	4.0	20.0	-	6.5	-	0.24, 0.51	18,200	[25]
26	TZ-3Cz	520	-	3.6	30.5	-	10.1	-	0.24, 0.51	22,950	[25]
27	TB2CZ-ACTRZ	520	-	4	30.8	24.2	9.5	-	0.32, 0.57	2336	[17]
28	PAPTC	521	-	2.6	37.1	41.8	12.6	-	0.25, 0.47	10,251	[26]
29	TPADSO2	521	-	4.8	15.0	-	5.1	-	0.21, 0.44	12,031	[27]
30	CDE2	522	118	7.7	-	-	5.2	-	0.32, 0.51	2512	[28]
31	2CzAcDBTO	538	-	4.0	13.9	5.5	4.5	-	0.36, 0.54	4525	[29]
32	G-mCBP	545	-	2.7	44.5	46.6	16.5	14.6	0.42, 0.55	18,800	[30]
33	TA-3CZ	546	-	2.4	39.0	40.8	11.8	-	0.39, 0.56	23,145	[31]
34	DCB-BP-PXZ	548	-	2.5	72.9	81.8	22.6	-	0.39, 0.57	95,577	[32]
35	PCzATD5	~550	-	2.6	48.7	50.5	15.5	-	0.41, 0.55	15,456	[33]
36	PABPC5	~550	-	2.6	60.5	61.2	18.1	17.8	0.40, 0.56	-	[34]
37	G-TCTA	550	-	4.4	1.40	0.93	0.50	0.26	0.46, 0.52	1200	[30]
38	G-mCP	550	-	2.7	44.5	46.6	16.5	14.6	0.42, 0.55	18,800	[30]
39	CDE1	552	114	4.4	38.9	17.3	13.8	-	0.40, 0.54	~10,000	[28]
40	TPA-AQ	612	-	3.8	10.6	-	7.5	-	0.60, 0.40	2200	[35]
41	MPPA-Cz	728	-	6.4	-	-	0.064	-	0.70, 0.29	24	[36]
42	MPPA-3Cz	715	-	6.2	-	-	0.254	-	0.69, 0.30	135	[36]

a) At the luminance of 1 cd m^{-2}

Reference

[1] A. R. Tiwari, S. R. Nath, K. A. Joshi, B. M. Bhanage, *J. Org. Chem.* **2017**, 82, 13239.

[2] P. Debnath, K. C. Majumdar, *Tetrahedron Lett.* **2014**, 55, 6976.

[3] V. V. Pavlishchuk, A. W. Addison, *Inorganica Chim. Acta* **2000**, 298, 97.

[4] C. M. Cardona, W. Li, A. E. Kaifer, D. Stockdale, G. C. Bazan, *Adv. Mater.* **2011**, 23, 2367.

[5] C. Adamo, V. Barone, *J. Chem. Phys.* **1999**, 110, 6158.

[6] A. D. Becke, *J. Chem. Phys.* **2019**, 150, 241101.

[7] a) S. Grimme, *Chem. phys. lett.* **1996**, 259, 128; b) S. Hirata, M. Head-Gordon, *Chem. phys. lett.* **1999**, 314, 291.

[8] M. Moral, L. Muccioli, W. J. Son, Y. Olivier, J. C. Sancho-García, *J. Chem. Theory Comput.* **2015**, 11, 168.

[9] J. Li, X. Liao, H. Xu, L. Li, J. Zhang, H. Wang, B. Xu, *Dyes Pigm.* **2017**, 140, 79.

[10] S. Shao, J. Hu, X. Wang, L. Wang, X. Jing, F. Wang, *J. Am. Chem. Soc.* **2017**, 139, 17739.

[11] X. L. Chen, J. H. Jia, R. Yu, J. Z. Liao, M. X. Yang, C. Z. Lu, *Angew. Chem. Int. Ed.* **2017**, 56, 15006.

[12] X. Zeng, J. Luo, T. Zhou, T. Chen, X. Zhou, K. Wu, Y. Zou, G. Xie, S. Gong, C. Yang, *Macromolecules* **2018**, 51, 1598.

[13] J. Luo, S. Gong, Y. Gu, T. Chen, Y. Li, C. Zhong, G. Xie, C. Yang, *J. Mater. Chem. C* **2016**, 4, 2442.

[14] X. Ban, W. Jiang, K. Sun, B. Lin, Y. Sun, *ACS Appl. Mater. Interfaces* **2017**, 9, 7339.

[15] J. Hu, X. Zhang, D. Zhang, X. Cao, T. Jiang, X. Zhang, Y. Tao, *Dyes Pigm.* **2017**, 137, 480.

[16] J. Luo, G. Xie, S. Gong, T. Chen, C. Yang, *Chem. Comm.* **2016**, 52, 2292.

[17] M. Godumala, S. Choi, H. J. Kim, C. Lee, S. Park, J. S. Moon, K. Si Woo, J. H. Kwon, M. J. Cho, D. H. Choi, *J. Mater. Chem. C* **2018**, 6, 1160.

[18] K. Albrecht, K. Matsuoka, K. Fujita, K. Yamamoto, *Angew. Chem. Int. Ed.* **2015**, 54, 5677.

[19] K. Albrecht, K. Matsuoka, D. Yokoyama, Y. Sakai, A. Nakayama, K. Fujita, K. Yamamoto, *Chem. Comm.* **2017**, 53, 2439.

[20] K. Matsuoka, K. Albrecht, K. Yamamoto, K. Fujita, *Sci. Rep.* **2017**, 7, 1.

[21] B. Huang, X. Ban, K. Sun, Z. Ma, Y. Mei, W. Jiang, B. Lin, Y. Sun, *Dyes Pigm.* **2016**, 133, 380.

[22] Y. Li, T. Chen, M. Huang, Y. Gu, S. Gong, G. Xie, C. Yang, *J. Mater. Chem. C* **2017**, 5, 3480.

[23] D. Liu, W. Tian, Y. Feng, X. Zhang, X. Ban, W. Jiang, Y. Sun, *ACS Appl. Mater. Interfaces* **2019**, 11, 16737.

[24] J. Wang, J. Peng, W. Yao, C. Jiang, C. Liu, C. Zhang, M. He, R. Liu, X. Xia, C. Yao, *Org. Electron.* **2017**, 48, 262.

[25] X. Ban, W. Jiang, T. Lu, X. Jing, Q. Tang, S. Huang, K. Sun, B. Huang, B. Lin, Y. Sun, *J. Mater. Chem. C* **2016**, 4, 8810.

[26] Y. Zhu, Y. Zhang, B. Yao, Y. Wang, Z. Zhang, H. Zhan, B. Zhang, Z. Xie, Y. Wang, Y. Cheng, *Macromolecules* **2016**, 49, 4373.

[27] K. Sun, Y. Sun, W. Jiang, S. Huang, W. Tian, Y. Sun, *Dyes Pigm.* **2017**, 139, 326.

[28] Y. Li, G. Xie, S. Gong, K. Wu, C. Yang, *Chem. Sci.* **2016**, 7, 5441.

[29] M. Huang, Y. Li, K. Wu, J. Luo, G. Xie, L. Li, C. Yang, *Dyes Pigm.* **2018**, 153, 92.

[30] K. Sun, Y. Sun, W. Tian, D. Liu, Y. Feng, Y. Sun, W. Jiang, *J. Mater. Chem. C* **2018**, 6, 43.

[31] K. Sun, Y. Sun, T. Huang, J. Luo, W. Jiang, Y. Sun, *Org. Electron.* **2017**, 42, 123.

[32] H. Liu, J. Zeng, J. Guo, H. Nie, Z. Zhao, B. Z. Tang, *Angew. Chem. Int. Ed.* **2018**, 57, 9290.

[33] Y. Wang, Y. Zhu, X. Lin, Y. Yang, B. Zhang, H. Zhan, Z. Xie, Y. Cheng, *J. Mater. Chem. C* **2018**, 6, 568.

[34] Y. Yang, S. Wang, Y. Zhu, Y. Wang, H. Zhan, Y. Cheng, *Adv. Funct. Mater.* **2018**, 28, 1706916.

[35] H. Bin, Y. Ji, Z. Li, N. Zhou, W. Jiang, Y. Feng, B. Lin, Y. Sun, *J. Lumin.* **2017**, 187, 414.

[36] K. Sun, D. Chu, Y. Cui, W. Tian, Y. Sun, W. Jiang, *Org. Electron.* **2017**, 48, 389.

S55

13 Low Efficiency Roll-off Blue TADF OLEDs Employing a Novel Acridine-Pyrimidine based High Triplet Energy Host

Francesco Rodella, **Rishabh Saxena**, *Sergey Bagnich, Dovydas Banevičius, Gediminas Kreiza, Stavros Athanasopoulos, Saulius Juršėnas, Karolis Kazlauskas, Anna Köhler*, and *Peter Strohriegl*

PAPER

Check for updates

Low efficiency roll-off blue TADF OLEDs employing a novel acridine–pyrimidine based high triplet energy host†

Francesco Rodella, [a] Rishabh Saxena, [b] Sergey Bagnich, [b]
Dovydas Banevičius, [c] Gediminas Kreiza, [c] Stavros Athanasopoulos, [d]
Saulius Juršėnas, [c] Karolis Kazlauskas, [c] Anna Köhler [be] and Peter Strohriegl*[ae]

The development of efficient blue emitter–host combinations is one of the biggest challenges in organic light-emitting diode (OLED) research. Host materials play a crucial role when it comes to enhancing the efficiency, improving the lifetime and decreasing the efficiency roll-off of the device. The need for new hosts is of prime importance, especially for blue phosphorescence and thermally activated delayed fluorescence (TADF) emitters, due to their high exciton energies. The hosts are less investigated than the emitters and require further progress. This work provides a new molecular strategy that combines an acridine derivative (donor) and pyrimidine moieties (acceptors) to obtain three novel host materials. This approach demonstrates that *via* careful selection of donor and acceptor units, it is possible to manage the properties of the host materials, obtaining at the same time superior thermal and morphological properties and high triplet energies up to 3.07 eV. The decrease of the conjugation in the acceptor unit was found to play a crucial role in increasing the triplet energy. The most promising host **1MPA** was used to fabricate blue TADF OLEDs. Using a sky-blue emitter, we achieved electroluminescence at 491 nm and a maximum external quantum efficiency (EQE) of 13.6%, combined with a low efficiency roll-off, even beyond the practical brightness of 1000 cd m^{-1}. The host **1MPA** was also combined with a deep blue emitter to deliver a blue OLED with color coordinates of x = 0.16 and y = 0.18.

Introduction

Presently, organic light-emitting diodes (OLEDs) are expanding their boundaries and applications, such as in flat panel displays and smartphones, due to their significant advantages like facile preparation, cost-effectiveness, and energy efficiency.[1,2] For these reasons, much effort is focused on developing this technology, both in academia and industry. Especially for display applications, commercial OLEDs contain stable and efficient green and red emitters based on iridium complexes.[3] In contrast, blue emitters suffer from lacking simultaneous efficiency and

stability.[4,5] In the last few years, thermally activated delayed fluorescence (TADF) emitters seemed to be among the most promising candidates to solve this problem. Their capacity of harvesting triplet excited states can allow for an internal quantum efficiency of up to 100% through prompt and delayed fluorescence emission. Rapid thermally activated transfer of the excitation from the triplet to the singlet state, followed by efficient delayed fluorescence, avoids degradation processes that could otherwise occur when the excitation prevails for a long time in the triplet state. TADF OLEDs contain purely organic molecules, which avoid rare and costly noble metals and allow a broad range of molecular engineering. Aside from emitters, host materials play an essential role in obtaining the desired performance of the OLED. Emitters are frequently doped in a host matrix to decrease detrimental bimolecular effects caused by longer-lived triplet states.[6] The dilution into the host is thus essential to enhance the lifetime, increase the efficiency, and reduce the efficiency roll-off of the device.[7] The hosts, in general, must have high and balanced charge carrier mobility, good thermal and morphological stability, and chemical stability. They also must have high triplet energy to confine the excitons on the emitter, which is particularly challenging for blue-emitting OLEDs.[8]

[a] Macromolecular Chemistry I, University of Bayreuth, Bayreuth 95440, Germany. E-mail: peter.strohriegl@uni-bayreuth.de

[b] Soft Matter Optoelectronics, University of Bayreuth, Bayreuth 95440, Germany

[c] Institute of Photonics and Nanotechnology, Vilnius University, Saulėtekio av. 3 LT-10257 Vilnius, Lithuania

[d] Departamento de Física, Universidad Carlos III de Madrid, Avenida Universidad 30, 28911 Leganés, Madrid, Spain

[e] Bayreuth Institute of Macromolecular Research (BIMF), University of Bayreuth, Bayreuth 95440, Germany

† Electronic supplementary information (ESI) available. See DOI: 10.1039/d1tc03598c

This journal is © The Royal Society of Chemistry 2021

J. Mater. Chem. C, 2021, **9**, 17471–17482 | **17471**

268

The majority of host materials adopt carbazole or less stable phosphine oxide groups.[9] In this work, we present host molecules based on acridine and pyrimidine groups instead. Acridine is often used as a donor (D) in emitter molecules because of its rigidity and strong donating feature.[10–13] Few cases report its use in hosts for red phosphorescence OLEDs.[14,15] Furthermore, what brought our attention to the acridine group is that it has a higher triplet energy than carbazole (due to less conjugation).[16] The pyrimidine unit is also a building block for TADF emitters due to its acceptor (A) properties.[17–20] It is also used as a building block for hosts in phosphorescence OLEDs, with triplet energies of these hosts lying below 3 eV.[21–23] Another use of pyrimidine is as an electron transport material (ETM).[24]

In this work, we report a strategy to obtain high triplet energy donor–acceptor host materials based on acridine and pyrimidine moieties. In particular, *via* careful molecular modification, it is possible to limit the conjugation of the acceptor pyrimidine, leading to a high triplet energy of more than 3 eV. To prove the strategy's applicability, we fabricated blue TADF OLEDs using the most promising host of the series (**1MPA**), expressing blue emission (from 461 nm to 493 nm) with low efficiency roll-off even beyond a practical brightness of 1000 cd m^{-2}.

Experimental

Materials

9,9-Diphenyl-9,10-dihydroacridine; 2-chloro-4,6-diphenylpyrimidine; 4,6-dichloro-2-phenylpyrimidine; 4,6-dichloro-2-methylpyrimidine; palladium(II) acetate and tri(*tert*-butyl)phosphine (10 wt% in hexane) were purchased from abcr. Sodium *tert*-butoxide was purchased from TCI.

Synthesis

10-(4,6-Diphenylpyrimidin-2-yl)-9,9-diphenyl-9,10-dihydroacridine (**2PPA**). 9,9-Diphenyl-9,10-dihydroacridine (1 g, 3 mmol, 1.1 eq.), 2-chloro-4,6-diphenylpyrimidine (727 mg, 2.73 mmol, 1 eq.), sodium *tert*-butoxide (340 mg, 3.54 mmol, 1.3 eq.), palladium(II) acetate (25 mg, 0.11 mmol, 0.04 eq.) and toluene (25 ml) were placed with a stirring bar in a Schlenk tube. The mixture was then degassed three times through freeze–pump–thaw cycles and the tube was backfilled with argon. Subsequently, tri(*tert*-butyl)phosphine(10 wt% in hexane) (0.07 ml, 0.22 mmol, 0.08 eq.) was added and the mixture was then refluxed for 12 h. The reaction mixture was extracted with water and the organic phase was dried over anhydrous sodium sulphate before evaporating the solvent with reduced pressure. Finally, the compound was purified by column chromatography on silica gel (20% ethyl acetate/hexane) and by train sublimation, obtaining 25% yield of pure product. 1H NMR (CDCl$_3$, 500 MHz, Me$_4$Si): δ [ppm] 8.01 (d, J = 7.5 Hz, 2H), 7.92 (d, J = 7.5 Hz, 4H), 7.45–7.42 (m, 7H), 7.39 (t, J = 7.5 Hz, 2H), 7.17 (t, J = 7.5 Hz, 2H), 7.05–6.99 (m, 6H), 6.96 (d, J = 7.0 Hz, 2H), 6.90 (d, J = 6.5 Hz, 4H). 13C NMR (CDCl$_3$, 500 MHz, Me$_4$Si): δ [ppm] 164.21, 160.05, 144.35, 142.55,

140.91, 137.73, 130.63, 130.27, 128.60, 128.04, 127.45, 127.28, 127.04, 126.32, 125.55, 124.07, 104.45, 58.62. EI-MS *m/z* [M]$^+$: 564.

10,10′-(2-Phenylpyrimidine-4,6-diyl)bis(9,9-diphenyl-9,10-dihydro-acridine) (**1PPA**). **1PPA** was synthesized following a similar procedure as described for **2PPA**; using 9,9-Diphenyl-9,10-dihydroacridine (977 mg, 2.93 mmol, 2.2 eq.), 4,6-dichloro-2-phenylpyrimidine (300 mg, 1.33 mmol, 1 eq.), sodium *tert*-butoxide (320 mg, 3.33 mmol, 2.5 eq.), palladium(II) acetate (25 mg, 0.11 mmol, 0.08 eq.), tri(*tert*-butyl)phosphine (10 wt% in hexane) (0.07 ml, 0.22 mmol, 0.16 eq.) and toluene (25 ml). Yield = 28%. 1H NMR (CDCl$_3$, 500 MHz, Me$_4$Si): δ [ppm] 8.27 (m, 2H), 7.44–7.37 (m, 7H), 7.22 (t, J = 7.5 Hz, 4H), 7.16–7.10 (m, 12H), 7.07 (t, J = 7.5 Hz, 4H), 6.89 (d, J = 7.5 Hz, 4H), 6.82 (d, J = 7.5 Hz, 8H), 5.65 (s, 1H). 13C NMR (CDCl$_3$, 500 MHz, Me$_4$Si): δ [ppm] 162.68, 161.44, 144.60, 140.17, 140.15, 138.37, 130.40, 130.15, 128.93, 128.30, 128.17, 127.56, 126.63, 126.09, 123.74, 123.69, 91.1, 58.12. EI-MS *m/z* [M]$^+$: 818.

10,10′-(2-Methylpyrimidine-4,6-diyl)bis(9,9-diphenyl-9,10-dihydro-acridine) (**1MPA**). **1MPA** was synthesized following a similar procedure as described for **2PPA**; using 9,9-diphenyl-9,10-dihydroacridine (2.35 g, 7.05 mmol, 2.3 eq.), 4,6-dichloro-2-methylpyrimidine (0.50 g, 3.07 mmol, 1 eq.), sodium *tert*-butoxide (0.77 g, 8.01 mmol, 2.6 eq.), palladium(II) acetate (55 mg, 0.25 mmol, 0.08 eq.), tri(*tert*-butyl)phosphine(10 wt% in hexane) (0.15 ml, 0.49 mmol, 0.16 eq.) and toluene (25 ml). Yield = 58%. 1H NMR (CDCl$_3$, 500 MHz, Me$_4$Si): δ [ppm] 7.23 (d, J = 7.5 Hz, 4H), 7.18 (t, J = 7.5 Hz, 4H), 7.14–7.10 (m, 12H), 7.04 (t, J = 7.5 Hz, 4H), 6.87 (d, J = 7.5 Hz, 4H), 6.80 (d, J = 7.5 Hz, 8H), 5.60 (s, 1H), 2.43 (s, 3H). 13C NMR (CDCl$_3$, 500 MHz, Me$_4$Si): δ [ppm] 144.76, 140.07, 138.81, 130.34, 130.06, 129.01, 127.88, 127.55, 126.60, 126.28, 123.36, 122.31, 94.77, 57.92, 26.17. EI-MS *m/z* [M]$^+$: 756.

Purification

The synthesized compounds **2PPA**, **1PPA**, and **1MPA** were purified by train sublimation in a Carbolite split tube furnace HZS 12/450.

Characterization

^{1}H NMR and ^{13}C NMR spectra were recorded on a Bruker Avance III HD (500 MHz), the chemical shifts were referred to chloroform-d3 (7.26 ppm), and the *J* values are given in Hz. MS spectra were obtained on a Finningan MAT 8500 using electron impact ionization.

Thermal measurements

Thermogravimetric analysis (TGA) was conducted on a Mettler TGA/DSC3 with a heating rate of 10 K min^{-1} under a nitrogen flow. Differential scanning calorimetry was performed with a Mettler DSC3+ in pierced Al pans at 10 K min^{-1} under a nitrogen flow. The glass transition T_g was determined as the midpoint temperature of the step. T_m and T_r were determined as the peak temperature of the melting peak and recrystallization peak, respectively. These calculations were performed by Mettler STARe 15.00a software.

17472 | *J. Mater. Chem. C*, 2021, **9**, 17471–17482

This journal is © The Royal Society of Chemistry 2021

269

Electrochemical measurements

Cyclic voltammetry measurements were carried out using a standard three electrode electrochemical micro-cell kit from Ametek Scientific Instruments, consisting of a Platinum wire counter electrode, a Platinum disk working electrode, and a Silver/Silver chloride reference electrode. A Gamry Interface 1010T served as the potentiostat. Electrochemistry grade solvent was used, and 100 mM tetrabutylammonium hexafluorophosphate was the supporting electrolyte. The solutions were thoroughly purged with dry nitrogen for 10 minutes before each measurement.

Computational details

We have used density functional theory to obtain the ground state geometries of the compounds employing the M06-2X exchange–correlation functional in combination with a 6-31+G(d,p) atomic basis set. Geometry optimizations were successfully converged, and no imaginary frequencies were observed following vibrational frequency analysis. Singlet and triplet emission energies were further obtained by optimizing the structures with linear response time-dependent density functional theory at the M06-2X/6-31+G(d,p) level[25] and within the Tamm–Dancoff approximation.[26] Electron–hole natural transition orbitals (NTOs) were calculated to characterize the excited state transitions.[27] All calculations were performed using the Gaussian 16 software package,[28] and orbitals were visualized using the Avogadro molecular editor software.[29] Charge transfer numbers ω_{CT} with values in the range between 0 (for a Frenkel exciton) and 1 (for a complete charge transfer exciton) were computed by a transition density matrix analysis,[30,31] based on defragmentation of the molecules in acridine and pyrimidine groups (D–A–D for **1PPA** and **1MPA** and D–A for **2PPA**). Electron–hole correlation plots of the Ω matrix for the excitations were also constructed based on the fragments. The average electron–hole distance Δr, based on the charge centroids of the orbitals involved in the transition,[32] was also computed as a complementary indicator to the nature of the states using Multiwfn software.[33]

Photophysical measurements

For measurements in solution, all the compounds were dissolved in toluene or mTHF at a concentration of $6–9 \times 10^{-5}$ M. Solutions were sonicated for 15 minutes after preparation. Absorption spectra were recorded using a Varian Cary 5000 spectrophotometer. Fluorescence spectra, phosphorescence spectra, and room temperature (RT) photoluminescence quantum yield (PLQY) were measured using a Jasco FP-8600 spectrofluorometer. For phosphorescence measurements, the detector unit was opened at a delay of 150 ms after excitation, and the signal was acquired for 50 ms. The excitation wavelength for both fluorescence and phosphorescence was 300 nm (unless specified in the text or figure). For the 77 K measurements, the sample or cuvette was immersed in liquid nitrogen. Values for the photoluminescence quantum yield of the molecules in solution were obtained using the Jasco FP-8600 spectrofluorometer equipped with an integrating sphere.

OLED fabrication and characterization

OLEDs were fabricated on pre-patterned indium tin oxide (ITO)-coated glass substrates (Kintec) with an ITO layer thickness of 100 nm and a sheet resistance of 15–20 $\Omega \; \square^{-1}$. Prior to device fabrication, the substrates were cleaned by sonicating consecutively in detergent (Hellmanex II), distilled water, acetone, isopropyl alcohol, boiling distilled water, and finally treated with O_2-plasma for 10 min. The substrates were then transferred into a vacuum evaporation chamber (Vacuum Systems and Technologies Ltd) integrated inside the nitrogen-filled glove box, where the stack of organic layers was deposited at a rate of 0.5–1 Å s^{-1} and a pressure $< 10^{-6}$ Torr. The doping of the emissive layer was accomplished by co-evaporating the host and guest materials from different evaporation sources at distinct rates for the desired doping concentration. Afterward, the samples were transported by the robotic arm to a metal deposition chamber without breaking the vacuum, which was followed by deposition of lithium fluoride (LiF) and aluminum (Al) layers at a rate of 0.2 and 2 Å s^{-1}, respectively. The active area of the devices was 4 mm^2 as defined by the ITO pattern and the shadow mask used for cathode deposition. The completed devices were removed from the vacuum chamber to the N_2-filled glove box without exposure to air and encapsulated by using a glass cover and UV-curable epoxy KATIOBOND LP655 (DELO). A system consisting of a calibrated integrating sphere (ORB Optronix), a spectrometer PMA-11 (Hamamatsu), and a source-meter unit 2601A (Keithley) was utilized for evaluation of the electrical-optical properties of OLEDs such as current–voltage–luminance (I–V–L) characteristics, EQE and efficiency roll-off.

Results and discussion

Design and synthesis

In this work, a strategy to increase the triplet energy of donor–acceptor molecules is shown. For this purpose, three novel host molecules were designed. As presented in previous work,[34] by direct connection of donors (acridine and carbazole) and acceptors (triazine), it is possible to increase the triplet energy of donor–acceptor molecules compared to the case where the connection occurs *via* a conjugated bridge. In this work, acridine (donor) and three different pyrimidines (acceptors) with a different size of the conjugated system of the pyrimidine were chosen to obtain three materials of different conjugation. In particular, we aim to see a decrease in the conjugation of the acceptor moiety, a key strategy to reach a high-energy triplet (Fig. 1). **2PPA** presents a donor–acceptor structure where the pyrimidine core is linked at positions 4 and 6 to two phenyl rings and at position 2 to one acridine. **1PPA** has a donor–acceptor–donor (DAD) structure; *i.e.*, the pyrimidine moiety is linked to just one phenyl ring (in position 2) while two acridines occupy positions 4 and 6. The last molecule of the series, **1MPA**, still has the same DAD configuration, but the pyrimidine is substituted with a methyl group (in position 2) and two acridines (in positions 4 and 6). By replacing the phenyl ring with a methyl group, the conjugation of the
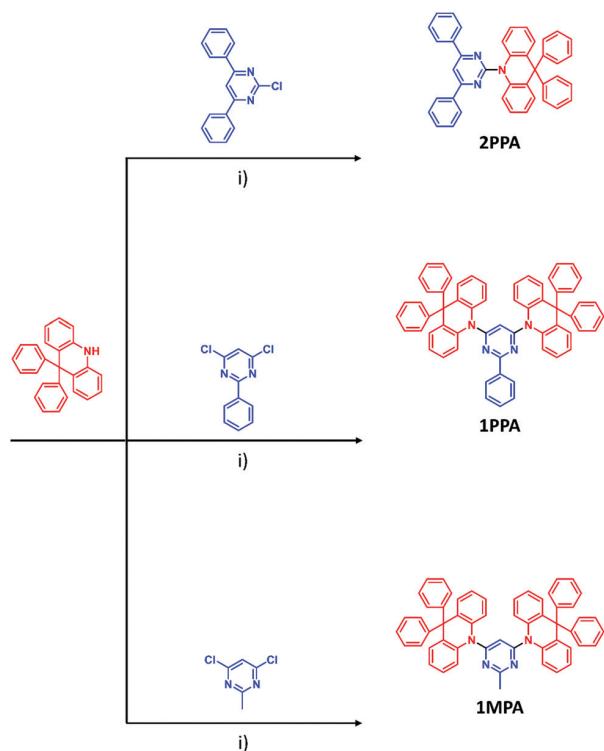
This journal is © The Royal Society of Chemistry 2021

J. Mater. Chem. C, 2021, **9**, 17471–17482 | **17473**

270

Paper

Journal of Materials Chemistry C

Fig. 1 Synthesis route to the three host materials **2PPA**, **1PPA** and **1MPA**. (i) Pd(Oac)$_2$, P(*t*Bu)$_3$, NaO*t*Bu, toluene, reflux, 12 h.

acceptor is limited to the central pyrimidine ring. The products were synthesized using a general Buchwald-Hartwig protocol between the donor acridine and the chlorinated pyrimidine acceptor, which provides an efficient way for the formation of C–N bonds (Fig. 1). Furthermore, all products were purified *via* train sublimation to obtain highly pure compounds.

Thermal and electrochemical analysis

The thermal properties of the compounds were investigated by differential scanning calorimetry (DSC) and thermogravimetric analysis (TGA), as shown in Fig. 2a and b. DSC shows that all the compounds are morphologically stable beyond 100 °C with glass transitions (T_g) of 108 °C (**2PPA**), 150 °C (**1PPA**), and 138 °C (**1MPA**) and that recrystallization (T_r) upon heating occurs above 100 °C for **2PPA** and above 200 °C for **1PPA** and **1MPA**, due to the addition of a second bulky acridine. The heating scan of **2PPA** was obtained after the sample was melted and directly cooled with liquid nitrogen. This was necessary to obtain the amorphous material during the cooling process. The melting temperatures (T_m) are around 300 °C for **2PPA** and **1PPA** and 273 °C for **1MPA**.

TGA data show high decomposition temperatures (T_d) above 300 °C for **2PPA** and above 400 °C for **1PPA** and **1MPA**. TGA also indicates that all the materials leave none or only minor residues which means that all three hosts completely evaporate already at normal pressure, which makes them ideal candidates for OLED fabrication *via* evaporation. Furthermore, throughout
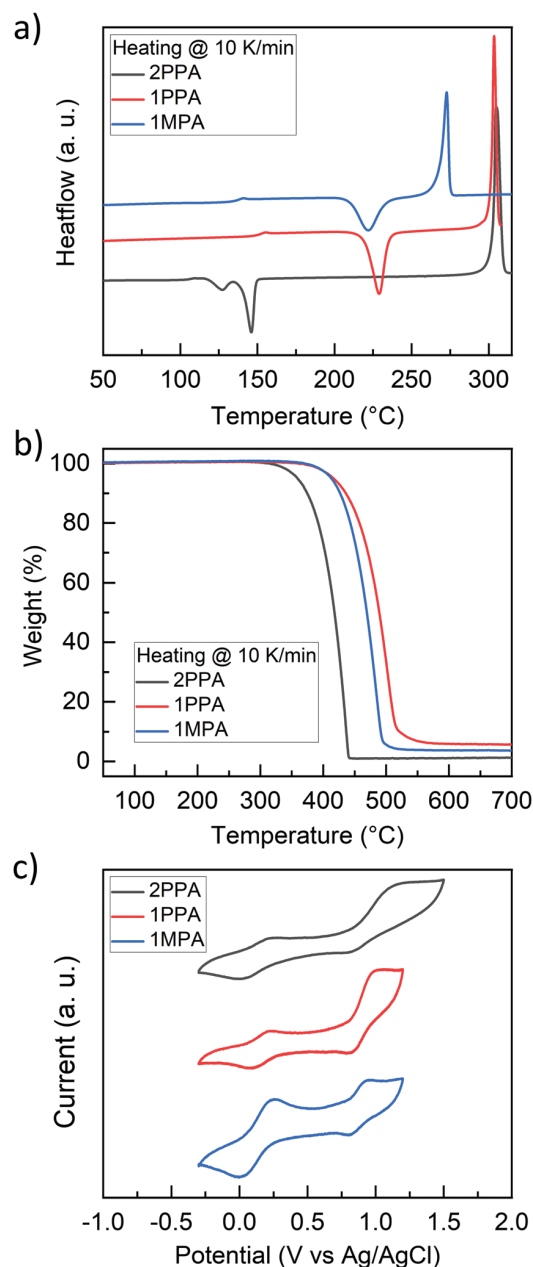
Fig. 2 Thermal and electrochemical properties of **2PPA**, **1PPA** and **1MPA**. (a) Differential scanning calorimetry showing the second heating scan. (b) Thermogravimetric analysis. (c) Cyclic voltammograms (cathodic scan) measured in CH$_2$Cl$_2$ at room temperature with tetra-*n*-butylammonium hexafluorophosphate (0.1 M) as the supporting electrolyte and a scan rate of 100 mV s^{-1}.

the series, it is possible to see that by adding a second acridine, the T_g, T_r, and T_d values of the materials are improved. The melting points are instead similar, with a small decrease in **1MPA**. These data confirm the high thermal stability of the materials and their potential applicability as hosts in OLEDs.

Furthermore, cyclic voltammetry of the three hosts was carried out to explore the electrochemical properties and to estimate the HOMO values (Fig. 2c). All the compounds show

17474 | *J. Mater. Chem. C*, 2021, **9**, 17471–17482

This journal is © The Royal Society of Chemistry 2021

271

two quasi-reversible oxidation peaks. The first oxidation peak always appears slightly above 0.2 V *vs.* Ag/AgCl, and it corresponds to the oxidation of the acridine donor moiety. The HOMO values for the three compounds were estimated by the half-wave potential of the first oxidation potential, considering the solvent correction according to Gräf *et al.*[35] The LUMO values were then calculated by adding the optical band gap to the HOMO values (Table 1).

Absorption and photoluminescence in solution

Absorption and photoluminescence studies of **2PPA**, **1PPA**, and **1MPA** were performed in dilute toluene solutions to analyze their intrinsic photophysical properties, with a focus on determining their triplet state energies. Fig. 3a shows the room temperature absorption spectrum of **2PPA**, **1PPA**, and **1MPA**. **2PPA** exhibits a band attributed to CT absorption from around 3.2–3.9 eV. This assignment is based on the structureless absorption profile and comparatively low extinction of this particular band. **1PPA** and **1MPA** do not show any pronounced signatures of a CT state absorption. The absorption of **2PPA**, **1PPA**, and **1MPA** differ significantly from the absorption of either donor or acceptor (Fig. S1a–c, ESI†). This indicates the existence of strong electronic interactions between the donor and acceptor units in these compounds.

In order to estimate the triplet and singlet energies of the host materials, phosphorescence (Ph) and steady-state (SS) measurements were carried out at liquid nitrogen temperature (77 K). For **2PPA** (Fig. 3b), the phosphorescence is structured with a 0–0 vibrational peak at 2.81 eV (442 nm). The steady-state spectrum is a combination of fluorescence and phosphorescence as the spectrum below 2.9 eV matches completely with the phosphorescence spectrum. Thus, the lowest singlet in **2PPA** is a state exhibiting a structureless emission centered around 3 eV, with an onset at 3.15 eV (394 nm), with the lack of vibrational structure probably indicating a CT-character. In **1PPA**, the lowest singlet and triplet states are both structured and have 0–0 peaks at 3.36 eV (369 nm) and 2.76 eV (449 nm), respectively, as shown in Fig. 3c. Thus, the T_1 state is at a lower energy in **1PPA** than in **2PPA**. This can be accounted for by the nature of this state. The phosphorescence of **2PPA** and **1PPA** are similar to the ones of their respective pyrimidine acceptors (Fig. S2, ESI†), indicating that the triplet is localized on the pyrimidine acceptor moieties, 2PhPy and 1PhPy, in agreement with the quantum chemical calculations (*vide infra*). The triplet energy of the hosts therefore reflects the phosphorescence energies of the respective

pyrimidine acceptors. The lower T_1 energy in **1PPA** results from the fact the phenyl ring is planar with the pyrimidine in **1PPA** whereas there is a torsion in **2PPA**, as evident in the quantum chemical calculations further below.

Due to the strong emission from the pyrimidine-based singlet state in **1PPA**, we cannot discern whether there is also a CT singlet state at about 3 eV with a lower oscillator strength buried under it. When we measured the spectra with different excitation wavelengths between 300 nm and 350 nm, we found them to be independent of excitation wavelength (Fig. S3, ESI†).

The emission of **1MPA**, in contrast, depends on the excitation wavelength, and the corresponding spectra are shown in Fig. 3d. As before, Ph and SS measurements were carried out at 77 K. For excitation at 300 nm and 320 nm (4.13 eV and 3.88 eV, respectively), we obtain a structured phosphorescence band with a 0–0 peak at 3.18 eV. However, when exciting at 335 nm and at 350 nm (3.70 eV and 3.54 eV), the emission band has a similar shape, yet it is shifted to lower energy, and it is broadened with a shoulder at 2.88 eV and an onset at 3.07 eV. To clarify the origin of these two bands, we performed photoluminescence excitation (PLE) spectra, and we also measured the phosphorescence of the acridine donor as well as the methylpyrimidine acceptor. These data are available in the ESI† (Fig. S4 and S5). For the higher energy phosphorescence, two assignments are principally possible, that is, to a locally excited (LE) state localized either on the acridine donor or on the pyrimidine acceptor. Based on the data in Fig. S4 and S5 and the arguments detailed in the ESI,† we tentatively assign the higher energy phosphorescence band to a ^{3}LE state localized on the acridine donor, and we attribute the lower energy phosphorescence band to a triplet state with mixed CT–LE character, where the LE contribution would be again from the acridine.

The fluorescence in **1MPA** shows the same excitation dependence. For excitation at 300 nm and 320 nm, we observe a broad band centered at about 3.6 eV (Fig. 3e), while for excitation at 335 nm and 350 nm, the fluorescence is centered at 3.0 eV (Fig. 3f). By comparison to the acridine fluorescence spectrum (Fig. S4, ESI†), the band at 3.6 eV is readily assigned to a ^{1}LE state localized mainly on the acridine. The band at 3.0 eV, by virtue of its lower energy, must have some significant CT contribution.

We also determined the S_1 and T_1 energies of all compounds in neat films at 77 K and found them to be shifted to lower energies by 0.1 eV (see Fig. S6, ESI†). We attribute this rather moderate shift in the neat film to energy transfer within the DOS, which is known to be efficient in neat films, so that the emission comes from sites with lower energy within the DOS.

Fig. 4a summarizes the insights obtained on the energies and character of the excited states in **2PPA**, **1PPA**, and **1MPA** based on the spectroscopic data. All energy values are taken from the onset of the emission spectra. It exemplifies the impact of reducing the conjugation length of the pyrimidine acceptor. While for 2PPA and 1PPA, the ^{3}LE state localized on the 2-phenylpyrimidine (2PhPy) and 1-phenylpyrimidine (1PhPy) is the lowest triplet state with an onset at around 2.9 eV, this is no longer the case when the conjugation is

Table 1 Glass transition (T_g), recrystallization (T_r), melting (T_m), and decomposition at 5 wt% loss (T_d) temperatures determined from differential scanning calorimetry and thermogravimetric analysis. HOMO and LUMO values of **2PPA**, **1PPA**, and **1MPA**, calculated from cyclic voltammetry and the optical bandgap, respectively

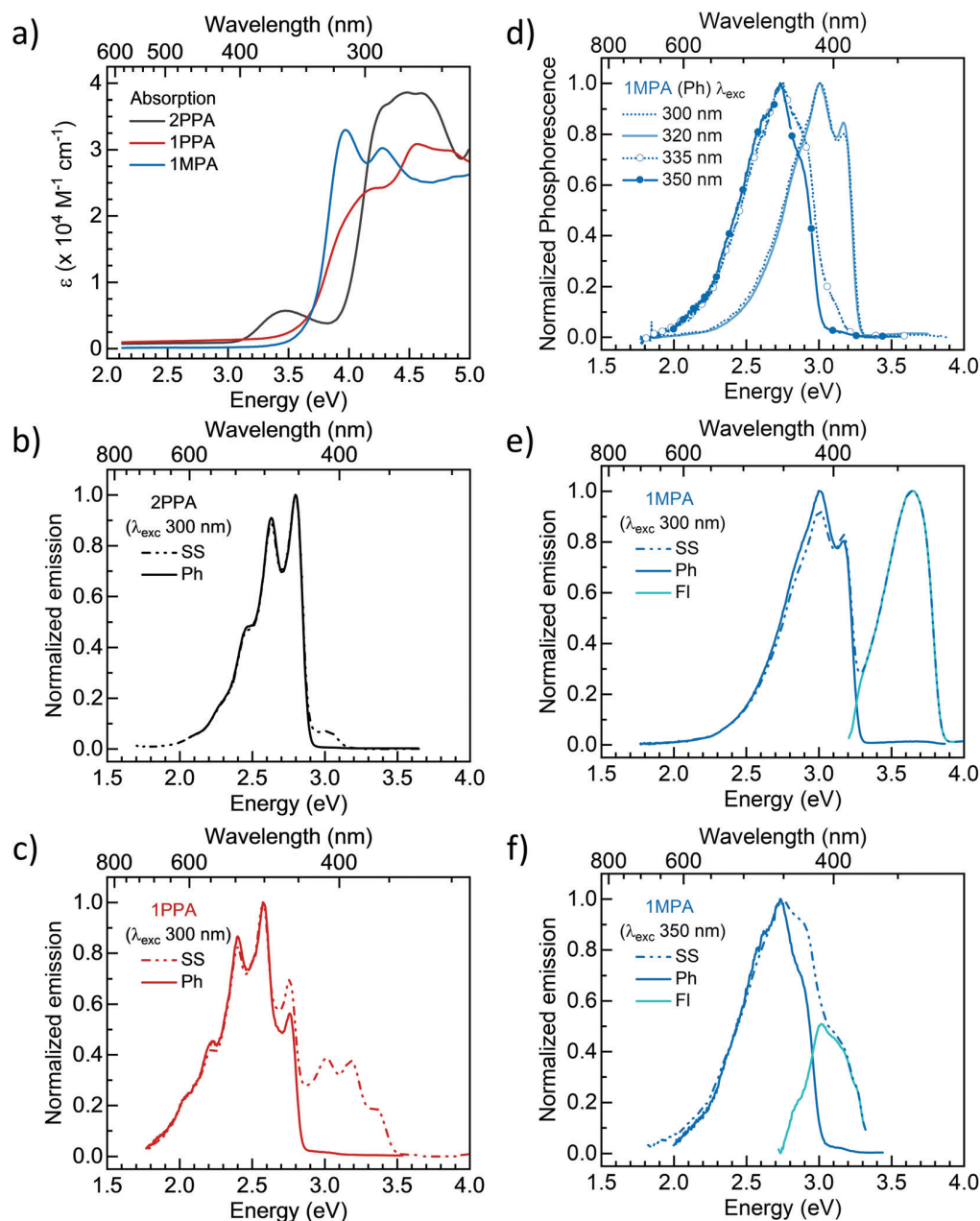|	T_g (°C)	T_r (°C)	T_m (°C)	T_d (°C)	HOMO (eV)	LUMO (eV)
2PPA	108	127, 147	305	359	−5.12	−2.00
1PPA	150	229	304	417	−5.11	−1.71
1MPA	138	222	273	413	−5.10	−1.55

272

Fig. 3 (a) The absorption spectra of **2PPA**, **1PPA**, and **1MPA** in toluene solution at 300 K. (b) The emission spectra of **2PPA** taken at 77 K in a toluene glass under steady-state conditions (SS), so that both fluorescence and phosphorescence show up, and taken with a delay of 150 ms after excitation and a gate width of 50 ms so that only phosphorescence (Ph) is visible. Excitation was at 300 nm. (c) The emission spectra were taken under the same conditions for **1PPA**. (d) The phosphorescence (Ph) spectra of **1MPA** in toluene glass at 77 K, taken for different excitation wavelengths as indicated. (e) Comparison of the Ph and SS spectra for excitation at 300 nm and (f) at 350 nm. Also indicated is the fluorescence spectrum obtained from subtracting the Ph from the SS.

reduced in methylpyrimidine (MePy). The triplet state for the units pyrimidine and methylpyrimidine have 0–0 peaks at 3.50 eV and 3.42 eV, respectively (see Nishi *et al.*[36] and Fig. S5b, ESI†), *i.e.*, well above the onset of phosphorescence for the acridine moiety (Fig. S4 and S5b, ESI†). As a result, in **1MPA**, the lowest triplet state becomes one with a mixed CT–LE character, where the LE contribution is from the acridine unit. We also comment on the

unusual observation of an excitation wavelength-dependent phosphorescence. This implies that when exciting into the acridine-based singlet LE state, the rates of intersystem crossing to its triplet state and phosphorescence can compete with the charge transfer required to form the CT-based singlet or triplet state. Evidently, the twists between the units slow down the charge transfer, which needs to take place through a bond.
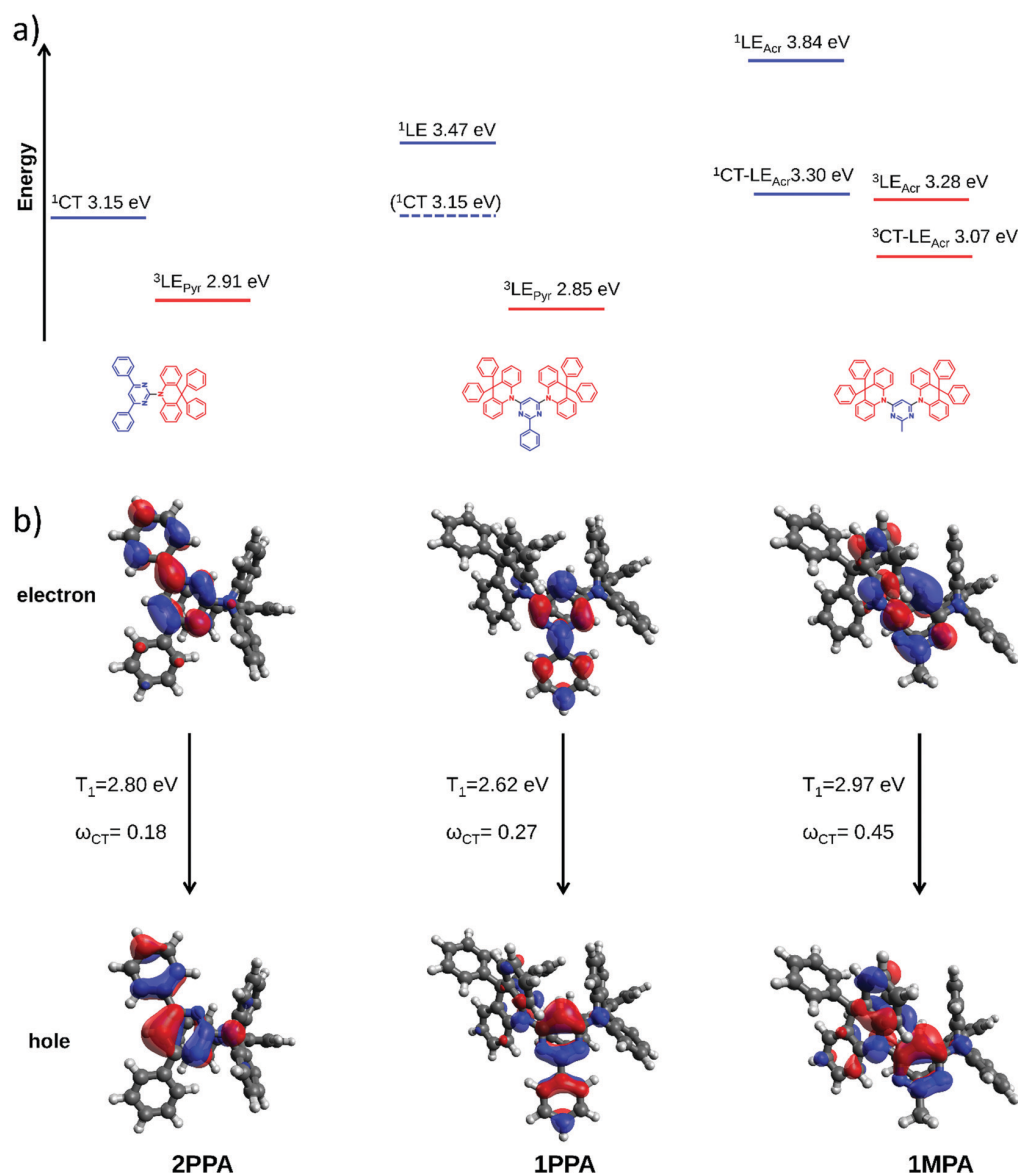
Fig. 4 (a) Excited state energy level diagram for **2PPA**, **1PPA**, and **1MPA**, based on the spectroscopic data, along with their structure (donor in red and acceptor in blue). The values are taken from the onset of the emission spectra. (b) TDA-DFT computed natural transition orbitals, emission energies, and charge transfer numbers for the lowest triplet state for **2PPA**, **1PPA**, and **1MPA** at the M06-2X/6-31+G(d,p) level. Pyr represents pyrimidine acceptors and Acr the acridine donor. A side view is displayed in Fig. S8 (ESI†).

Theoretical calculations

For a deeper understanding of the excited states, we turn our attention to the electronic structure calculations. We find that for all molecules, acridine units lose planarity, and their central ring adopts a distorted boat conformation both at the ground and excited state geometries. This boat conformation is in agreement with results on related compounds.[37,38] At the same time, there is an intramolecular pi-stacking arrangement between the phenyl ring of one of the acridine donor units and the pyrimidine acceptor moiety (Fig. S7, ESI†). The obtained conformations suggest a strong electronic mixing between the donor and acceptor units, consistent with the observations made in the absorption spectra. The TDA-DFT calculated lowest excited singlet and triplet energies are in very good agreement with the fluorescence and phosphorescence spectroscopic data, respectively, as summarized in Table 2. Calculations support the above spectroscopic assignment on the nature of the emissive triplet states. Fig. 4b illustrates the spatial extent of the hole–electron NTO pairs for the optimized lowest triplet state of **2PPA**, **1PPA**, and **1MPA**, along with the calculated charge transfer numbers ω_{CT}. These transitions can be described by a single NTO pair. The calculated relaxed T_1 state for **2PPA** and **1PPA** has a LE character and is localized on the pyrimidine unit, whereas the relaxed T_1 state for **1MPA** has

Table 2 TDA-DFT computed singlet ($S_1 \rightarrow S_0$) and triplet ($T_1 \rightarrow S_0$) emission energies of **2PPA**, **1PPA**, and **1MPA** at the M06-2X/6-31+G(d,p) level along with the energy values of fluorescence (Fl) and phosphorescence (Ph) taken from the onset of the spectra at 77 K in toluene solution for 300 nm excitation

Compound	Theory S_1 (eV)	Experiment S_1 (eV)	Theory T_1 (eV)	Experiment T_1 (eV)
2PPA	3.23	3.15	2.80	2.91
1PPA	3.41	3.47	2.62	2.85
1MPA	3.50 ($S_2 \rightarrow S_0$)	3.84	2.97	3.28
	3.13 ($S_1 \rightarrow S_0$)	3.30^a		3.07^a

^{a} Excitation at 350 nm.

a mixed CT–LE character, with the LE part on the acridine. An energy level diagram based on the spectroscopic data is depicted in Fig. 4a. The NTOs for fluorescence can be found in Fig. S7 (ESI†). The emissive singlet for **2PPA** is localized on the pyrimidine, which is in contrast to the spectroscopic assignment of a CT state. This comes from the fact that the obtained gas-phase geometry from the TDA-DFT calculations leads to a distorted acridine. However, in the solid state, intermolecular interactions might favor pi–pi stacking configurations between the acridine units of the molecules and result in a twisted intramolecular CT state. For 1PPA, the obtained lowest singlet is at 3.41 eV and has a CT character. The lowest singlet state for 1MPA is at 3.13 eV, which displays a strong charge transfer character as depicted by the hole–electron pair natural transition orbitals and the electron–hole correlation plot of the Ω matrix (Fig. S9, ESI†) and has a weak oscillator strength $f = 0.0037$. Following optimization of the second lowest singlet state, S_2, we find that it is located at 3.50 eV and has an oscillator strength $f = 0.0134$ (Fig. S7, ESI†). Although the charge transfer numbers obtained are similar for the two states, the electron–hole distance index Δr is larger for the S_1 state ($\Delta r = 3.26$ Å) than for the S_2 state ($\Delta r = 2.07$ Å), indicating a larger CT length for the S_1 state. The hole NTO for S_2 is delocalized across both acridine units. This could explain the experimentally observed excitation wavelength dependent emission described in the previous section. Given the relatively large energy difference between the S_2 and S_1 states and the fact that relaxation from the Franck–Condon state requires large conformational rearrangement, vibrational relaxation and internal conversion to S_1 might compete with radiative emission from the S_2 state leading to non-Kasha emission.[39]

OLED properties

After having established that the acridine–pyrimidine based compound **1MPA** is the one with the highest triplet energy (> 3.0 eV) among the studied compounds, we employed it as a host for the fabrication of blue OLED. We combined it with the previously reported blue TADF emitters **mPTC**[40] and **OBA-O**[41] as dopants (Fig. S10e, ESI†). In the case of **mPTC**, a doping concentration of 12 wt% was used based on photoluminescence quantum yield measurements (Table S1, ESI†). For the emitter **OBA-O** we used several doping concentrations (5, 8, and 13 wt%) with a view to examine the emission wavelength tunability of the

device. The choice of **mPTC** and **OBA-O** as TADF emitters was based on (i) their shallow HOMO levels (-5.12 and -5.15 eV, respectively), which were similar to that of **1MPA**, (ii) their triplet energies being lower than that of the host to allow for triplet exciton confinement and (iii) their high photoluminescence quantum yields. OLEDs were fabricated using the following simple device architecture: ITO (100 nm)/TAPC (30 nm)/EML (x wt% **mPTC** and **OBA-O** in **1MPA**, 30 nm)/TmPyPB (40 nm)/LiF (0.8 nm)/Al (100 nm). Here, ITO was used as a transparent anode, (1,1-bis[[(di-4-tolylamino)phenyl]cyclohexane) TAPC and (1,3,5-tri(*m*-pyridin-3-ylphenyl)benzene) TmPyPB for hole and electron injection/transport, respectively, LiF/Al as the reflective cathode, whereas x denotes the doping concentration (in weight percentage) of the particular TADF emitter in the emissive layer (EML).

The configuration and the energy level diagram of the device with the EML (12 wt% **mPTC** in **1MPA**) are displayed in Fig. 5a. The main device characteristics are provided in Fig. 5b–d and Table 3. The OLED demonstrated a low turn-on voltage (V_{on}) of 3.25 V, greenish-blue electroluminescence at 491 nm with the full width at half maximum (FWHM) of 75 nm resulting in Commission Internationale de L'Eclairage (CIE) coordinates of (0.2, 0.4). The maximum external quantum efficiency (EQE_{max}) was determined to be 13.6%, which is in good agreement with PLQY of **mPTC** in **1MPA** (PLQY $\approx$ 70%, see Table S1 of the ESI†)[40] if typical device outcoupling efficiency of about 20% is taken into account.[42] The fabricated device exhibited low efficiency roll-off at practically useful brightness, *i.e.*, EQE dropped down to 12.3% at the brightness of 100 cd m^{-2} and to 11.6% at 1000 cd m^{-2} (Fig. 5b). Notably, EQE remained above 10% up to the very high brightness of 5000 cd m^{-2}. This behavior could be explained by the optimal device architecture and well-balanced electron and hole currents. The maximum luminance achieved by the device was nearly 44 000 cd m^{-2}. The properties of analogous devices based on the same host, yet the different TADF emitter **OBA-O** at various doping concentrations in the EML, are presented in Fig. S10 (ESI†) and Table 3. The **OBA-O** device with a similar doping concentration (13 wt%) as the previous one based on **mPTC** expressed comparable emission properties. Explicitly, peak emission wavelength, bandwidth, CIE color coordinates, and maximum EQE were found to be alike. On the other hand, the much steeper *I–V* and *L–V* curves in the **OBA-O** device indicated a significantly improved charge carrier mobility in the EML. Importantly, the reduced **OBA-O** concentration down to 5 wt% in the EML shifted the emission wavelength from greenish-blue (493 nm) to deep-blue (461 nm), demonstrating the potential of **1MPA** to host deep-blue TADF emitters. The picture of the deep-blue emitting OLED is shown in the inset of Fig. S10 (ESI†). The reduced emitter concentration concomitantly caused a broadening of emission bandwidth (up to 94 nm) and an accelerated EQE roll-off. In OLEDs, EQE roll-off typically arises from exciton–polaron quenching and from exciton–exciton annihilation. The increased roll-off with lower emitter concentrations can arise from either effect. Since there is a barrier of about 1.15 eV for electron injection onto the host yet not for injection onto the emitter, the likely scenario is that electron transport
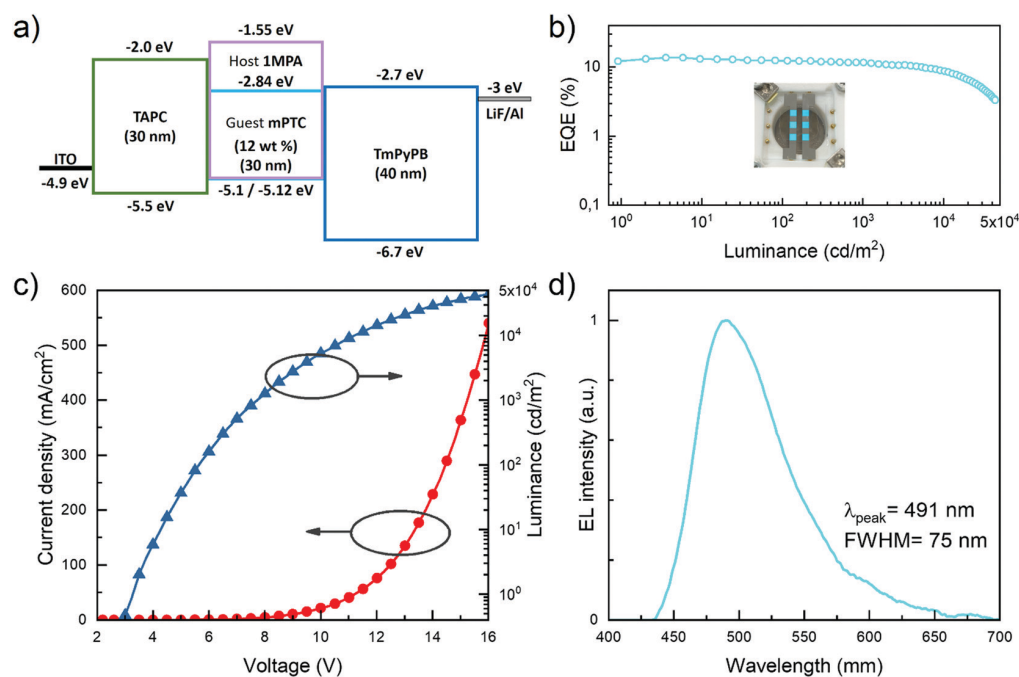
17478 | *J. Mater. Chem. C*, 2021, **9**, 17471–17482

This journal is © The Royal Society of Chemistry 2021

275

Fig. 5 Main properties of the TADF OLED based on the **1MPA** host doped with 12 wt% of **mPTC**. (a) Energy level diagram. (b) EQE *vs.* luminance. (c) Current density and luminance *vs.* applied voltage. (d) Electroluminescence spectrum with working device picture shown in the inset.

Table 3 Main parameters of blue TADF OLEDs based on the **1MPA** host doped with **mPTC** and **OBA-O** emitters

Emitter	V_{on}^{a} (V)	EQE^{b} (%)	L_{max}^{c} (cd m^{-2})	CE_{max}^{d} (cd A^{-1})	LE_{max}^{e} (lm W^{-1})	λ_{max}^{f} (nm)	$FWHM^{g}$ (nm)	CIE 1931^{h} (x, y)
mPTC (12 wt%)	3.25	13.6/12.3/11.5	43 911	33.3	27.5	491	75	(0.2, 0.4)
OBA-O (13 wt%)	2.75	14.2/11.9/8.9	30 247	36.6	36.4	493	83	(0.2, 0.38)
OBA-O (8 wt%)	3.25	14.9/6.8/2.9	8449	26.2	24.5	475	93	(0.16, 0.21)
OBA-O (5 wt%)	3.5	10.6/3.5/1.6	52 83	14.4	12.1	461	94	(0.16, 0.18)

^{a} Turn-on voltage at 1 cd m^{-2}. ^{b} Maximum EQE/EQE at 100 cd m^{-2}/EQE at 1000 cd m^{-2}. ^{c} Maximum brightness. ^{d} Maximum current efficiency. ^{e} Maximum luminous efficiency. ^{f} Peak emission wavelength. ^{g} Full width at half maximum. ^{h} Commission Internationale de L'Eclairage color coordinates (x, y).

proceeds by hopping between emitter molecules while hole transport occurs *via* the host, where hole injection is barrier-free. This results in a charge carrier imbalance that favors exciton–hole quenching. However, at low emitter concentrations percolative transport across emitting sites is no longer possible, so that the recombination zone narrows towards the electron injecting side. This decrease in recombination zone implies an increase of both exciton and charge carrier density, so that in addition to exciton–hole quenching there can also be a contribution from triplet–triplet annihilation. (see Fig. S10b, ESI†). We note that the dominant lifetime of delayed fluorescence in **mPTC** (2 μs) is shorter than that in **OBA-O** (9 μs), consistent with its lower susceptibility to exciton quenching processes (Fig. S12 and Table S2, ESI†). Furthermore, we fabricated an identical **mPTC**-based device where the **1MPA** host is replaced with the benchmark host **mCBP**. In Fig. S11 (ESI†) we provide the comparison of OLED properties of the two identical devices differing only by the host material (**1MPA** *vs.* benchmark **mCBP**). Due to the lower LUMO of **mCBP** compared to **1MPA**, many more electrons are being injected into the **mCBP** host

resulting in significantly higher current densities flowing through the device, and subsequently, higher luminance attained at the same driving voltage. EL spectra of both devices utilizing the same **mPTC** dopant concentration (12 wt%) are found to be very similar. The device featuring benchmark **mCBP** host exhibits a higher EQEmax of 21% and similar efficiency roll-off as the other one based on the **1MPA** host. Nevertheless, the obtained results show that high-triplet-energy host **1MPA** is suitable for the fabrication of efficient blue TADF OLEDs, delivering low efficiency roll-off even beyond the practical brightness of 1000 cd m^{-2}.

Conclusions

In this work, we present three newly synthesized host molecules that adopt acridine and pyrimidine units. The bulky acridine provides superior thermal and morphological properties, further improved when two acridines are used, like in **1PPA** and **1MPA**. The donor and acceptor combination allows

276

transporting both holes and electrons. Throughout the series, it is possible to observe a decrease in the conjugation of the acceptor moiety within the hosts. When the acceptor unit is limited to only one pyrimidine ring (**1MPA** host), the triplet energy is the highest, with a value of 3.07 eV. Through theoretical calculations and spectroscopy, we attribute its nature to a mixed CT–LE state. Finally, to demonstrate the potential of these molecules, **1MPA** is employed as the host material to fabricate blue TADF OLEDs. Using the emitter **mPTC** we achieved a sky-blue OLED with electroluminescence at 491 nm and a maximum EQE of 13.6%, combined with a low roll-off. The host **1MPA** is also shown to be suitable for deep-blue emitters like OBA-O, delivering blue OLEDs with color coordinates of $x = 0.16$ and $y = 0.18$.

Author contributions

F. Rodella performed the synthesis and characterization of the host materials, as well as the thermal and electrochemical analysis. R. Saxena and S. Bagnich performed the photophysical studies. D. Banevičius and G. Kreiza fabricated OLED devices. S. Athanasopoulos was responsible for DFT calculations. S. Juršėnas, K. Kazlauskas, A. Köhler and P. Strohriegl supervised the experiments and corrected the manuscript.

Conflicts of interest

There are no conflicts to declare.

Acknowledgements

References

1 Q. Wei, N. Fei, A. Islam, T. Lei, L. Hong, R. Peng, X. Fan, L. Chen, P. Gao and Z. Ge, Small-Molecule Emitters with High Quantum Efficiency: Mechanisms, Structures, and Applications in OLED Devices, *Adv. Opt. Mater.*, 2018, **6**, 1800512.

2 M. Y. Wong and E. Zysman-Colman, Purely Organic Thermally Activated Delayed Fluorescence Materials for Organic Light-Emitting Diodes, *Adv. Mater.*, 2017, **29**, 1605444.

3 H. Xu, R. Chen, Q. Sun, W. Lai, Q. Su, W. Huang and X. Liu, Recent progress in metal-organic complexes for optoelectronic applications, *Chem. Soc. Rev.*, 2014, **43**, 3259–3302.

4 Y. Zhang, J. Lee and S. R. Forrest, Tenfold increase in the lifetime of blue phosphorescent organic light-emitting diodes, *Nat. Commun.*, 2014, **5**, 5008.

5 Z. Xu, B. Z. Tang, Y. Wang and D. Ma, Recent advances in high performance blue organic light-emitting diodes based on fluorescence emitters, *J. Mater. Chem. C*, 2020, **8**, 2614–2642.

6 Z. Yang, Z. Mao, Z. Xie, Y. Zhang, S. Liu, J. Zhao, J. Xu, Z. Chi and M. P. Aldred, Recent advances in organic thermally activated delayed fluorescence materials, *Chem. Soc. Rev.*, 2017, **46**, 915–1016.

7 Y. Wang, J. H. Yun, L. Wang and J. Y. Lee, High Triplet Energy Hosts for Blue Organic Light-Emitting Diodes, *Adv. Funct. Mater.*, 2020, 2008332.

8 M. Godumala, S. Choi, M. J. Cho and D. H. Choi, Thermally activated delayed fluorescence blue dopants and hosts: from the design strategy to organic light-emitting diode applications, *J. Mater. Chem. C*, 2016, **4**, 11355–11381.

9 T. Chatterjee and K.-T. Wong, Perspective on Host Materials for Thermally Activated Delayed Fluorescence Organic Light Emitting Diodes, *Adv. Opt. Mater.*, 2019, **7**, 1800565.

10 Q. Zhang, B. Li, S. Huang, H. Nomura, H. Tanaka and C. Adachi, Efficient blue organic light-emitting diodes employing thermally activated delayed fluorescence, *Nat. Photonics*, 2014, **8**, 326–332.

11 T.-A. Lin, T. Chatterjee, W.-L. Tsai, W.-K. Lee, M.-J. Wu, M. Jiao, K.-C. Pan, C.-L. Yi, C.-L. Chung, K.-T. Wong and C.-C. Wu, Sky-Blue Organic Light Emitting Diode with 37% External Quantum Efficiency Using Thermally Activated Delayed Fluorescence from Spiroacridine-Triazine Hybrid, *Adv. Mater.*, 2016, **28**, 6976–6983.

12 I. E. Serdiuk, C. H. Ryoo, K. Kozakiewicz, M. Mońka, B. Liberek and S. Y. Park, Twisted acceptors in the design of deep-blue TADF emitters: crucial role of excited-state relaxation in the photophysics of methyl-substituted s-triphenyltriazine derivatives, *J. Mater. Chem. C*, 2020, **8**, 6052–6062.

13 T. Serevičius, R. Skaisgiris, I. Fiodorova, G. Kreiza, D. Banevičius, K. Kazlauskas, S. Tumkevičius and S. Juršėnas, Single-exponential solid-state delayed fluorescence decay in TADF compounds with minimized conformational disorder, *J. Mater. Chem. C*, 2021, **9**, 836–841.

14 X.-Y. Liu, F. Liang, Y. Yuan, L.-S. Cui, Z.-Q. Jiang and L.-S. Liao, An effective host material with thermally activated delayed fluorescence formed by confined conjugation for red phosphorescent organic light-emitting diodes, *Chem. Commun.*, 2016, **52**, 8149–8151.

15 X.-Y. Liu, Y.-Y. Ma, W. Zhang, B. Song, L. Ding, M.-K. Fung and J. Fan, A Novel Linking Strategy of Using 9,10-Dihydroacridine to Construct Efficient Host Materials for Red Phosphorescent Organic Light-Emitting Diodes, *Chemistry*, 2018, **24**, 11755–11762.

16 Y. Im, M. Kim, Y. J. Cho, J.-A. Seo, K. S. Yook and J. Y. Lee, Molecular Design Strategy of Organic Thermally Activated

17480 | *J. Mater. Chem. C*, 2021, **9**, 17471–17482

This journal is © The Royal Society of Chemistry 2021

Delayed Fluorescence Emitters, *Chem. Mater.*, 2017, **29**, 1946–1963.

17 B. Li, Z. Li, T. Hu, Y. Zhang, Y. Wang, Y. Yi, F. Guo and L. Zhao, Highly efficient blue organic light-emitting diodes from pyrimidine-based thermally activated delayed fluorescence emitters, *J. Mater. Chem. C*, 2018, **6**, 2351–2359.

18 K. Wu, T. Zhang, L. Zhan, C. Zhong, S. Gong, N. Jiang, Z.-H. Lu and C. Yang, Optimizing Optoelectronic Properties of Pyrimidine-Based TADF Emitters by Changing the Substituent for Organic Light-Emitting Diodes with External Quantum Efficiency Close to 25% and Slow Efficiency Roll-Off, *Chemistry*, 2016, **22**, 10860–10866.

19 I. S. Park, J. Lee and T. Yasuda, High-performance blue organic light-emitting diodes with 20% external electroluminescence quantum efficiency based on pyrimidine-containing thermally activated delayed fluorescence emitters, *J. Mater. Chem. C*, 2016, **4**, 7911–7916.

20 H.-J. Park, S. H. Han and J. Y. Lee, Molecular Design of Thermally Activated Delayed-Fluorescent Emitters Using 2,2'-Bipyrimidine as the Acceptor in Donor-Acceptor Structures, *Chem. – Asian J.*, 2017, **12**, 2494–2500.

21 K. S. Son, M. Yahiro, T. Imai, H. Yoshizaki and C. Adachi, Blue organic electrophosphorescence diodes using diarylamino-substituted heterocyclic compounds as host material, *J. Photopolym. Sci. Technol.*, 2007, 47–51.

22 S.-J. Su, C. Cai and J. Kido, RGB Phosphorescent Organic Light-Emitting Diodes by Using Host Materials with Heterocyclic Cores: Effect of Nitrogen Atom Orientations, *Chem. Mater.*, 2011, **23**, 274–284.

23 S.-J. Su, C. Cai and J. Kido, Three-carbazole-armed host materials with various cores for RGB phosphorescent organic light-emitting diodes, *J. Mater. Chem.*, 2012, **22**, 3447.

24 R. Komatsu, H. Sasabe and J. Kido, Recent progress of pyrimidine derivatives for high-performance organic light-emitting devices, *J. Photonics Energy*, 2018, **8**, 1.

25 Y. Zhao and D. G. Truhlar, The M06 suite of density functionals for main group thermochemistry, thermochemical kinetics, noncovalent interactions, excited states, and transition elements: two new functionals and systematic testing of four M06-class functionals and 12 other functionals, *Theor. Chem. Acc.*, 2008, **120**, 215–241.

26 S. Hirata and M. Head-Gordon, Time-dependent density functional theory within the Tamm–Dancoff approximation, *Chem. Phys. Lett.*, 1999, 291–299.

27 R. L. Martin, Natural transition orbitals, *J. Chem. Phys.*, 2003, **118**, 4775–4777.

28 M. J. Frisch, G. W. Trucks, H. B. Schlegel, G. E. Scuseria, M. A. Robb, J. R. Cheeseman, G. Scalmani, V. Barone, G. A. Petersson, H. Nakatsuji, X. Li, M. Caricato, A. V. Marenich, J. Bloino, B. G. Janesko, R. Gomperts, B. Mennucci, H. P. Hratchian, J. V. Ortiz, A. F. Izmaylov, J. L. Sonnenberg, D. Williams-Young, F. Ding, F. Lipparini, F. Egidi, J. Goings, B. Peng, A. Petrone, T. Henderson, D. Ranasinghe, V. G. Zakrzewski, J. Gao, N. Rega, G. Zheng, W. Liang, M. Hada, M. Ehara, K. Toyota,

R. Fukuda, J. Hasegawa, M. Ishida, T. Nakajima, Y. Honda, O. Kitao, H. Nakai, T. Vreven, K. Throssell, J. A. Montgomery Jr., J. E. Peralta, F. Ogliaro, M. J. Bearpark, J. J. Heyd, E. N. Brothers, K. N. Kudin, V. N. Staroverov, T. A. Keith, R. Kobayashi, J. Normand, K. Raghavachari, A. P. Rendell, J. C. Burant, S. S. Iyengar, J. Tomasi, M. Cossi, J. M. Millam, M. Klene, C. Adamo, R. Cammi, J. W. Ochterski, R. L. Martin, K. Morokuma, O. Farkas, J. B. Foresman and D. J. G. Fox, *Gaussian 16, Revision C.01*, Gaussian Inc., Wallingford CT, 2016.

29 M. D. Hanwell, D. E. Curtis, D. C. Lonie, T. Vandermeersch, E. Zurek and G. R. Hutchison, Avogadro: an advanced semantic chemical editor, visualization, and analysis platform, *J. Cheminf.*, 2012, **4**, 17.

30 F. Plasser, TheoDORE: A toolbox for a detailed and automated analysis of electronic excited state computations, *J. Chem. Phys.*, 2020, **152**, 84108.

31 F. Plasser and H. Lischka, Analysis of Excitonic and Charge Transfer Interactions from Quantum Chemical Calculations, *J. Chem. Theory Comput.*, 2012, **8**, 2777–2789.

32 C. A. Guido, P. Cortona, B. Mennucci and C. Adamo, On the Metric of Charge Transfer Molecular Excitations: A Simple Chemical Descriptor, *J. Chem. Theory Comput.*, 2013, **9**, 3118–3126.

33 T. Lu and F. Chen, Multiwfn: a multifunctional wavefunction analyzer, *J. Comput. Chem.*, 2012, **33**, 580–592.

34 F. Rodella, S. Bagnich, E. Duda, T. Meier, J. Kahle, S. Athanasopoulos, A. Köhler and P. Strohriegl, High Triplet Energy Host Materials for Blue TADF OLEDs-A Tool Box Approach, *Front. Chem.*, 2020, **8**, 657.

35 K. Gräf, M. A. Rahim, S. Das and M. Thelakkat, Complementary co-sensitization of an aggregating squaraine dye in solid-state dye-sensitized solar cells, *Dyes Pigm.*, 2013, **99**, 1101–1106.

36 N. Nishi, R. Shimada and Y. Kanda, The Phosphorescence Processes in Pyrimidine and 2-Chloropymidine, *Bull. Chem. Soc. Jpn.*, 1970, 41–46.

37 G. F. Makhaeva, S. V. Lushchekina, N. P. Boltneva, O. G. Serebryakova, E. V. Rudakova, A. A. Ustyugov, S. O. Bachurin, A. V. Shchepochkin, O. N. Chupakhin, V. N. Charushin and R. J. Richardson, 9-Substituted acridine derivatives as acetylcholinesterase and butyrylcholinesterase inhibitors possessing antioxidant activity for Alzheimer's disease treatment, *Bioorg. Med. Chem.*, 2017, **25**, 5981–5994.

38 K. G. Thorat, R. P. Tayade and N. Sekar, Acridine-1, 8-diones – A new class of thermally stable NLOphores: Photophysical, (hyper)polarizability and TD-DFT studies, *Opt. Mater.*, 2016, **62**, 306–319.

39 A. P. Demchenko, V. I. Tomin and P.-T. Chou, Breaking the Kasha Rule for More Efficient Photochemistry, *Chem. Rev.*, 2017, **117**, 13353–13381.

40 D.-Y. Chen, W. Liu, C.-J. Zheng, K. Wang, F. Li, S. L. Tao, X.-M. Ou and X.-H. Zhang, Isomeric Thermally Activated Delayed Fluorescence Emitters for Color Purity-Improved Emission in Organic Light-Emitting Devices, *ACS Appl. Mater. Interfaces*, 2016, **8**, 16791–16798.

41 D. Song, Y. Yu, L. Yue, D. Zhong, Y. Zhang, X. Yang, Y. Sun, G. Zhou and Z. Wu, Asymmetric thermally activated delayed

This journal is © The Royal Society of Chemistry 2021

J. Mater. Chem. C, 2021, **9**, 17471–17482 | 17481

278

fluorescence (TADF) emitters with 5,9-dioxa-13 b-boranaphtho[3,2,1-de]anthracene (OBA) as the acceptor and highly efficient blue-emitting OLEDs, *J. Mater. Chem. C*, 2019, **7**, 11953–11963.

42 N. C. Greenham, R. H. Friend and D. D. Bradley, Angular Dependence of the Emission from a Conjugated Polymer Light-Emitting Diode: Implications for efficiency calculations, *Adv. Mater.*, 1994, **6**, 491–494.

17482 | *J. Mater. Chem. C*, 2021, **9**, 17471–17482

This journal is © The Royal Society of Chemistry 2021

279

Supporting Information

Low efficiency roll-off blue TADF OLEDs employing a novel acridine-pyrimidine based high triplet energy host

Francesco Rodella,[a] Rishabh Saxena,[b] Sergey Bagnich,[b] Dovydas Banevičius,[c] Gediminas Kreiza,[c] Stavros Athanasopoulos,[d] Saulius Juršėnas,[c] Karolis Kazlauskas,[c] Anna Köhler[b,e] and Peter Strohriegl[a,e].

[a] Macromolecular Chemistry I, University of Bayreuth, Bayreuth 95440, Germany.

[b] Soft Matter Optoelectronics, University of Bayreuth, Bayreuth 95440, Germany.

[c] Institute of Photonics and Nanotechnology, Vilnius University, Saulėtekio av. 3, LT-10257 Vilnius, Lithuania.

[d] Departamento de Física, Universidad Carlos III de Madrid, Avenida Universidad 30, 28911 Leganés, Madrid, Spain.

[e] Bayreuth Institute of Macromolecular Research (BIMF), University of Bayreuth, Bayreuth 95440, Germany.

280

Table of contents:

Donors and acceptors used for spectroscopic studies:

2PhPy   1PhPy   MePy   Acridine
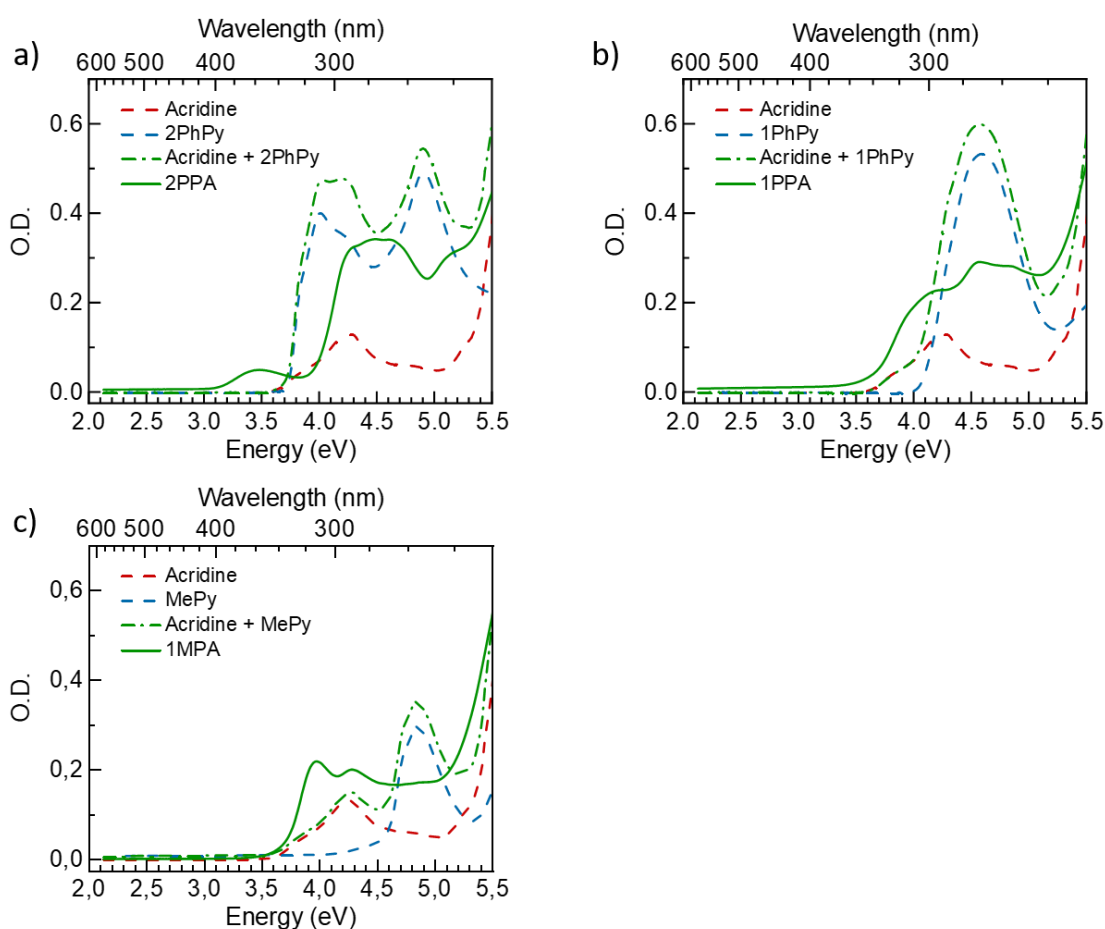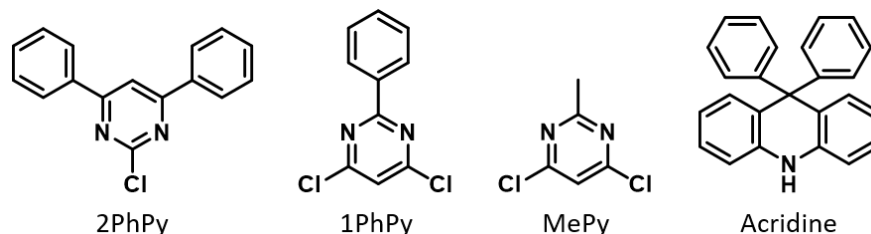
Figure S1: a), b) and c) show the absorption spectra (solid green line) of **2PPA**, **1PPA** and **1MPA** solutions (concentration = 0.05 mg/mL) in toluene along with acridine absorption (dashed red line) and **2PhPy**, **1PhPy** and **MePy** acceptors (dashed blue line) respectively. The sum of donor and acceptor absorption is shown by green dash-dot line. d) Acridine and 2PhPy (red and blue dashed

3

line) absorption spectra in Figure S1 a are shifted in energy to match the sum of acridine + 2PhPy spectrum (green dash-dot line) with the absorption spectrum of **2PPA** (solid green line).
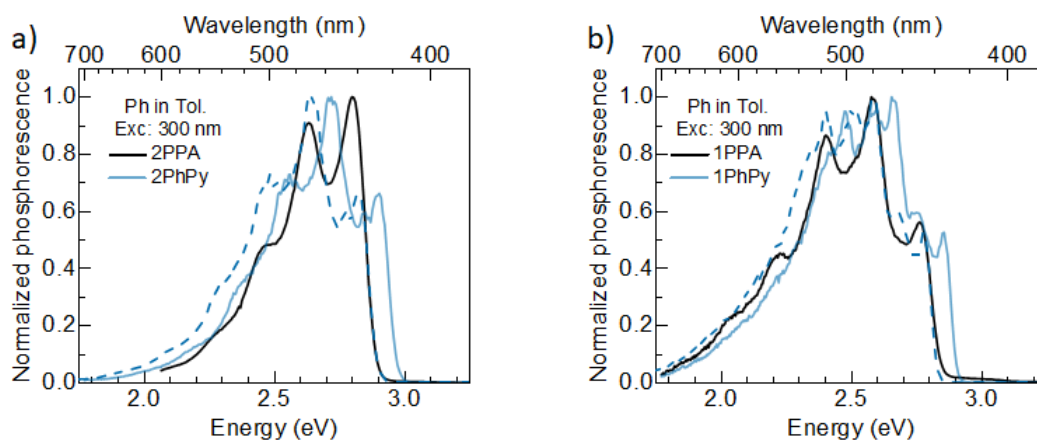
Figure S2: a) and b) show the comparison of **2PPA** and **1PPA** spectra (black line) with the horizontally translated Ph spectra of **2PhPy** and **1PhPy** spectra (blue dashed line) respectively. For reference the original **2PhPy** and **1PhPy** spectra is shown with a semi-transparent blue line.
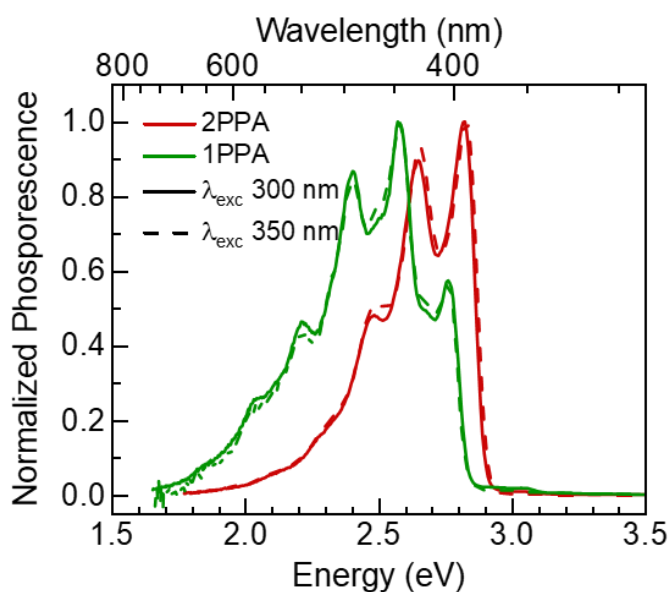
Figure S3: Excitation wavelength Ph spectra is shown for **2PPA** and **1PPA** in mTHF.

4
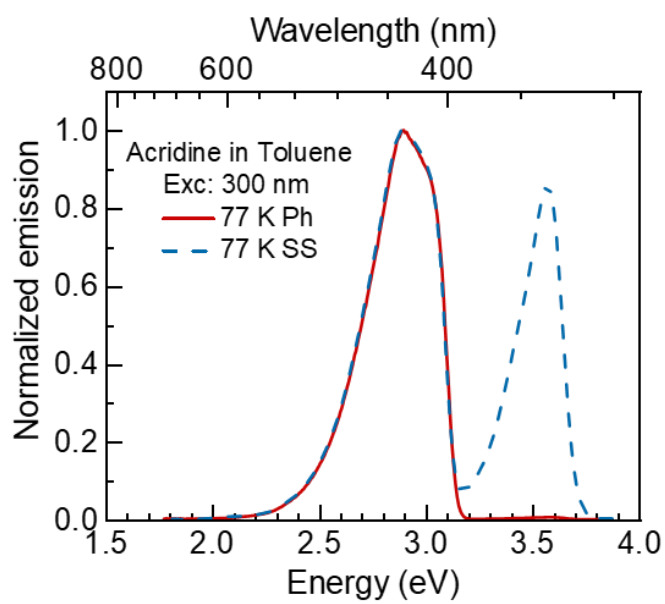
Figure S4: 77 K phosphorescence (red solid line) and steady-state (blue dashed line) for acridine solution in toluene (concentration = 0.05 mg/mL). Phosphorescence is collected with a delay time of 150 ms and a gate width of 50 ms.
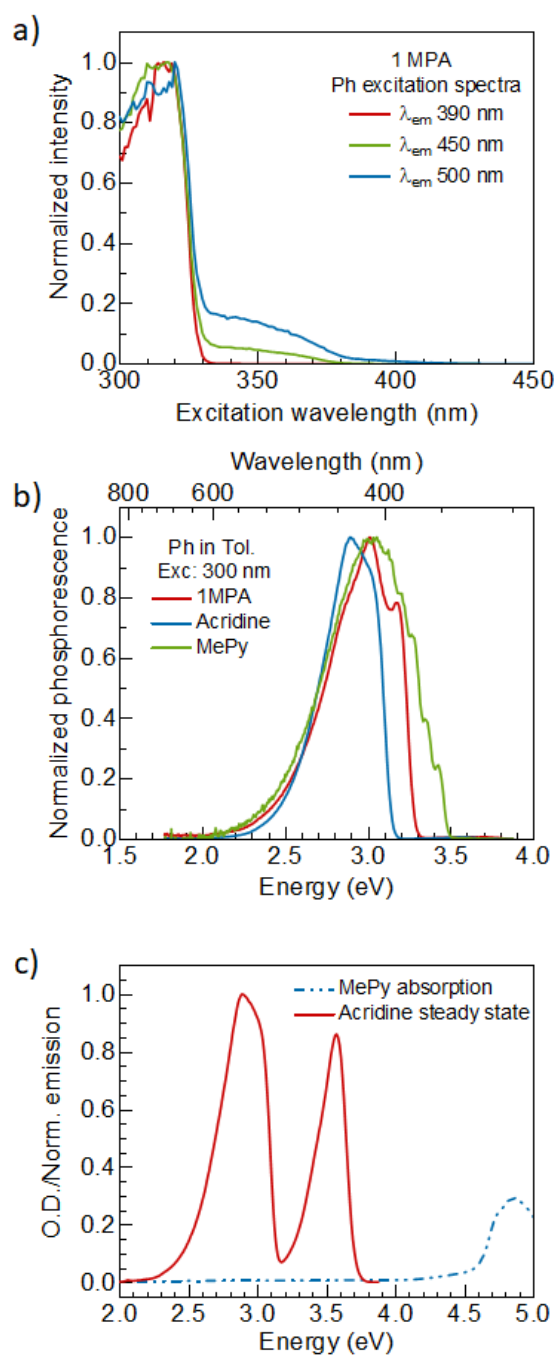
Figure S5: a) Phosphorescence (delay time 50 ms, gating time 50 ms) excitation spectrum for 1MPA solution in toluene glass (77 K). b) 77 K phosphorescence for 1MPA (red), acridine (blue) and methylpyriminine (MePy – green) solution in toluene (concentration = 0.05 mg/mL). Phosphorescence is collected with a delay time of 150 ms and a gate width of 50 ms. c) MePy absorption (blue dash-dot-dot line) and 77 K SS steady state emission of acridine solution (red solid) in toluene.

6
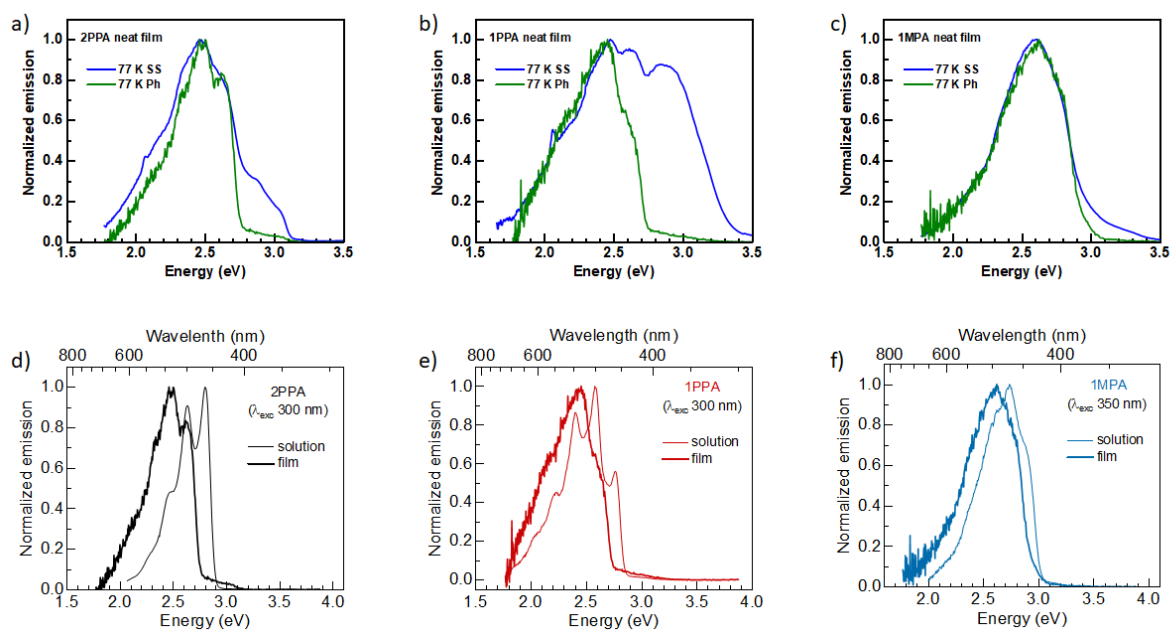
Figure S6: 77 K steady state (SS) and phosphorescence (delay time: 150 ms, gating time: 50 ms) spectra for a) 2PPA b) 1PPA and c) 1MPA neat films. 77 K phosphorescence (Ph) spectra in neat films compared with the Ph spectra in frozen toluene solution for d) 2PPA e) 1PPA and f) 1MPA.

Assignment of singlet and triplet states for 1MPA

S_2 is an acridine based locally excited (LE) state (by comparison of steady state emission of 1MPA in **Figure 3e** with the steady state emission of acridine in **Figure S4**).

Option A: High energy 1MPA phosphorescence (T_2) is acridine based phosphorescence as it is observed only when acridine is excited, i.e. when $\lambda_{exc} < 330$ nm (**Figure S5a** and **Figure S1**). This also implies that the intersystem crossing (ISC) rate on acridine is faster and that the charge transfer (CT) from acridine to methylpyrimidine (MePy) to form a CT state is slower. The internal conversion from the high energy triplet state (T_2) to the low energy triplet state (T_1) is also slow because of the required CT.

Option B: High energy 1MPA phosphorescence (T_2) is from MePy based LE.

- **Argument in favor of it:** The MePy phosphorescence is close in energy to the observed T_2 emission (**Figure 5b**).
- **Arguments against it:** the absorption from MePy is very far away from the excitation energy ($\lambda_{exc} = 300$ nm, $E_{exc} = 4.13$ eV), i.e. MePy cannot be excited. Thus, the excitation would need to be transferred from acridine to MePy. However, the emission of acridine has negligible overlap with the MePy absorption (**Figure S5c**), implying poor energy transfer between these two units, since for excitations to be transferred efficiently via Förster/Dexter process some overlap is required.

Low energy 1MPA phosphorescence (T_1): It is assigned as an acridine based hybrid CT-LE state because emission at both 450 and 500 nm have strong contribution from acridine excitation ($\lambda_{exc} < 330$ nm) in the phosphorescence excitation spectrum (**Figure 5a**). The phosphorescence spectral shape (**Figure 3f**) has some signatures of acridine phosphorescence (**Figure S4**). Also, there is some weak absorption between 330-380 nm (**Figure S5a**) consistent with the expected position of CT absorption.

8
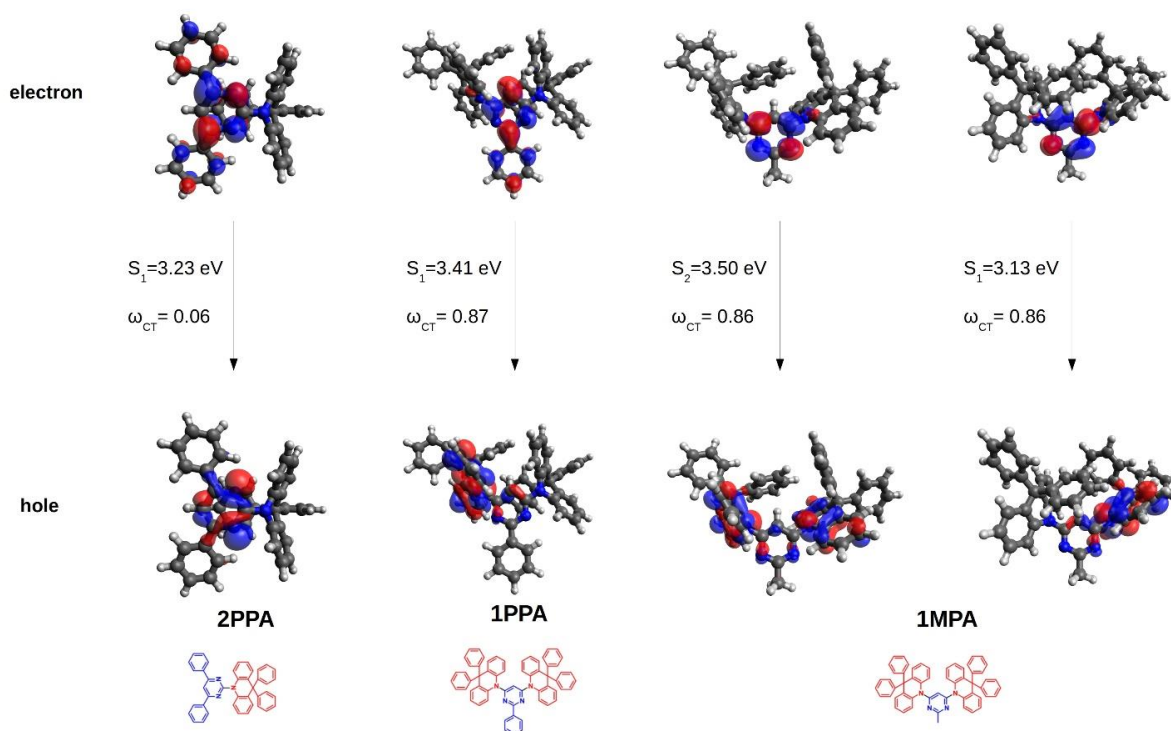
Figure S7: TDA-DFT computed natural transition orbitals, emission energies and charge transfer numbers for the lowest relaxed singlet states for **2PPA**, **1PPA** and **1MPA** at the M06-2X/6-31+G(d,p) level. For **1MPA** both the S_2 and S_1 state NTOs are shown. The relevant arrangement of the acridine and pyrimidine units is shown at the bottom.
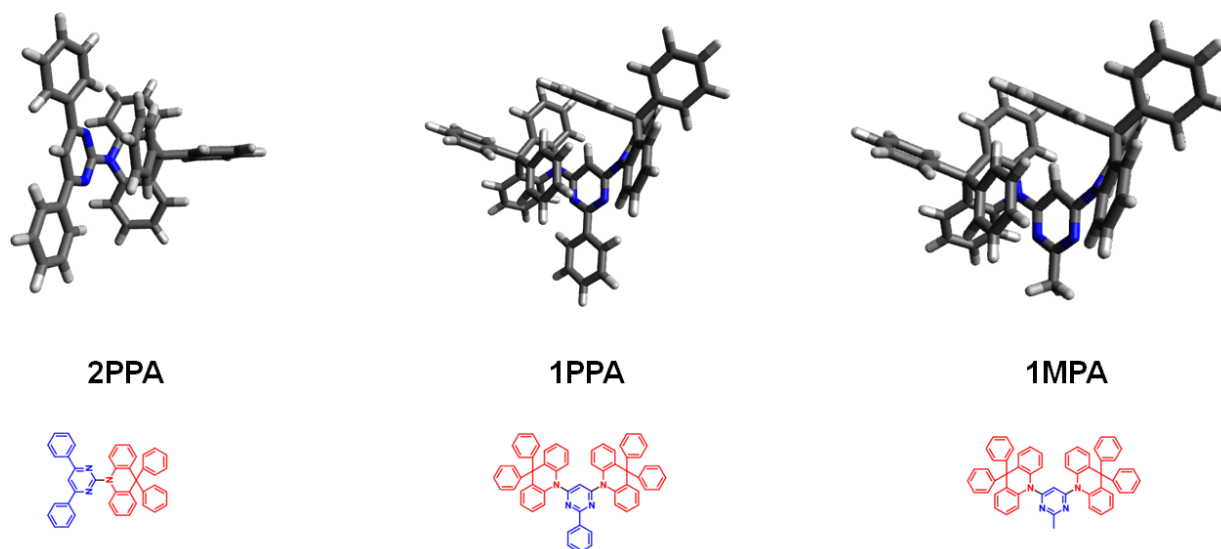
Figure S8: TDA-DFT optimized structures for the lowest triplet state for **2PPA**, **1PPA,** and **1MPA** at the M06-2X/6-31+G(d,p) level. The structures from Figure 4b (top view) of the main text are reproduced here to present a side view of the optimized triplet geometries.

Table S3: Charge transfer numbers ω_{CT} and average electron-hole separation distance Δr for the lowest relaxed singlet and triplet excited states of **1PPA** and **1MPA**.

compound/state	ω_{CT}	Δr (Å)
1PPA/S$_1$	0.87	4.44
1PPA/T$_1$	0.27	3.09
1MPA/S$_2$	0.86	2.07
1MPA/S$_1$	0.86	3.26
1MPA/T$_1$	0.45	1.92
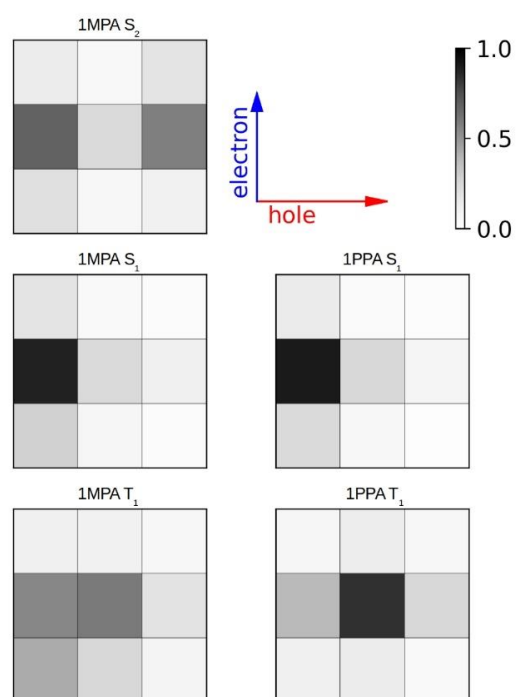
Figure S9: Electron-hole pair correlation plots of the Ω matrix with respect to the acridine-pyrimidine-acridine fragments for the lowest singlet and triplet state of **1PPA** and **1MPA.**
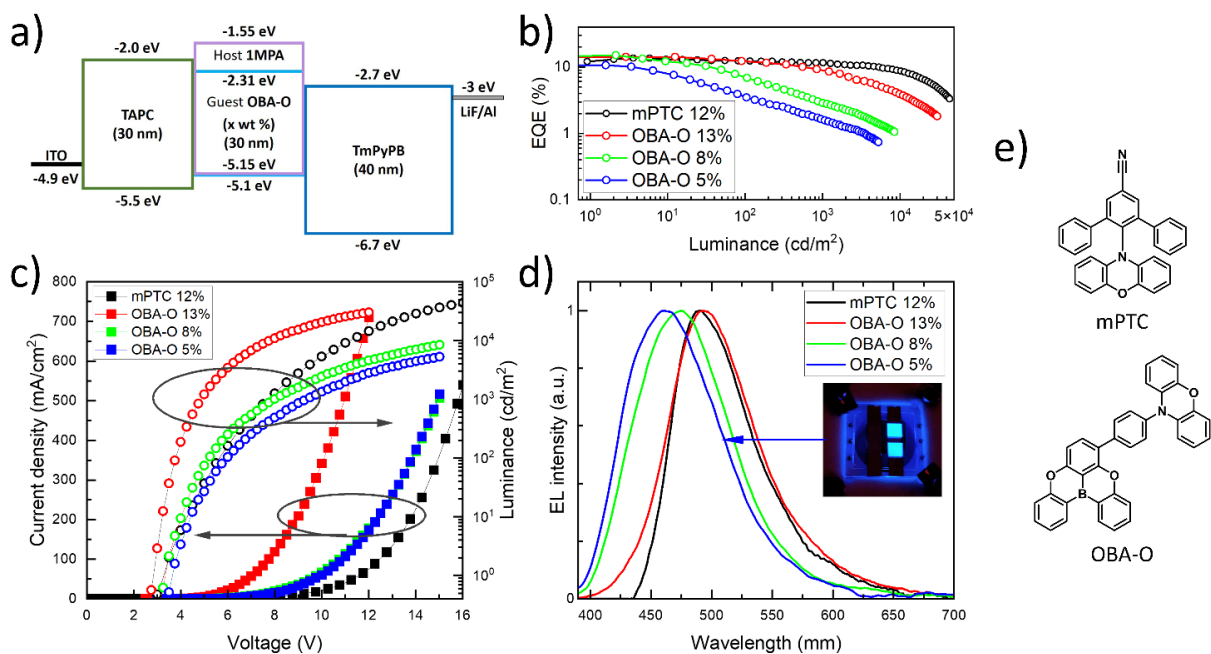
Figure S10: Main properties of the TADF OLED based on **1MPA** host doped with 5, 8 and 13 wt% of **OBA-O**. a) energy level diagram. b) EQE vs. luminance. c) current density and luminance vs. applied voltage. d) electroluminescence spectrum with working device picture shown in the inset. The properties of analogous device with **mPTC** (12 wt%) emitter is shown for reference. e) Molecular structure of the emitters.

290
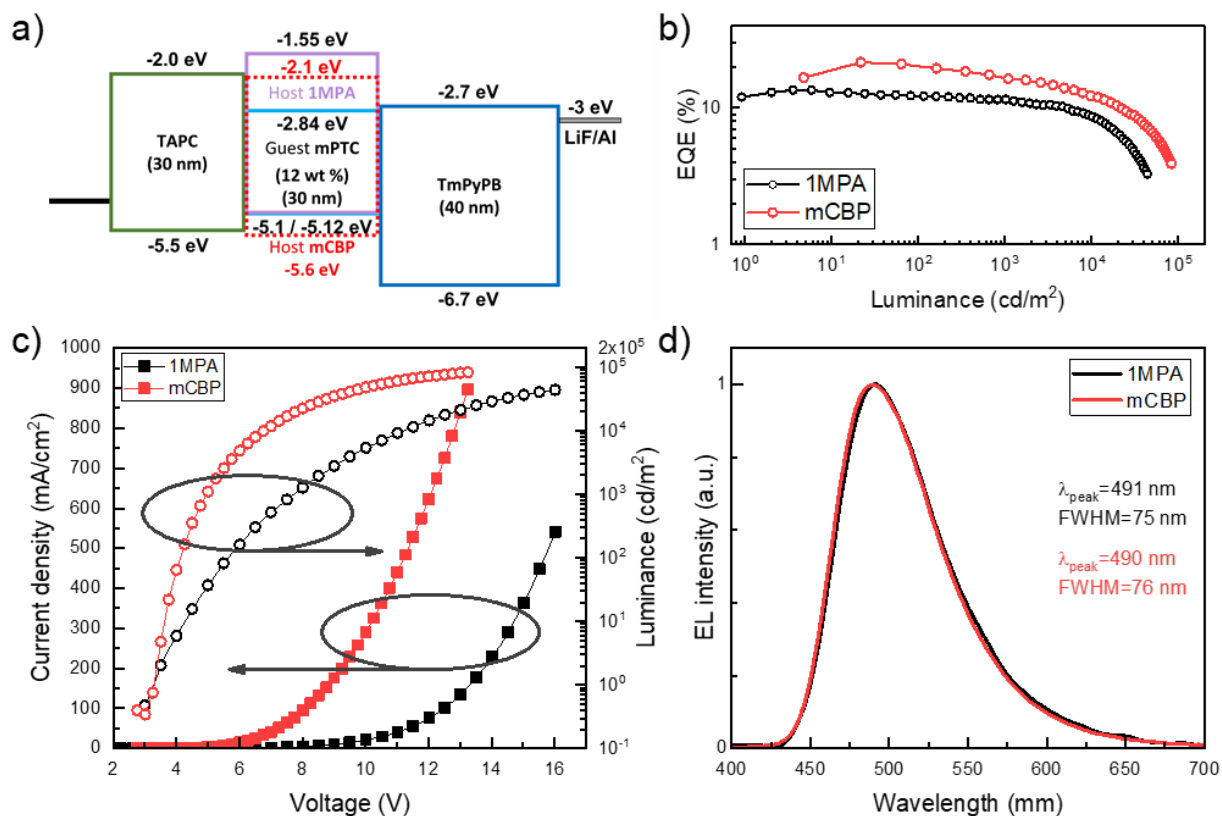
Figure S11: Comparison of the TADF OLEDs based on the new host **1MPA** vs. the benchmark host **mCBP**. Both the OLEDs have a doping concentration of 12 wt% of **mPTC**. a) energy level diagram. b) EQE vs. luminance. c) current density and luminance vs. applied voltage. d) electroluminescence spectrum.
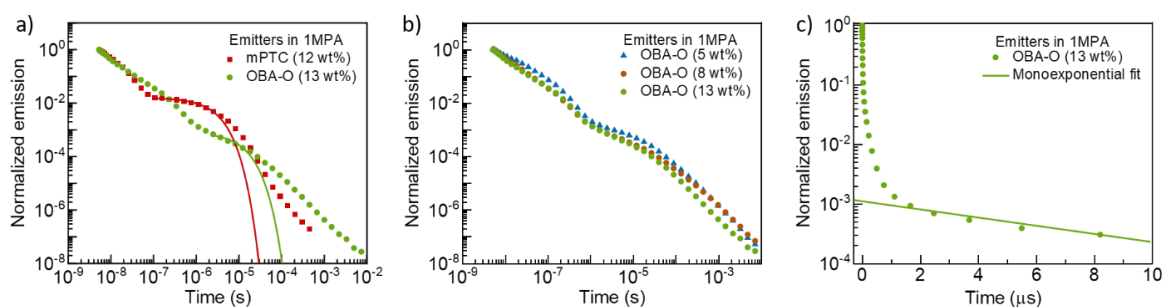
Figure S12: a) RT PL decay of **mPTC** (12 wt%) and **OBA-O** (13 wt%) doped films in **1MPA**. Also shown are monoexponential fits to the decay of the delayed component of 2μs and 9μs, respectively. b) RT PL decay of **OBA-O** (5, 8 and 13 wt%) doped films in **1MPA**. c) RT PL decay of OBA-0 in 1MPA (13 wt%) on a semilogarithmic scale, along with a monoexonential fit of 9μs lifetime.
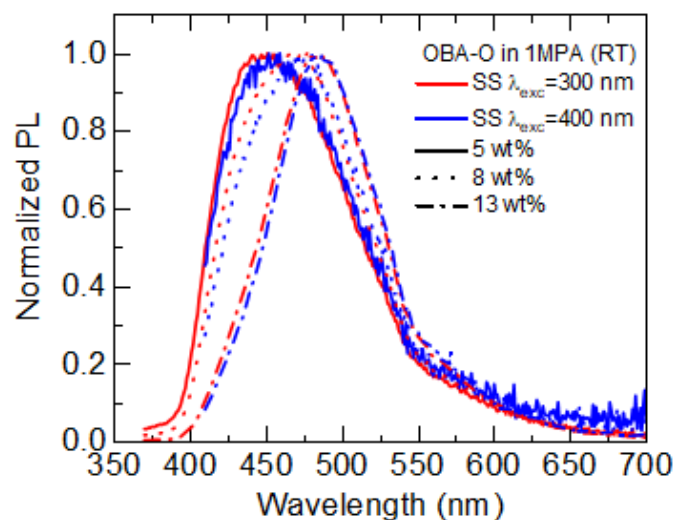
Figure S13: Room temperature photoluminescence spectra of OBA-O doped films (5, 8 and 13 wt%) in 1MPA. The spectra are shown for two excitation wavelengths: when excitons are generated only on emitter molecules ($\lambda_{exc} = 400$ nm - blue lines) and on both host and emitter ($\lambda_{exc} = 300$ nm - red lines).

Table S1: Photolominescence quantum yield measurements of mPTC and OBA-O with different doping percentage in **1MPA** host.

mPTC (wt%) in 1MPA	PLQY (%)	OBA-O (wt%) in 1MPA	PLQY (%)
5	53	5	29
10	69	10	51
12	71	20	42
20	72		

Table S2: A summary of average delayed fluorescence (DF) lifetimes for the PL decays of doped emitter films in **1MPA**.

Emitter in 1MPA	Doping concentration	Monoexponential delayed lifetime	Average delayed lifetime
mPTC	12 wt%	2 μs	6 μs
OBA-O	5 wt%	11 μs	218 μs
	8 wt%	11 μs	343 μs
	13 wt%	9 μs	191 μs

The monoexponential delayed lifetime gives the dominant contribution to the decay. In the film, there are further contributions at longer lifetimes that can arise from tail states in the DOS, triplet-triplet annihilation and phosphorescence. If these longer-lived contributions are included, an average delayed fluorescence (DF) lifetime is obtained according to $\left(\tau_{avg} = \frac{\int t.I_{DF}dt}{\int I_{DF}dt} \right)$.

14 Full list of publications

Publications included in this thesis:

1. **Saxena, R.**[‡]; Nikitenko, V. R.; Fishchuk, I. I.; Burdakov, Y. V.; Metel, Yu. V.; Genoe, J; Bässler, H; Köhler, A; Kadashchuk, A; Role of the Reorganization Energy for Charge Transport in Disordered Organic Semiconductors. *Phys. Rev. B* 103, 165202 (**2021**). (Chapter 8)

2. Stankevych, A[‡]; **Saxena, R.**[‡]; Vakhnin, A.; Pflumm, C.; Genoe, J; Bässler, H; Köhler, A; Kadashchuk, A; Impact of Energy Correlations on Narrowing of Occupied Density of State Distribution for Charge Carriers at Low Temperatures in Disordered Organic Semiconductors. Manuscript in preparation. (Chapter 9)

3. **Saxena, R.**[‡]; Meier, T.; Athanasopoulos, S.; Bässler, H.; Köhler, A.; Kinetic Monte Carlo Study of Triplet-Triplet Annihilation in Conjugated Luminescent Materials. *Phys. Rev. Applied* 14, 034050 (**2020**). (Chapter 10)

4. Sun, D.[‡]; **Saxena, R.**[‡]; Fan, X.; Athanasopoulos, S.; Duda, E.; Zhang, M.; Bagnich, S.; Zhang, X.; Zysman-Colman, E.; Köhler, A.; Regiochemistry of Donor Dendrons Controls the Performance of Thermally Activated Delayed Fluorescence Dendrimer Emitters Translating in Their Use in High Efficiency Solution-Processed Organic Light-Emitting Diodes. *Adv. Sci.*, **2022**, 2201470. (Chapter 11)

5. Sun, D.[‡]; Duda, E.[‡]; Fan, X.; **Saxena, R.**; Zhang, M.; Bagnich, S.; Zhang, X.; Köhler, A.; Zysman-Colman, E.; Thermally Activated Delayed Fluorescent Dendrimers that Underpin High-efficiency Host-Free Solution-Processed Organic Light Emitting Diodes. *Adv. Mater.*, **2022**, 2110344. (Chapter 12)

6. Rodella, F.[‡]; **Saxena, R.**; Bagnich, S.; Banevičius, D.; Kreiza, G.; Athanasopoulos, S.; Juršėnas, S.; Kazlauskas, K.; Köhler, A.; and Strohriegl, P.; Low Efficiency Roll-off Blue TADF OLEDs Employing a Novel Acridine-Pyrimidine based High Triplet Energy Host. *J. Mater. Chem. C*, **2021**, 9, 17471. (Chapter 13)

[‡] indicates first author

Publications not included in this thesis:

7. Duda, E.; Hall, D.; Bagnich, S.; Carpenter-Warren, C.; **Saxena, R.**; Wong, M. Y.; Cordes, D. B.; Slawin, A. M. Z.; Beljonne, D.; Olivier, Y.; Zysman-Colman, E.; Köhler, A.; Enhancing TADF Emission by Fine-Tuning the Dendron Donor Strength. *J. Phys. Chem. B*, **2022**, 126, 2, 552–562.

8. Kahle F.-J.; Rudnick A.; Wedler S.; **Saxena R.**; Ammenhäuser R.; Scherf U.; Bagnich S.; Bässler H.; Köhler A.; Static and Dynamic Disorder of Charge Transfer States Probed by Optical Spectroscopy. *Adv. Energy Mater.*, **2022**, 2103063.

9. Banapanavar, G.; **Saxena, R.**; Köhler, A.; Kabra, D.; Micrometer Long Triplet Exciton Diffusion Length in Polymeric Semiconductor. Submitted.

10. Duda, E.; Suresh, S. M.; Bagnich, S.; Hall, D.; **Saxena, R.**; Slawin, A. M. Z.; Beljonne, D.; Olivier, Y.; Zysman-Colman, E.; Köhler, A.; Controlling the RISC-related Parameters by Employing an Extendable Molecular Design for Blue TADF Emitters. Prepared for submission.

11. Duda, E.; **Saxena, R.**; Kahle, F.-J.; Bagnich, S.; Köhler, A.; The Effects of TADF versus Non-TADF Host Materials on TADF Properties of Guest-Host Systems for OLEDs. Manuscript in preparation.

Appendix

List of abbreviations

AOSF	Amorphous Organic Semiconductor Film
CDM	Correlated Disorder Model
CT	Charge Transfer
D-A	Donor-Acceptor
DET	Dexter Energy Transfer
DF	Delayed Fluorescence
DOS	Density of States
DSCC	Display Supply Chain Consultants
ECDM	Extended Correlated Disorder Model
EGDM	Extended Gaussian Disorder Model
EL	Electroluminescence
EML	Emissive Layer
EQE	External Quantum Efficiency
ETL	Electron Transport Layer
FRET	Förster Resonance Energy Transfer
GDM	Gaussian Disorder Model
HOMO	Highest Occupied Molecular Orbital
HTL	Hole Transport Layer
IC	Internal Conversion
IQE	Internal Quantum Efficiency
ISC	Intersystem Crossing
ITO	Indium Tin Oxide
KMC	Kinetic Monte Carlo
LCAO	Linear Combination of Atomic Orbitals

LE	Local Excitation
LUMO	Lowest Unoccupied Molecular Orbital
MA	Miller-Abrahams
MO	Molecular Orbital
NNH	Nearest Neighbor Hopping
NTO	Natural Transition Orbital
ODOS	Occupational Density of States
OLED	Organic Light Emitting Diode
PF	Prompt Fluorescence
Ph	Phosphorescence
PL	Photoluminescence
PLQY	Photoluminescence Quantum Yield
RISC	Reverse Intersystem Crossing
SOC	Spin-Orbit Coupling
SPQ	Singlet-Polaron Quenching
SSA	Singlet-Singlet Annihilation
STA	Singlet-Triplet Annihilation
TADF	Thermally Activated Delayed Fluorescence
TOF	Time of Flight
TSL	Thermally Stimulated Luminescence
TTA	Triplet-Triplet Annihilation
TPQ	Triplet-Polaron Quenching
VRH	Variable Range Hopping
vt-KMC	Variable Time step Kinetic Monte Carlo

Acknowledgements

Erklärung und eidesstattliche Versicherung

Hiermit versichere ich an Eides statt, dass ich die vorliegende Arbeit selbstständig verfasst und keine anderen als die von mir angegebenen Quellen und Hilfsmittel verwendet habe.

Weiterhin erkläre ich, dass ich die Hilfe von gewerblichen Promotionsberatern bzw.-vermittlern oder ähnlichen Dienstleistern weder bisher in Anspruch genommen habe, noch künftig in Anspruch nehmen werde.

Zusätzlich erkläre ich hiermit, dass ich keinerlei frühere Promotionsversuche unternommen habe.

Bayreuth, den

Rishabh Saxena